AD-A099 014 NAVAL OCEAN RESEARCH AND DEVELOPMENT ACTIVITY NSTL S--ETC F/G 8/10
OCEANIC ENVIRONMENTAL BACKGROUND OBSERVATIONS IN THE SARGASSO S--ETC(U)
MAR 80 H PERKINS

UNCLASSIFIED NORDA-TN-58 NL

1 OF 3
AD A
099014

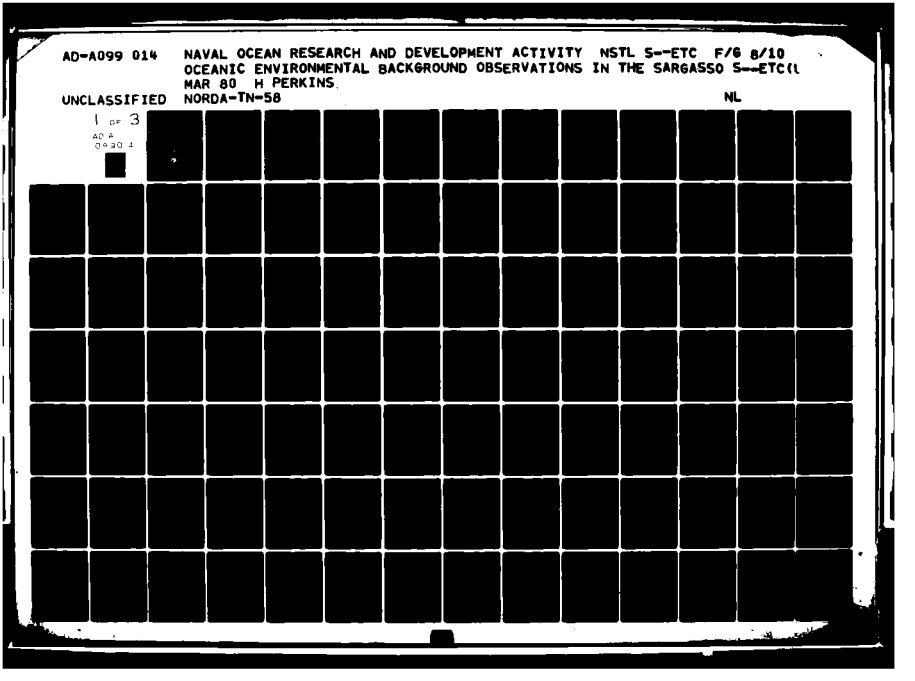

NORDA Technical Note 58

AD A099014

Oceanic Environmental Background Observations in the Sargasso Sea During September 1979.

NORDA-TN-58

Final rept.,

Oceanography Division
Ocean Science and Technology Laboratory

Mar 80

Henry/Perkins

279

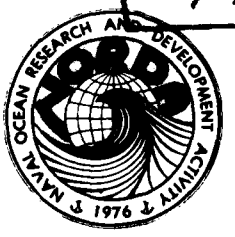

Naval Ocean Research And Development Activity
NSTL Station, Mississippi 39529

392 172

Compiled and Edited by

Henry Perkins[1]

with contributions by

Walter Grabowski[5]

Michael Harris[1]

Zachariah Hallock[2]

Kenneth Nelson[4]

Henry Perkins[1]

Thomas Sanford[3]

Peter Smith[1]

Robert Wahl[2]

William Teague[2]

1) Naval Ocean Research and Development Activity, NSTL Station, MS 39529

2) U.S. Naval Oceanographic Office, Bay St. Louis, MS 39522

3) Applied Physics Laboratory, University of Washington, 1013 NE 40th St., Seattle, WA 98105

4) Arete' Associates, P.O. Box 3800, Santa Monica, CA 90403

5) Science applications, Inc., 8400 Westpark Dr., McLean, VA 22101

TABLE OF CONTENTS

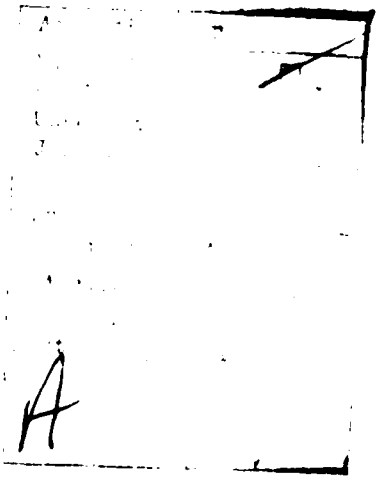

Section 1.0

INTRODUCTION

by Henry Perkins

1.0 INTRODUCTION

This document presents the results of an experiment, conducted jointly by the Naval Ocean Research and Development Activity (NORDA) and the Naval Oceanographic Office (NAVOCEANO), to measure the environmental background in the upper layers of the Sargasso Sea during late summer. The experiment focuses on physical oceanography and attendant meteorology on scales ranging from tens of meters to tens of kilometers in the horizontal, and on scales of order one meter or more over the upper several hundred meters of the ocean. The measurement platforms were the USNS KANE, a Navy P-3 aircraft (two flights) and the Tiros N and GOES satellites. A summary of the types of data collected is given in Table 1.1.

The report is organized into sections which reflect observational methods rather than specific phenomena. Thus, information on mixed layer depth is found in individual sections reporting AXBT, XBT, and CTD measurements; information on currents, in sections devoted to current meter and to shear probe (XTVP) results; and so on. This has expedited production of the report and has permitted a more complete discussion of instrument performance.

Further information regarding these data may be obtained from the editor or from the individual identified in the relevant section.

Table 1.1
PLATFORMS, SENSORS AND DATA SETS

USNS KANE	
Expendable current probe (XCP)	Shear, temperature
XBT's (0.05°C)	Temperature, fine structure
Meteorological observations	Wind speed, rainfall, humidity, insolation, etc.
Wave rider buoy	Wave height, direction
Still camera	Cloud distribution images
Current meter mooring	Current velocity and direction
CTD	Conductivity, temperature, depth, B-V frequency
P-3 AIRCRAFT	
AXBT's	Temperature profiles
Photo camera	Sea surface roughness
Video tape	Color, sea surface roughness
PRT-5 radiation thermometer	Sea surface temperature
PRT-4 radiation thermometer	Sky radiance
IR scanner	Sea surface temperature
TIROS-N	
Infrared data	Sea surface temperature
Visible reflectance images	Sea surface roughness
GOES	
Infrared data	Sea surface temperature
Visible reflectance images	Sea surface roughness

Section 2.0

CRUISE NARRATIVE

by Michael Harris

2.0 CRUISE NARRATIVE

Prior to the USNS KANE's departure from Charleston, South Carolina, a tentative operating area was selected based on satellite and aircraft observations. This technique was used to reduce ship survey time in locating an area free of energetic eddies. A large area, some 300 km square, was monitored by satellite infrared observations shortly before seagoing operations commenced. These were used as a guide for an AXBT survey of the same area. Finally, based on both satellite and aircraft measurements, a 100 km square within the larger square was chosen for shipboard measurements.

On 1 September 1979, the USNS KANE left port and proceeded to the selected operating area (near 31°30'N, 71°30'W). Time enroute was used for equipment testing. On the second day at sea, detailed logging of meteorological measurements commenced.

Once in the area, a detailed bathymetric and hydrographic survey was conducted to verify the presence of a smooth bottom and absence of energetic eddies in order to avoid a pointlessly complex or atypical environment. This survey was followed by a determination of dominant scales conducted as follows. Along a 10 km track XCP's were dropped every 2 km and XBT's every 0.5 km. From these measurements, distances between subsequent drops were determined for each of the two types of probes according to the criterion that consecutive drops be recognizably similar, but alternate drops much less so. These trial spacings proved satisfactory and were used for most subsequent drops.

A subsurface mooring, containing VACM and Aanderaa current meters concentrated near the seasonal thermocline, was deployed by NAVOCEANO on Day 4. The mooring was recovered approximately six weeks after implantation during a subsequent cruise.

Following these preliminaries, the first intensive experiment was conducted on Days 6 and 7. An "L" shaped pattern, some 20 km on each leg and located near the current meter mooring, was traversed three times, with XBT's and XCP's dropped every 0.5 and 2.7 km, respectively. The pattern was traversed three times at intervals of about eight hours, thus permitting resolution of the inertial period motion, which is believed to be the major contributor to small scale vertical shear.

The XCP's, used here in quantity for the first time, provide vector current measurements at about 10 m intervals from the surface to 800 m depth. Thus, the pattern of drops provides resolution of currents as a function of horizontal and vertical distance and, to a limited extent, of time.

The closely spaced XBT drops permit detailed statistical characterization of the small-scale structure of the temperature field, measurement of the horizontal extent of finestructure patches, and redundant sampling of the large-scale temperature field which can be used for smoothing and/or detection of defective probes. To accommodate the rapid drop rate of the XBT's, a multiple launch system capable of simultaneous digitization of up to four probes had been developed and was employed for the first time during this cruise.

CTD stations were taken at the extremities of each "L" pattern.

Coincident with the shipboard program, remote sensing measurements of sea surface roughness and sea surface temperature were made from satellite and aircraft. Measurements of radiometric temperature, sea state observations, and specialized

photographs were taken from the ship to assist in analysis and correlation of the remotely sensed data.

The first intensive experiment was followed by a star-shaped survey employing XBT's, XCP's and CTD casts. This survey served to monitor the mesoscale variability of the selected site and verified that no eddies had entered the area.

A second intensive experiment, again consisting of three traverses of the "L" pattern, commenced on Day 9. A few refinements, consisting of improved XBT and XCP launching and recording techniques, were incorporated into this second experiment, based on the results of the first.

On Day 11, after completion of the intensive shear experiments, repeated CTD lowerings were made near the current meter mooring to sample the finestructure at smaller vertical and horizontal scales than was possible with XBT's. During the same interval, XCP drops were made every few hours for an intercomparison with the current meter data.

The CTD series was completed on Day 12 and the USNS KANE began its transit back to Charleston, arriving on Day 14, the 14th of September.

Figure 2.1 graphically displays the major events of the cruise.

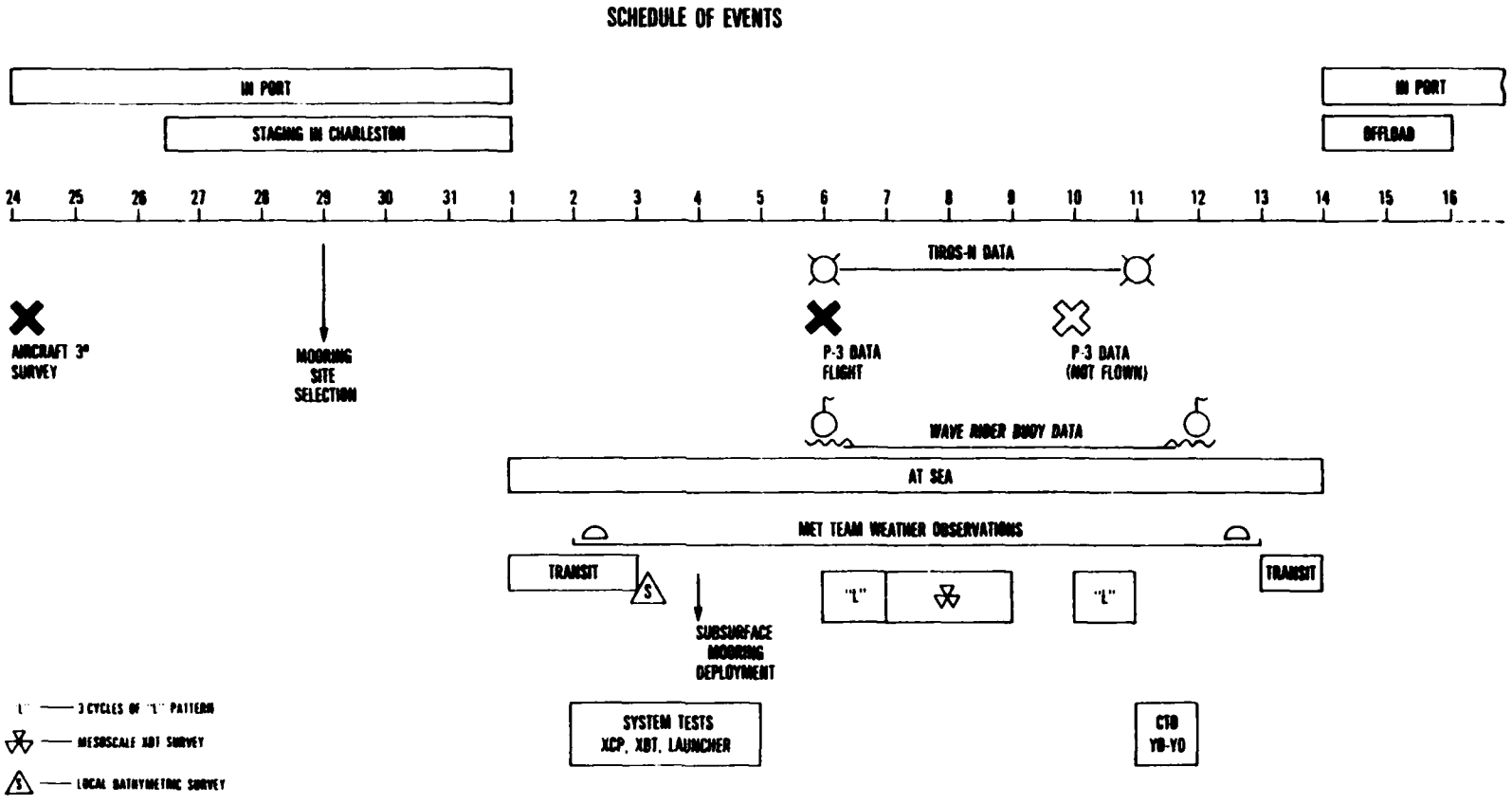

Figure 2.1. Diagrammatic representation of events during the observation period

Section 3.0

NAVIGATION

by Henry Perkins

3.0 NAVIGATION

3.1 INTRODUCTION

The requirement for navigational information is common to many sections of this report. Thus, although positional data are found in most of the sections, some aspects of navigation are reported here only, rather than being duplicated or scattered throughout the report.

3.2 EQUIPMENT AND METHODS

During the data-collecting portion of the cruise, ship's navigation was performed by members of the scientific party (Boyd, Harris and Morton) using two types of LORAN-C receivers. Two units were normally run simultaneously and checked against each other. Satellite fixes were obtained whenever possible and used as a further check. This combination of systems provided uninterrupted data of good quality throughout the cruise.

While underway, the practice was to steer a constant course and speed (based on screw r.p.m.) between fixes so that intermediate positions could be found by interpolation with respect to time. This proved especially useful during the intensive "L" pattern measurements, during which the rapidity of drops permitted only time of drop to be recorded.

Aircraft navigation during overflights was by VLF/Omega with an absolute accuracy of about 1 nm.

3.3 SELECTED PLOTS

An overview of the operating area is given in Figure 3.1.

Detailed ship tracks during the first intensive experiment, involving three circuits around the "L" pattern (legs a-f), are shown in Figures 3.2a-c, and those for the second experiment (legs g-l), in Figures 3.3a-c. During part of these operations, a manned rubber boat was being towed astern for launching shear probes, giving rise to occasional pauses during which this boat was serviced. These occurred either at the ends of legs or, since the boat was not used after dark, at sundown.

The aircraft track during the overflight of 6 September and its relation to the "L" pattern can be seen in Figure 3.4.

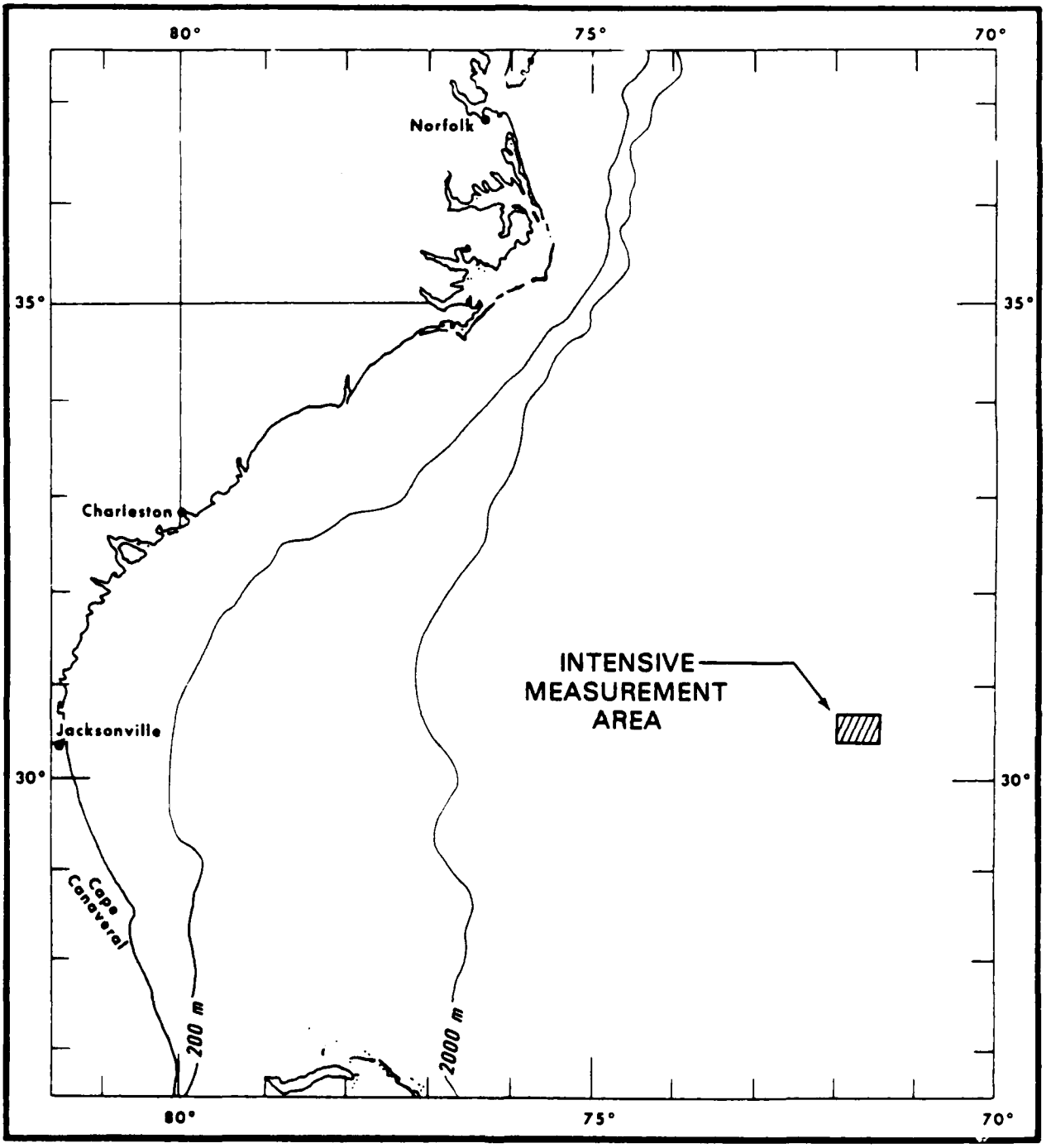

Figure 3.1 General view of operating area.

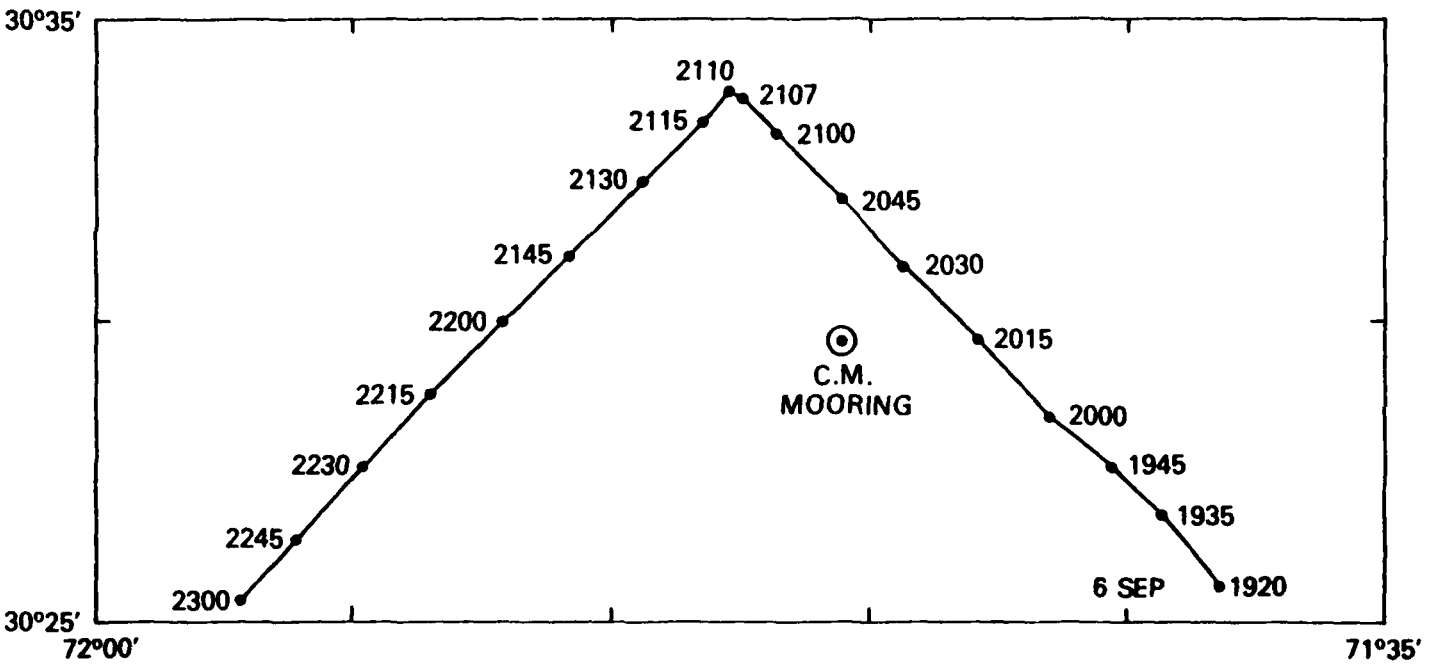

Figure 3.2a. Ship track during legs a and b of "L" pattern
Times are GMT.

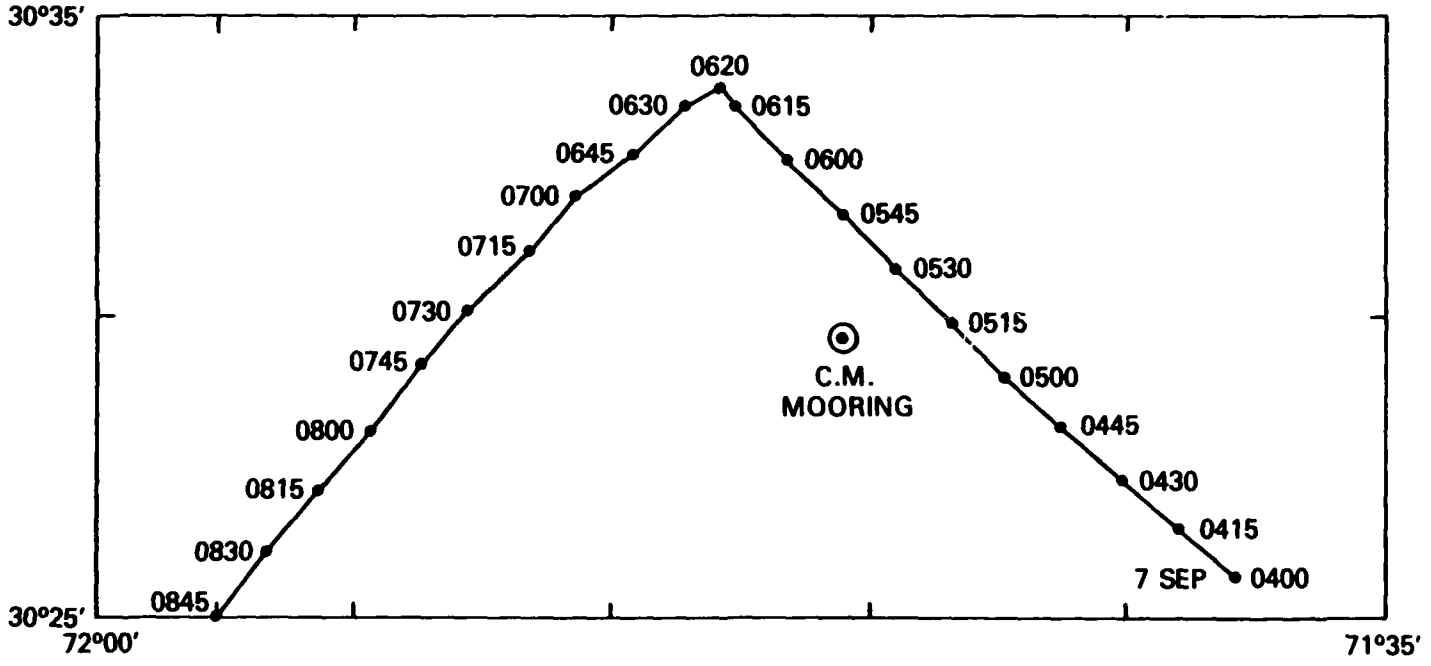

Figure 3.2b. Ship track during legs c and d of "L" pattern

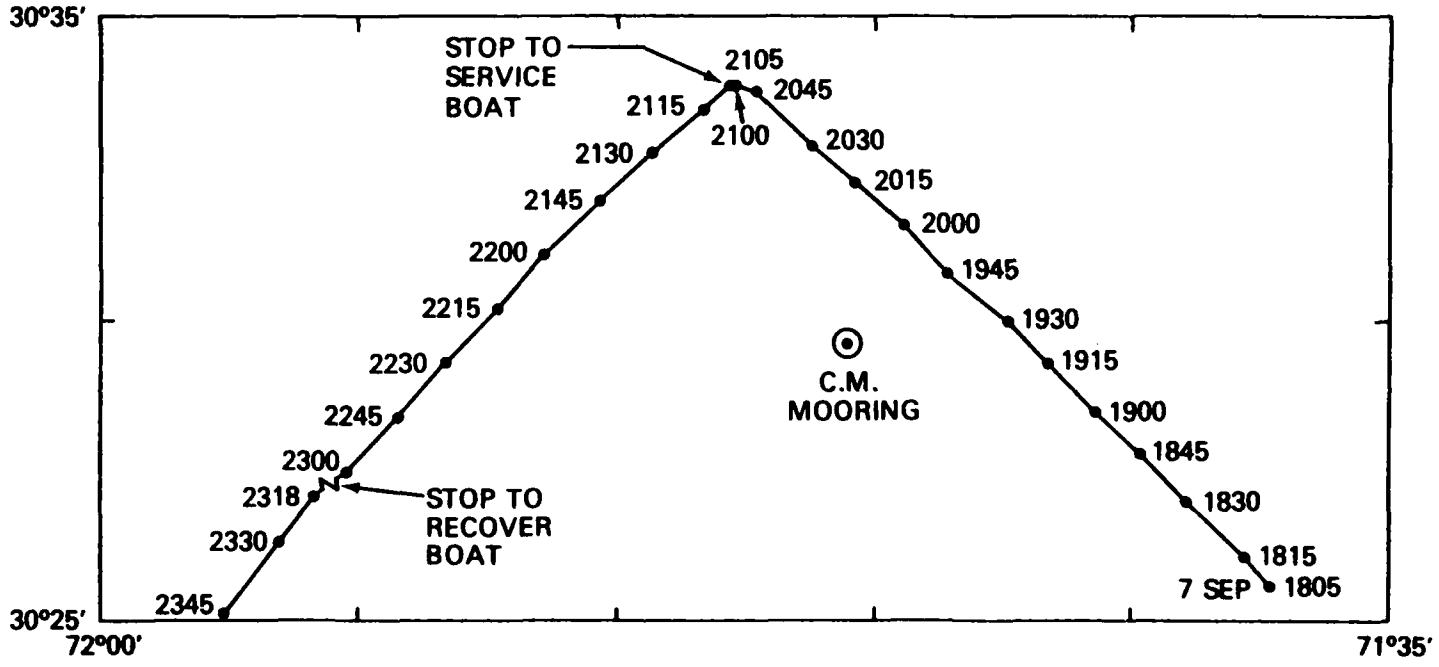

Figure 3.2c. Ship track during legs e and f of "L" pattern

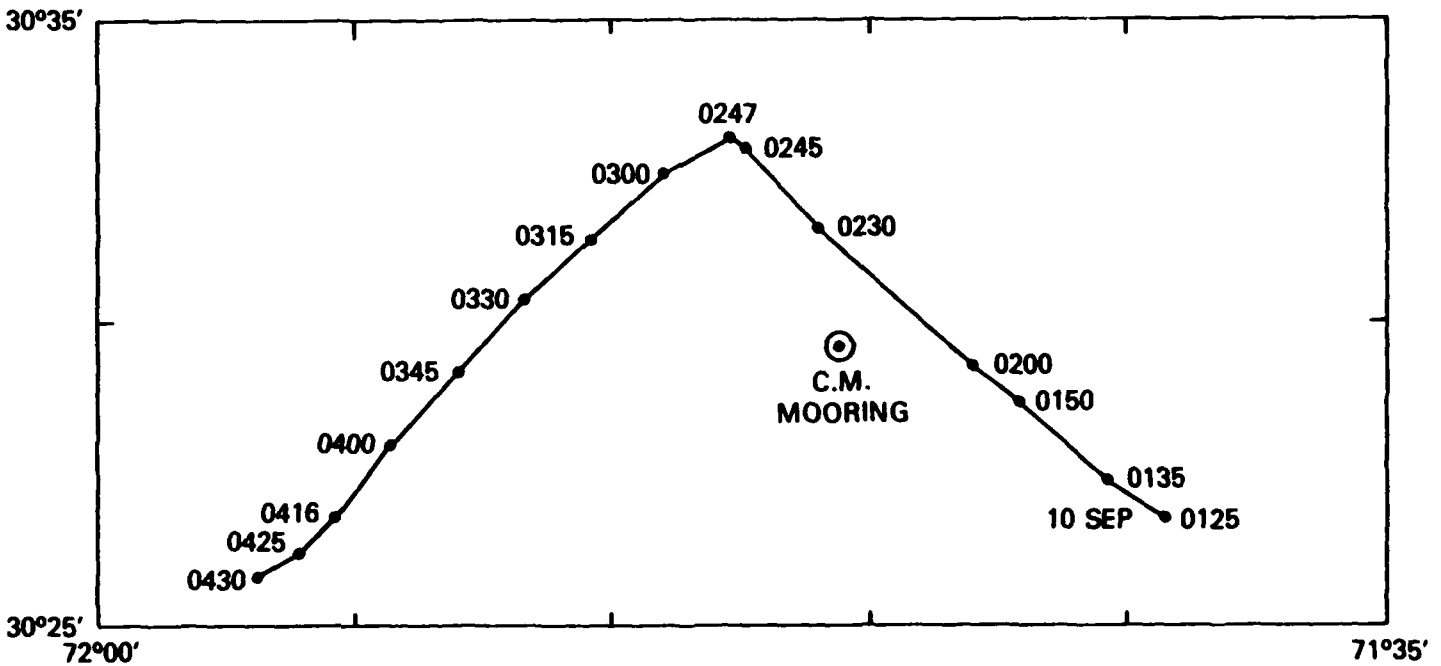

Figure 3.3a Ship track during legs g and h of "L" pattern
Times are GMT.

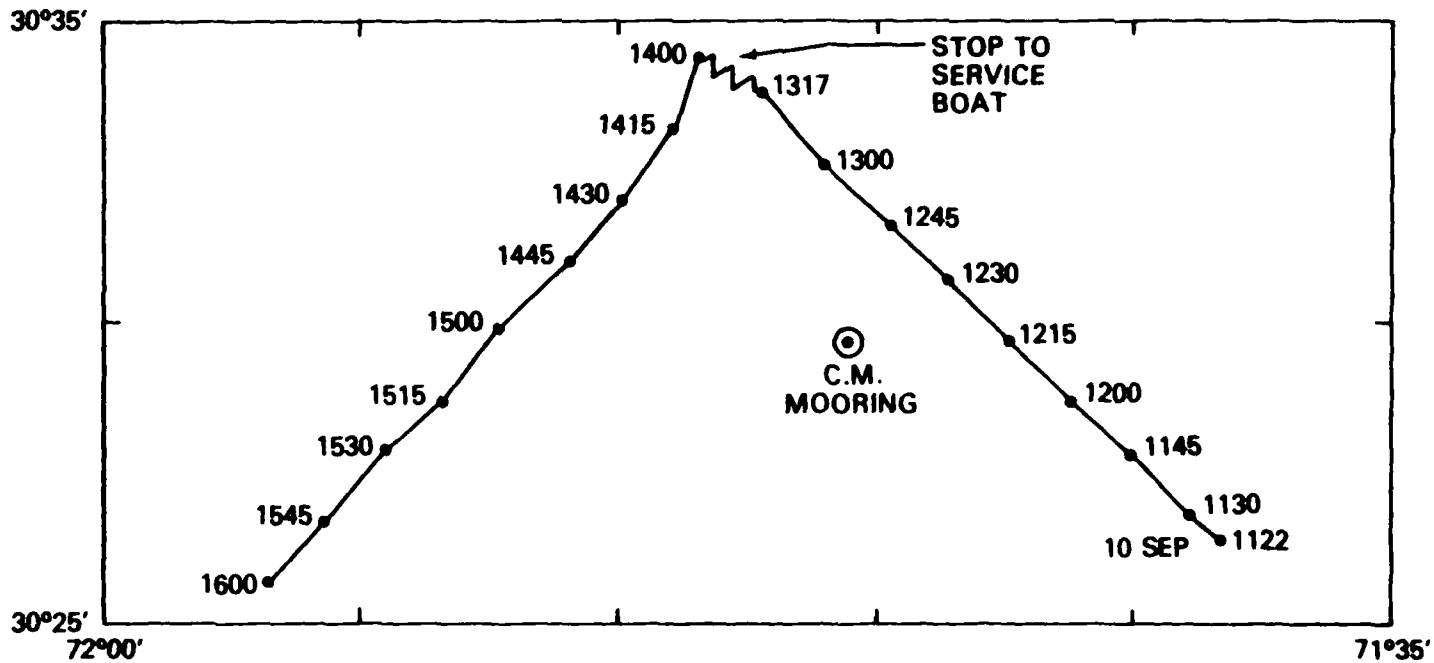

Figure 3.3b. Ship track during legs i and j of "L" pattern

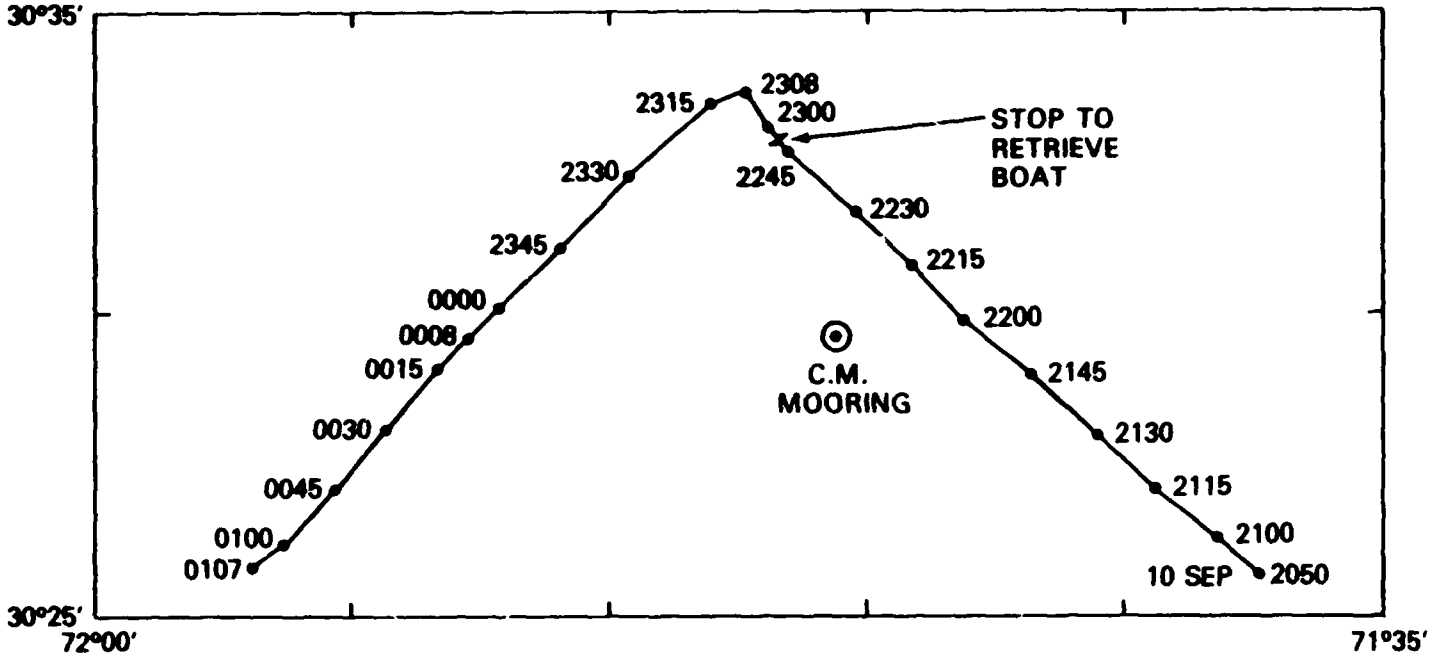

Figure 3.3c. Ship track during legs k and l of "L" pattern

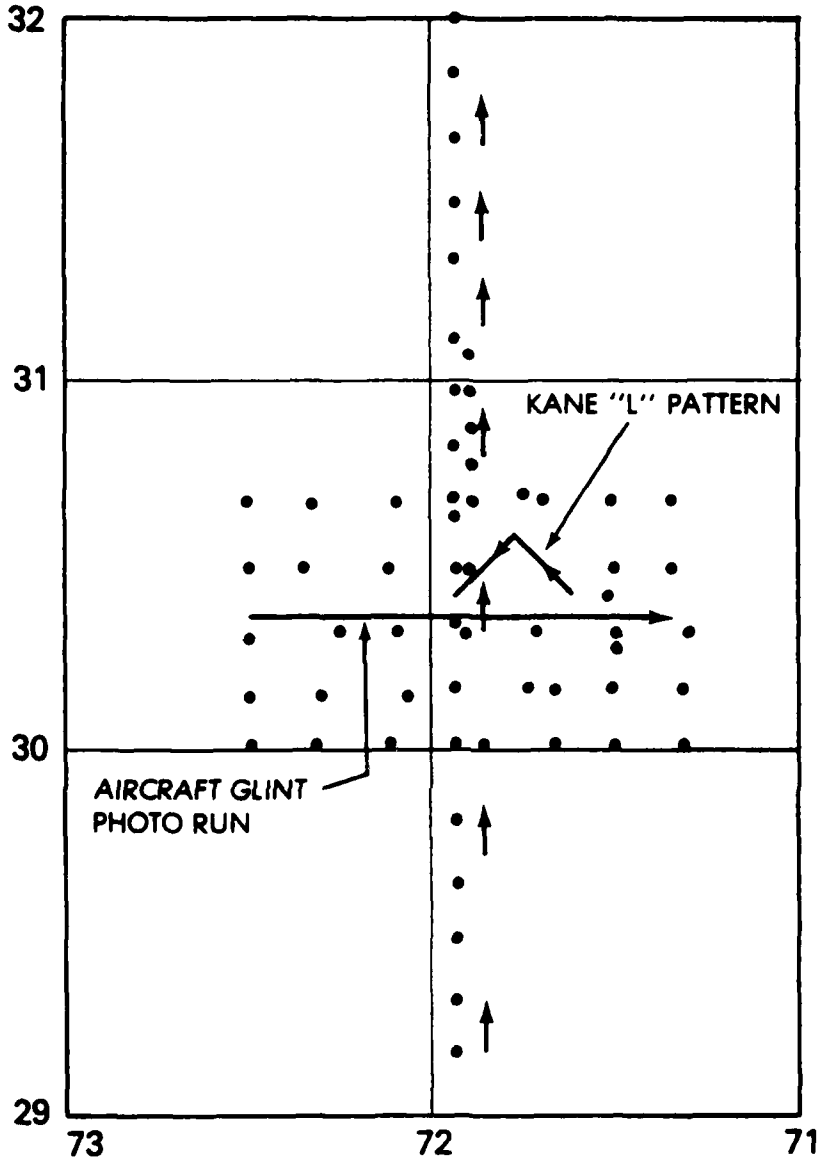

Figure 3.4. Aircraft track during survey of 6 September
Dots denote AXBT drop points.

Section 4.0

CTD MEASUREMENTS

by Zachariah Hallock and William Teague

4.0 CTD MEASUREMENTS

4.1 INTRODUCTION

During the interval reported here, a total of 42 CTD casts were made from the USNS KANE using a Neil Brown Instrument Systems Mark III CTD. The purpose of these measurements was threefold: to provide estimates of the level of mesoscale activity during the cruise; to provide measurements of the vertical stability in support of the current meter, shear probe and XBT programs; and to measure, through rapidly repeated casts, the evolution of the temperature and salinity fields on scales smaller than those accessible by other available instruments.

A tabulation of the stations taken is given in Table 4.1. Data was recorded during both downgoing and upgoing portions of each cast but, as is common practice, only the downgoing are displayed here.

4.2 SELECTED STATION DATA

Stations were taken at the beginning and end of each travers of the "L" pattern, a total of twelve in all (casts 56-61 and 73-78). These are representative of all stations in the area, are located very close to the XBT and shear probe intensive measurements, and lie in reasonable proximity to the current meter mooring. Hence, they have been selected for presentation here.

Figures 4.1a-f show the first group of six stations, corresponding to the intensive measurements made during the first three traverses of the "L" pattern. Temperature, salinity, sigma-t, sound velocity, and Brunt-Vaisala frequency profiles are given for each station, together with a T-S plot. Figures 4.2a-f give comparable displays for the second group of six casts, corresponding to the second set of intensive "L" pattern measurements.

4.3 TIME SERIES DATA

A total of nine time series, or "yo-yo", casts were made in the vicinity of the mooring. These consisted of repeated lowerings of the CTD between closely spaced depth limits while the ship drifted. Typical time intervals between consecutive lowerings were on the order of 6 min. The corresponding distance between lowerings is, of course, dependent on the rate at which the instrument was translated relative to the layer being profiled. This velocity is typically of order 30 cm s^{-1}, corresponding to a profile separation of some 108m.

Figures 4.3a-i are displays of these casts. The same parameters are plotted as for the station data, with each of the profiles (except for the T-S plots) being offset from its predecessor by a uniform amount.

4.4 MESOSCALE MEASUREMENTS

The first of two sets of mesoscale measurements consisted of several widely spaced (30 nm) stations taken at the start of the cruise (casts 50, 55, 62, 63), supplemented by intervening XBT drops. Only weak mesoscale features were found, confirming the results reported for the upper ocean by previous AXBT measurements (See Section 8).

The second set of measurements taken during the middle of the cruise consisted of a cloverleaf pattern (casts 64-73) centered at 30°30'N, 71°42'W; also supplemented with XBT drops. Again, no strong mesoscale features were found.

The two surveys served to monitor the level of mesoscale activity in the area where smaller scale measurements were being made, and so are invaluable for interpretation of those measurements. But since no significant mesoscale features were found, and since the survey stations are reported in detail elsewhere (Broome et al., 1980), these stations are not considered further in this report.

The steepest large-scale thermocline slope observed during the cruise is shown in Figure 4.4. It was observed by XBT's during a northward transect as the ship departed from the operating area.

An eddy in the main thermocline was found during an earlier cruise to this area and has been described by Broome et al., (1979).

4.5 REFERENCES

Broome, R. D., W. Teague and Z. Hallock (1979). Observations of an Anticyclonic Mid-Ocean Eddy With a Deep Homogeneous Layer (abs.). Trans., Am. Geophys. Union, 60, p. 862.

Broome, R., R. Karpas, F. Muhler, Z. Hallock, and W. Teague (1980). CTD and XBT Profiles in the Western North Atlantic Ocean, August - October 1979. U.S. Naval Oceanographic Office Technical Note - Data Report, No. TN 7210-6-80.

TABLE 4.1

Summary of CTD Data Collected

STATION NUMBER	LATITUDE	LONGITUDE
26050	30 30.0 N	71 41.5 W
26051	30 31.8 N	71 44.2 W
26052	30 28.6 N	71 51.6 W
32053	30 31.0 N	71 6.1 W
33054	30 56.9 N	71 24.2 W
34055	30 20.0 N	72 6.0 W
26056	30 25.8 N	71 37.0 W
26057	30 24.6 N	71 57.8 W
26058	30 25.8 N	71 37.5 W
26059	30 24.8 N	71 57.8 W
26060	30 25.8 N	71 37.4 W
26061	30 24.6 N	71 57.8 W
35062	30 9.8 N	71 54.5 W
35063	30 9.9 N	71 28.0 W
37064	30 29.8 N	71 53.2 W
26065	30 30.1 N	71 41.2 W
38066	30 29.9 N	71 30.6 W
39067	30 21.7 N	71 35.8 W
26068	30 30.0 N	71 41.5 W
40069	30 38.6 N	71 47.5 W
41070	30 38.5 N	71 36.5 W
26071	30 29.9 N	71 41.9 W
42072	30 21.5 N	71 47.3 W
26073	30 25.7 N	71 38.6 W
26074	30 25.5 N	71 57.1 W
26075	30 25.9 N	71 37.6 W
26076	30 25.5 N	71 57.5 W
26077	30 25.3 N	71 37.3 W
26078	30 25.7 N	71 57.2 W
26079	30 29.7 N	71 47.0 W
26080	30 31.1 N	71 48.3 W
26081	30 30.0 N	71 47.0 W
26082	30 30.1 N	71 46.7 W
26083	30 30.1 N	71 47.2 W
26084	30 30.3 N	71 47.8 W
26085	30 30.0 N	71 47.3 W
26086	30 30.3 N	71 46.9 W
26087	30 30.2 N	71 47.0 W
26088	30 30.5 N	71 46.9 W
26089	30 32.2 N	71 47.7 W
26090	30 30.2 N	71 46.8 W
26091	30 43.9 N	71 47.8 W

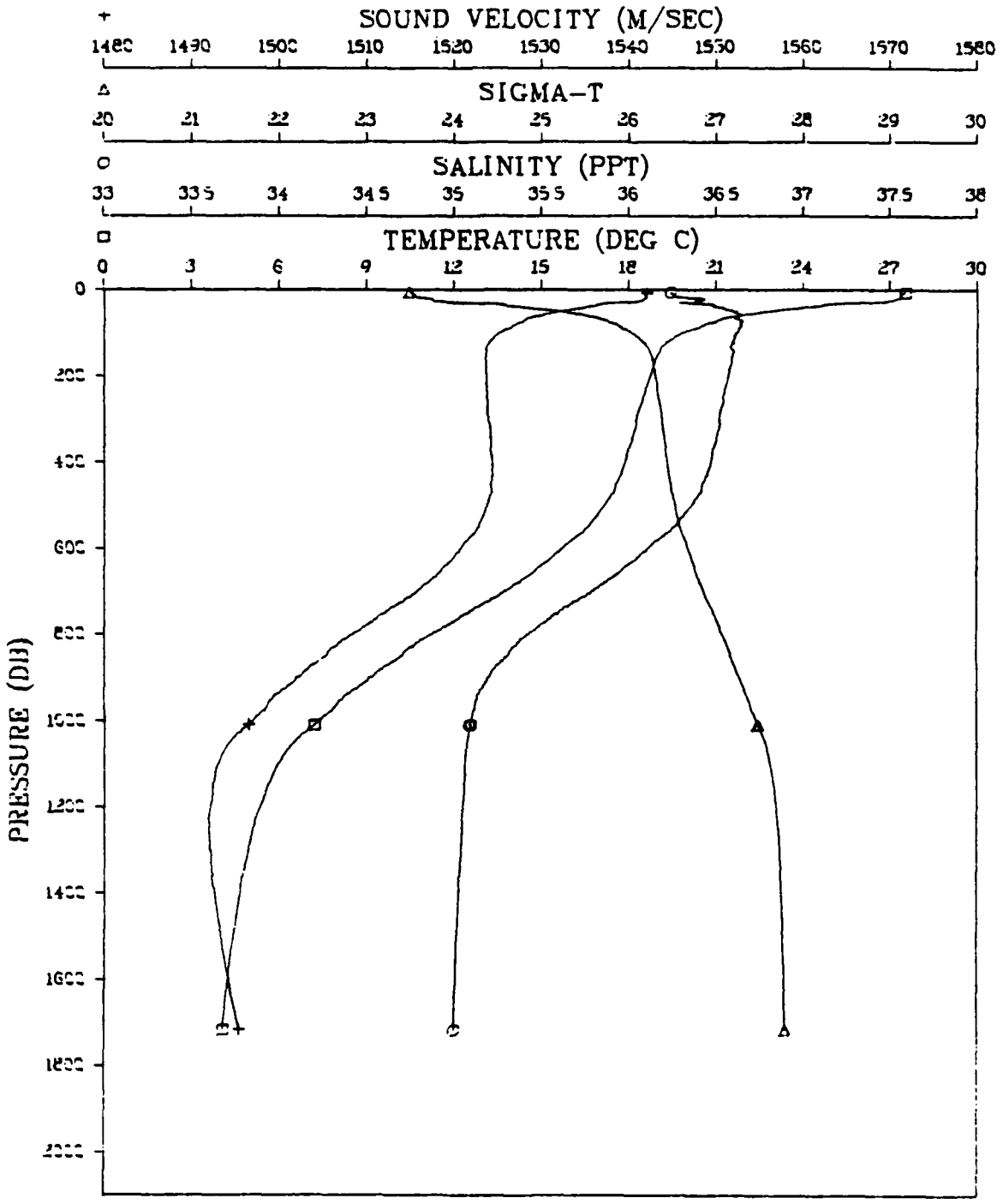

Figure 4.1a. CTD station 026056
Start: 6 Sept 1657Z, 30°25.8'N, 71°37.0W

STATION 026056

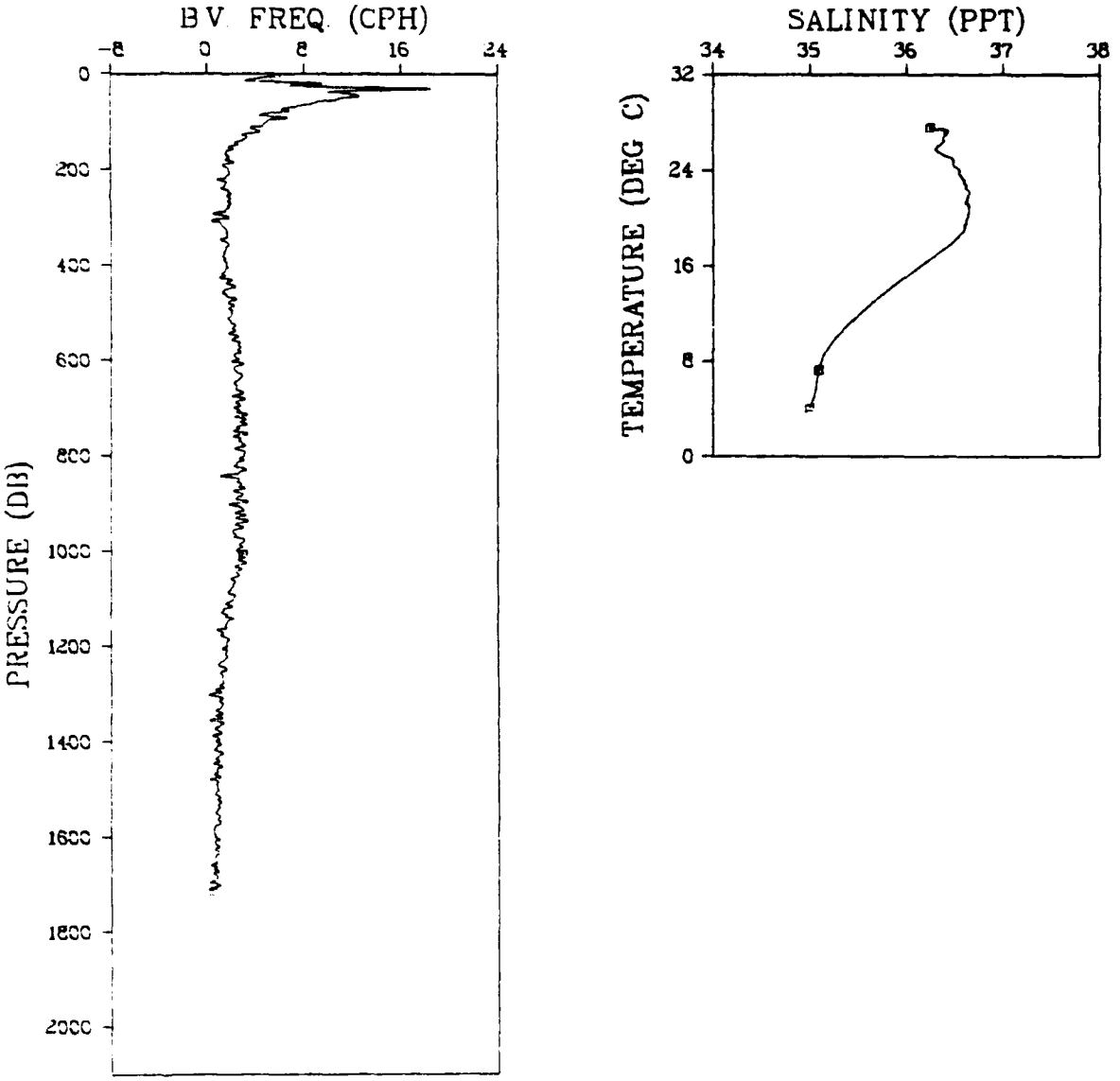

Figure 4.1a. (continued)

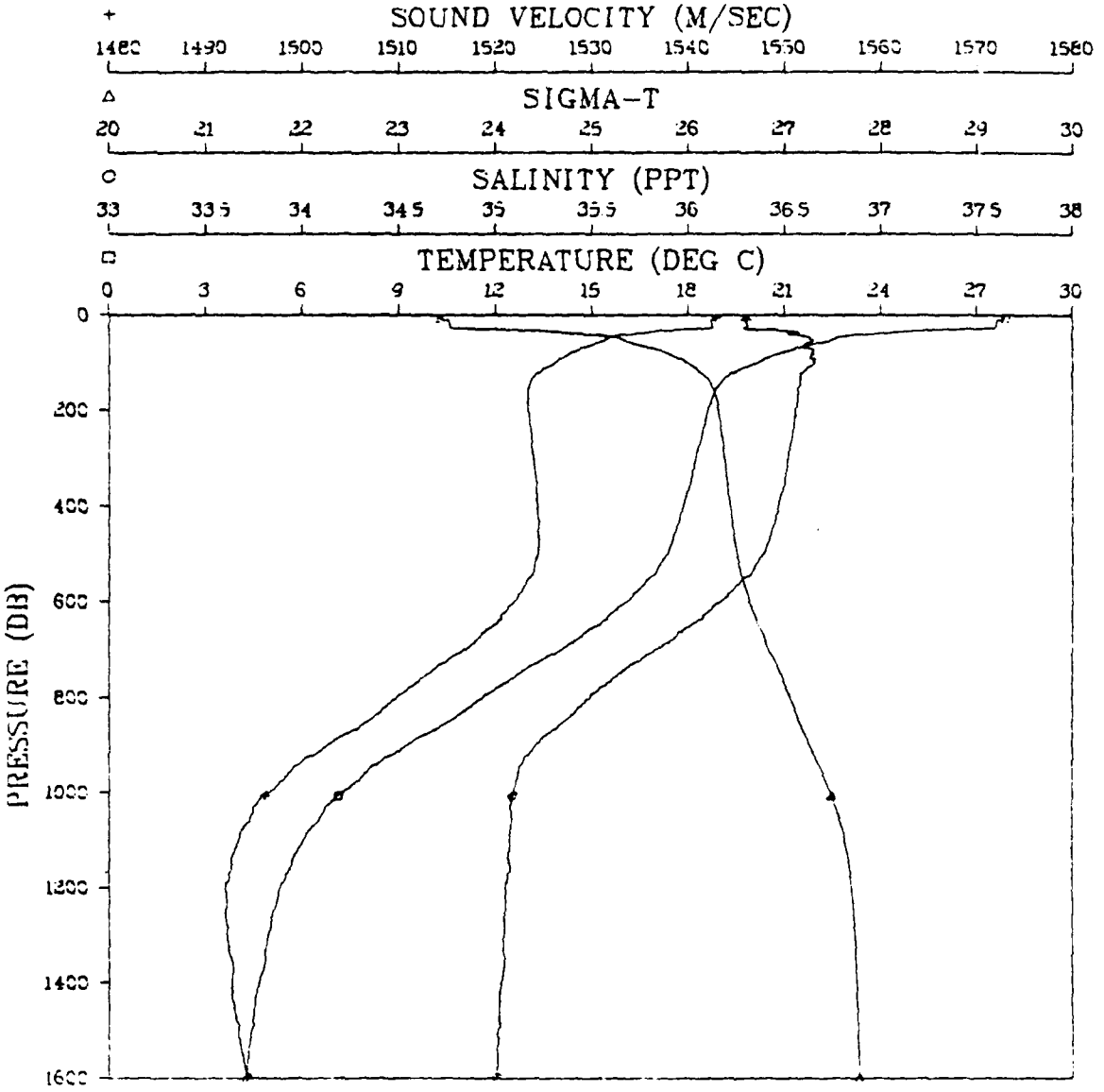

Figure 4.1b. CTD station 026057
Start: 6 Sept 2316Z, 30°24.6'N, 71°57.8'W

STATION 026057

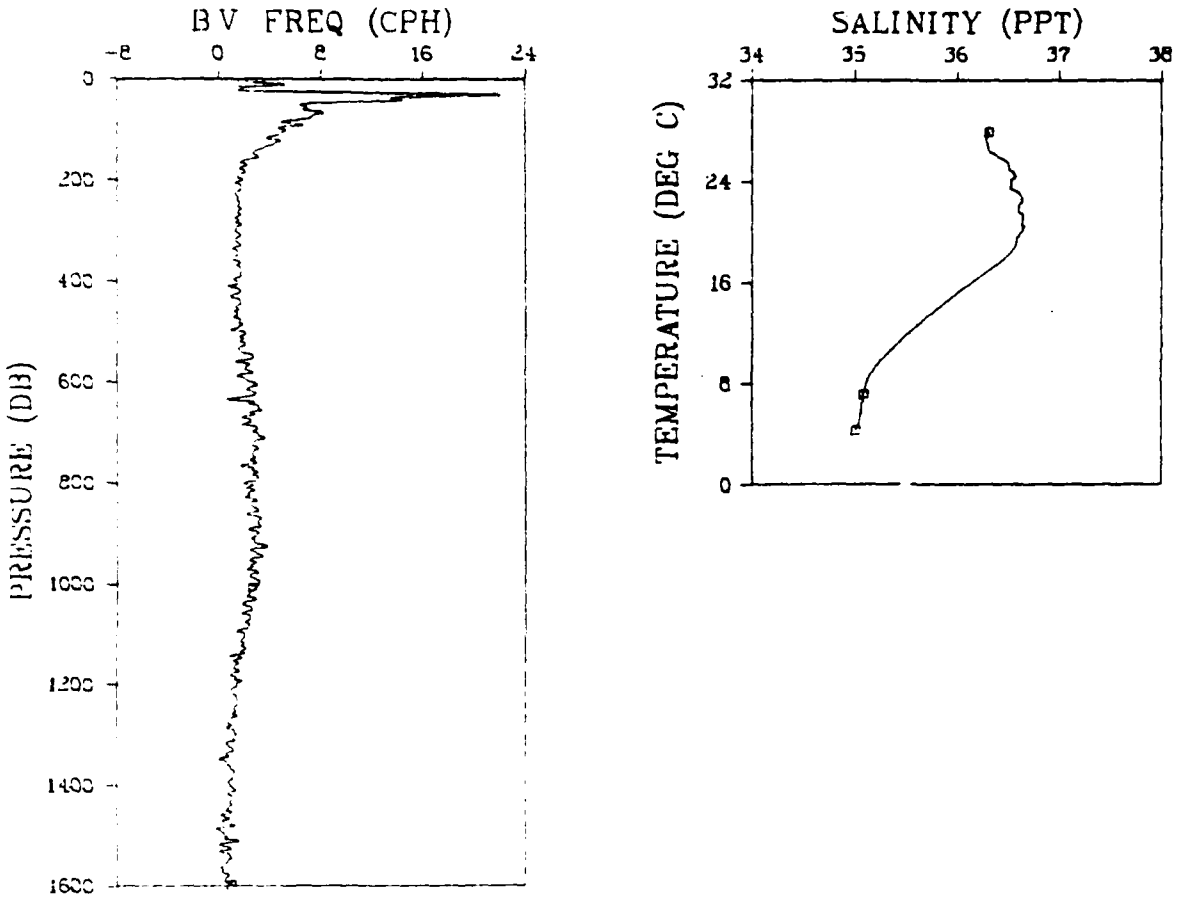

Figure 4.1b. (continued)

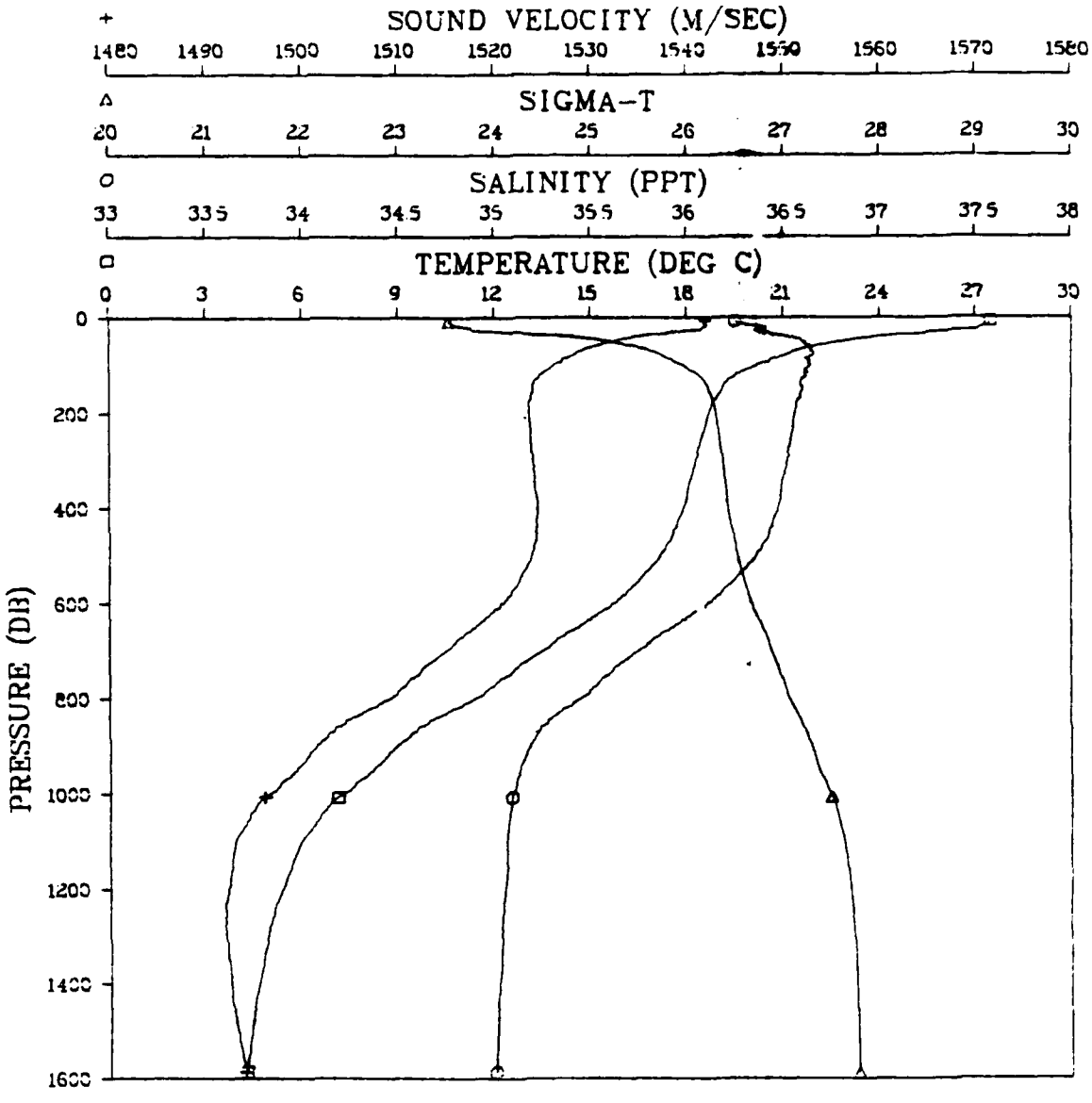

Figure 4.1c. CTD station 026058
Start: 7 Sept 0213Z, 30°25.8'N, 71°37.5'W

STATION 026058

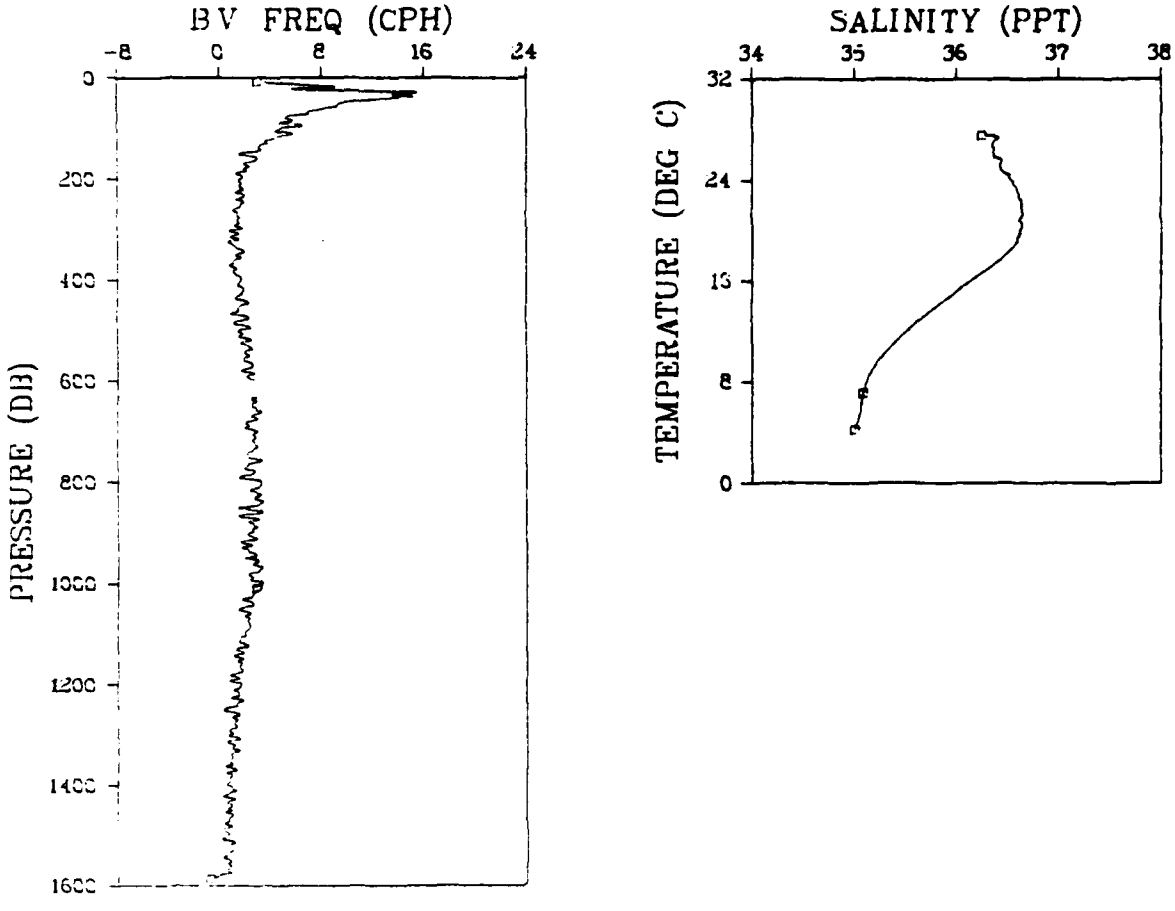

Figure 4.1c. (continued)

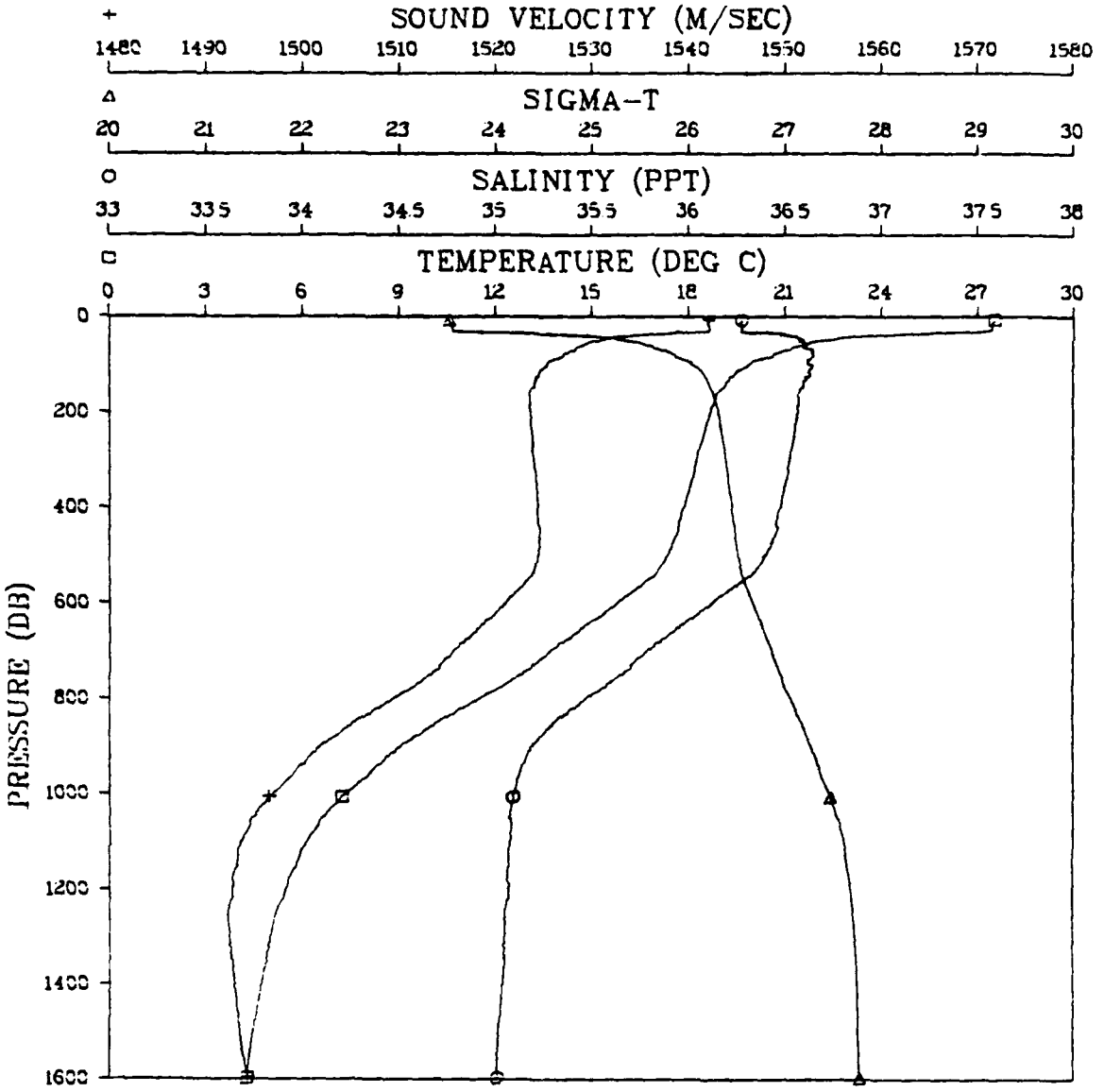

Figure 4.1d. CTD station 026059
Start: 7 Sept 0800Z, 30°24.8'N, 71°57.8'W

STATION 026059

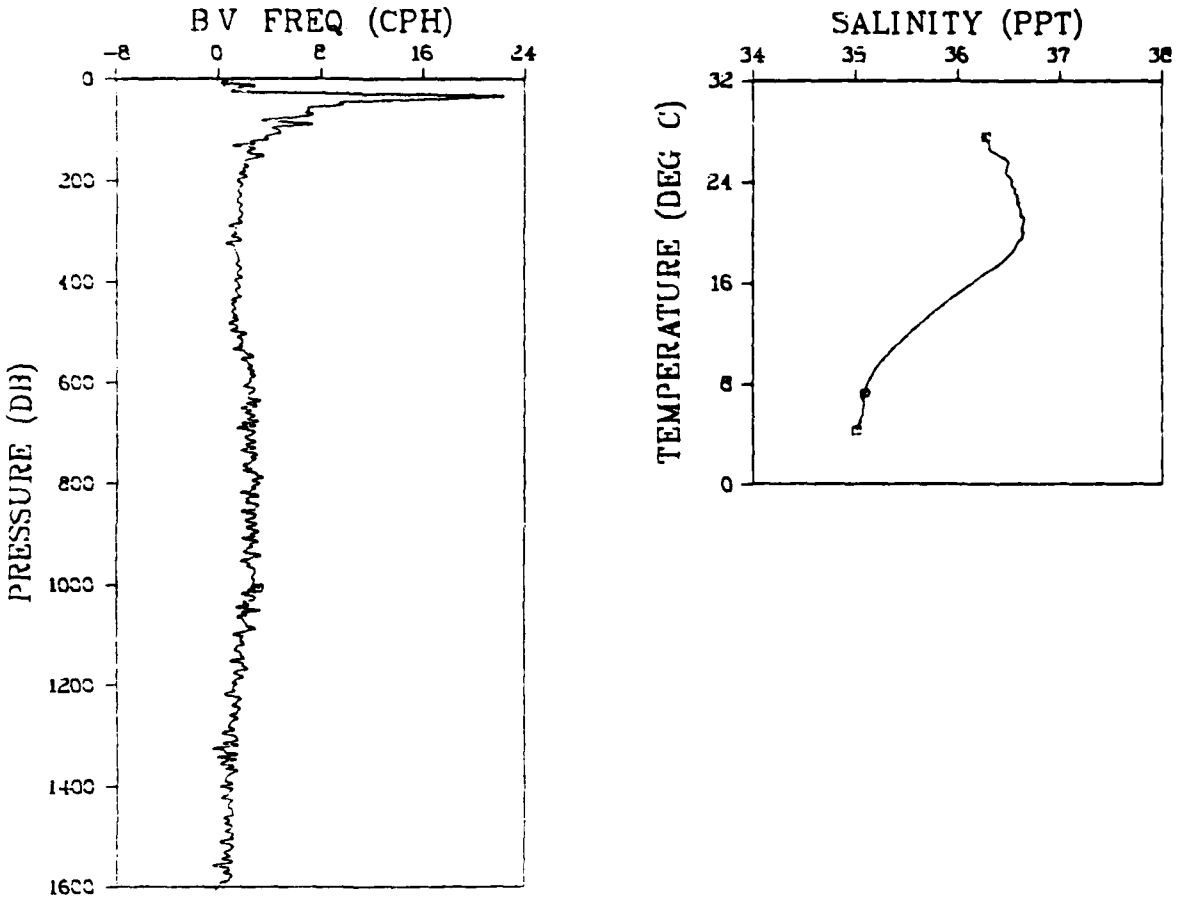

Figure 4.1d. (continued)

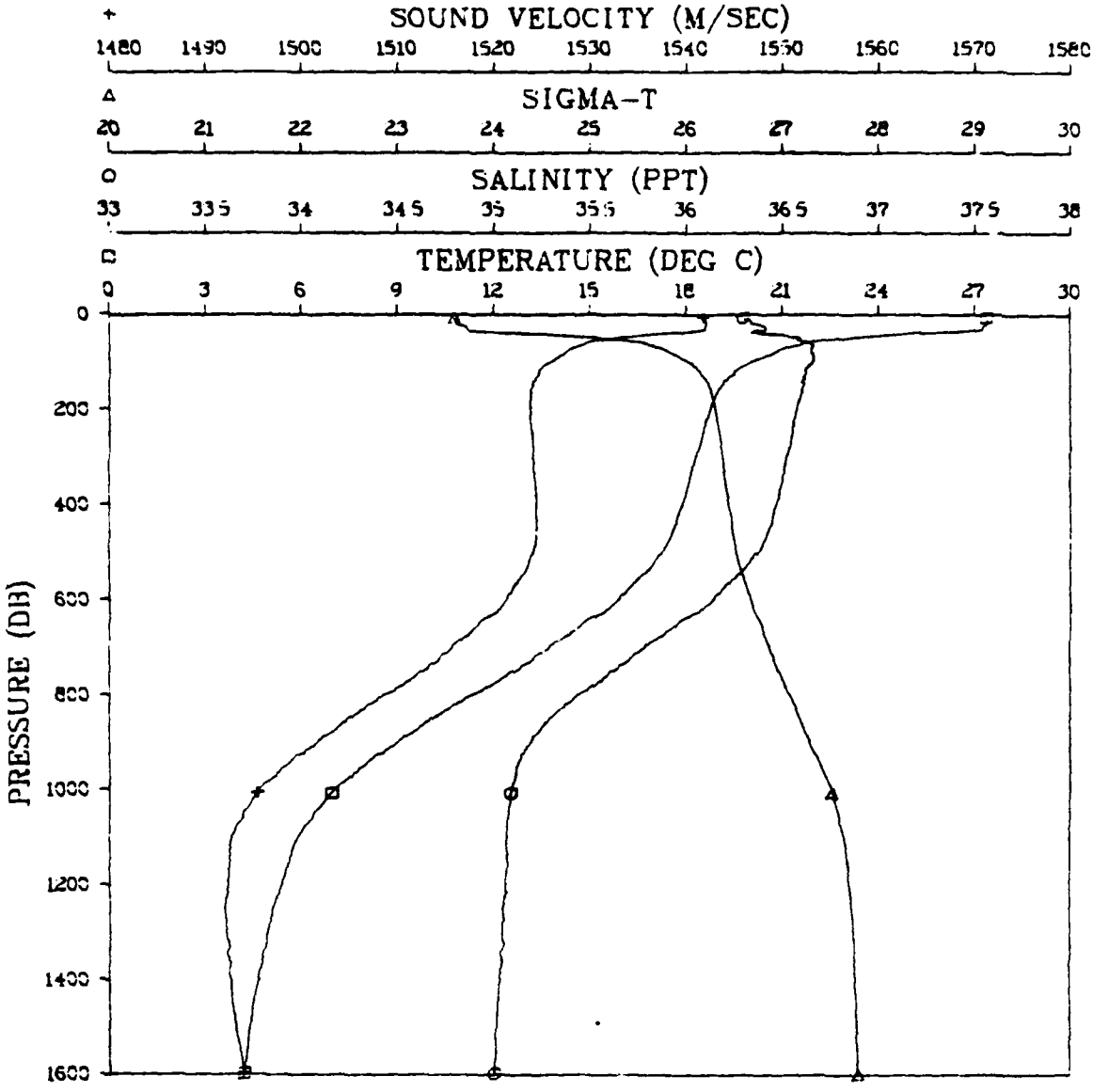

Figure 4.1e. CTD station 026060
Start: 7 Sept 1141Z, 30°25.8'N, 71°37.4'W

STATION 026060

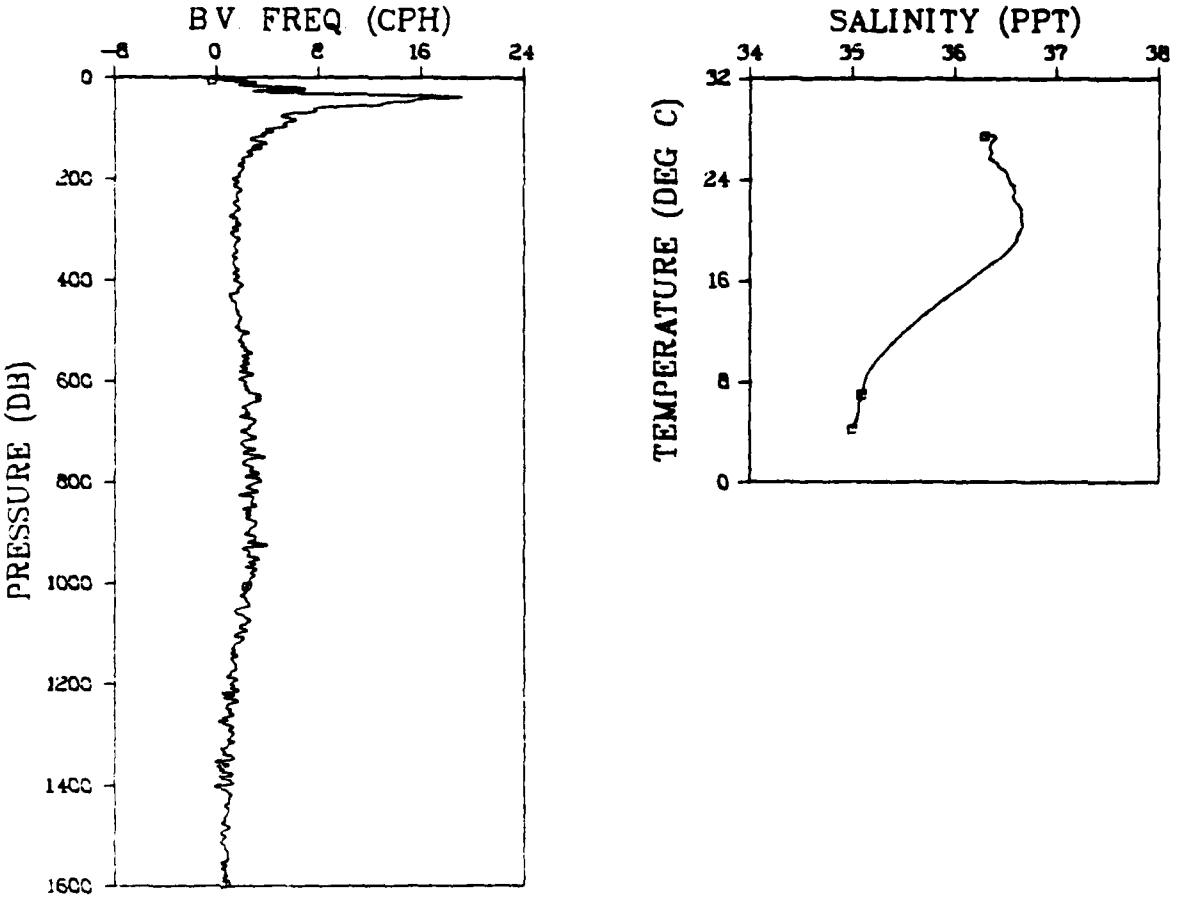

Figure 4.1e. (continued)

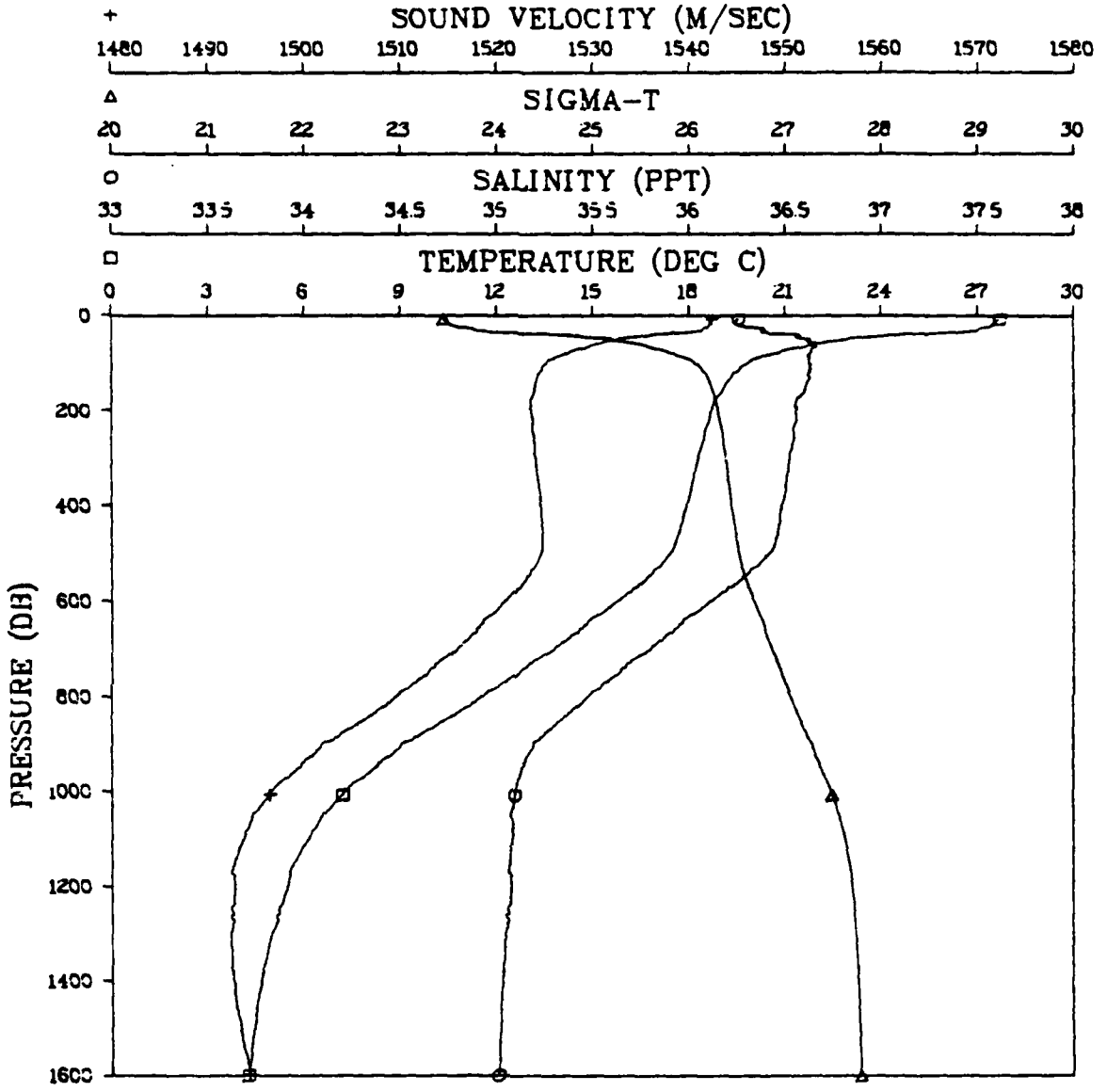

Figure 4.1f. CTD station 026061
Start: 8 Sept 0008Z, 30°24.6'N, 71°57.8'W

STATION 026061

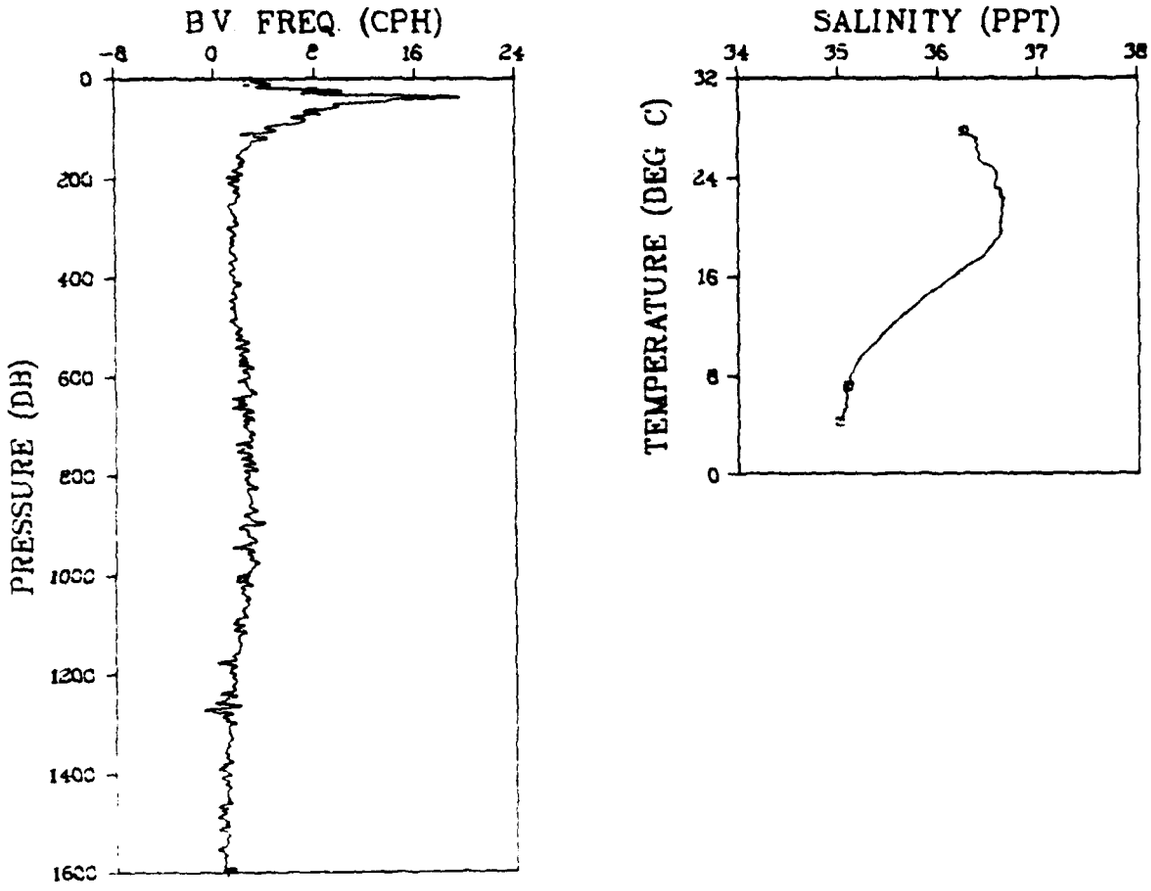

Figure 4.1f. (continued)

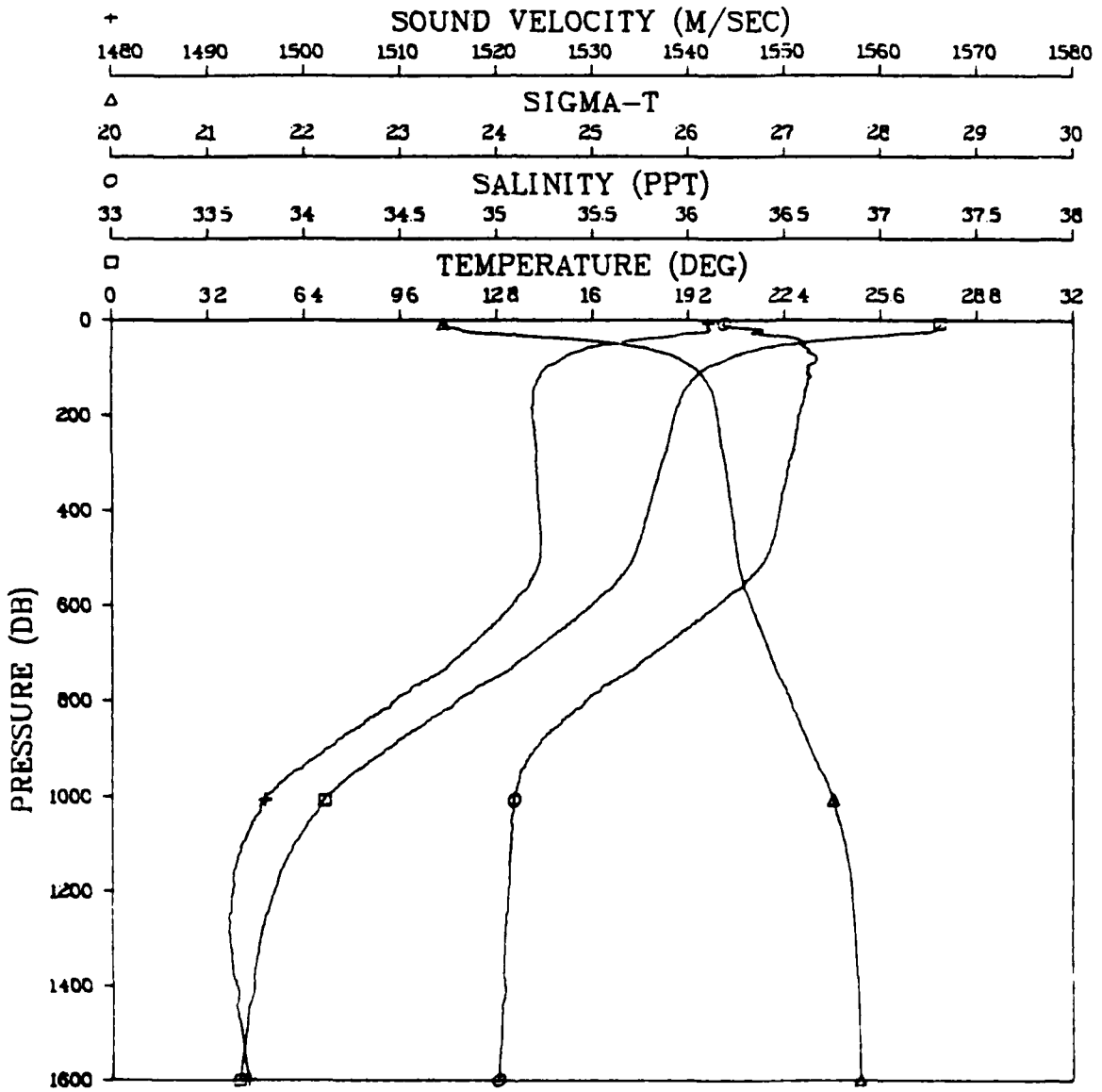

Figure 4.2a. CTD station 026073
Start: 10 Sept 0009Z, 30°25.7'N, 71°38.6'W

STATION 026073

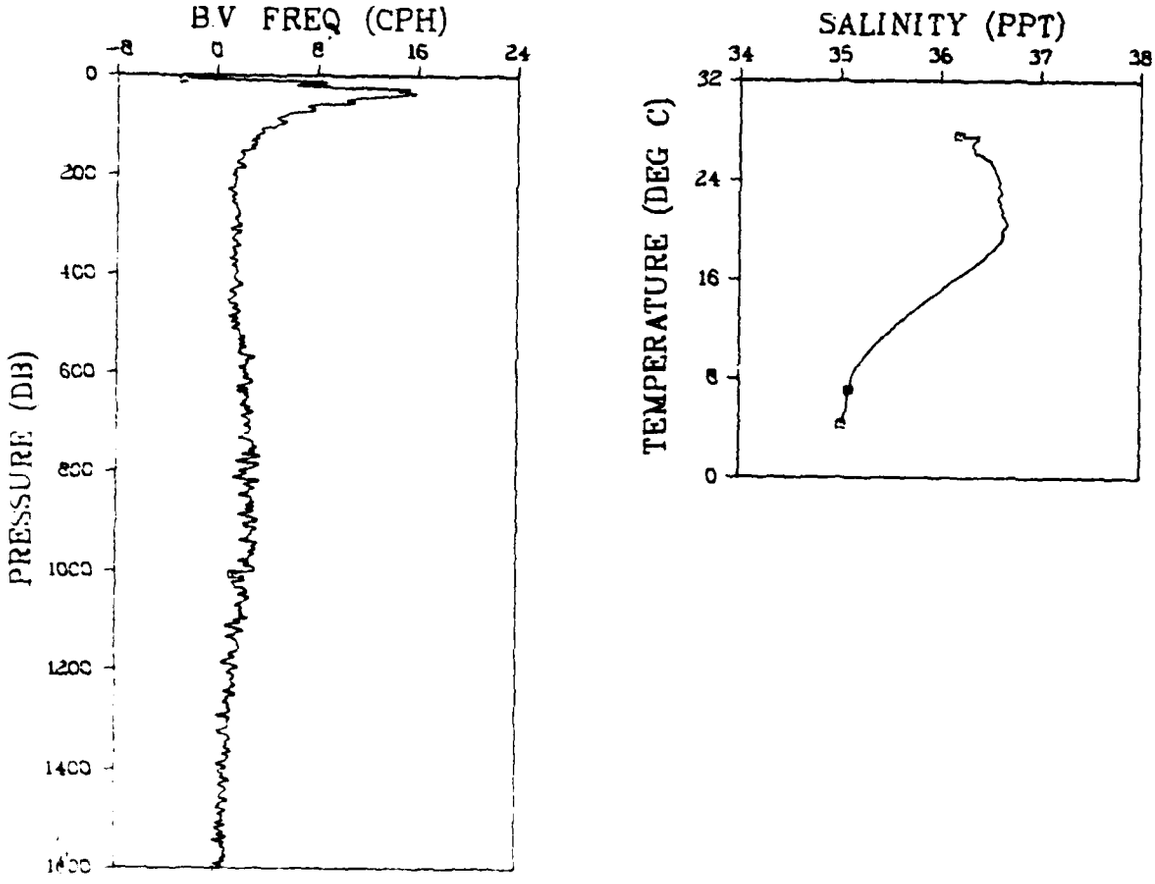

Figure 4.2a. (continued)

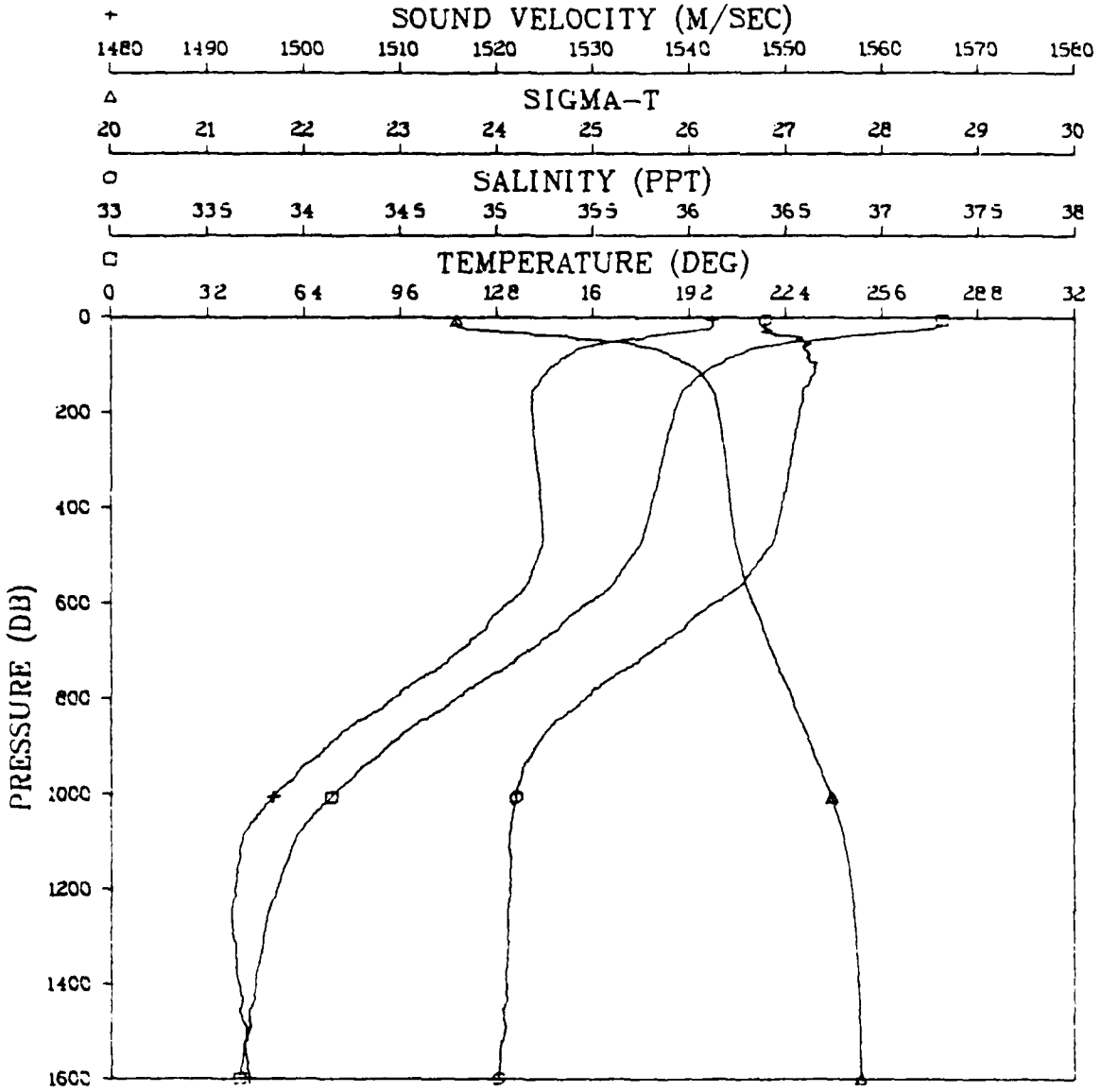

Figure 4.2b. CTD station 026074
Start: 10 Sept 0443Z, 30°25.5'N, 71°57.1'W

STATION 026074

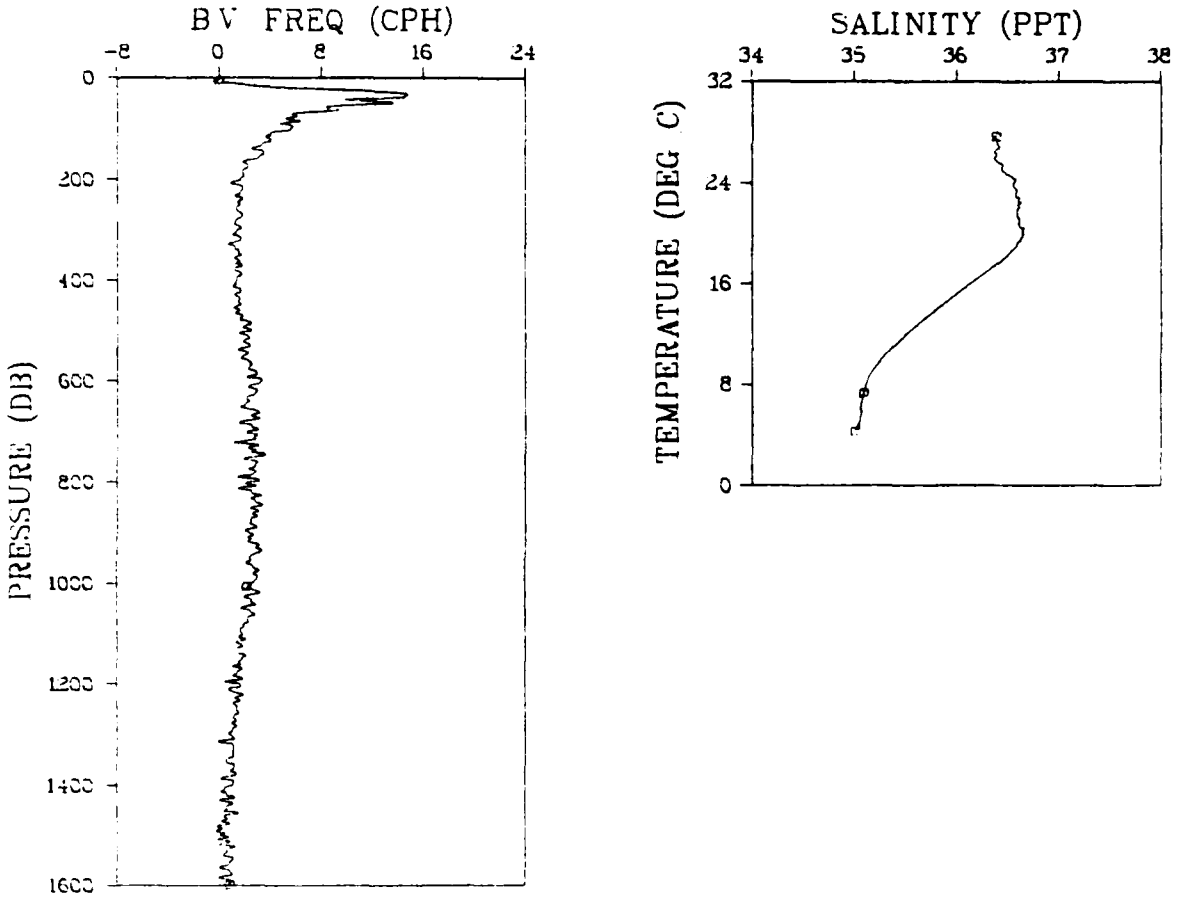

Figure 4.2b. (continued)

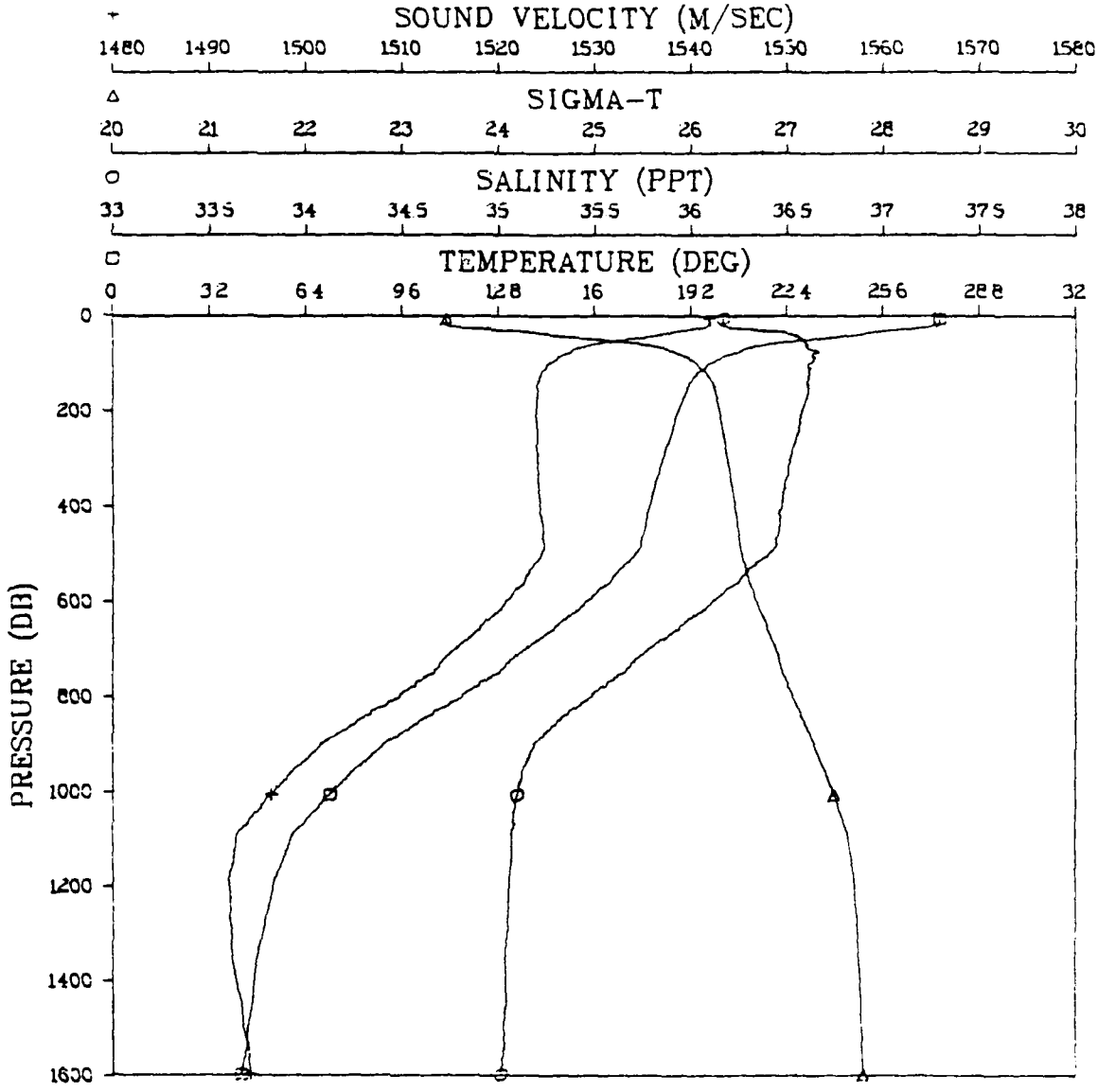

Figure 4.2c. CTD station 026075
Start: 10 Sept 1750Z, 30°25.9'N, 71°37.6'W

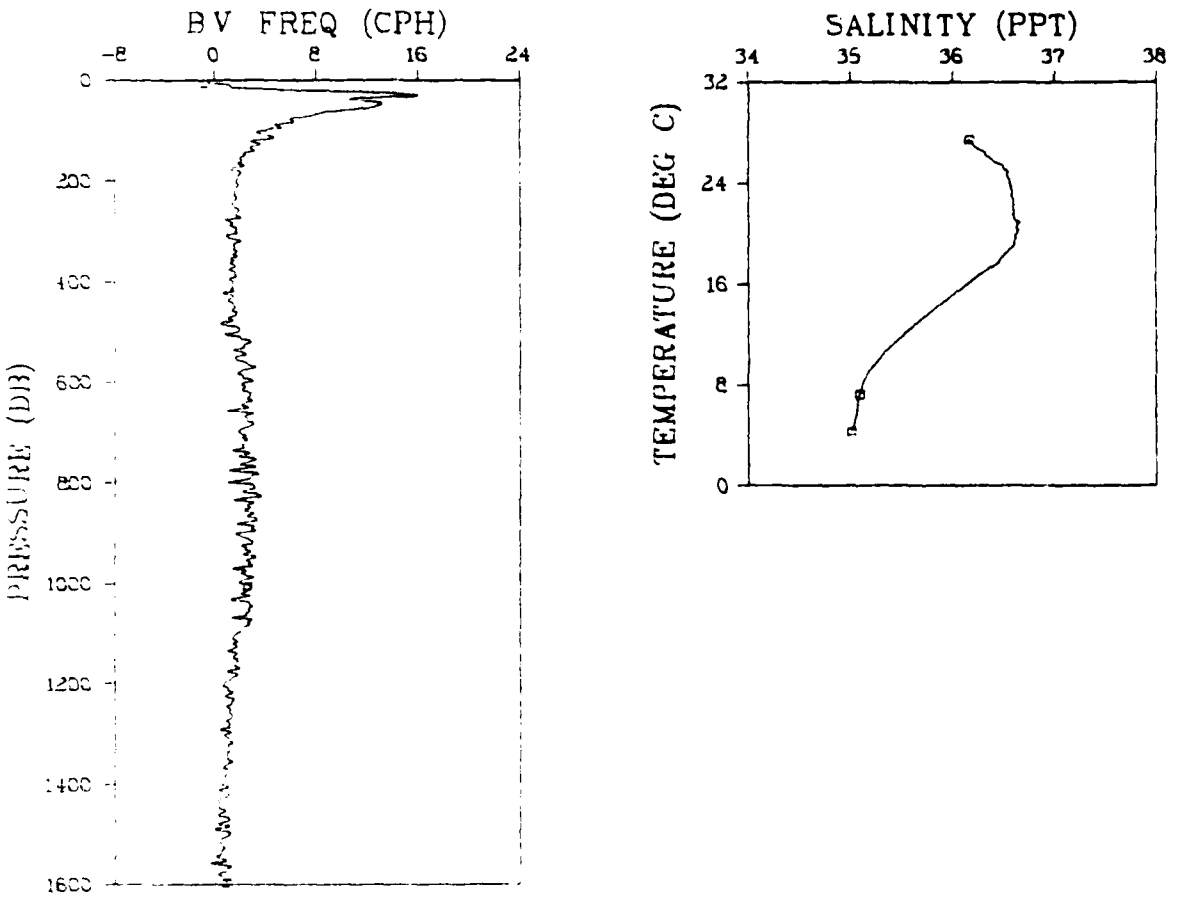

Figure 4.2c. (continued)

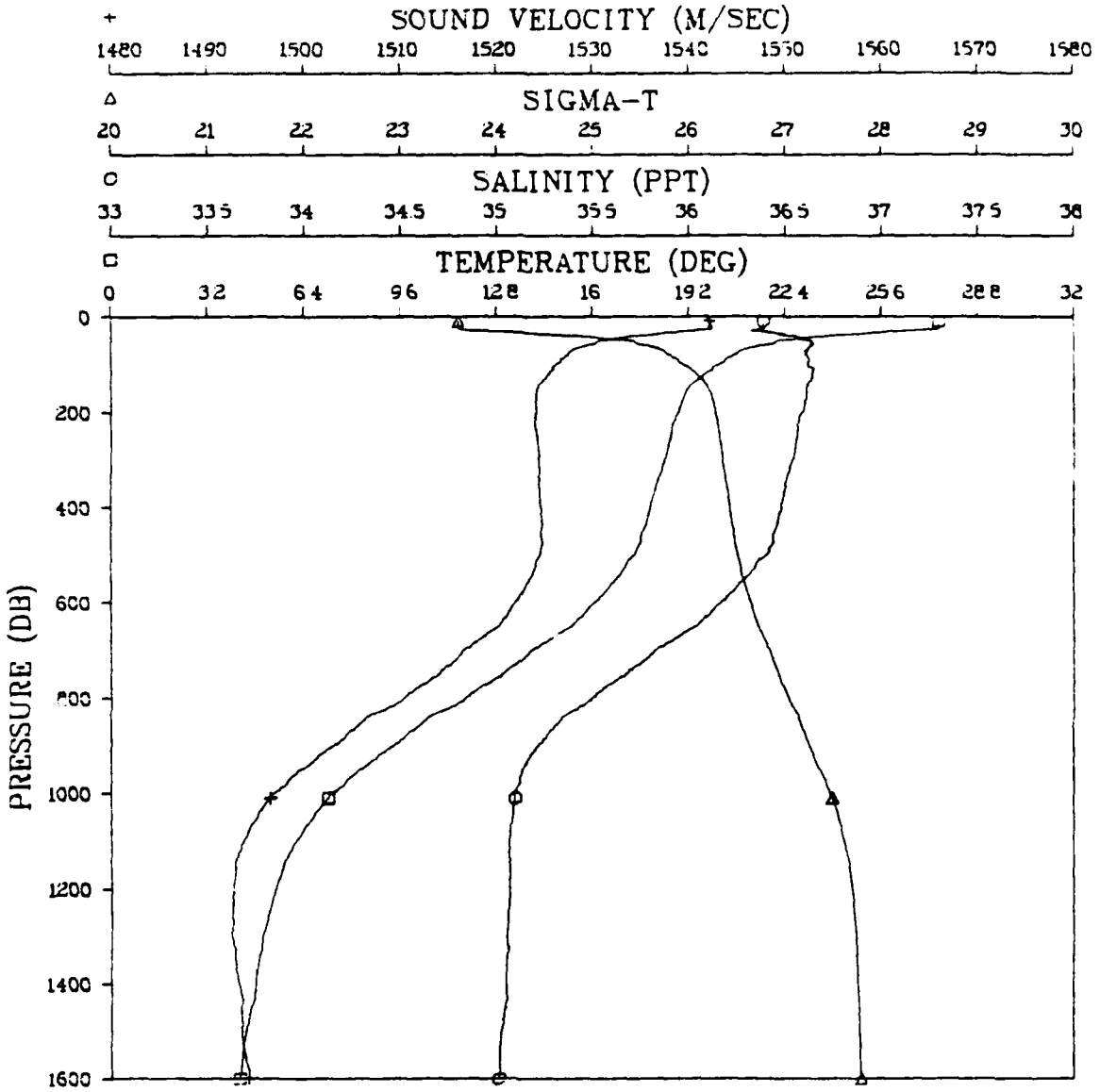

Figure 4.2d. CTD station 026076
Start: 10 Sept 1652Z, 30°25.5'N, 71°57.5'W

STATION 026076

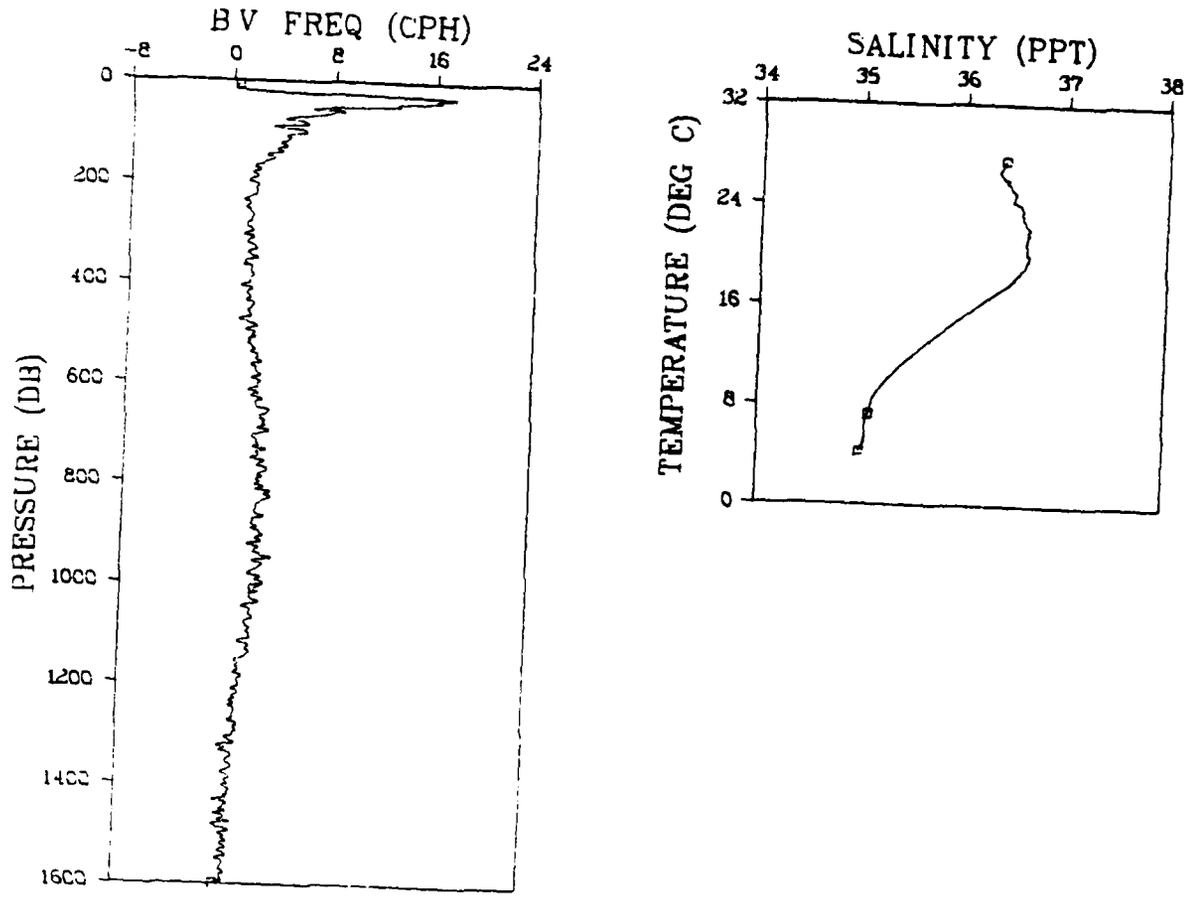

Figure 4.2d. (continued)

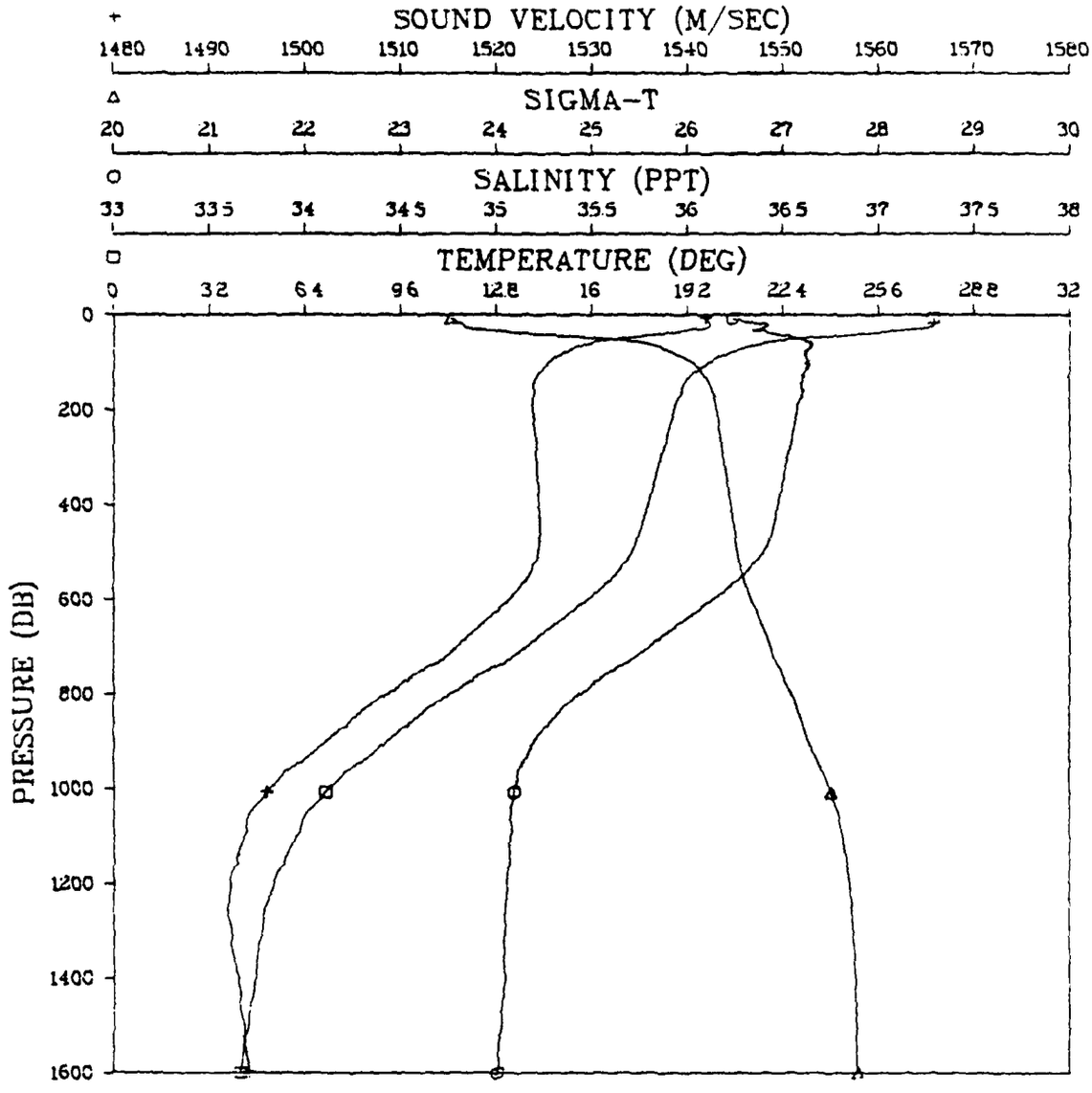

Figure 4.2e. CTD station 026077
Start: 10 Sept 1934Z, 30°25.3'N, 71°37.3'W

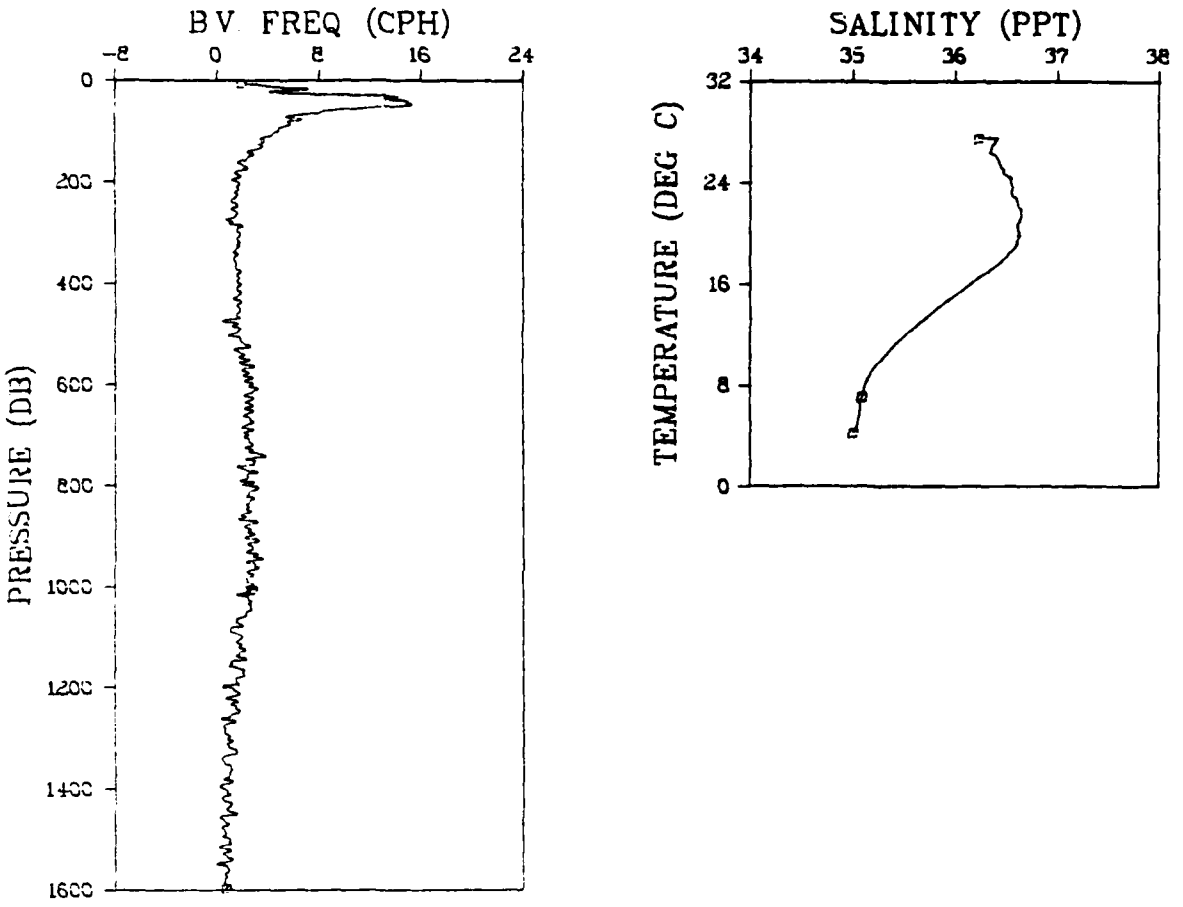

Figure 4.2e. (continued)

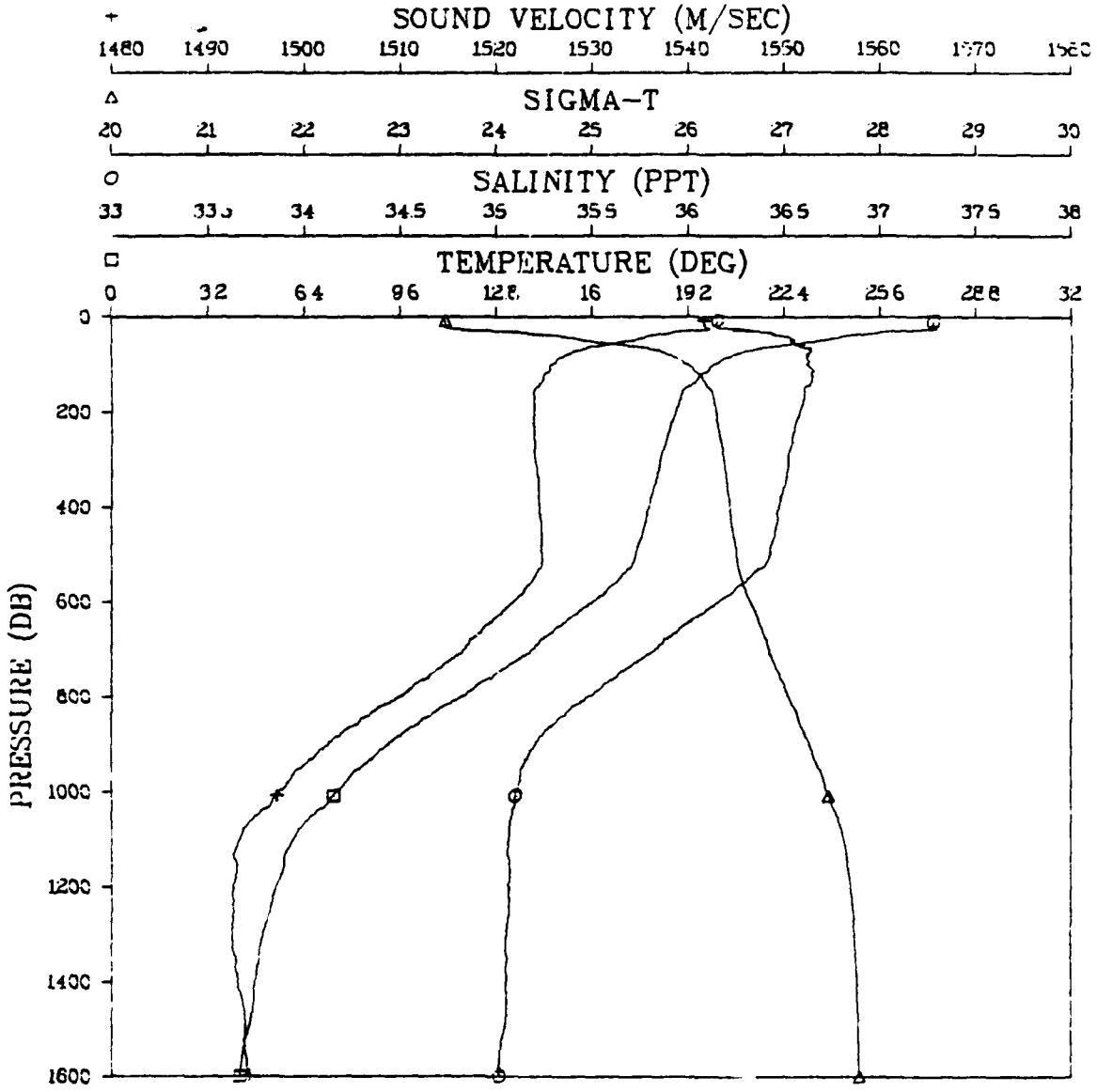

Figure 4.2f. CTD station 026078
Start: 11 Sept 0122Z, 30°25.7'N, 71°57.2'W

STATION 026078

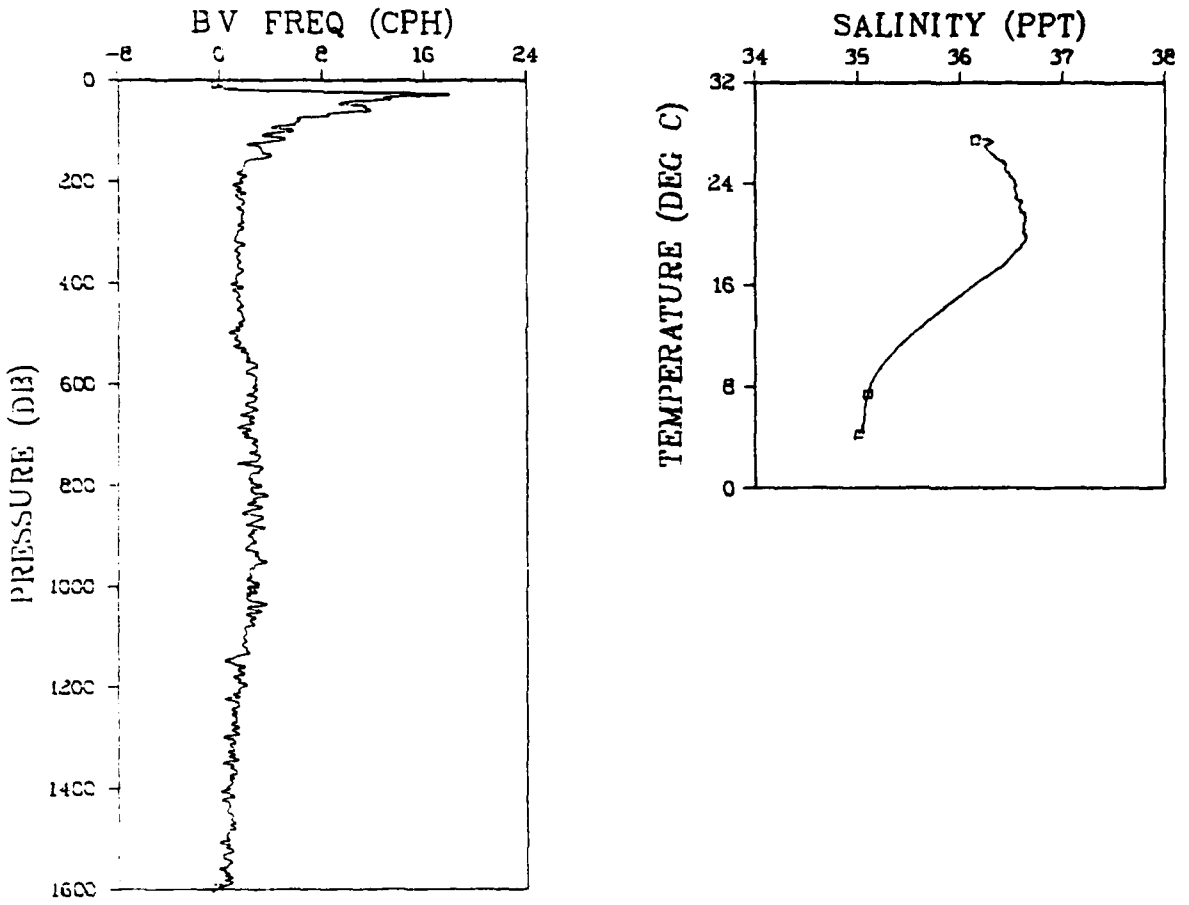

Figure 4.2f. (continued)

STATION 026081

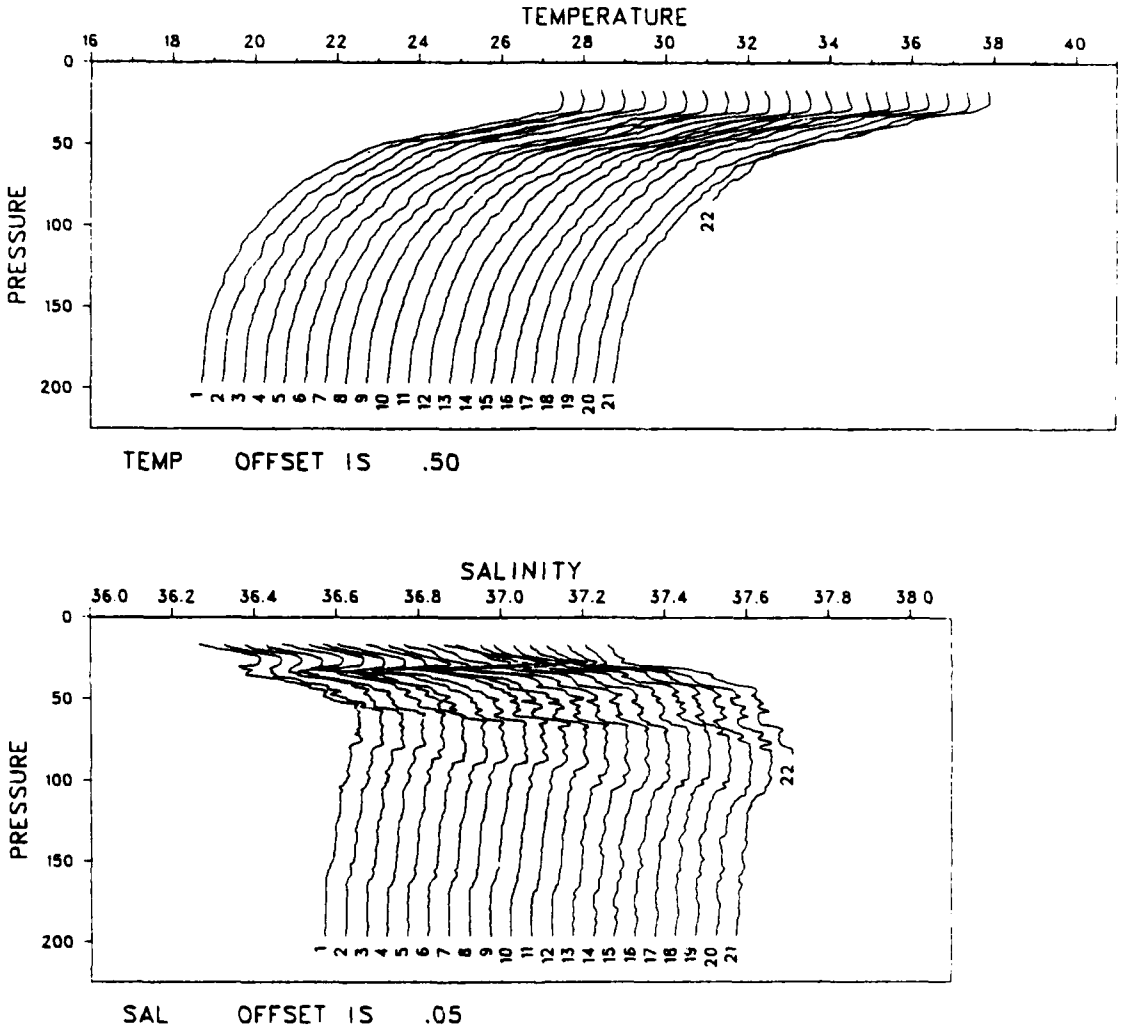

Figure 4.3a. CTD time series 026081
Start: 11 Sept 0252Z, 30°30.0'N, 71°47.0'W
Stop : 11 Sept 1010Z, 30°31.4'N, 71°46.9'W

STATION 026081

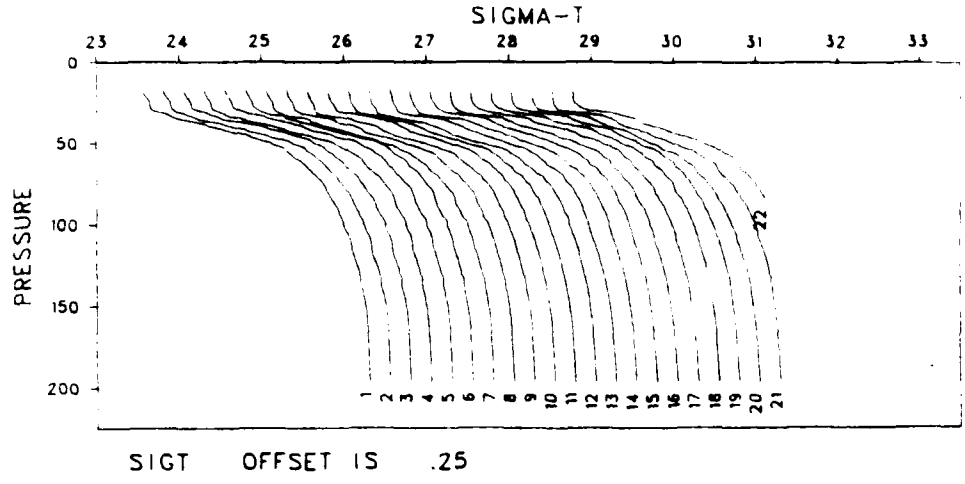

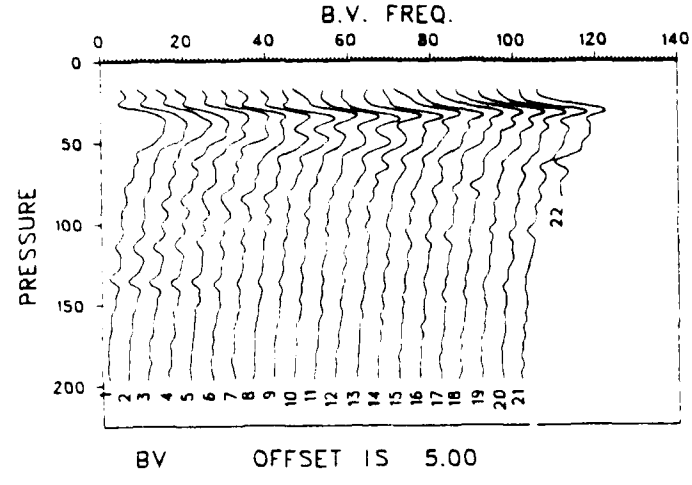

Figure 4.3a. (continued)

STATION 026081

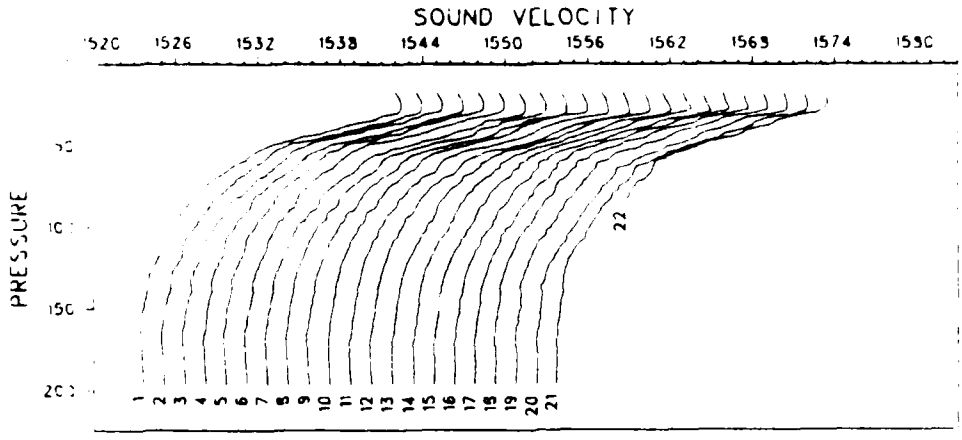

SDVOL OFFSET IS 1.50

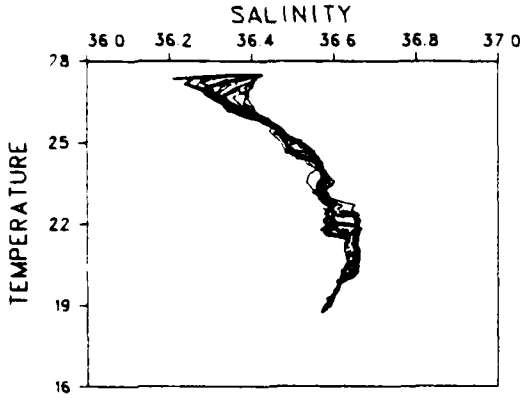

Figure 4.3a. (continued)

STATION 026082

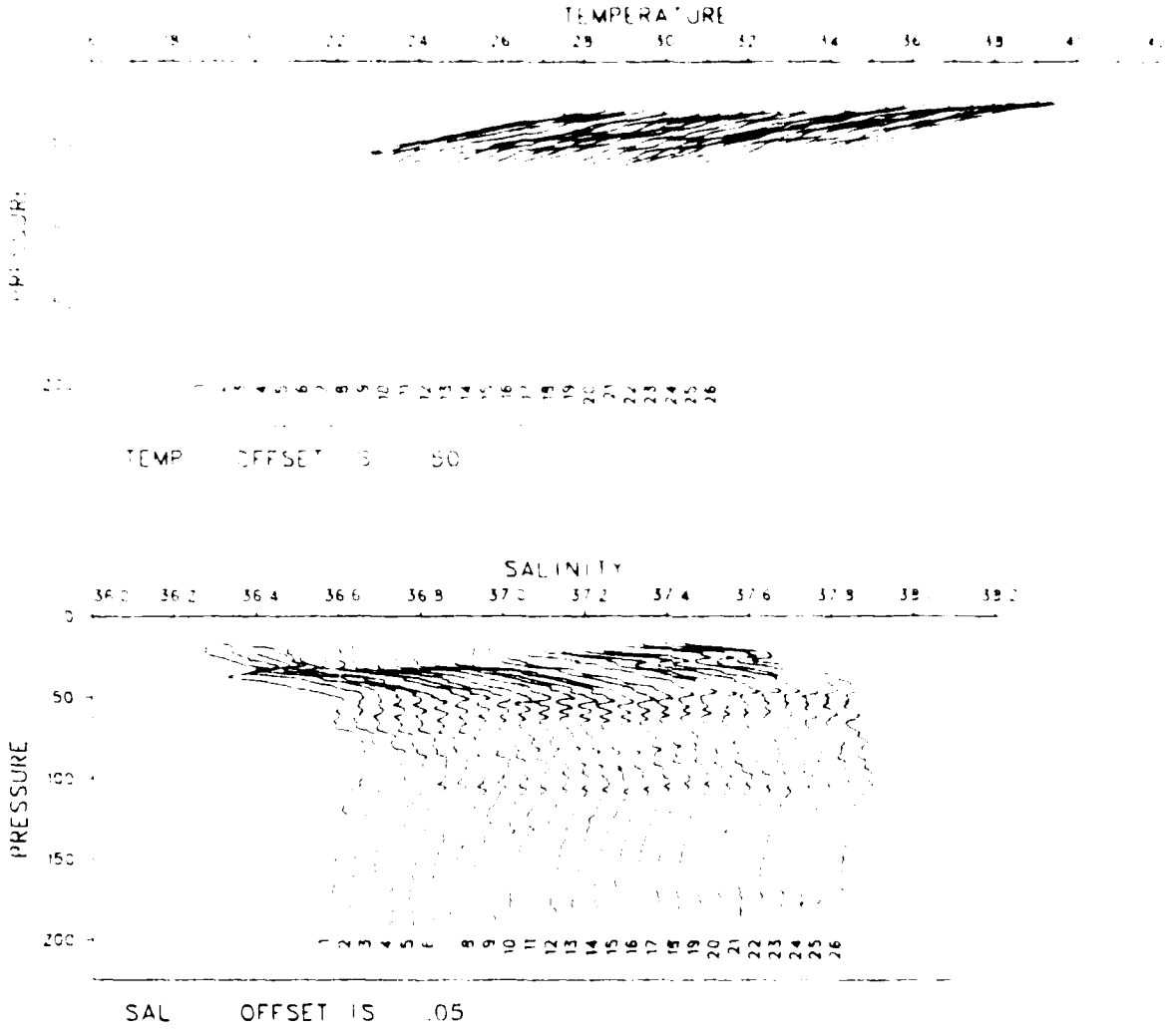

Figure 4.3b. CTD time series 026082
Start: 11 Sept 1154Z, 30°30.1'N, 71°46.7'W
Stop : 11 Sept 1451Z, 30°31.7'N, 71°48.0'W

STATION 026082

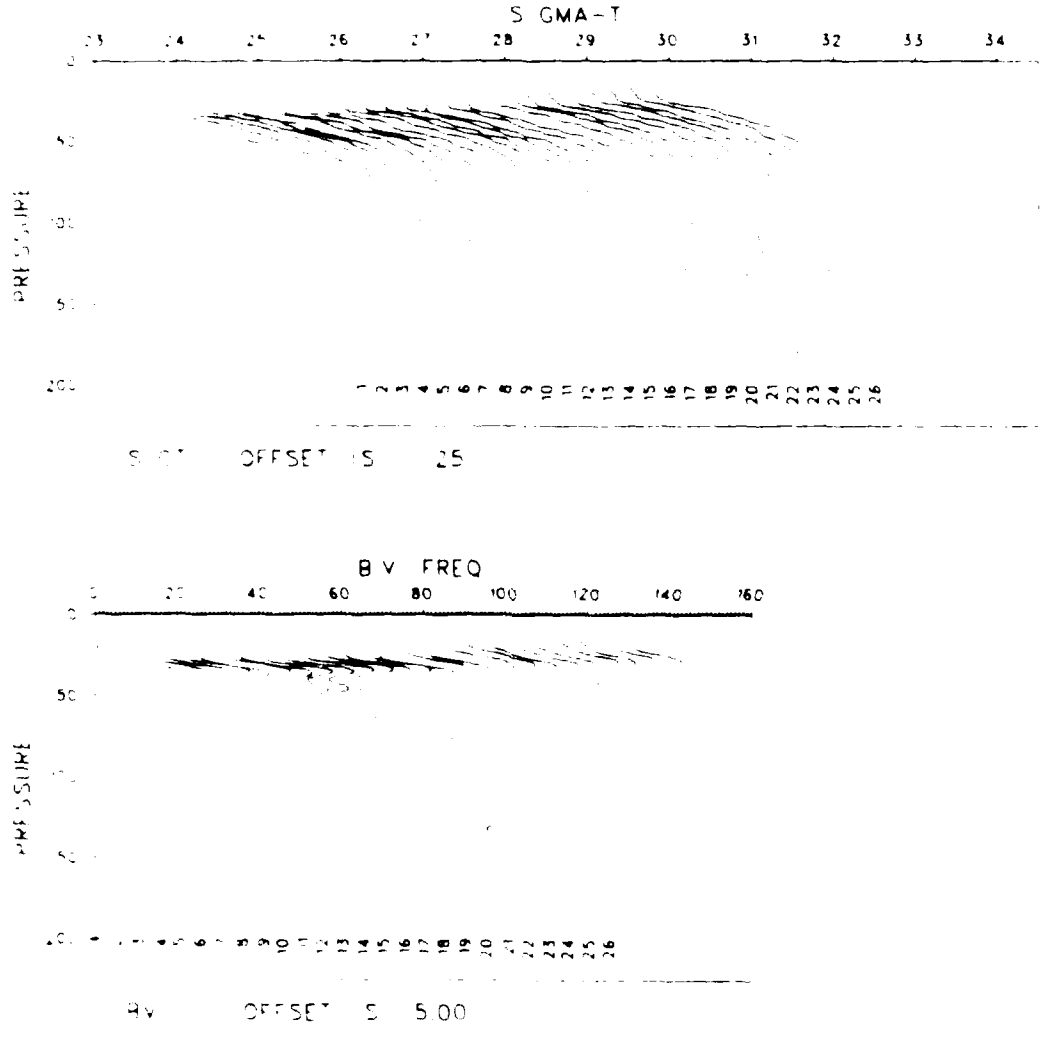

Figure 4.3b. (continued)

STATION 026082

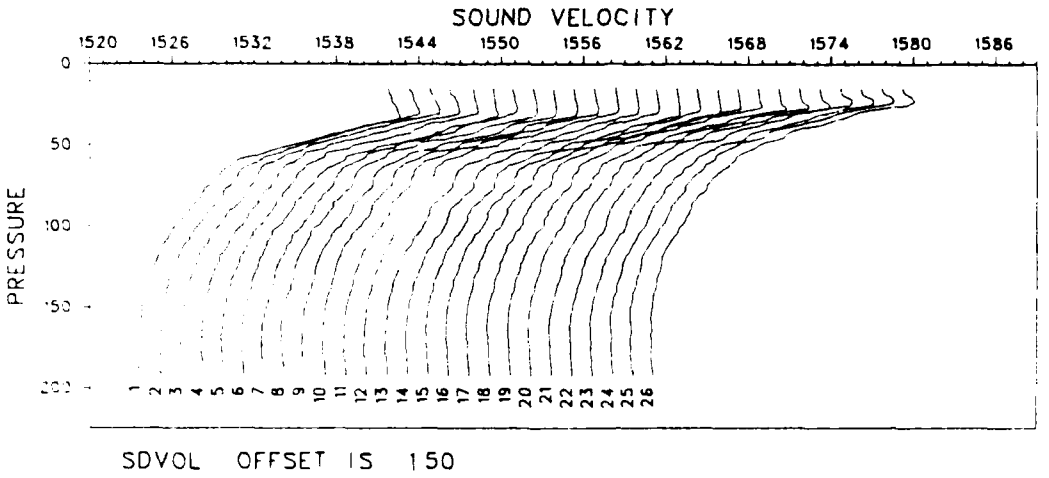

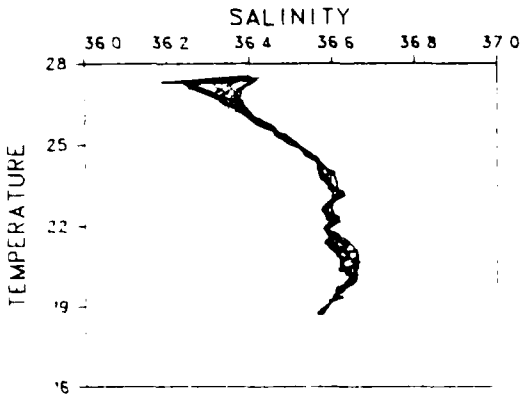

Figure 4.3b. (continued)

STATION 026083

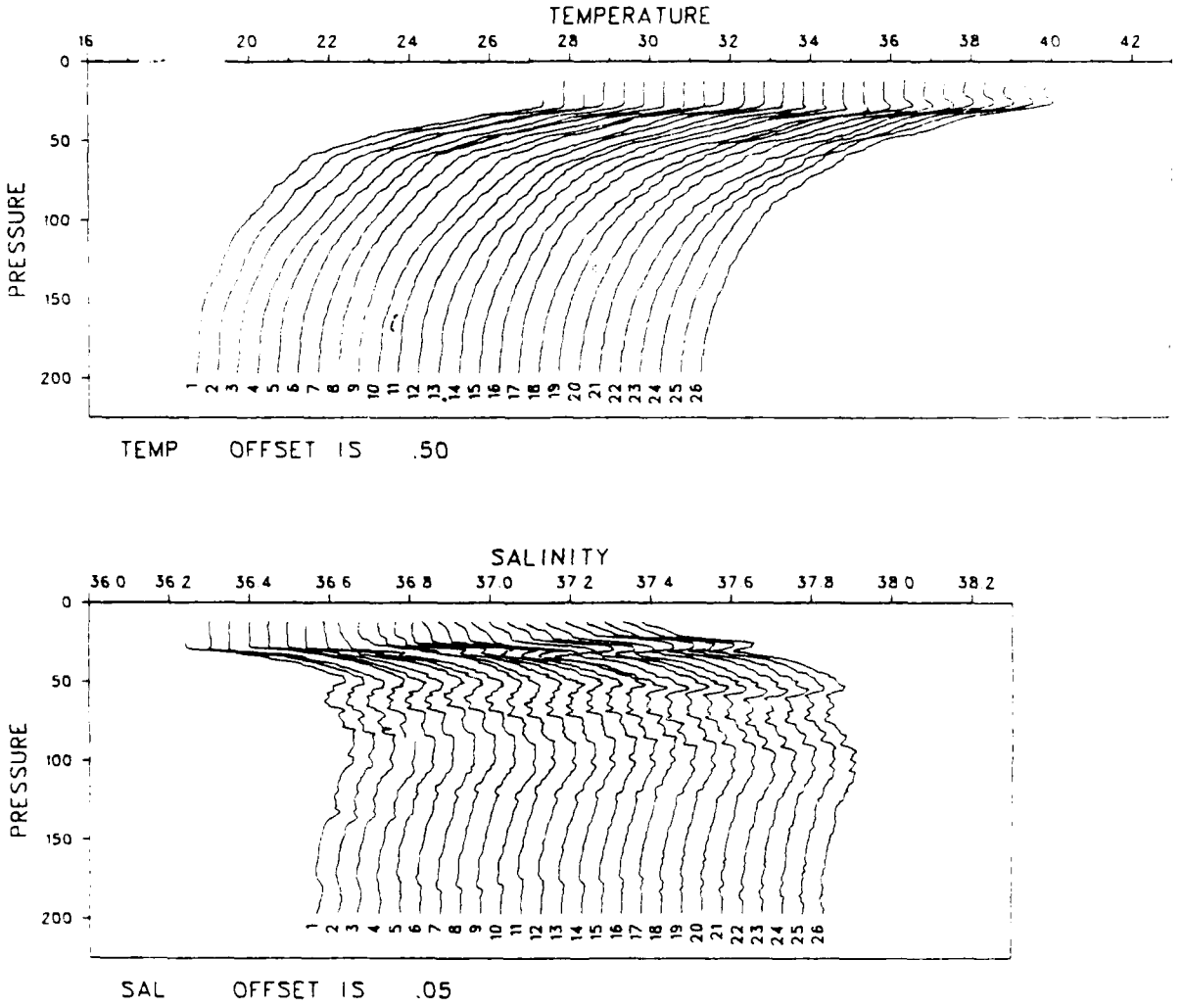

Figure 4.3c. CTD time series 026083
Start: 11 Sept 1554Z, 30°30.1'N, 71°47.2'W
Stop : 11 Sept 1853Z, 30°30.7'N, 71°49.0'W

STATION 026083

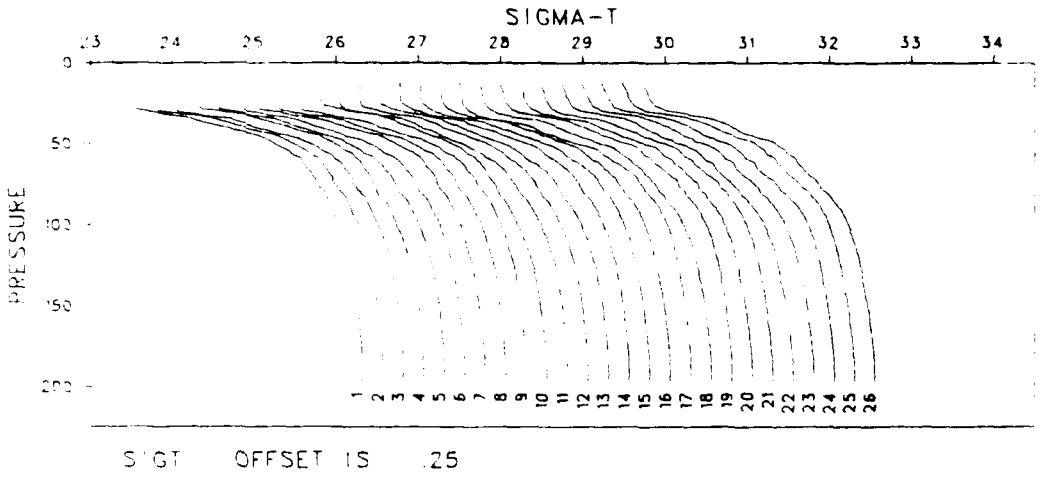

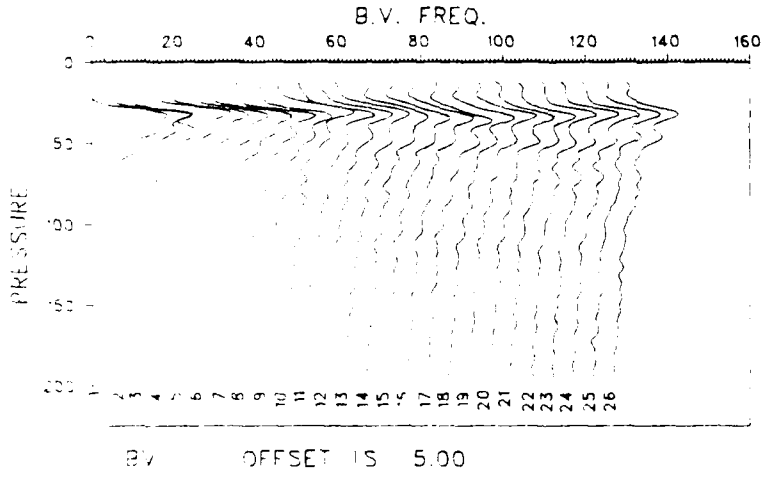

Figure 4.3c. (continued)

STATION 026083

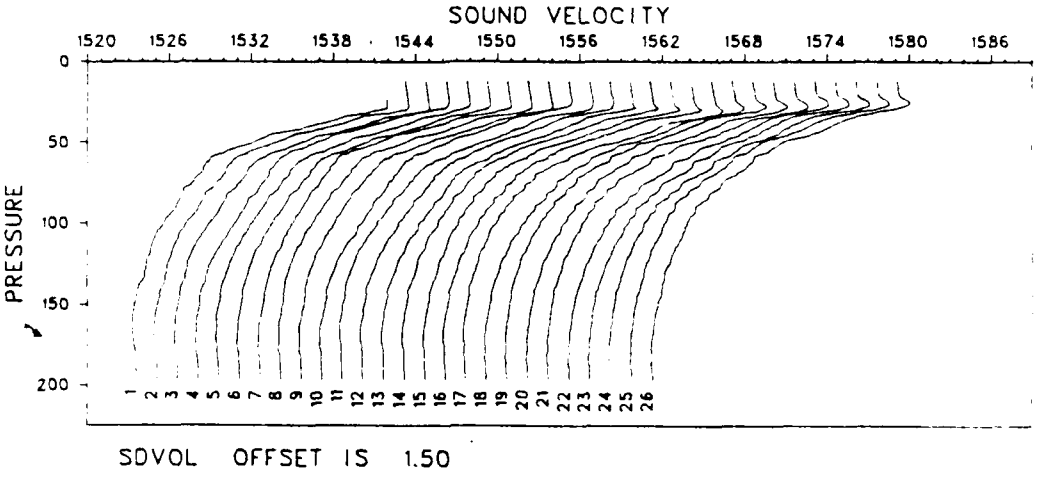

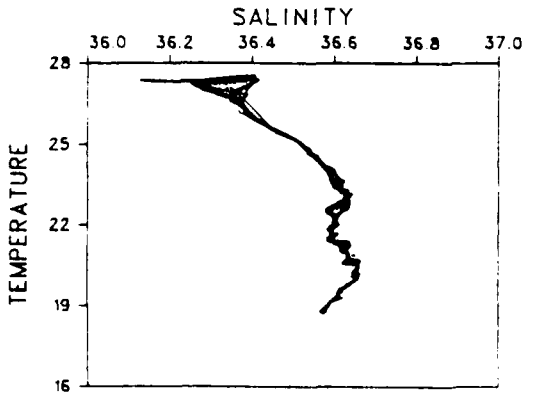

Figure 4.3c. (continued)

STATION 026084

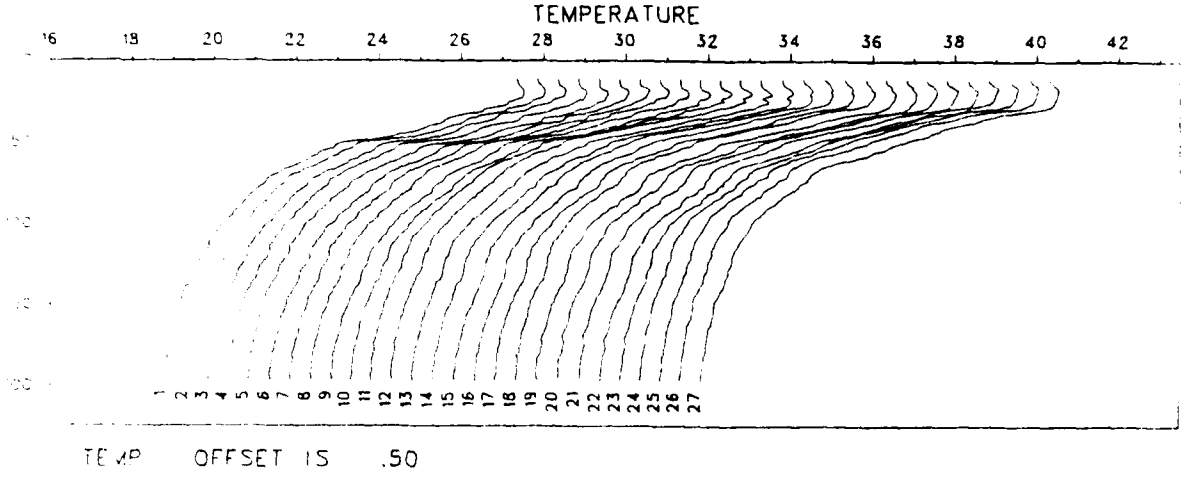

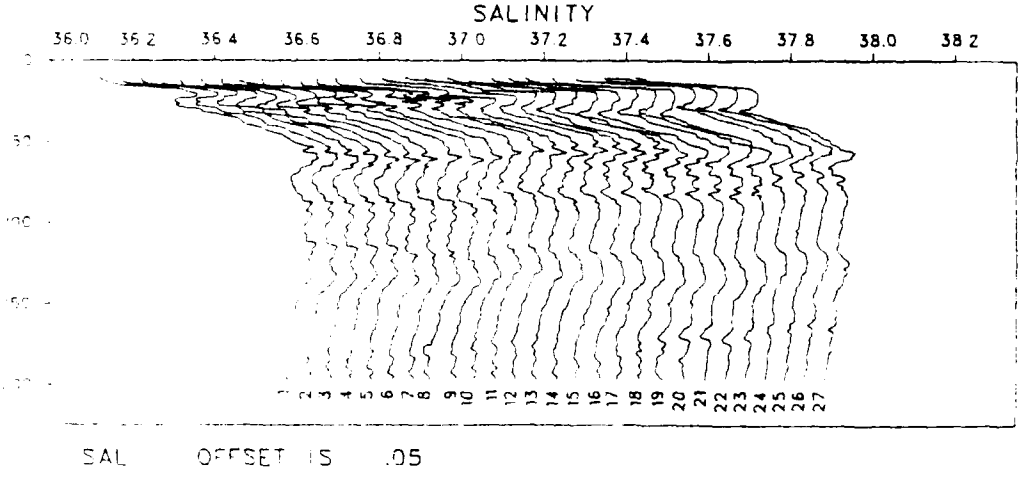

Figure 4.3d. CTD time series 026084
Start: 11 Sept 1944Z, 30°30.3'N, 71°47.3'W
Stop : 11 Sept 2246Z, 30°31.5'N, 71°47.3'W

STATION 026084

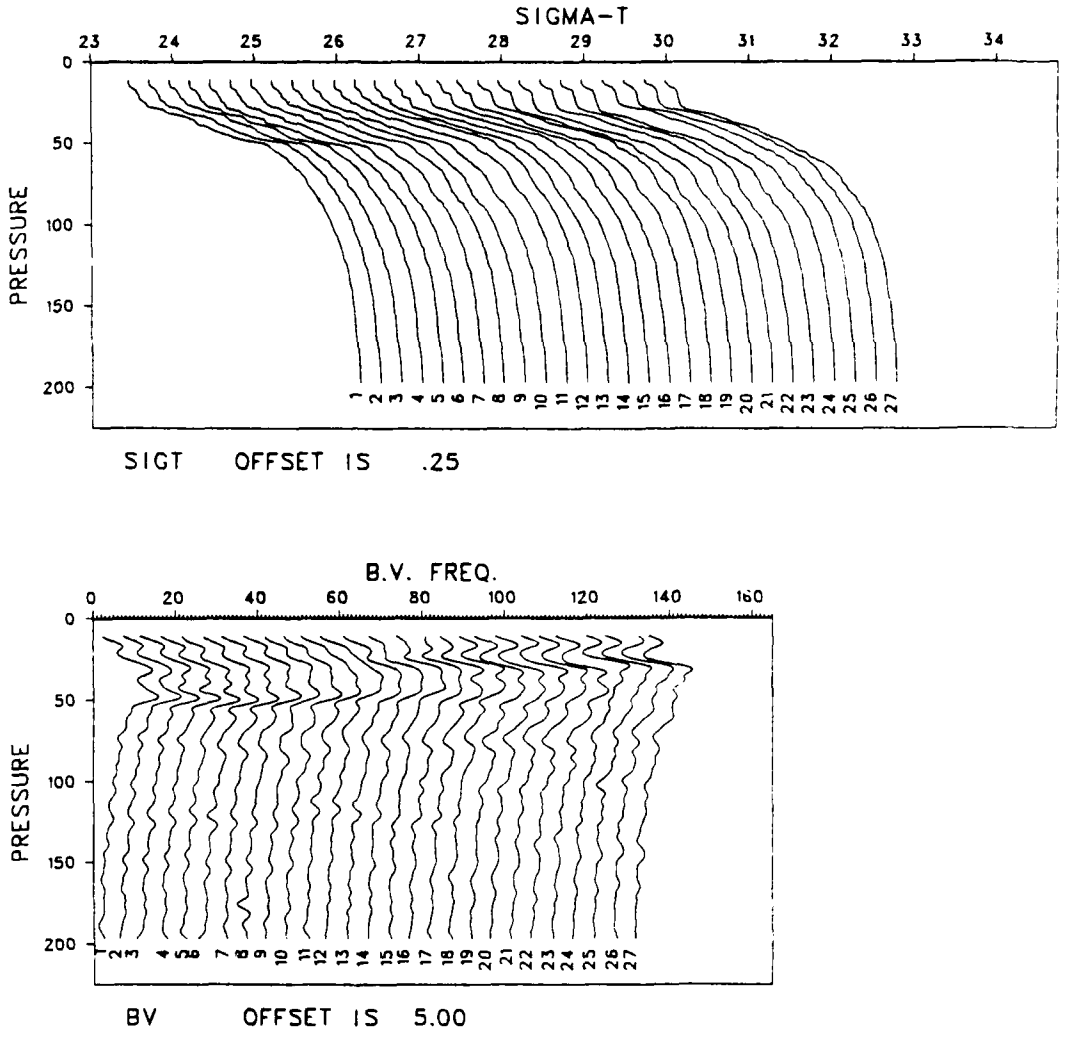

Figure 4.3d. (continued)

STATION 026084

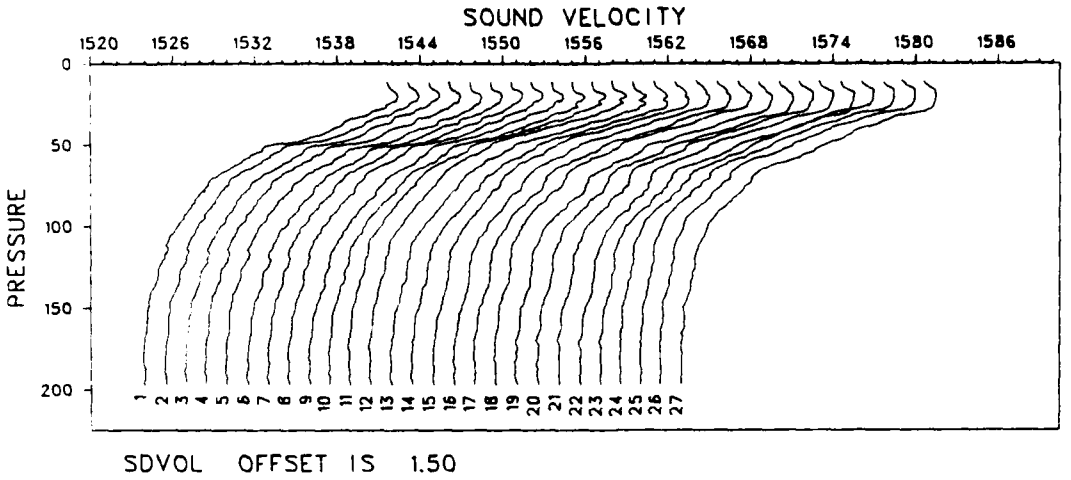

SDVOL OFFSET IS 1.50

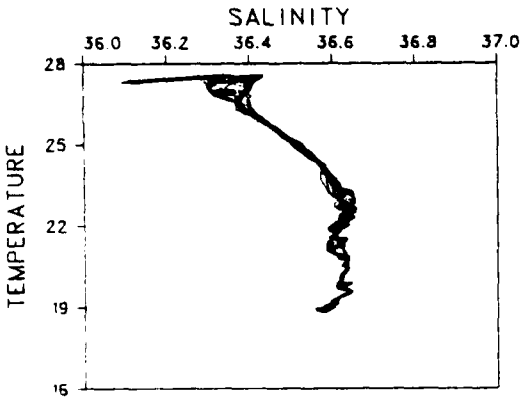

Figure 4.3d. (continued)

STATION 026085

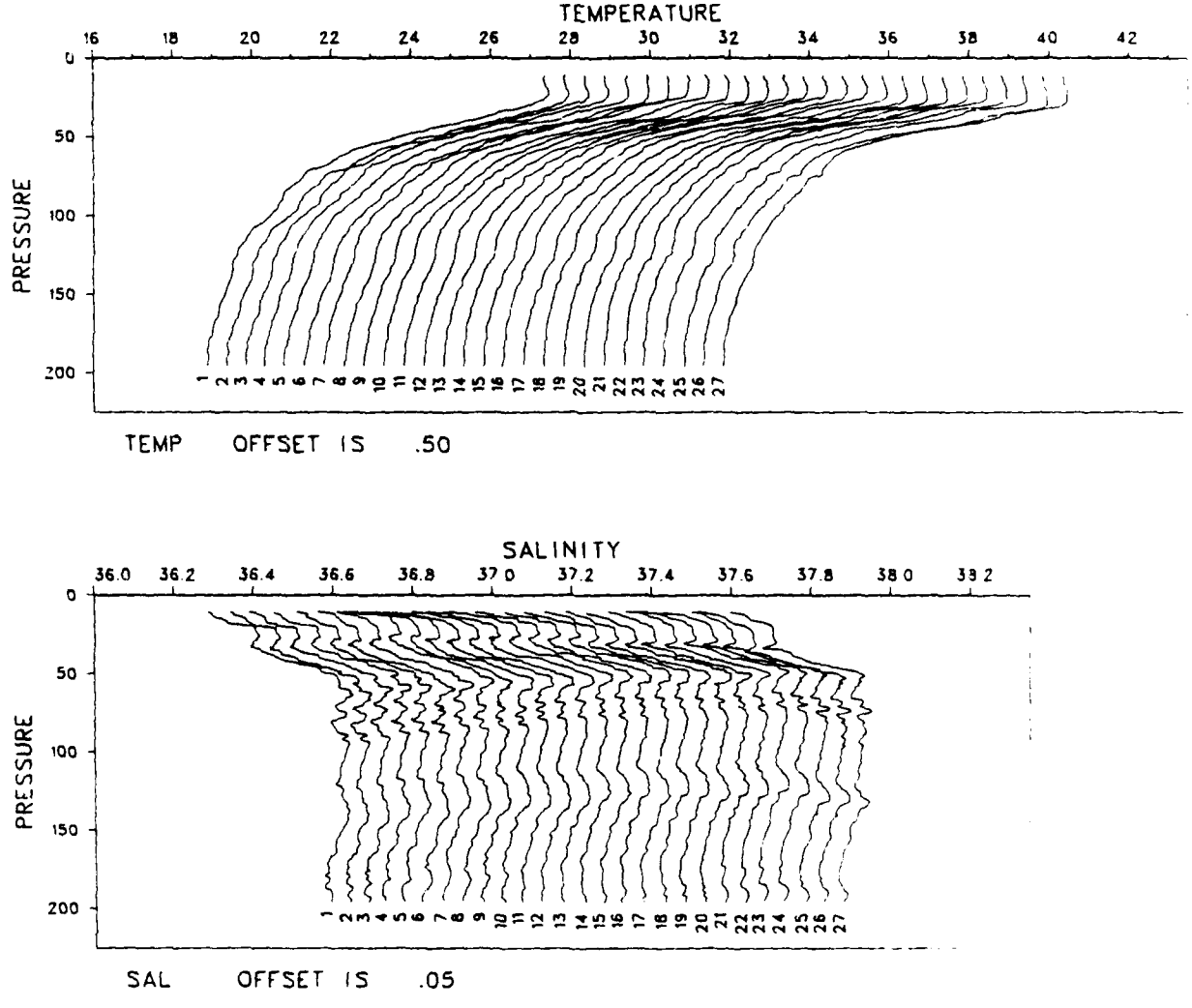

Figure 4.3e. CTD time series 026085
Start: 11 Sept 2344Z, 30°30.0'N, 71°47.3'W
Stop : 12 Sept 0245Z, 30°32.2'N, 71°50.6'W

STATION 026085

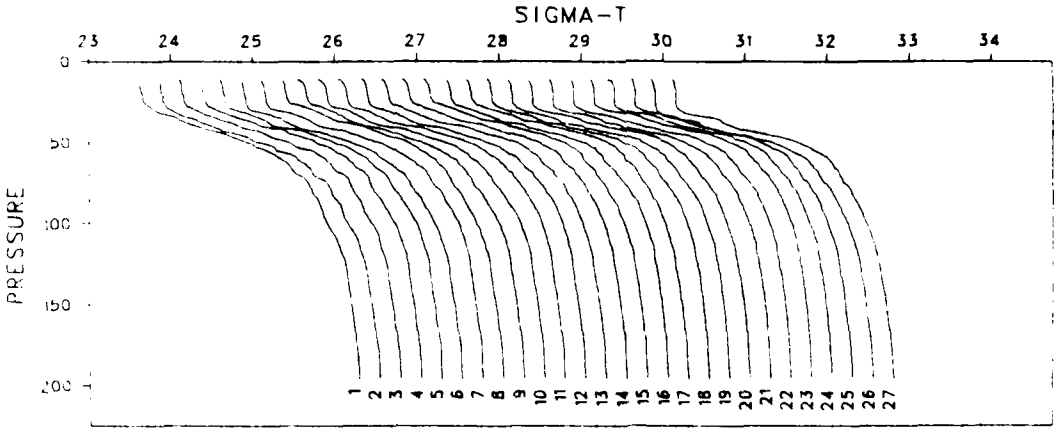

SIGT OFFSET IS .25

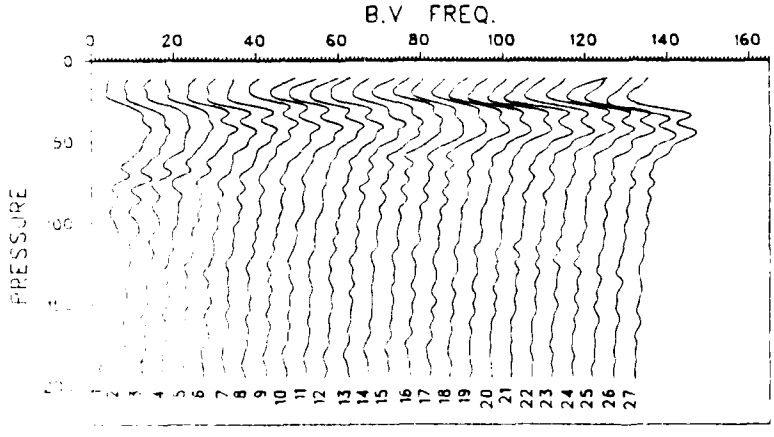

BV OFFSET IS 5.00

Figure 4.3e. (continued)

STATION 026085

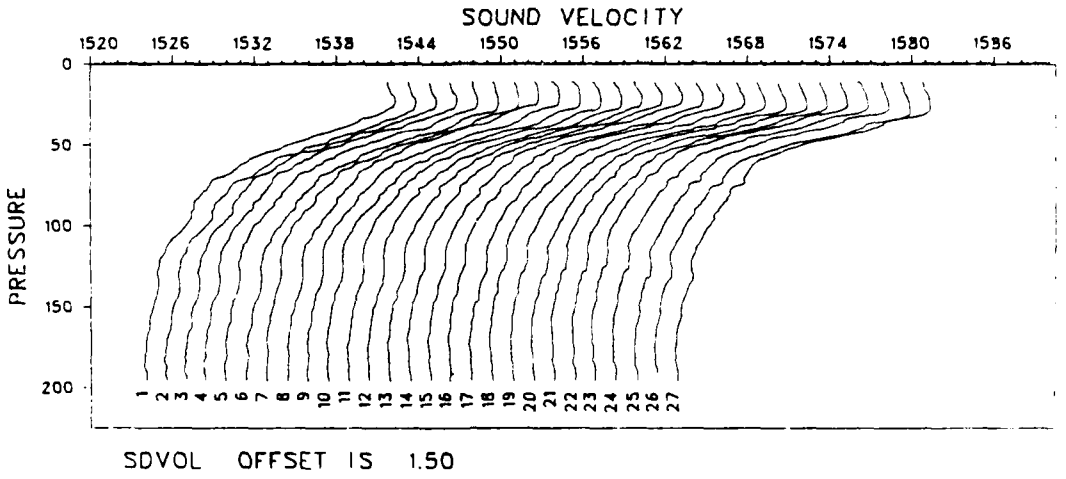

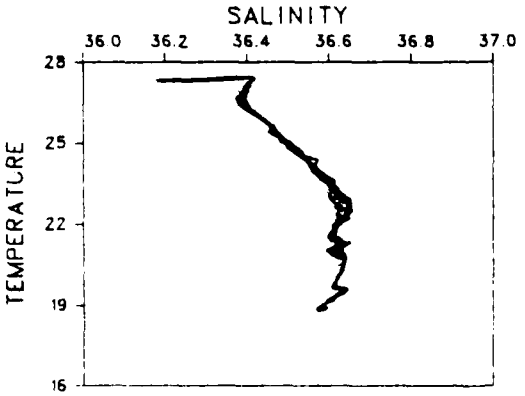

Figure 4.3e. (continued)

STATION 026086

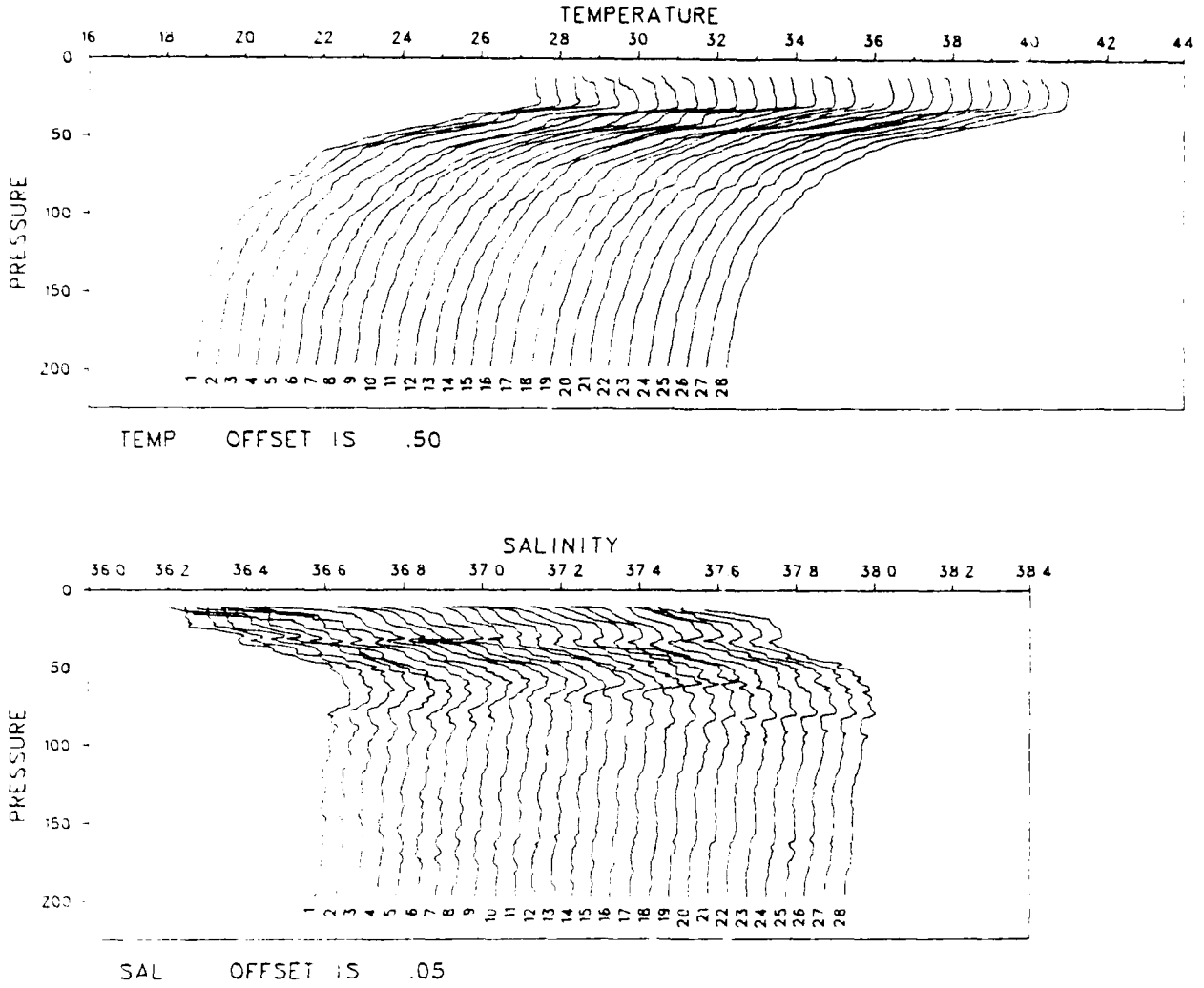

Figure 4.3f. CTD time series 026086
Start: 12 Sept 0359Z, 30°30.3'N, 71°46.9'W
Stop : 12 Sept 0702Z, 30°32.8'N, 71°50.5'W

STATION 026086

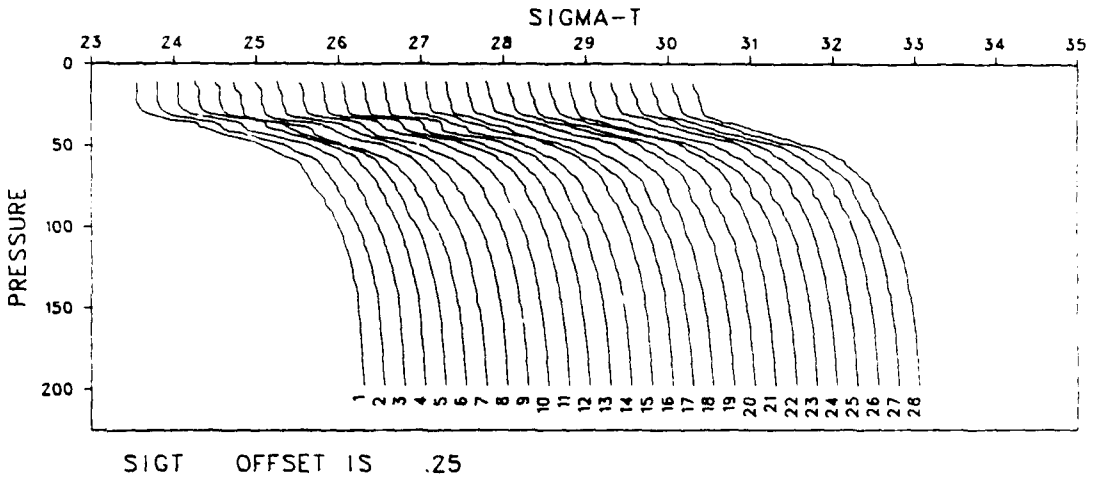

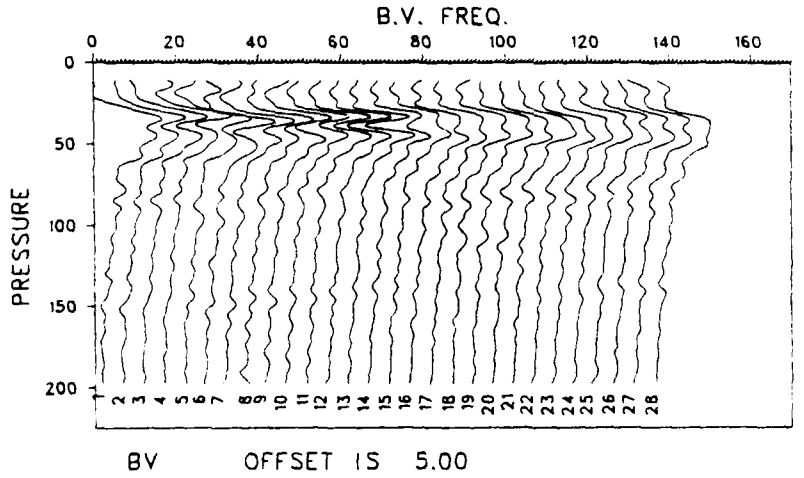

Figure 4.3f. (continued)

STATION 026086

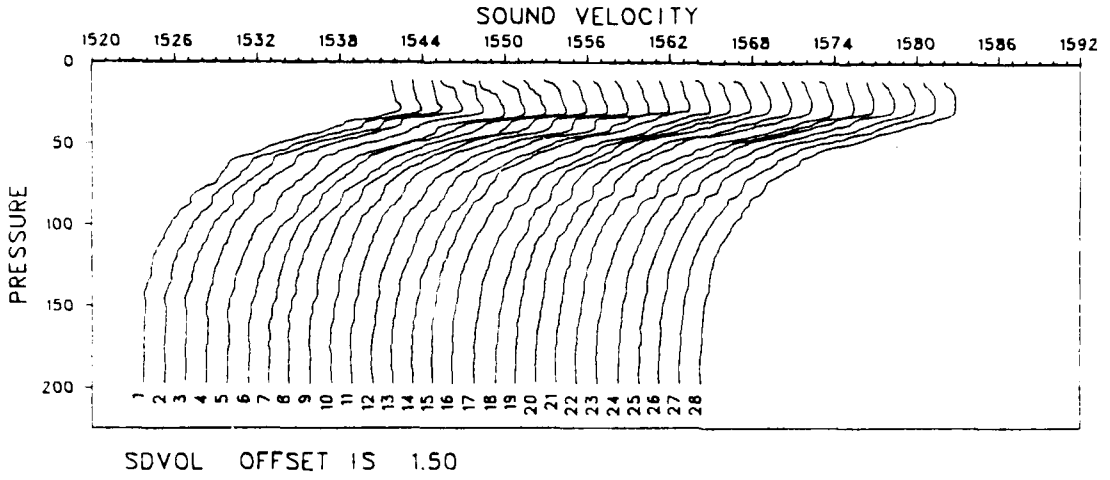

SDVOL OFFSET IS 1.50

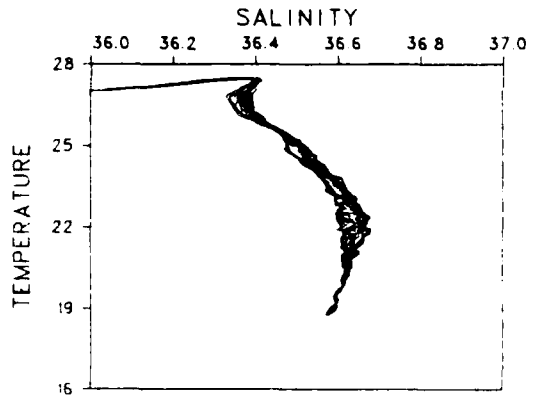

Figure 4.3f. (continued)

STATION 026087

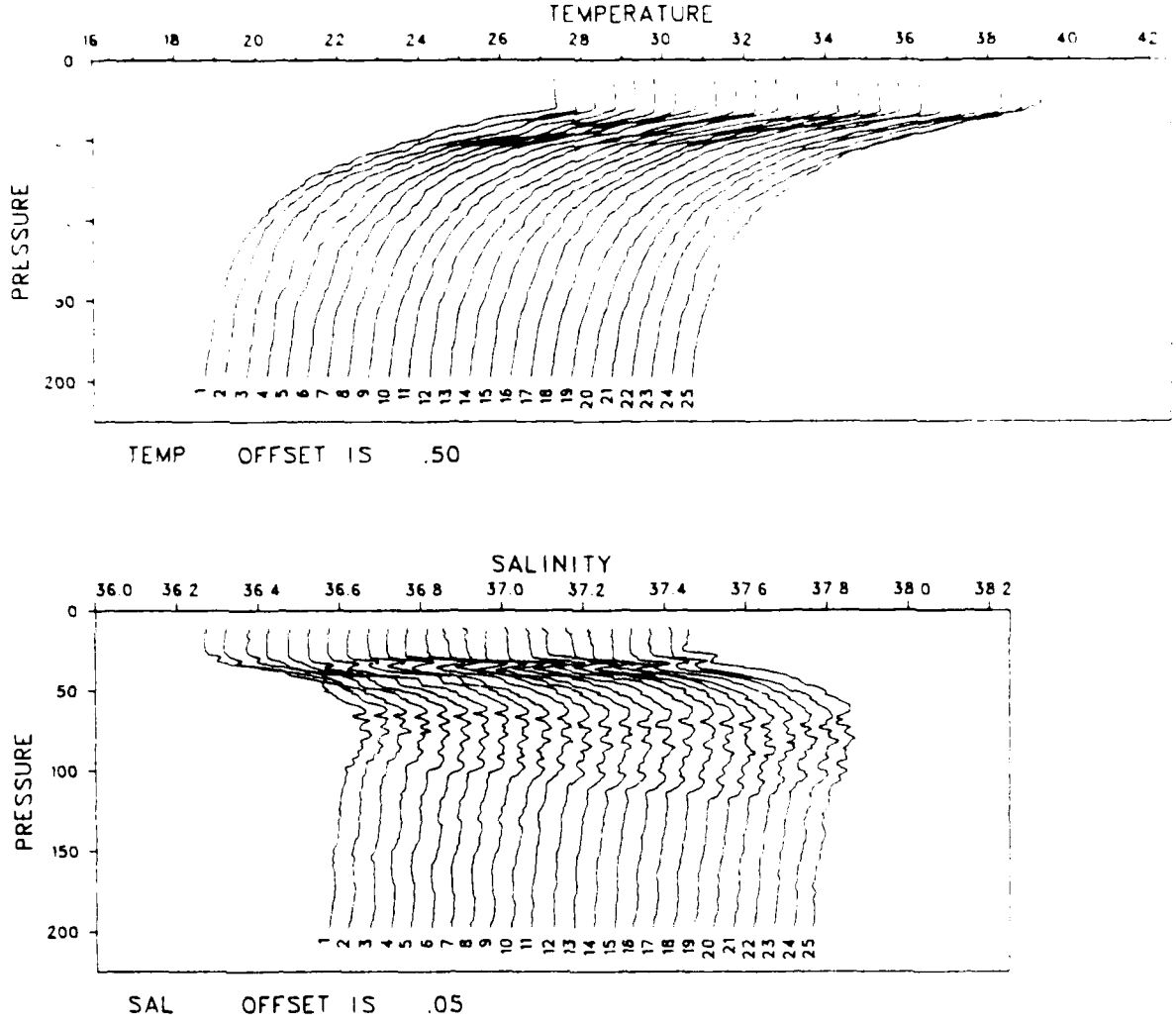

Figure 4.3g. CTD time series 026087
Start: 12 Sept 0814Z, 30°30.2'N, 71°47.0'W
Stop : 12 Sept 1103Z, 30°31.4'N, 71°46.0'W

STATION 026087

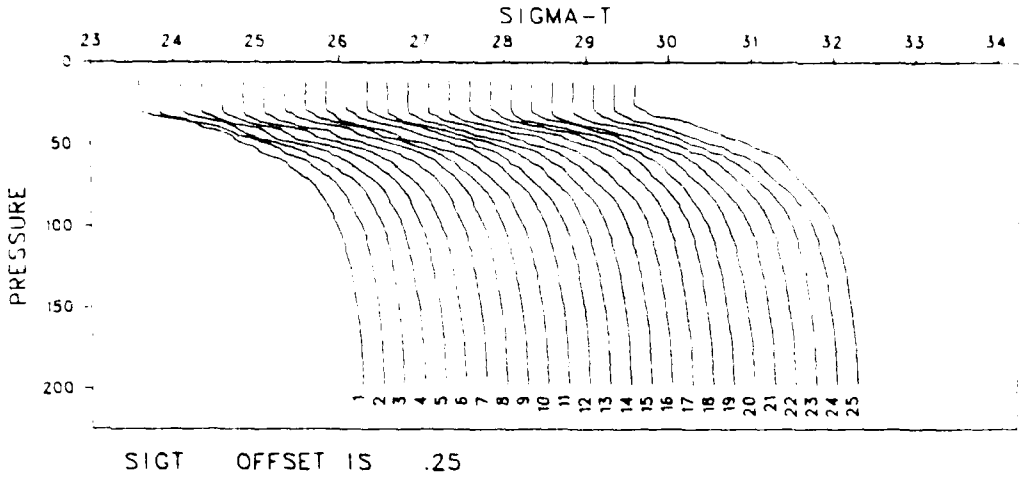

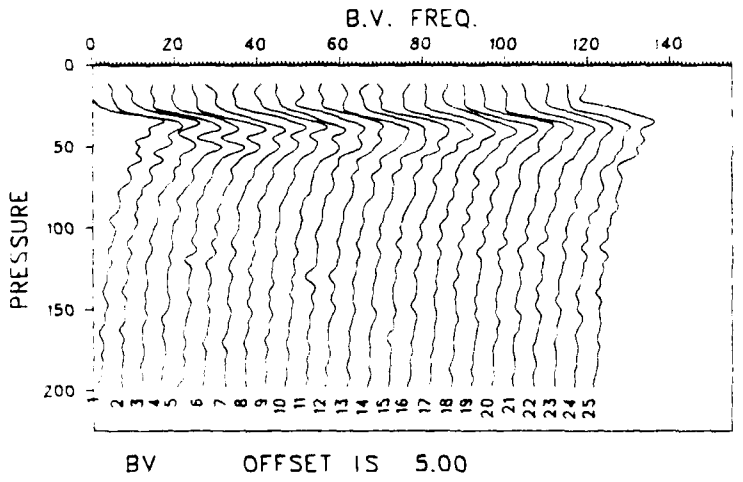

Figure 4.3g. (continued)

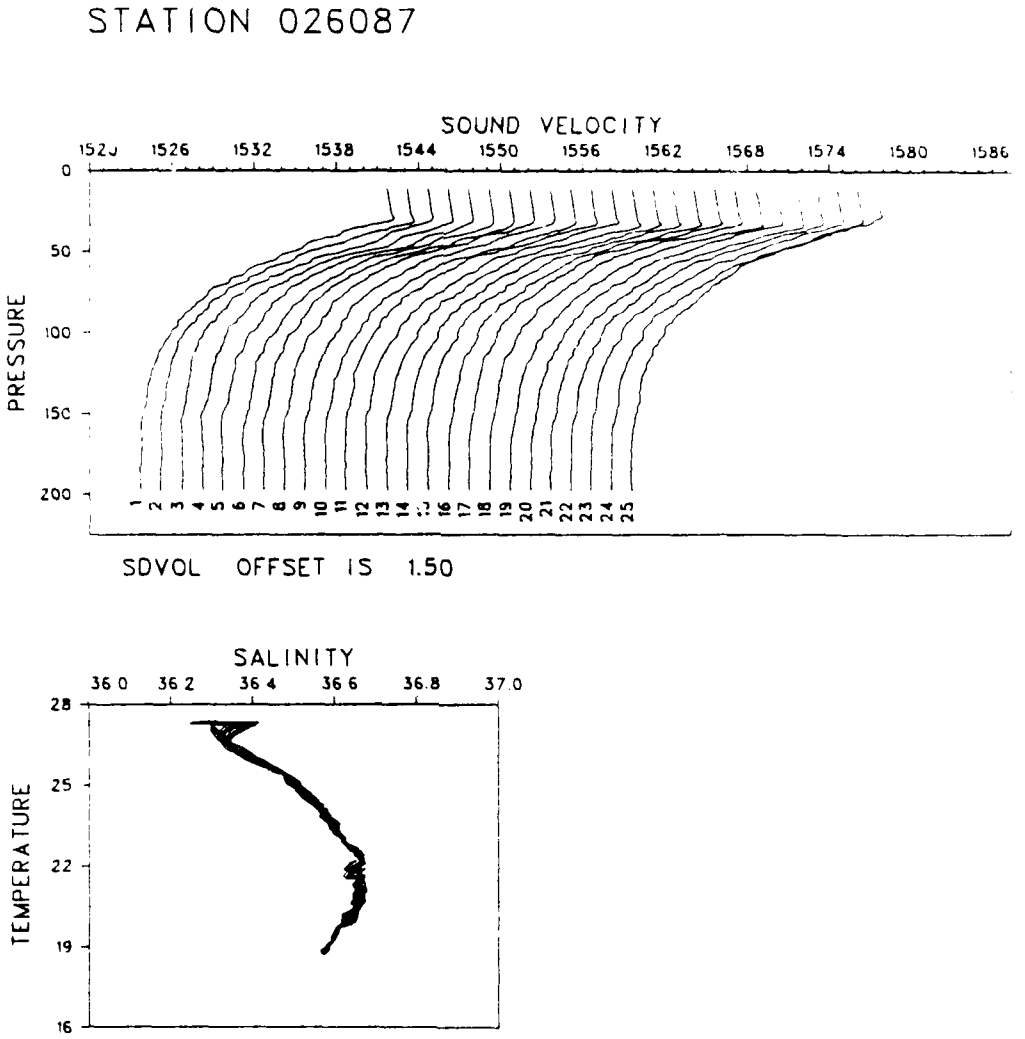

Figure 4.3g. (continued)

STATION 026088

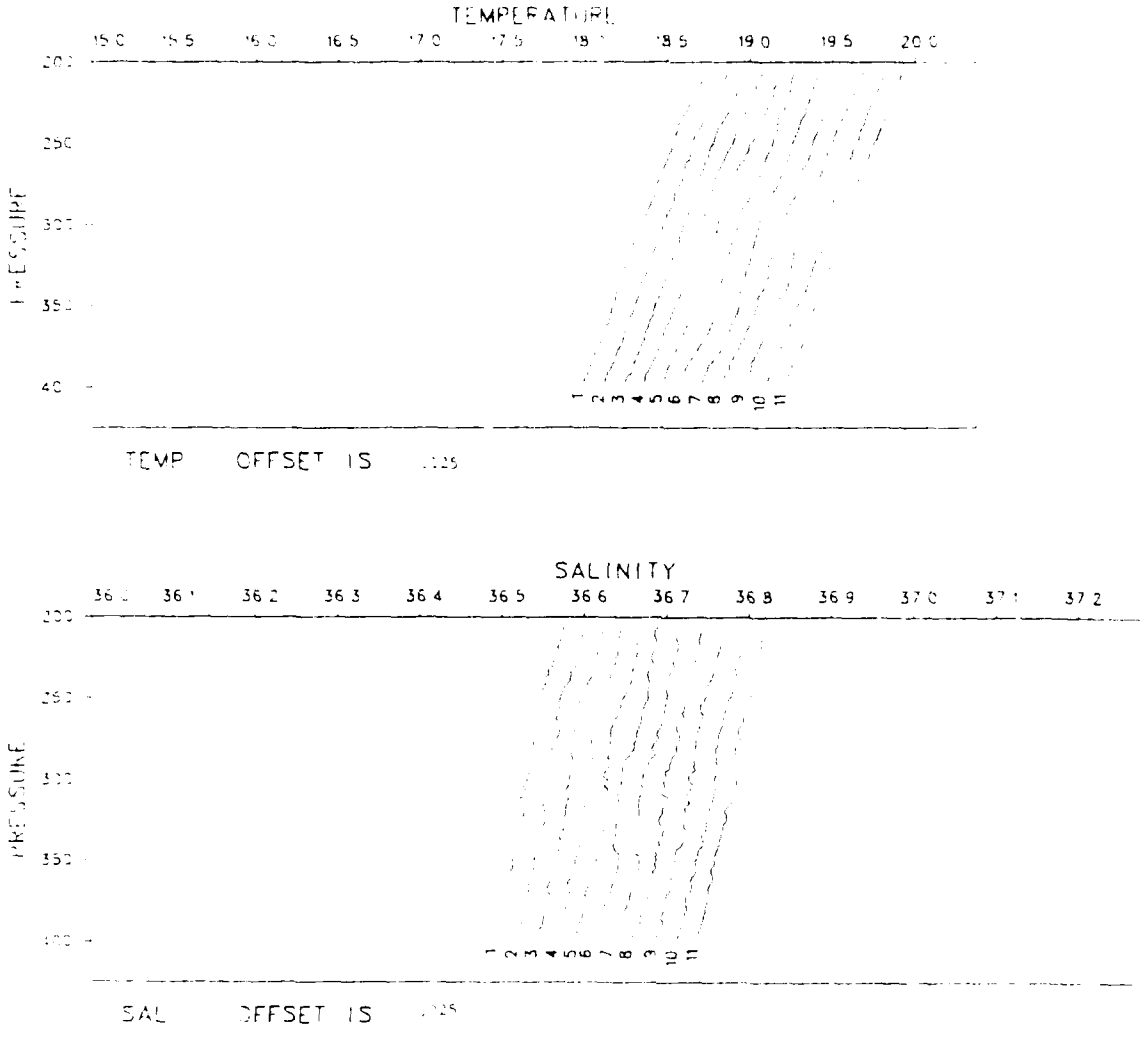

Figure 4.3h. CTD time series 026088
Start: 12 Sept 1201Z, 30°30.5'N, 71°46.9'W
Stop : 12 Sept 1400Z, 30°31.9'N, 71°47.5'W

STATION 026088

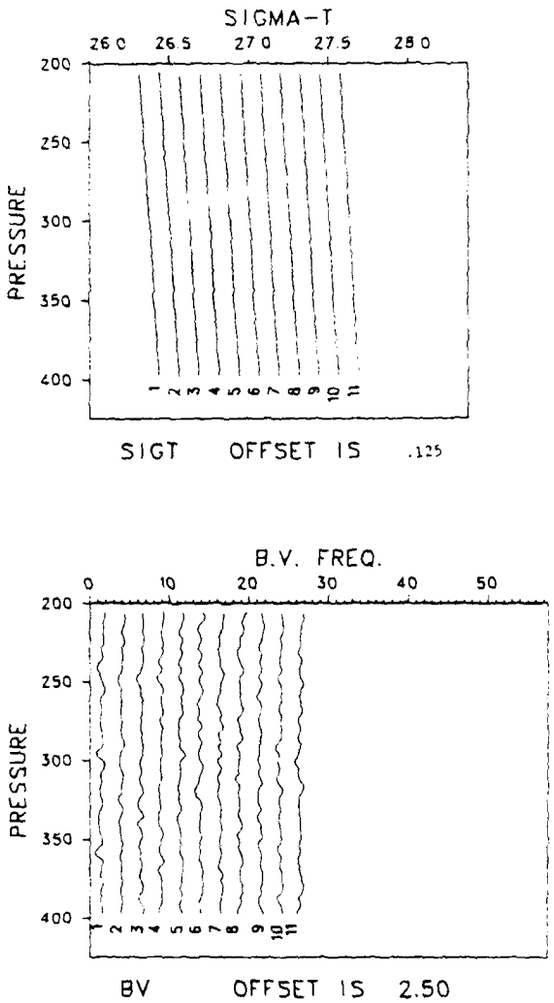

Figure 4.3h. (continued)

STATION 026088

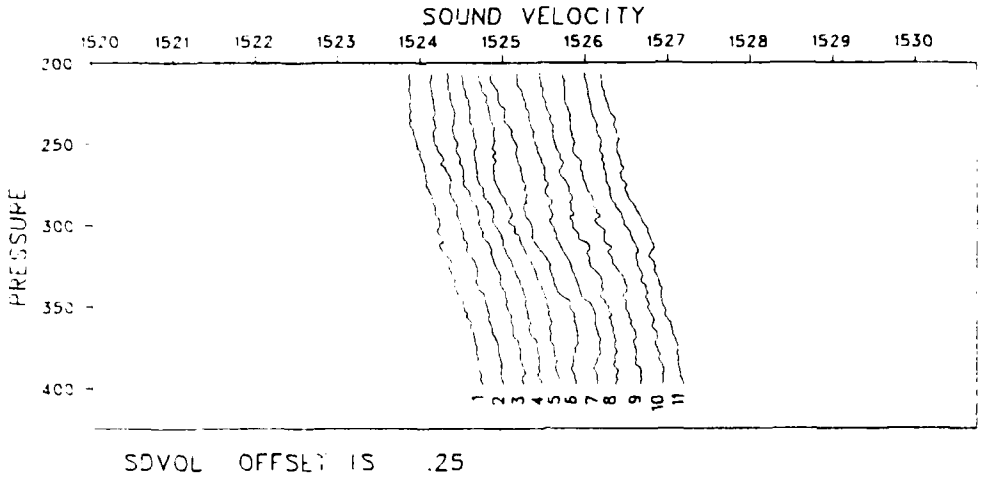

SDVOL OFFSET IS .25

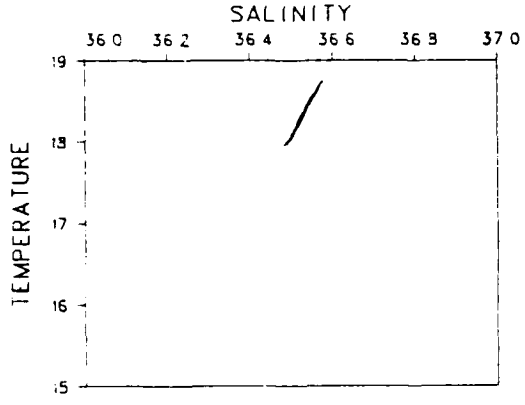

Figure 4.3h. (continued)

STATION 026089

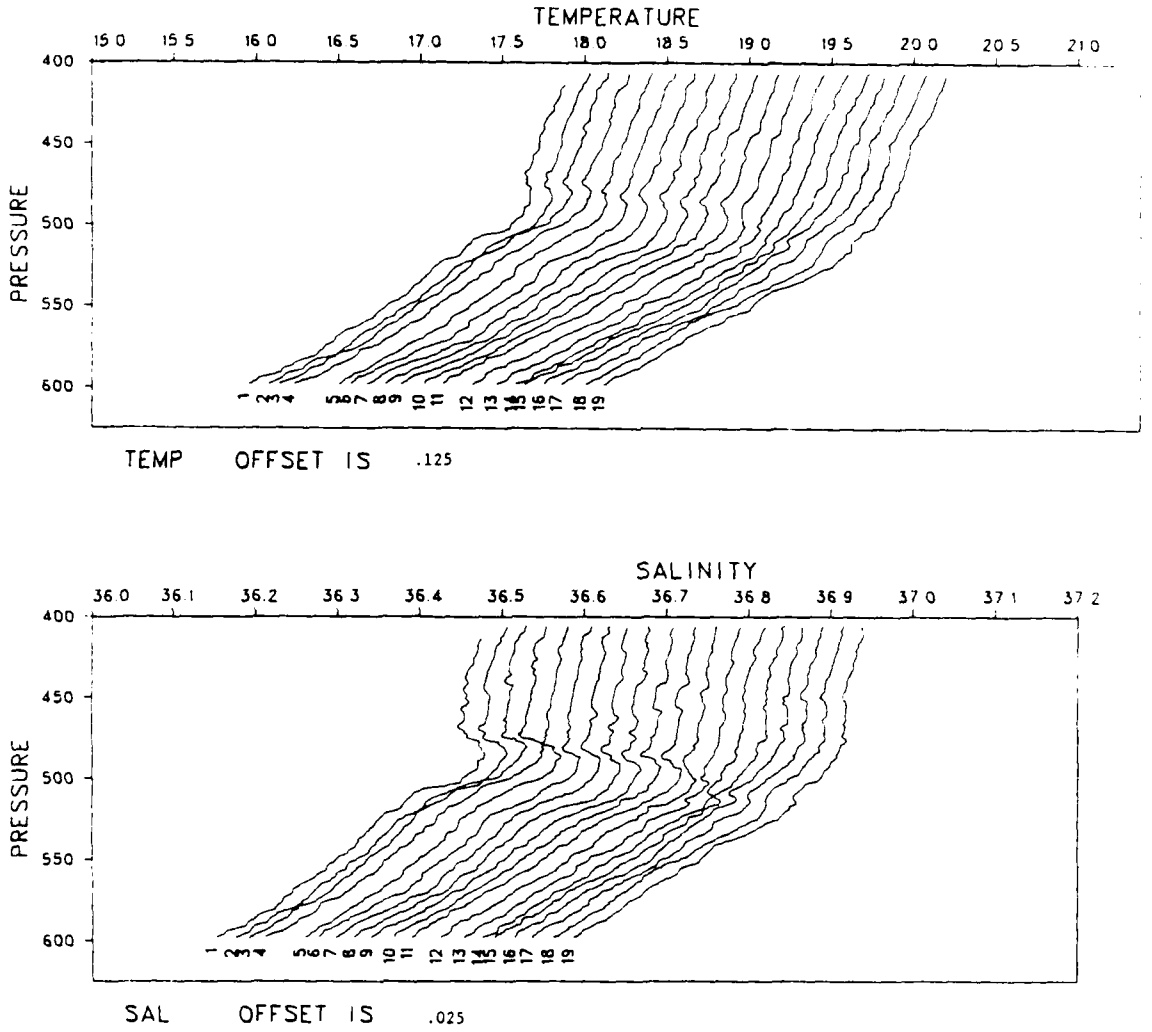

Figure 4.3i. CTD time series 026089
Start: 12 Sept 1425Z, 30°32.2'N, 71°47.7'W
Stop : 12 Sept 1632Z, 30°34.0'N, 71°48.1'W

STATION 026089

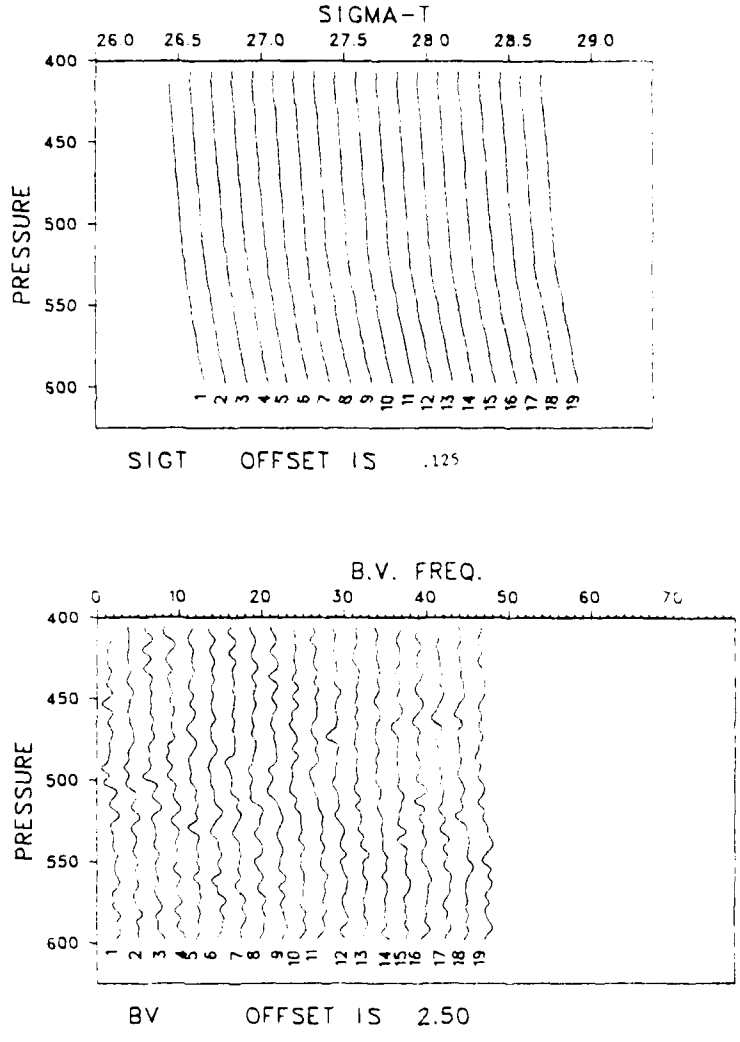

Figure 4.3i. (continued)

STATION 026089

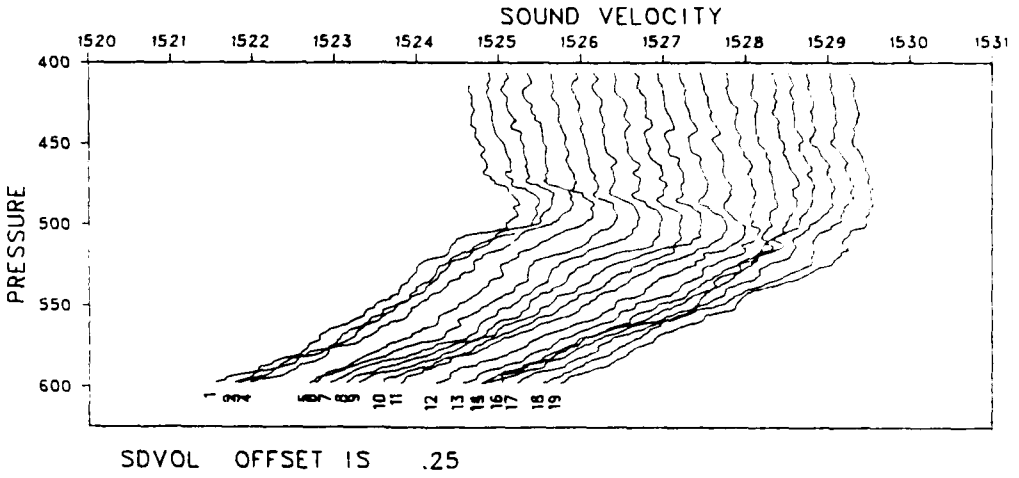

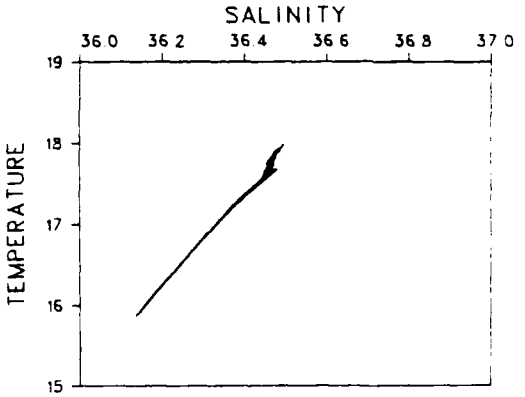

Figure 4.3i. (continued)

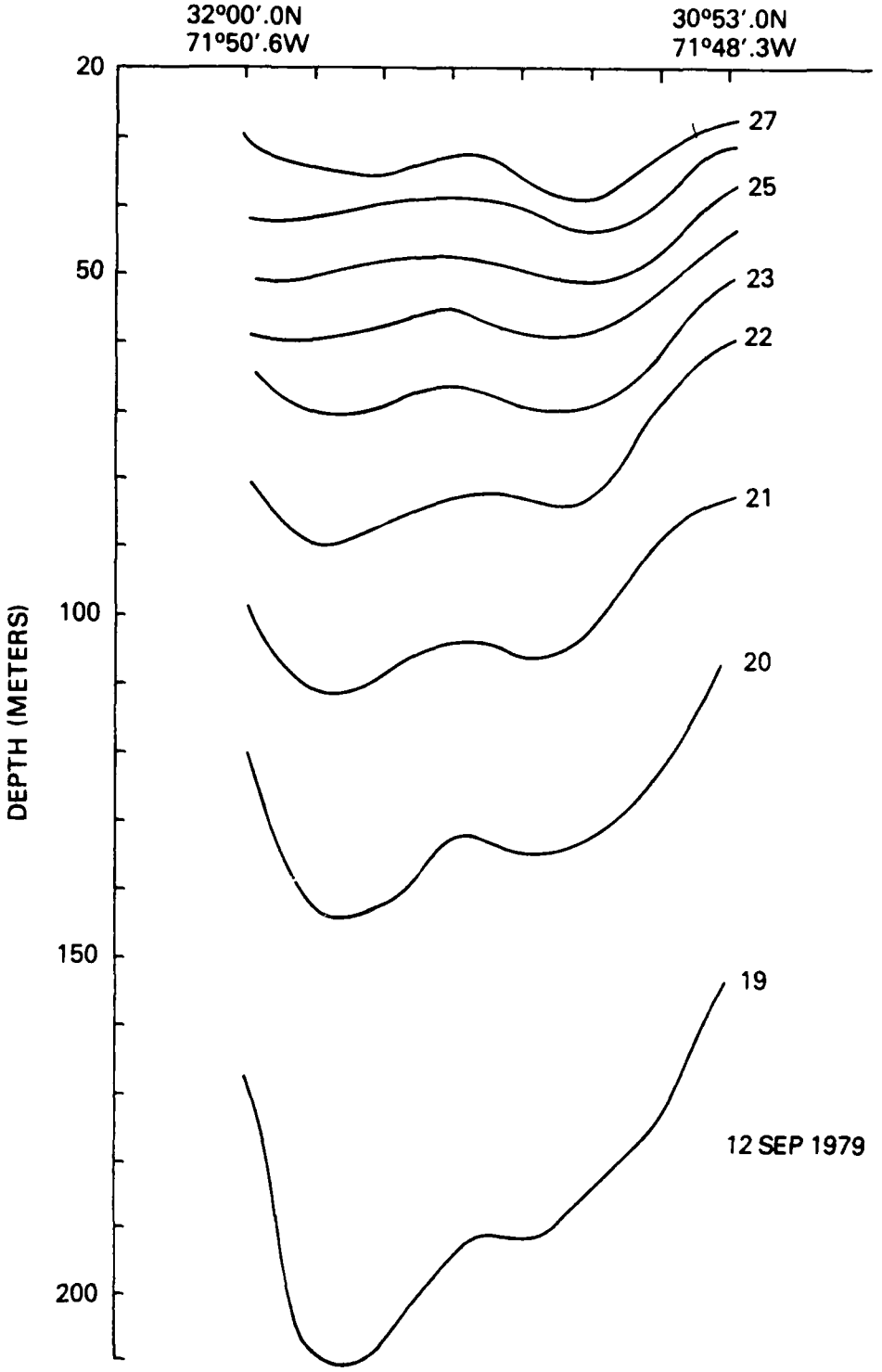

Figure 4.4. XBT section taken as the ship departed the operating area, heading northward (right to left). Drop positions, spaced 10 nm apart, are indicated by tics on the horizontal axis.

Section 5

XBT DATA

by Henry Perkins and Kenneth Nelson

5.0 XBT DATA

5.1 INTRODUCTION

The XBT, normally used for large scale surveys, has recently been successful, with suitable signal processing, in the measurement of finestructure; that is, temperature features having vertical scales of tens of centimeters. The XBT experiment reported here was designed to exploit this possibility and, by making a number of closely spaced drops, to measure the horizontal extent of finestructure or other small-scale features.

A total of 502 XBT's were launched and digitally recorded (at a rate of approximately 20 Hz) as the ship traversed six L-shaped patterns, each beginning and ending at nearly the same location. Each "L" pattern consisted of a northwesterly leg of about 20 km length, followed by a southwesterly leg of the same length (See Section 3), thus giving a total of twelve nearly straight legs.

5.2 HARDWARE DESCRIPTION

A system for digitally logging XBT data was built at NORDA and used at sea for the first time during the cruise reported here. The system consists of four launch station interfaces feeding through a common junction box into a four channel scanning analog to digital converter (see Fig. 5.1). The digital outputs of the four channel converter are processed within the calculator to produce calibrated and formatted data values, which are then recorded on the internal cassette tape drive or on an optional external 9-track digital tape recorder. An X-Y plotter permits graphic presentation of collected temperature profiles for the purpose of assessing data quality and completeness. A real-time clock provides time tagging of data points and sequencing control of the data collection operation.

Resistance measurements by the XBT probe are converted to a voltage output at the launch station and this voltage expanded at the junction box so that the desired temperature range corresponds to ±10 v, the full range of the digitizer, thereby minimizing least count errors. Final conversion to temperature and calculation of depth, based on elapsed probe fall time, is done by the calculator. During the cruise, the temperature range was from 10°C to 30°C which, combined with the 11-bit digitizer, gave a least significant count of 0.01°C. The signal was digitized at intervals of 0.0508 sec, corresponding to a vertical interval of approximately 21 cm between samples.

The XBT's which were used, Type T-7's manufactured by the Sippican Corporation, provided data from the surface to 760 m. They were purchased with the high precision option to minimize variability between probes and so were accurate to ±0.09°, twice the standard accuracy.

5.3 CALIBRATION PROCEDURES

Three types of calibration were performed. These were laboratory tests, shipboard tests, and in situ comparisons with CTD casts, as discussed in turn below.

Two randomly selected XBT's were submerged in a controlled temperature bath at the NAVOCEANO calibration facility. After calibration of the system using three precision resistors, corresponding to the bottom of the and the middle of the system range, the XBT's were connected to the system, the bath cycled from 10°C to 30°C, and the temperatures measured by the system were compared with independent measurements by

a primary platinum resistance standard (Guideline Model 9975) and a secondary quartz standard (Hewlett-Packard Model 2801A). This provided a full system test of all the circuitry and software, as well as a spot check of the probes. In all cases, total error was within 0.05°C. The error was dominated by 60 Hz pick-up (not present on shipboard) corresponding to about 0.02°C.

During shipboard operations, calibrations were checked regularly at three points by substitution of known resistors for the XBT. In no case were errors found which exceed one least significant count of the digitizer (about 0.011°C).

At the extremities of each "L" pattern, CTD casts were made and these were compared with the nearest XBT drop, thereby giving a total of 12 intercomparisons. Homogeneity of the upper mixed layer provided a one-point calibration check, indicating all XBT's to be within the specified 0.05°C. However, a serious discrepancy of some 30 m was found in the depth at which isotherms were intercepted toward the bottom of the drops, between 600 and 750 m in the top of the main thermocline. By eliminating all other possibilities, this discrepancy has been traced to an error in the standard formula used to compute depth as a function of time for T-7 probes. The depth was found to be given much better by

$$z = 6.47t - 0.00025t^2$$

than by the standard formula

$$z = 6.47t - 0.00216t^2$$

where z is in meters and t is in seconds. That is, the coefficient of the quadratic or "despooling" term was found to be nearly an order of magnitude smaller than that commonly used. Similar results have been obtained by other investigators (Seaver and Kuleshov, 1979; McDowell, 1977). However, caution should be observed in applying this formula in other cases where the mass or geometry of the probes may be different, or in other areas where temperatures, and hence viscosity of the water, may be different. The revised formula was used exclusively in this report.

5.4 DATA PROCESSING

The XBT data were initially edited to remove obvious errors, usually associated with breaks or leakage in the XBT wire. Operationally, obvious errors were defined as either a failure to record data or a discontinuity in the temperature profile. Data below any discontinuity were considered as suspect and omitted from further analysis. Temperature averages over short depth intervals from each remaining XBT drop were then compared at several d[illegible]s to further edit the data. Mean temperatures were calculated for 5 m dept[illegible] i[illegible]vals centered at the following depths: 17 m, 100 m, 200 m, 300 m, 400 m, [illegible] m, [illegible] m, and 700 m. If a temperature profile was biased at all depths by mo[illegible] than 0.40°C from neighboring profiles, it was omitted from further analysis. Additionally, comparisons of mean temperatures at the depth intervals specified above revealed occasional intermittent sensor malfunctions. Data below any such intermittency were also omitted.

Of the 502 XBT's employed during the experiment, 398 recorded temperature for the full depth range (0.33 m - 785.35 m), 61 XBT's recorded partial temperature records (failure occurring between 40 m and 785 m), and 43 XBT's did not produce any reliable data.

5.5 DATA PRESENTATION

Two sets of temperature profiles were plotted from the edited XBT data from each of the twelve legs. One set is for the full depth range 0 - 785 m (Fig. 5.2a-l). The other is for the subrange 0 - 150 m (Fig. 5.3a-l), the fivefold increase in resolution being useful in the mixed layer and seasonal thermocline. Position and time information for each XBT drop is given in Table 5.1. The temperature profiles reveal evidence of diurnal heating and cooling near the surface, as well as occasional temperature anomalies such as in the beginning of leg b near 150 m.

Differences between consecutive temperature samples were computed and are plotted for the upper 150 m in Fig. 5.4a-l. The approximate vertical temperature gradient in ^{o}C per meter can be obtained from these by multiplying the given temperature scale by three. Depth of the seasonal thermocline is seen to vary by about ±10 m over distances of 8 to 12 km. Contours were prepared for each leg, but do not add to the impressions gained from Figures 5.2-5.4, and so are not reproduced here.

Overall, gradients and their variability are much more pronounced in the seasonal thermocline than in the permanent thermocline, while the very weak gradients in the 18^{o} water are not resolved because of least count resolution in the digitizer.

Smoothed versions of temperature gradient, computed in the least squares sense over 5 consecutive points, corresponding to about 1.5 m in the vertical, provide another view of selected profiles. Regions in the pronounced seasonal thermocline can be found where the gradient nearly vanishes (40 m level in Fig. 5.5), deeper regions where the gradient is indistinguishable from zero over several meters (125 to 130 m in Fig. 5.6), or pronounced temperature inversions in the surface mixed layer (Fig. 5.7).

Vertical wavenumber spectra were computed for the three depth intervals 50 - 200 m (just below the seasonal thermocline), 200 - 500 m (18^{o} water), and 500 - 785 m (top of the permanent thermocline). Each time series was detrended by a second order polynomial least squares fit and a cosine-taper data window was applied before the spectra were computed. Samples of the temperature data after detrending are shown in Figure 5.8. Frequency spectra for each depth range were first ensemble averaged for each leg. Differences in spectral level between legs were small. The spectra were further averaged according to whether the data were taken on a northwesterly or on a southwesterly leg. No significant differences were observed. Finally, the spectra were ensemble averaged over all legs for each depth range (see Table 5.2 for number of records included in each ensemble), and the results are shown in Figure 5.9.

A least square fit was performed on the spectral estimates between 0.13 Hz and 1.3 Hz to estimate the slope of the spectrum for each depth range. Table 5.3 lists these results, along with the total temperature variance in each depth region after detrending. The present spectra were compared with the results of Hayes et al., (1975), who presented vertical wavenumber spectra from the Sargasso Sea (within 400 km of the present measurements). Their data were collected during October, 1971, and July 1973. The present spectral levels agree within a factor of 2 with Hayes et al., for the 50-200 m and 200-500 m depth ranges at frequencies below 1 Hz (wavelengths greater than about 1 m). The noise level appears to be reached in the present data between 1 and 2 Hz at these depth ranges, and is in reasonable agreement with the [illegible] of the XBT digital system.

Coherence calculations were also performed for the three depth regions between several representative adjacent XBT drops (after prewhitening the temperature data by first differencing in the vertical direction). As expected for the large horizontal XBT drop separations (of order 0.5 km) [Desaubies (1976), and Joyce and Desaubies (1977)], the dropped horizontal temperature coherence levels were not significant at the vertical wavenumbers resolved in the present data.

5.6 REFERENCES

Desaubies, Y.J.F. (1976). Analytical Representation of Internal Wave Spectra. J. Phys. Oceanography, 6, p. 976-981.

Hayes, S.P., T. M. Joyce, R. C. Millard, Jr. (1975). Measurements of Vertical Fine Structure in the Sargasso Sea. J. Geo. Res., 80, p. 314-318.

Joyce, T. M. and Y. J. F. Desaubies (1977). Discrimination Between Internal Waves and Temperature Finestructure. J. Phys. Oceanography, 7, p. 22-32.

McDowell, S. (1977). A Note on XBT Accuracy. Polymode News, no. 29, June 17.

Seaver, G. and S. Kuleshov (1979). XBT Accuracy. Polymode News, no. 72, Nov. 16.

Table 5.1

XBT drop time and position

No	Leg a Day	Time	Lat.	Long.	Leg b Day	Time	Lat.	Long.
1	9/6	19:24:01	30 25.9	71 34.5	9/7	21:11:14	30 33.7	71 47.8
2		27:01	26.2	35.7		14:00	33.4	48.1
3		30:18	26.4	37.1		17:00	33.2	48.4
4		33:00	26.3	38.0		20:00	33.0	48.7
5		36:02	26.4	39.4		23:01	32.8	49.0
6		39:02	27.1	39.7		26:01	32.6	49.3
7		42:00	27.4	41.0		28:59	32.4	49.6
8		45:00	27.6	42.2		31:59	32.1	49.9
9		48:01	27.8	43.5		34:59	31.8	50.2
10		51:02	27.9	46.8		38:01	31.7	50.4
11		53:59	28.1	44.0		41:00	31.4	50.7
12		57:00	28.2	41.3		44:00	31.2	51.0
13						50:03	30.7	51.2
14		20:01:03	28.5	41.6		53:01	30.5	51.4
15		04:01	28.7	41.9		55:00	30.3	51.7
16		07:00	29.0	42.2		58:21	30.1	52.
17		10:00	29.3	42.4	[illegible]	[illegible]	29.8	52.4
18		13:00	29.5	42.7		07:02	29.6	52.6
19		16:01	29.7	43.0		10:59	29.4	52.9
20		19:00	30.0	43.3		13:59	29.1	53.1
21		22:01	30.3	43.6		16:59	28.9	53.4
22		25:06	30.5	43.9		19:59	28.6	53.7
23		28:00	30.7	44.1		30:00	28.4	53.9
24		32:48	31.1	44.5				
25		36:00	31.3	44.8		33:36	28.1	54.2
26		38:48	31.5	45.0		36:05	27.9	54.5
27		42:00	31.8	45.3		28:57	27.7	54.7
28		45:02	32.0	45.6		32:01	27.4	55.0
29		48:02	32.2	45.9		34:59	27.2	55.
30		51:01	32.4	46.2		37:59	27.0	55.5
31		54:02	32.7	46.5				
32						43:59	26.5	56.
33		58:05	33.1	47.1		47:01	26.3	56.2
34		59:14	33.1	47.1		49:59	26.1	56.5
35		21:02:01	33.3	47.1		53:02	25.1	57.
36						56:06	25.7	56.2
37						59:14	25.5	57.1
38					31	2:21	25.3	57.

Table 5.1 (cont.)

XBT drop time and position

No	Leg c Day	Time	Lat.	Long.	Leg d Day	Time	Lat.	Long.
1	9/7	3:58:01	30 25.6	71 37.8	9/7	6:23:00	30 33.7	71 48.1
2						26:00	33.6	48.3
3		4:03:02	25.9	38.1		29:28	33.5	48.6
4		06:02	26.0	38.3		32:01	33.4	48.7
5		09:01	26.2	38.6		35:00	33.2	48.9
6		12:11	26.3	38.8		38:00	33.1	49.1
7		15:32	26.5	39.0		41:00	32.9	49.3
8		18:03	26.7	39.2				
9		21:01	26.8	39.4		44:53	32.7	49.6
10		24:00	27.0	39.7		48:00	32.6	49.8
11		27:00	27.1	39.9		51:00	32.4	50.0
12		30:00	27.3	40.1		54:00	32.3	50.3
13		33:01	27.5	40.3		57:01	32.1	50.5
14		36:25	27.7	40.6		7:00:00	32.0	50.7
15		38:59	27.8	40.8		03:24	31.8	50.9
16		42:00	28.0	41.1		06:00	31.6	51.1
17		45:00	28.2	41.3		09:00	31.5	51.2
18		48:00	28.4	41.5		12:00	31.3	51.4
19		51:00	28.5	41.7		15:00	31.1	51.6
20		54:00	28.7	42.0		18:00	30.9	51.8
21		57:00	28.8	42.2		21:00	30.7	52.1
22		5:00:00	29.0	42.4				
23		03:01	29.2	42.6				
24		06:00	29.4	42.8		28:00	30.2	52.6
25		09:00	29.5	43.0		31:00	30.0	52.9
26		12:00	29.7	43.2		34:00	29.9	53.0
27		15:00	29.9	43.4		37:00	29.7	53.2
28		18:00	30.1	43.6		40:00	29.5	53.4
29		21:00	30.3	43.8		43:00	29.3	53.6
30		24:00	30.4	44.1		46:00	29.1	53.8
31		27:00	30.6	44.3				
32		30:00	30.8	44.5		52:00	28.7	54.2
33		33:00	31.0	44.7		55:00	28.5	54.4
34		36:05	31.2	44.9		58:01	28.2	54.6
35		39:00	31.3	45.1		8:01:00	28.0	54.8
36		42:00	31.5	45.3		04:02	27.8	55.0
37		45:00	31.7	45.5		07:00	27.6	55.2
38		48:00	31.9	45.7		10:01	27.4	55.4
39		51:00	32.1	45.9		13:02	27.2	55.6
40		54:00	32.2	46.2		16:02	27.0	55.8
41		56:59	32.4	46.4		19:00	26.8	56.0
42						22:00	26.6	56.2
43						25:00	26.4	56.4
44		6:04:00	32.8	46.9		28:00	26.2	56.6
45						31:00	26.0	56.8
46		08:13	33.1	47.1		34:03	25.8	57.0
47		11:00	33.3	47.3		37:00	25.6	57.2
48		14:00	33.4	47.5		40:00	25.4	57.4
49		17:00	33.6	47.7		43:00	25.1	57.6
50		20:00	33.8	47.9		46:00	24.9	57.8

Table 4.1 cont.

XBT drop time and position

No	Leg e Day	Time	Lat.	Long.	Leg f Day	Time	Lat.	Long.
1	9/7	18:05:	30 25.8	71 37.3	9/7	21:	32	71 47.9
2		08:01	25.8	37.9		11:	33.7	47.1
3		11:01	25.9	37.6		14:	33.5	47.9
4		14:38	26.1	37.6		17:	33.4	48.4
5		20:04	26.4	38.2		20:00	33.3	48.6
6		23:02	26.6	38.4		23:01	33.1	48.8
7		26:17	26.8	38.6		26:01	33.0	49.0
8		29:00	26.9	38.8		29:01	32.8	49.2
9		32:01	27.1	39.0				
10		35:01	27.3	39.2		34:58	32.6	49.6
11		38:16	27.4	39.4		38:00	32.4	49.8
12		40:59	27.6	39.6		41:00	32.2	50.0
13		44:00	27.7	39.7		44:00	32.1	50.2
14		46:59	27.9	39.9		47:00	31.9	50.4
15		50:13	28.0	40.1				
16		53:01	28.2	40.3		53:00	31.5	50.9
17		56:00	28.3	40.5				
18		59:00	28.5	40.6		59:00	31.2	51.3
19		19:02:00	28.6	40.8		22:02:00	31.0	51.5
20		05:00	28.8	41.0		05:00	30.8	51.7
21		08:00	28.9	41.2		08:00	30.6	51.9
22		11:01	29.1	41.4		11:00	30.4	52.1
23		13:59	29.2	41.5		14:00	30.3	52.2
24		17:00	29.4	41.7		17:00	30.1	52.4
25		20:01	29.5	41.9				
26		22:59	29.7	42.0				
27		25:59	29.8	42.2		26:01	29.5	53.0
28		29:02	30.0	42.3		29:00	29.4	53.2
29		33:01	30.2	42.6		32:00	29.2	53.4
30		36:00	30.3	42.9		35:00	29.0	53.6
31		38:59	30.5	43.1				
32		41:59	30.6	43.4		39:06	28.8	53.8
33		45:00	30.8	43.6		42:21	28.6	54.0
34		48:00	31.0	43.8		45:04	28.4	54.2
35		50:59	31.1	43.9		48:01	28.2	54.4
36		54:00	31.3	44.1		51:00	28.0	54.6
37		57:00	31.4	44.2		54:00	27.9	54.8
38		20:00:00	31.6	44.4		57:31	27.6	55.0
39		03:01	31.7	44.6		23:00:22	27.5	55.2
40		06:01		44.8				
41		09:01		45.0		21:31	26.9	56.0
42		12:01	32.	45.2		24:03	26.7	56.2
43		15:00	32.3	45.4		27:00	26.5	56.4
44		17:59	32.4	45.6		30:01	26.3	56.6
45		20:59	32.5	45.7		33:00	26.1	56.8
46						36:02	25.9	57.0
47		27:00	32.8	46.0		39:00	25.8	57.2
48		30:00	32.9	46.2		42:01	25.4	57.4
49		33:	33.	46.				
50		36:	33.3	46.5		45:04	25.1	57.6
						49:	24.9	57.8
		39:44	33.5	47.1				

Table [illegible]

XBT drop time and position

No	Leg g Day	Time	Lat.	Long.	Leg f Day	[illegible]	[illegible]	[illegible]
1	9/10	1:28:59	30 27.0	71 39.4	[illegible]	[illegible]	[illegible]	[illegible]
2		31:59	27.2	40 [illegible]		[illegible]	[illegible]	[illegible]
3		35:00	27.4	40.4		[illegible]	[illegible]	[illegible]
4		38:01	27.7	40.7				
5		41:00	27.9	41.1		[illegible]	38.3	49.
6		44:00	28.2	41.4		[illegible]	38.1	49.
7		47:00	28.4	41.8		[illegible]	[illegible]	[illegible]
8		50:00	28.7	42.1		[illegible]	[illegible]	
9						[illegible]		
10		56:00	29.1	42.6		[illegible]		[illegible]
11		59:00	29.2	42.9		[illegible]		[illegible]
12		2:02:00	29.5	43.2				
13		05:00	29.7	43.5		[illegible]	[illegible]	[illegible]
14		08:00	29.9	43.8		[illegible]	[illegible]	[illegible]
15		11:01	30.1	44.1		[illegible]	[illegible]	[illegible]
16		14:00	30.4	44.4		[illegible]	[illegible]	[illegible]
17		17:00	30.6	44.7				
18		20:00	30.8	45.0		[illegible]	[illegible]	[illegible]
19		23:00	31.1	45.3		[illegible]	[illegible]	[illegible]
20		26:00	31.3	45.6		[illegible]	[illegible]	[illegible]
21						[illegible]	[illegible]	[illegible]
22		32:02	31.8	46.2		[illegible]	[illegible]	[illegible]
23		35:00	32.0	46.5		[illegible]	[illegible]	[illegible]
24		38:30	32.3	46.8		[illegible]	[illegible]	[illegible]
25		41:07	32.6	47.0				
26		44:11	32.8	47.3				
27		47:12	33.1	47.7		[illegible]	[illegible]	[illegible]
28								[illegible]
29								
30						[illegible]	[illegible]	[illegible]
31						[illegible]	[illegible]	[illegible]
32						[illegible]	[illegible]	[illegible]
33						[illegible]	[illegible]	[illegible]
34						[illegible]	[illegible]	[illegible]
35						[illegible]	[illegible]	[illegible]
36						[illegible]	[illegible]	[illegible]

Table 5.1 (cont.)

XBT drop time and position

No	Leg i Day	Time	Lat.	Long.	Leg j Day	Time	Lat.	Long.
1	9/10	11:26:03	30 26.6	71 38.6	9/10	14:00:00	30 34.4	71 48.4
2		29:00	26.7	38.8		03:00	34.2	48.5
3						06:00	33.9	48.6
4		32:53	27.0	39.1		09:00	33.7	48.7
5		35:19	27.2	39.3		12:00	33.4	48.8
6		37:30	27.3	39.4		15:00	33.2	48.9
7		40:00	27.5	39.6		18:01	33.0	49.1
8		43:01	27.7	39.9		21:00	32.7	49.3
9		45:01	27.8	40.0		24:00	32.5	49.5
10		48:00	28.0	40.2				
11		51:00	28.2	40.5				
12		54:00	28.3	40.7		31:02	31.9	50.0
13		56:59	28.5	41.0		34:02	31.7	50.2
14		59:59	28.7	41.2		37:00	31.5	50.4
15		12:02:59	28.9	41.4		40:00	31.3	50.6
16		05:59	29.1	41.7		43:00	31.1	50.8
17		08:59	29.3	41.9		46:11	30.9	51.0
18		11:59	29.5	42.2		49:02	30.7	51.3
19		15:00	29.7	42.4		52:00	30.5	51.6
20		17:59	29.9	42.6		55:01	30.3	51.8
21		20:59	30.1	42.9		58:01	30.0	52.1
22		23:59	30.3	43.1		15:01:00	29.8	52.4
23		26:59	30.5	43.4		04:00	29.6	52.6
24		29:59	30.7	43.6		07:19	29.3	52.8
25		32:59	30.9	43.8		10:01	29.1	53.0
26		35:59	31.1	44.0		13:12	28.8	53.3
27		39:00	31.2	44.3		16:01	28.6	53.5
28		42:00	31.4	44.5				
29		45:06	31.6	44.7		19:31	28.5	53.7
30		48:00	31.8	45.0		22:02	28.3	53.9
31						24:59	28.2	54.1
32		52:00	32.1	45.3		28:00	28.0	54.4
33		55:00	32.3	45.6		31:00	27.8	54.6
34		58:01	32.5	45.8		34:02	27.6	54.8
35		13:01:01	32.7	46.1		37:01	27.3	55.1
36		04:00	32.9	46.3		40:00	27.1	55.3
37		07:00	33.1	46.5		43:01	26.9	55.5
38		10:00	33.3	46.7		46:00	26.6	55.8
39						49:00	26.4	56.0
40	9/10	14:00	33.6	47.0		52:01	26.2	56.2
41						55:01	26.0	56.4
42						58:00	25.8	56.7

Table 5.1 (cont.)

XBT drop time and position

No	Leg k Day	Time	Lat.	Long.	Leg l Day	Time	Lat.	Long.
1	9/10	20:52:00	30 25.8	71 37.6	9/11	1:16:01	30 [illegible]	[illegible]
2		55:00	26.0	37.8		19:[illegible]	33.[illegible]	[illegible]
3		58:00	26.2	38.0		22:[illegible]	[illegible].9	[illegible]
4		21:01:02	26.4	38.		25:00	[illegible].7	[illegible]
5		03:59	26.5	38.5		28:01	32.5	4[illegible]
6		07:00	26.7	38.8		[illegible]:[illegible]	32.2	49.7
7		10:00	26.8	39.0		[illegible]:[illegible]	32.0	[illegible]
8		13:00	27.0	39.2		[illegible]:[illegible]	[illegible].7	[illegible]
9		16:00	27.2	39.5		[illegible]:[illegible]	[illegible]	[illegible]
10		19:00	27.3	39.7		[illegible]	[illegible]	[illegible]
11		21:59	27.5	39.9				
12		25:00	27.7	40.1		[illegible]:[illegible]	[illegible]	[illegible]
13		28:02	27.9	40.4		[illegible]:[illegible]	[illegible]	[illegible]
14		31:00	28.1	40.6		[illegible]:[illegible]	[illegible]	[illegible]
15	9/10	34:00	28.3	40.8		[illegible]:[illegible]	[illegible]	[illegible]
16		37:00	28.5	41.1		[illegible]:[illegible]	[illegible]	[illegible]
17		40:00	28.7	41.4	9/11	[illegible]:[illegible]	[illegible]	[illegible]
18		43:00	28.9	41.6		[illegible]:[illegible]	[illegible]	[illegible]
19		46:00	29.1	41.9		[illegible]:[illegible]	[illegible]	[illegible]
20		49:00	29.2	42.1		[illegible]:[illegible]	[illegible]	[illegible]
21		52:00	29.4	42.4		[illegible]:[illegible]	[illegible]	[illegible]
22		55:00	29.6	42.7		[illegible]:[illegible]	[illegible]	[illegible]
23		58:00	29.8	42.9		[illegible]:[illegible]	[illegible]	[illegible]
24		22:01:00	30.0	43.2		[illegible]:[illegible]	[illegible]	[illegible]
25		04:00	30.1	43.4		[illegible]:[illegible]	[illegible]	[illegible]
26		07:00	30.3	43.6		[illegible]:[illegible]	[illegible]	[illegible]
27		09:59	30.5	43.8		[illegible]:[illegible]	[illegible]	[illegible]
28						[illegible]:[illegible]	[illegible]	[illegible]
29		16:00	30.9	44.2		[illegible]:[illegible]	[illegible]	[illegible]
30		19:00	31.0	44.4		[illegible]:[illegible]	[illegible]	[illegible]
31		22:00	31.2	44.8		[illegible]:[illegible]	[illegible]	[illegible]
32		25:00	31.4	44.8		[illegible]:[illegible]	[illegible]	[illegible]
33		27:01	31.5	45.0		[illegible]:[illegible]	[illegible]	[illegible]
34		31:00	31.8	45.3		[illegible]:[illegible]	[illegible]	[illegible]
35		33:59	32.0	45.5		[illegible]:[illegible]	[illegible]	[illegible]
36		37:00	32.2	45.8		[illegible]:[illegible]	[illegible]	[illegible]
37		40:01	32.4	46.1		1:01:[illegible]	[illegible]	[illegible]
38		43:00	32.6	46.3				
39					9/11	[illegible]:[illegible]	[illegible]	[illegible]

TABLE 5.2

Number of Records Averaged Per Leg

LEG (Number of XBTs)	60-200m	200-500m	500-785m
A (38)	33	31	26
B (39)	33	33	32
C (50)	45	42	41
D (50)	44	42	41
E (52)	48	47	46
F (51)	43	39	39
G (27)	25	23	22
H (36)	27	26	25
I (40)	35	31	27
J (42)	36	35	34
K (38)	36	34	34
L (39)	35	31	31
CROSSWIND	222	208	196
DOWNWIND	218	206	202

TABLE 5.3

Vertical Wave Number Spectral Slopes and Temperature Variance

	DEPTH RANGE		
	60-200m	200-500m	500-785m
SLOPE	-3.2 ± 0.4	-2.6 ± 0.1	-2.5 ± 0.2
VARIANCE	$8.4\times10^{-3}\,^{o}C^{2}$	$5.7\times10^{-4}\,^{o}C^{2}$	$3.3\times10^{-3}\,^{o}C^{2}$

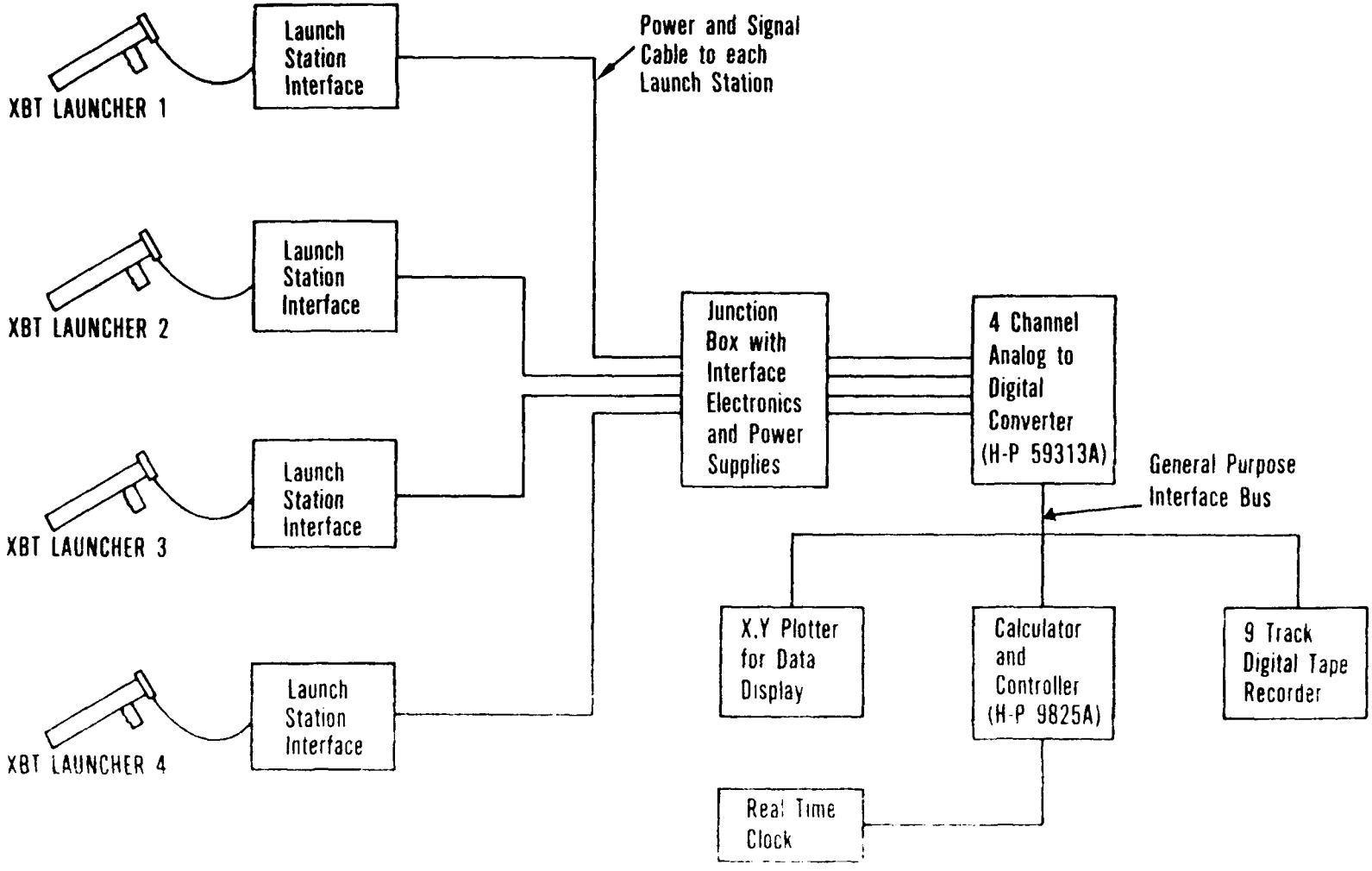
XBT LAUNCHER 1
XBT LAUNCHER 2
XBT LAUNCHER 3
XBT LAUNCHER 4
Launch Station Interface
Launch Station Interface
Launch Station Interface
Launch Station Interface
Power and Signal Cable to each Launch Station
Junction Box with Interface Electronics and Power Supplies
4 Channel Analog to Digital Converter (H-P 59313A)
General Purpose Interface Bus
X,Y Plotter for Data Display
Calculator and Controller (H-P 9825A)
9 Track Digital Tape Recorder
Real Time Clock

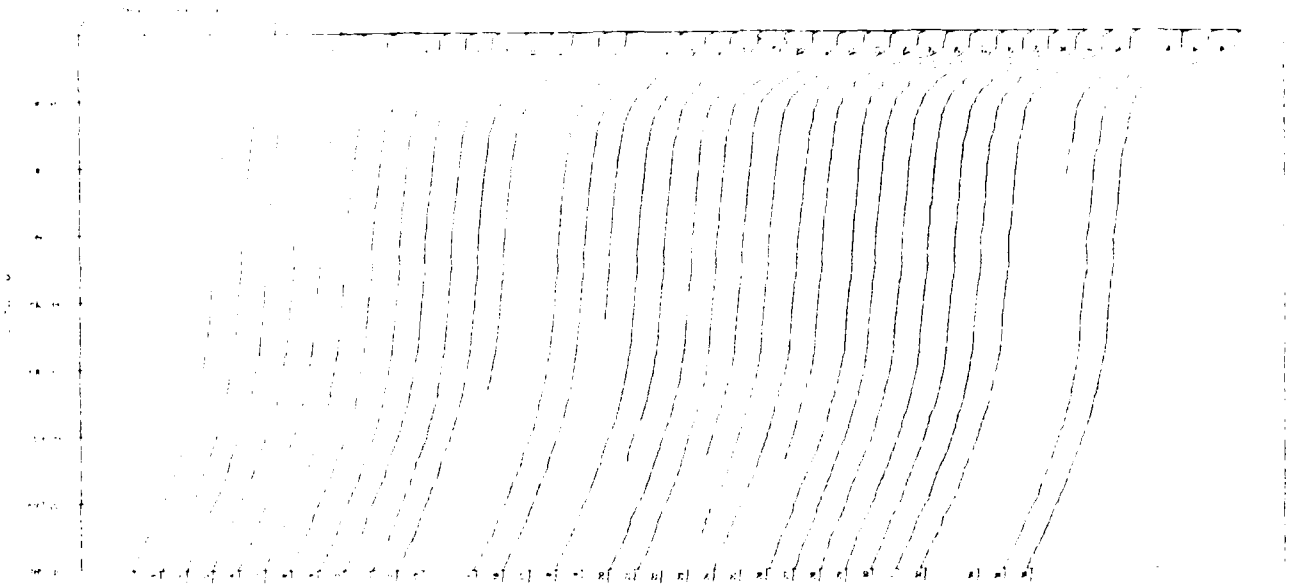

Figure 5.2a. XBT profiles, leg a of "L" pattern

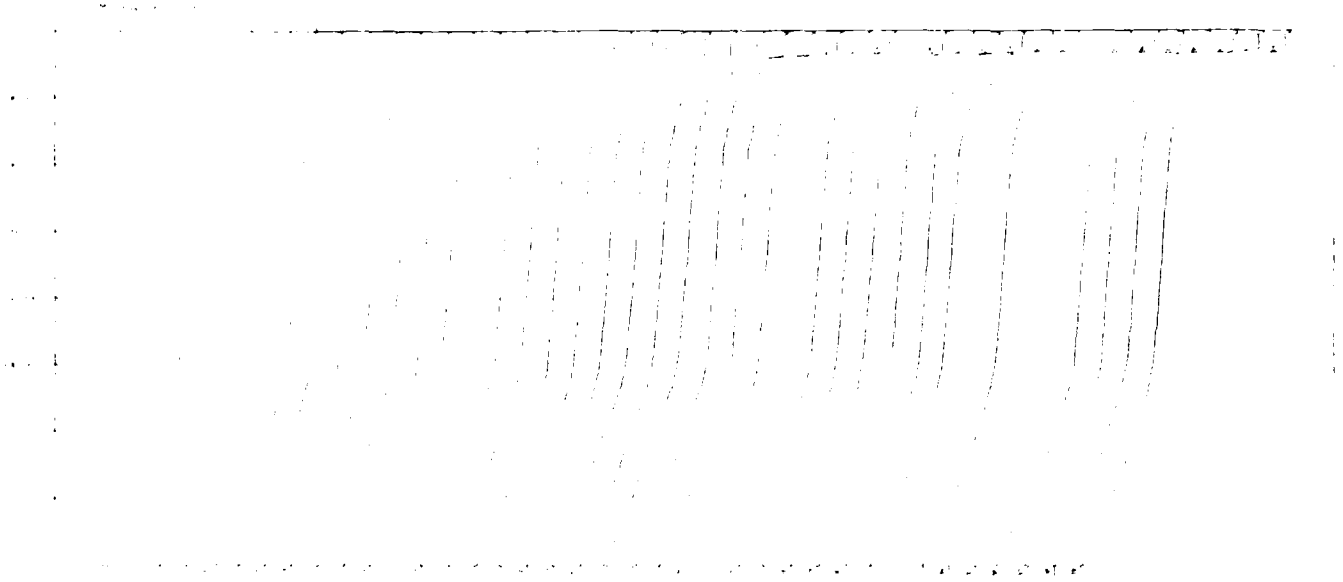

Figure 5.2b. XBT profiles, leg b of "L" pattern

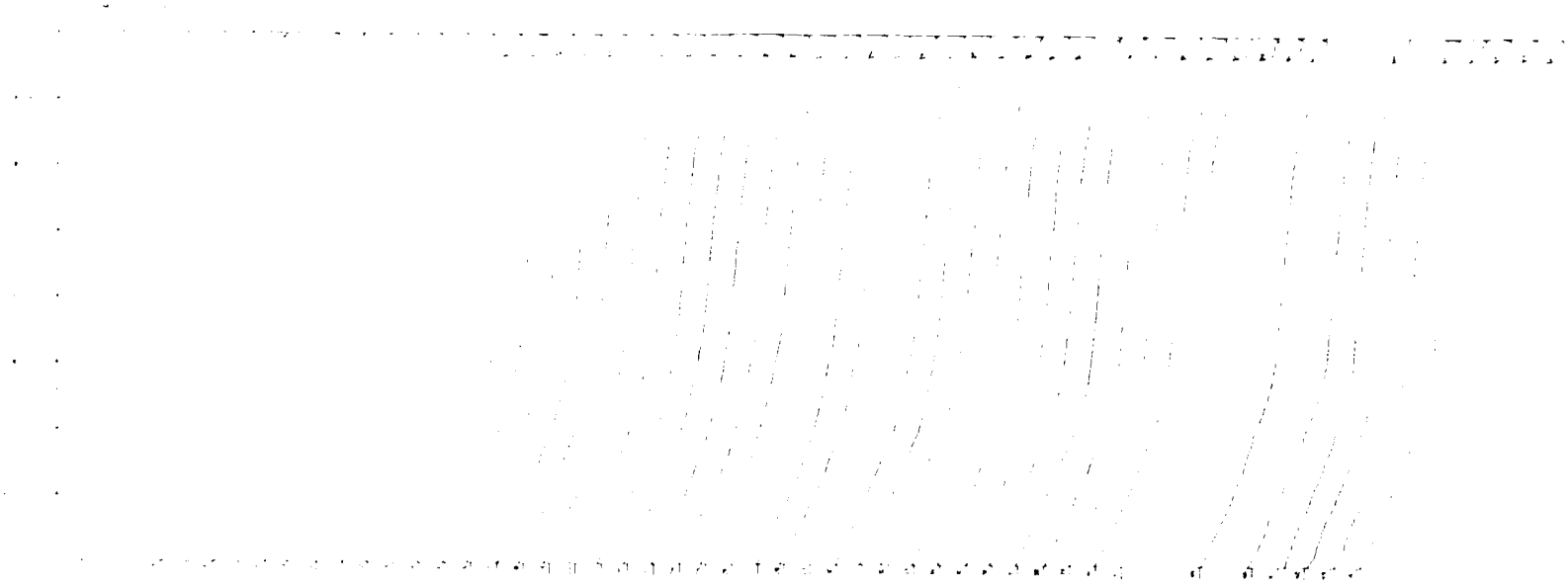

Figure 5.2c. XBT profiles, leg c of "L" pattern

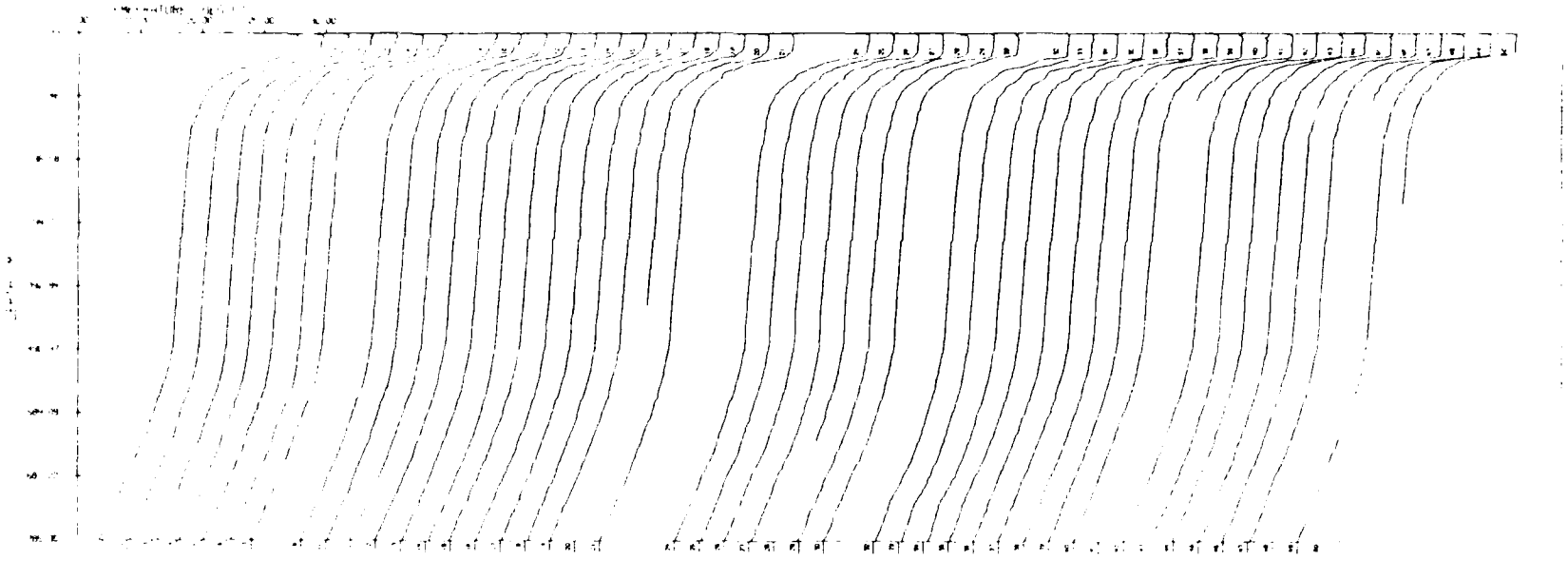

Figure 5.2d. XBT profiles, leg d of "L" pattern

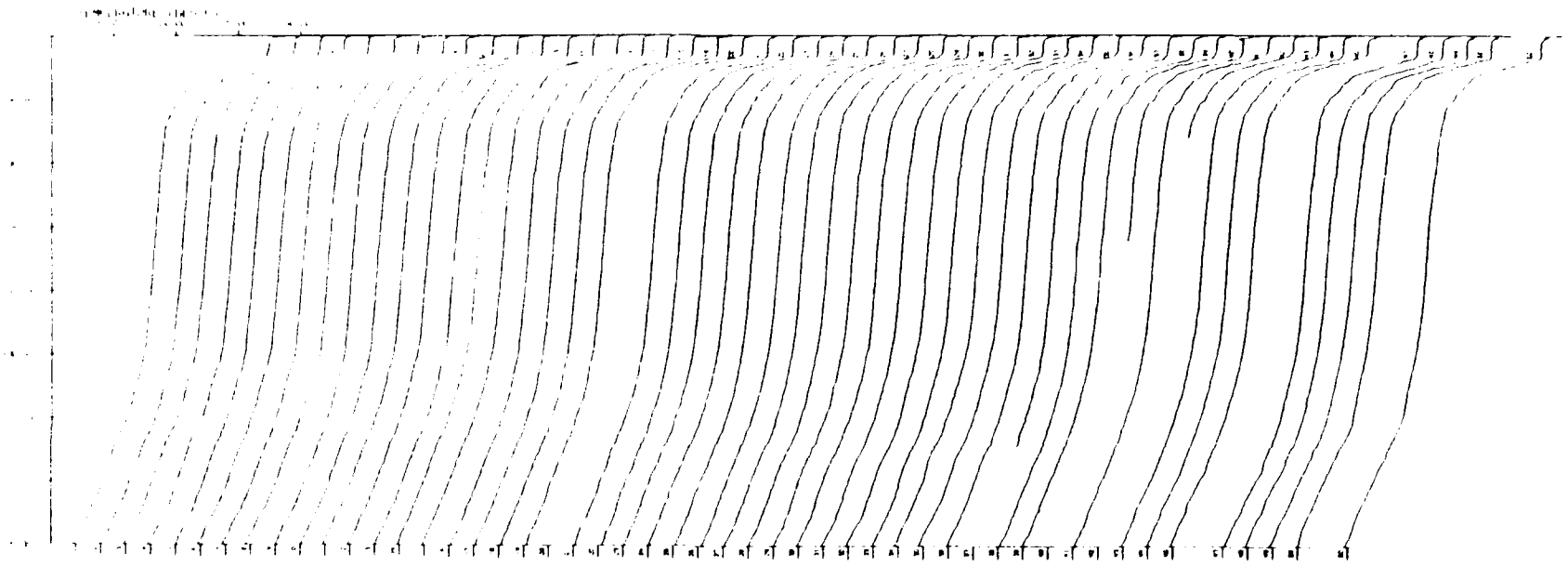

Figure 5.2e. XBT profiles, leg e of "L" pattern

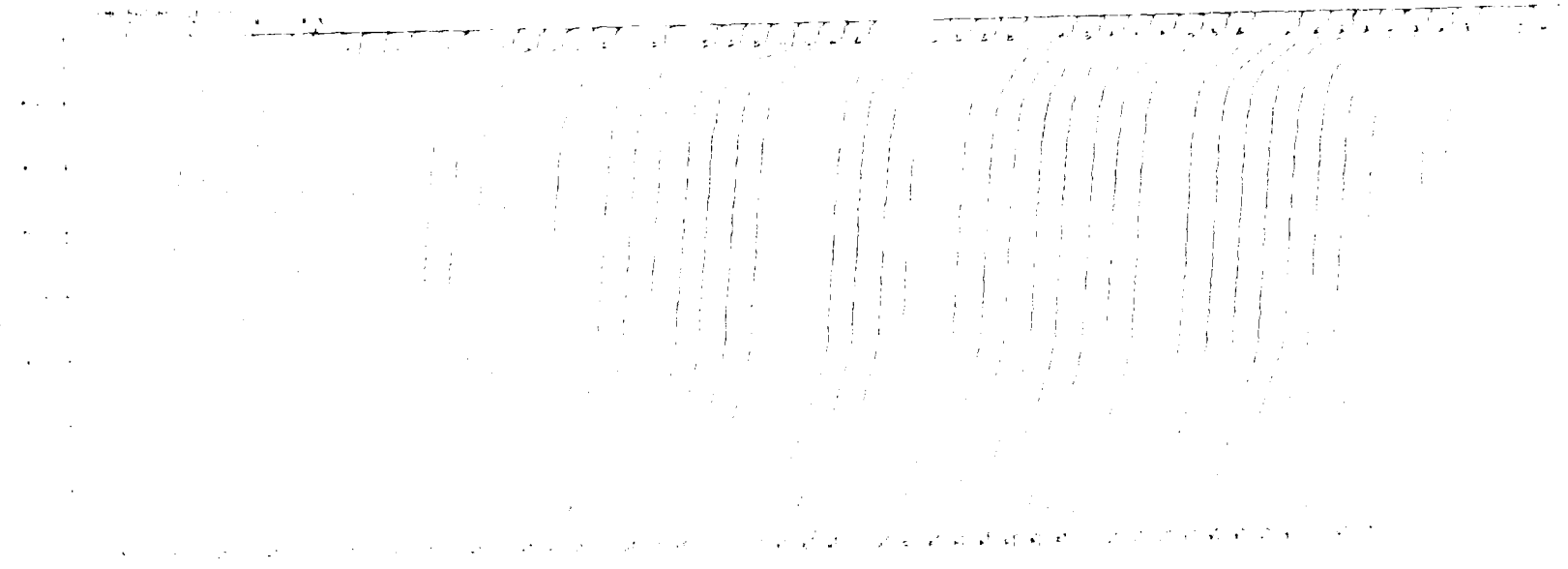

Figure 5.2f. XBT profiles, leg f of "L" pattern

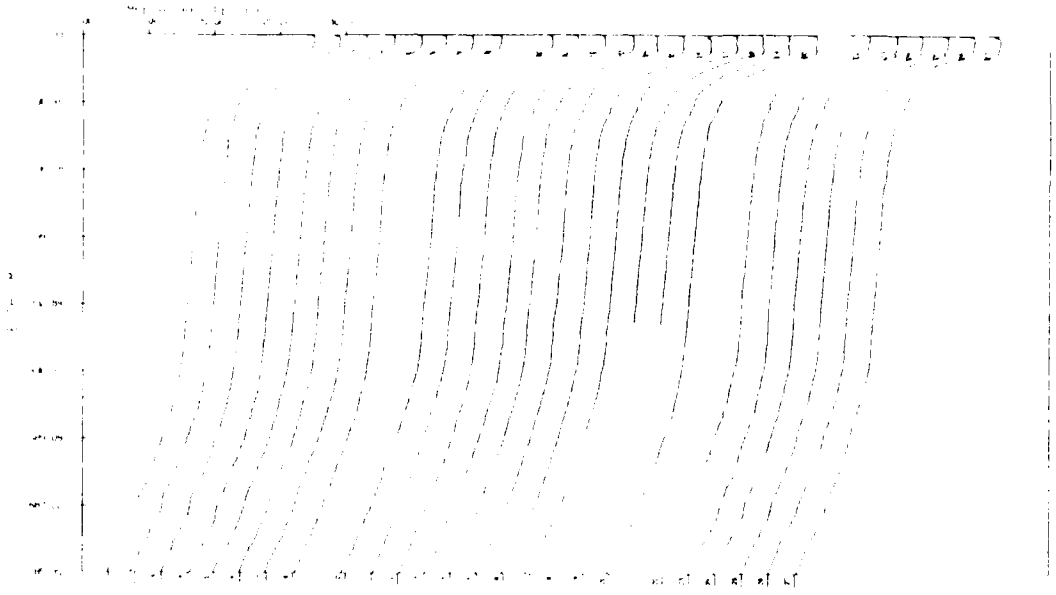

Figure 5.2g. XBT profiles, leg g of "L" pattern

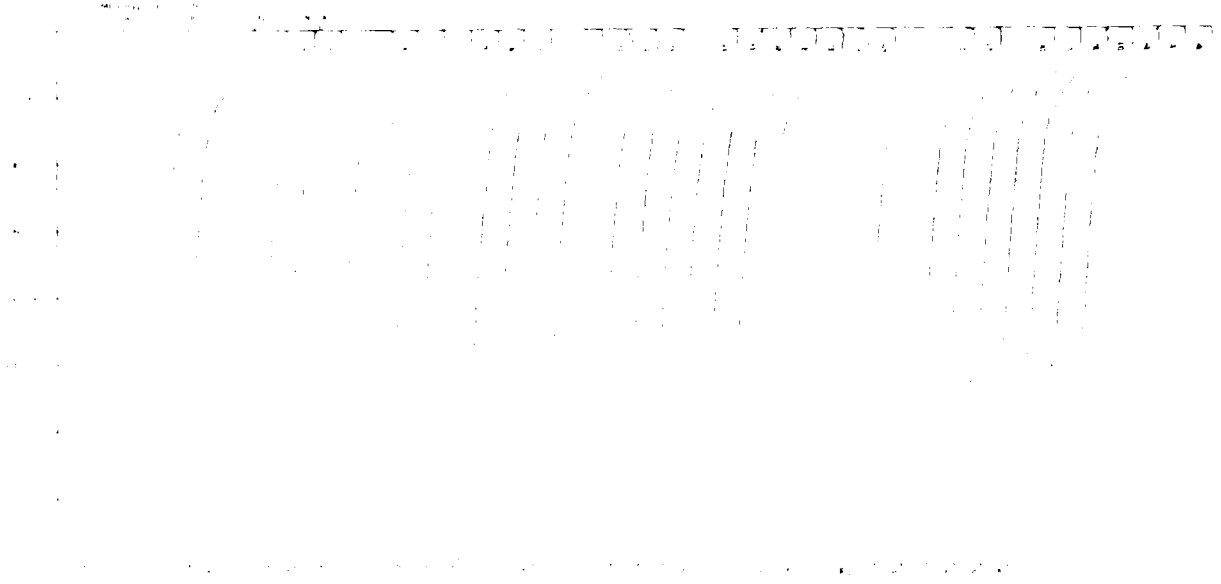

Figure 5.2b. XBT profiles, leg b of "L" pattern

AD-A099 014 NAVAL OCEAN RESEARCH AND DEVELOPMENT ACTIVITY NSTL S--ETC F/G 8/10
OCEANIC ENVIRONMENTAL BACKGROUND OBSERVATIONS IN THE SARGASSO S--ETC(U
MAR 80 H PERKINS
UNCLASSIFIED NORDA-TN-58 NL

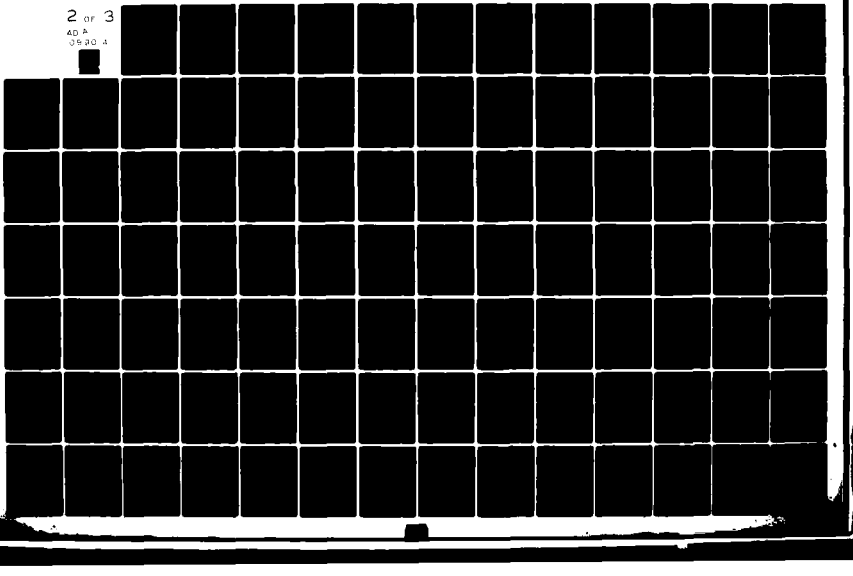

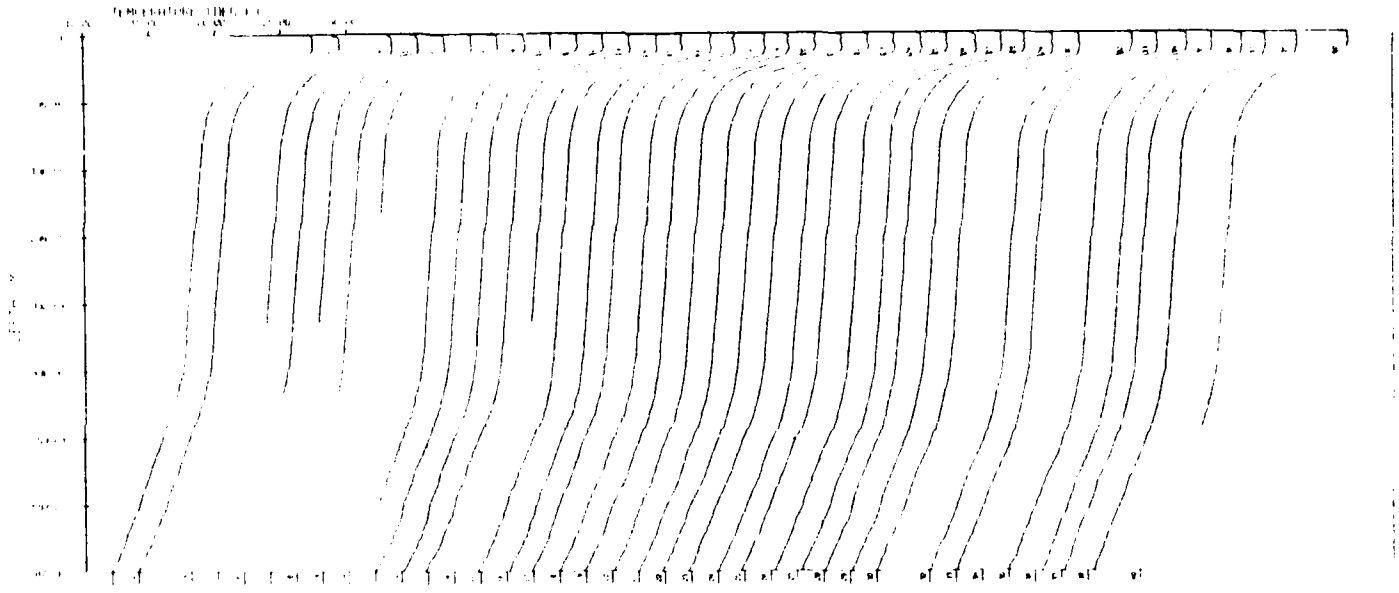

Figure 5.2i. XBT profiles, leg i of "L" pattern

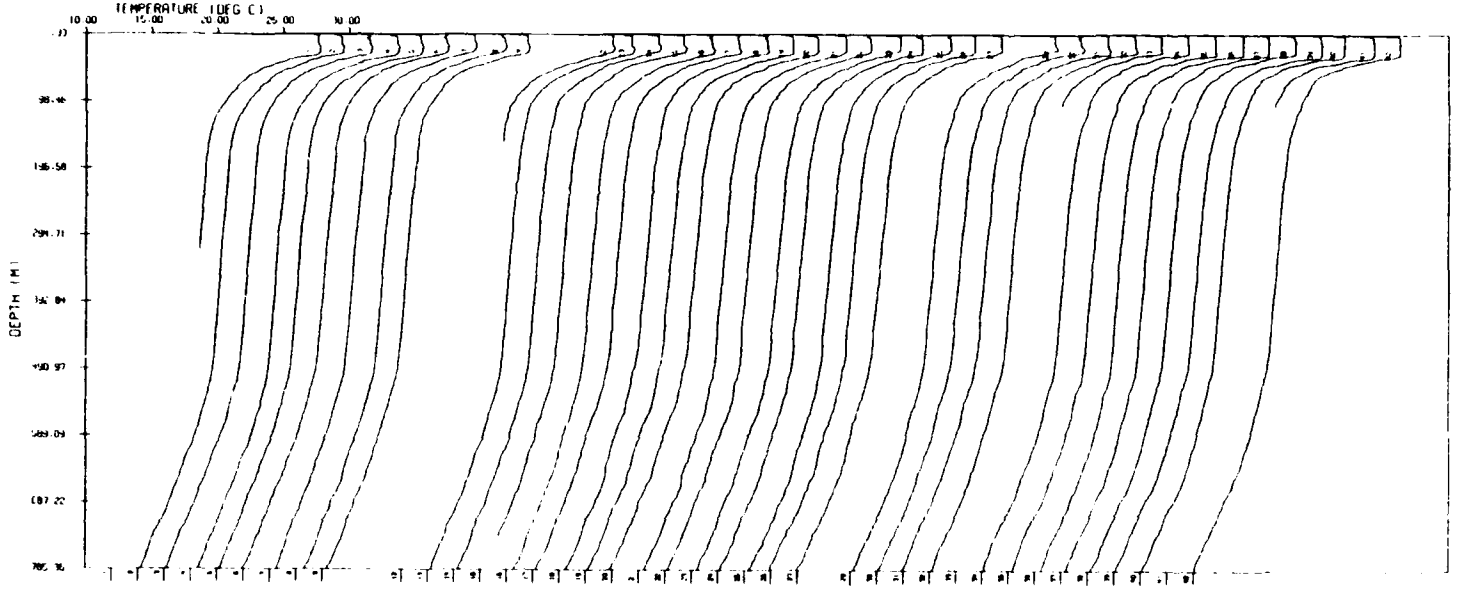

Figure 5.2j. XBT profiles, leg j of "L" pattern

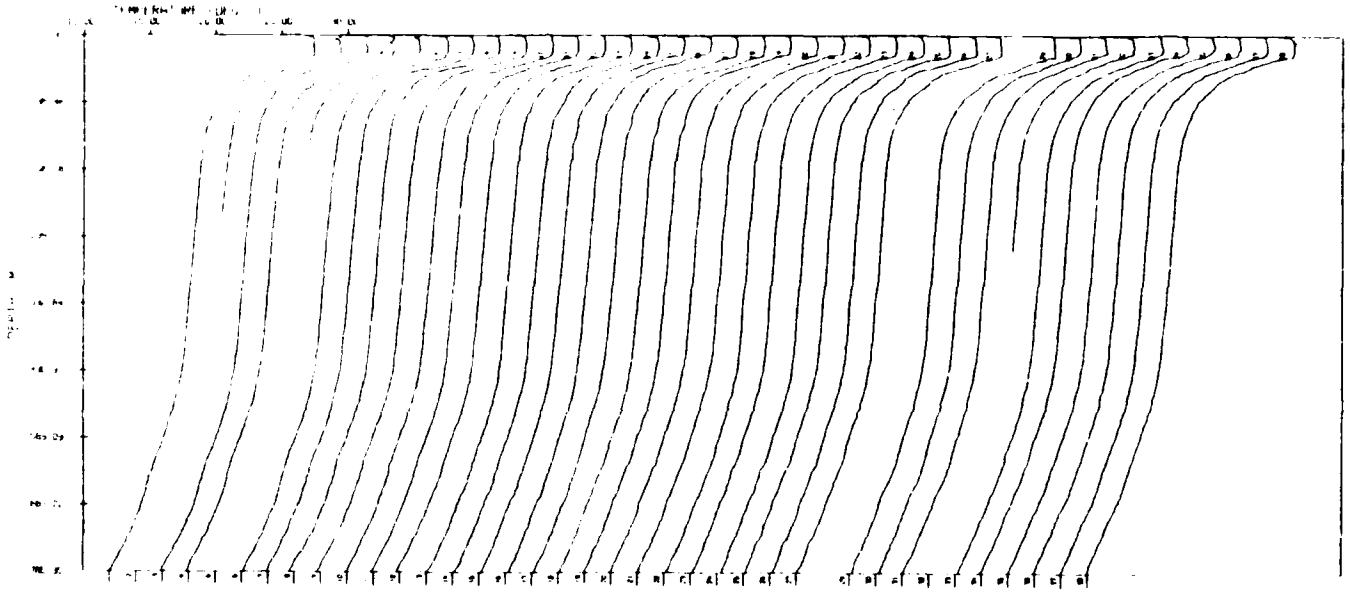

Figure 5.2k. XBT profiles, leg k of "L" pattern

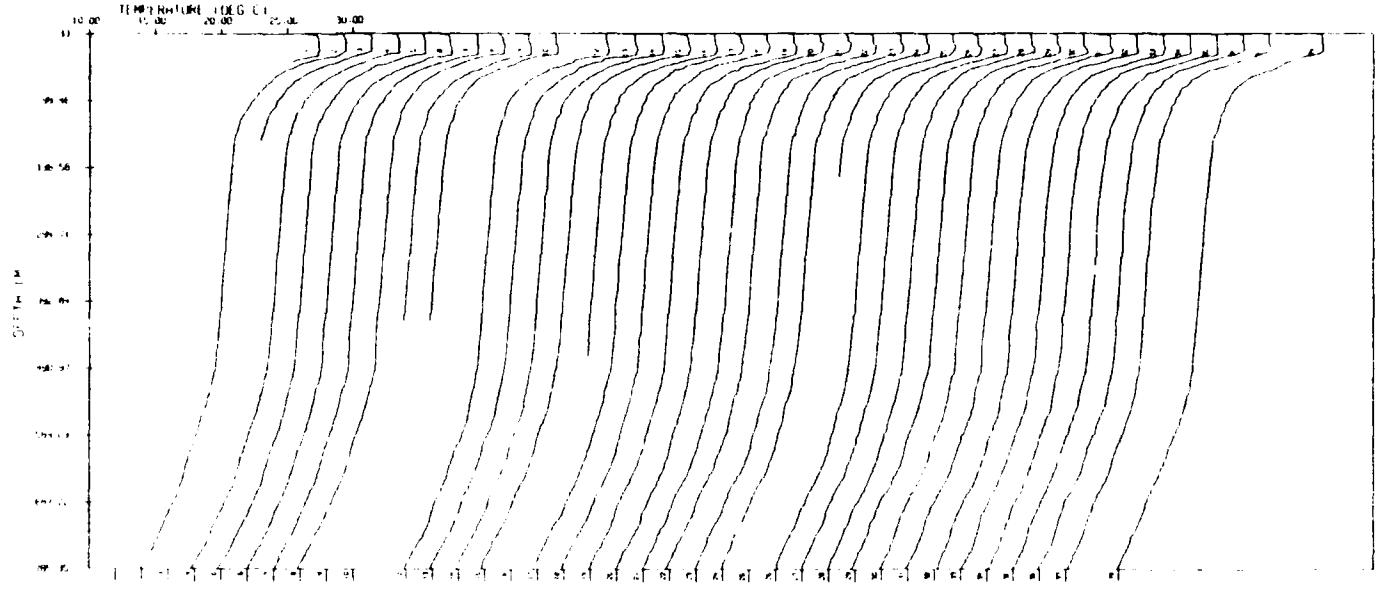

Figure 5.21. XBT profiles, leg 1 of "L" pattern

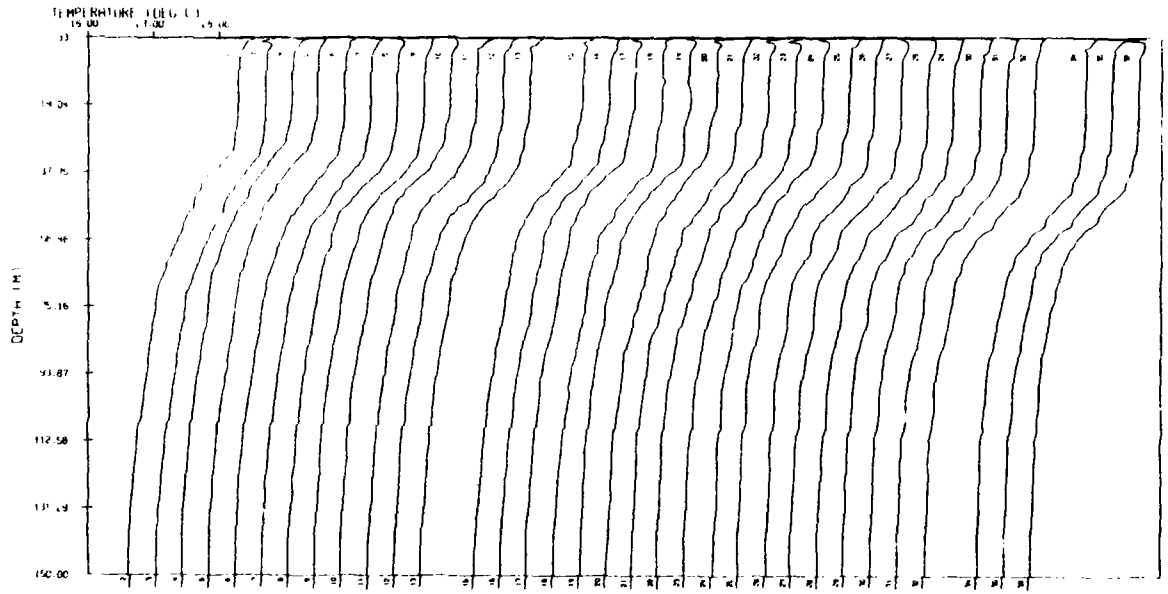

Figure 5.3a. XBT profiles, upper portion, leg a of "L" pattern

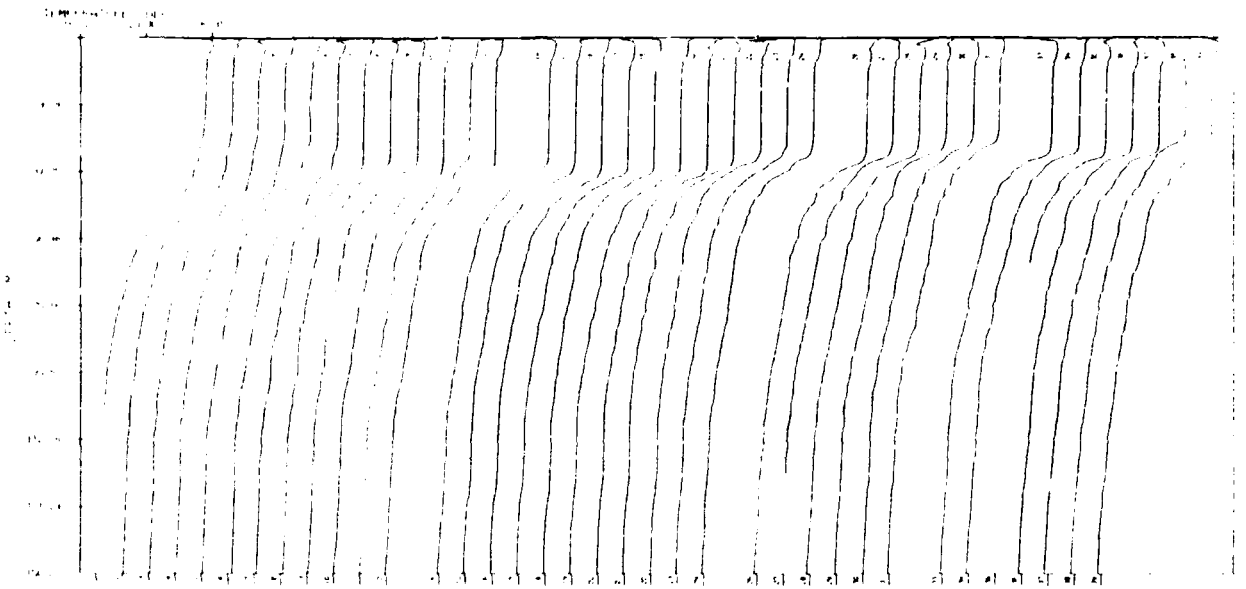

Figure 5.3b. XBT profiles, upper portion, leg b of "L" pattern

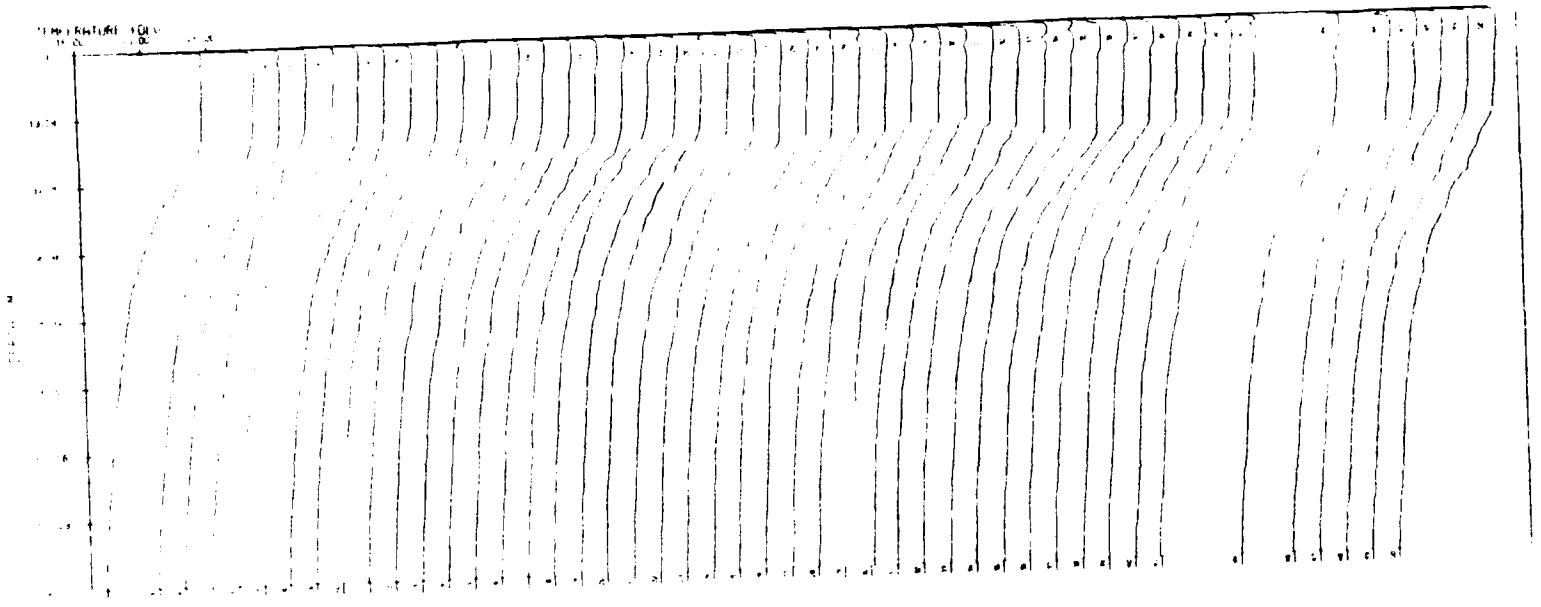

Figure 5.3c. XBT profiles, upper portion, leg c of "L" pattern

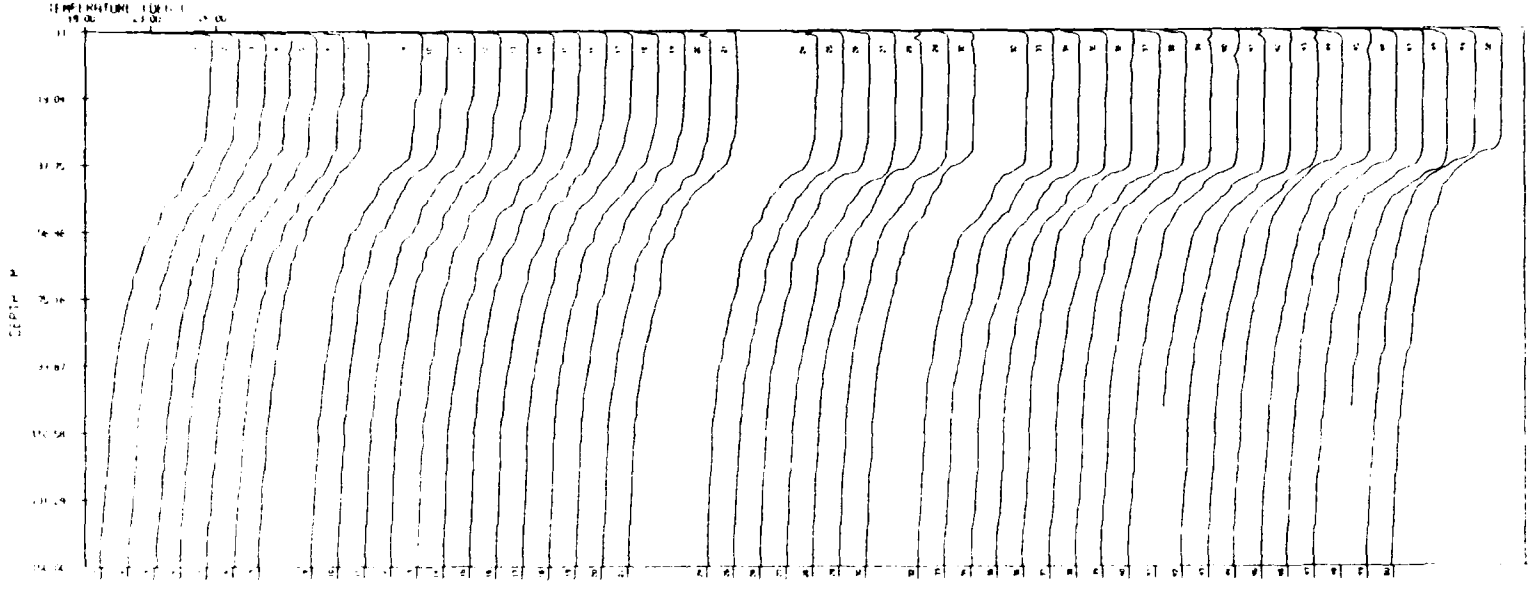

Figure 5.3d. XBT profiles, upper portion, leg d of "L" pattern

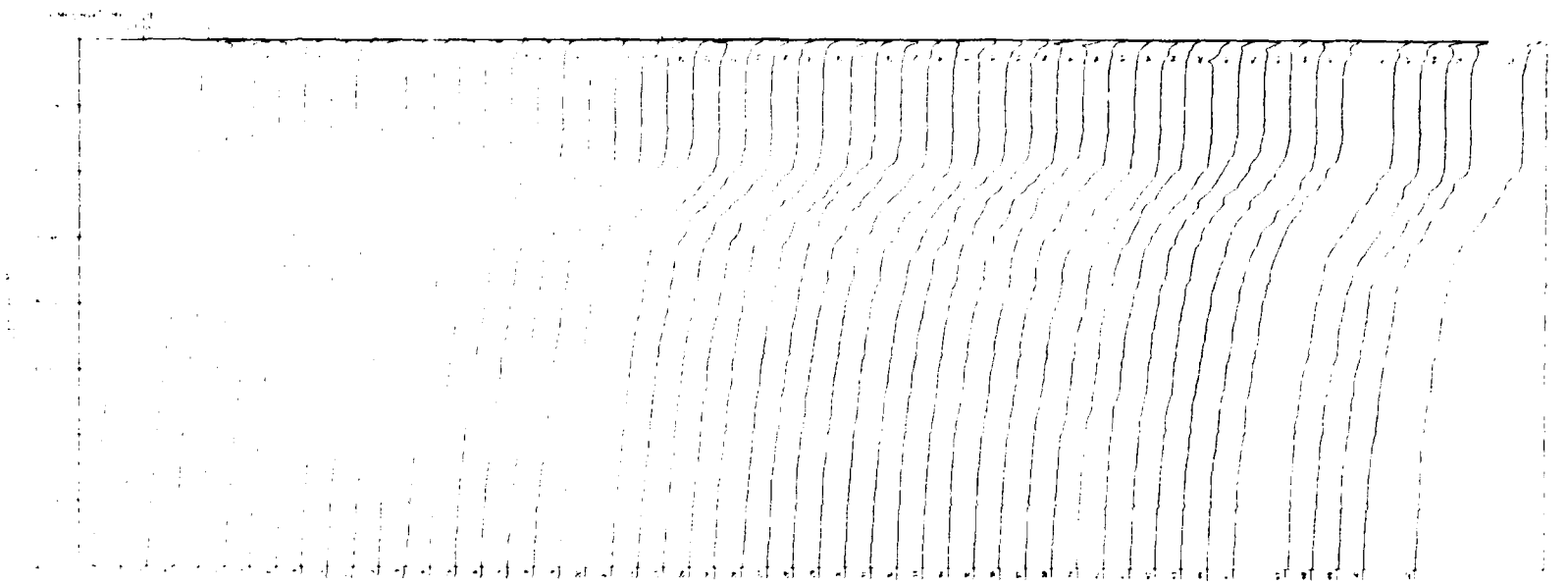

Figure 5.3e. XBT profiles, upper portion, leg e of "L" pattern

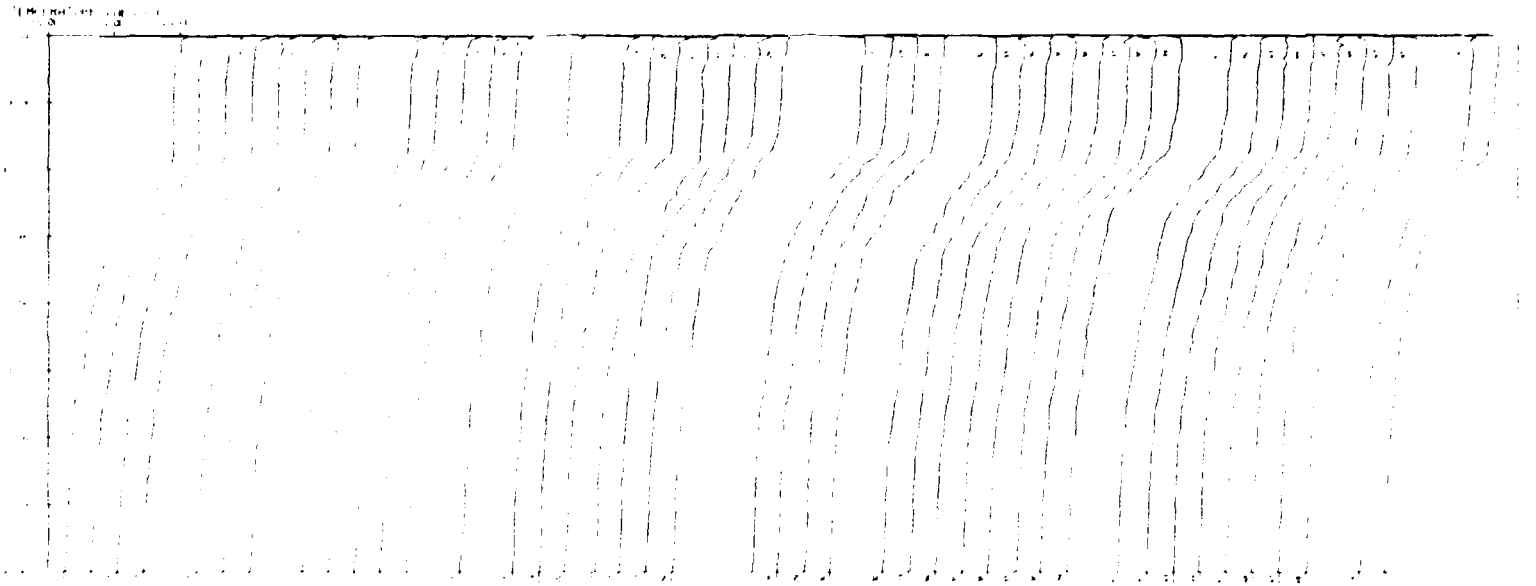

Figure 5.3f. XBT profiles, upper portion, leg f of "L" pattern

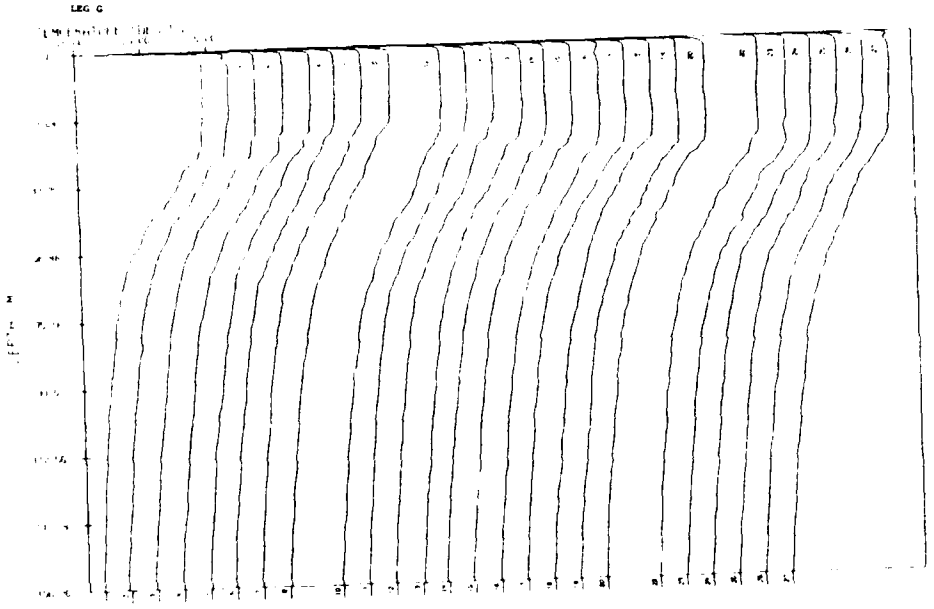

Figure 5.3g. XBT profiles, upper portion, leg g of "L" pattern

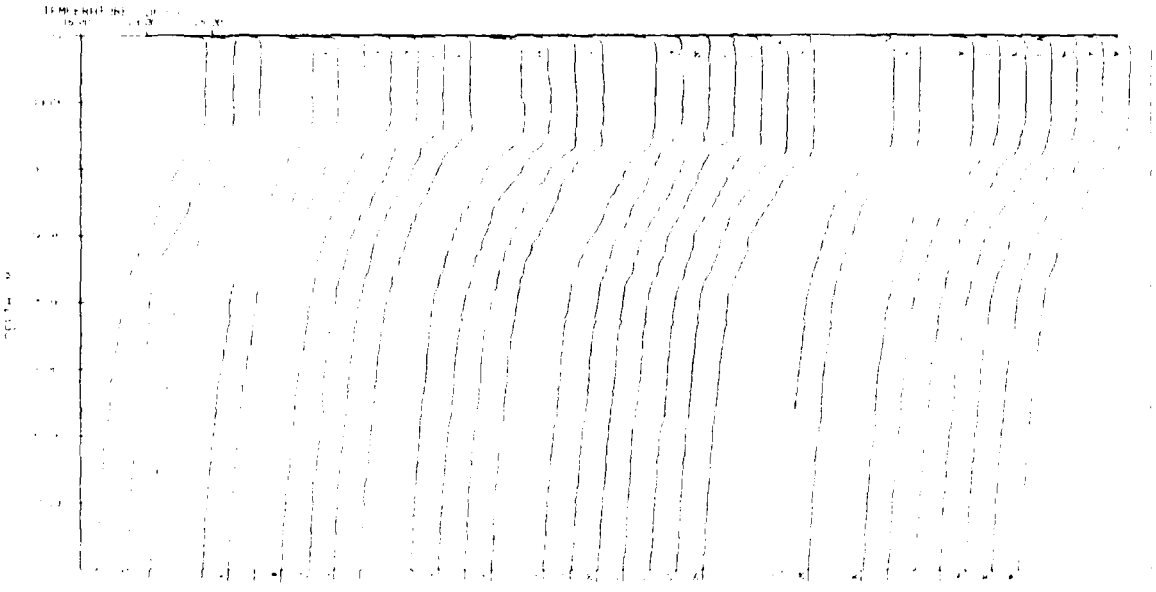

Figure 5.3h. XBT profiles, upper portion, leg h of "L" pattern

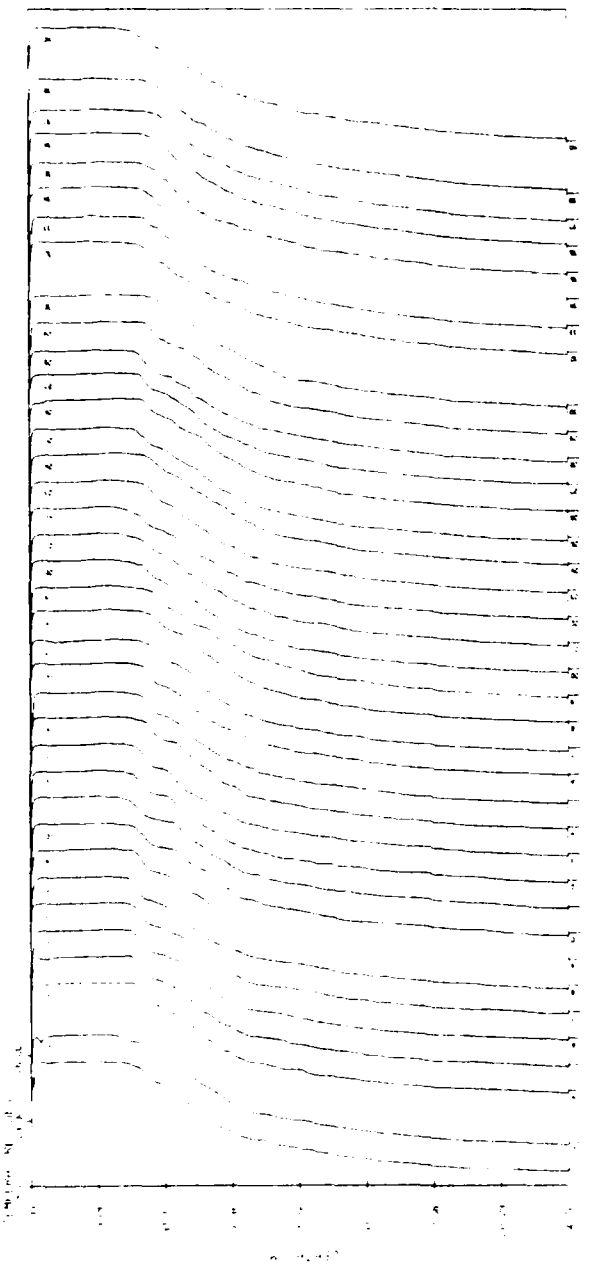

Figure 5.3i. XBT profiles, upper portion, leg i of "L" pattern

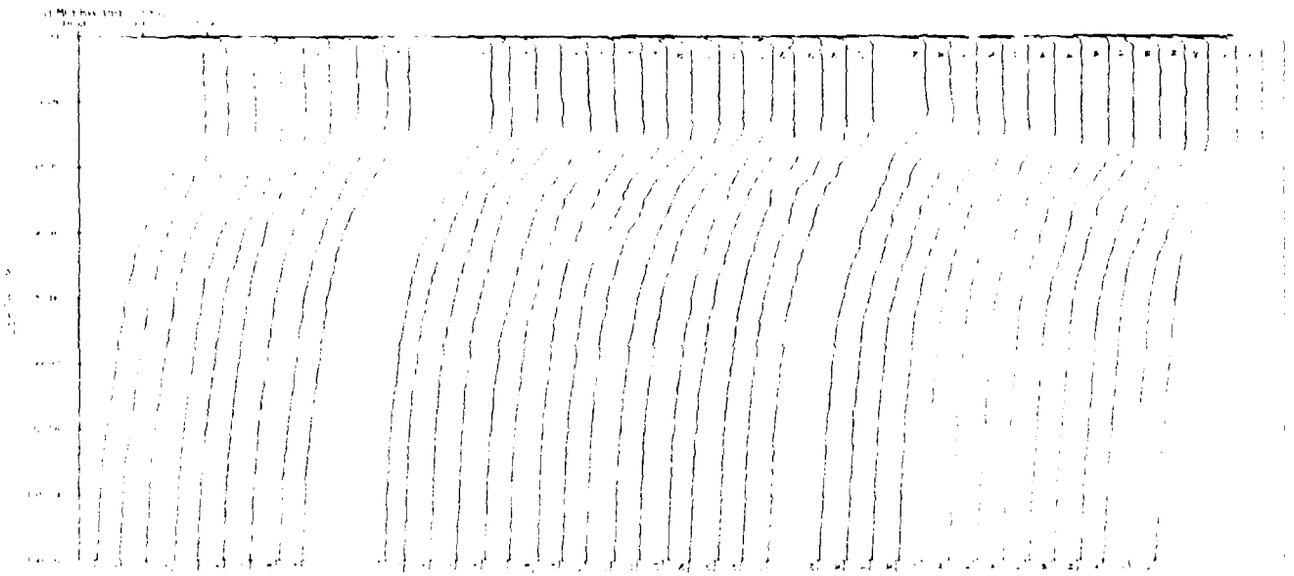

Figure 5.3j. XBT profiles, upper portion, leg j of "L" pattern

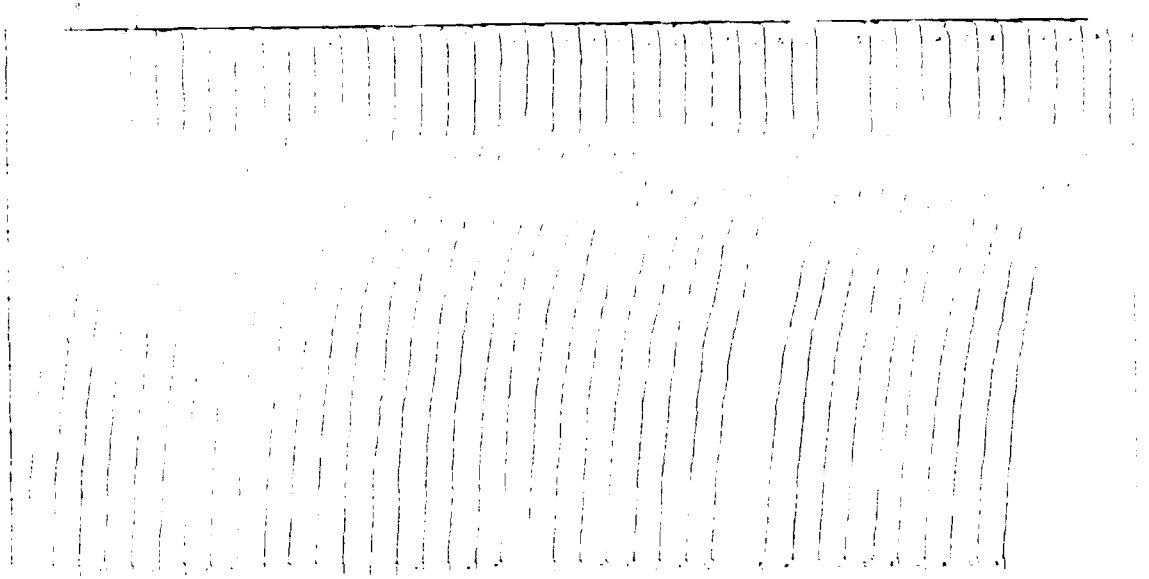

Figure 5.3k. XBT profiles, upper portion, leg k of "L" pattern

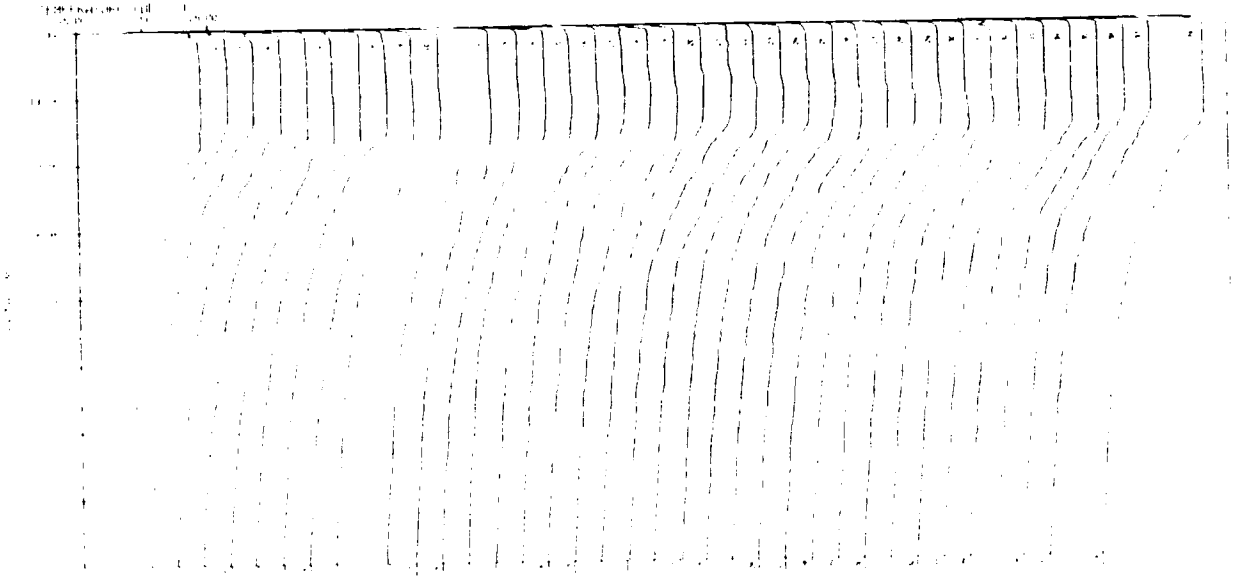

Figure 5.31. XBT profiles, upper portion, leg 1 of "L" pattern

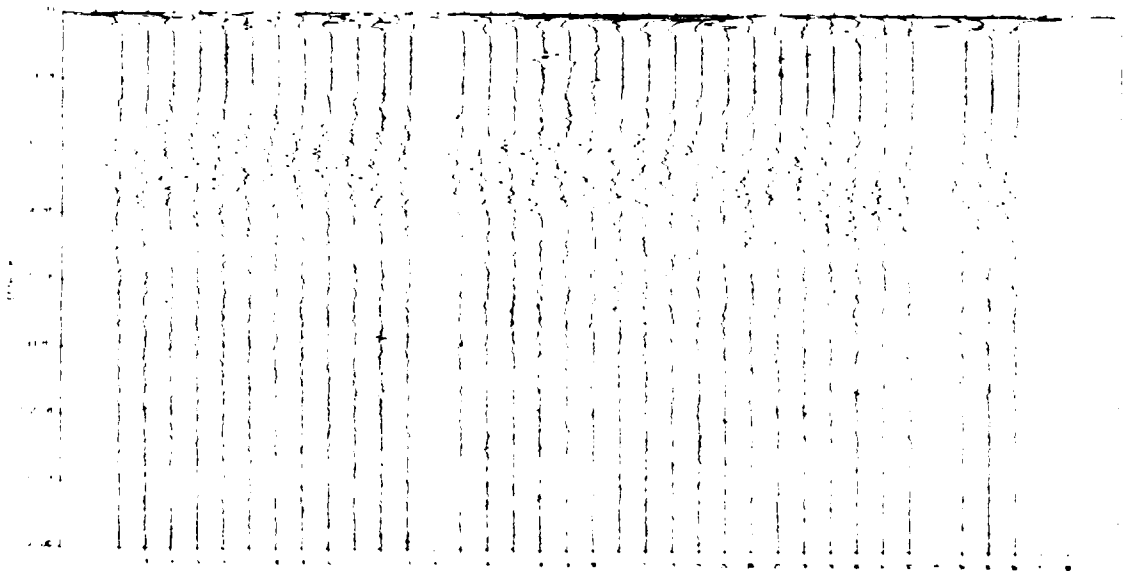

Figure 5.4a. First vertical difference profile of XBT data, leg a

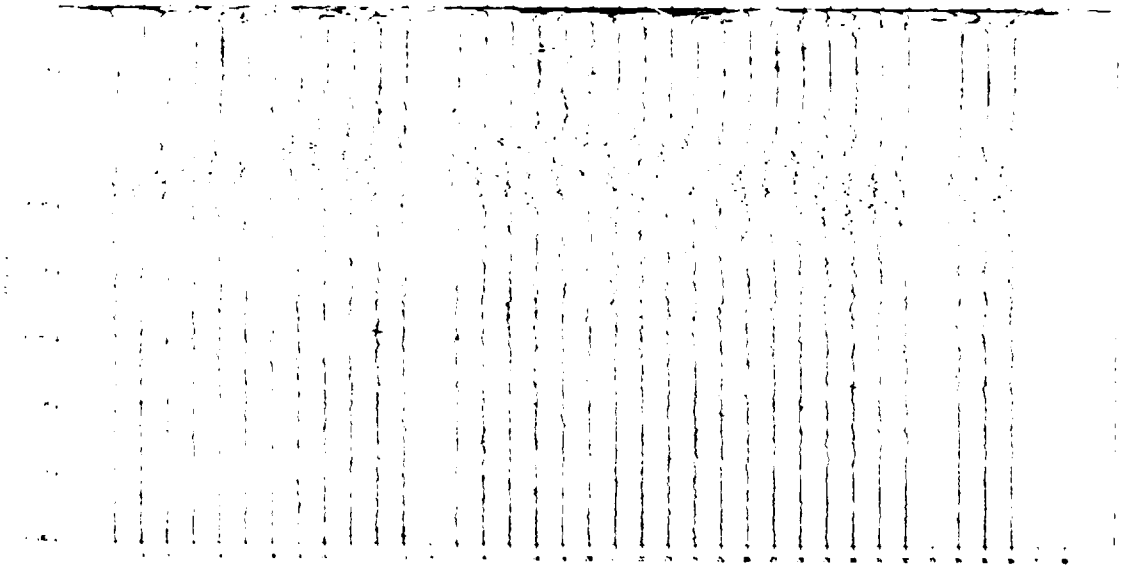

Figure 5.4a. First vertical difference profile of XBT data, leg a

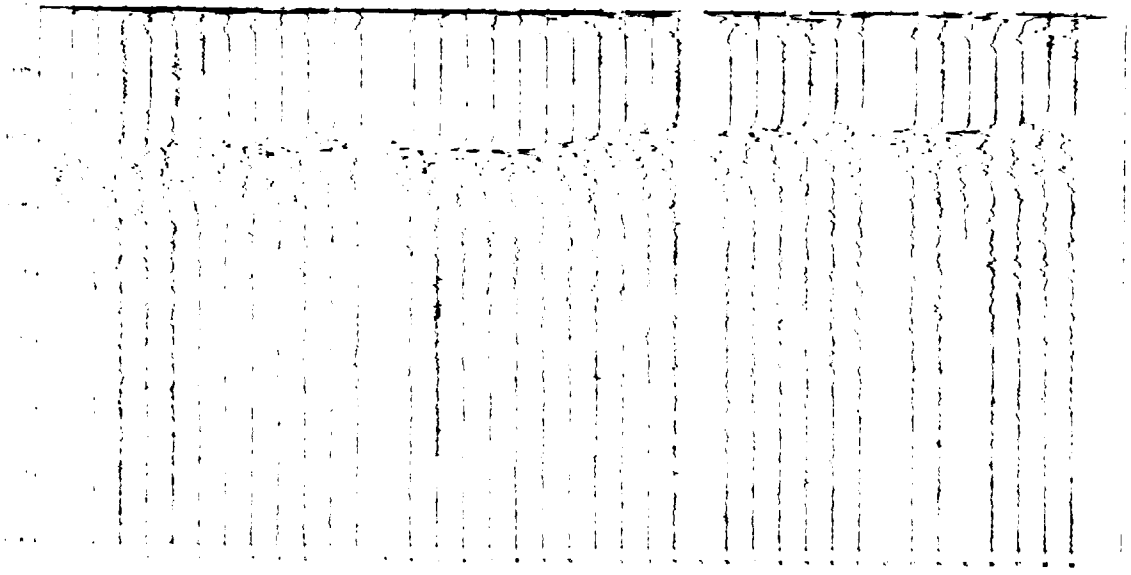

Figure 5.4b. First vertical difference profile of XBT data, leg b

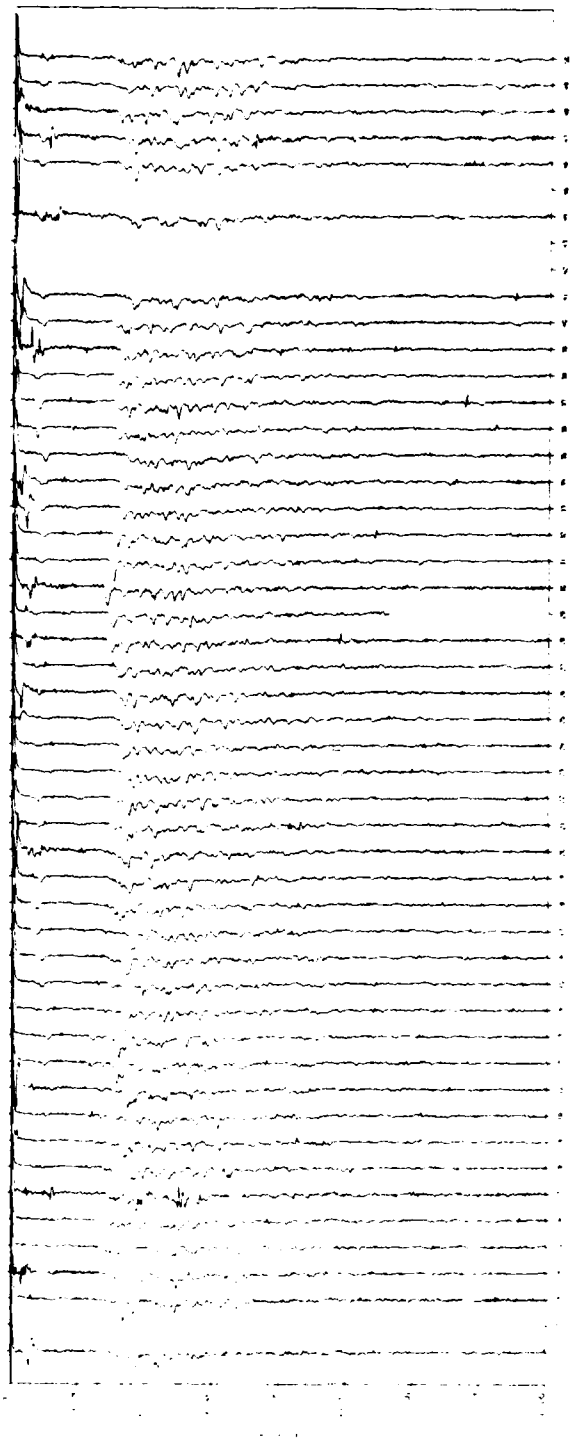

Figure 5.4c. First vertical difference profile of XBT data, leg c

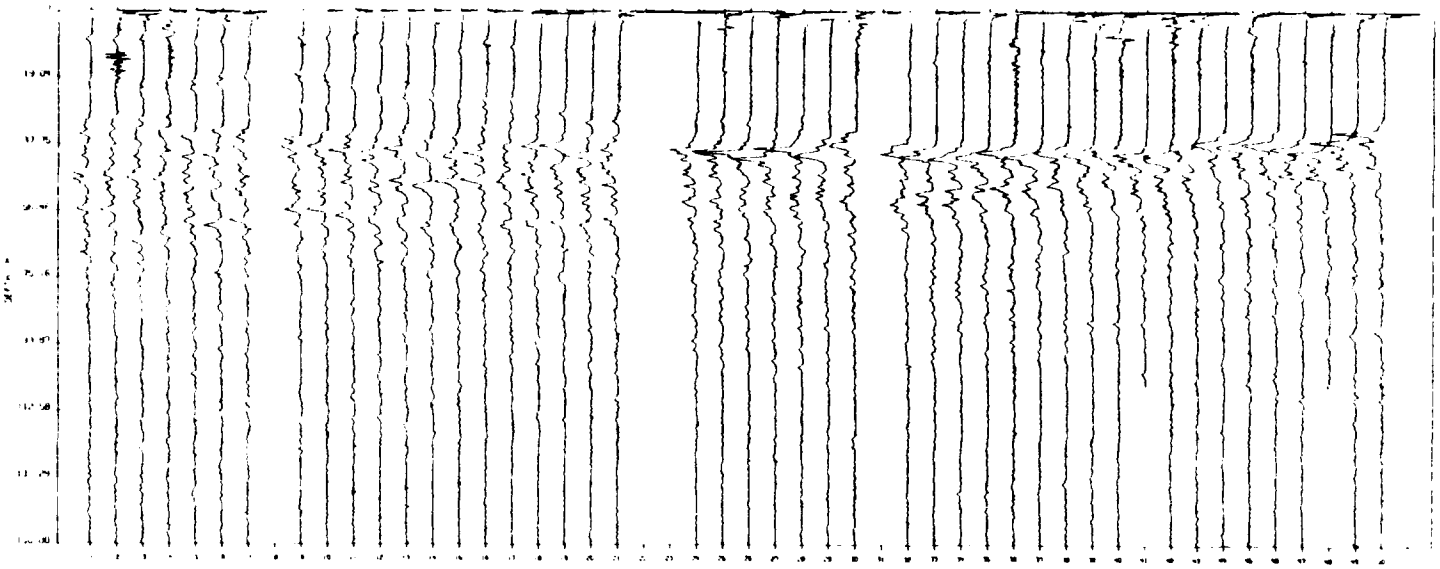

Figure 5.4d. First vertical difference profile of XBT data, leg d

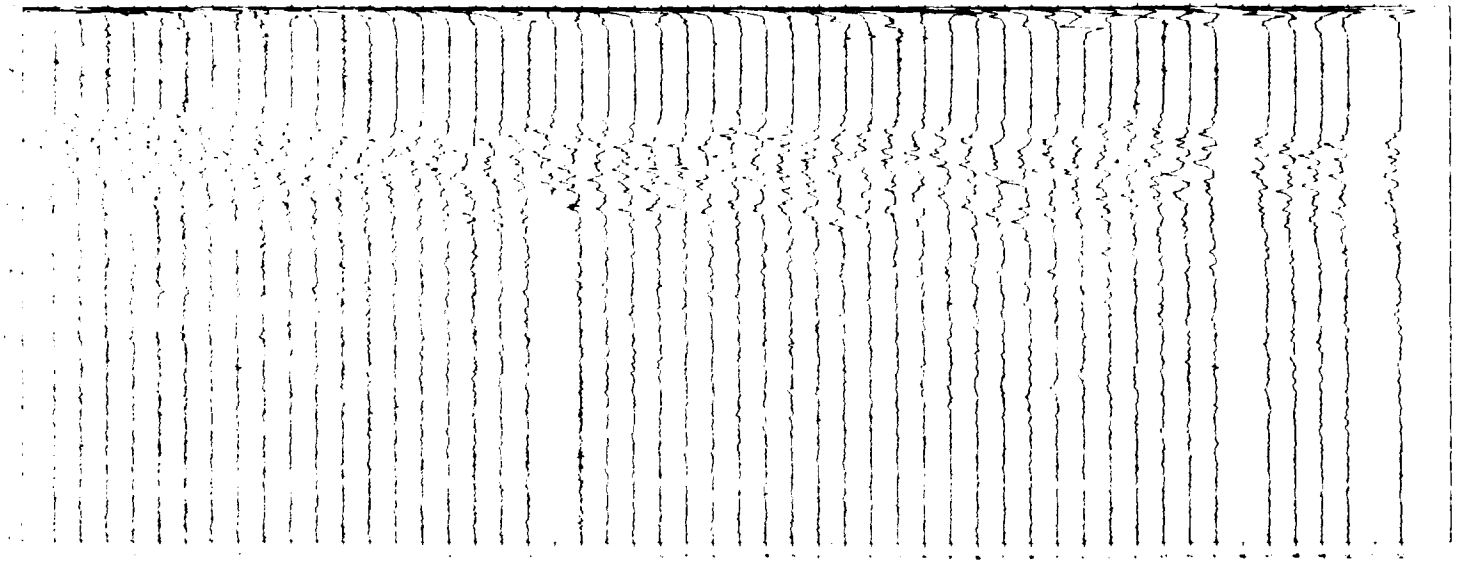

Figure 5.4e. First vertical difference profile of XBT data, leg e

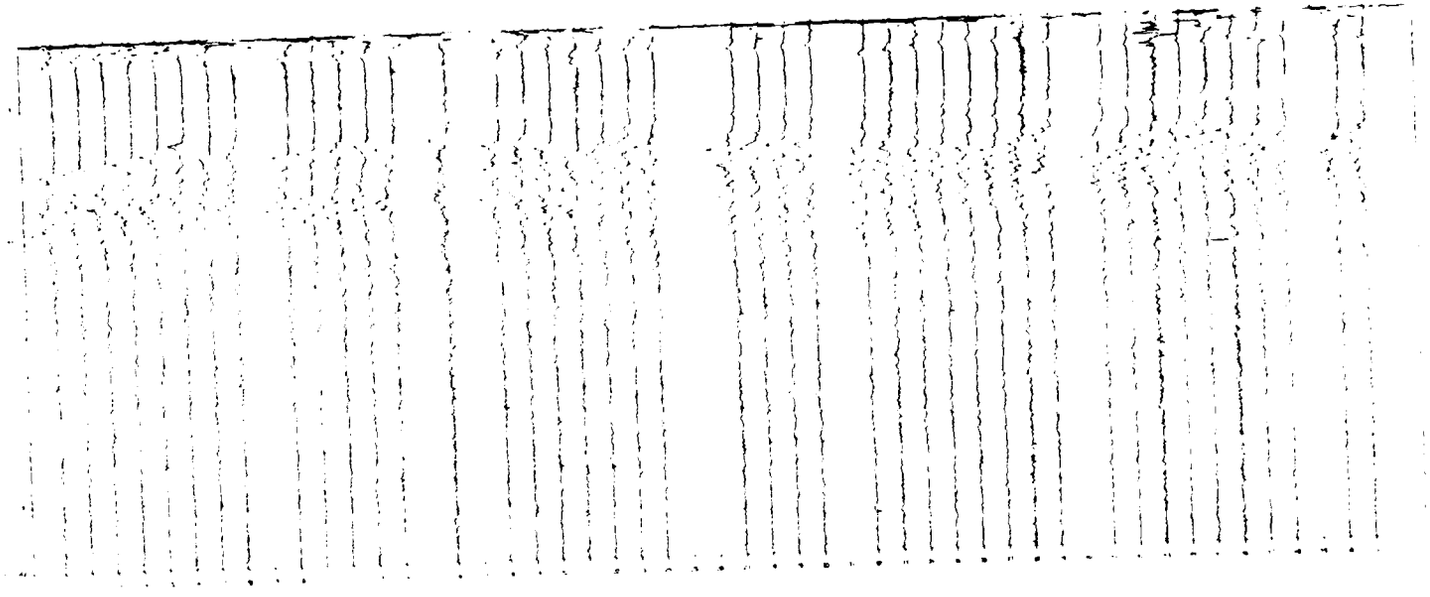

Figure 5.4f. First vertical difference profile of XBT data, leg f

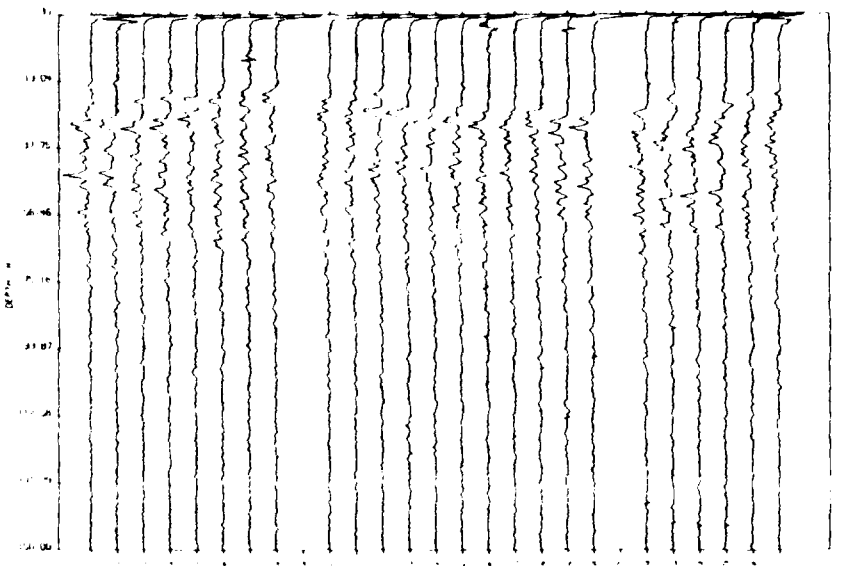

Figure 5.4g. First vertical difference profile of XBT data, leg g

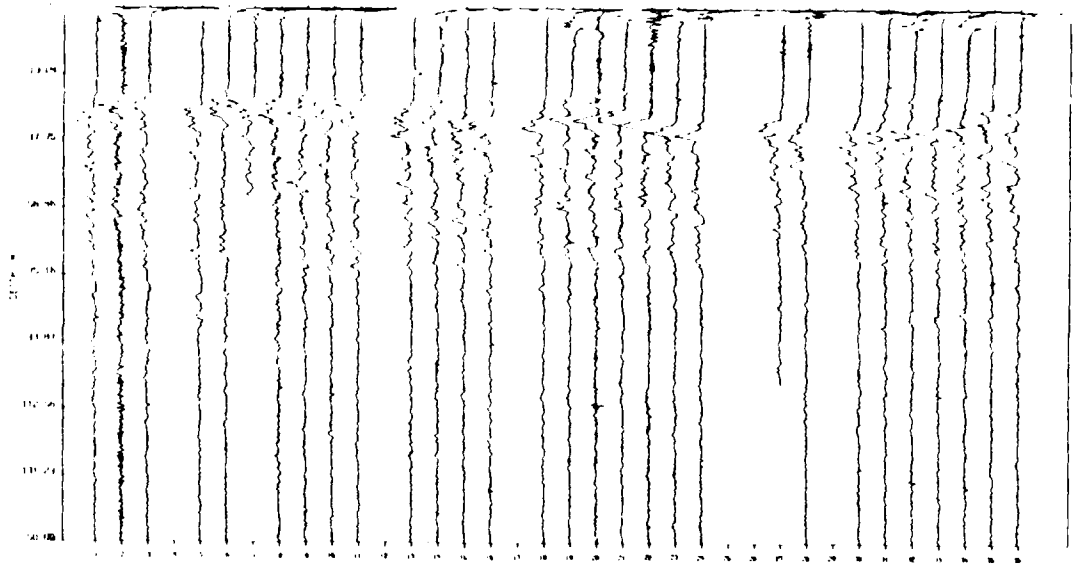

Figure 5.4h. First vertical difference profile of XBT data, leg h

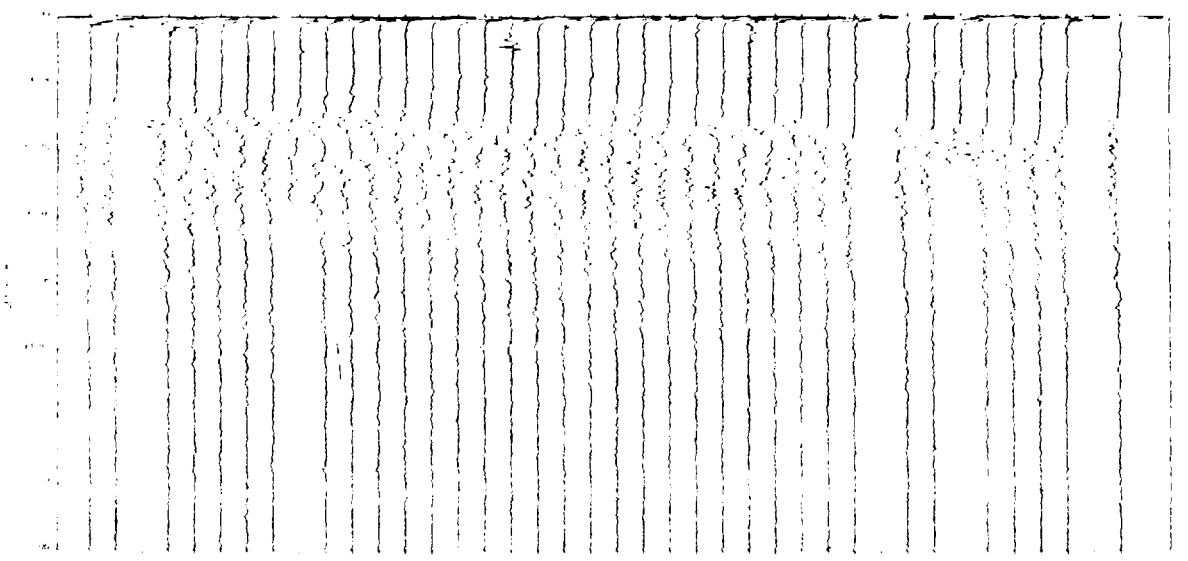

Figure 5.4i. First vertical difference profile of XBT data, leg 1

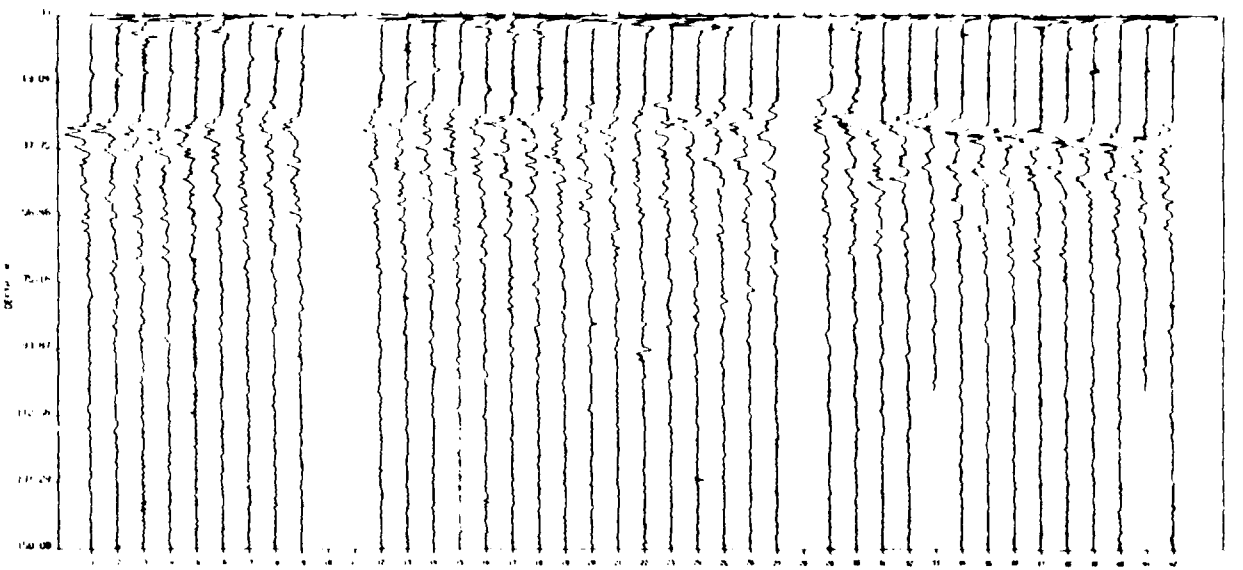

Figure 5.4j. First vertical difference profile of XBT data, leg j

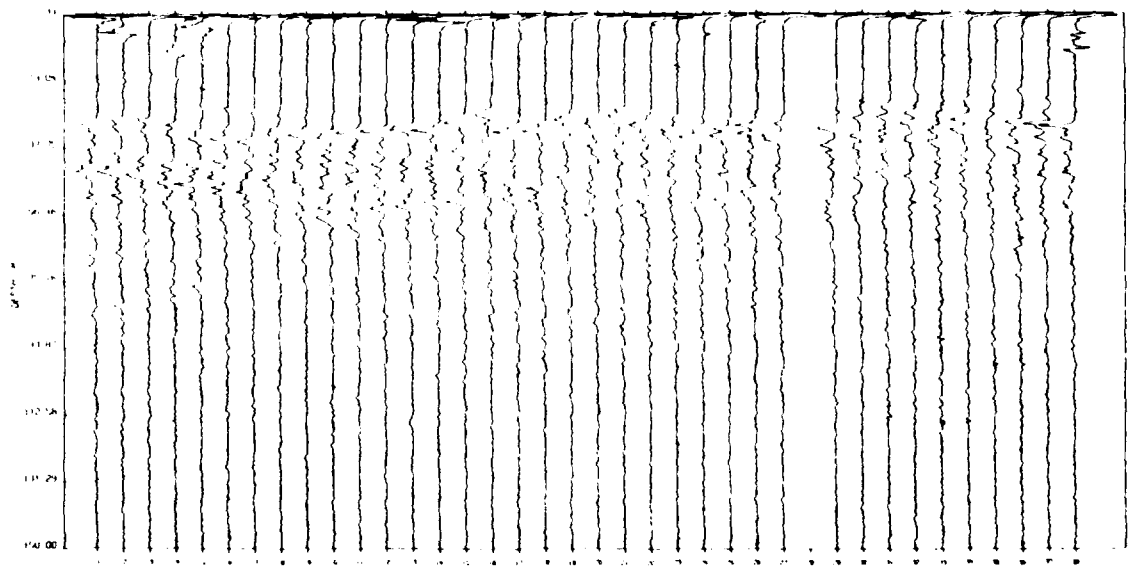

Figure 5.4k. First vertical difference profile of XBT data, leg k

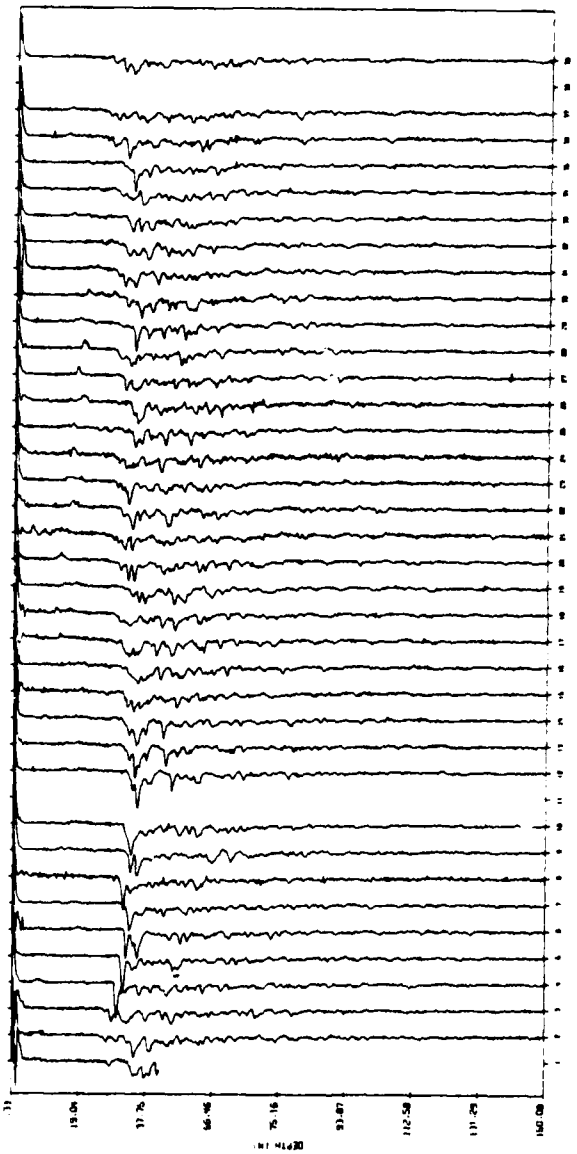

Figure 5.41. First vertical difference profile of XBT data, leg 1

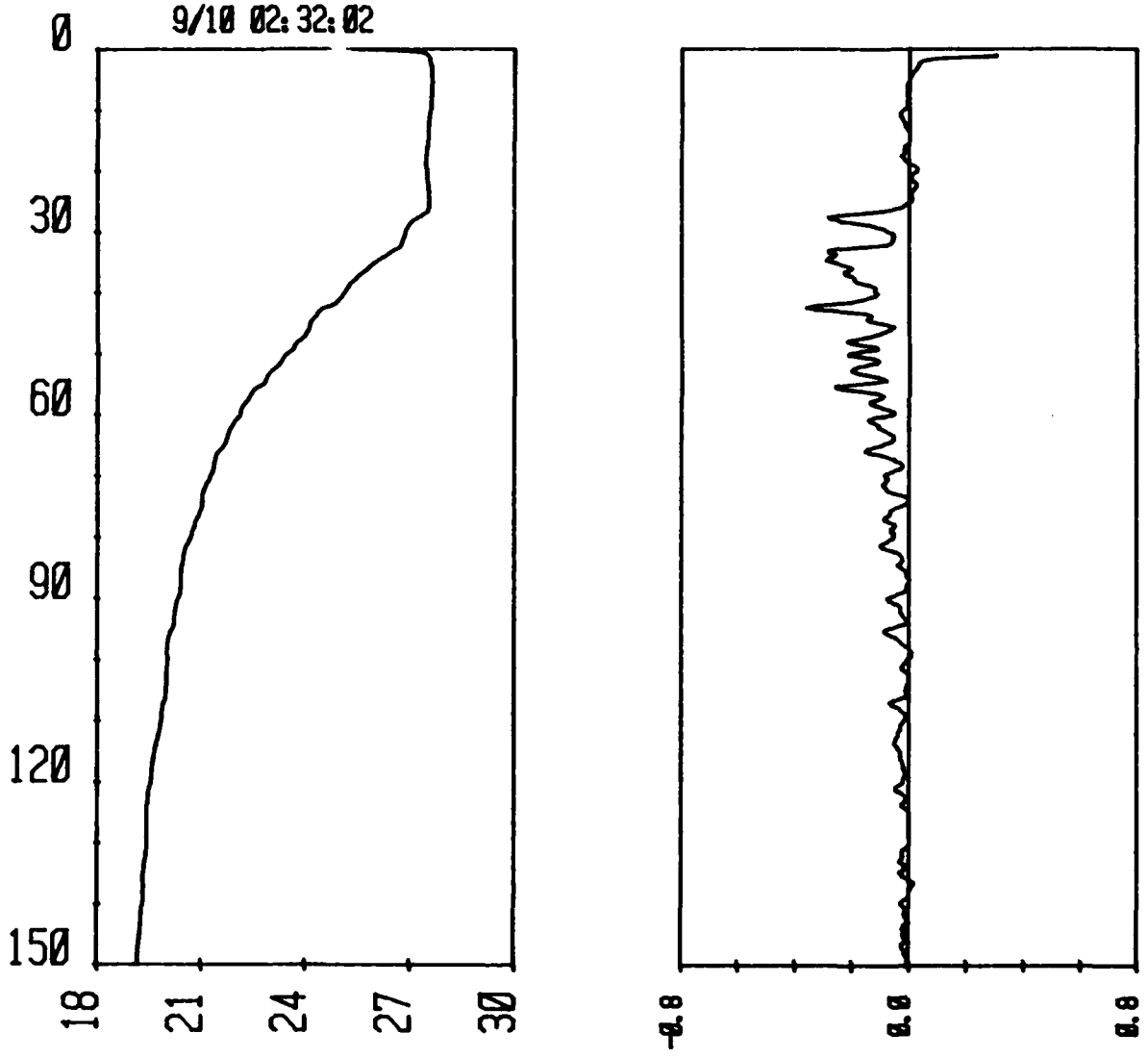

Figure 5.5. Leg g, drop 22. Temperature and temperature gradient versus depth; temperature gradient (right panel) is in ^{o}C per meter.

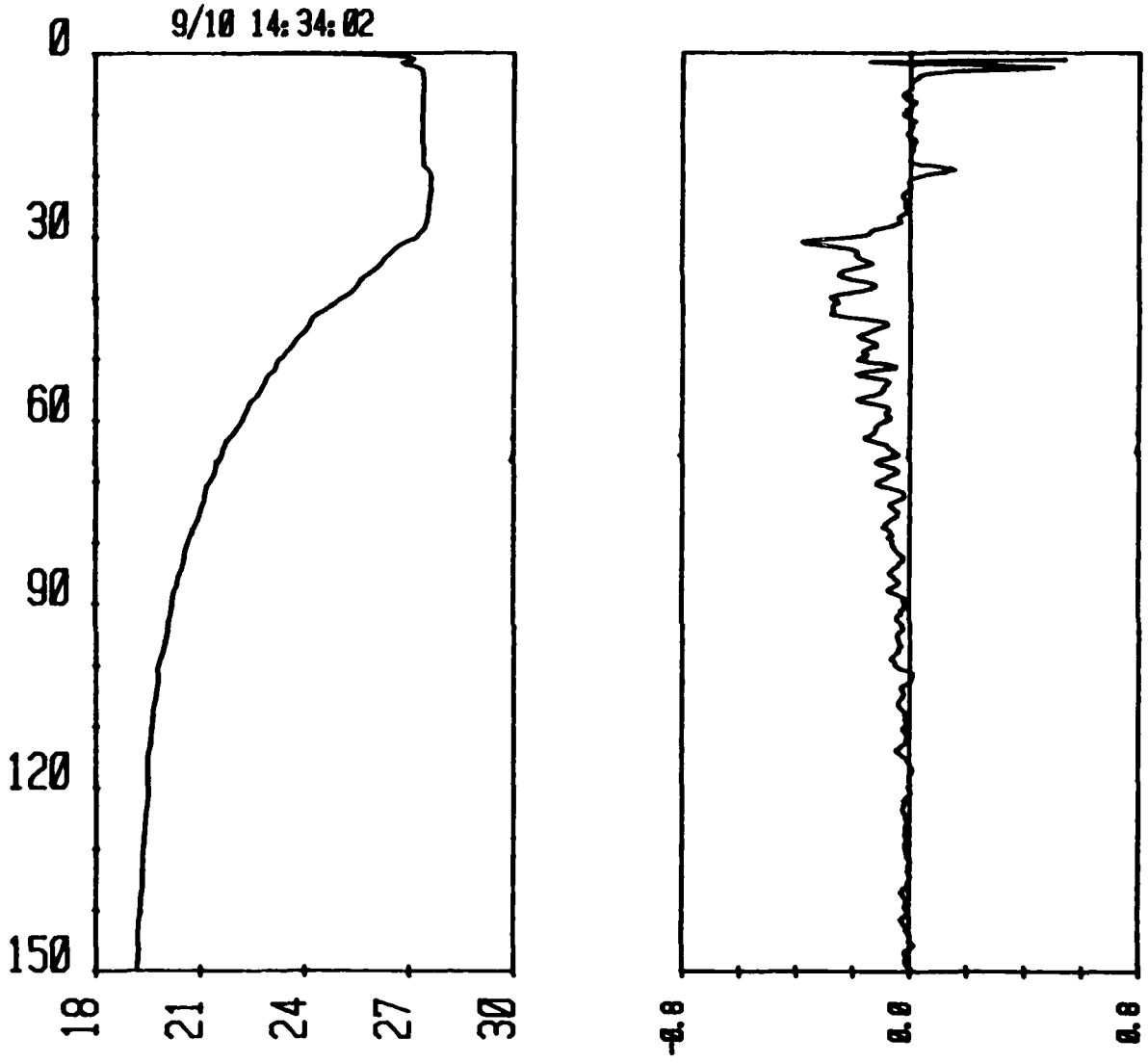

Figure 5.6. Leg j, drop 13. Temperature and temperature gradient versus depth; temperature gradient (right panel) is in ^{o}C per meter.

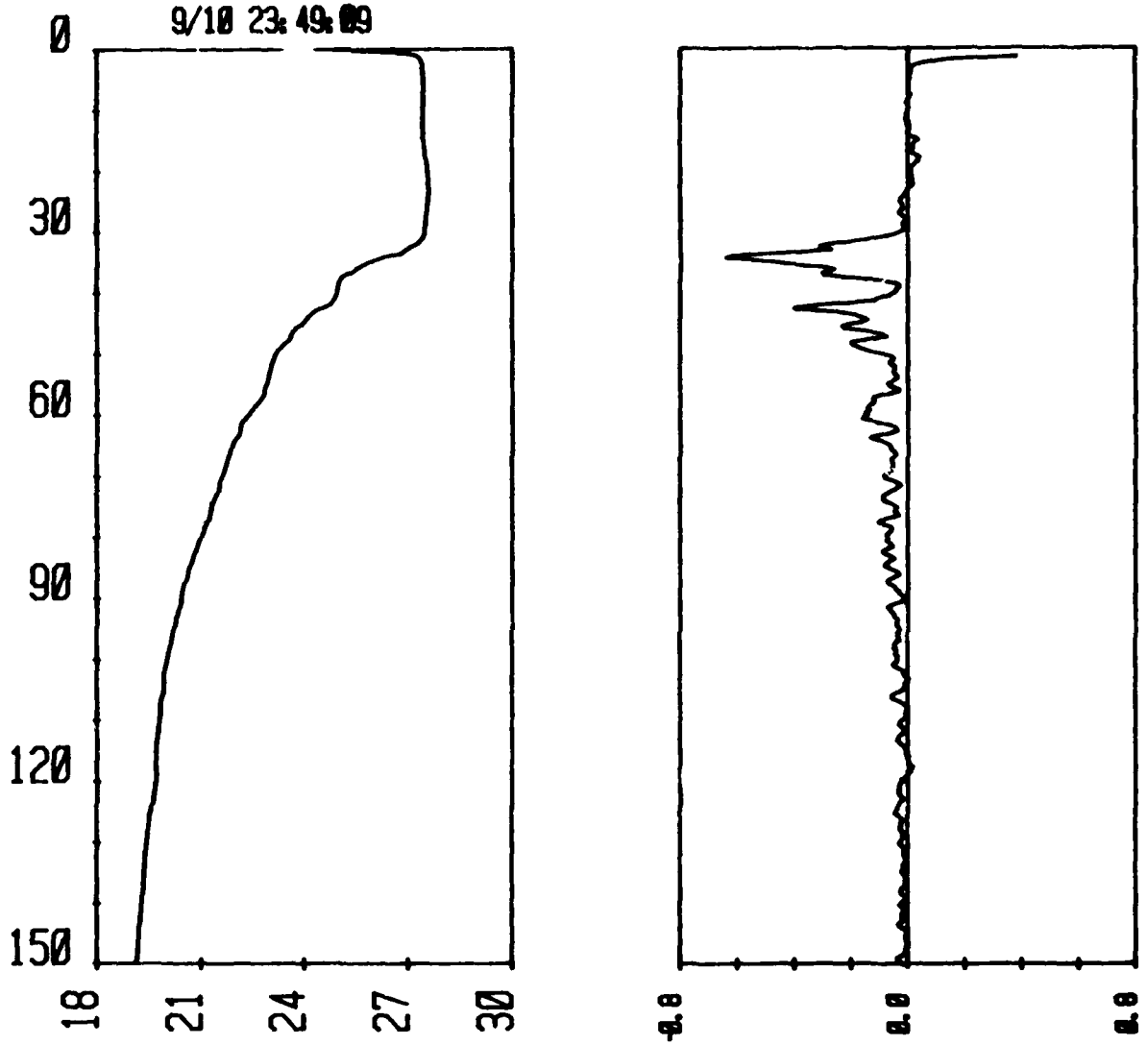

Figure 5.7. Leg ℓ, drop 13. Temperature and temperature gradient versus depth; temperature gradient (right panel) is in ^{o}C per meter.

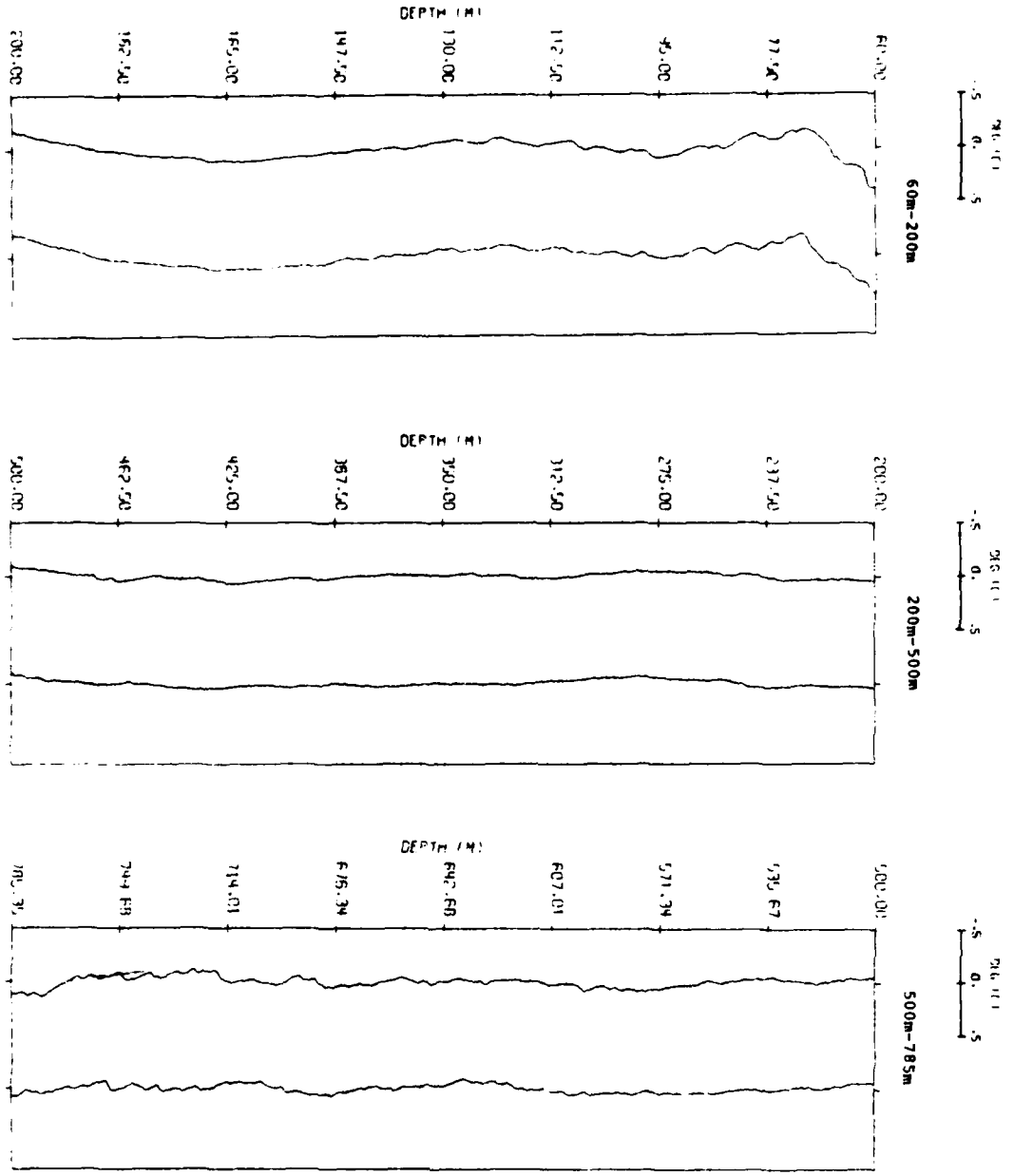

Figure 5.8. Sample plots of temperature residuals, used for computing vertical wavenumber spectra in the three depth ranges indicated, after second-order detrending.

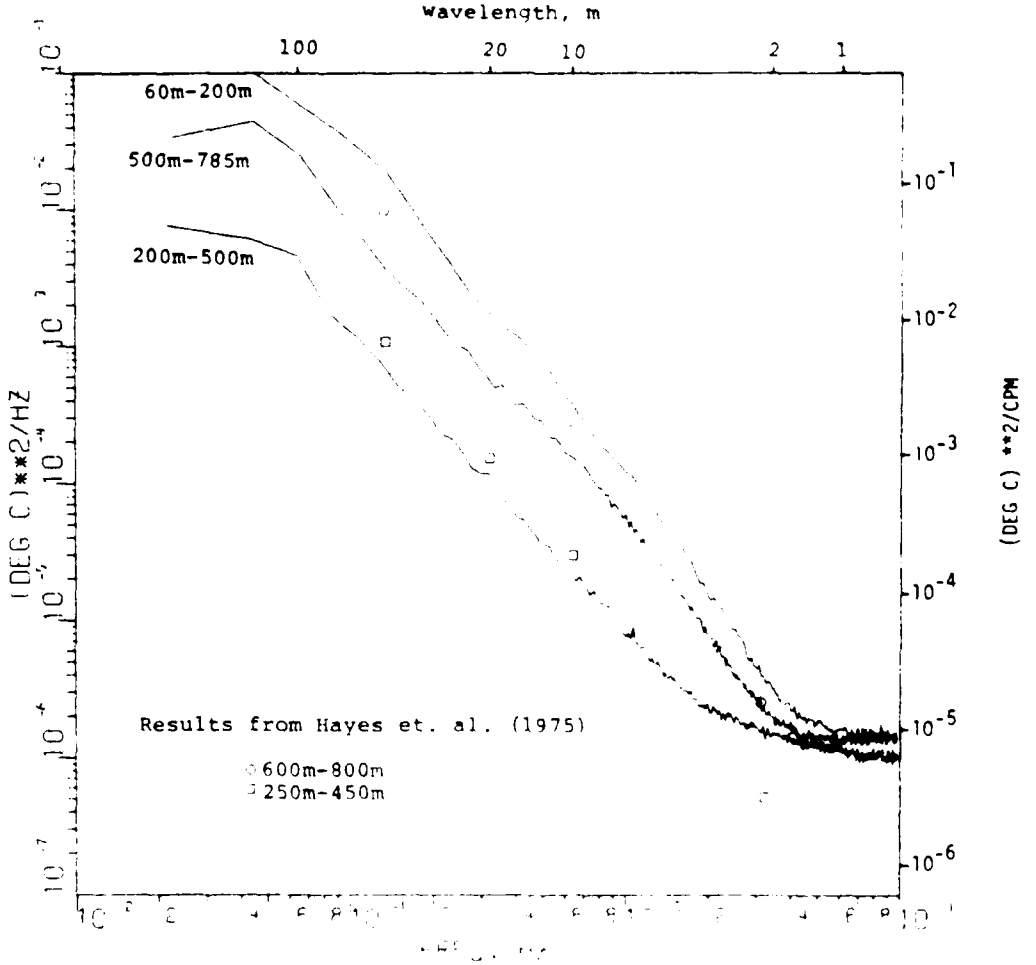

Figure 5.9. Vertical wavenumber spectra of temperature, ensemble averaged over all drops in each of three depth ranges, compared with the results from Hayes, et.al. (1975).

Section 6.0

CURRENT METER DATA

by Ortwin von Zweck and Robert Wahl

6.0 CURRENT METER DATA

6.1 INTRODUCTION

A subsurface mooring containing 12 current meters was deployed at 30°29.7'N, 71°45.6'W in some 5300 m of water. The mooring was deployed on 4 September 1979 and recovered on 16 October 1979 using the USNS KANE. In order to display this data on a scale which permits intercomparison with other measurements, only the first ten-day segment is shown here. A description of the full-length data series is reported by von Zweck and Wahl (1980).

6.2 INSTRUMENTATION

A total of 12 meters, 8 AMF vector averaging (VACM) and 4 Aanderaa current meters, were mounted on the mooring. The VACM's were mounted at depths between 132 and 372 m. The Aanderaa instruments were spaced 500 m apart at depths of 522, 1022, 1522 and 2022 m. A schematic of the mooring configuration is shown in Figure 6.1. Pertinent information on meter depths and the data records can be found in Table 6.1.

Aanderaa current meters determine current speed by counting the number of revolutions of a Savonius rotor over a chosen sampling time interval. Current direction is determined each sampling interval by measuring instantaneously the orientation of a current vane with respect to magnetic north. The current speed and direction are recorded every sampling time interval in digital form on quarter-inch magnetic tape. Some of these instruments are equipped to measure and record, in addition, instantaneous values of temperature, conductivity and pressure.

The VACM measures current speed (using a Savonius rotor) and direction (using a magnetic compass and current vane) and computes north-south and east-west vector components of the current eight times per rotor revolution. The individual vector components are then averaged over the sampling interval and recorded, together with a temperature measurement, on a magnetic cassette tape. The VACM temperatures presented in this data report were obtained using thermistors mounted into the endcap of the VACM, replacing the internally mounted thermistors of the same type. This modification decreased the temperature time constant from about 5 or 6 minutes to 1 minute.

6.3 CALIBRATION

Calibration coefficients for the temperature sensors were obtained individually for each meter and applied to the recorded temperature measurements. The temperature calibration curves and procedure are described by Mayoral (1978). The worst RMS error of the least square fitted calibration curves for all VACM's was [illegible].

The threshold speed of the VACM [illegible] is 3 cm/sec; the instrument is incapable of measuring current speeds less than that value. However, due to the vector averaging nature of the instrument it is possible to obtain a vector averaged current speed which is smaller than the threshold if the instantaneous speed fluctuates above and below the threshold during the averaging interval. Whenever the speed of the vector averaged current is below the threshold, its value is set to zero.

For the Aanderaa meters [illegible] when it falls below the [illegible]

The compasses of all current meters are checked for error and, if necessary, are adjusted to fall within specifications prior to meter deployment.

6.4 DATA PROCESSING

The Aanderaa and VACM current meter data tapes were transcribed to 7-track computer-compatible tape using Virginia Instruments, Inc., translators. The data were then placed into FEB (fast and easy binary) data files, truncated to remove mooring deployment and recovery noise and edited for occasional spurious spikes in the data.

Meter depths are based on the mooring design and the pressure measurements from the Aanderaa A-2926, assuming 1 m = 1 db. The record from A-2926 is generally of a poor quality and so is not included in this report. Nevertheless, a 24-hour section of the pressure record was of sufficient quality to provide a reliable estimate of the meter depth.

The edited data are stored on computer tape in FEB file format at the Naval Oceanographic Office and are undergoing further analyses.

6.5 DATA PRESENTATION

Time series of current speed and direction, east-west current component (u), and north-south current component (v) for each instrument are shown in Figures 6.2a-k in order of increasing instrument depth. Similar series for temperature, when available, are given in Figures 6.3a-k. The figures include all observed values within the specified time interval. The values have been edited to remove occasional spurious values, but have not been otherwise smoothed. As is characteristic of open-ocean current measurements, oscillations of inertial period, indistinguishable from diurnal period at this latitude, are prominent.

Progressive vector diagrams are displayed in Figures 6.4a-k. These hodographs describe, as a function of time, the cumulative sum of current vectors which have been low-pass filtered at 1 cph and subsampled at hourly intervals. The curves do not, in general, correspond to the trajectory of a water particle. Note that the mean current has a component toward the west in all cases.

Power spectra of the u and v current components were computed and the results are given in Figure 6.5a-k. The technique used for these calculations is a standard one: a linear trend was removed from each series, a cosine bell window applied in the time domain, the series Fourier transformed, spectral estimates obtained by averaging the squared Fourier coefficients at several adjacent frequencies, and, finally, the spectral estimates corrected for the loss of variance induced by the data window. The number of frequency bands over which averaging took place was variable, giving the frequency dependent confidence limits seen in Figures 6.5a-k.

Alternate spectral representations available for vector time series (Gonella, 1972) have also been prepared. Figures 6.6a-k show the series decomposed spectrally into circular clockwise and counter-clockwise components, and Figures 6.7a-k give the orientation and stability of the current ellipse defined by each vector spectral component.

The spectra show the characteristic features expected at this location. The dominant spectral peak is at inertial (or diurnal tidal) period and the motion there is largely polarized in the circular, clockwise sense. Energy levels decrease roughly as the inverse square of the frequency for frequencies greater than tidal.

No change of spectral slope is evident at the local Brunt-Vaisala frequency, which is nearly constant at 2 or 3 cph over the depth range spanned by the current meters (see Figs. 4.1 and 4.2).

6.6 REFERENCES

Gonella, J. (1972). A Rotary-component Method for Analysing Meteorological and Oceanographic Vector Time Series. Deep-Sea Res., 19, p. 833-846.

Mayoral, Carlos (1978). Vector Averaging Current Meter Temperature Accuracy and Response Time Test. NAVOCEANO Technical Note No. 6320-1-78.

McCullough, James R. (1975). Vector Averaging Current Meter Speed Calibration and Recording Technique. Unpublished manuscript, Woods Hole Oceanographic Institution, Technical Report Number WHOI-75-44.

Von Zweck, O. and R. Wahl (1980). Upper Ocean Current Measurements in the Sargasso Sea. NAVOCEANO Technical Note No. 7210-1-80.

TABLE 6.1

CURRENT METER MOORING SUMMARY

METER	DEPTH (M)	USABLE DATA START	USABLE DATA END	SAMPLING INTERVAL (SEC)	VARIABLES
V561	132	0000Z 5 SEP 79	1248Z 16 OCT 79	112	U,V,T
V217	147	0000Z 5 SEP 79	1248Z 16 OCT 79	112	U,V,T
V538	162	0000Z 5 SEP 79	1248Z 16 OCT 79	112	U,V,T
V256	177	0000Z 5 SEP 79	1248Z 16 OCT 79	112	U,V,T
V539	192	0000Z 5 SEP 79	1248Z 16 OCT 79	112	U,V,T
V532	222	0000Z 5 SEP 79	1248Z 16 OCT 79	112	U,V,T
V254	272	0000Z 5 SEP 79	1248Z 16 OCT 79	112	U,V,T
V559	372	0000Z 5 SEP 79	1248Z 16 OCT 79	112	U,V,T
A2926	522	0000Z 5 SEP 79	1300Z 8 SEP 79	600	P
A2930	1022	0000Z 5 SEP 79	1241Z 16 OCT 79	600	S,D
A2797	1522	0000Z 5 SEP 79	1241Z 16 OCT 79	600	S,D
A2796	2022	NO DATA		600	

SYMBOLS

A - AANDERAA RCM 5
V - AMF-VACM

S - SPEED
D - DIRECTION
P - PRESSURE

U - EAST-WEST COMPONENT OF CURRENT
V - NORTH-SOUTH COMPONENT OF CURRENT
T - TEMPERATURE

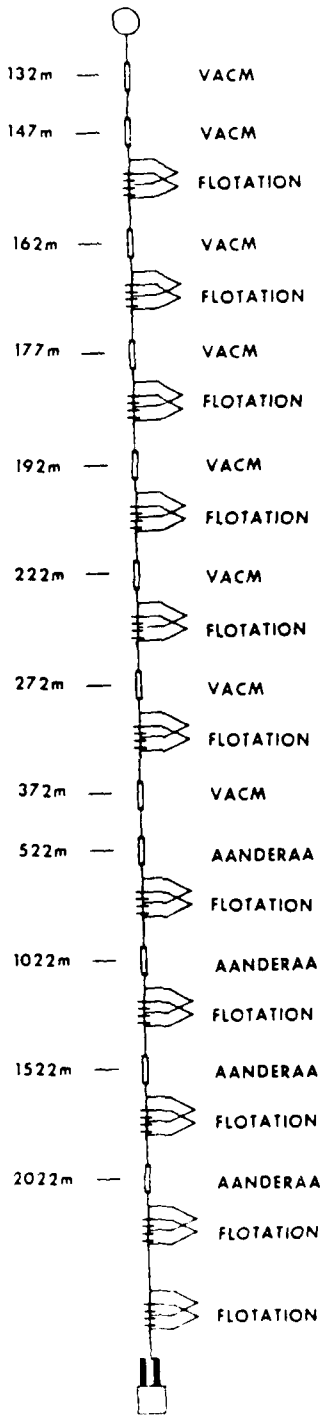

Figure 6.1. Current meter mooring schematic.

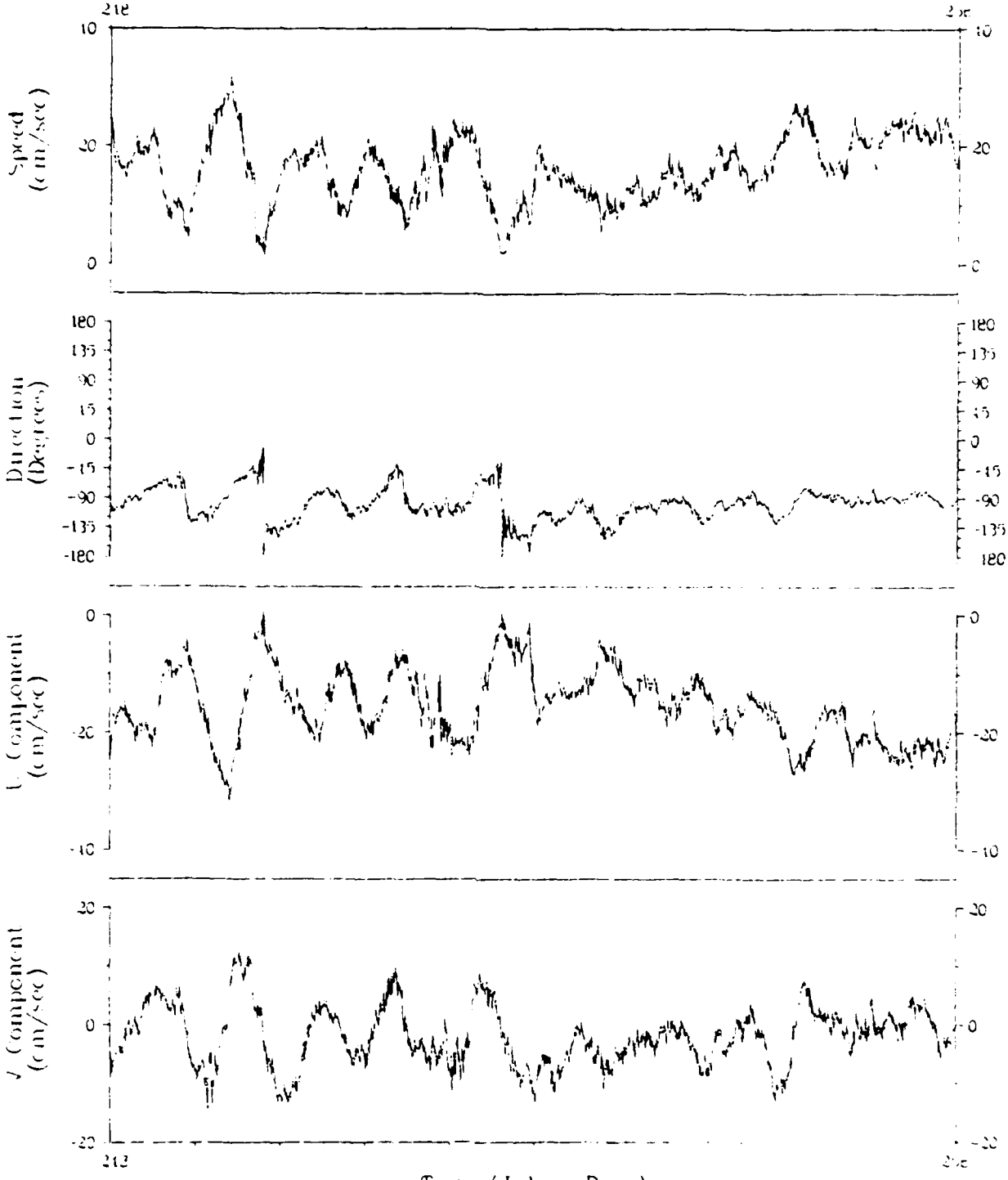

File	VA0879	Array	2
Meter	V-0561	Depth	132 M
Latitude	30 29.7 N	Start	5 SEP 1979
Longitude	71 15.6 W	End	11 SEP 1979

Figure 6.2a. Current time series

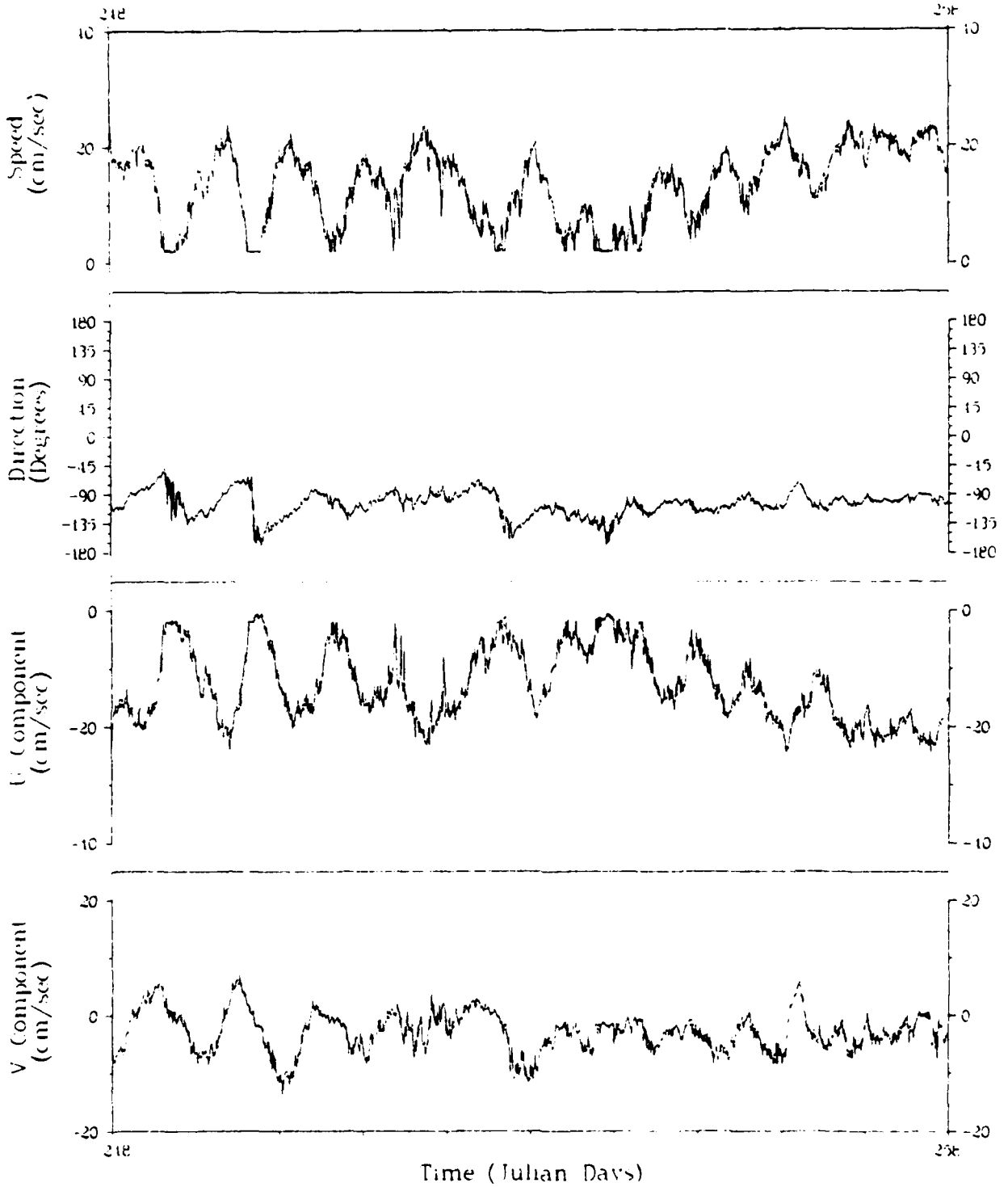

File	VA0879	Array	2
Meter	V-0217	Depth	117 M
Latitude	30 29.7 N	Start	5 SEP 1979
Longitude	71 15.6 W	End	11 SEP 1979

Figure 6.2b. Current time series

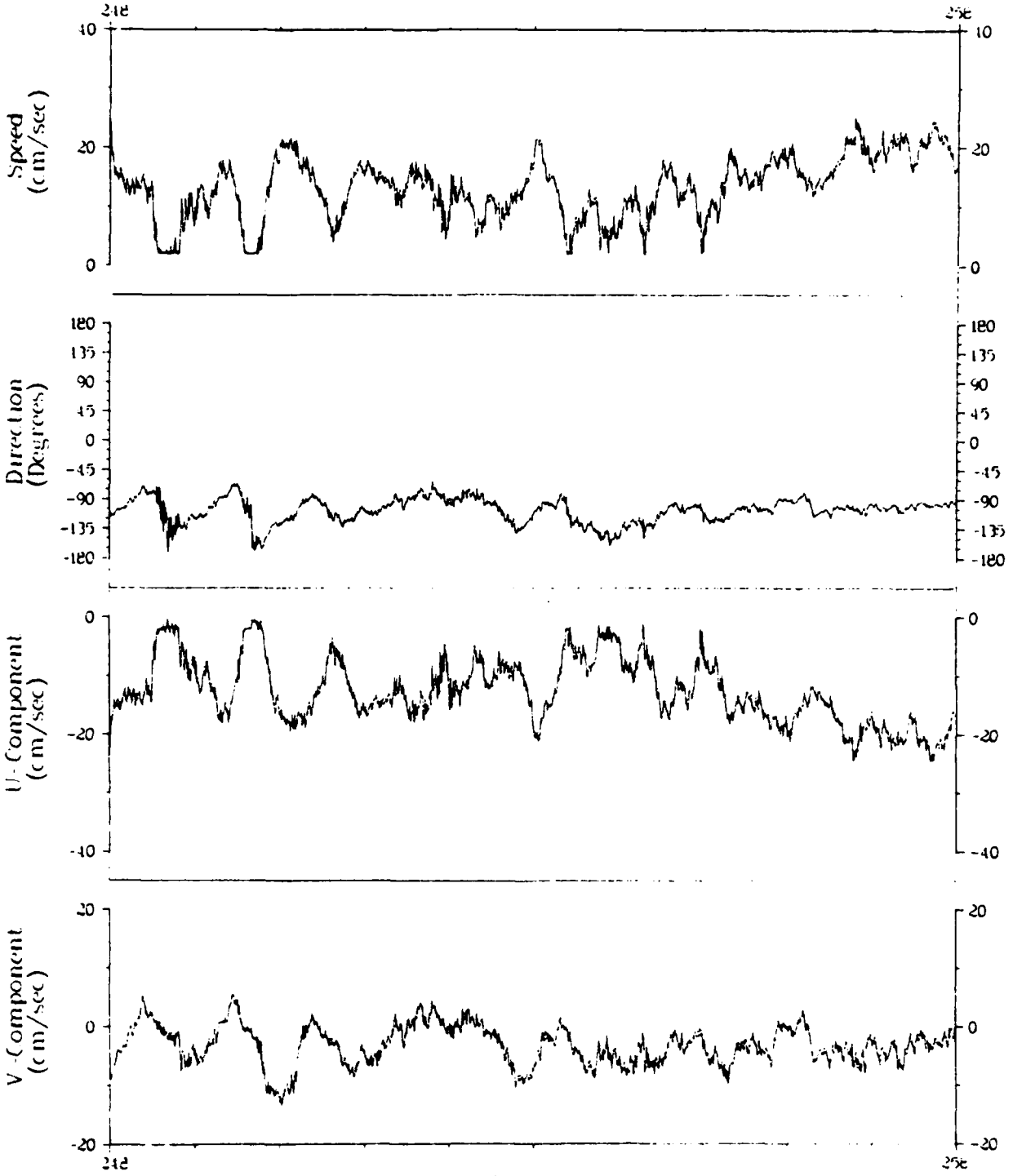

File	VA0879	Array	2
Meter	V-0538	Depth	162 M
Latitude	30 29.7 N	Start	5 SEP 1979
Longitude	71 15.6 W	End	11 SEP 1979

Figure 6.2c. Current time series

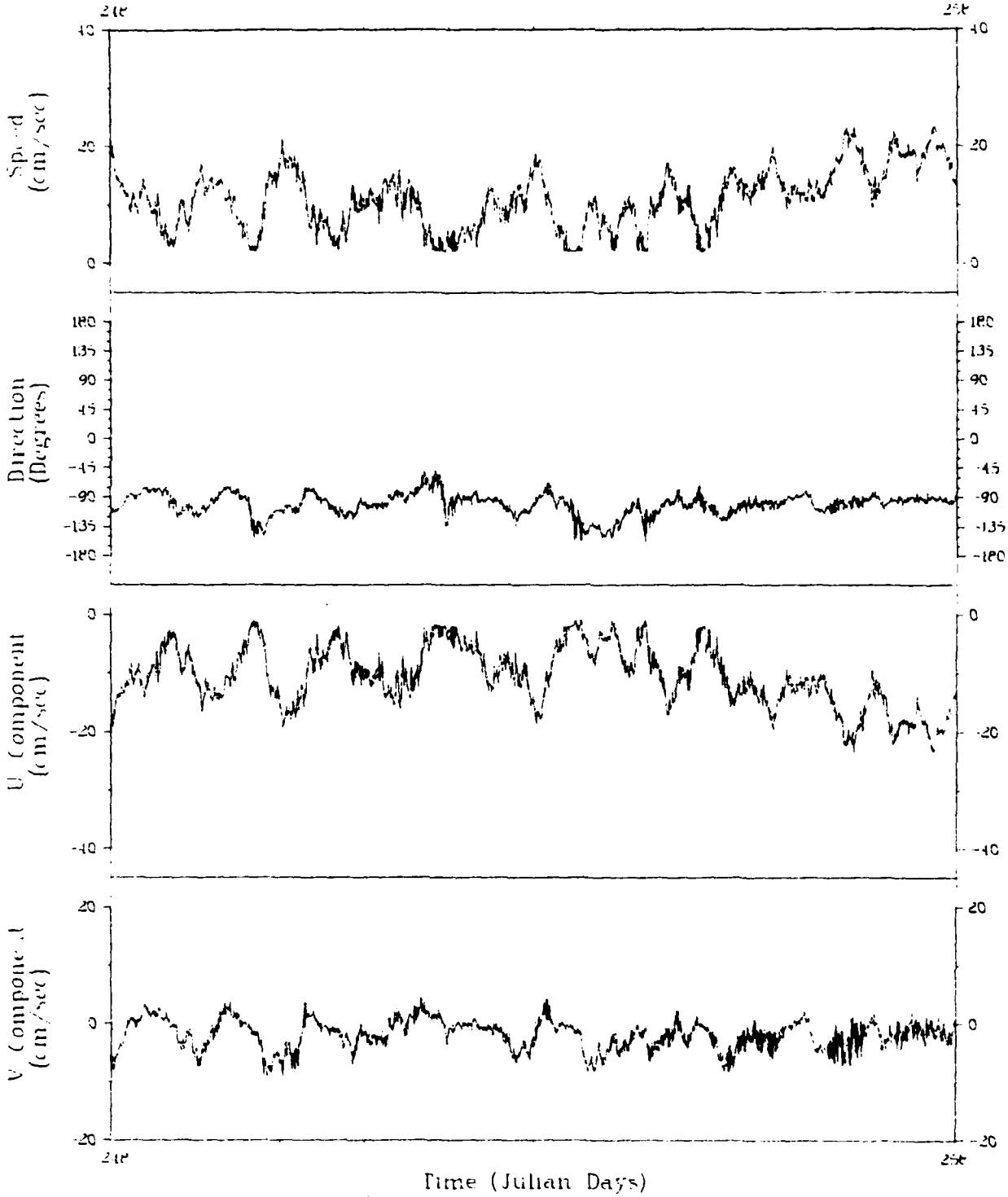

File	VA0879	Array	2
Meter	V-0256	Depth	177 M
Latitude	30 29.7 N	Start	5 SEP 1979
Longitude	71 43.6 W	End	14 SEP 1979

Figure 6.2d. Current time series

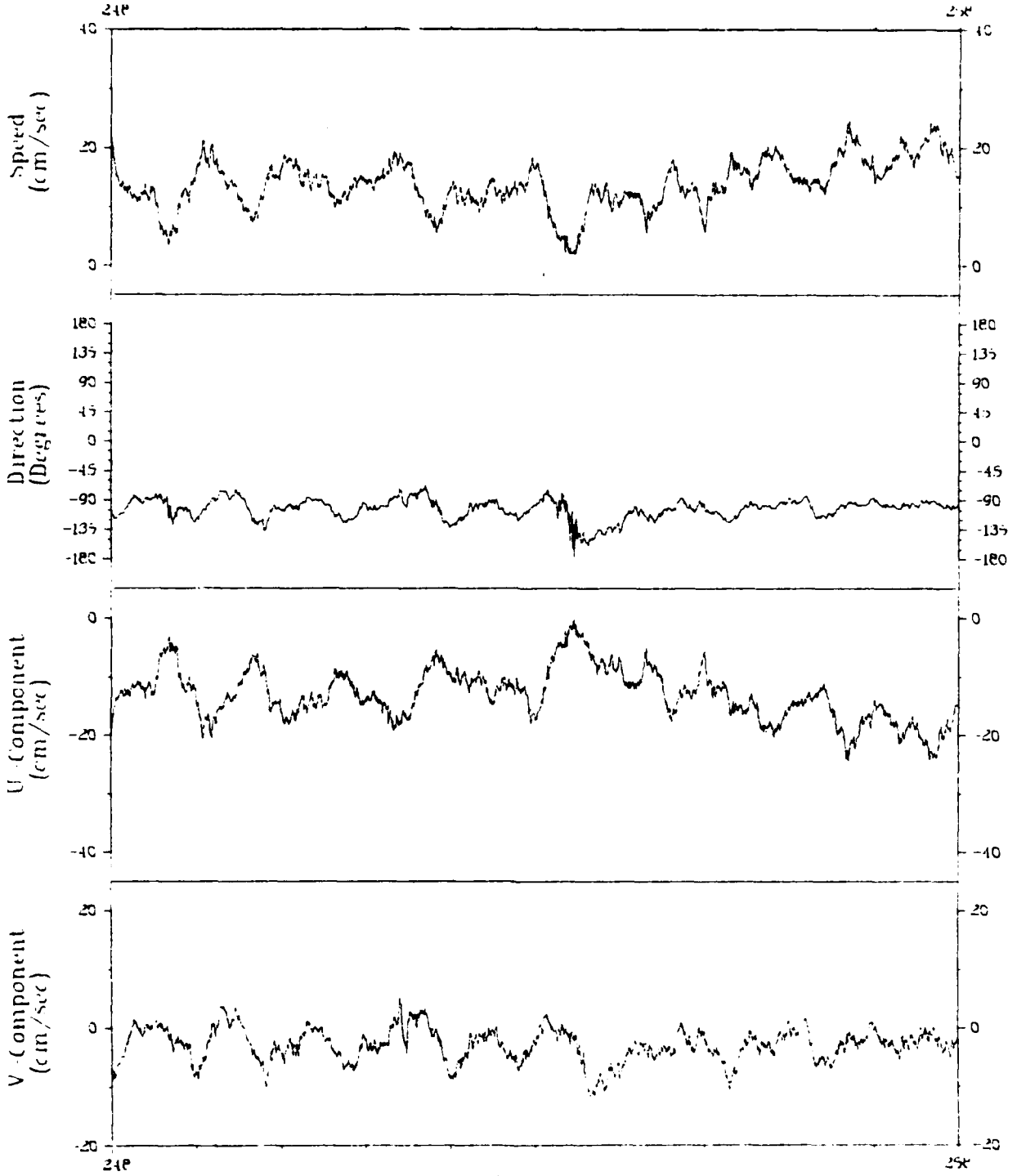

File	VA0879	Array	2
Meter	V-0539	Depth	192 M
Latitude	30 29.7 N	Start	5 SEP 1979
Longitude	71 45.6 W	End	14 SEP 1979

Figure 6.2e. Current time series

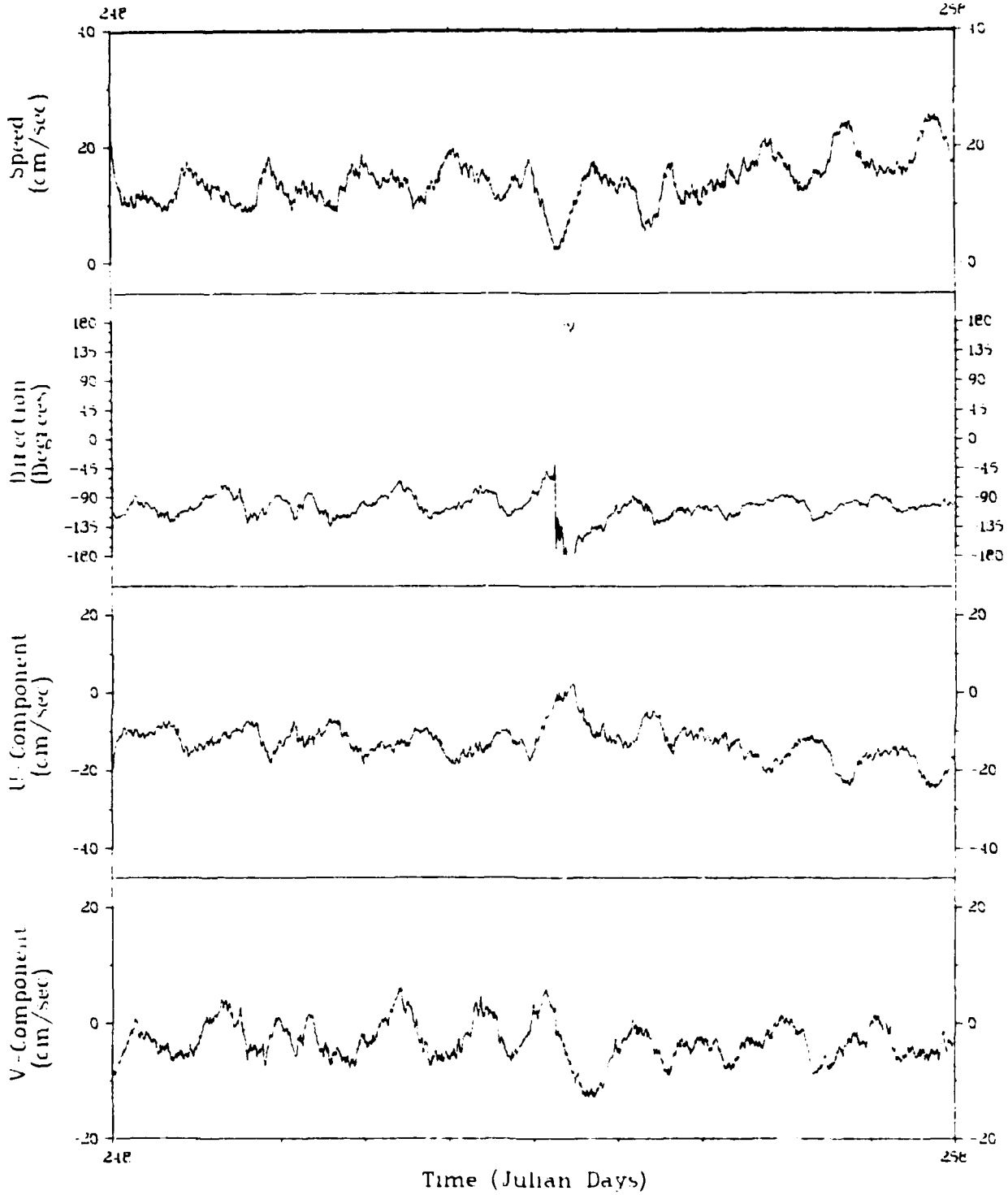

File	VA0879	Array	2
Meter	V-0532	Depth	222 M
Latitude	30 29.7 N	Start	5 SEP 1979
Longitude	71 45.6 W	End	14 SEP 1979

Figure 6.2f. Current time series

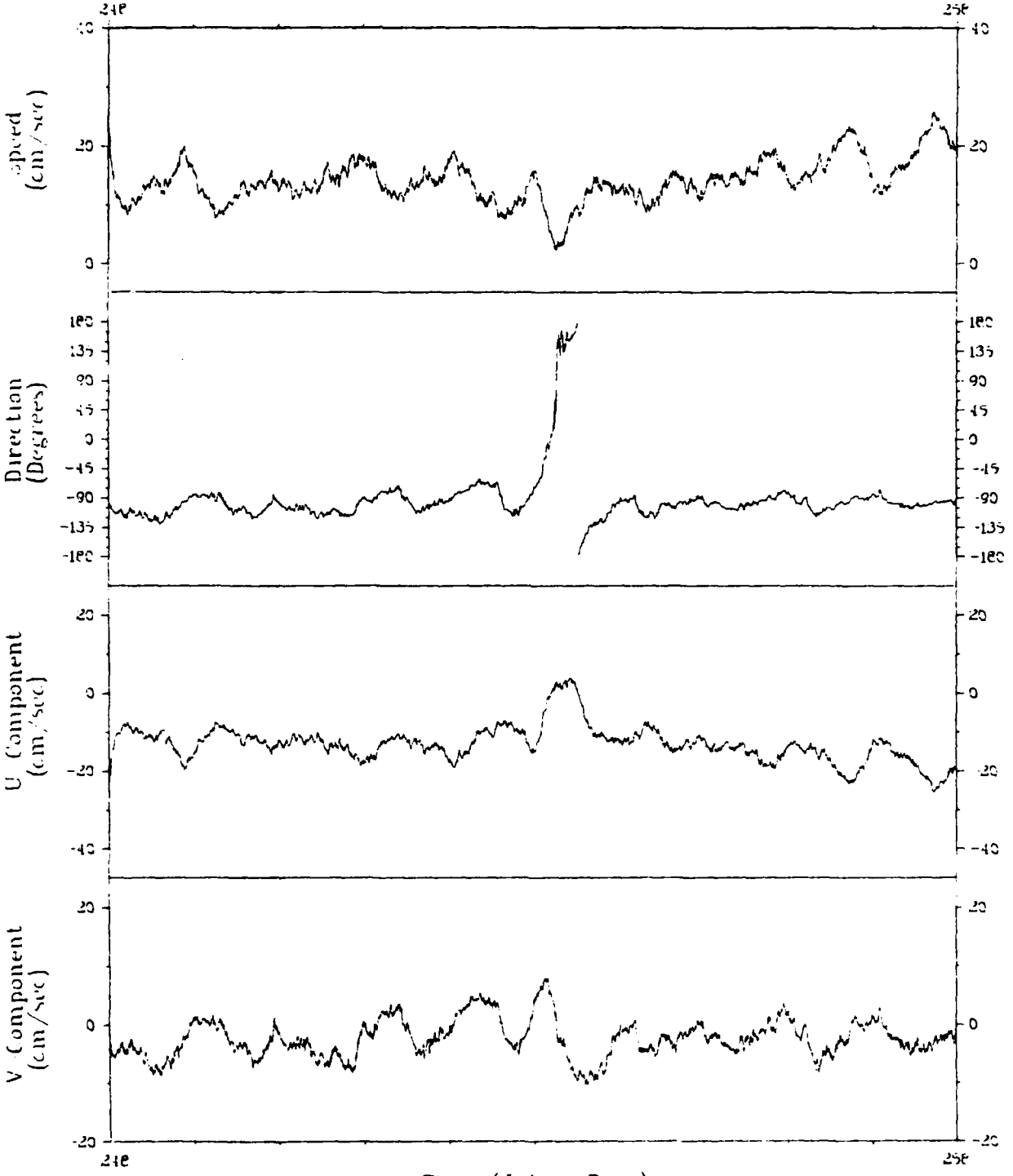

File	VA0879	Array	2
Meter	V-0254	Depth	272 M
Latitude	30 29.7 N	Start	5 SEP 1979
Longitude	71 45.6 W	End	14 SEP 1979

Figure 6.2g. Current time series

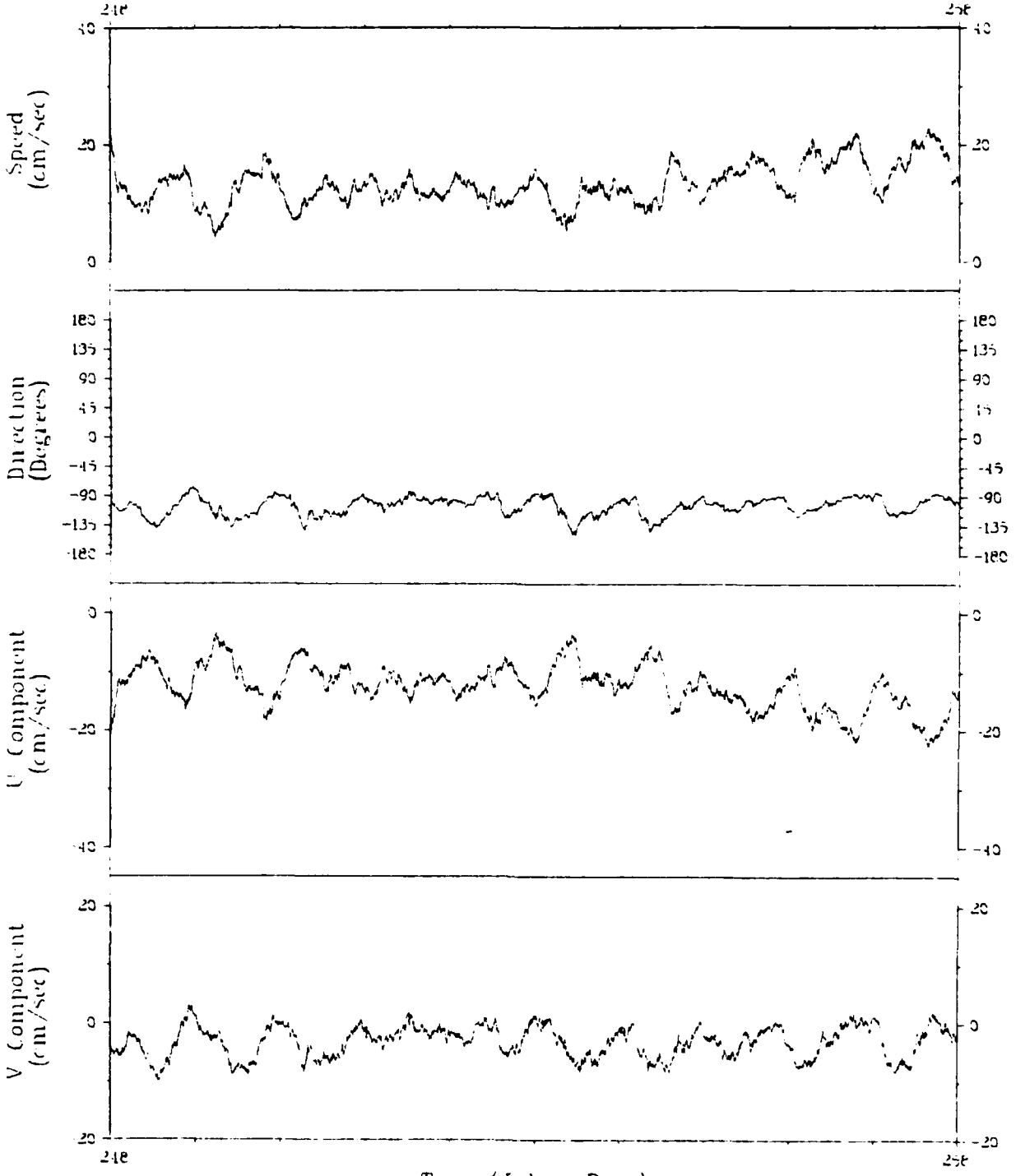

File	VA0879	Array	2
Meter	V-0559	Depth	372 M
Latitude	30 29.7 N	Start	5 SEP 1979
Longitude	71 45.6 W	End	14 SEP 1979

Figure 6.2h. Current time series

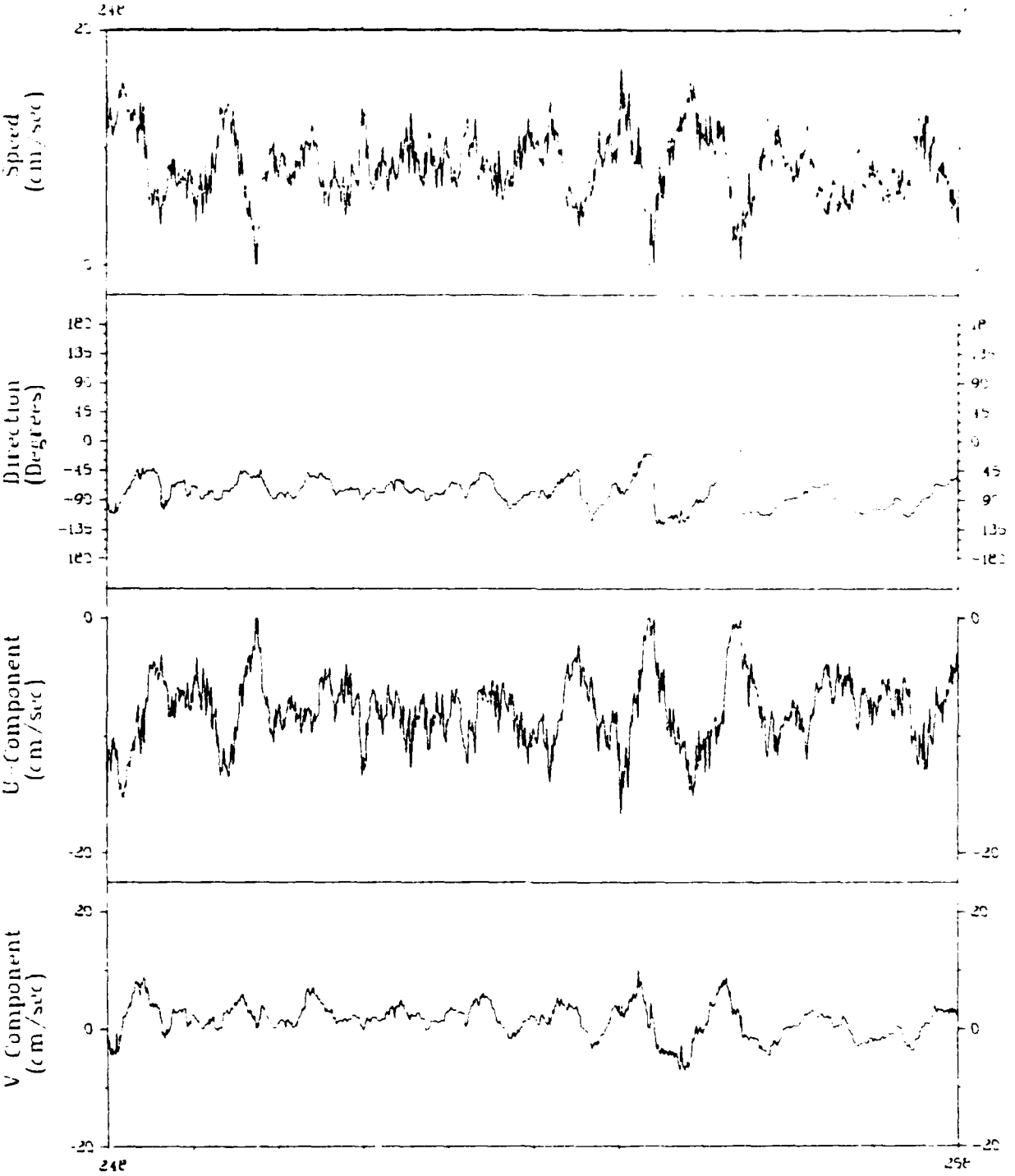

File	AA0879	Array	2
Meter	A-2930	Depth	1022 M
Latitude	30 29.7 N	Start	5 SEP 1979
Longitude	71 45.6 W	End	15 SEP 1979

Figure 6.2j. Current time series

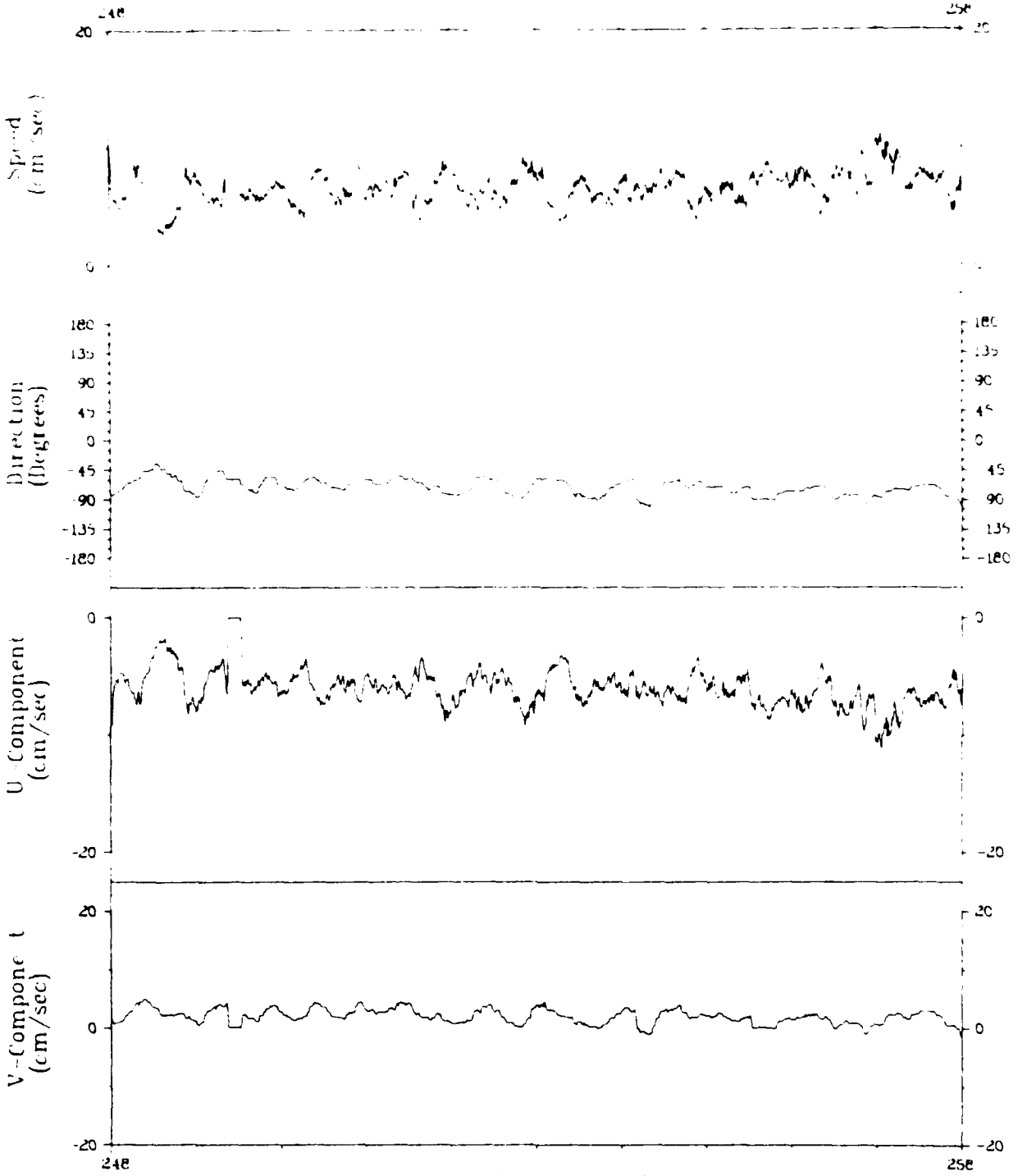

File	AA0879	Array	2
Meter	A-2797	Depth	1522 M
Latitude	30 29.7 N	Start	5 SEP 1979
Longitude	71 45.6 W	End	15 SEP 1979

Figure 6.2k. Current time series

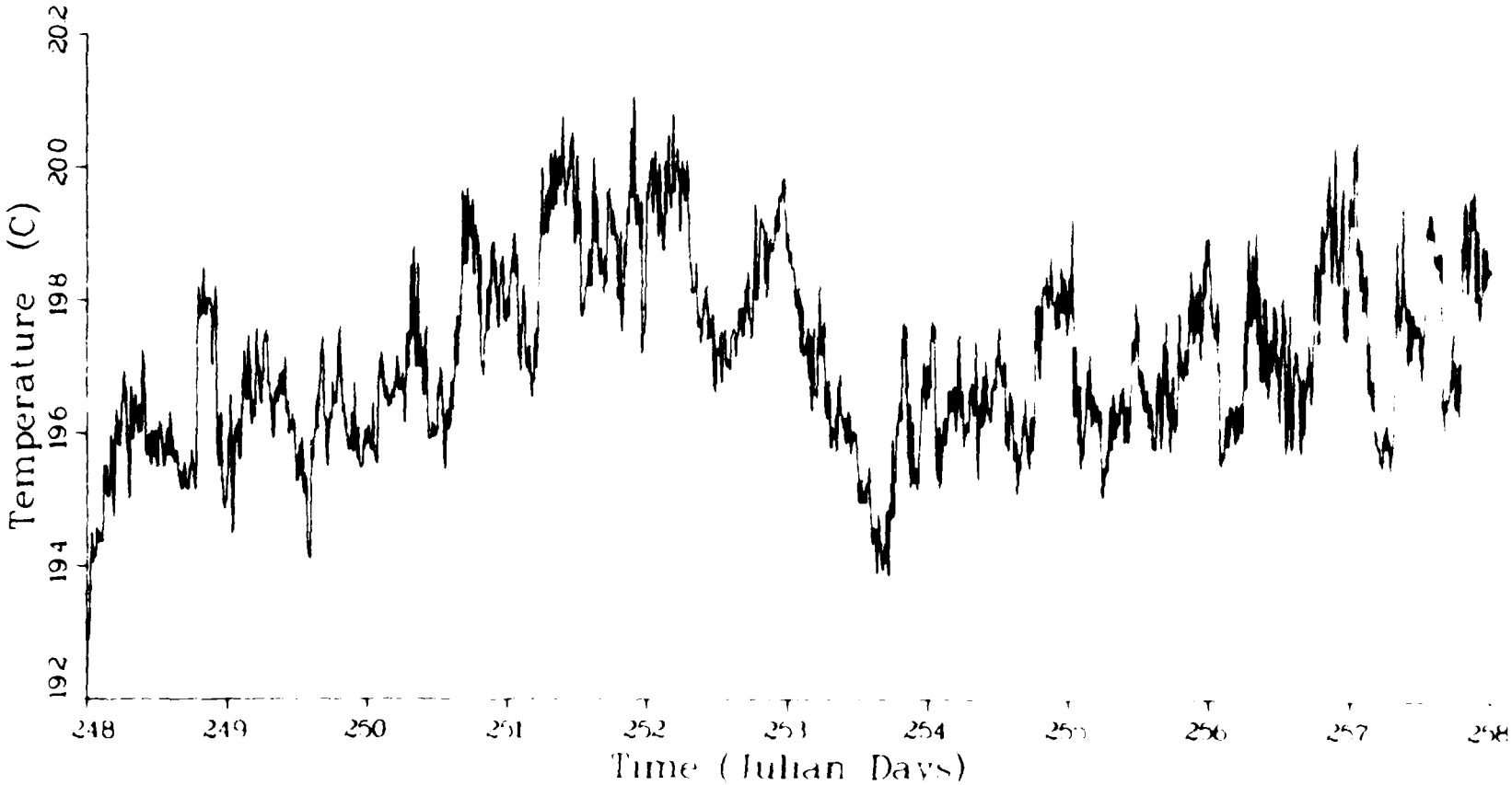

File	VA0879	Array	2
Meter	V 0561	Depth	132 M
Latitude	30 29.7 N	Start	5 SEP 1979
Longitude	71 [illegible] W	End	11 SEP 1979

[illegible] Temperature Time Series

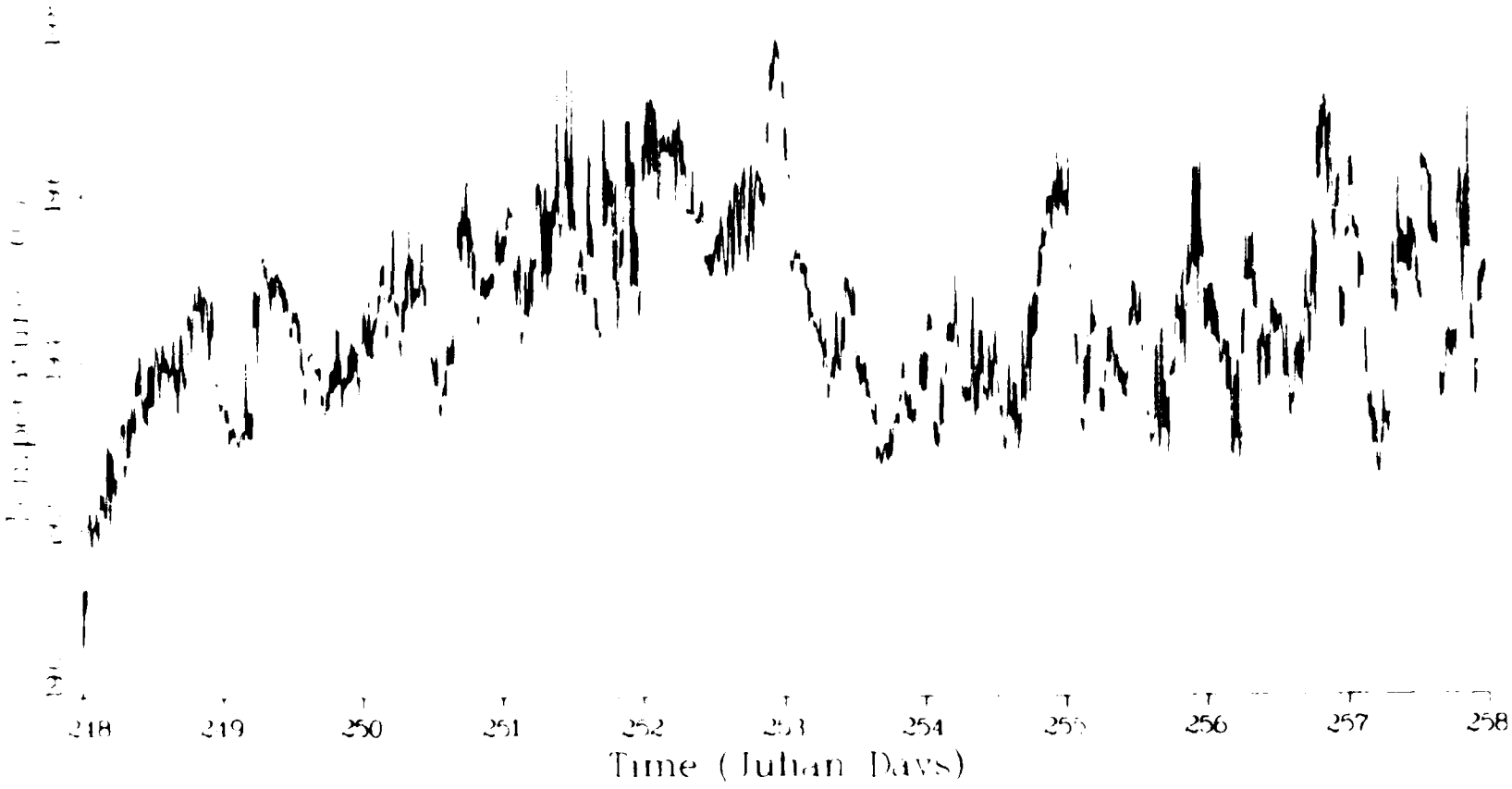

File	VA0879	Array	2
Meter	V 0217	Depth	147 M
Latitude	30 29.7 N	Start	5 SEP 1979
Longitude	71 45.6 W	End	14 SEP 1979

Figure 6.3b. Temperature time series

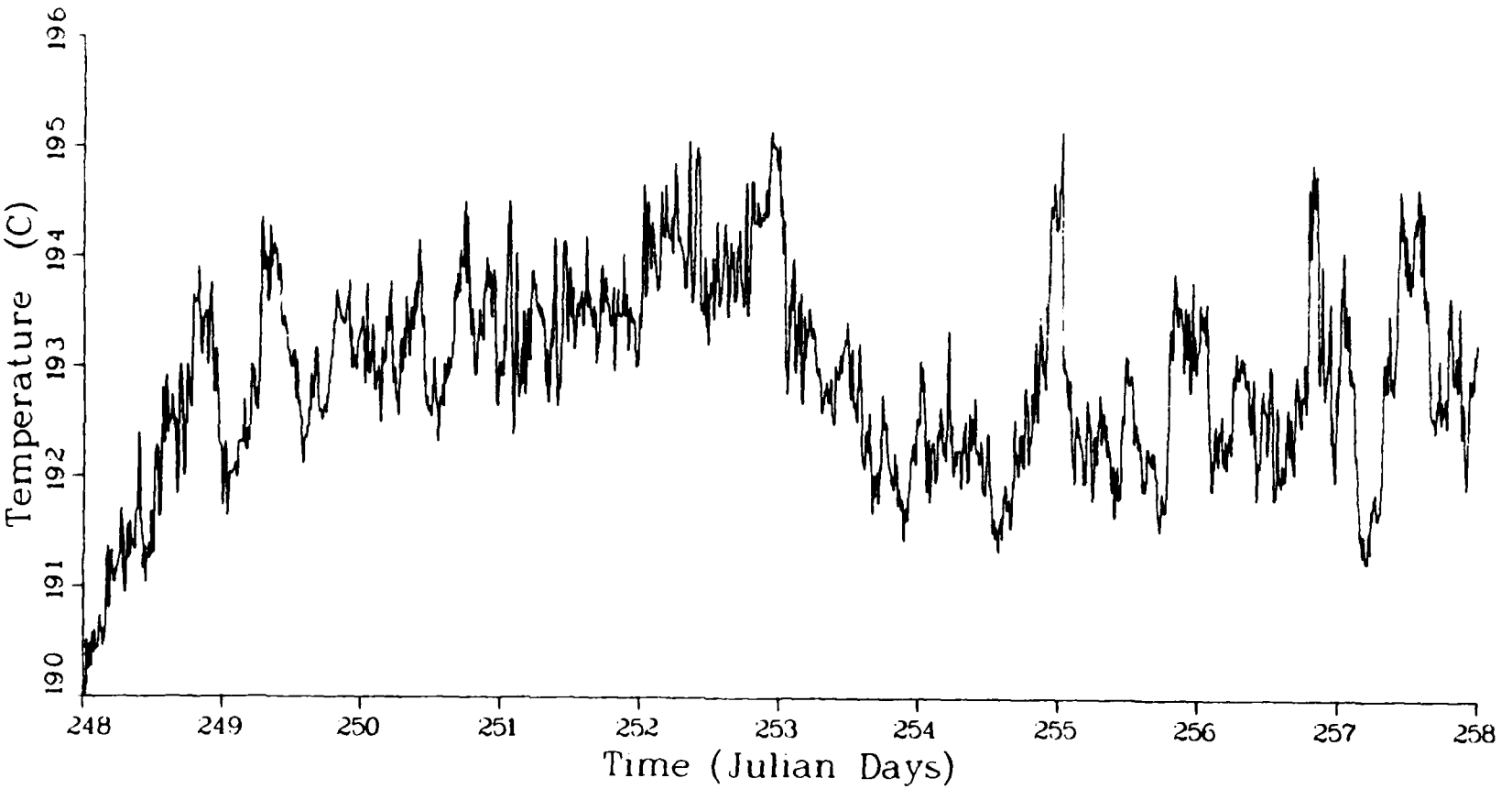

File	VA0879	Array	2
Meter	V-0538	Depth	162 M
Latitude	30 29.7 N	Start	5 SEP 1979
Longitude	71 45.6 W	End	14 SEP 1979

Figure 6.3c. Temperature time series

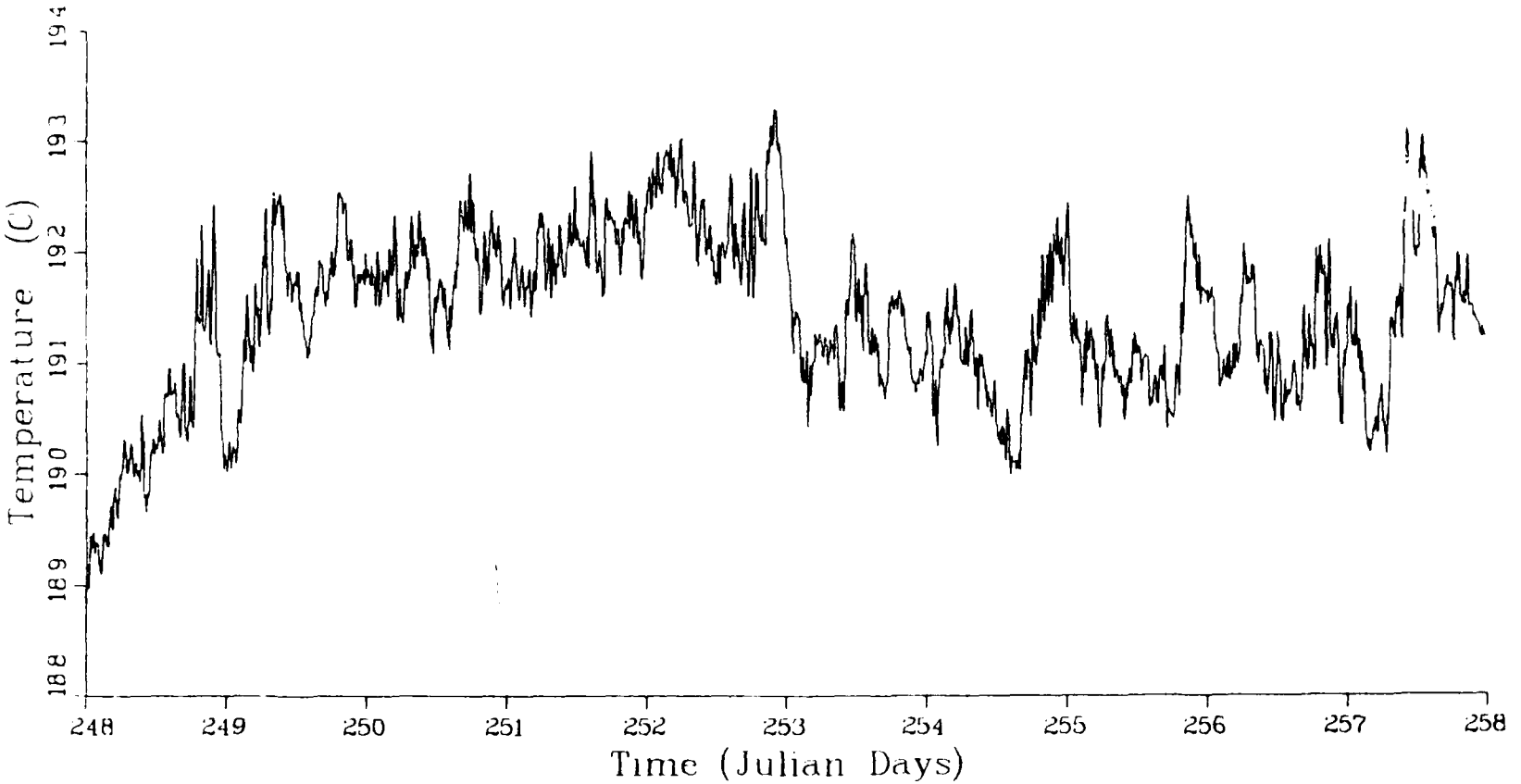

File	VA0879	Array	2
Meter	V-0256	Depth	177 M
Latitude	30 29.7 N	Start	5 SEP 1979
Longitude	71 45.6 W	End	14 SEP 1979

Figure 6.3d. Temperature time series

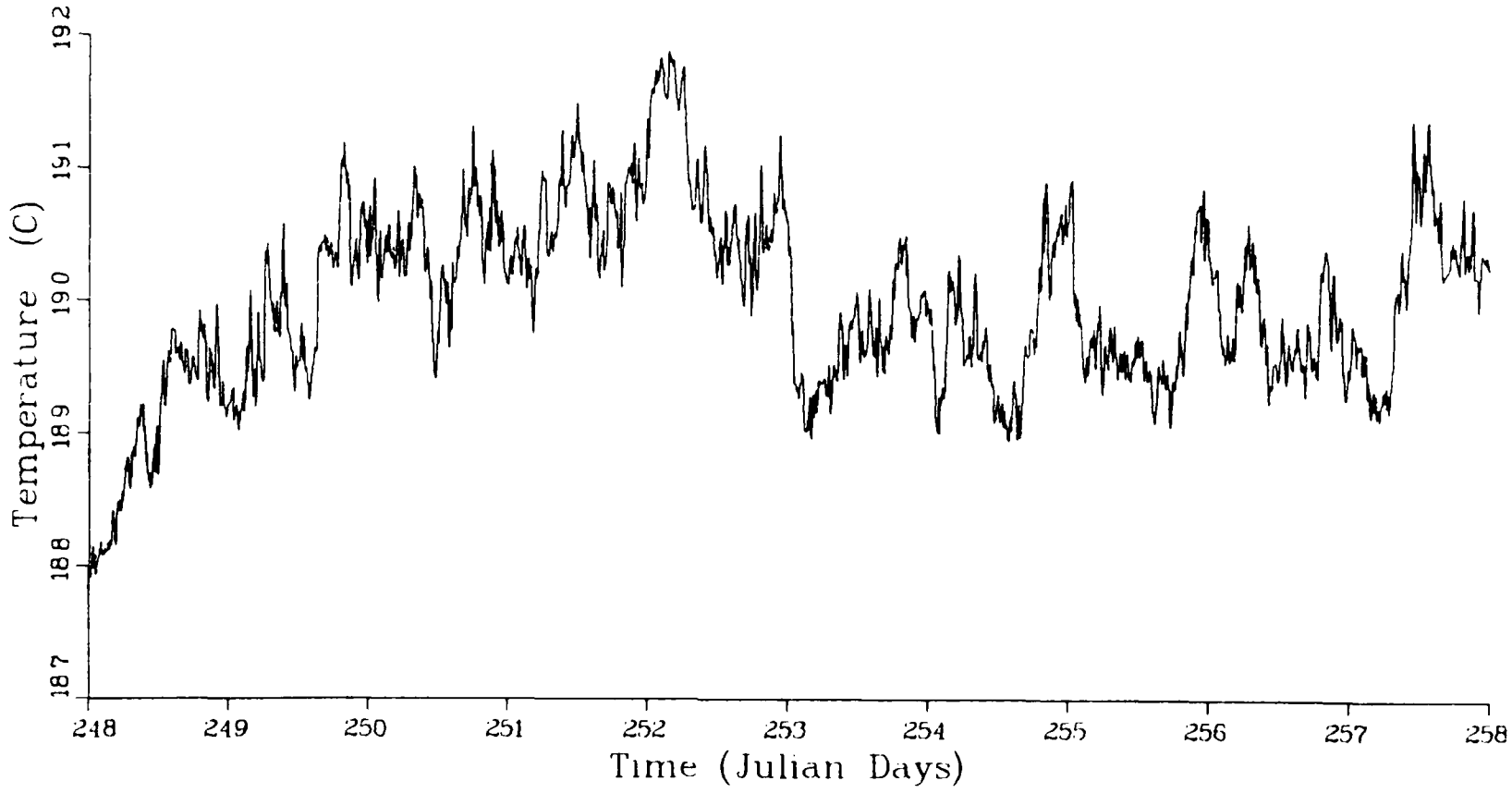

File	VA0879	Array	2
Meter	V-0539	Depth	192 M
Latitude	30 29.7 N	Start	5 SEP 1979
Longitude	71 45.6 W	End	14 SEP 1979

Figure 6.3e. Temperature time series

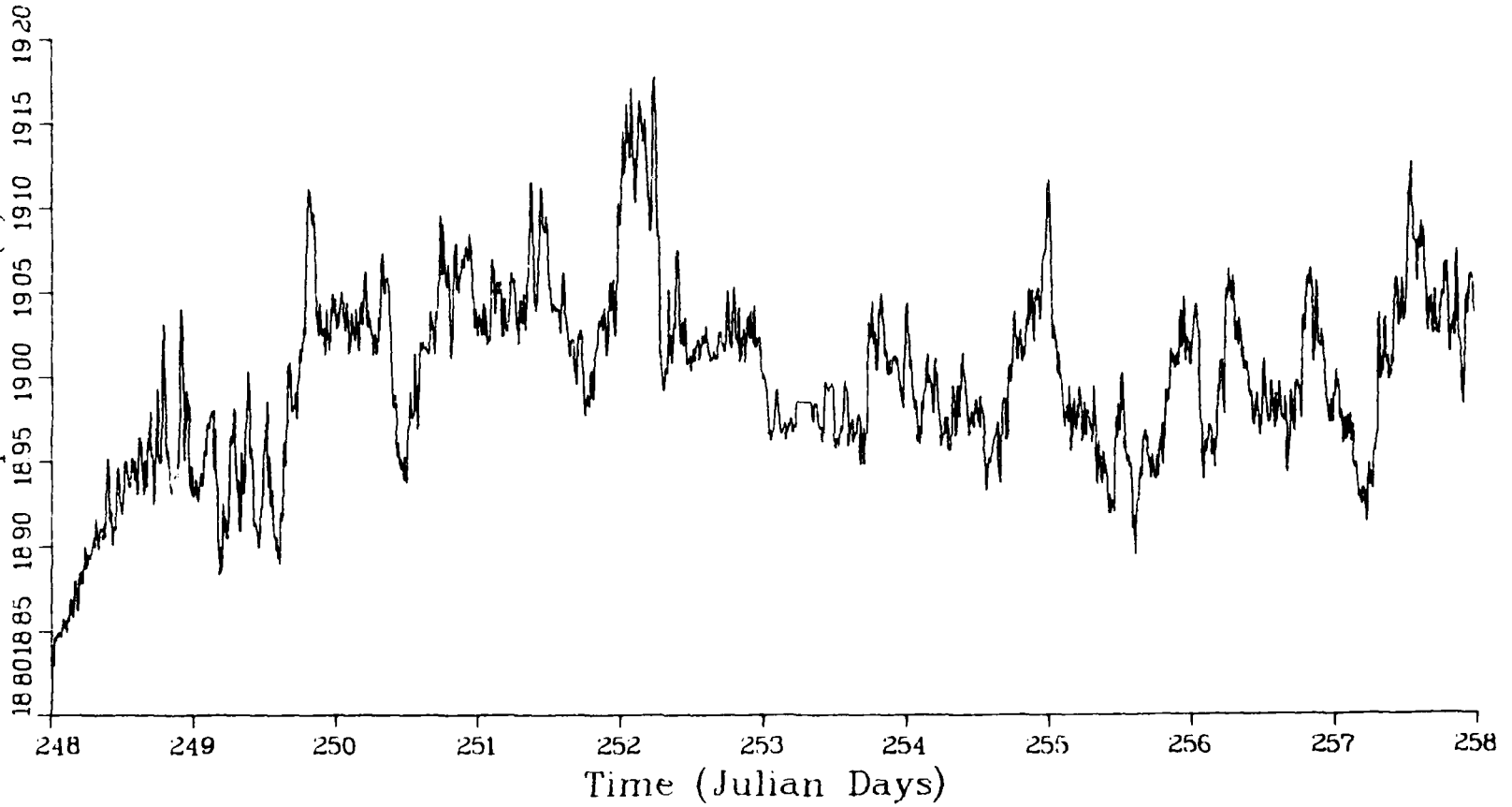

File	VA0879	Array	2
Meter	V-0532	Depth	222 M
Latitude	30 29.7 N	Start	5 SEP 1979
Longitude	71 45.6 W	End	14 SEP 1979

Figure 6.3f. Temperature time series

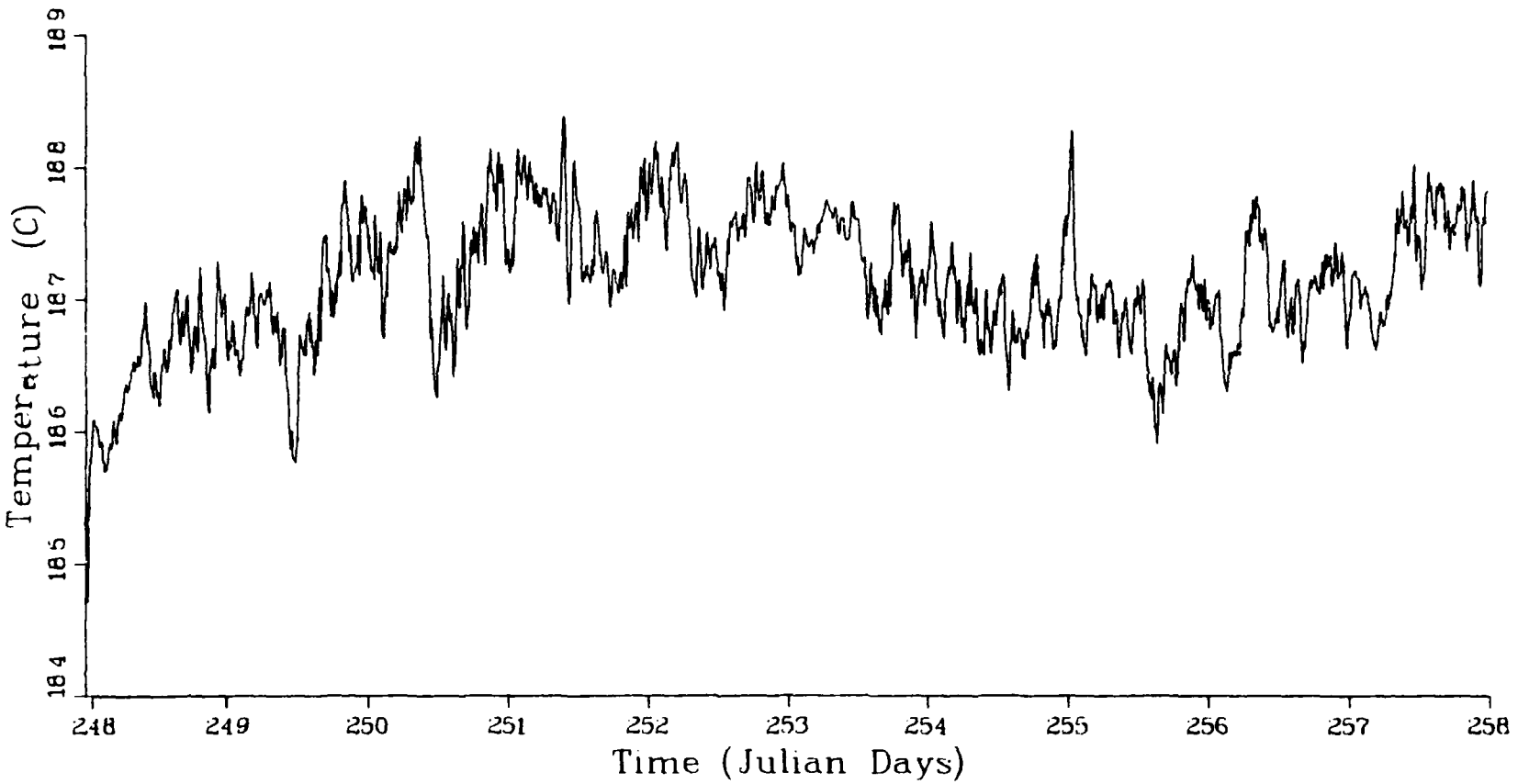

File	VA0879	Array	2
Meter	V-0254	Depth	272 M
Latitude	30 29.7 N	Start	5 SEP 1979
Longitude	71 45.6 W	End	14 SEP 1979

Figure 6.3g. Temperature time series

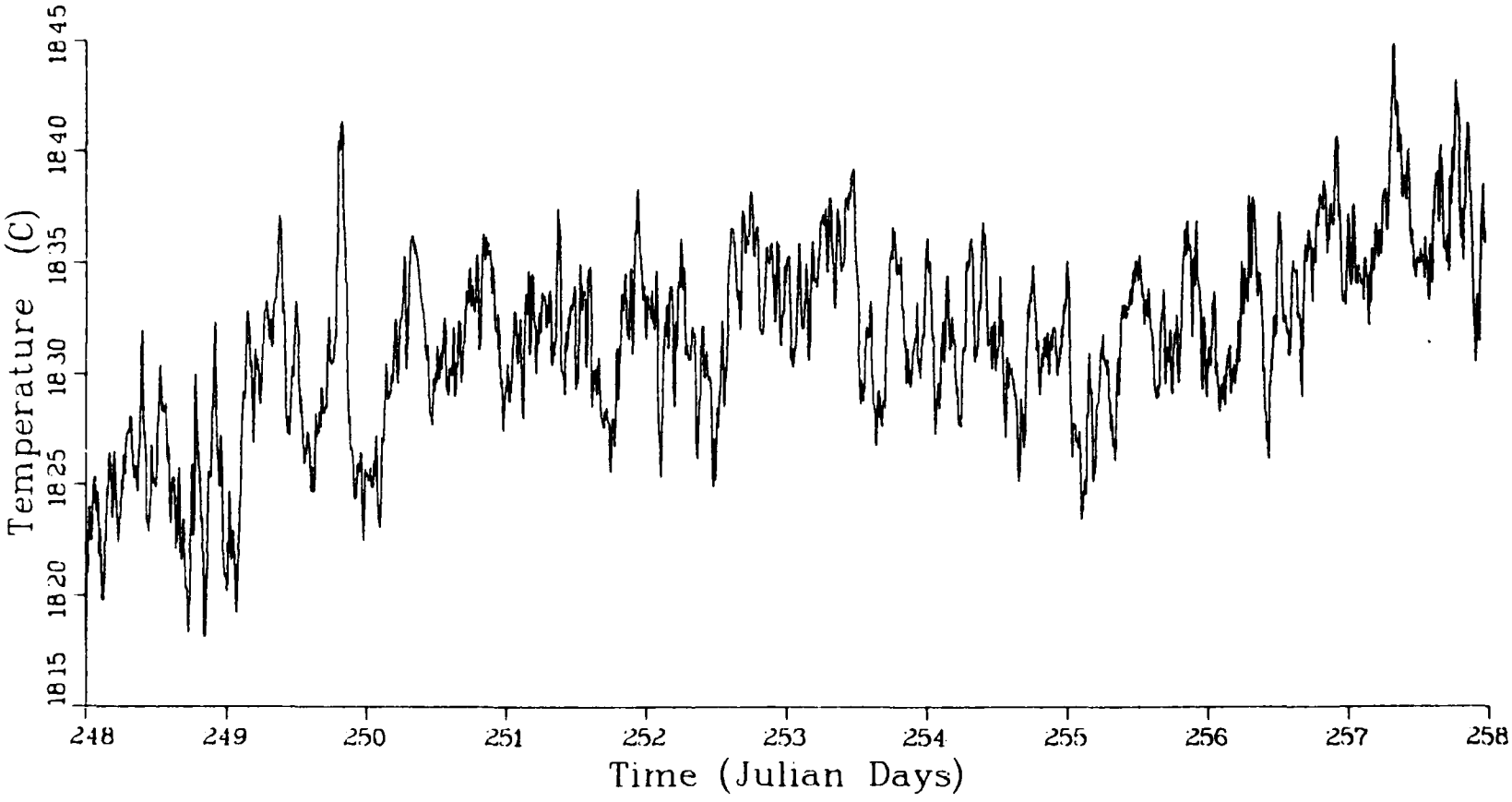

File	VA0879	Array	2
Meter	V-0559	Depth	372 M
Latitude	30 29.7 N	Start	5 SEP 1979
Longitude	71 45.6 W	End	14 SEP 1979

Figure 6.3h. Temperature time series

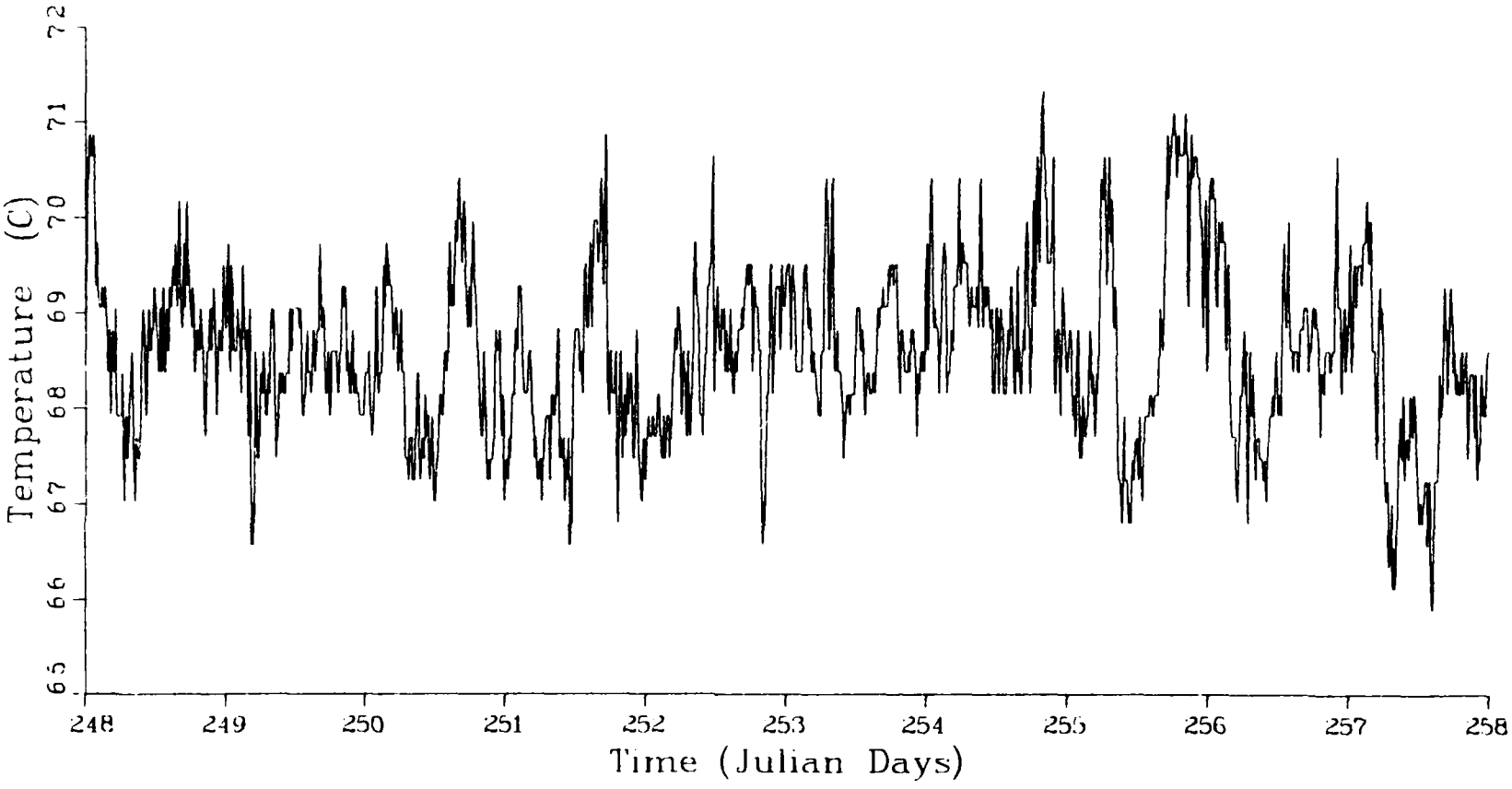

File	AA0879	Array	2
Meter	A-2930	Depth	1022 M
Latitude	30 29.7 N	Start	5 SEP 1979
Longitude	71 45.6 W	End	15 SEP 1979

Figure 6.3j. Temperature time series

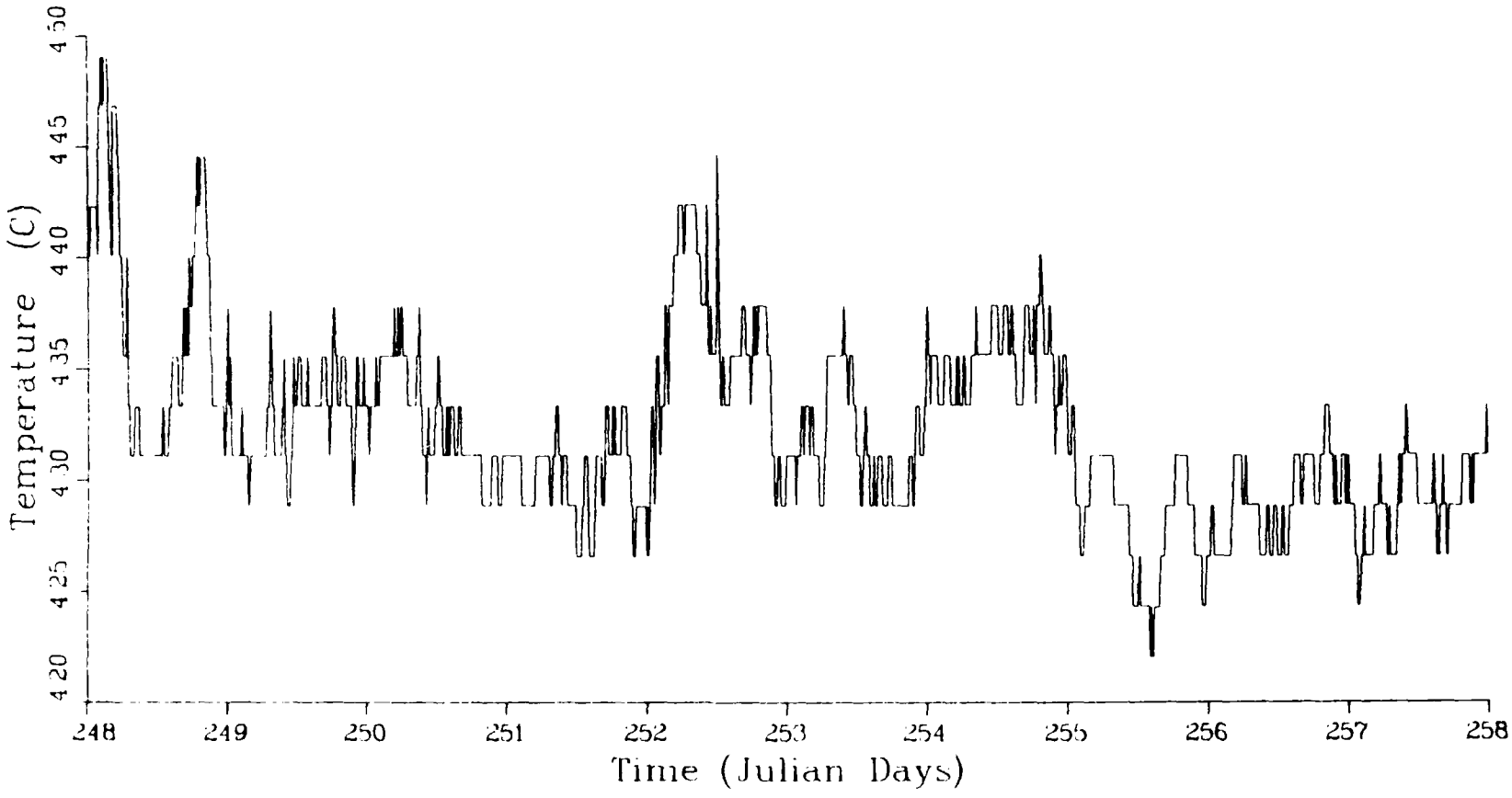

File	AA0879	Array	2
Meter	A-2797	Depth	1522 M
Latitude	30 29.7 N	Start	5 SEP 1979
Longitude	71 45.6 W	End	15 SEP 1979

Figure 6.3k. Temperature time series

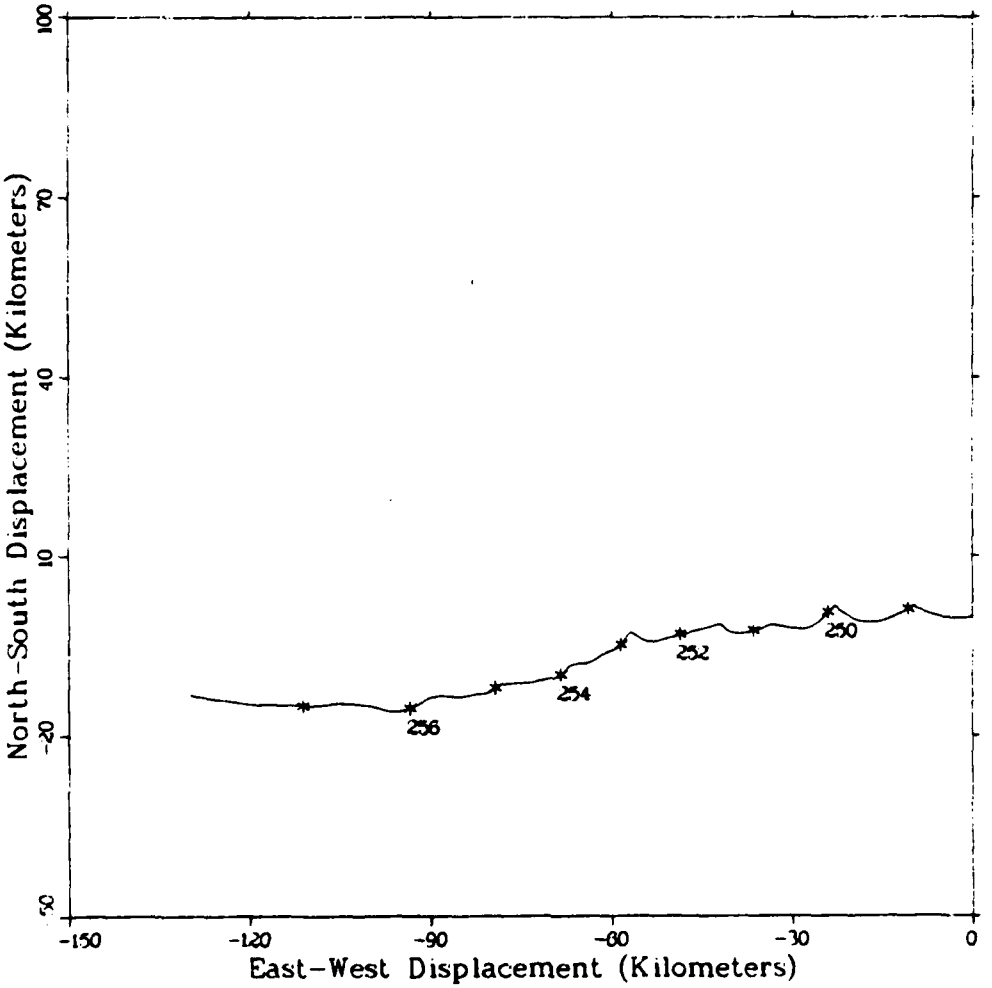

* Every 24 Hours Starting At 0000 Julian Day 249

File	VA0879	Array	2
Meter	V-0561	Depth	132 M
Latitude	30 297 N	Start	5 SEP 1979
Longitude	71 456 W	End	14 SEP 1979

Figure 6.4a. Progressive vector diagram

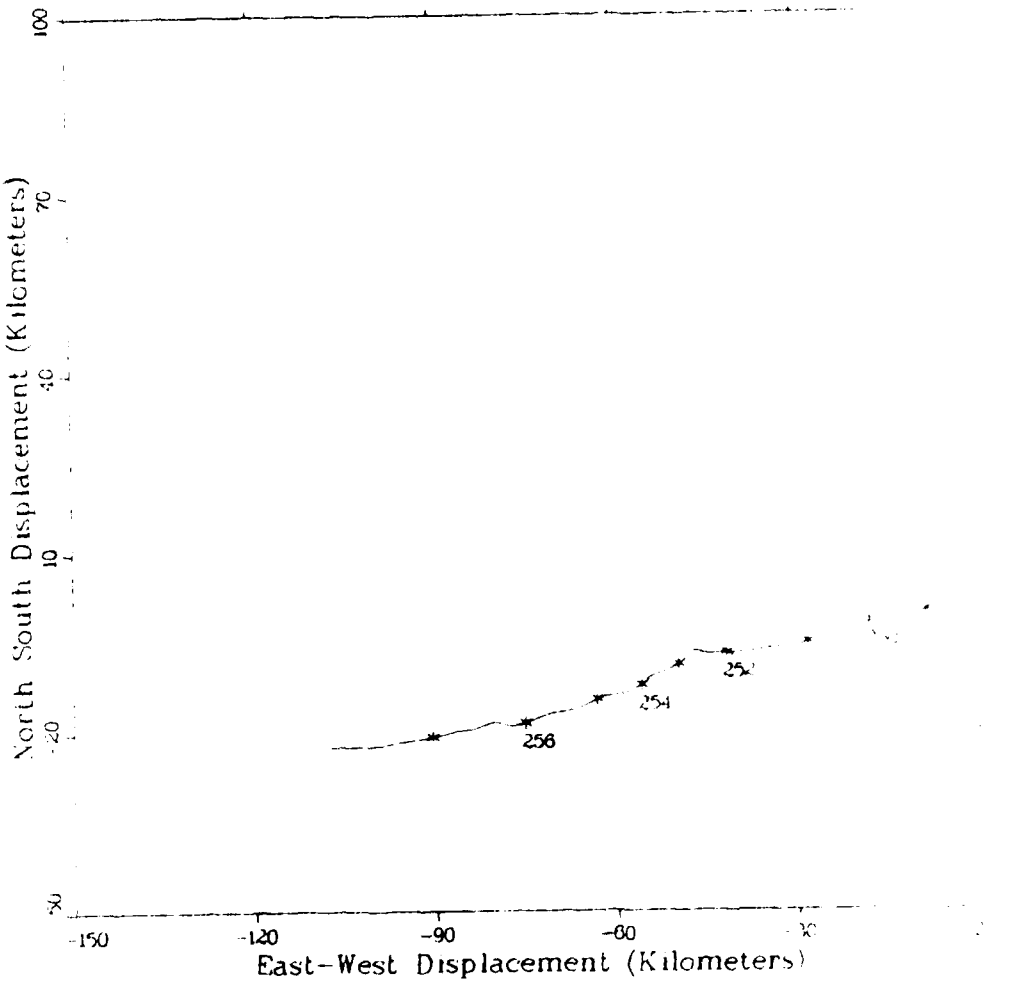

* Every 24 Hours Starting At 0000 Julian [illegible]

File	VA0879	Array	2
Meter	V-0217	Depth	[illegible] M
Latitude	30 29.7 N	Start	[illegible] 1979
Longitude	71 45.6 W	End	[illegible] 1979

Figure 6.4b. Progressive vector diagram

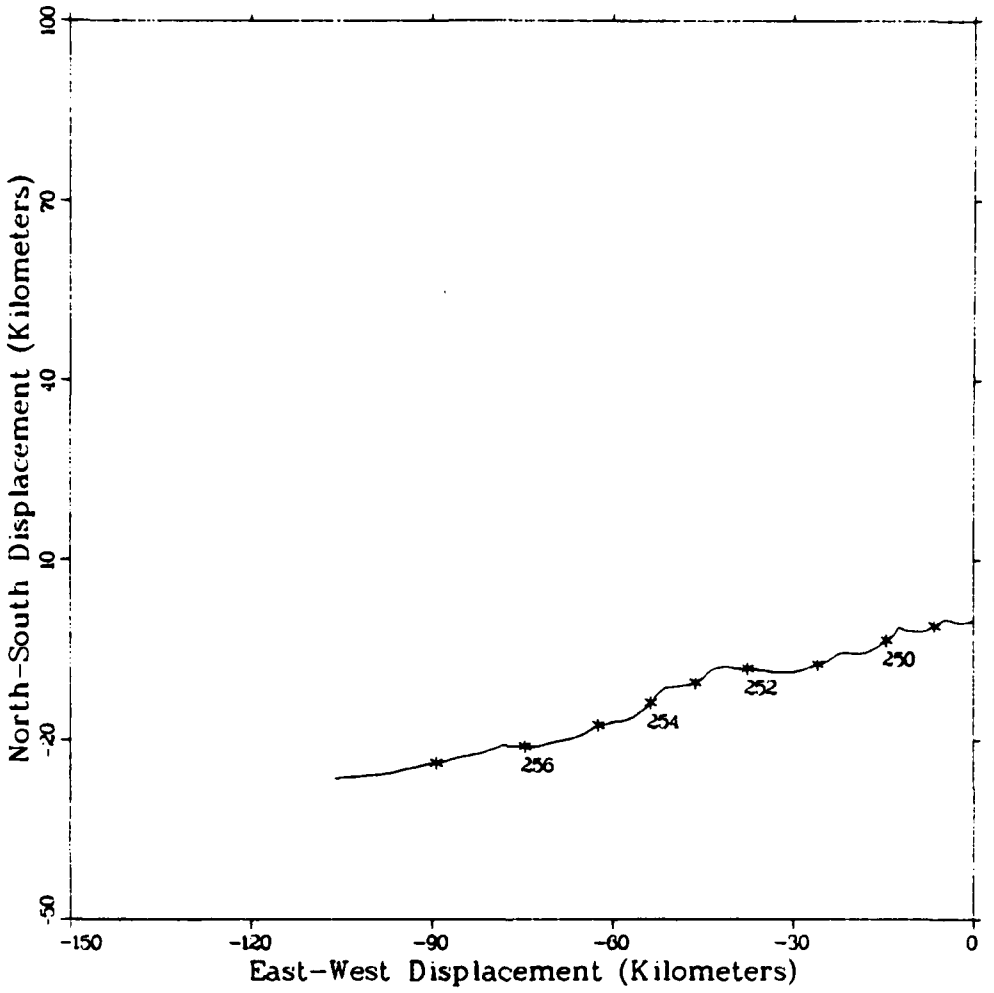

* Every 24 Hours Starting At 0000 Julian Day 249

File	VA0879	Array	2
Meter	V-0538	Depth	162 M
Latitude	30 29.7 N	Start	5 SEP 1979
Longitude	71 45.6 W	End	14 SEP 1979

Figure 6.4c. Progressive vector diagram

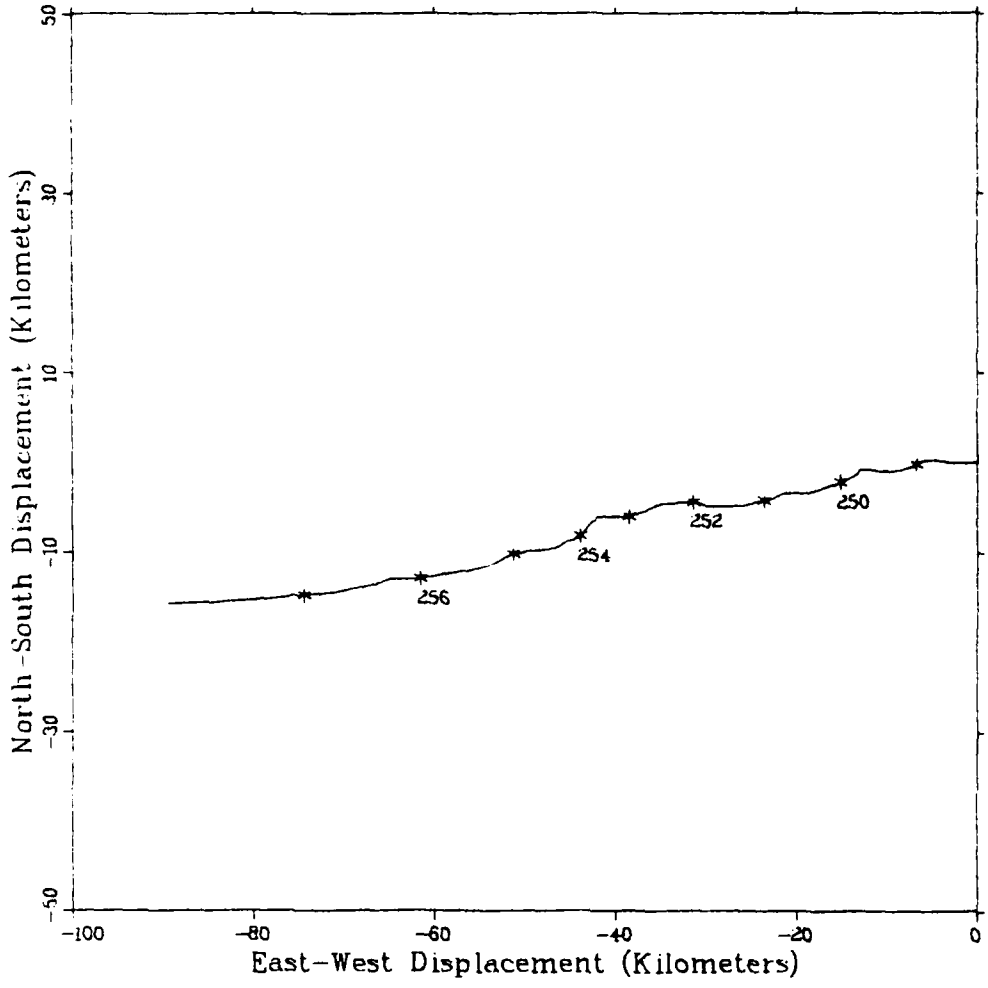

* Every 24 Hours Starting At 0000 Julian Day 249

File	VA0879	Array	2
Meter	V-0256	Depth	177 M
Latitude	30 29.7 N	Start	5 SEP 1979
Longitude	71 45.6 W	End	14 SEP 1979

Figure 6.4d. Progressive vector diagram

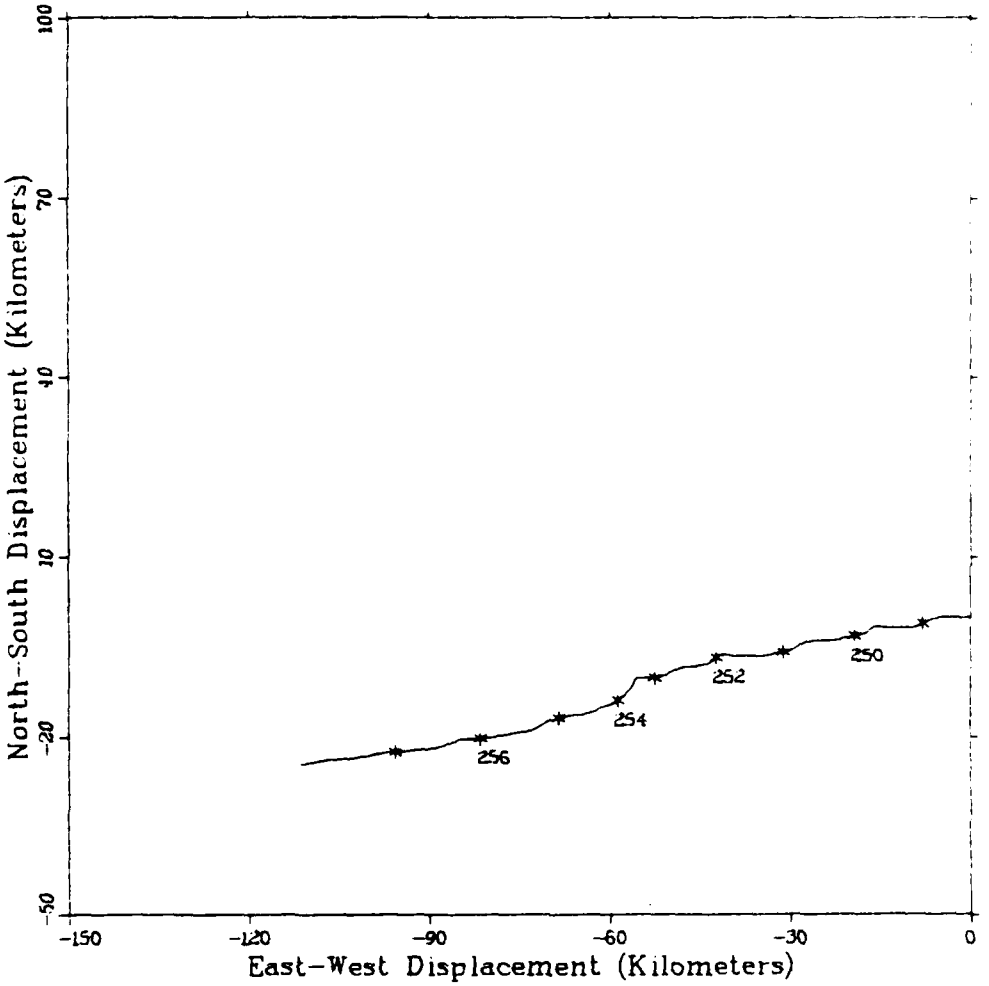

* Every 24 Hours Starting At 0000 Julian Day 249

File	VA0879	Array	2
Meter	V-0539	Depth	192 M
Latitude	30 29.7 N	Start	5 SEP 1979
Longitude	71 45.6 W	End	14 SEP 1979

Figure 6.4e. Progressive vector diagram

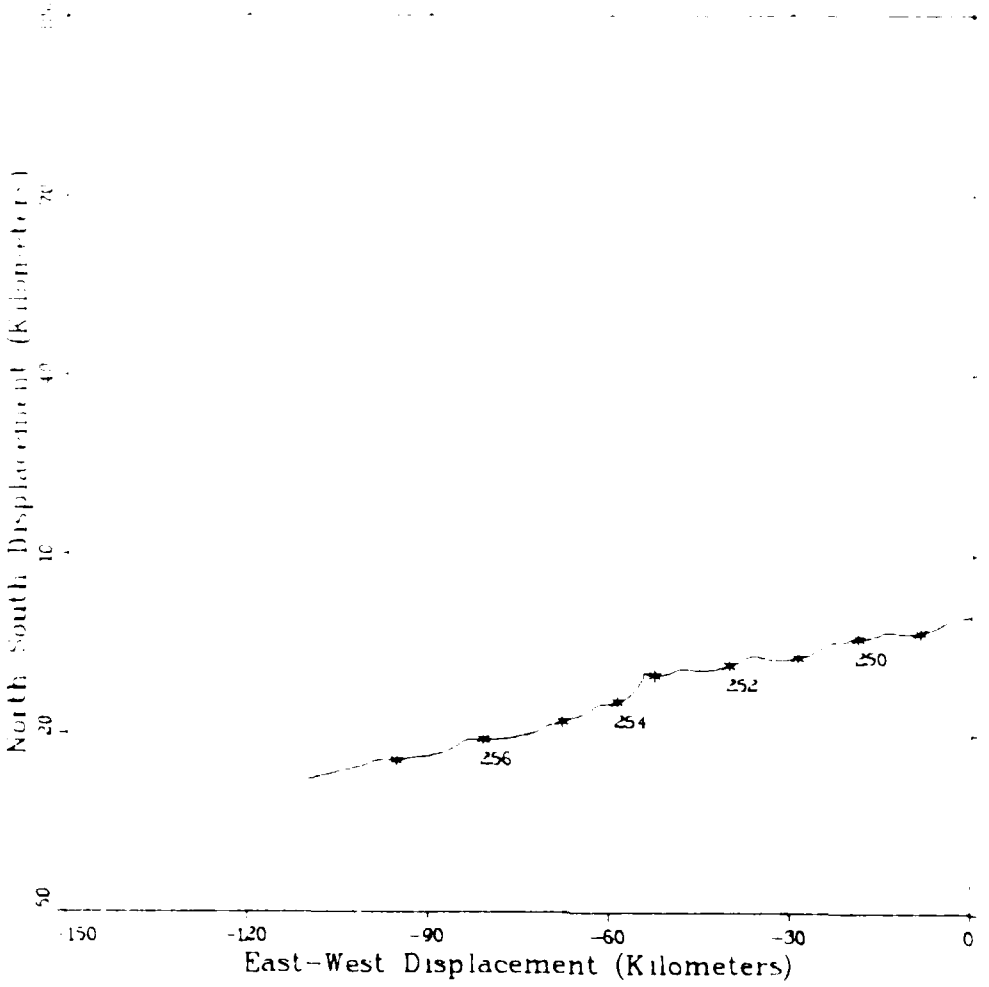

* Every 24 Hours Starting At 0000 Julian Day 249

File	VA0879	Array	2
Meter	V-0532	Depth	222 M
Latitude	30 29.7 N	Start	5 SEP 1979
Longitude	71 45.6 W	End	14 SEP 1979

Figure 6.4f. Progressive vector diagram

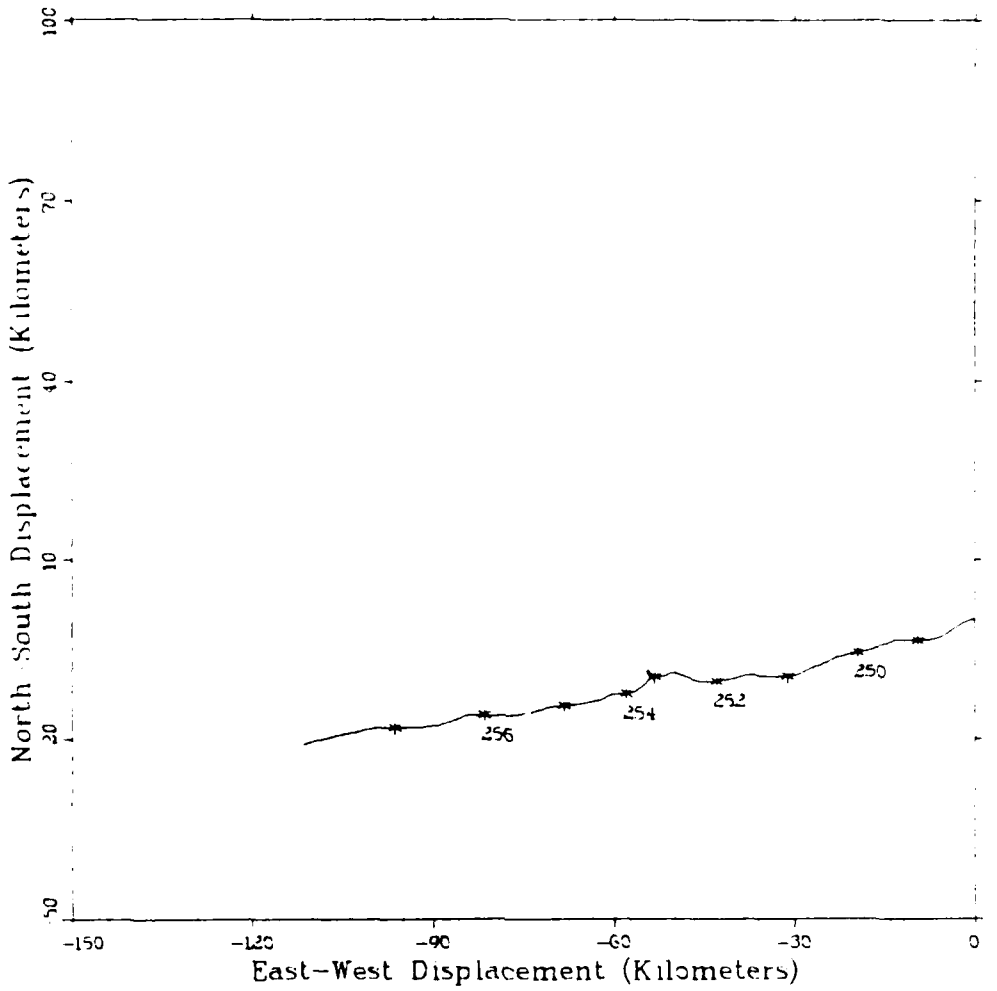

* Every 24 Hours Starting At 0000 Julian Day 249

File	VA0879	Array	2
Meter	V-0254	Depth	272 M
Latitude	30 29.7 N	Start	5 SEP 1979
Longitude	71 45.6 W	End	14 SEP 1979

Figure 6.4g. Progressive vector diagram

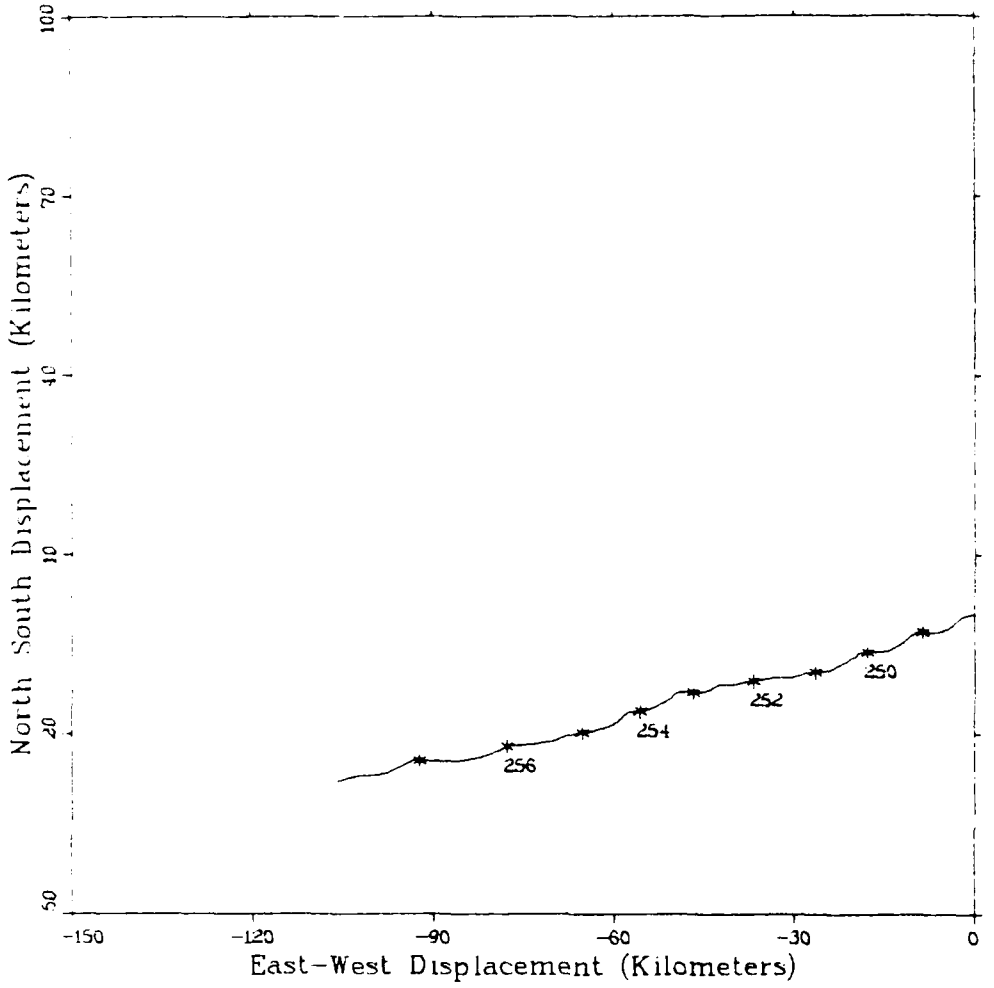

* Every 24 Hours Starting At 0000 Julian Day 249

File	VA0879	Array	2
Meter	V-0559	Depth	372 M
Latitude	30 29.7 N	Start	5 SEP 1979
Longitude	71 45.6 W	End	14 SEP 1979

Figure 6.4h. Progressive vector diagram

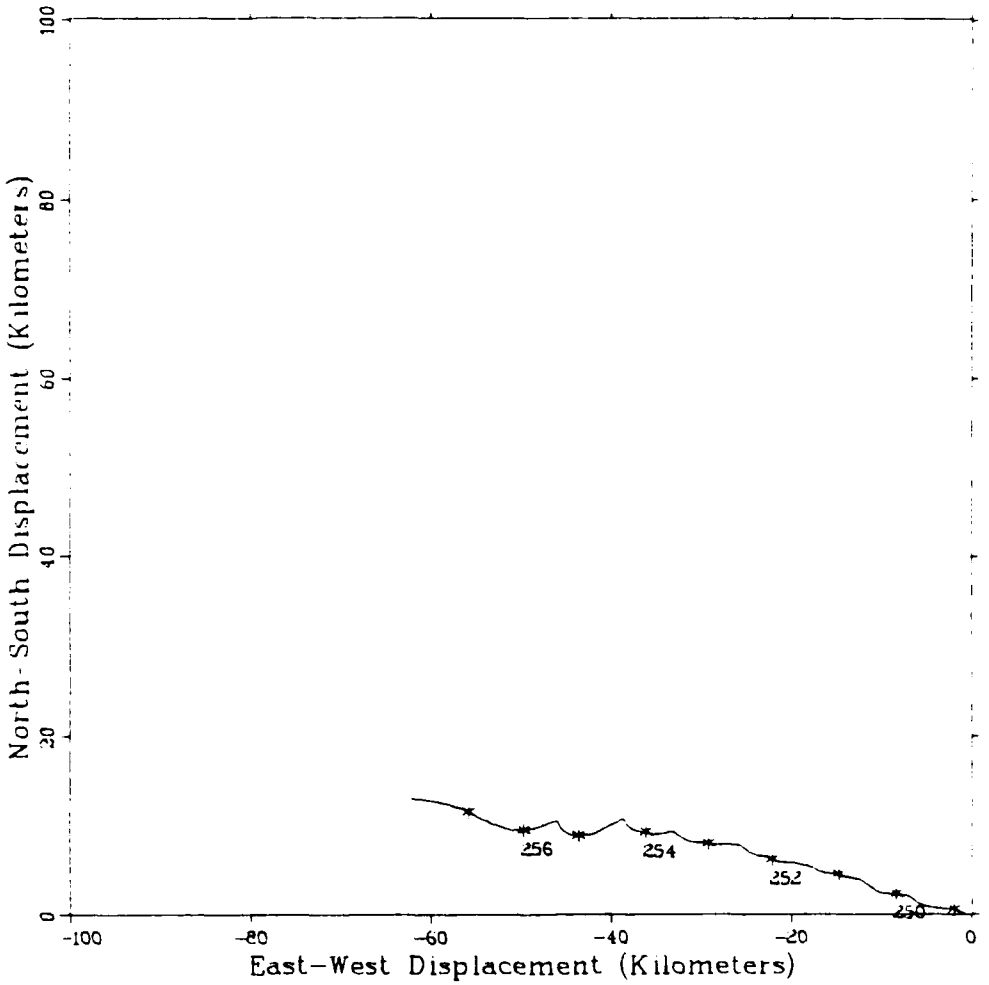

* Every 24 Hours Starting At 0000 Julian Day 249

File	AA0879	Array	2
Meter	A-2930	Depth	1022 M
Latitude	30 29.7 N	Start	5 SEP 1979
Longitude	71 45.6 W	End	15 SEP 1979

Figure 6.4j. Progressive vector diagram

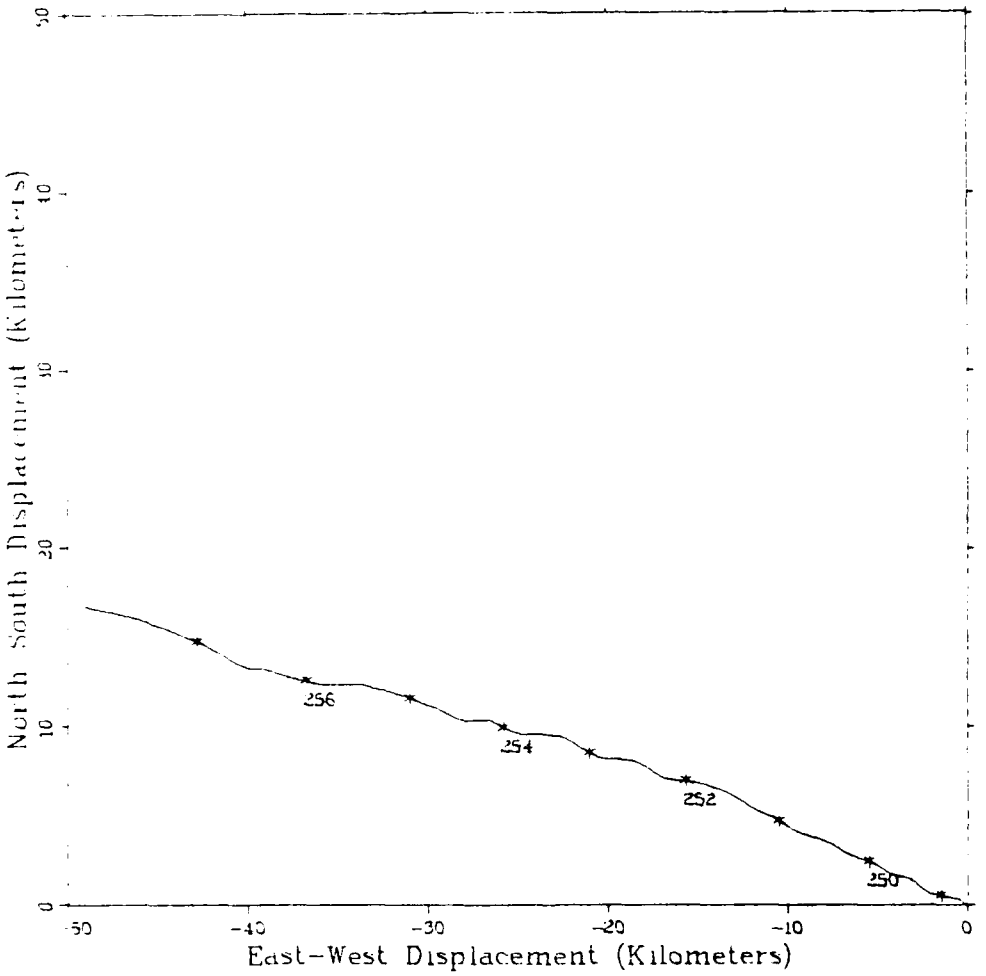

* Every 24 Hours Starting At 0000 Julian Day 249

File	AA0879	Array	2
Meter	A-2797	Depth	1522 M
Latitude	30 29.7 N	Start	5 SEP 1979
Longitude	71 45.6 W	End	15 SEP 1979

Figure 6.4k. Progressive vector diagram

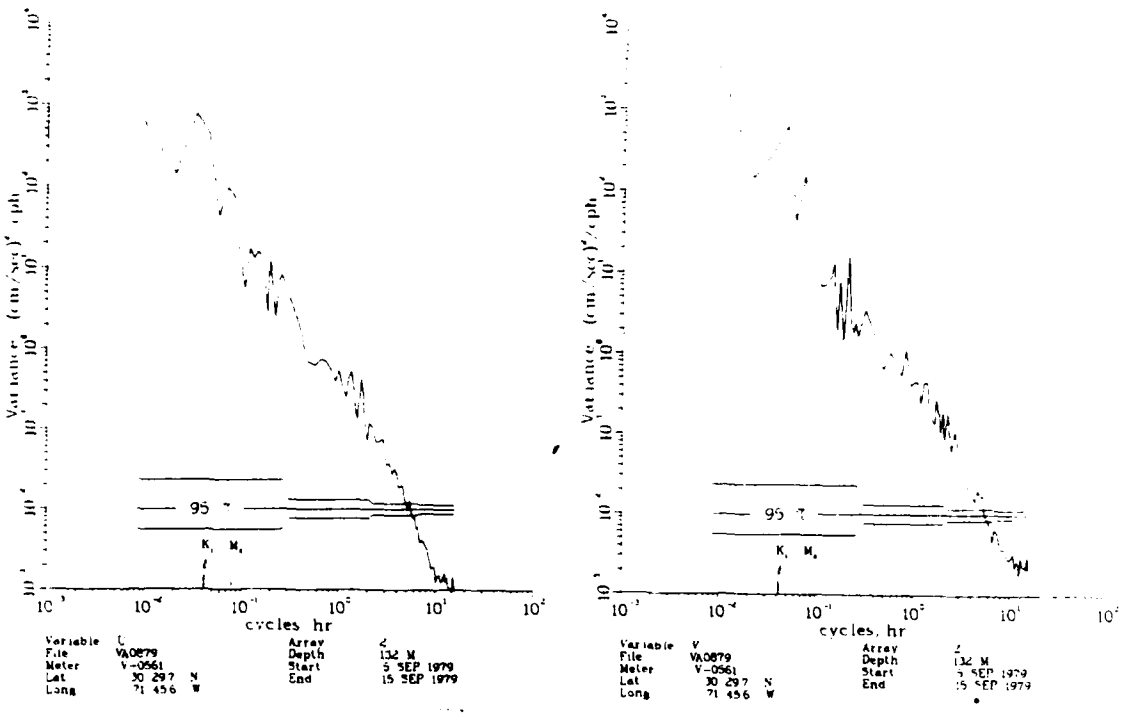

Figure 6.5a. Current spectrum

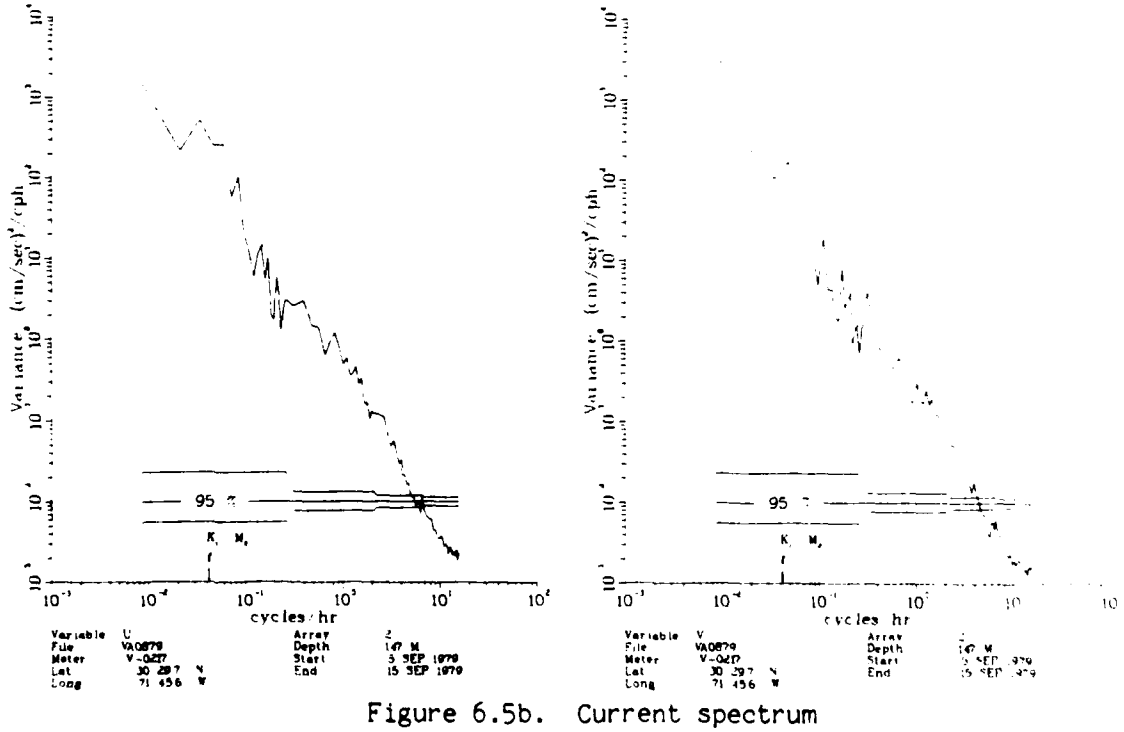

Figure 6.5b. Current spectrum

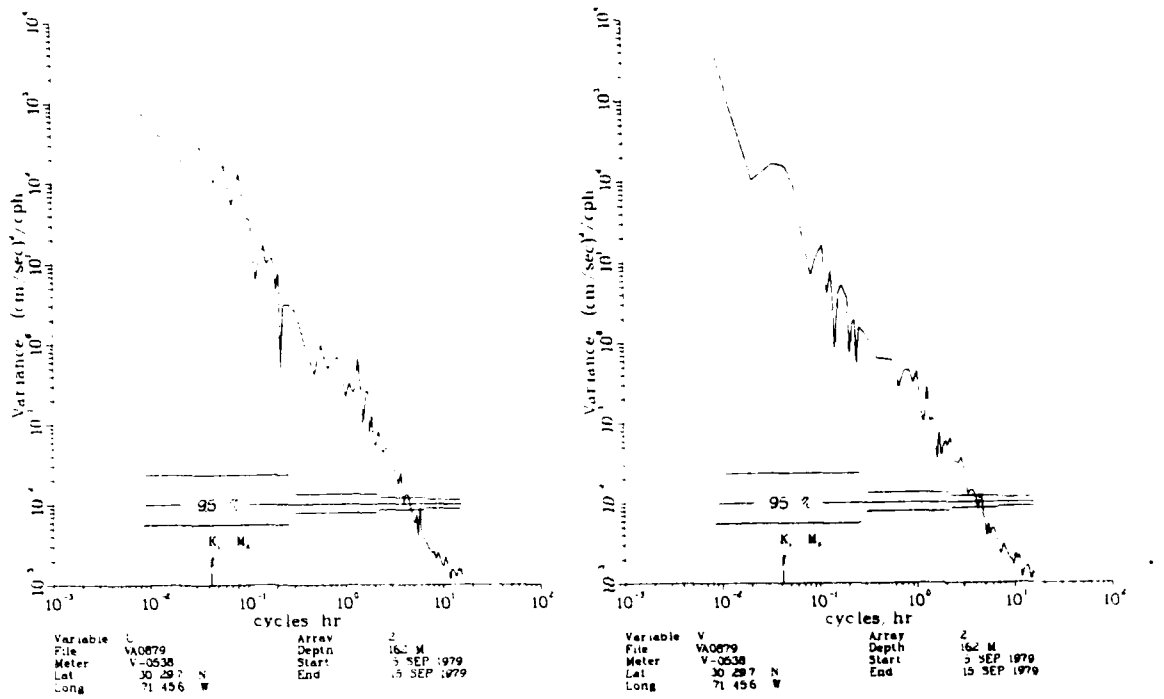

Figure 6.5c. Current spectrum

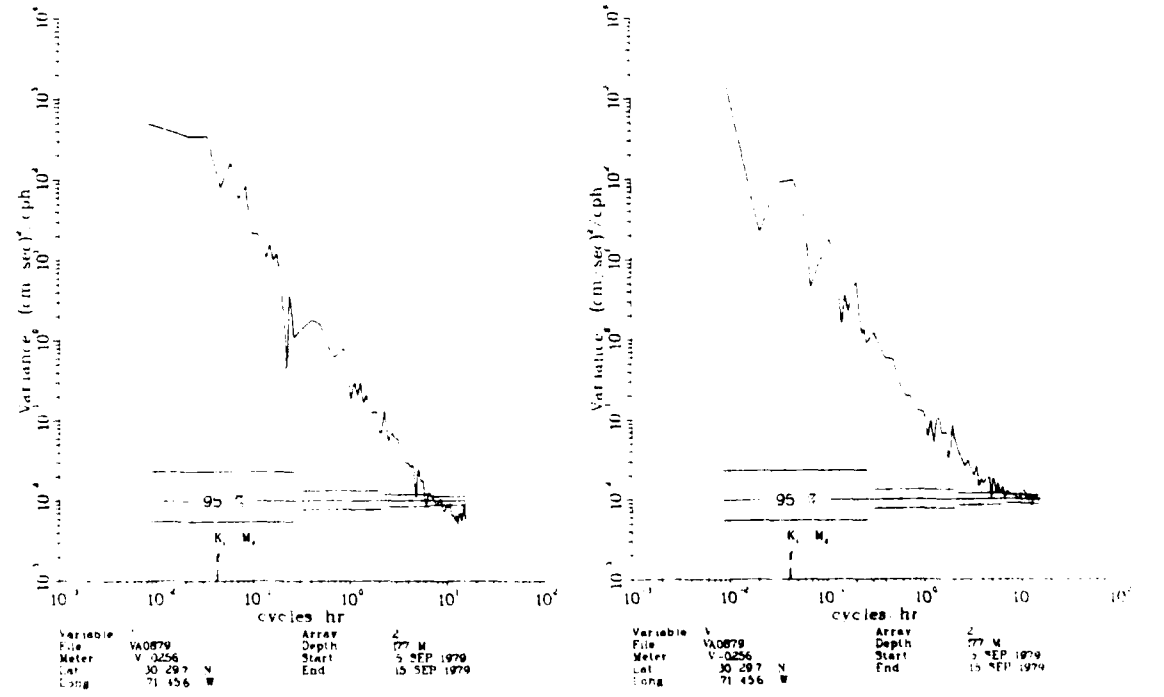

Figure 6.5d. Current spectrum

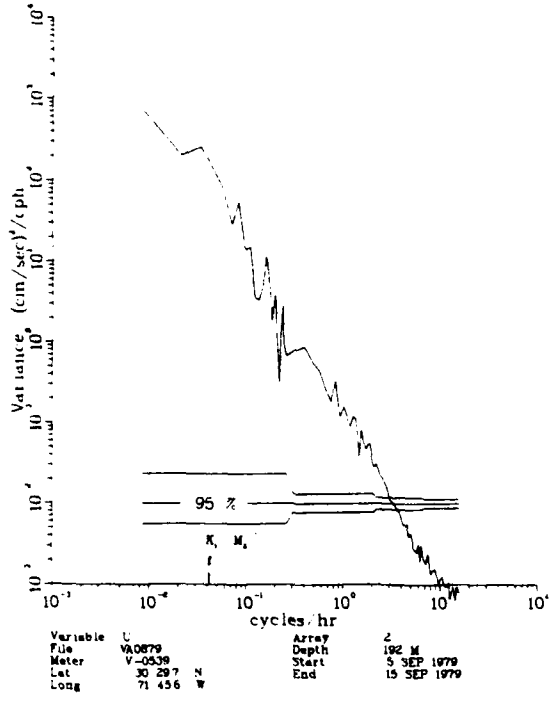

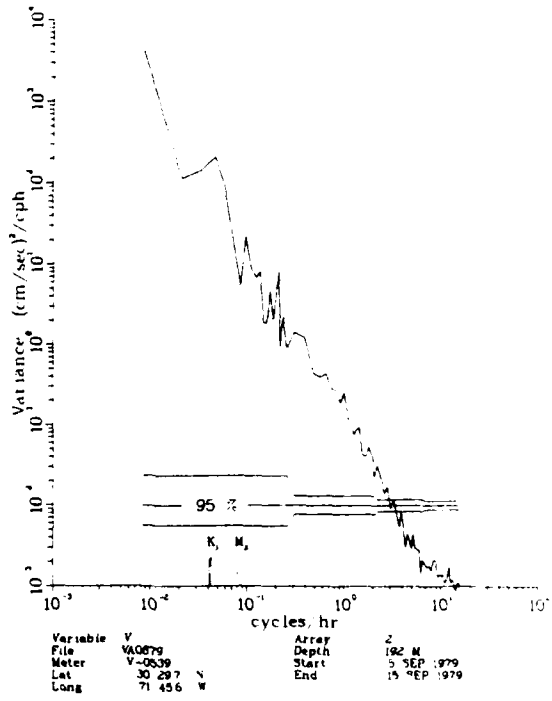

Figure 6.5e. Current spectrum

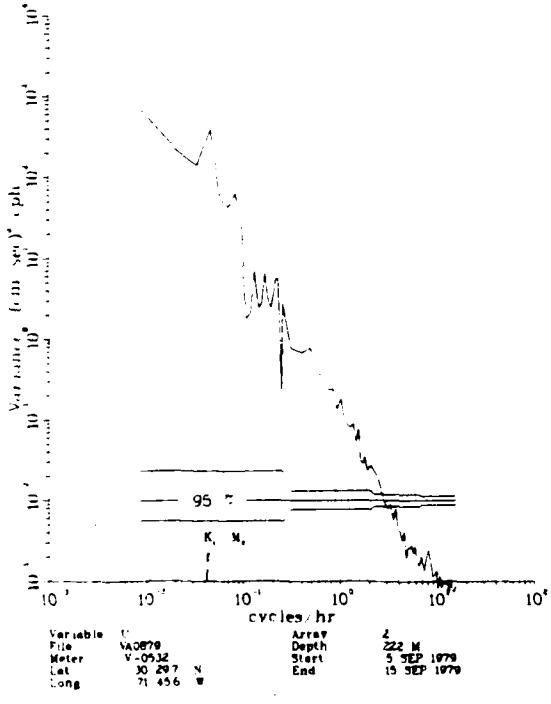

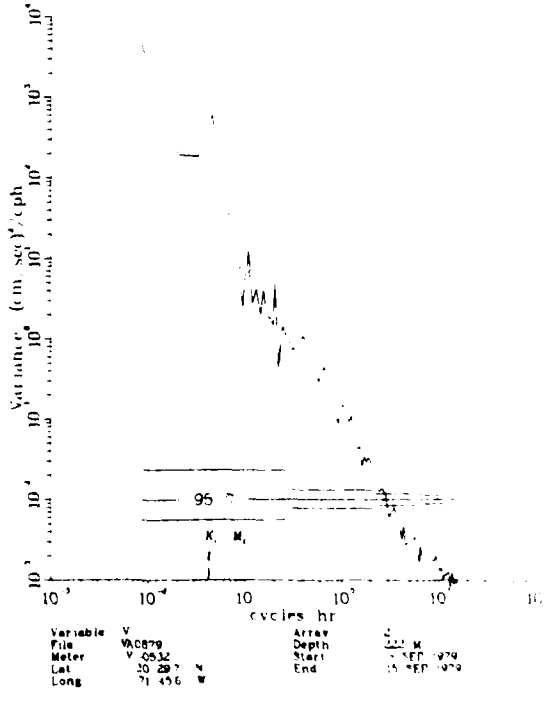

Figure 6.5f. Current spectrum

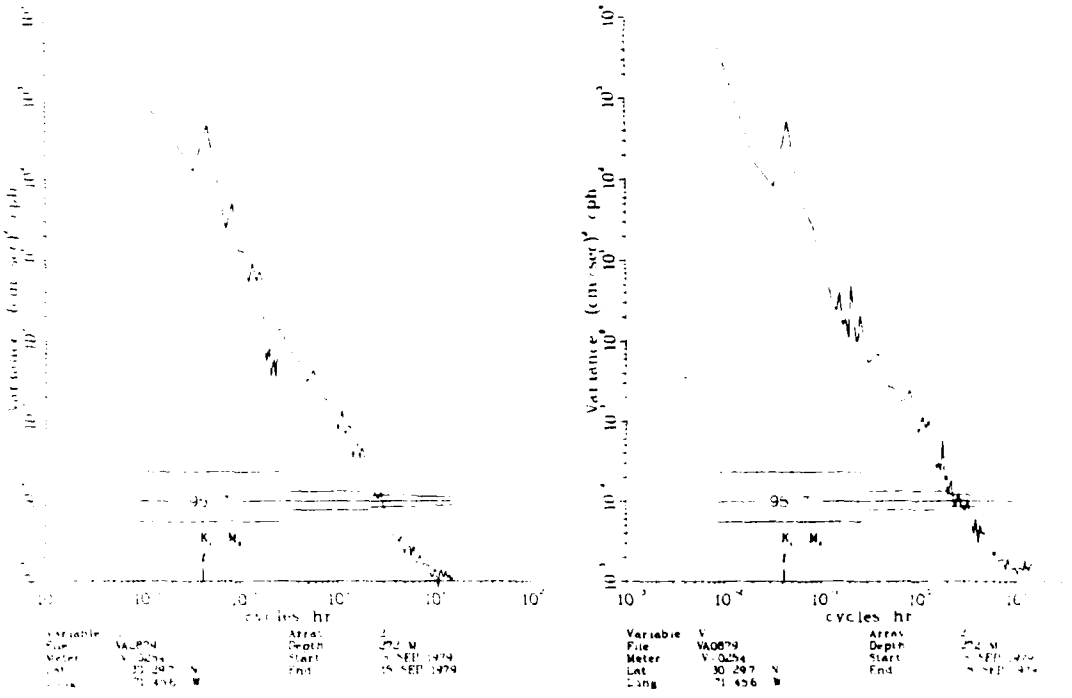

Figure 6.5g. Current spectrum

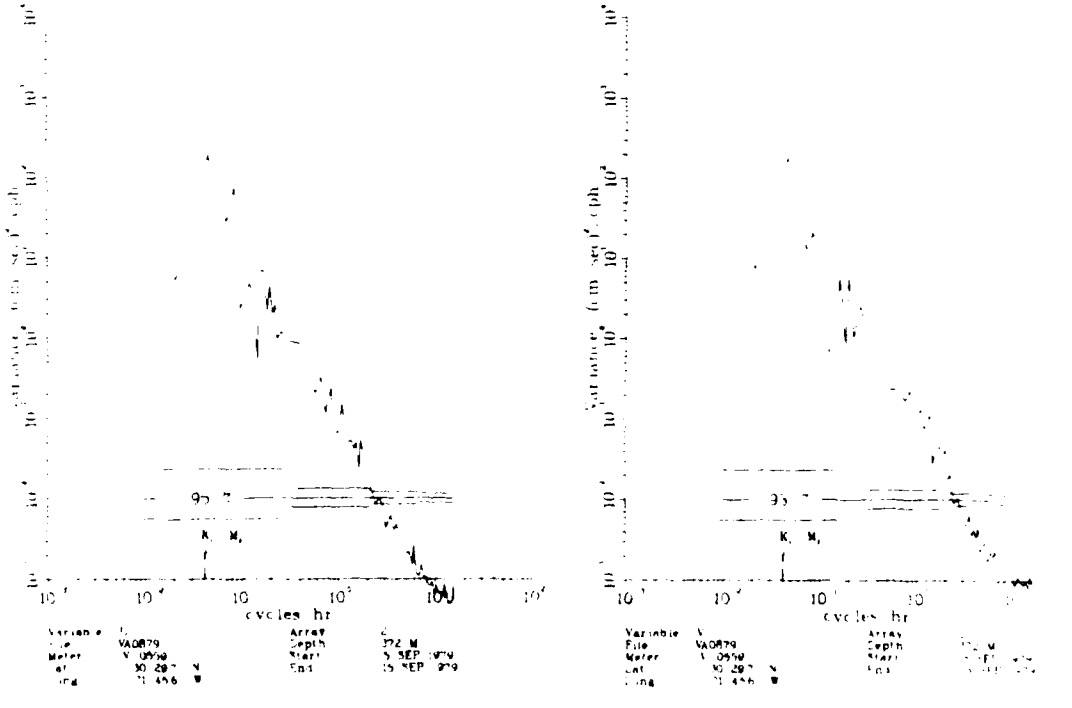

Figure 6.5h. Current spectrum

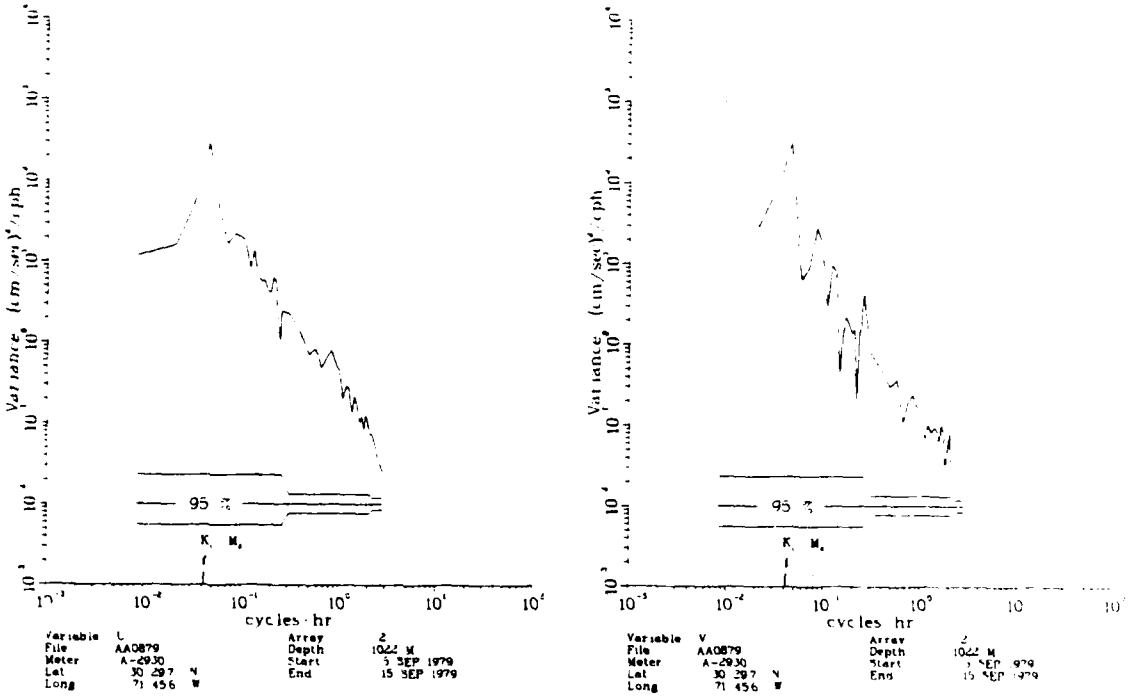

Figure 6.5j. Current spectrum

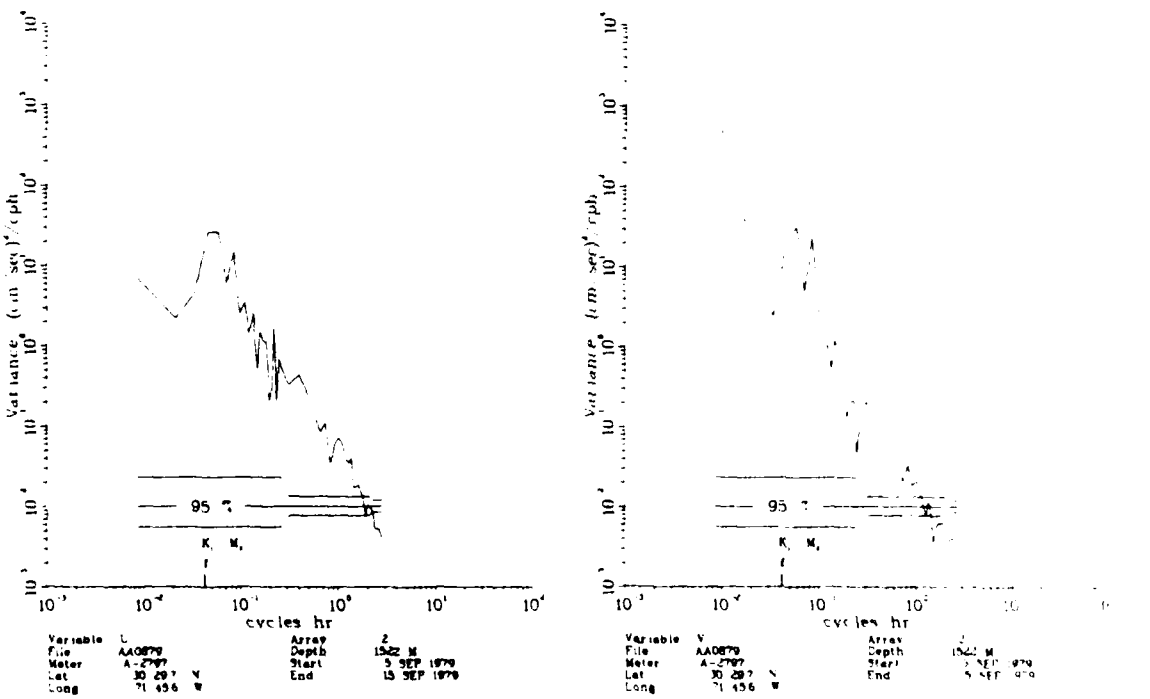

Figure 6.5k. Current spectrum

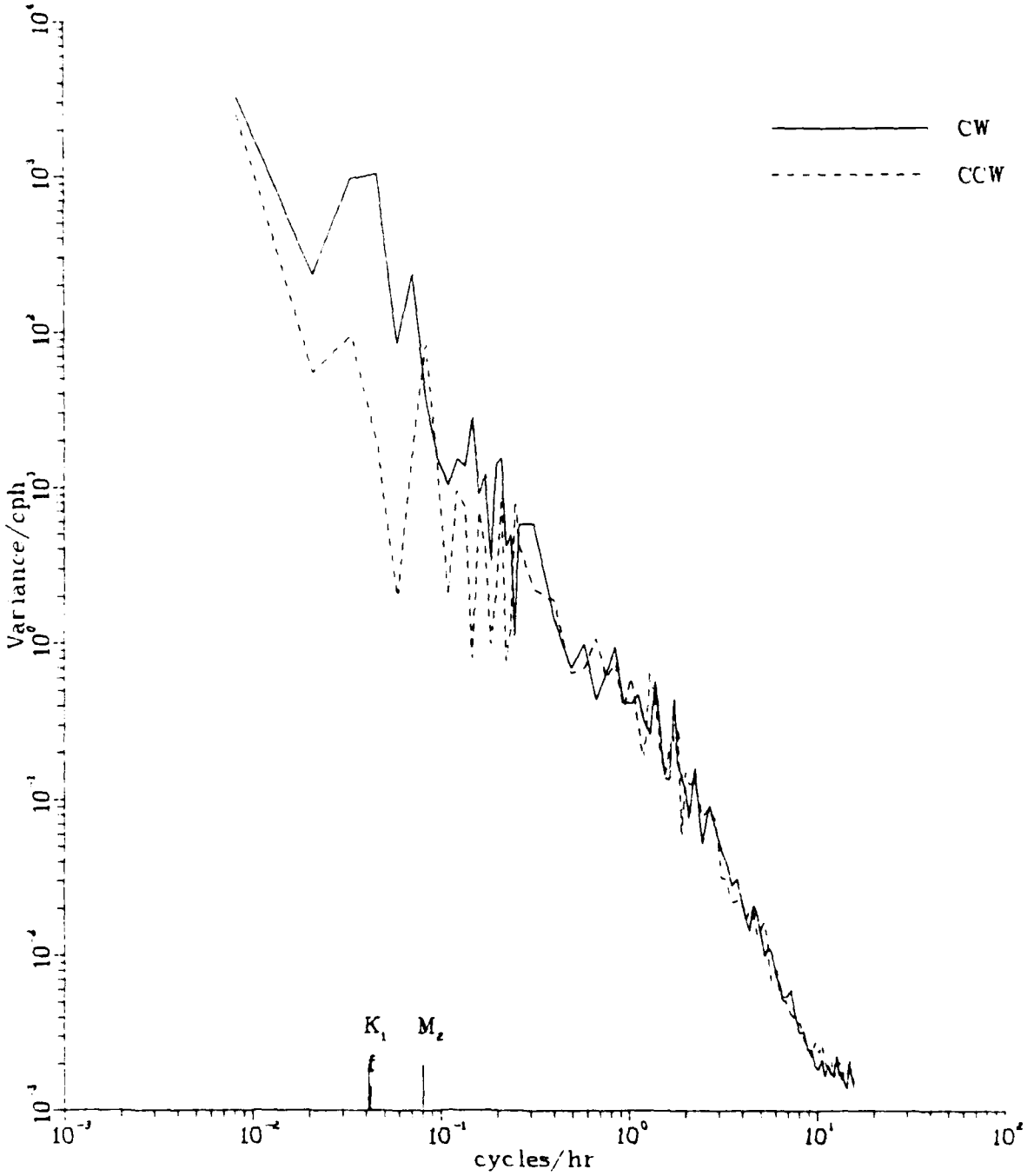

Variable	U		Variable	V	
Depth	132 M		Depth	132 M	
Meter	V-0561		Meter	V-0561	
Lat	30 29.7	N	Lat	30 29.7	N
Long	71 45.6	W	Long	71 45.6	W

Figure 6.6a. Rotary spectrum

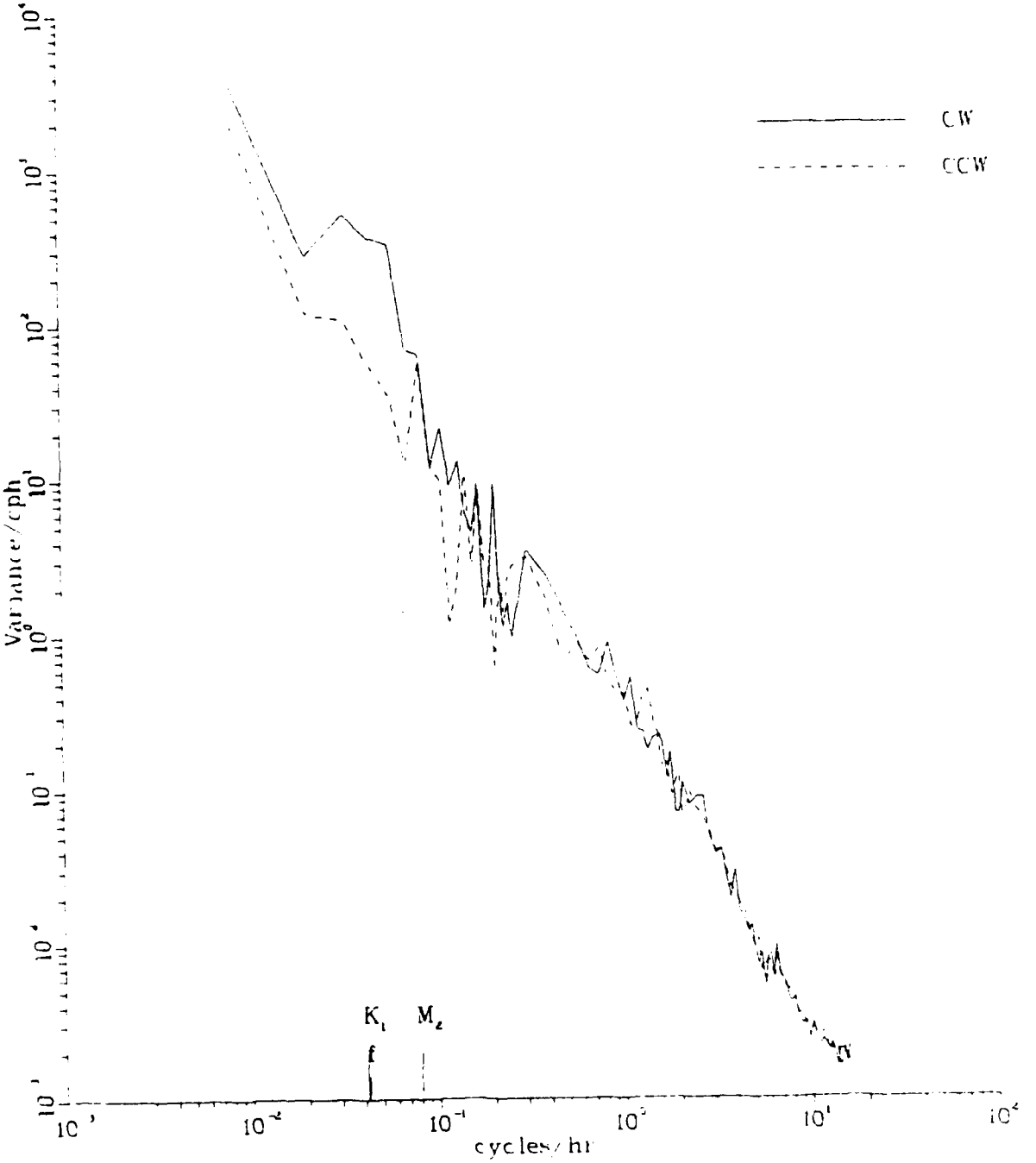

Variable	U	Variable	V
Depth	147 M	Depth	147 M
Meter	V-0217	Meter	V-0217
Lat	30 29.7 N	Lat	30 29.7 N
Long	71 45.6 W	Long	71 45.6 W

Figure 6.6b. Rotary spectrum

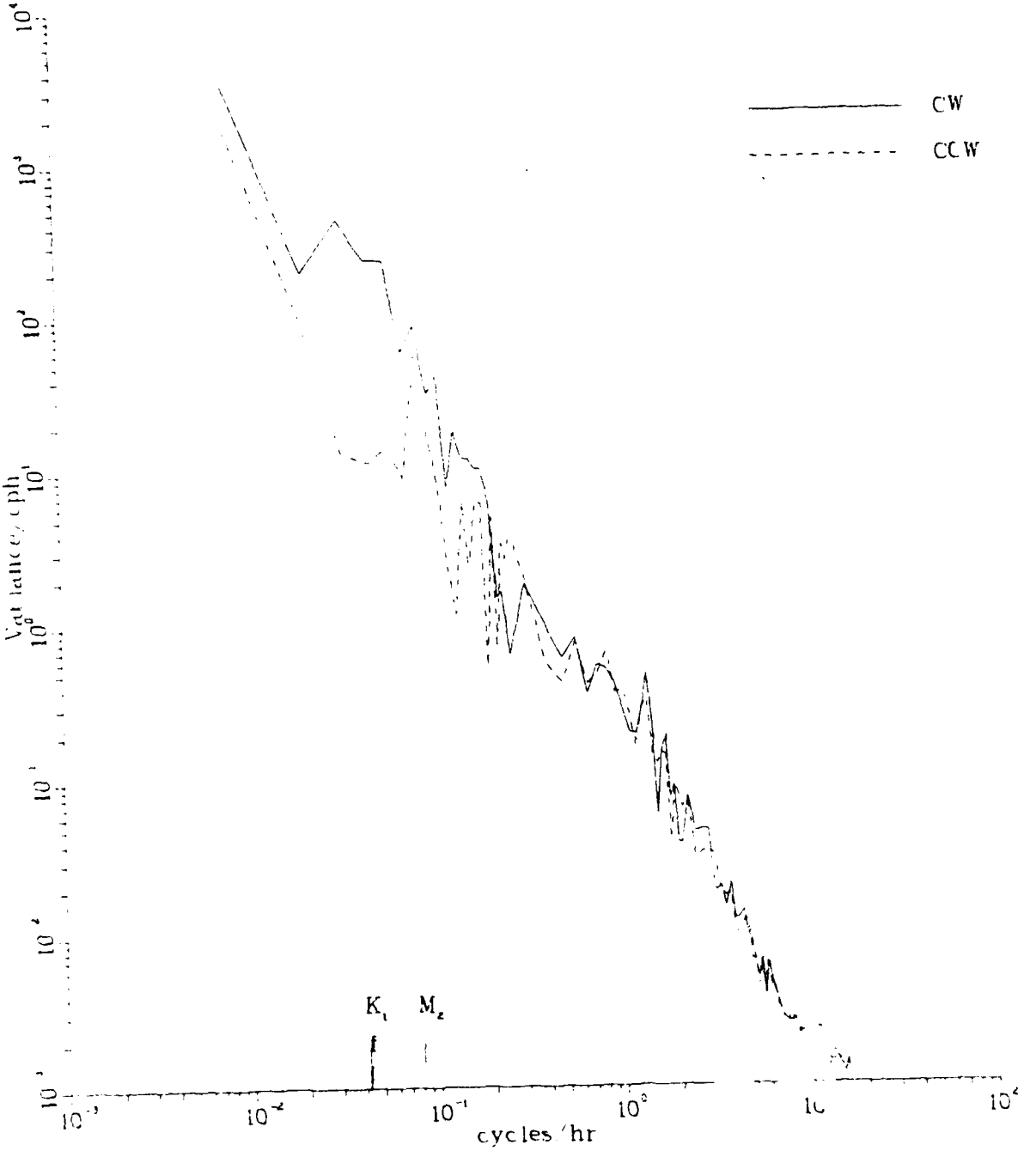

Variable	U		Variable	V	
Depth	162 M		Depth	162 M	
Meter	V-0538		Meter	V-0538	
Lat	30 29.7	N	Lat	30 29.7	N
Long	71 45.6	W	Long	71 45.6	W

Figure 6.6c. Rotary spectrum

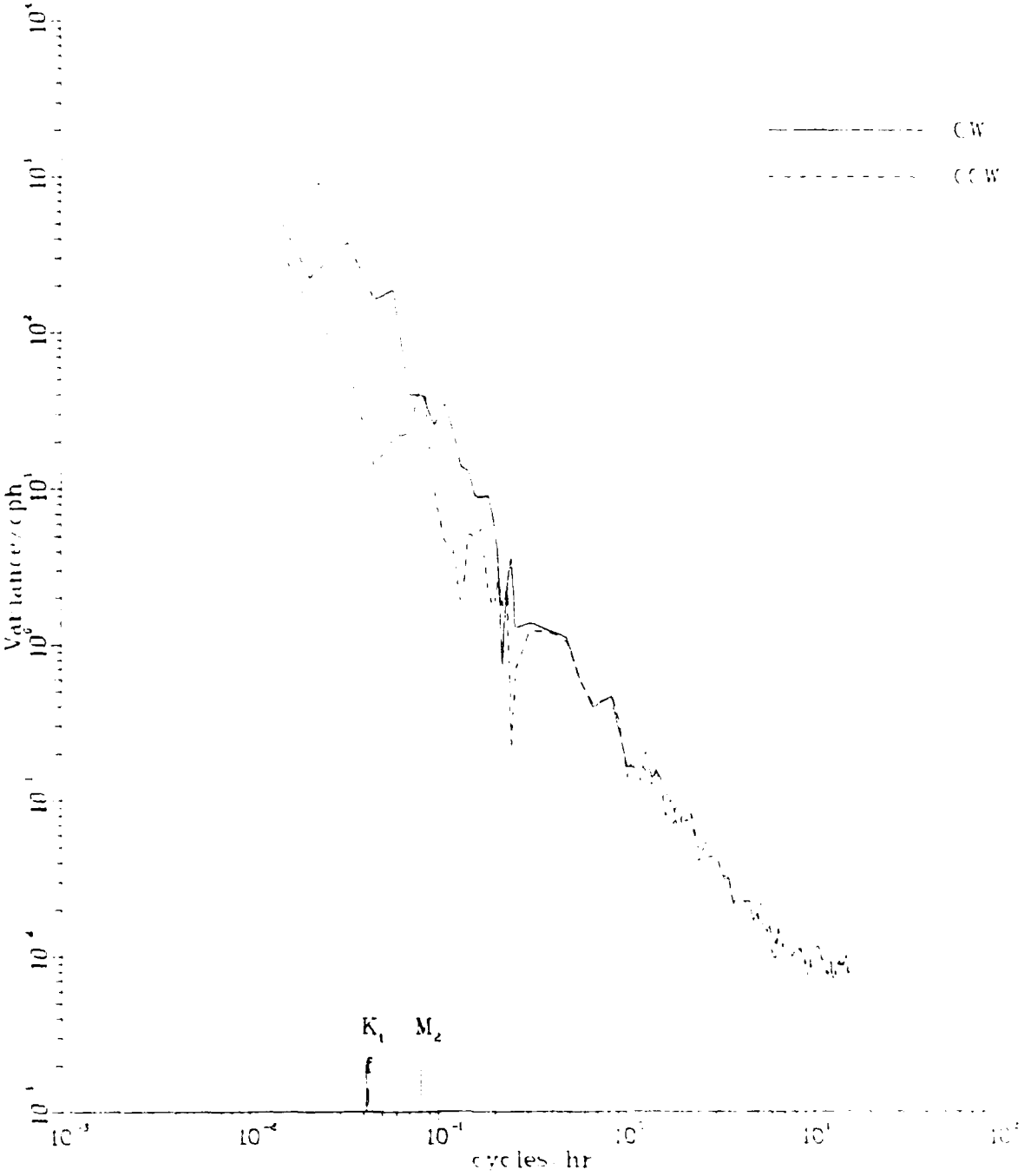

Variable	U	Variable	V
Depth	177 M	Depth	177 M
Meter	V 0256	Meter	V 0256
Lat	30 29.7 N	Lat	30 29.7 N
Long	71 45.6 W	Long	71 45.6 W

Figure 6.6d. Rotary spectrum

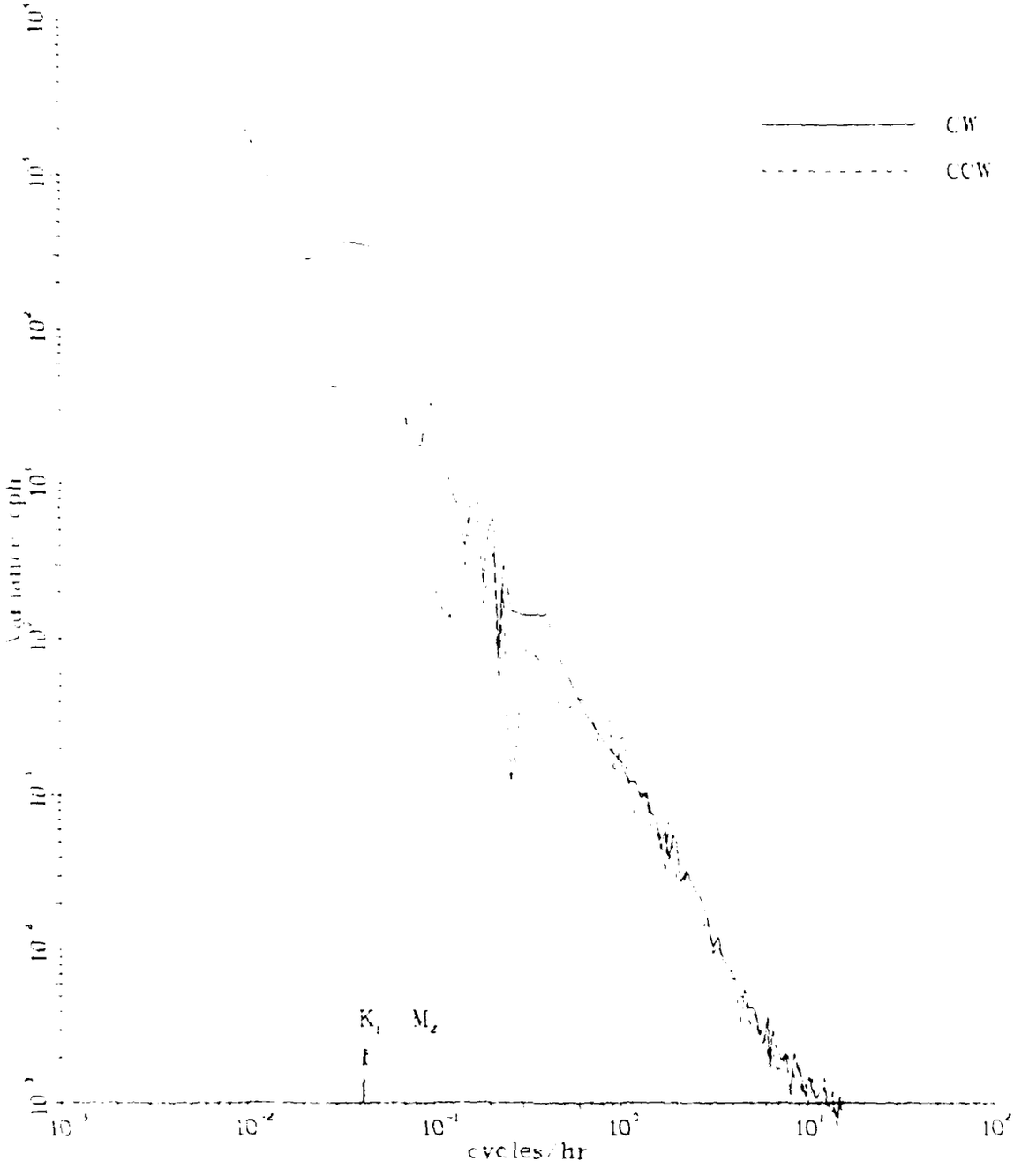

Variable	U		Variable	V	
Depth	192 M		Depth	192 M	
Meter	V-0539		Meter	V-0539	
Lat	30 29.7	N	Lat	30 29.7	N
Long	71 45.6	W	Long	71 45.6	W

Figure 6.6e. Rotary spectrum

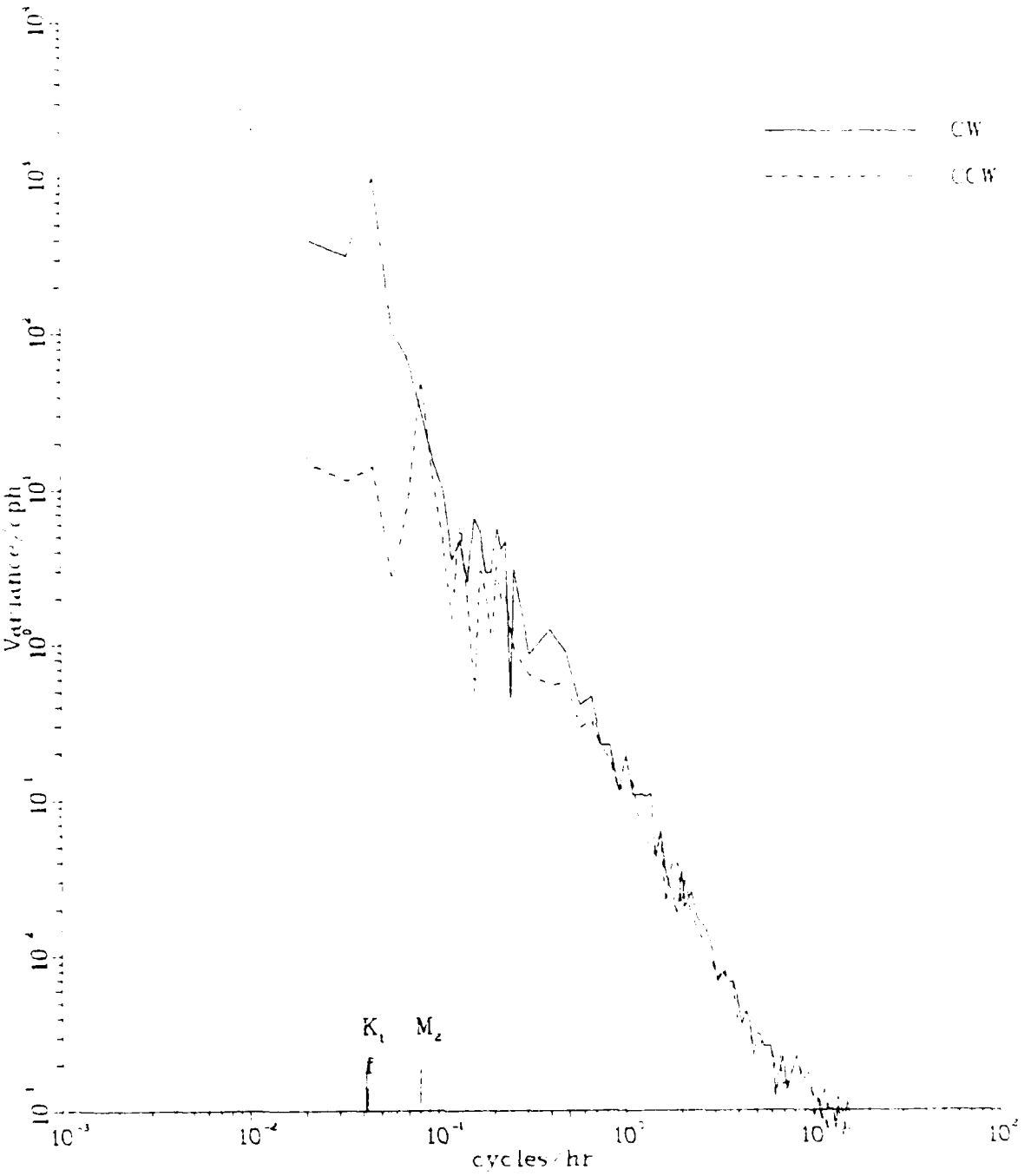

Variable	U		Variable	V	
Depth	222 M		Depth	222 M	
Meter	V-0532		Meter	V-0532	
Lat	30 297	N	Lat	30 297	N
Long	71 456	W	Long	71 456	W

Figure 6.6f. Rotary spectrum

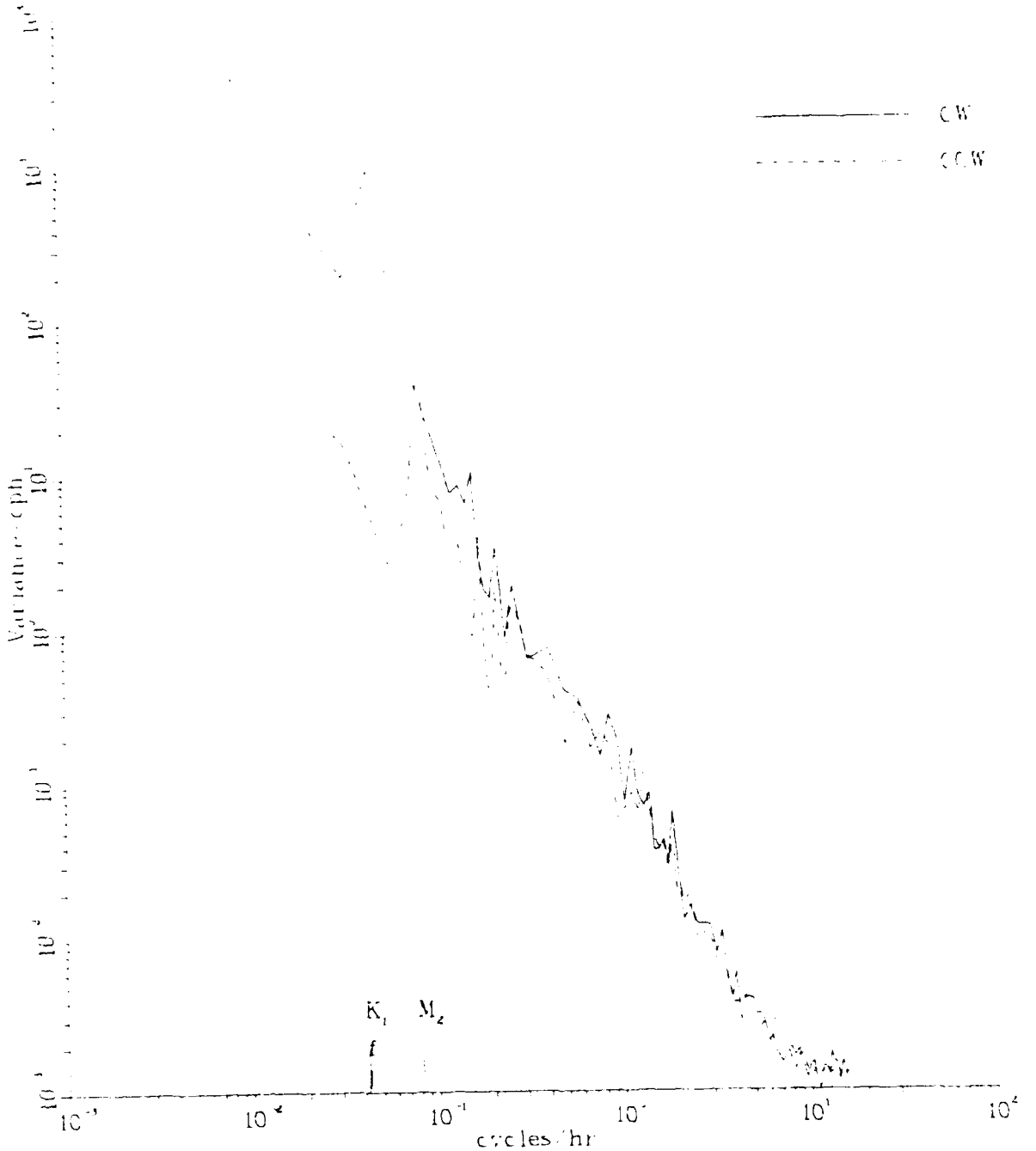

Variable	U		Variable	V	
Depth	272 M		Depth	272 M	
Meter	V-0254		Meter	V-0254	
Lat	30 29.7	N	Lat	30 29.7	N
Long	71 45.6	W	Long	71 45.6	W

Figure 6.6g. Rotary spectrum

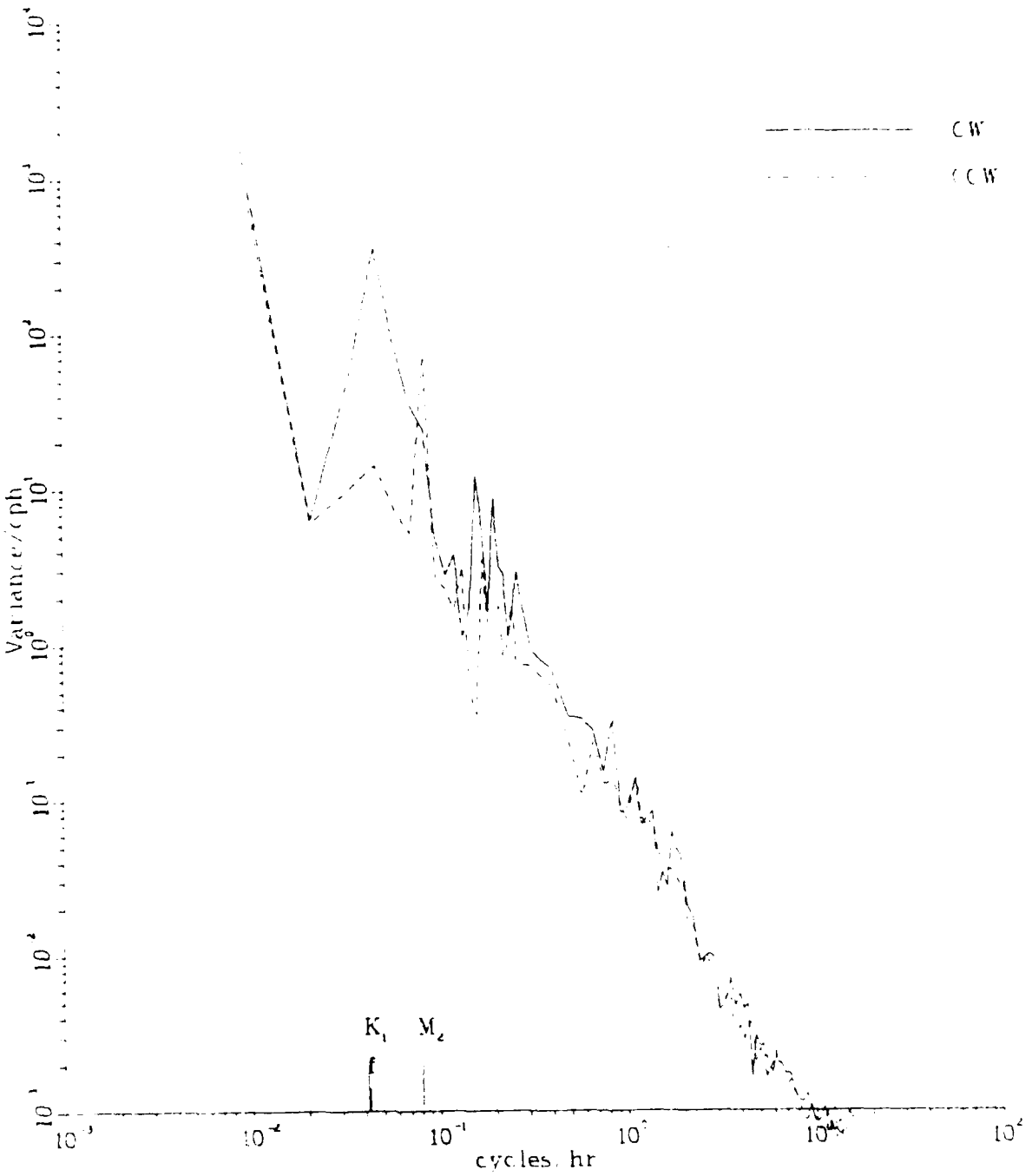

Variable	U		Variable	V	
Depth	372 M		Depth	372 M	
Meter	V-0559		Meter	V-0559	
Lat	30 29.7	N	Lat	30 29.7	N
Long	71 45.6	W	Long	71 45.6	W

Figure 6.6h. Rotary spectrum

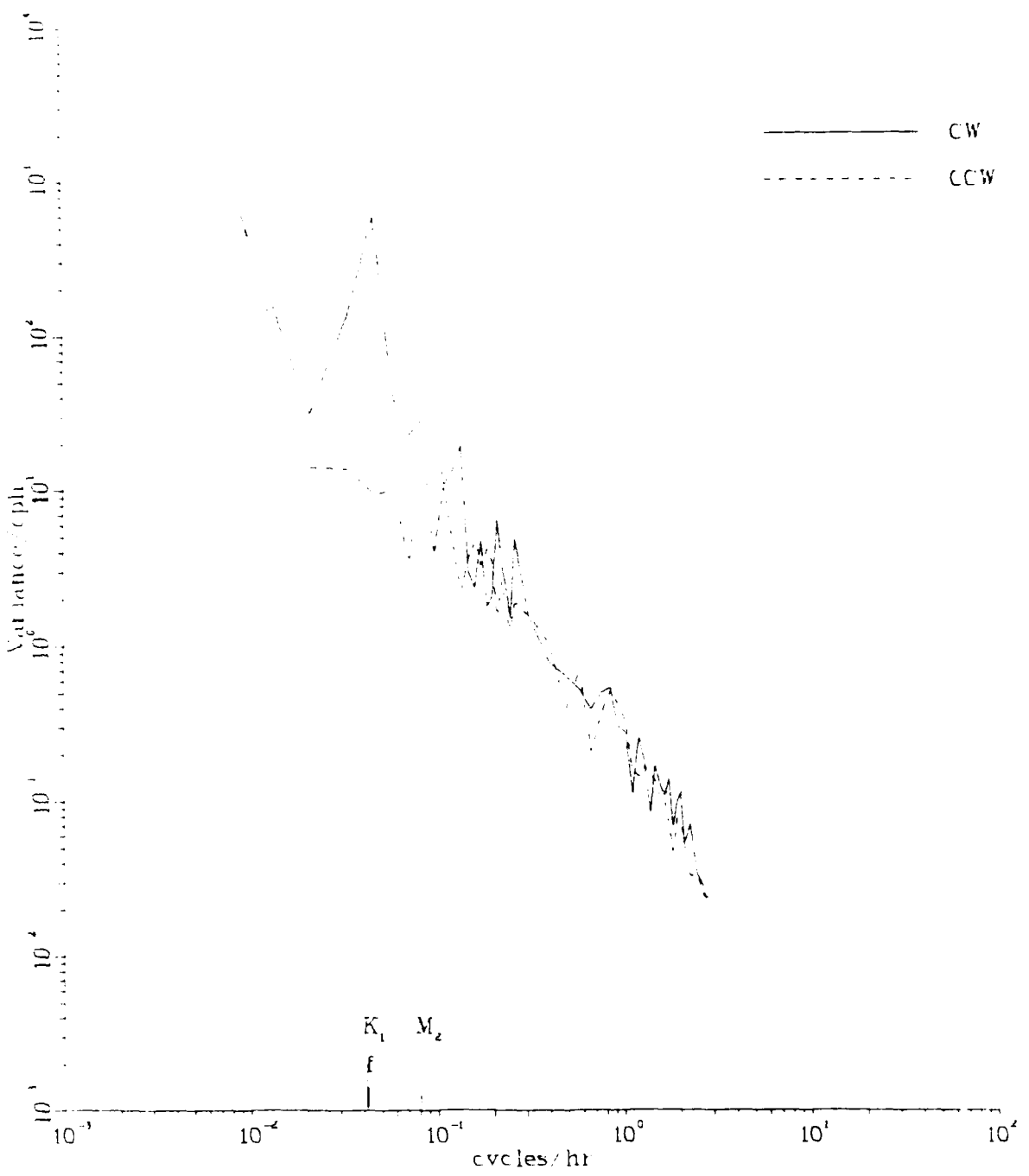

Variable	U	Variable	V
Depth	1022 M	Depth	1022 M
Meter	A-2930	Meter	A-2930
Lat	30 29? N	Lat	30 29 7 N
Long	71 456 W	Long	71 456 W

Figure 6.6j. Rotary spectrum

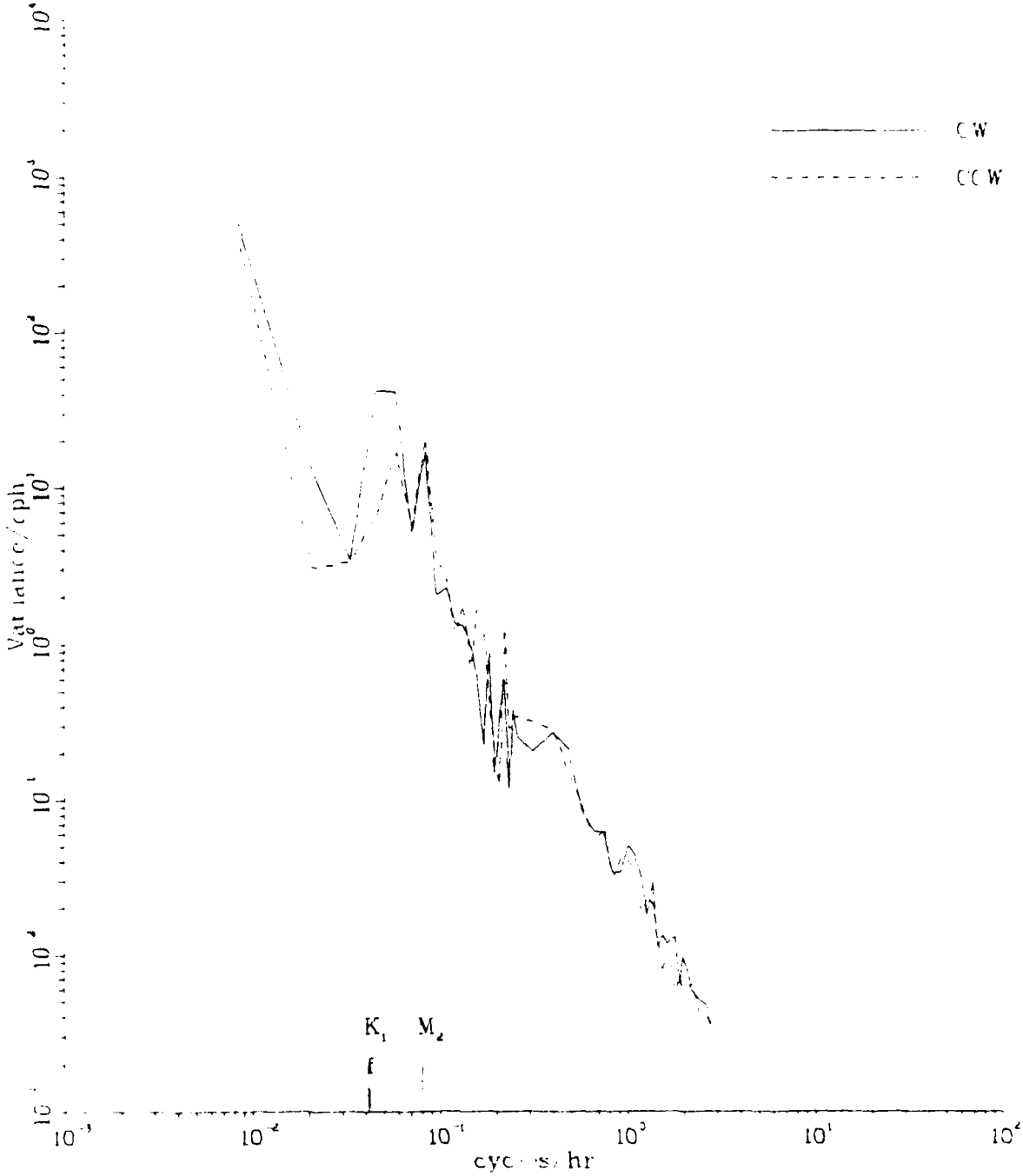

Variable	U		Variable	V	
Depth	1522 M		Depth	1522 M	
Meter	A-2797		Meter	A-2797	
Lat	30 297	N	Lat	30 297	N
Long	71 456	W	Long	71 456	W

Figure 6.6k. Rotary spectrum

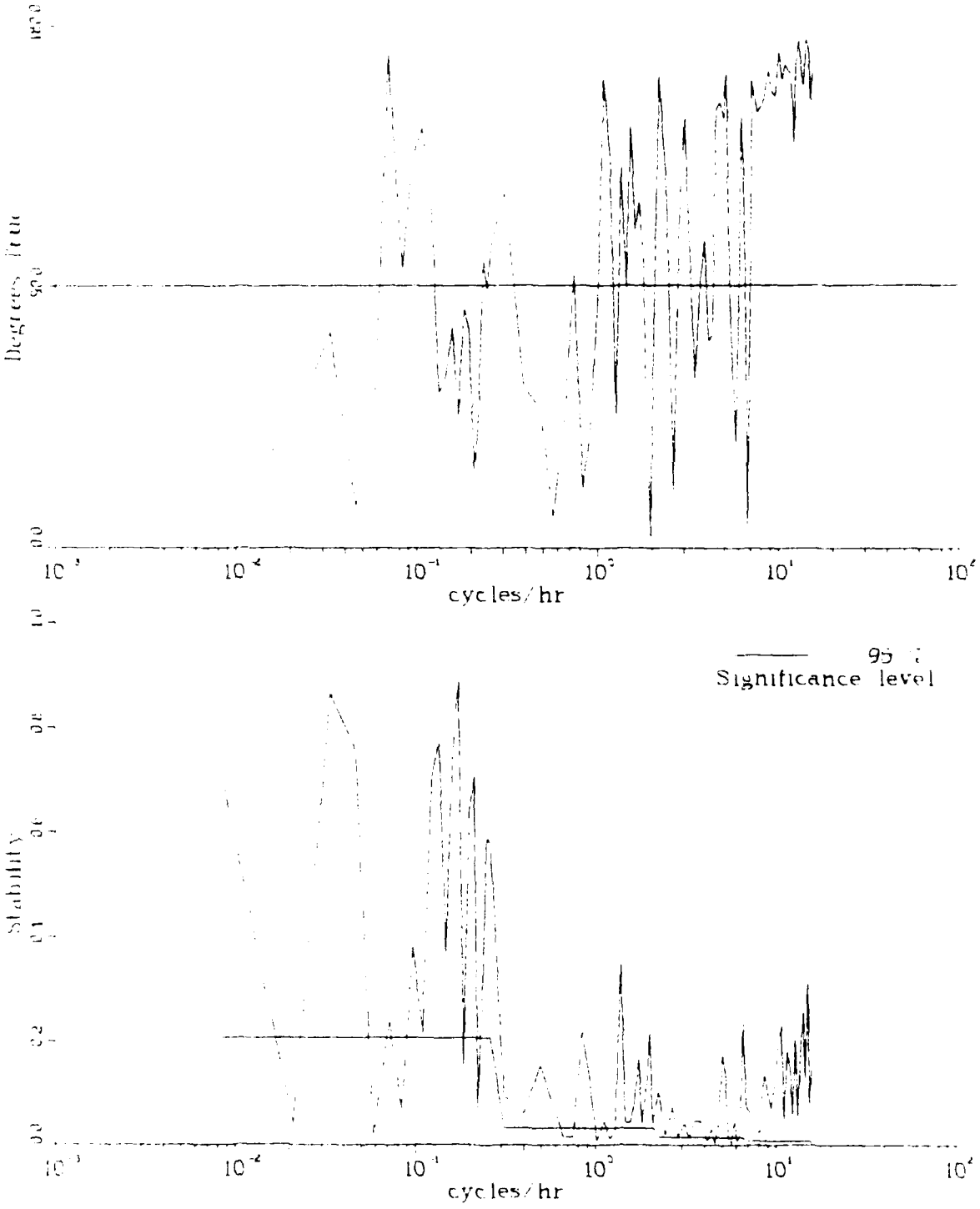

Variable	U	Variable	V
Depth	132 M	Depth	132 M
Meter	V-0561	Meter	V-0561
Lat	30 29.7 N	Lat	30 29.7 N
Long	71 45.6 W	Long	71 45.6 W

Figure 6.7a. Ellipse orientation and stability

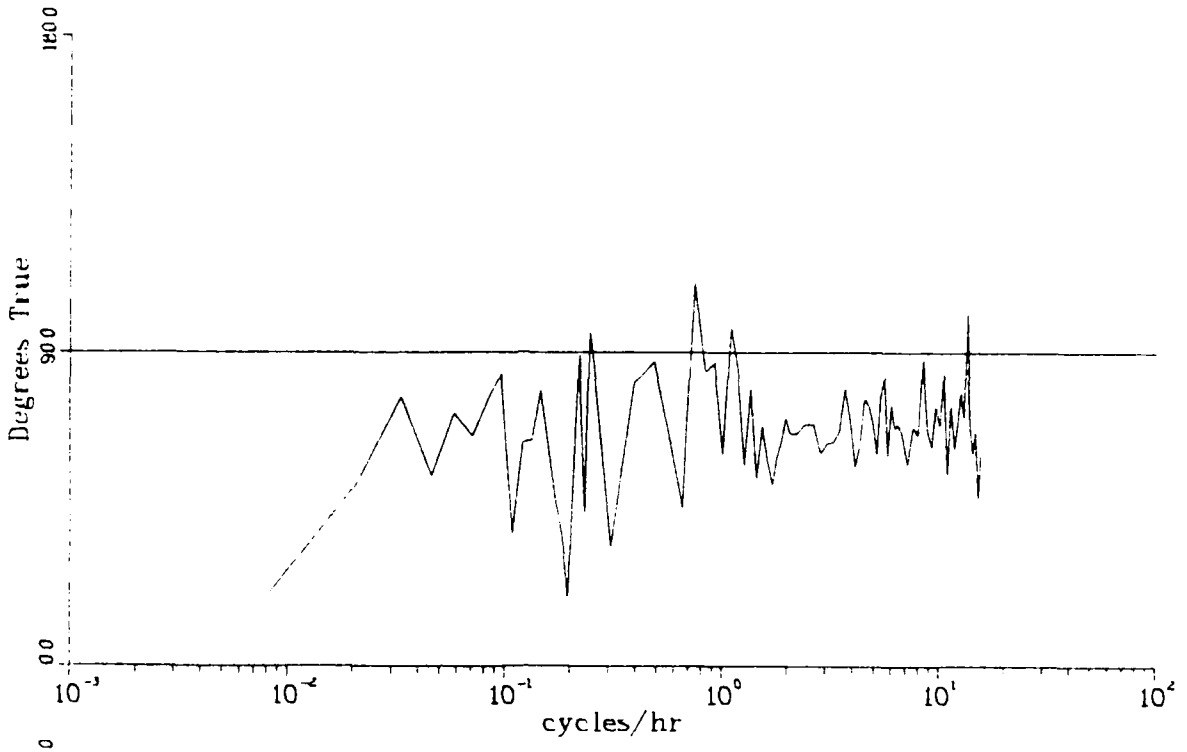

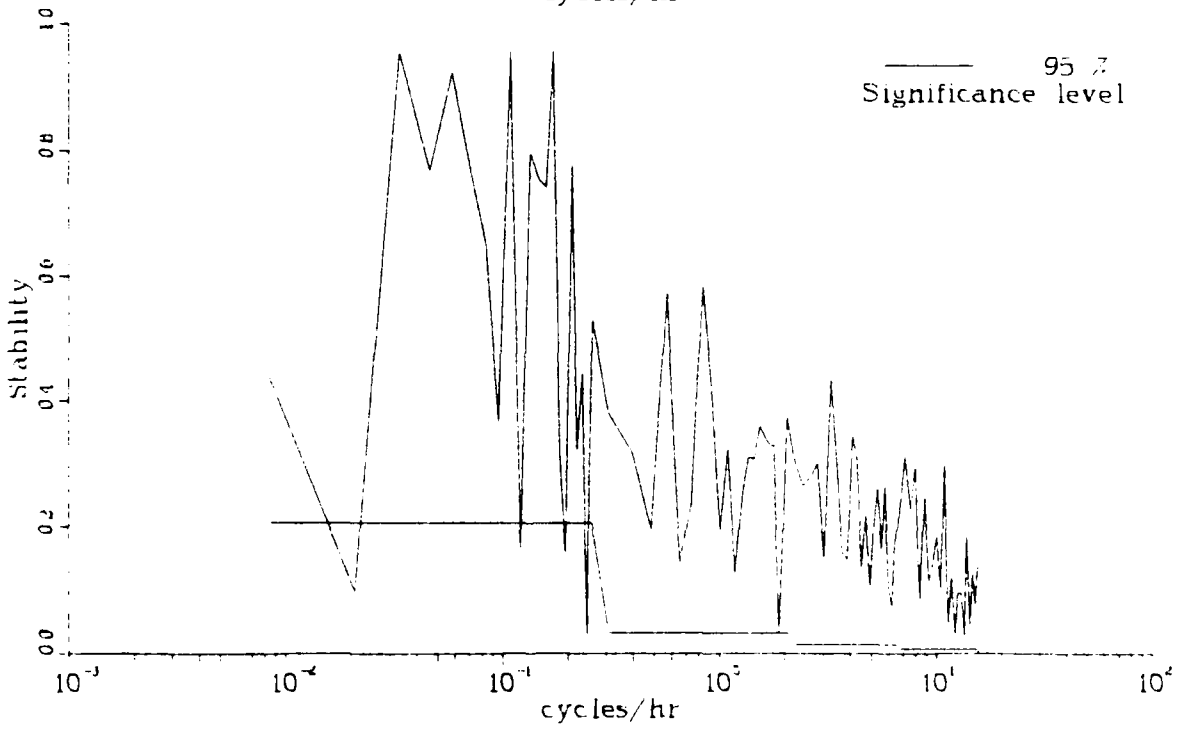

Variable	U	Variable	V
Depth	147 M	Depth	147 M
Meter	V-0217	Meter	V-0217
Lat	30 29.7 N	Lat	30 29.7 N
Long	71 45.6 W	Long	71 45.6 W

Figure 6.7b. Ellipse orientation and stability

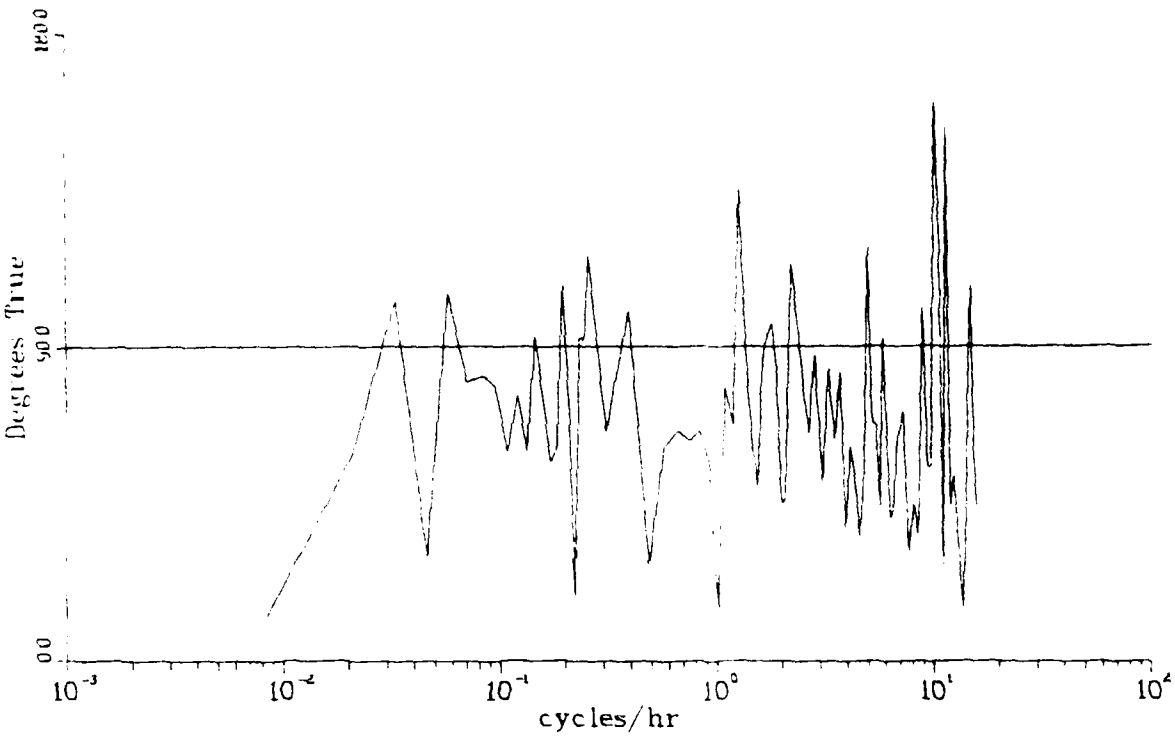

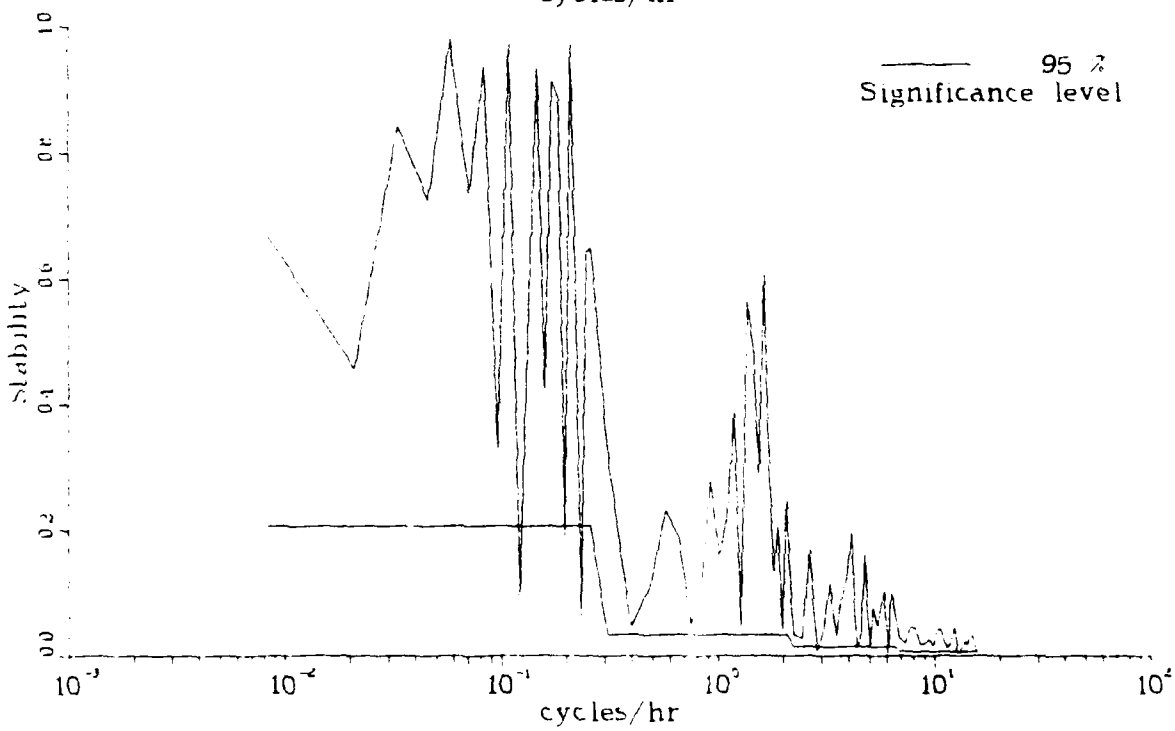

Variable	U	Variable	V
Depth	162 M	Depth	162 M
Meter	V-0538	Meter	V-0538
Lat	30 29.7 N	Lat	30 29.7 N
Long	71 45.6 W	Long	71 45.6 W

Figure 6.7c. Ellipse orientation and stability

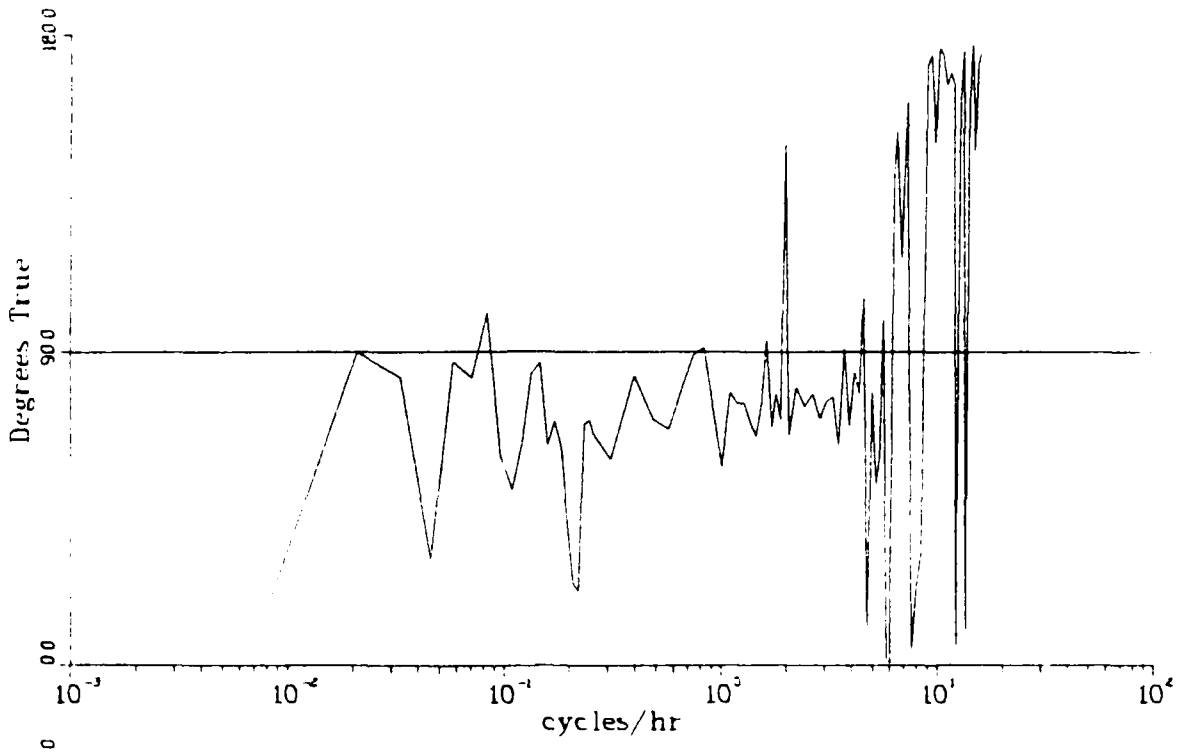

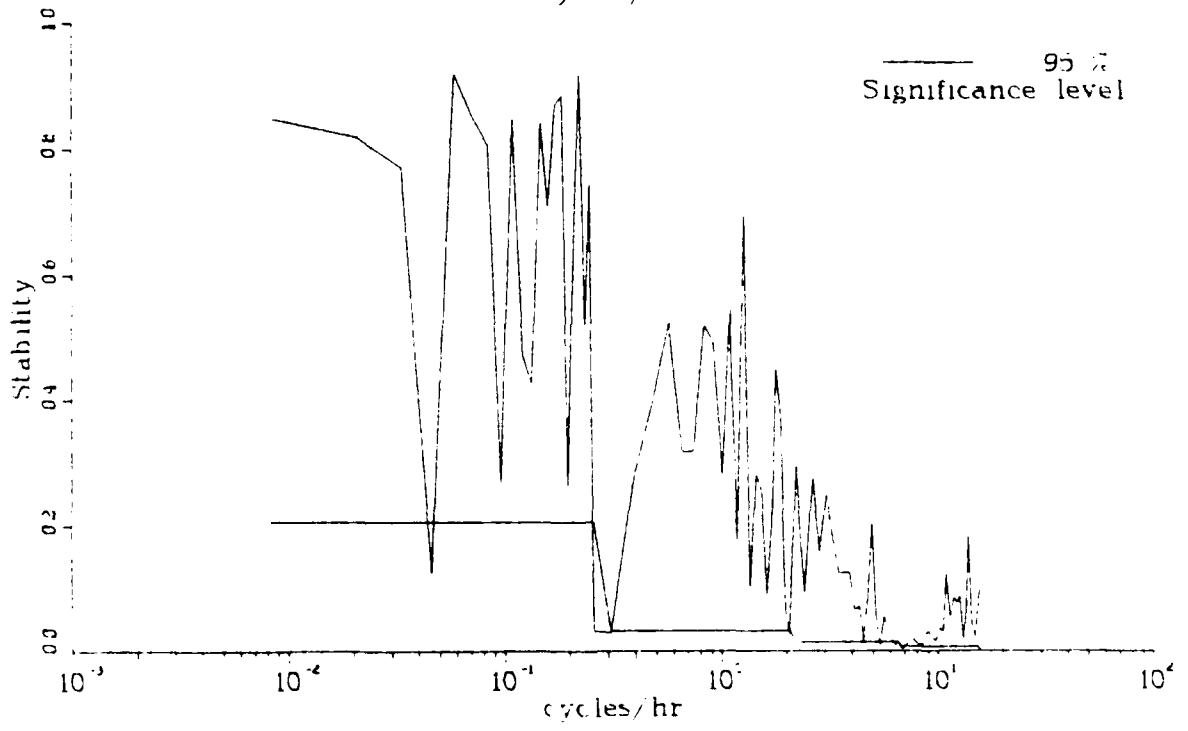

Variable	U
Depth	177 M
Meter	V-0256
Lat	30 29.7 N
Long	71 45.6 W

Variable	V
Depth	177 M
Meter	V-0256
Lat	30 29.7 N
Long	71 45.6 W

Figure 6.7d. Ellipse orientation and stability

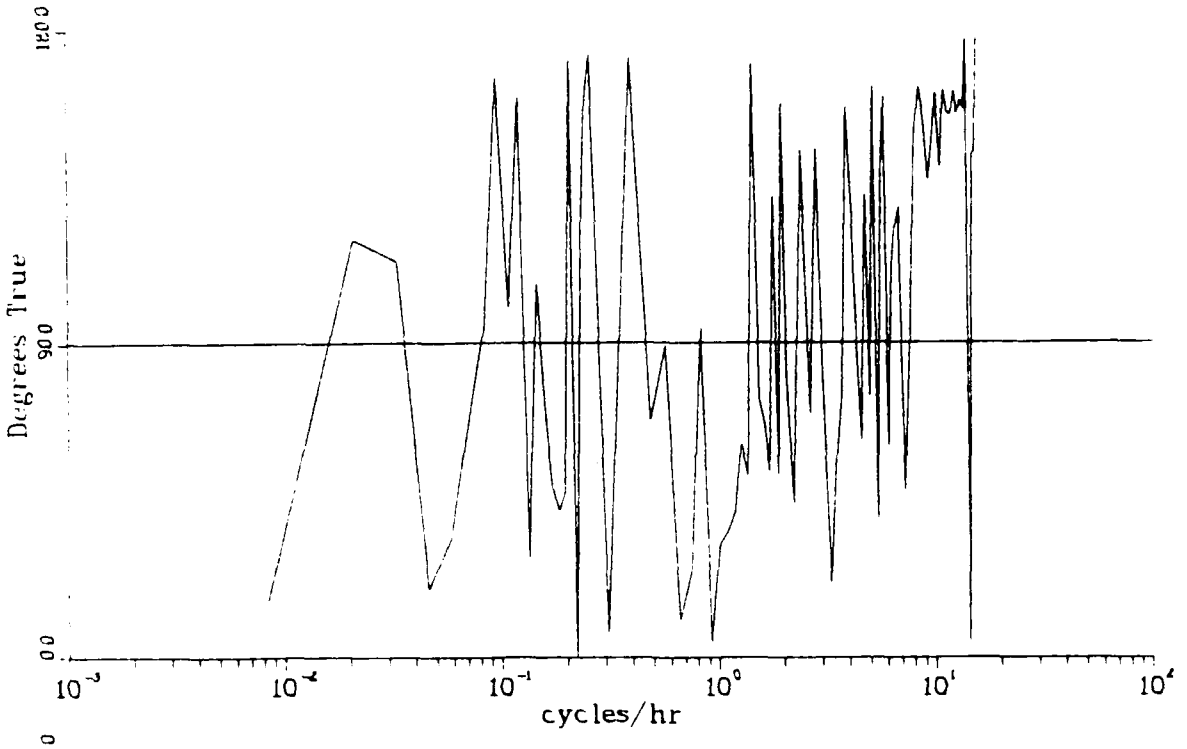

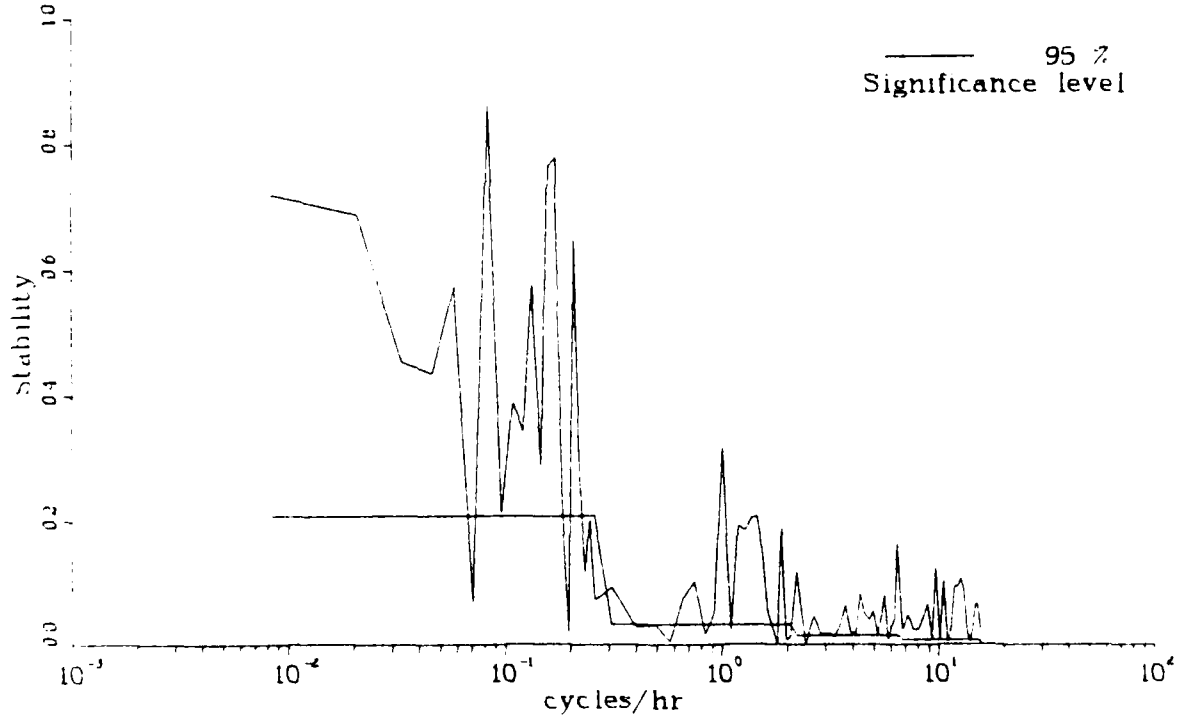

Variable	U	Variable	V
Depth	192 M	Depth	192 M
Meter	V-0539	Meter	V-0539
Lat	30 29.7 N	Lat	30 29.7 N
Long	71 45.6 W	Long	71 45.6 W

Figure 6.7e. Ellipse orientation and stability

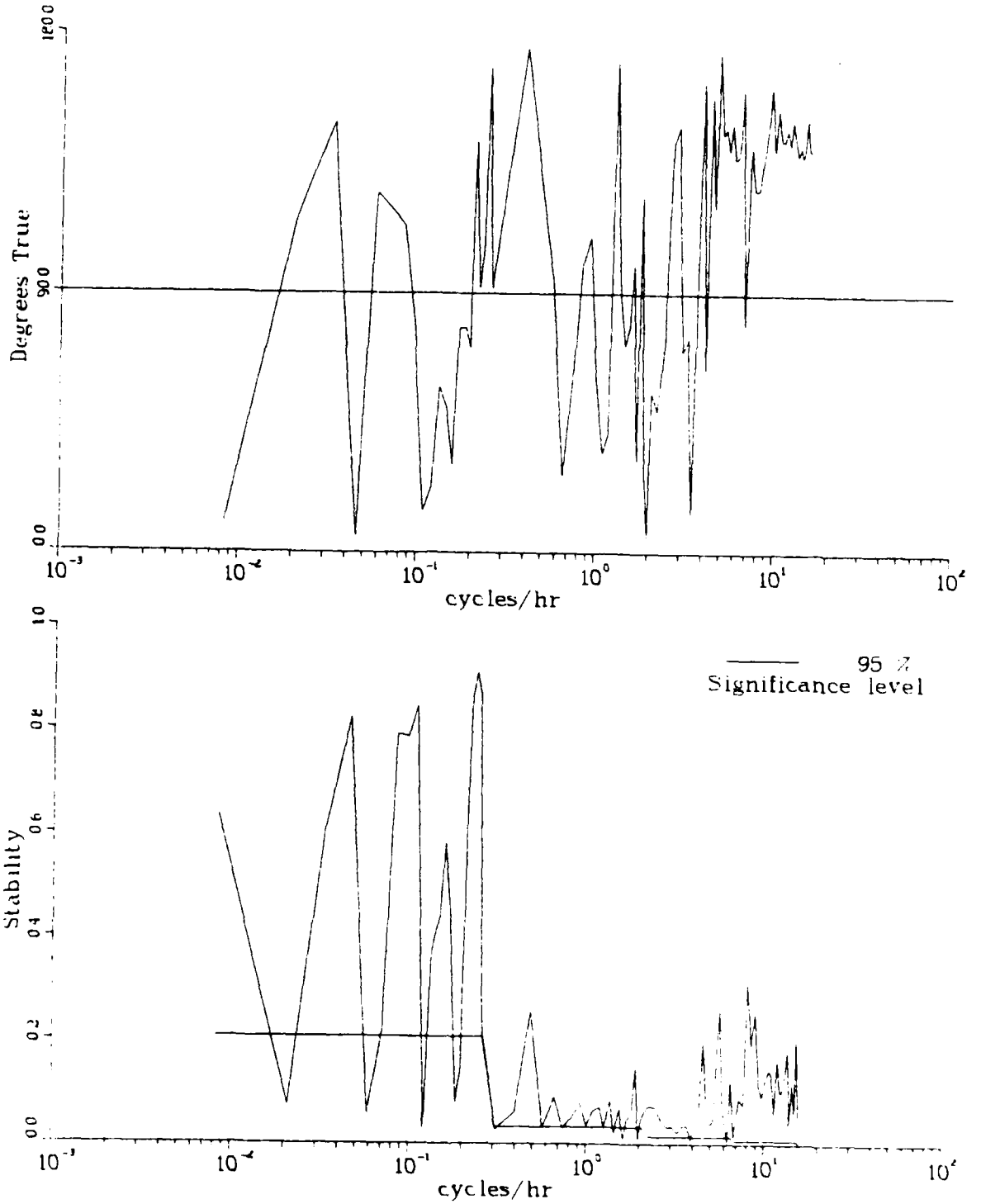

Variable	U
Depth	222 M
Meter	V-0532
Lat	30 29.7 N
Long	71 45.6 W

Variable	V
Depth	222 M
Meter	V-0532
Lat	30 29.7 N
Long	71 45.6 W

Figure 6.7f. Ellipse orientation and stability

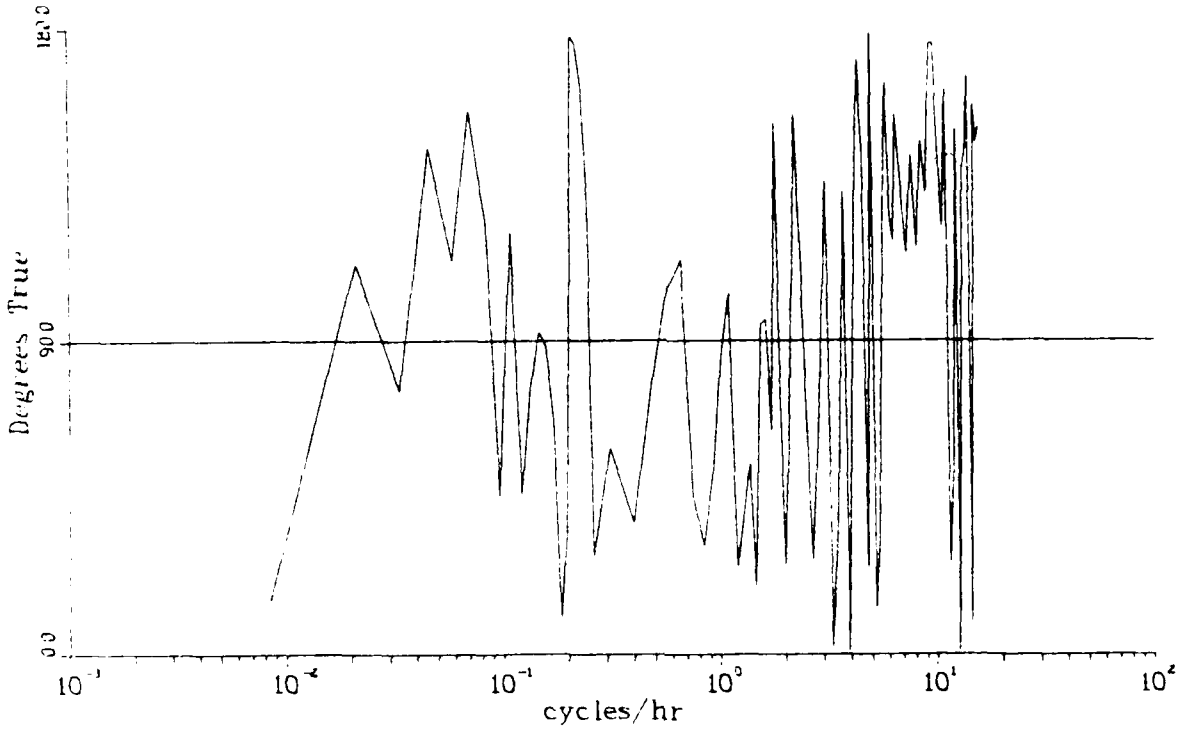

95 %
Significance level

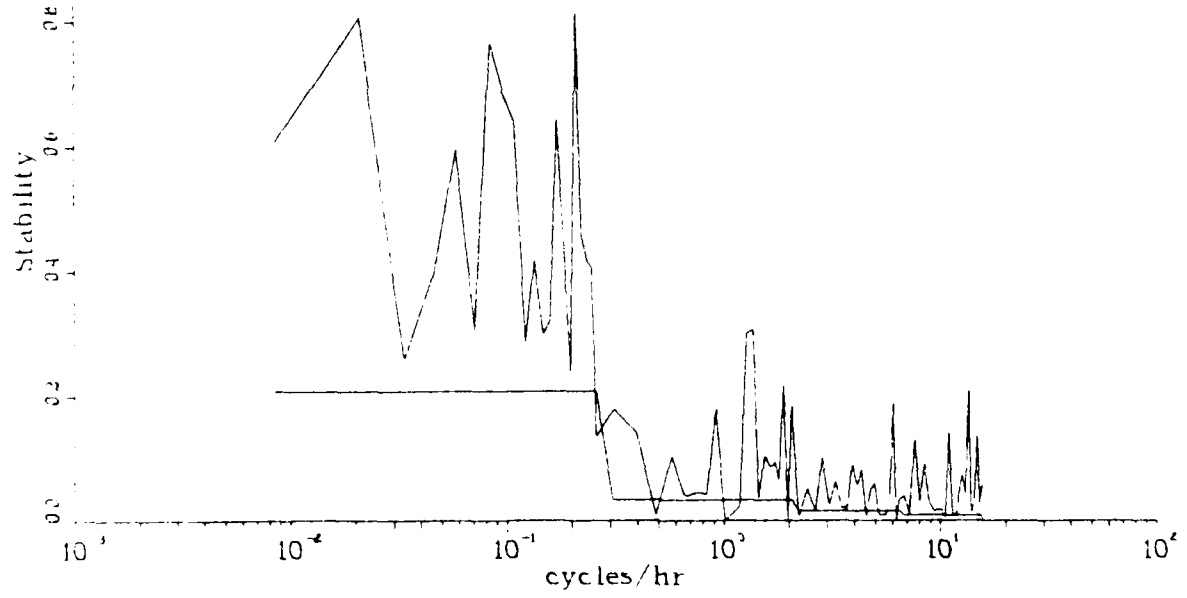

Variable	U	Variable	V
Depth	272 M	Depth	272 M
Meter	V-0254	Meter	V-0254
Lat	30 29.7 N	Lat	30 29.7 N
Long	71 45.6 W	Long	71 45.6 W

Figure 6.7g. Ellipse orientation and stability

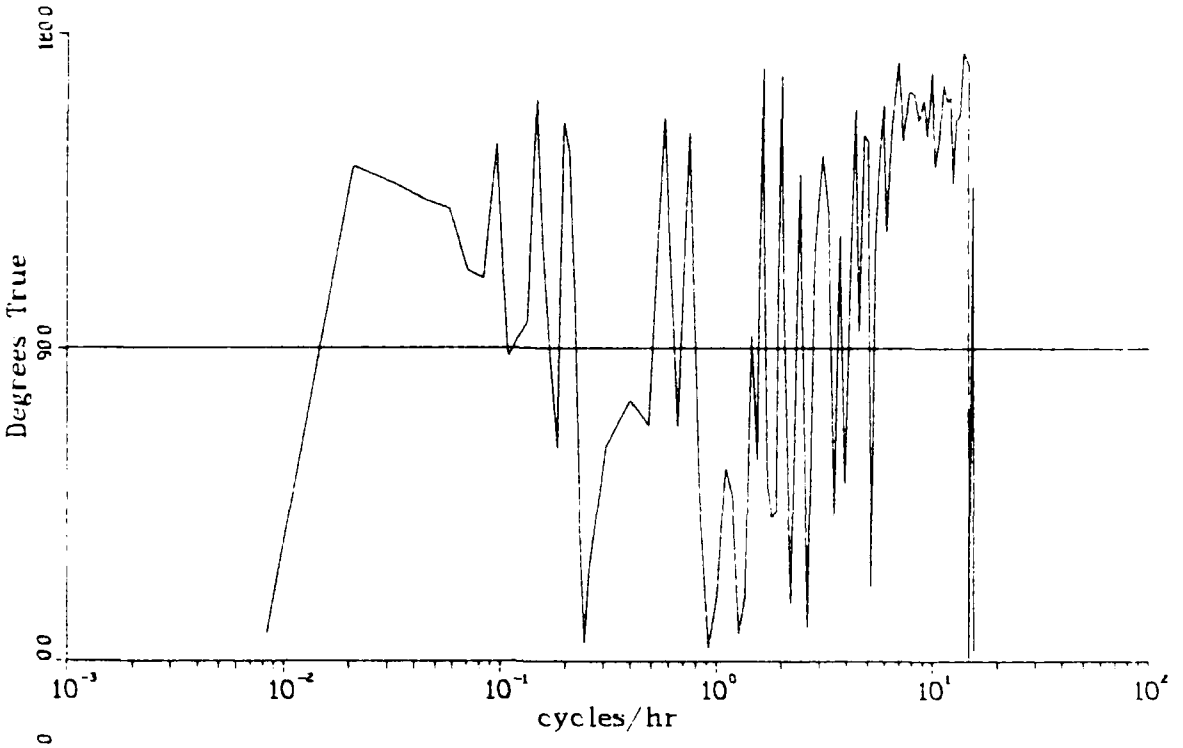

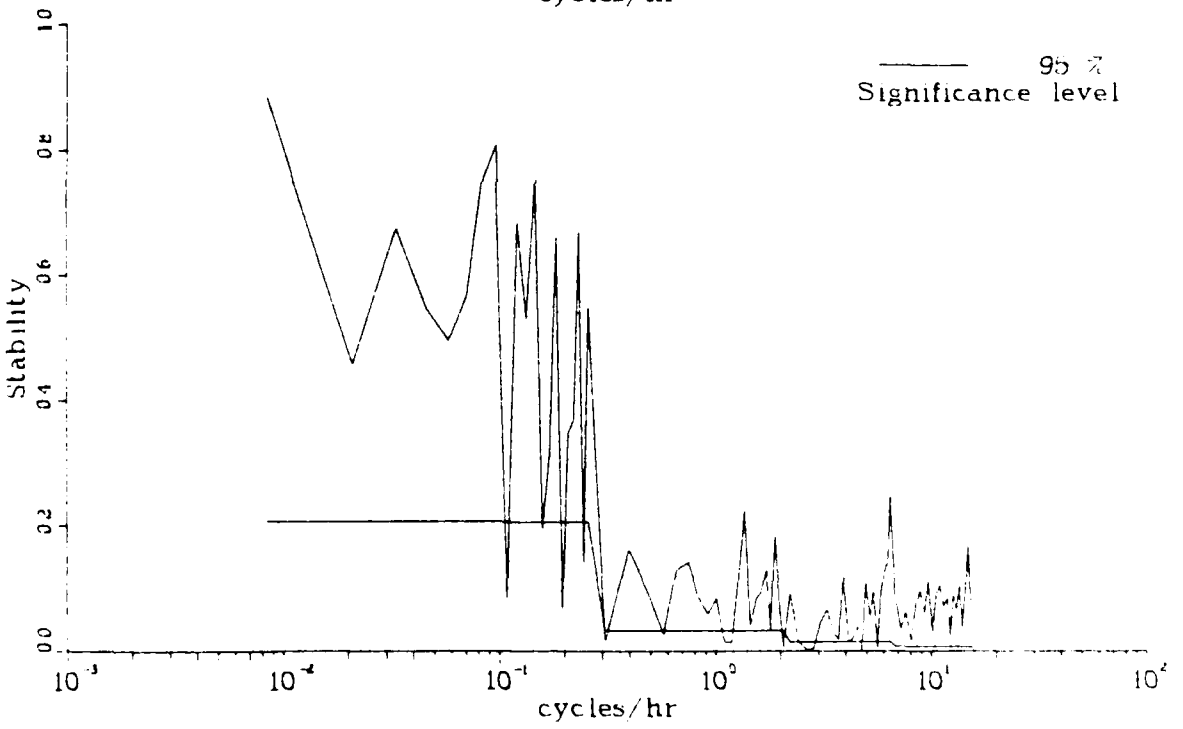

Variable	U	Variable	V
Depth	372 M	Depth	372 M
Meter	V-0559	Meter	V-0559
Lat	30 297 N	Lat	30 297 N
Long	71 456 W	Long	71 456 W

Figure 6.7h. Ellipse orientation and stability

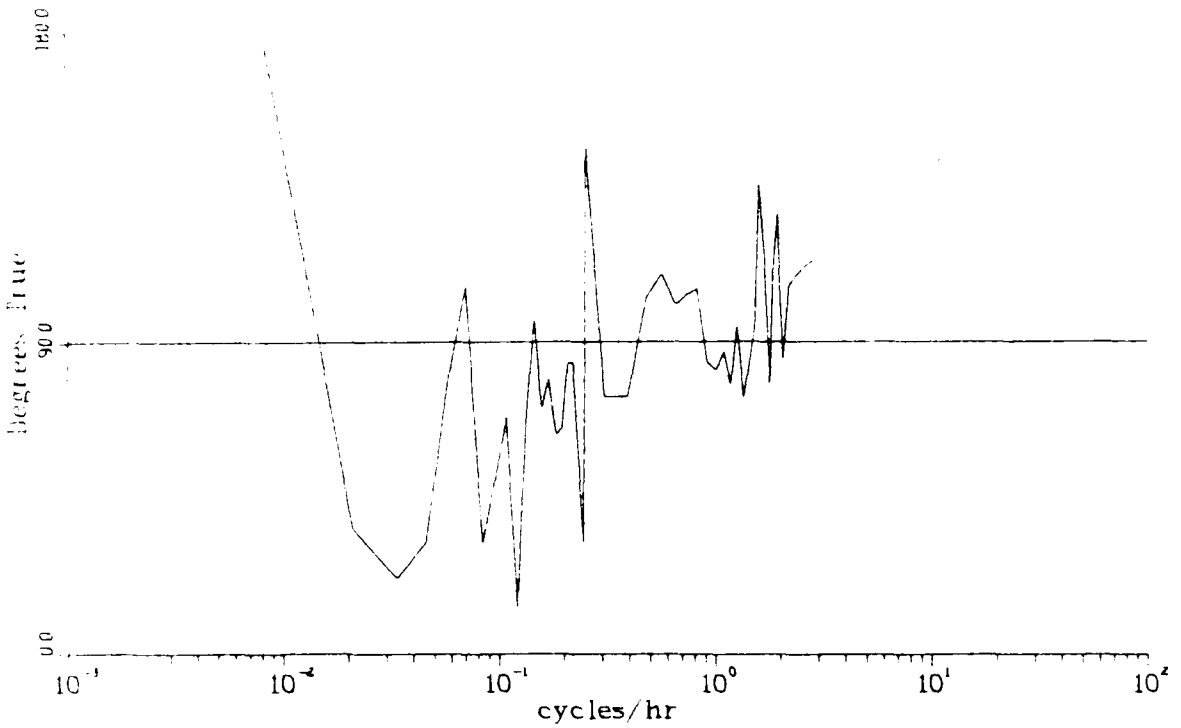

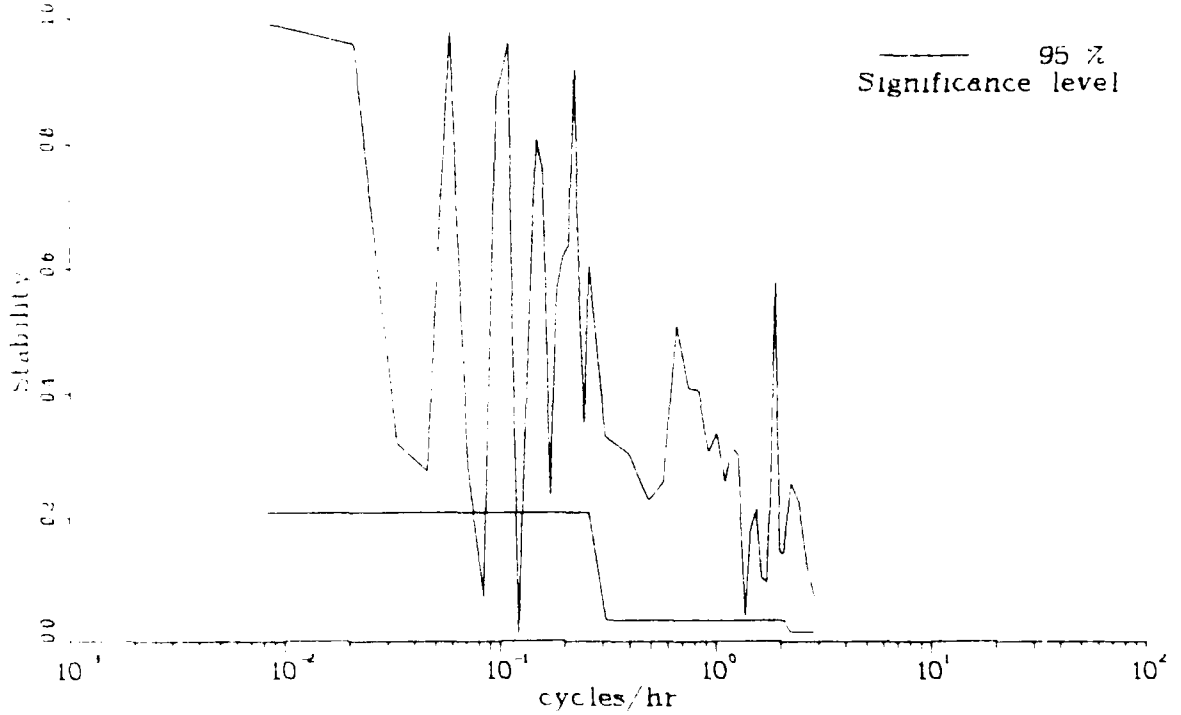

Variable	U	Variable	V
Depth	1022 M	Depth	1022 M
Meter	A-2930	Meter	A-2930
Lat	30 29.7 N	Lat	30 29.7 N
Long	71 45.6 W	Long	71 45.6 W

Figure 6.7j. Ellipse orientation and stability

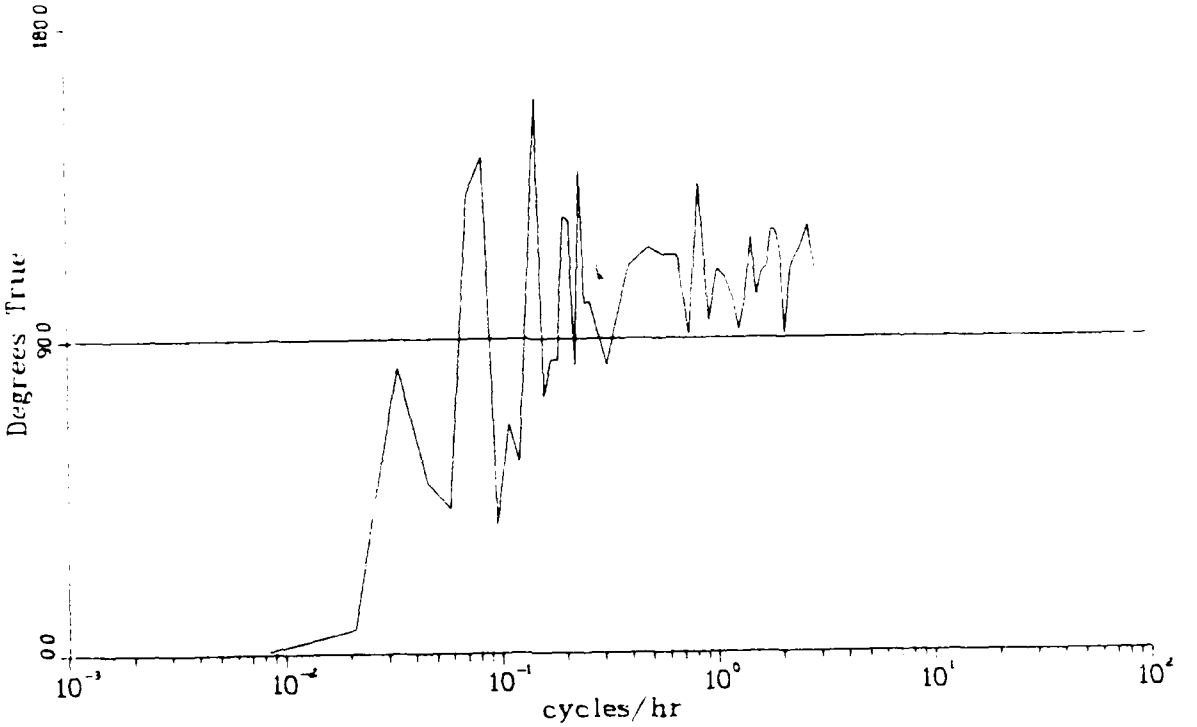

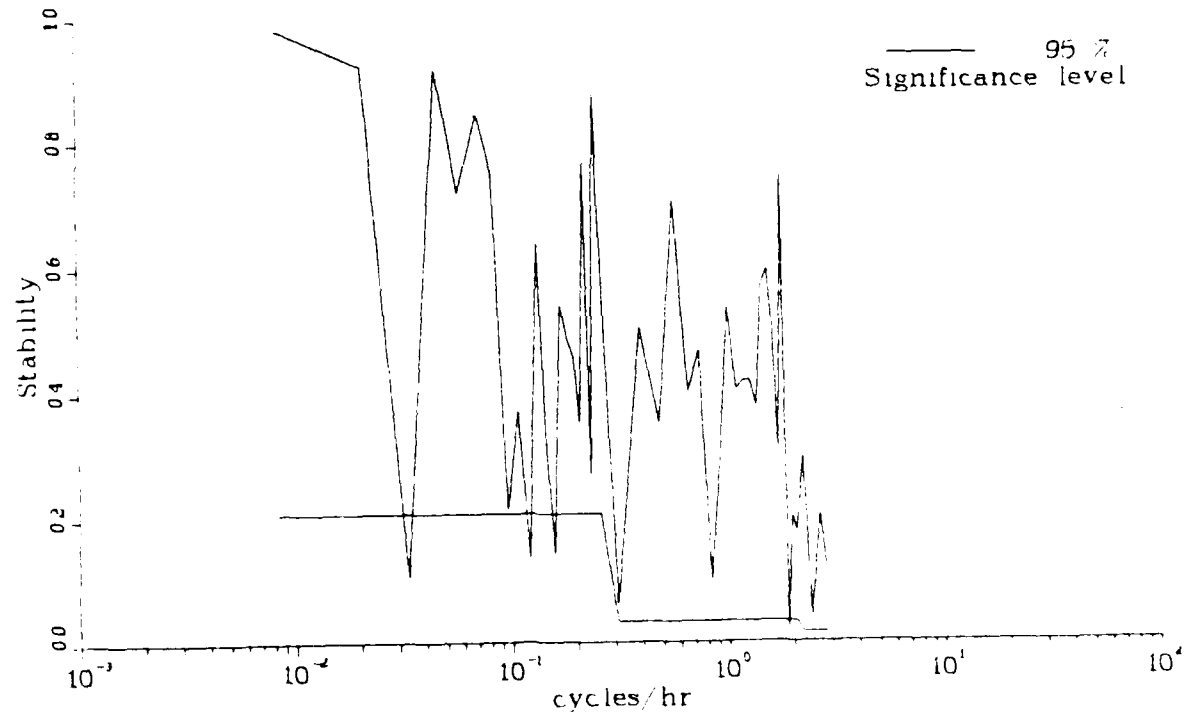

Variable	U
Depth	1522 M
Meter	A-2797
Lat	30 29.7 N
Long	71 45.6 W

Variable	V
Depth	1522 M
Meter	A-2797
Lat	30 29.7 N
Long	71 45.6 W

Figure 6.7k. Ellipse orientation and stability

Section 7.0

SHEAR PROBE DATA

by Thomas B. Sanford

AD-A099 014 NAVAL OCEAN RESEARCH AND DEVELOPMENT ACTIVITY NSTL S--ETC F/G 8/10
OCEANIC ENVIRONMENTAL BACKGROUND OBSERVATIONS IN THE SARGASSO S--ETC(U)
MAR 80 H PERKINS

UNCLASSIFIED NORDA-TN-58 NL

3 OF 3
AD A 099014

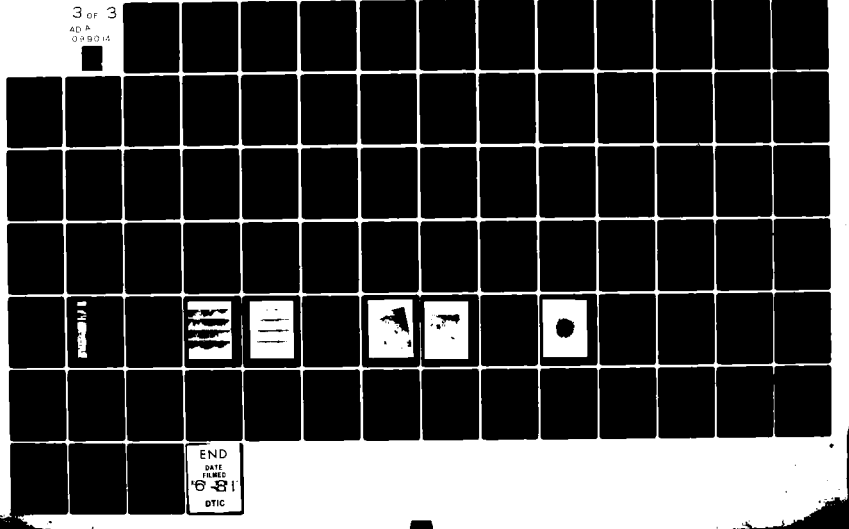

7.0 SHEAR PROBE DATA

7.1 INTRODUCTION

Profiles of ocean velocity as a function of depth between the sea surface and about 800 m were obtained in a two-dimensional pattern during USNS KANE Cruise 343918. These data were obtained with an expendable velocity and temperature profiler under NORDA-sponsored development. This project explored velocity shears with a 10 m vertical resolution and a 2.5 km horizontal resolution. The plan was to deploy shear probes at horizontal spacings short enough that strong features were correlated from one profile to its near neighbor and to continue the profiling until the correlation was lost between more distantly separated pairs. A limited amount of previous experience suggested that inter-probe separations of about 2-4 km would be appropriate in the open ocean. A second consideration influencing the experimental plan was that most of the strong, deep velocity fluctuations at sea are due to inertial period motions. Hence several repetitions of the profile section spaced over an inertial period (24 hr. at latitude 30°) were planned to resolve this dominant motion. The third consideration was the desire to obtain at least a second realization of the above experiment. A repeat experiment several days later was scheduled to examine the evolution of the observed structure after several cycles of its motion.

7.2 MEASUREMENT SYSTEM

The expendable probes were manufactured by the Sippican Corporation, Marion, Massachusetts. This device has been described by Drever and Sanford (1979) and is shown in Fig. 7.1. The device is made from standard Sippican parts, such as nose weight, probe spool and afterbody, combined with special electronics and sensors. The purpose of the device is to measure weak electric currents in the sea generated by the motion of the sea water through the geomagnetic field. These currents produce a signal at the probe electrodes of approximately 50 nV per cm/s of water flow. The electic voltage is converted to an FM signal which is sent to the surface vessel along with similar compass and temperature signals. The resulting electric current profile corresponds to the velocity profile relative to an unknown, depth-independent reference velocity. The reference velocity influences transport but not vertical shear measurements. Performance trials show the method to have an uncertainty of about 1 cm/s. During periods of geomagnetic activity earth currents may arise and reduce the above performance. An examination of geomagnetic records from San Juan, Puerto Rico, shows that there were no unusual magnetic events during the period when the profiles were being made.

The deck unit, called the receiver and processing system, is shown in Fig. 7.2. The three channels of FM data are transmitted to the ship by way of the expendable wire link. The signals are transformer coupled, amplified and filtered into the three separate frequency bands. These three FM signals are recorded on a HP3960 tape recorder so the data can be replayed after the drop. The period of the temperature signal is measured in a counter and converted to a voltage, V_T, which can be displayed on the XY plotter. The electric field and compass frequencies are converted to voltages, V_E and V_C, respectively, which are a linear representation of the voltages sensed by the probe.

The compass voltage, V_C , is used as a reference signal for the two-phase, lock-in amplifier. The lock-in amplifier synchronously demodulates the electric field voltage into in-phase (north-south) and quadrature (east-west) components with respect to the compass signal. These signals are recorded on the two-pen XY recorder as a function of time (depth) in real time as the probe is falling. Thus

the velocity data is available for immediate examination and analysis in analog form.

The processing system also measures and plots the in-phase and quadrature of the compass signal and the period of the compass signal.

Currently the analog plots are digitized after the cruise and processed on a HP9845S computer. The east and north velocity components are compensated for the fall-rate-induced contribution and for the probe and receiver transfer functions.

7.3 DESCRIPTION OF EXPERIMENT

During Cruise 343918 of the USNS KANE, Messrs. Drever and Bartlett of our lab, with the assistance of NORDA, NAVOCEANO and APL/JHU personnel, deployed 116 expendable velocity probes. An additional 22 probes were not deployed because of mechanical or electrical malfunctions.

Several drops were made prior to the beginning of the main experiment which served to determine a suitable distance between drops. Based on this, subsequent drops were made about 2.5 km apart.

The primary deployment pattern was two-dimensional, consisting of an L-shaped array of 20 km long legs oriented SE to NW and NE to SW. This pattern was executed three times in about a day, followed by a repetition of this sequence two days later. At the start the towed launcher was used, but at the end of the first leg it was decided to suspend use of this unit and rely on the deck launcher or on a hand-held launcher used from a towed rubber boat. The numbers of deck and rubber-boat launches are 57 and 39, respectively, with 20 probes launched from the towed launcher. It should be noted that profiles from deck-launched probes are contaminated by vessel-produced electric and magnetic disturbances in the upper 100 m.

The few probes remaining after the L-shaped pattern were deployed near the mooring to provide a short time series in that area.

The pattern and station positions are shown in Figure 7.3 for the first three repetitions of the L-shaped track and in Figure 7.4 for the second three repetitions. Drop time, positions, and relevant comments are provided in Table 7.1 covering the whole cruise. Three types of probe launchers were used: Deck denotes use of a conventional breech-loaded, Sippican-made XBT launcher; RB stands for rubber boat, from which probes were launched 200 m astern of the ship from a hand launcher; and Hand represents use of a standard Sippican-made, hand-held XBT launcher.

7.4 PERFORMANCE SUMMARY

Of the 116 probes launched, our preliminary analysis indicates that

a. 72 produced good profiles,

b. 34 produced portions of good data (about 3 drops were degraded by operator error, especially in making proper ground),

c. 10 were launched but failed to produce any usable data (we estimate that six failed due to operator error causing the wire to break during rubber boat launches).

Of the 22 probes which were taken to sea but were not launched, we find that

a. 12 had dead or weak batteries,

b. 8 had the wire link broken,

c. 2 came apart due to insufficient bonding between parts.

We experienced several problems with the towed launcher. The principal difficulty was that the probe would separate from the upper canister and either leave the launcher before it was deliberately released or become jammed and unable to be released at all. The winch was not able to be braked or locked and was not powerful enough to raise the launcher out of the water. The experience with the towed launcher was, however, valuable in that it showed clearly that a delayed release as an integral part of each probe is needed. With such a device the launch and recording could be performed by one person.

The overall quality of the data is good. Some of the drops have intermittent noise from an unknown source and some have a tendency for the in-phase signal to drift with depth, probably due to a pressure-induced error. Of the probes dropped, it is estimated that the data return is greater than 80%. It may be possible to recover additional portions of noisy drops with special processing. The possibility will be examined.

7.5 PRESENTATION OF RESULTS

Figures 7.5a - o present all of the usable velocity profiles for the cruise. The presentation is of the east velocity component plotted in the upper panel and north component plotted in the lower. The scales are 20 cm s^{-1} per tic in velocity and 200 m per tic in depth. Each profile is offset from its neighbor by about 20 cm/s. The profiles are grouped into those before the experiment (250-259), the individual legs of the first "L"-shaped pattern (6 groups), miscellaneous profiles between patterns (317-320), the 6 legs of the second "L"-shaped pattern, and the time-series at the mooring (359-363).

These profiles are digitized and processed versions of the analog plots are produced in real time at sea by the analog deck unit. Each profile has been processed to remove the effects of the two-pole analog filter in the deck unit and smoothed with a triangular filter at a total width of about 25 m. With comparable vertical filtering, the XTVP probes have demonstrated a performance uncertainty at AUTEC of about 1 cm/s RMS.

These plots reveal several important characteristics about the oceanic shear field, such as the temporal and spatial scales of variability. There exist strong gradients in the velocity field over distances of order 100 m in the vertical and 10 km in the horizontal. Moreover, numerous noticeable features change from leg to leg. The purpose of the next analysis is to try to differentiate between temporal and spatial structure in these observations.

The principal use of these profiles is to study zones of strong vertical shear and internal waves. The average shear over, say, 100-800 m is not large, seldom exceeding $10^{-3}s^{-1}$ (10 cm/s/100 m) and is composed primarily of steady and low-frequency currents. One method to separate these low-frequency currents from the shear-contributing internal waves is to fit a second order (quadratic) polynomial to the profile and subtract this fit from the original profile. This simple scheme is very effective in emphasizing the internal wave shears.

A second processing step has been followed whereby the residue profiles (original minus fit) are rotated to a reference time. Since most of the energy is due to inertial period motions, it is quite effective to rotate profiles at the inertial period to the same reference time. Under this demodulation scheme, each profile of a time series can be rotated to the same time with the result that inertial currents appear to be steady and very similar in each profile. When used on a spatial section, the method tends to eliminate the temporal structure, revealing more clearly the underlying spatial dependence. The reference times used are 1950Z on 6 September 1979 for "L" series 1 and 0130Z on 10 September for "L" series 2. The fitted and rotated "L"-pattern profiles are plotted in Figures 7.6a-l.

7.6 REFERENCE

Drever, Robert G. and Thomas B. Sanford, An expendable temperature and velocity profiler (XTVP), in Proceedings of a Workshop on Near Surface Ocean Experimental Technology, 6-8 November 1979, at the Naval Ocean Research and Development Activity, Bay St. Louis, MS.

Table 7.1

XTVP - LOG
USNS KANE - September 1979

Drop No.	Date 9-79	Time (Z) hr.min:sec.	Launcher Used	Lat. (N)	Long. (W)	Comments
250	2	2014:02	Deck	30°59.8	73°38.5	Good drop: In transit to test site.
251	2	2019:01	Deck	30°59.8	73°38.2	Poor quality.
252	2	2227:50	Remote	30°53.4	73°31.5	Good drop: Solenoid would not fire. Gnd wire broken. Some RFI.
253	4	0347:30	Remote	30°35.7	71°47.3	Good drop: Difficulty firing solenoid.
254	4	0358	Remote	30°35.7	71°46.4	Good drop, but probe released early.
255	4	unknown	Remote	---	---	Performance unknown: probe released after launcher put into water.
256	4	2312:00	Remote	30°29.4	71°46.4	Performance unknown: slowly rotating 3Hz.
257	4	2336:00	Remote	30°28.7	71°48.9	Good drop.
258	4	2347:36	Remote	30°28.0	71°49.9	Good drop.
259	4	2538:00	Remote	30°27.4	71°51.0	Noisy drop.
260	6	1925:22	Remote	20°26.0	71°38.5	After 80s cable accidentally disconnected at winch. Start of L #1.
261	6	1938:45	Remote	30°27.1	71°39.7	Probe seemed to die before launch, although worked some deep.
262	6	1950:08	Remote	30°27.8	71°40.7	Good drop.
263	6	2007:09	Remote	30°29.0	71°42.1	Good drop.
264	6	2020:07	Remote	30°30.1	71°43.3	Good drop.
265	6	2034:16	Remote	30°31.1	71°44.6	Good drop for 160s.
266	6	2053:25	Remote	30°32.5	71°46.1	Good drop: took 4 min to release probe.
267	6	2118:00	Deck	30°33.1	71°48.4	Good drop: some cc noise. Vertex of L #1.

Table 7.1 XTVP - LOG (cont.)

Drop No.	Date 9-79	Time (Z) hr.min:sec.	Launcher Used	Lat. (N)	Long. (W)	Comments
268	6	2130:00	Deck	30°32.3	71°49.4	Good drop.
269	6	2151:00	Deck	30°30.6	71°51.3	Good drop.
270	6	2200:00	Deck	30°30.0	71°52.1	Good drop: trend to 1.
271	6	2215:02	Deck	30°28.8	71°53.5	Good drop.
272	6	2230:02	Deck	30°27.6	71°54.8	Good drop except for 2 60-s section.
273	6	2245:01	Deck	30°26.4	71°56.1	Good drop.
274	6	2300:02	Deck	30°25.4	71°57.2	Good drop, end of L #1.
275	7	0407:10	Remote	30°26.0	71°38.4	Poor drop: start of L #2.
276	7	0421:02	Remote	30°26.8	71°39.4	Fair drop, noise spikes.
277	7	0433:31	Remote	30°27.4	71°40.3	Good drop.
278	7	0448:00	Remote	30°28.3	71°41.5	Good drop.
279	7	0503:01	Deck	30°29.1	71°42.6	Noisy drop.
280	7	0517:47	Remote	30°30.0	71°43.5	Bad drop.
281	7	0533:54	Deck	30°31.0	71°44.7	Good drop, some noise.
282	7	0548:01	Deck	30°31.8	71°45.7	Good drop, some noise.
283	7	0603:56	Deck	30°32.8	71°46.8	Good drop.
284	7	0618:01	Deck	30°33.6	71°47.7	Good drop, vertex of L #2.
285	7	0635:34	Deck	30°33.1	71°49.0	Noisy drop, -V low.
286	7	0650:30	Deck	30°32.4	71°50.0	Good drop.
287	7	0704:00	Deck	30°31.7	71°50.9	Possibly temp related; noise, deep 1 trend.
288	7	0721:05	Deck	30°30.7	71°52.0	Good drop.
289	7	0735:02	Deck	30°29.8	71°53.1	Good drop.
290	7	0750:01	Deck	30°28.8	71°54.0	Noisy drop.
291	7	0805:01	Deck	30°27.7	71°55.0	Noisy drop, F_T noticed.
292	7	0820:00	Deck	30°26.7	71°56.0	Good drop.

Table 7.1 XTVP - LOG (cont.)

Drop No.	Date 9-79	Time (Z) hr.min:sec.	Launcher Used	Lat. (N)	Long. (W)	Comments
293	7	0835:00	Deck	30°25.7	71°57.0	1st 1/2 noisy: end of L #2.
294	7	1455:05	RB	30°27.1	71°38.2	Good drop. Rubber boat: 50' behind.
295	7	1807:22	RB	30°25.6	71°37.3	Bad drop: rubber boat 600' behind (Gnd not present at launch). Start of L #3.
296	7	1822:20	RB	30°26.5	71°38.3	Bad drop (Gnd not corrected until Drop 297)
297	7	1835:51	RB	30°27.3	71°39.2	Fair drop.
298	7	1852:05	RB	30°28.1	71°40.2	Noisy drop.
299	7	1906:30	RB	30°28.8	71°41.1	Good drop.
300	7	1921:00	RB	30°29.5	71°41.9	Good drop: some noise.
301	7	1938:48	RB	30°30.4	71°43.1	Good drop.
302	7	1951:14	RB	30°31.1	71°43.9	Good drop.
303	7	2006:00	RB	30°31.8	71°44.8	Good drop.
304	7	2021:26	RB	30°32.5	71°45.7	Good drop.
305	7	2031:29	RB	30°32.9	71°46.2	Good drop.
306	7	2122:41	RB	30°33.1	71°48.8	Good drop: vertex of L #3.
307	7	2138:04	RB	30°32.4	71°49.8	Good for 180s.
308	7	2152:53	RB	30°31.5	71°50.9	Good drop.
309	7	2209:54	RB	30°30.5	71°52.0	Good drop.
310	7	2222:23	RB	30°29.8	71°52.9	Bad drop: +V problem?
311	7	2228:33	RB	30°29.4	71°53.2	Good drop.
312	7	2240:04	RB	30°28.7	71°53.9	Good drop.
313	7	2254:43	RB	30°27.8	71°54.8	Good drop.
314	7	2326:40	Hand	30°26.5	71°56.4	CC half amplitude.
315	7	2340:00	Deck	30°25.6	71°57.3	Bad probe launched inadvertently.
316	7	2348:00	Deck	30°25.1	71°57.7	Good drop: end of L #3.

Table 7.1 XTVP - LOG (cont.)

Drop No.	Date 9-79	Time hr.min:sec.	Launcher Used	Lat. (N)	Long. (W)	Comments
317	9	0337:10	Deck	30°30.4	71°41.4	Good drop.
318	9	1018:00	Deck			Good beyond 1st 50s: deep I trend.
319	9	1726:40	Deck	30°23.0	71°41.4	Good drop: deep I trend.
320	9	2051:00	Deck	30°29.6	71°42.1	Good drop.
321	10	0130:00	Deck	30°27.1	71°39.8	Good drop: start of L #4.
322	10	0150:00	Deck	30°28.7	71°42.1	Good drop.
323	10	0210:00	Deck	30°30.0	71°44.0	Good drop.
324	10					Good drop.
325	10	0250:00	Deck	30°32.9	71°48.0	Good drop: vertex of L #4.
326	10	0310:00	Deck	30°31.7	71°49.9	Noisy drop: deep I trend.
327	10	0330:00	Deck	30°30.4	71°51.7	Good drop.
328	10	0350:00	Deck	30°28.8	71°53.4	Good drop.
329	10	0410:00	Deck	30°27.1	71°55.0	Good drop: deep I trend.
330	10	0430:00	Deck	30°25.8	71°56.9	Good drop: end of L #4.
331	10	1127:03	RB	30°26.6	71°38.6	Good drop: start of L #5.
332	10	1149:05	RB	30°28.0	71°40.3	Good drop.
333	10	1212:19	RB	30°29.5	71°42.1	Good drop.
334	10	1230:20	RB	30°30.7	71°43.6	Good drop: raining.
335	10	1230:20	Deck	30°30.7	71°43.6	Some noise, simult. w/334
336	10	1250:20	RB	30°31.9	71°45.1	Some noise: rain.
337	10	1310:10	RB	30°33.3	71°46.7	Some noise, rain, deep I trend.
338	10	1312:30	Deck	30°33.5	71°46.9	Nearly simult. w/337.
339	10	1401:17	RB	30°34.3	71°48.4	Good drop: vertex of L #5.
340	10	1420:05	RB	30°32.8	71°49.2	Fair drop: rain: 1/2 cc.
341	10	1440:00	RB	30°31.3	71°50.5	Good drop.

Table 7.1 XTVP - LOG (cont.)

Drop No.	Date 9-79	Time (Z) hr.min:sec.	Launcher Used	Lat. (N)	Long. (W)	Comments
342	10	1459:44	RB	30°29.9	71°52.3	Good drop.
343	10	1521:50	RB	30°28.3	71°53.9	Good drop.
344	10	1540:06	RB	30°27.1	71°55.3	Good drop.
345	10	1601:54	RB	30°25.6	71°57.0	CC half size: NG End of L #5.
346	10	2055:20	RB	30°26.0	71°37.8	Good drop: start of L #6.
347	10	2122:20	RB	30°27.5	71°39.9	Good drop.
348	10	2140:08	RB	30°28.6	71°41.3	Good drop.
349	10	2201:19	RB	30°29.9	71°43.1	Good drop but no temp.
350	10	2222:25	RB	30°31.2	71°44.6	Good drop.
351	10	2240:50	RB	30°32.4	71°46.1	Good drop.
352	10	2315:30	Deck	30°33.4	71°48.1	Bad drop: vertex of L #6.
353	10	2321:10	Deck	30°33.0	71°48.6	Good drop.
354	10	2340:00	Deck	30°31.5	71°50.4	Good drop.
355	11	0000:00	Deck	30°30.1	71°52.1	Good drop.
356	11	0020:00	Deck	30°28.7	71°53.6	Good drop.
357	11	0040:00	Deck	30°27.4	71°54.9	Good drop.
358	11	0100:00	Deck	30°26.2	71°56.3	Good drop: end of L #6.
359	11	0411:15	Deck	30°28.7	71°46.2	Good [illegible] time series.
360	11	1531:00	Deck	30°30.7	71°47.5	Good drop.
361	11	2324:00	Deck	30°31.1	71°47.8	Good drop.
362	12	0800:00	Deck	30°30.8	71°47.6	Good drop.
363	12	1714:00	Deck	30°30.4	71°47.1	Good drop.
364	12	2148:00	Deck	30°53.2	71°48.3	Test of high speed launch: noisy drop.
365	12	2154:00	Deck	30°54.6	71°48.4	2nd high speed launch. Good drop.

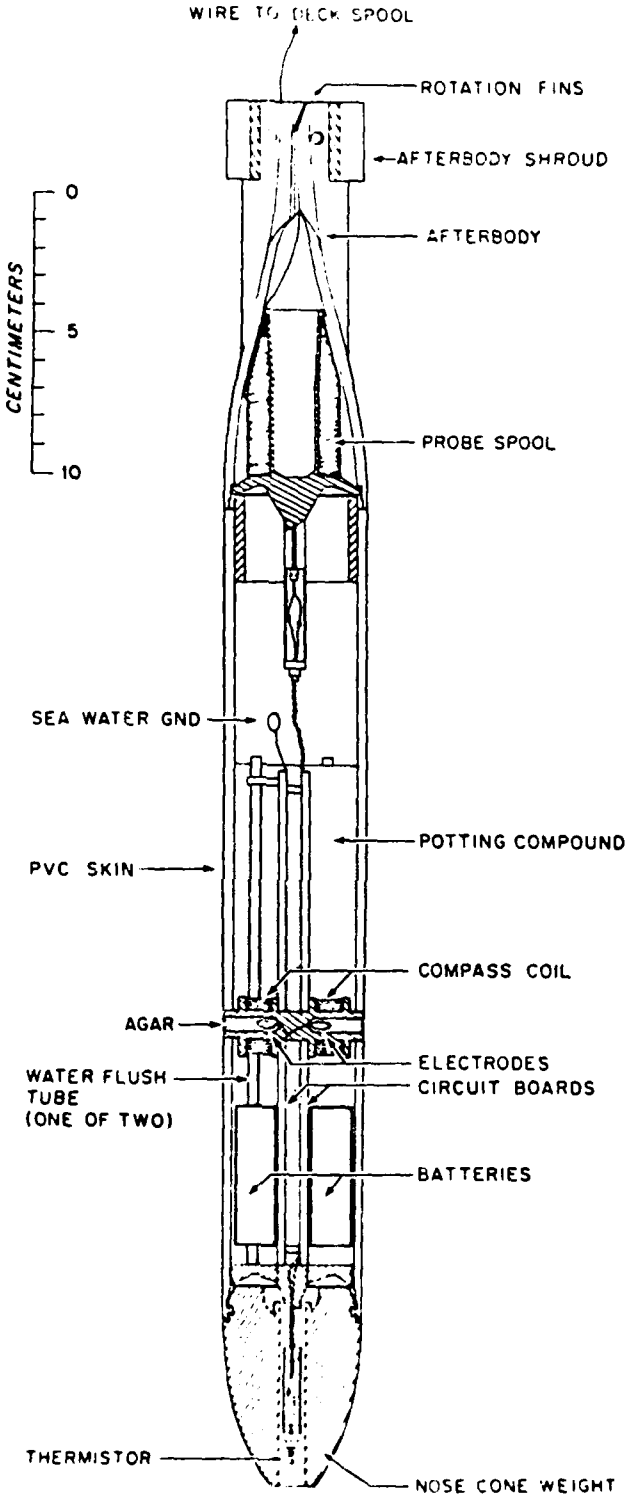

Figure 7.1. Expendable temperature and velocity profiler (XTVP)

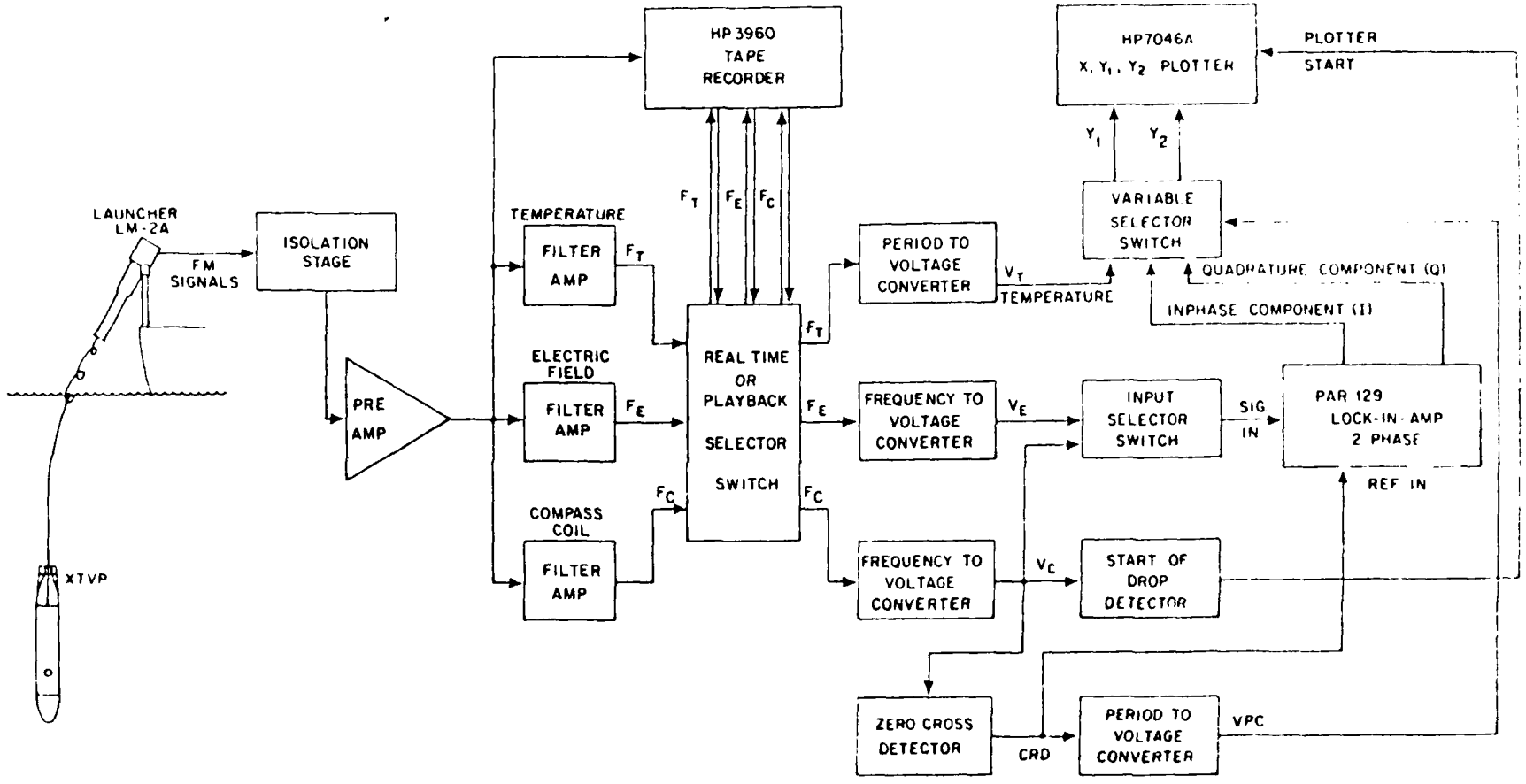

Figure 7.2. Processing system used on board USNS KANE

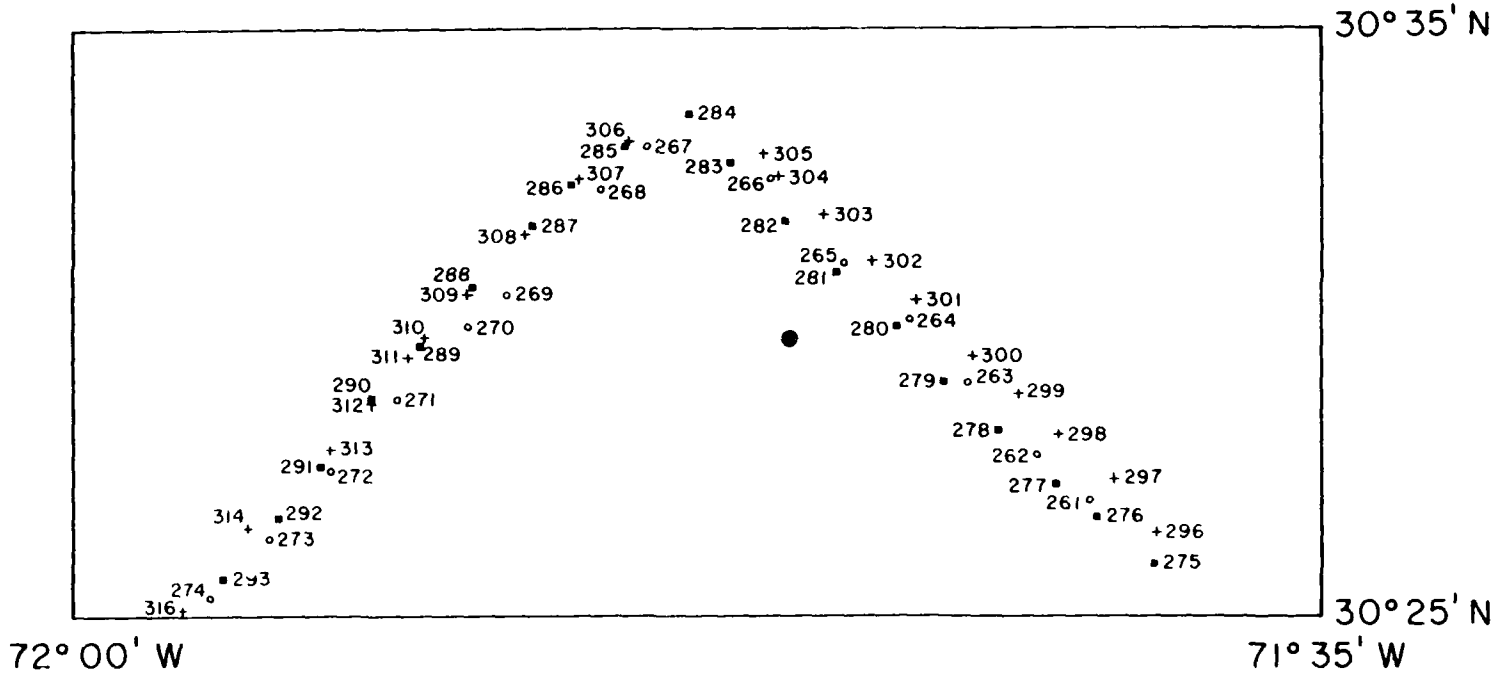

Figure 7.3. XTVP launch positions for first three repetitions of L-shaped pattern. Large dot is position of current meter mooring.

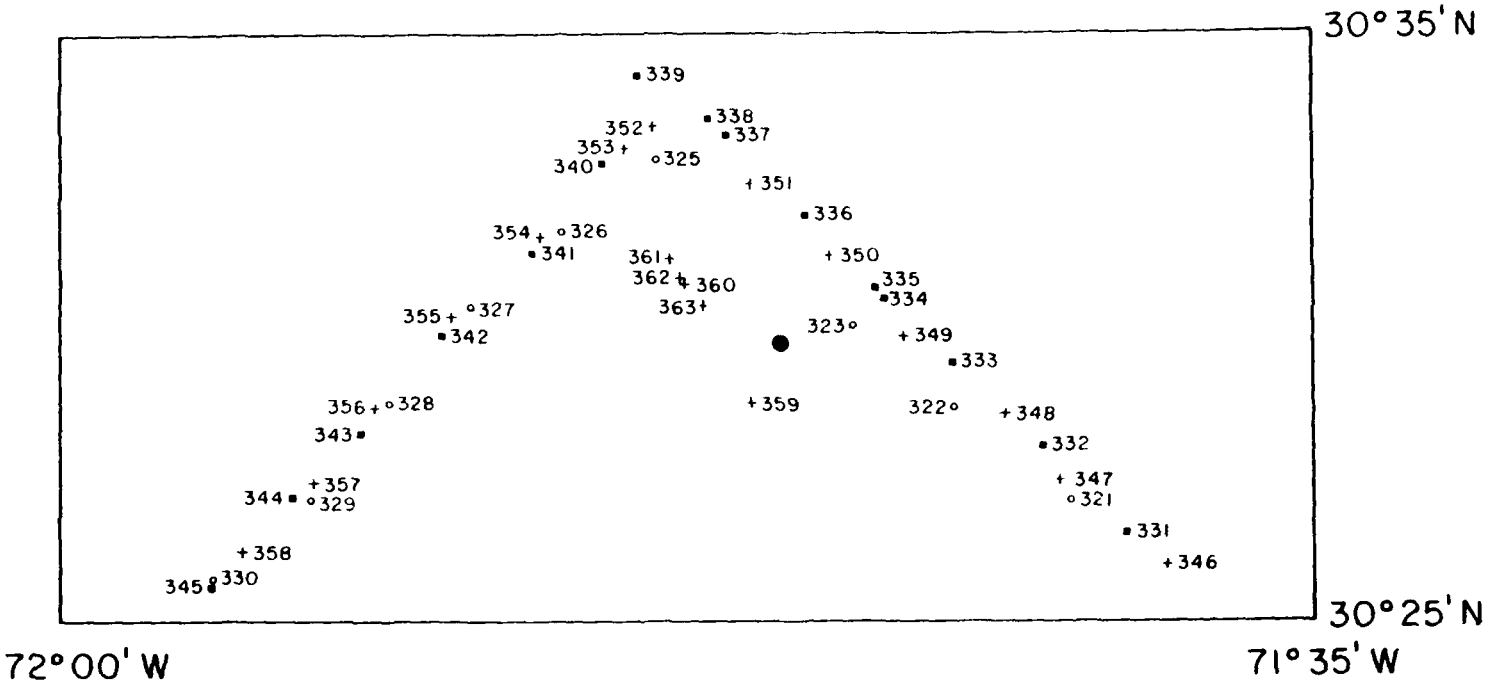

Figure 7.4. XTVP launch positions for second three repetitions of L-shaped pattern. Large dot is position of current meter mooring. Profiles 360 - 363 comprise a brief time-series station.

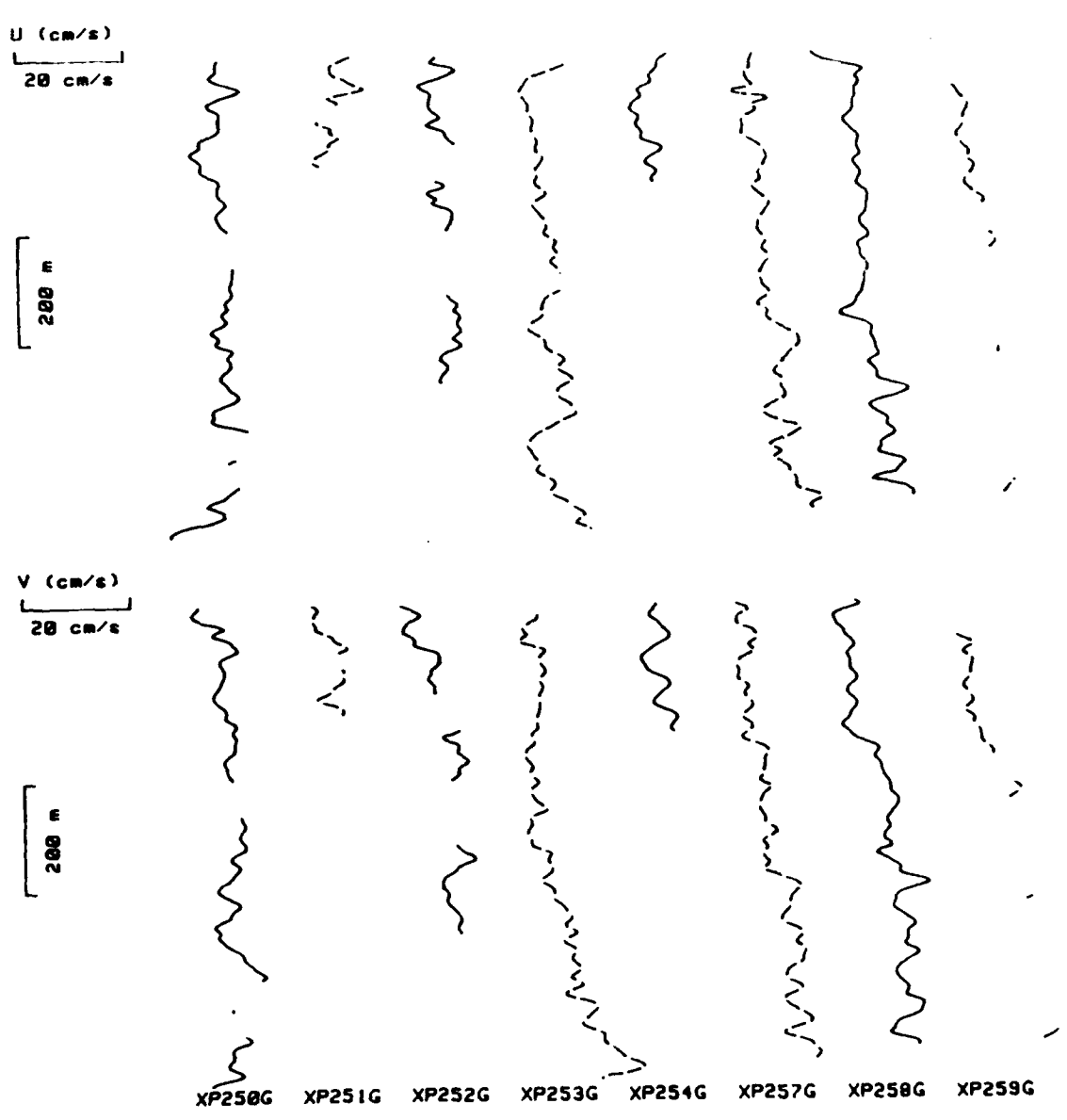

Figure 7.5a. East (U) and North (V) velocity profiles prior to start of experiment.

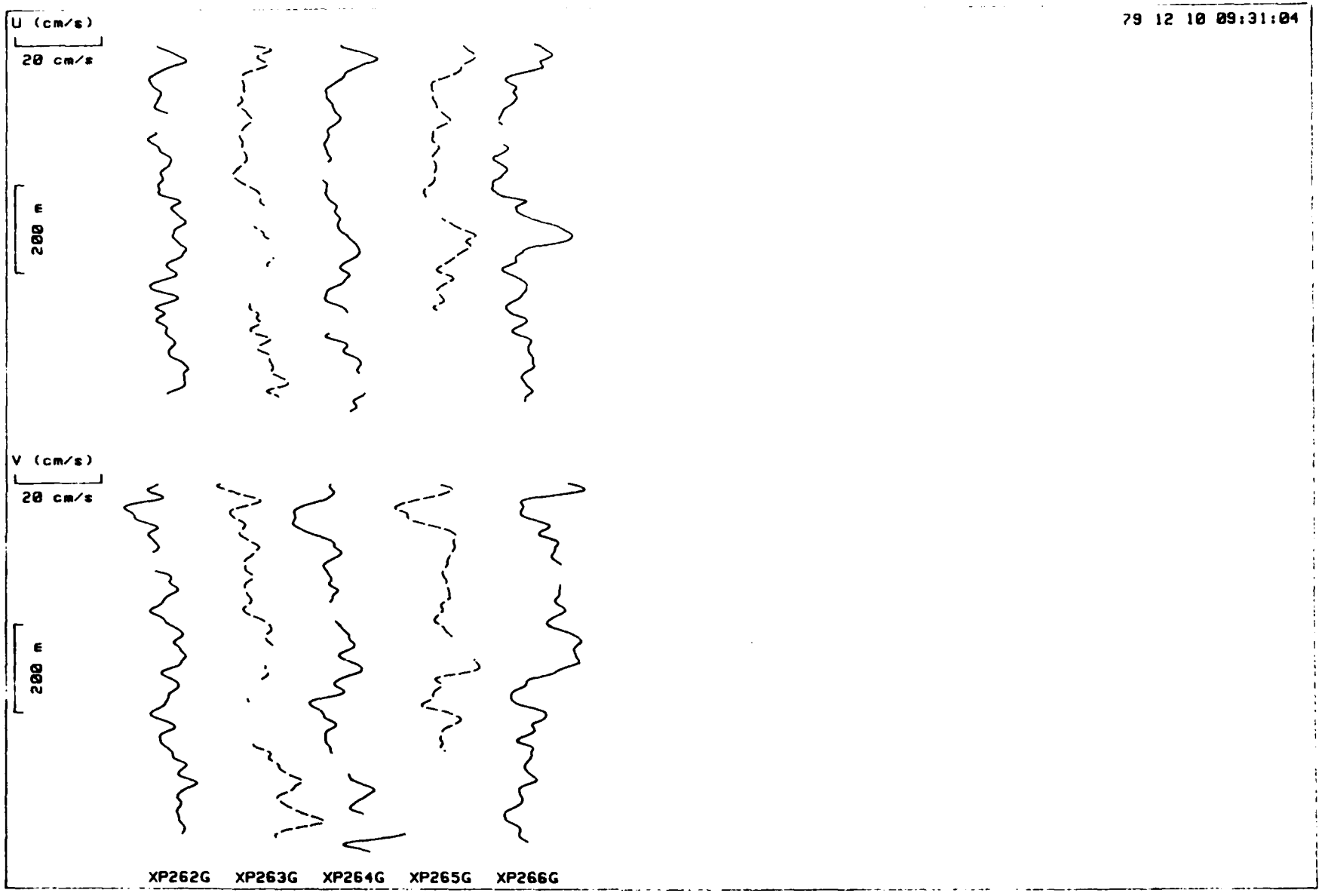

Figure 7.5b. East (U) and North (V) velocity profiles for first leg of first L-shaped pattern of first series.

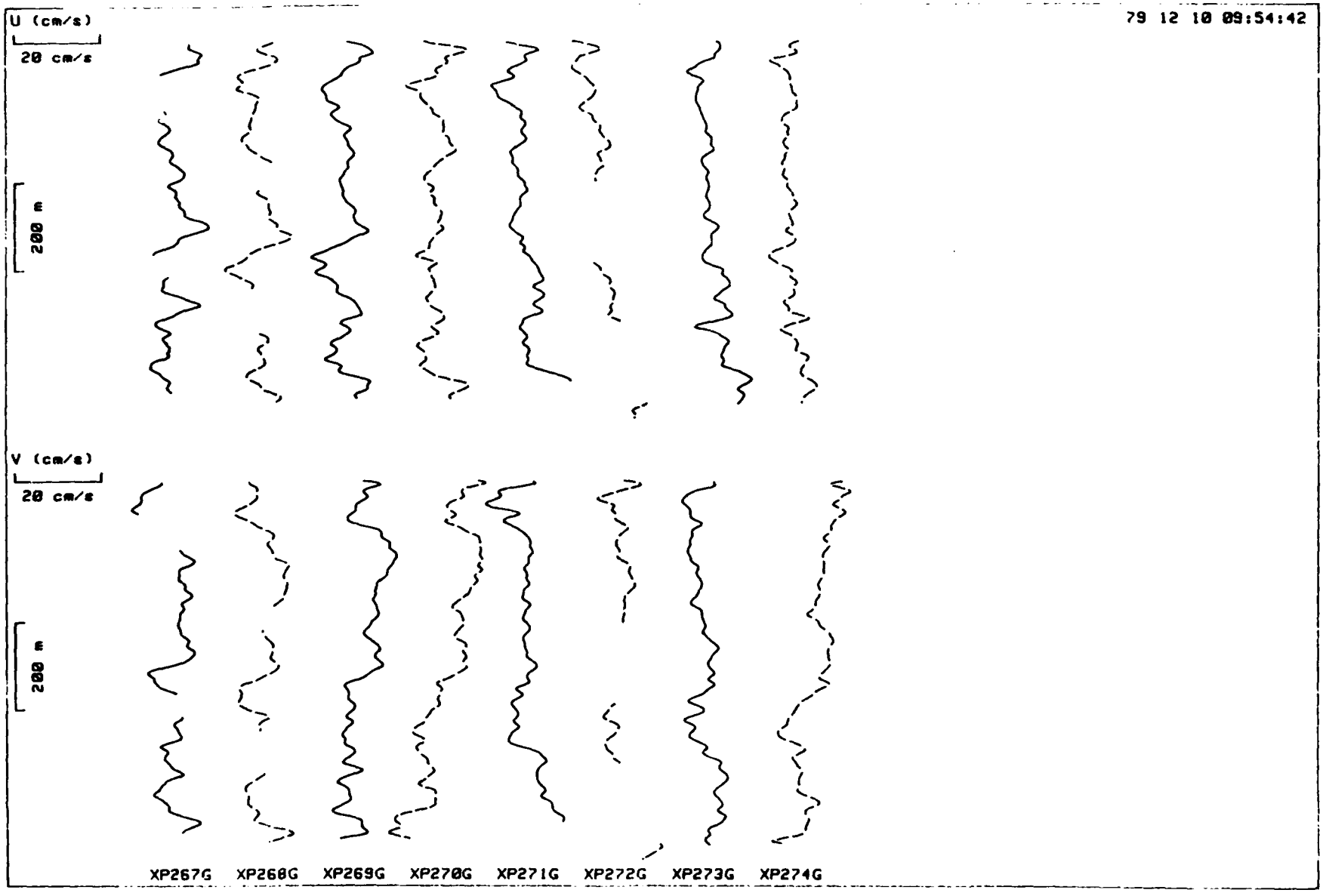

Figure 7.5c. East (U) and North (V) velocity profiles for second leg of first L-shaped pattern of first series.

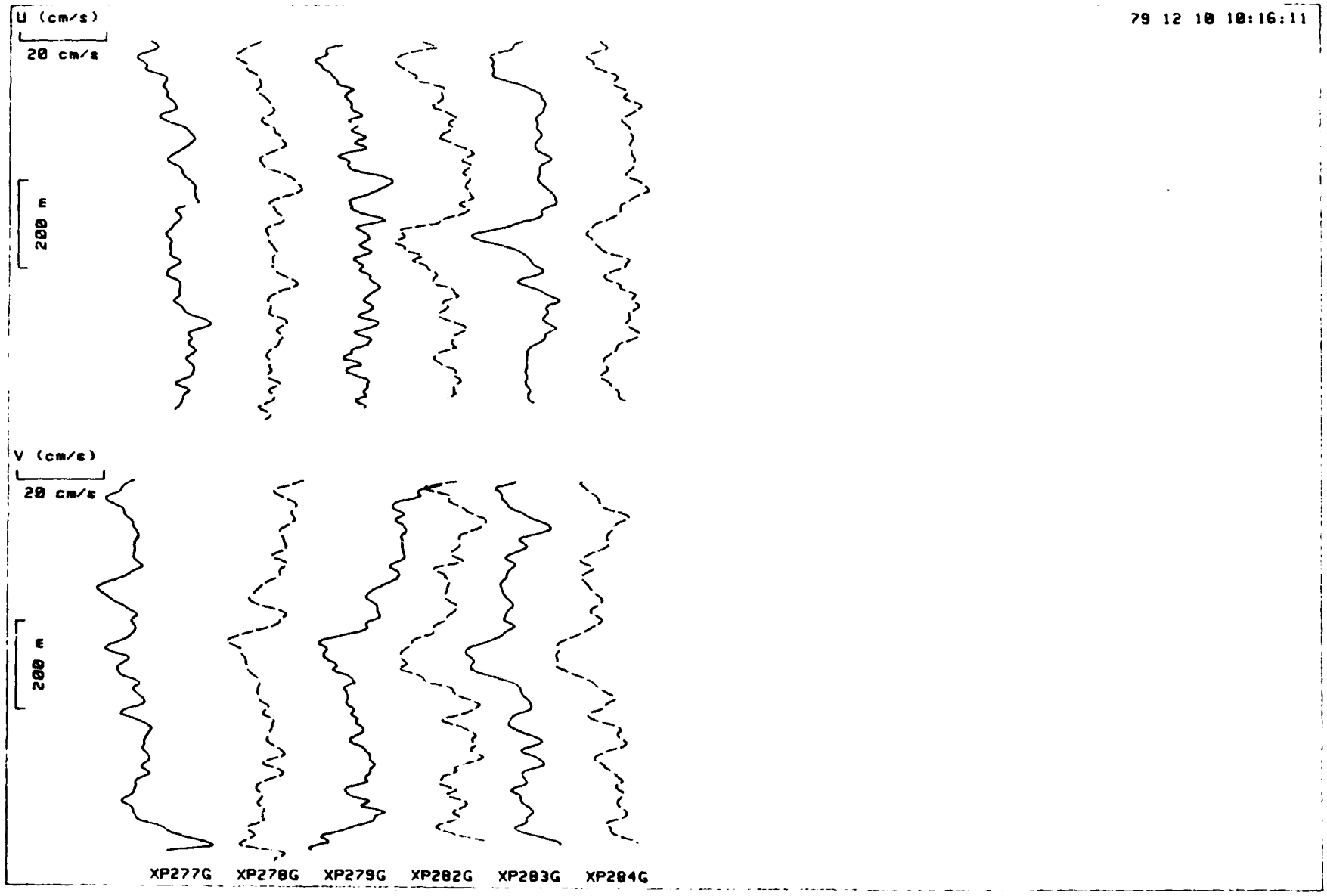

Figure 7.5d. East (U) and North (V) velocity profiles for first leg of second L-shaped pattern of first series.

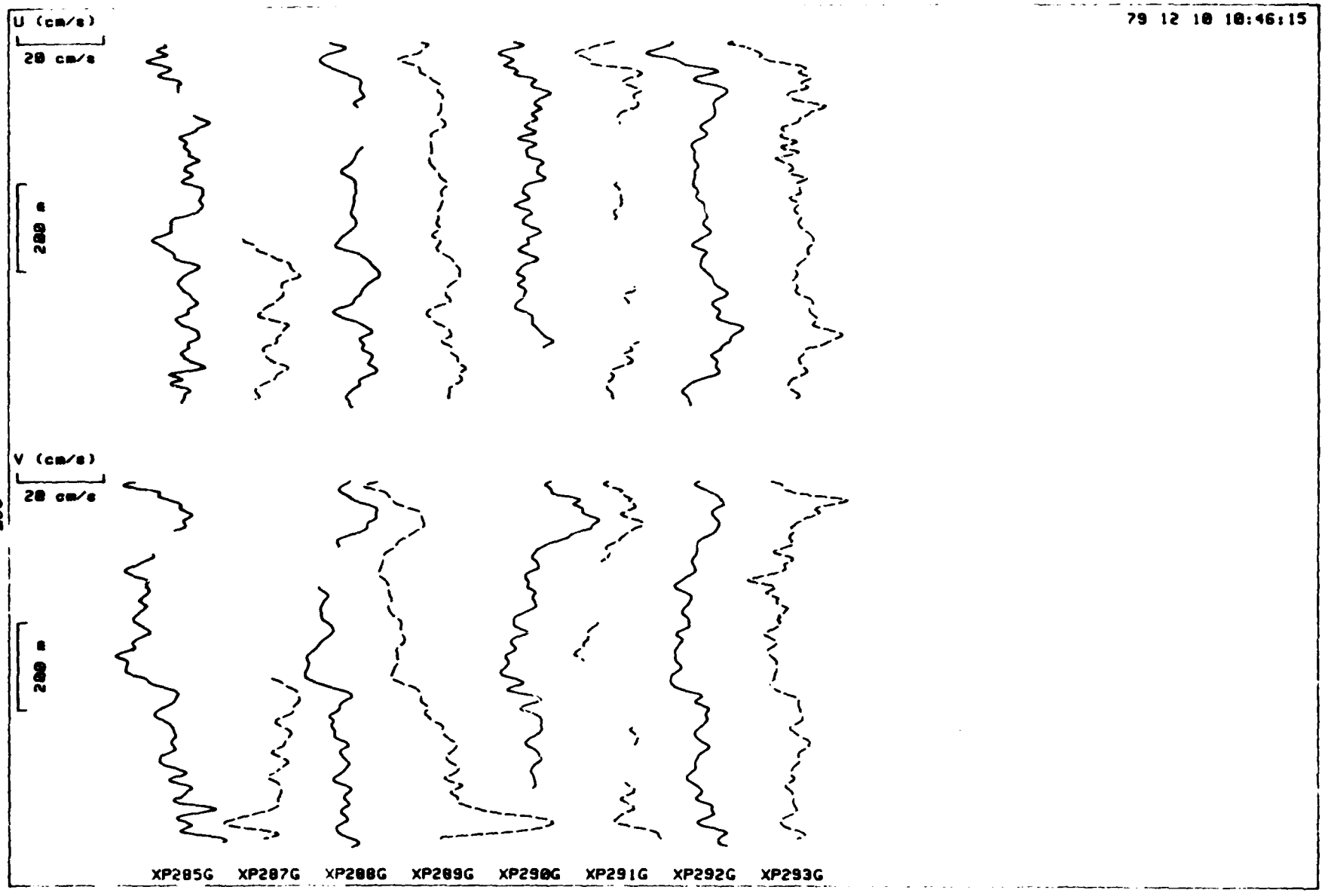

Figure 7.5e. East (U) and North (V) velocity profiles for second leg of second L-shaped pattern of first series.

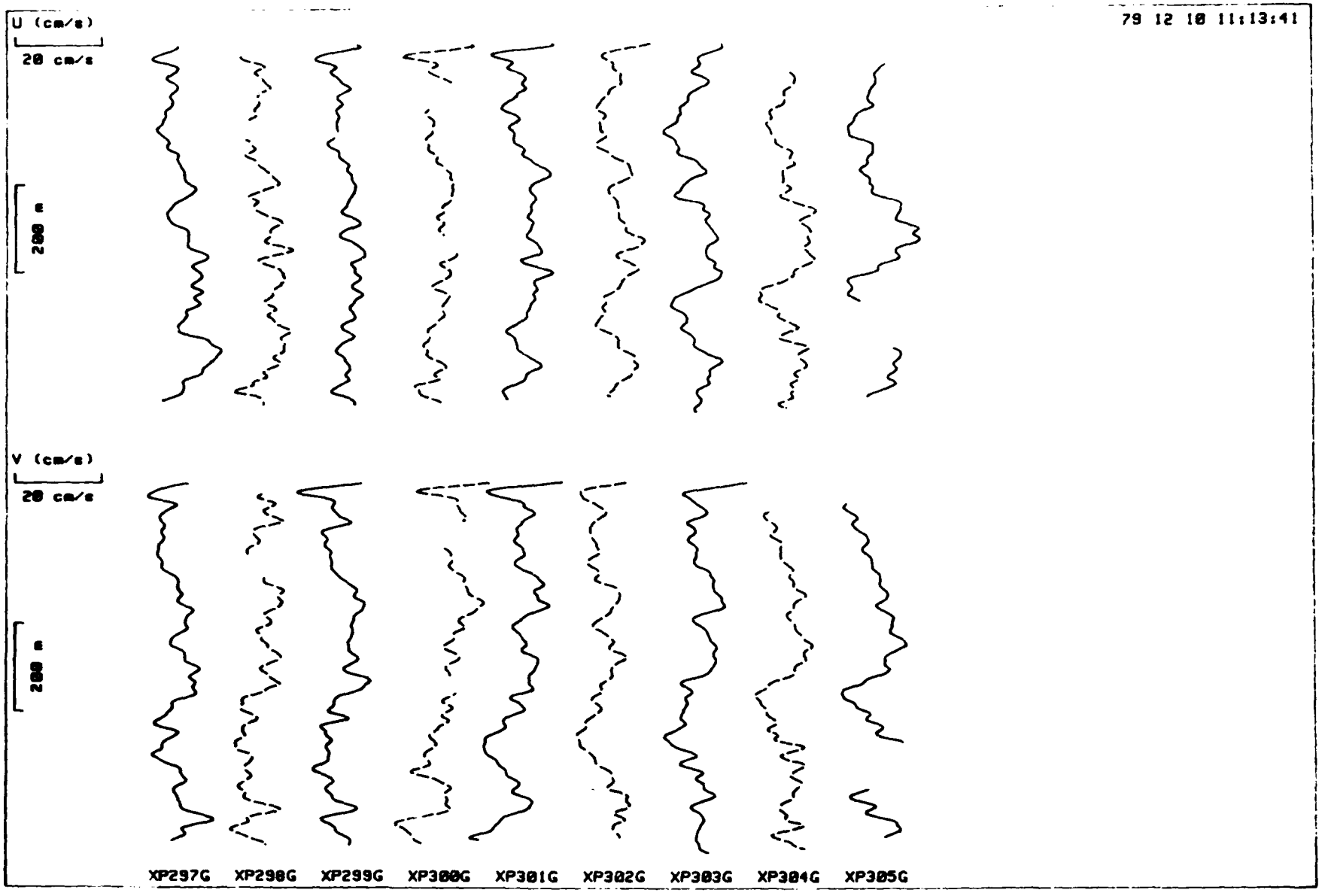

Figure 7.5f. East (U) and North (V) velocity profiles for first leg of third L-shaped pattern of first series.

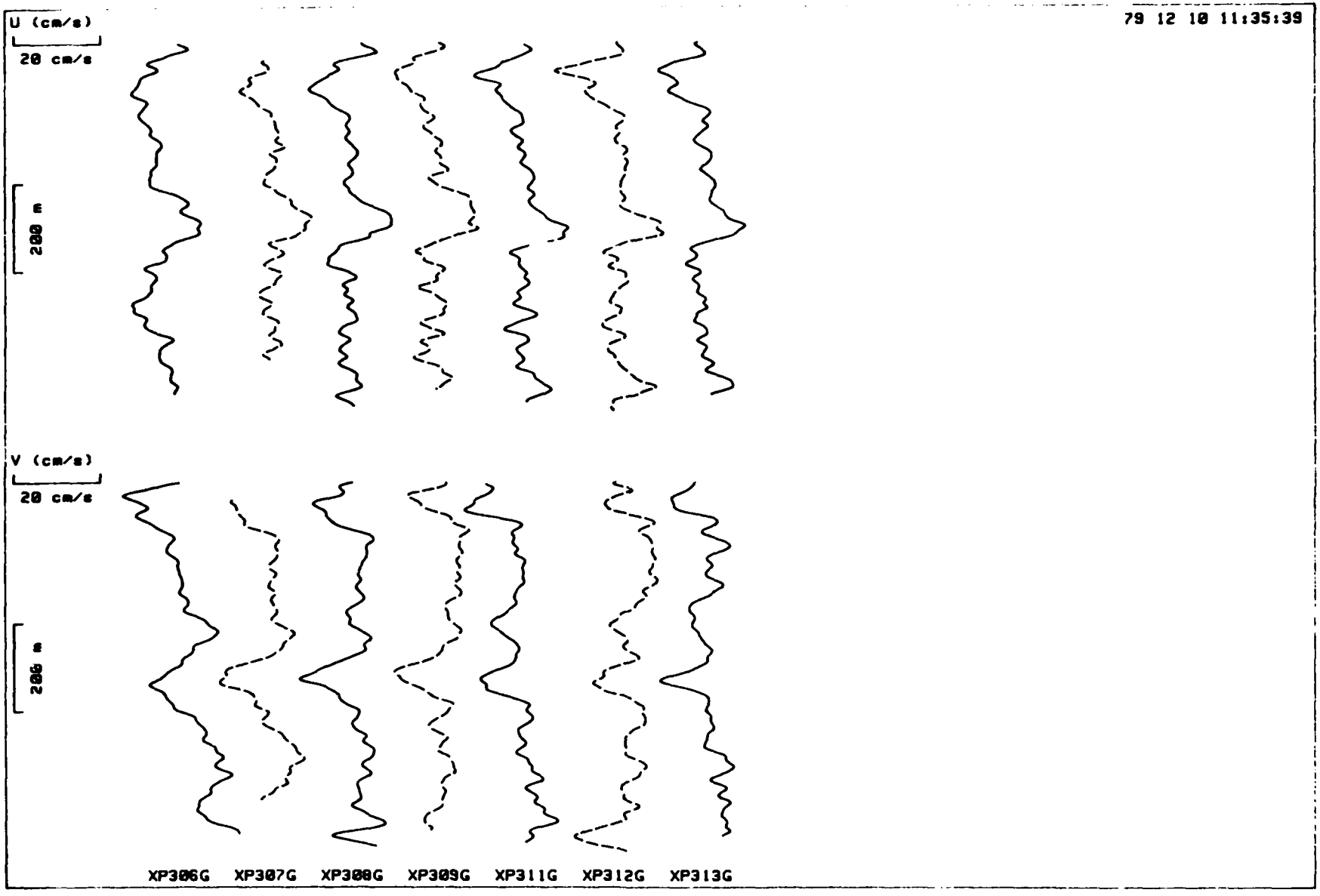

Figure 7.5g. East (U) and North (V) velocity profiles for second leg of third L-shaped pattern of first series. Profiles 314 and 316 belong to this series but are presented in Figure 7.5h.

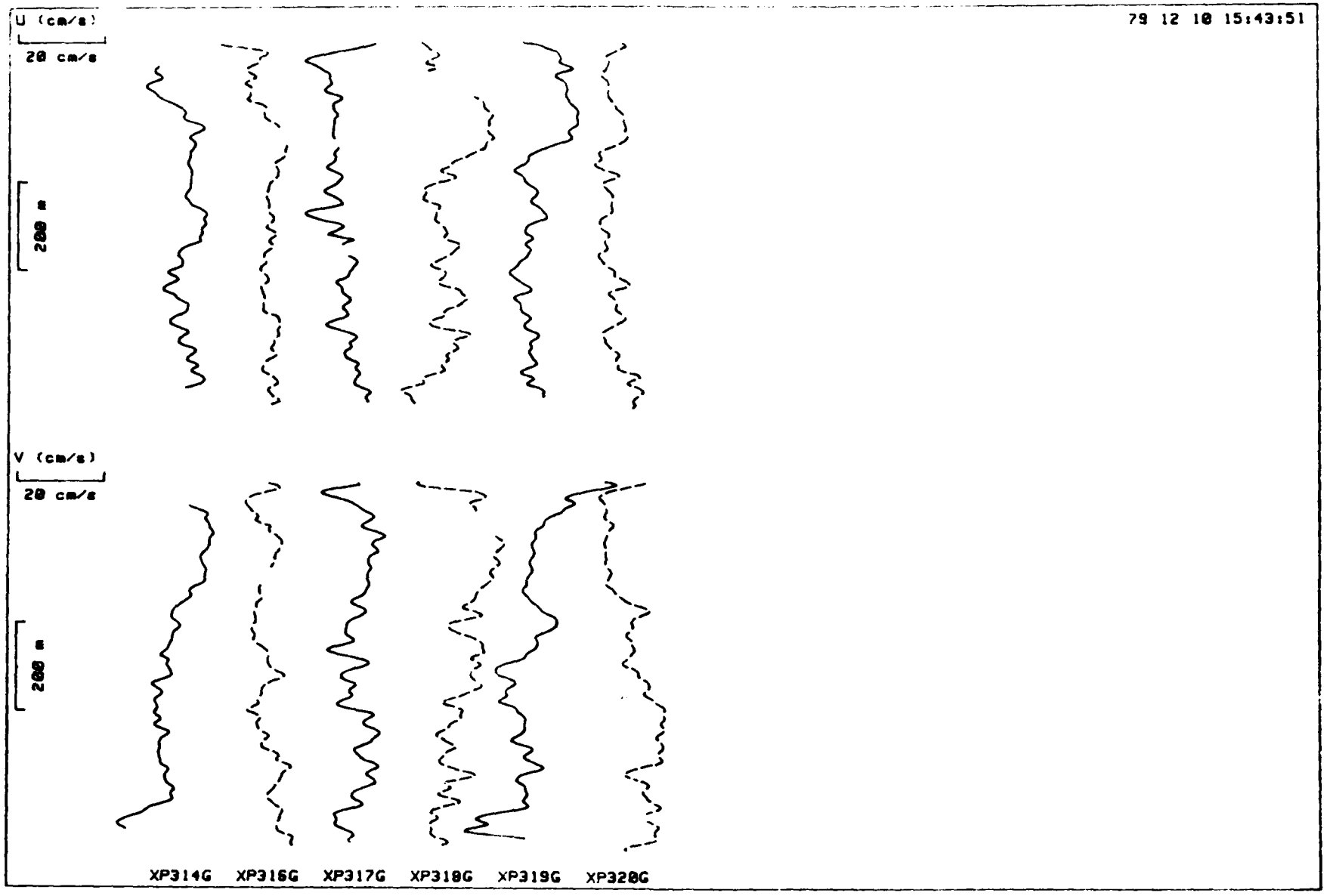

Figure 7.5h. East (U) and North (V) velocity profiles taken at various times and places between the the two series, except for drops 314 and 316 which belong with the leg shown in Figure 7.5g.

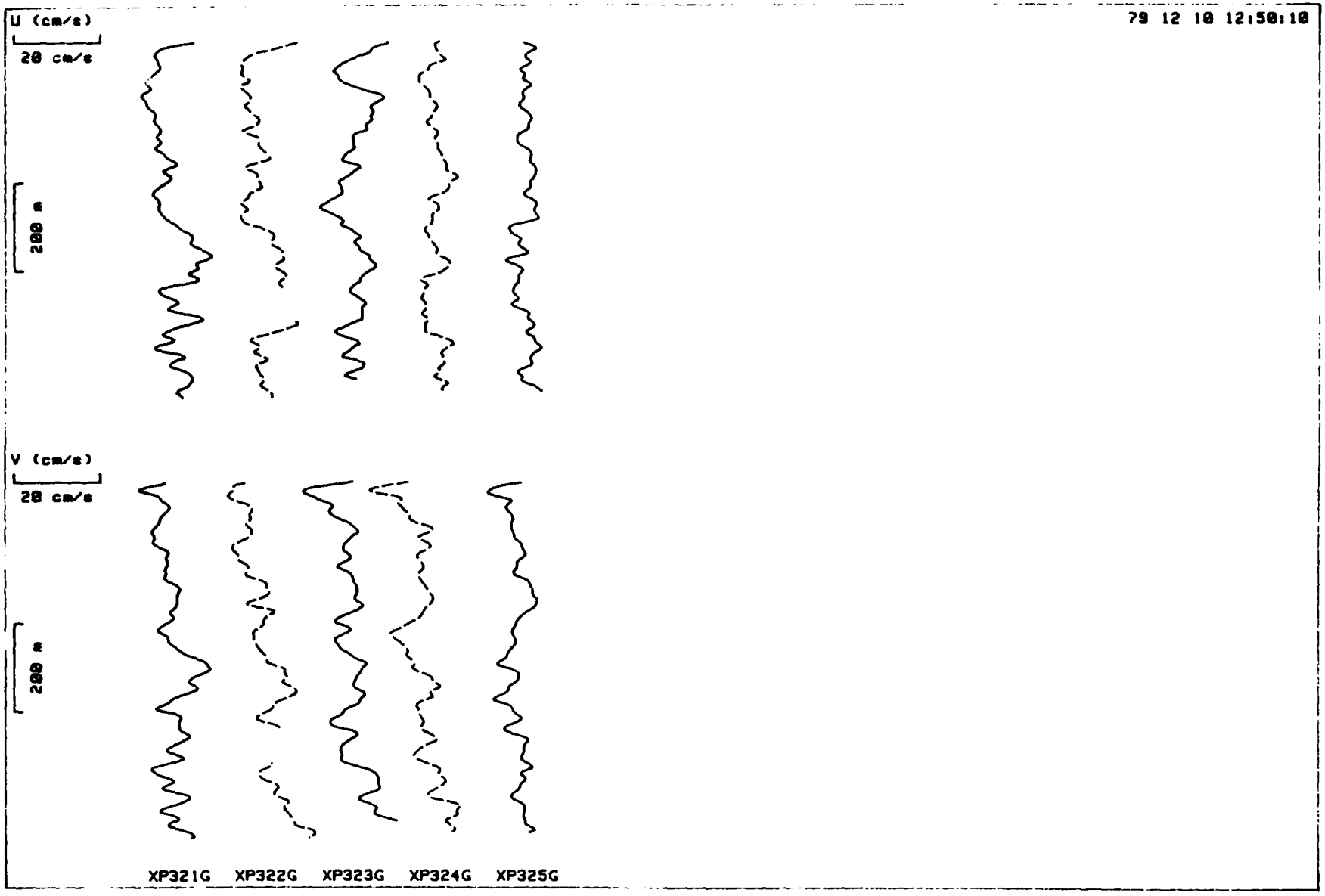

Figure 7.5i. East (U) and North (V) velocity profiles for first leg of first L-shaped pattern of second series.

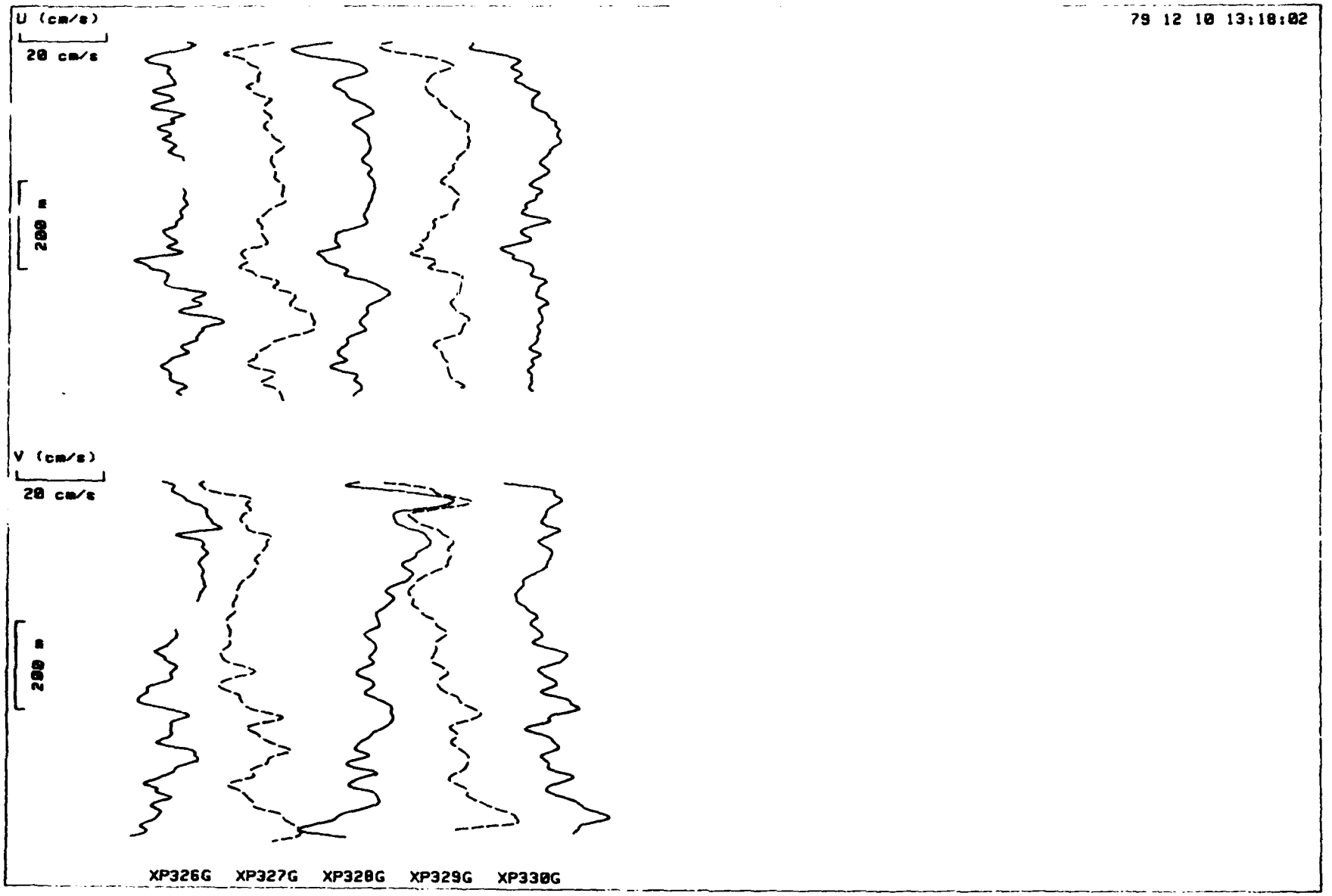

Figure 7.5j. East (U) and North (V) velocity profiles for second leg of first L-shaped pattern of second series.

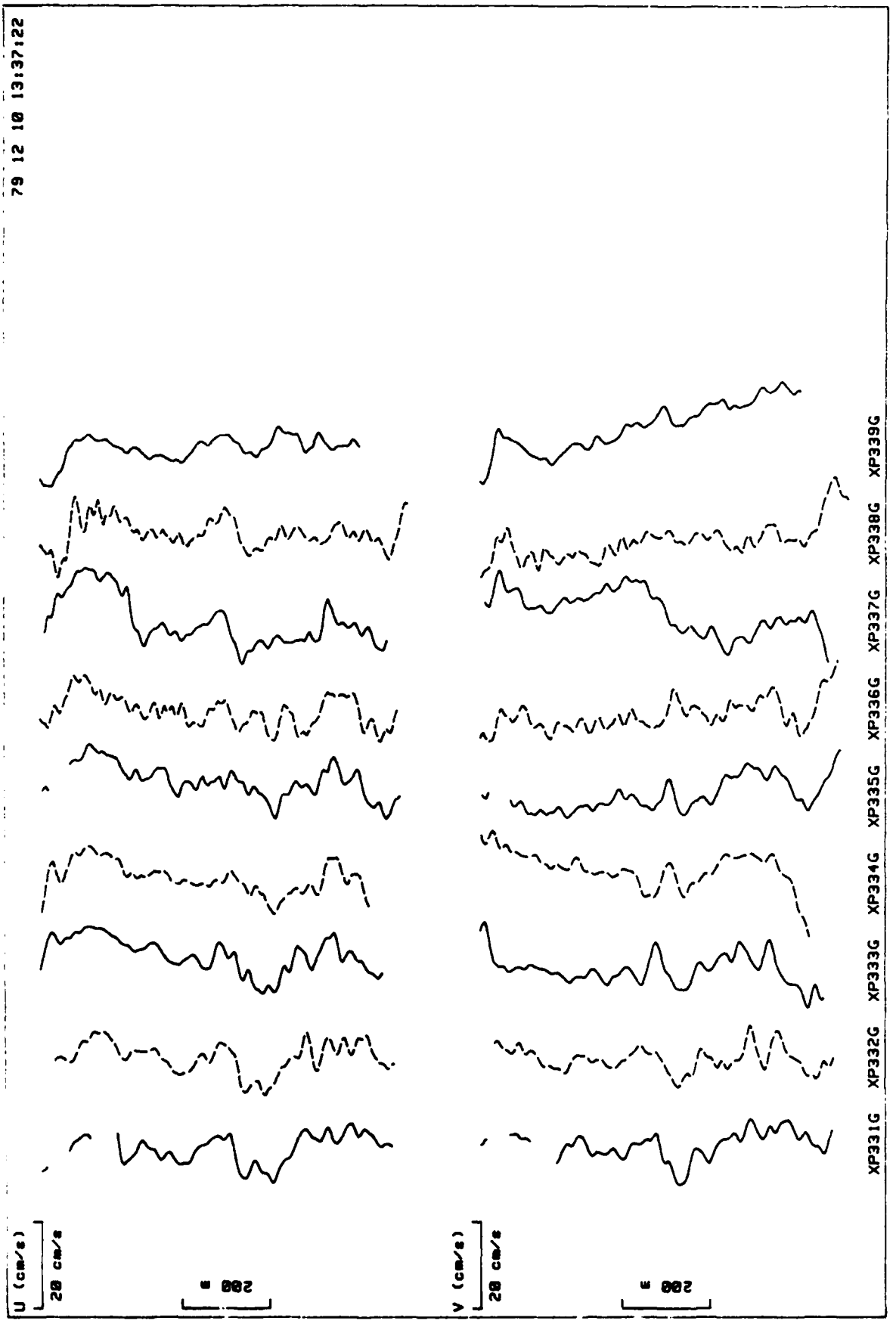

Figure 7.5k. East (U) and North (V) velocity profiles for first leg of second L-shaped pattern of second series.

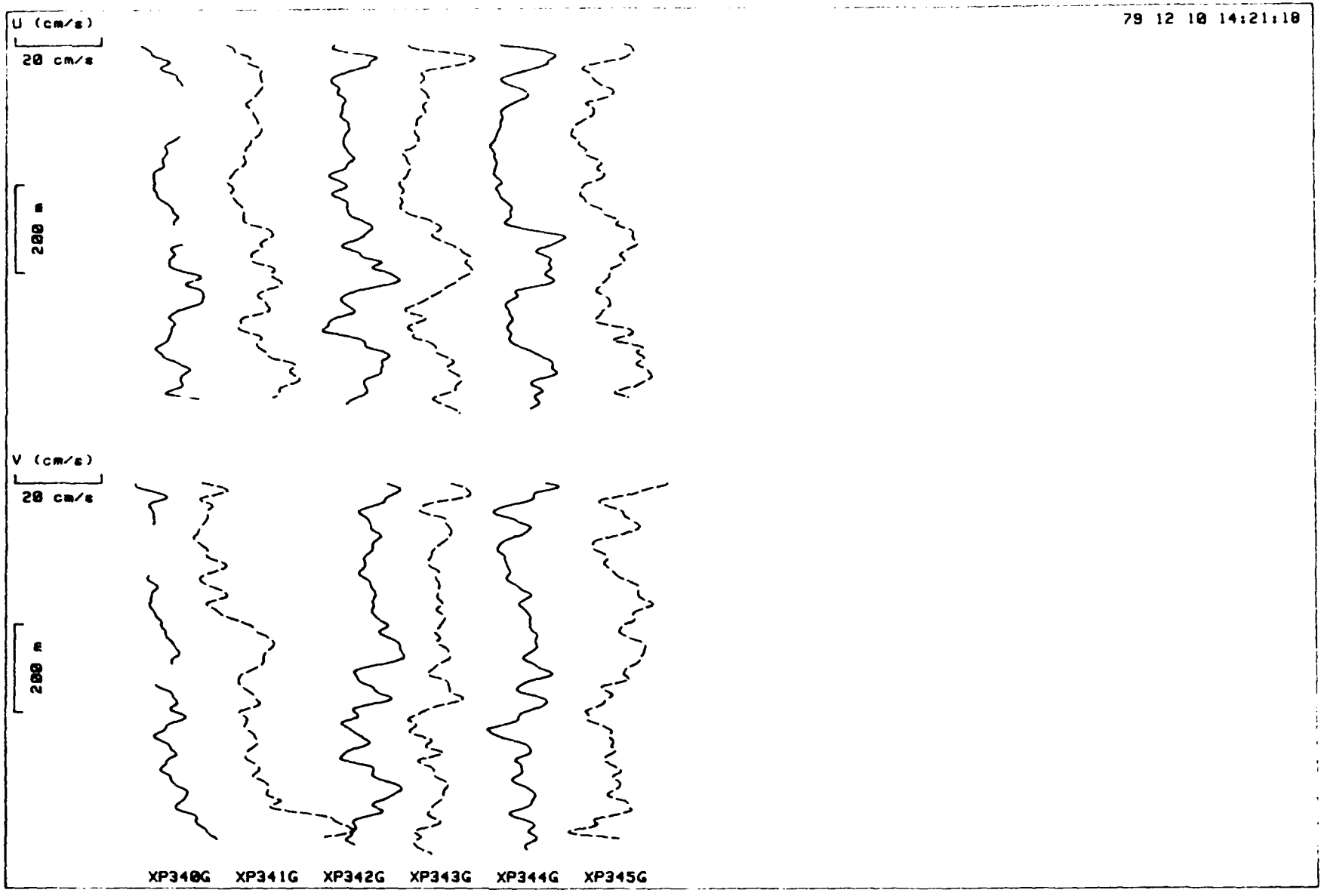

Figure 7.51. East (U) and North (V) velocity profiles for second leg of second L-shaped pattern of second series.

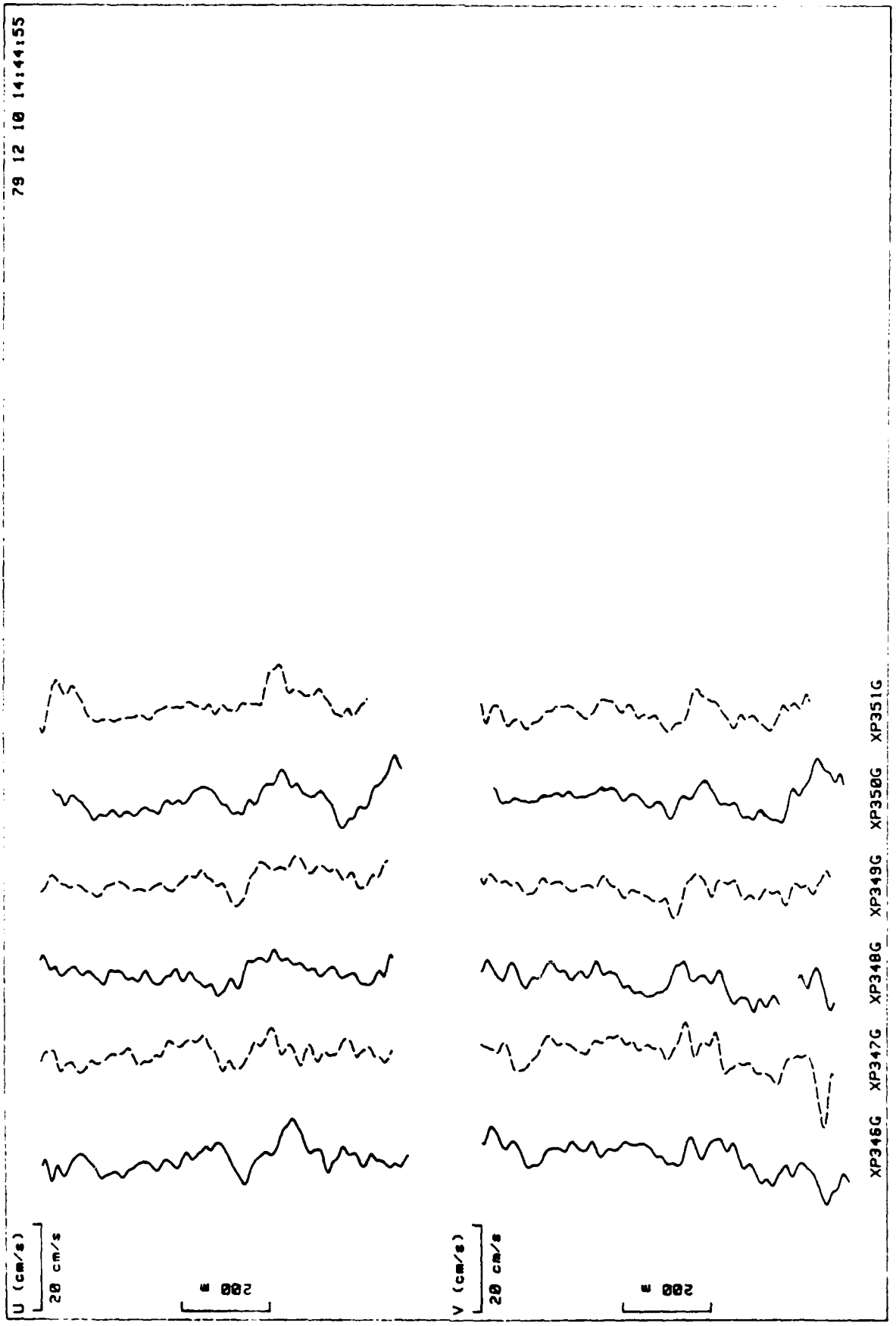

Figure 7.5m. East (U) and North (V) velocity profiles for first leg of third L-shaped pattern of second series.

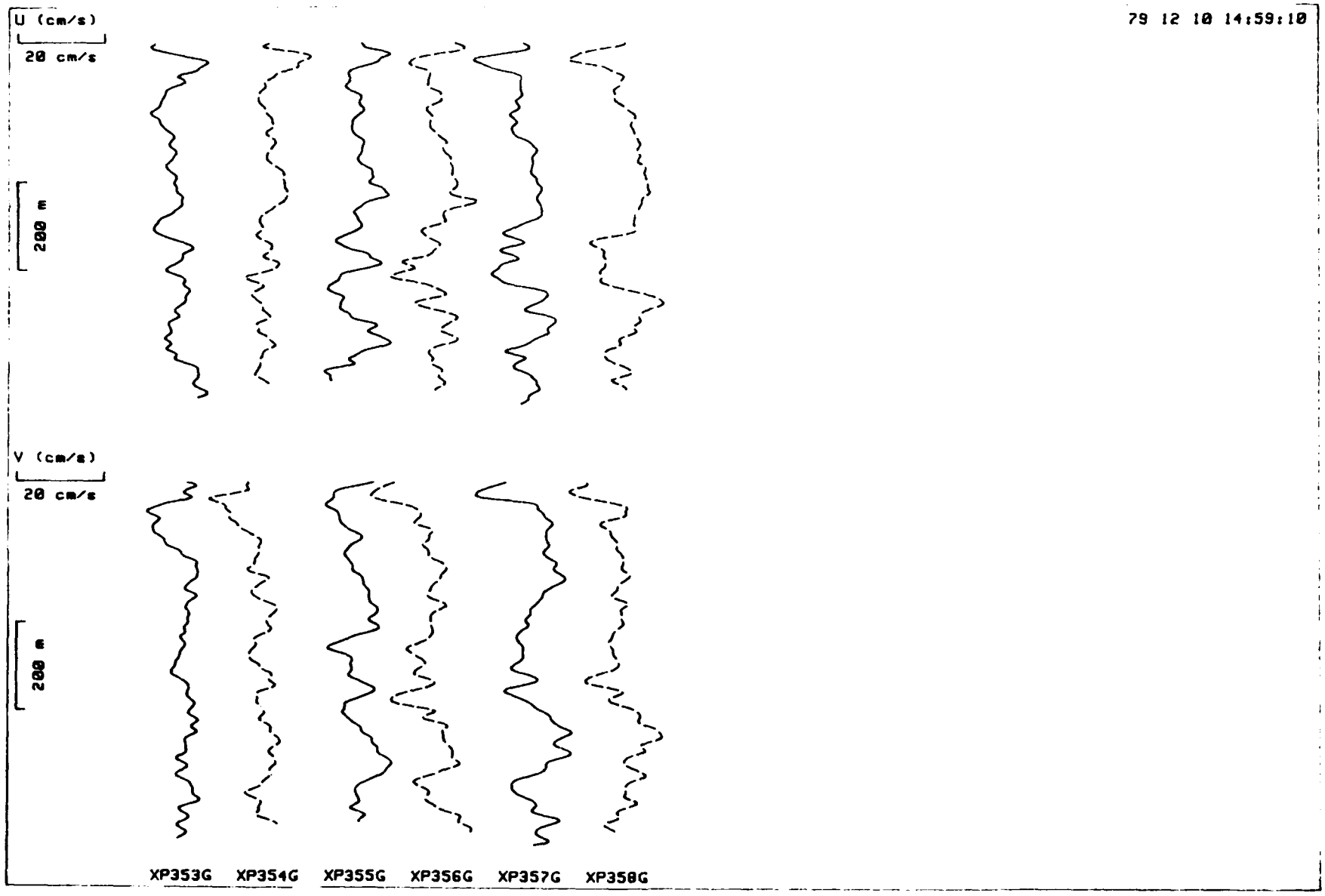

Figure 7.5n. East (U) and North (V) velocity profiles for second leg of third L-shaped pattern of second series.

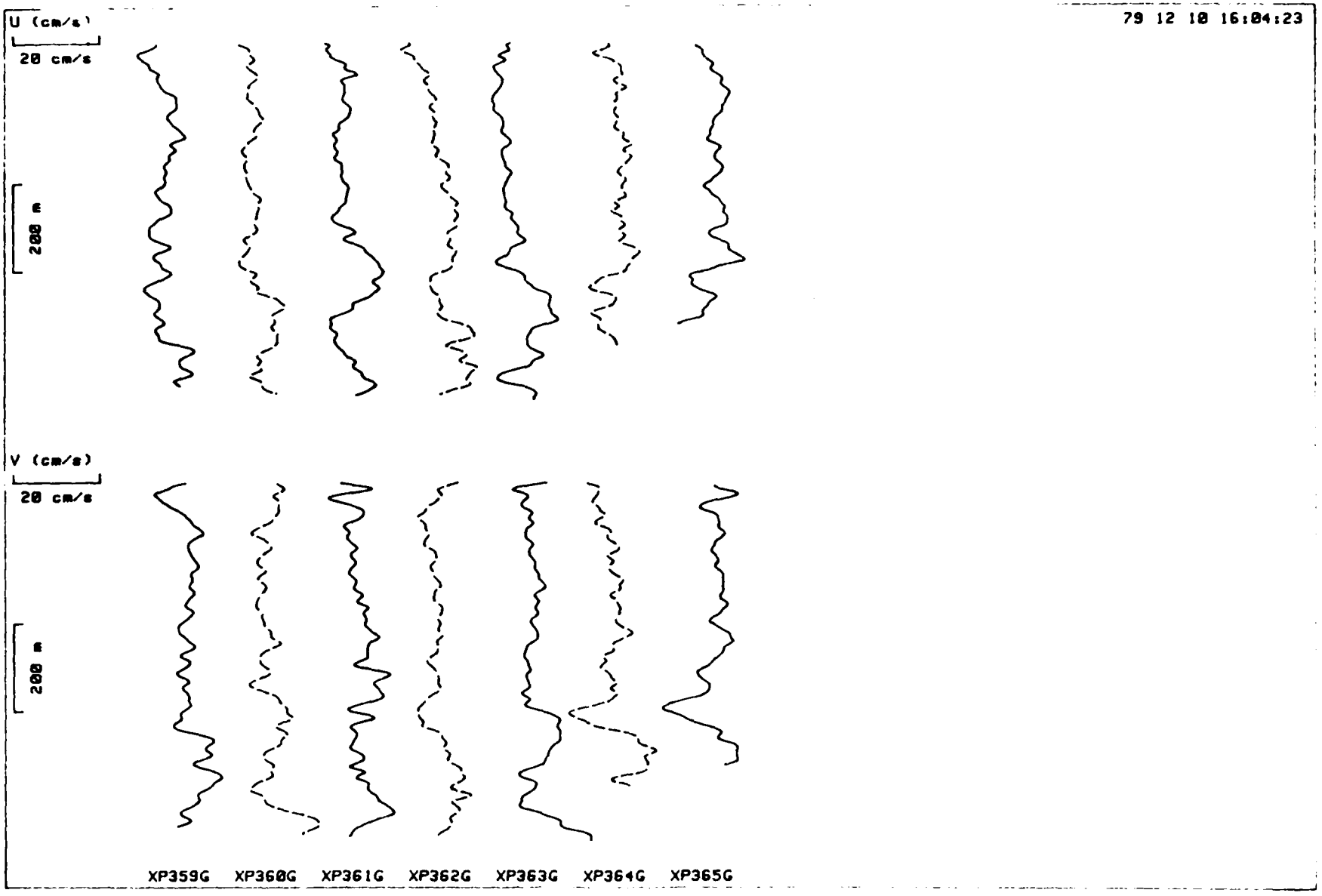

Figure 7.5o. East (U) and North (V) velocity profiles taken after the completion of second series including the time-series drops, 360 -363.

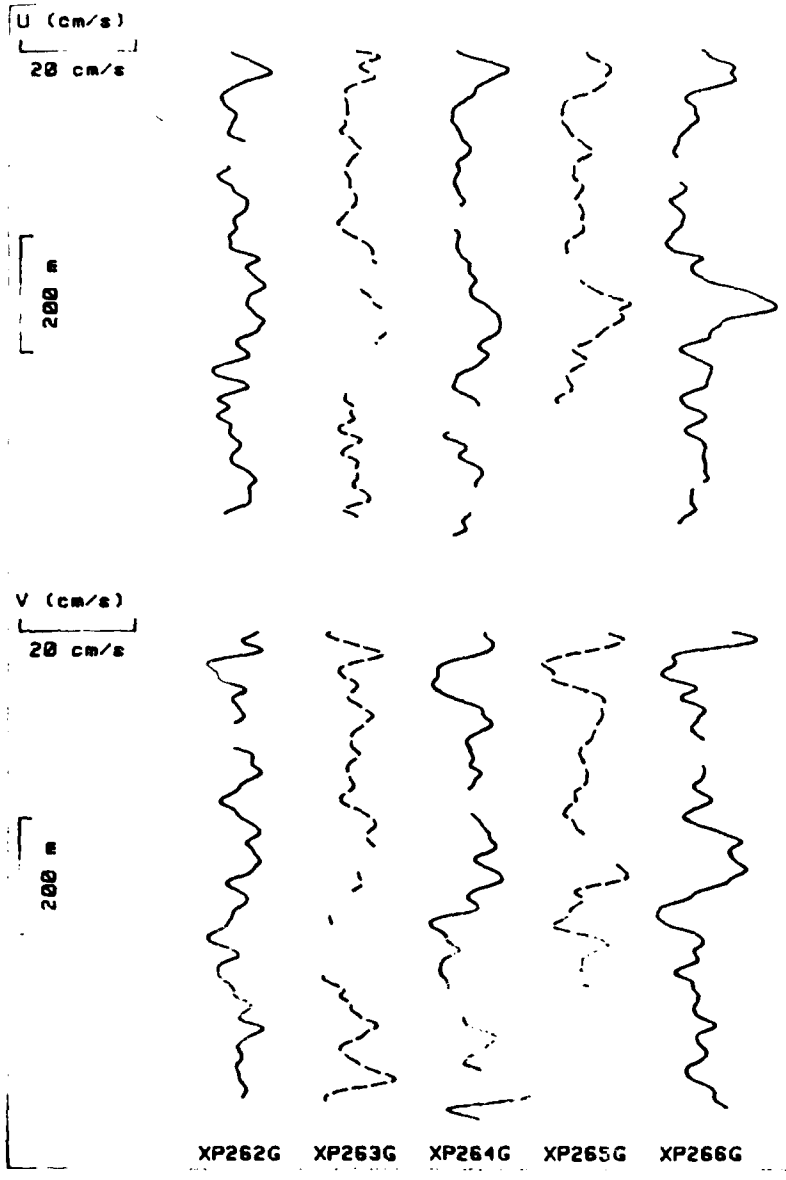

79 12 20 13:27:17
ROTATED TO 19:50

Figure 7.6a. East (U) and North (V) components of residue and rotated profiles for first leg of first L-shaped pattern of first series.

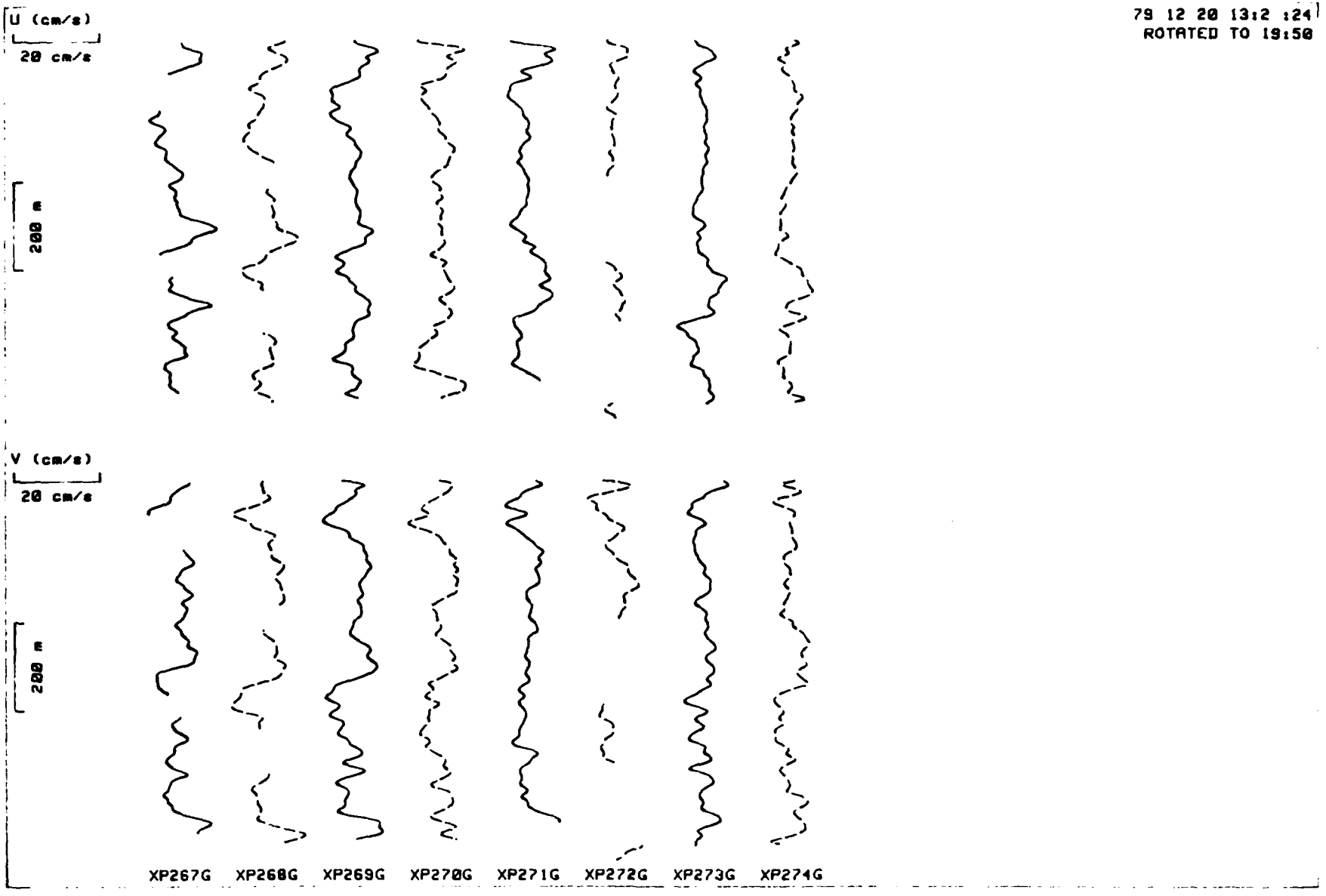

Figure 7.6b. East (U) and North (V) components of residue and rotated profiles for second leg of first L-shaped pattern of first series.

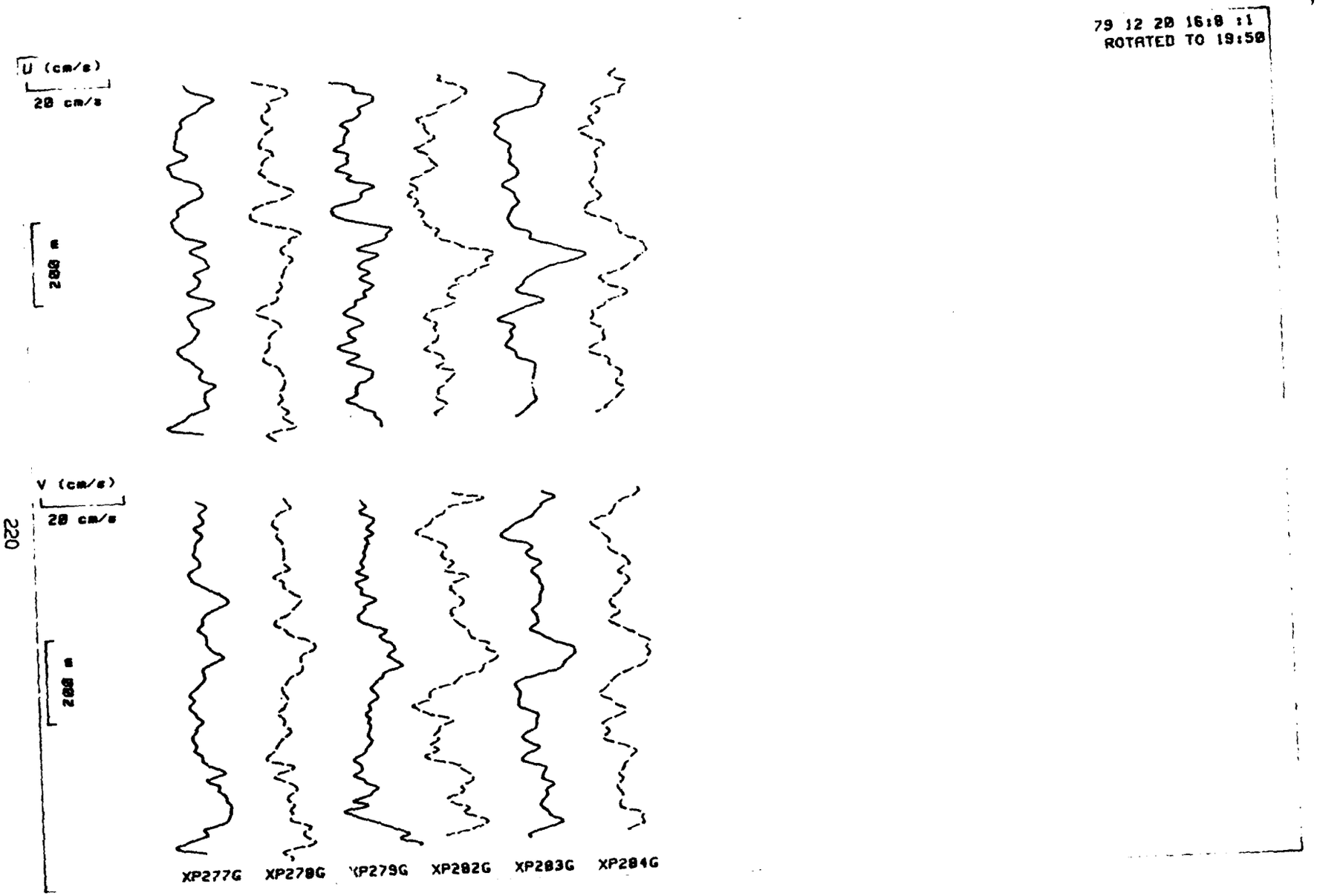

Figure 7.6c. East (U) and North (V) components of residue and rotated profiles for first leg of second L-shaped pattern of first series.

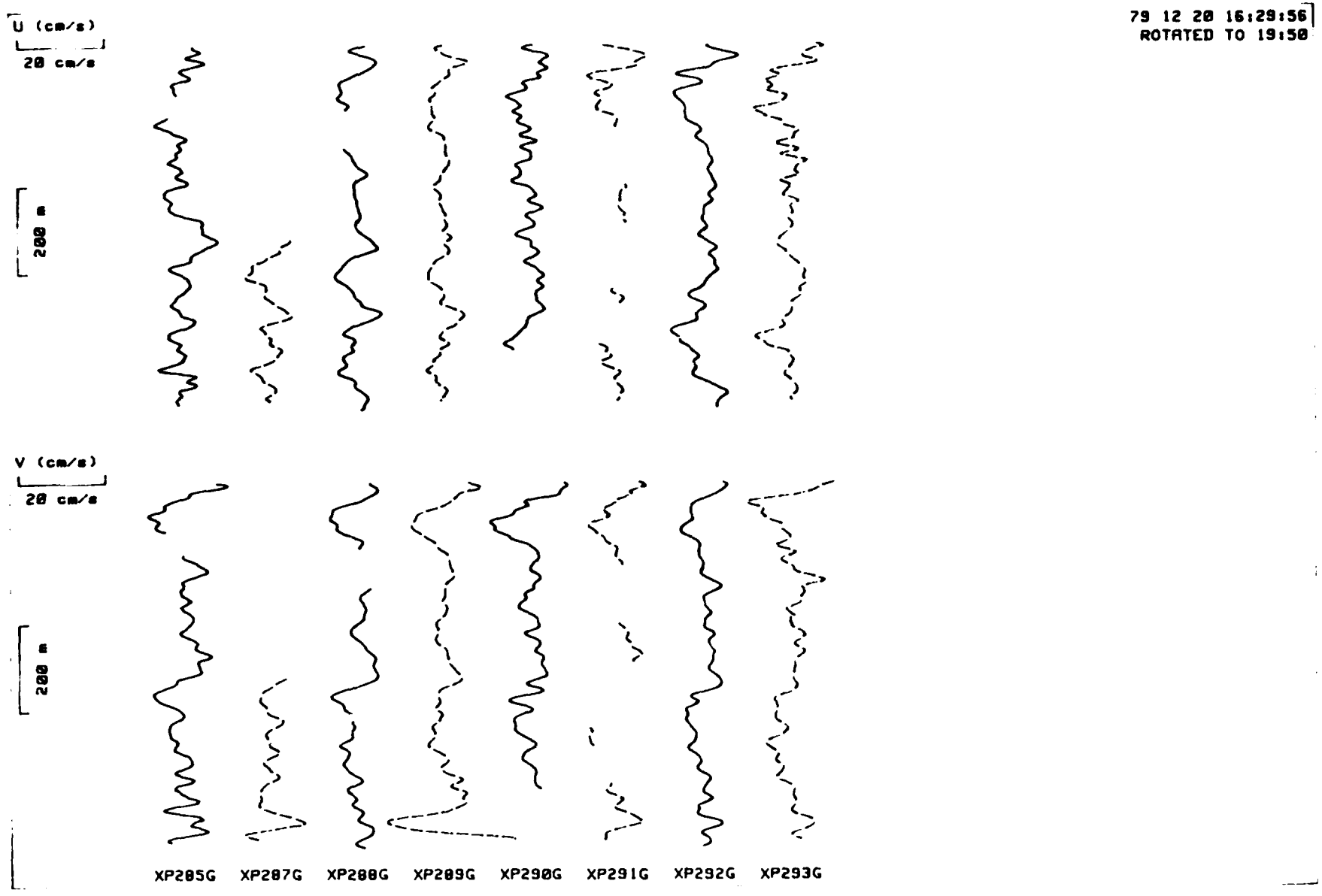

Figure 7.6d. East (U) and North (V) components of residue and rotated profiles for second leg of second L-shaped pattern of first series.

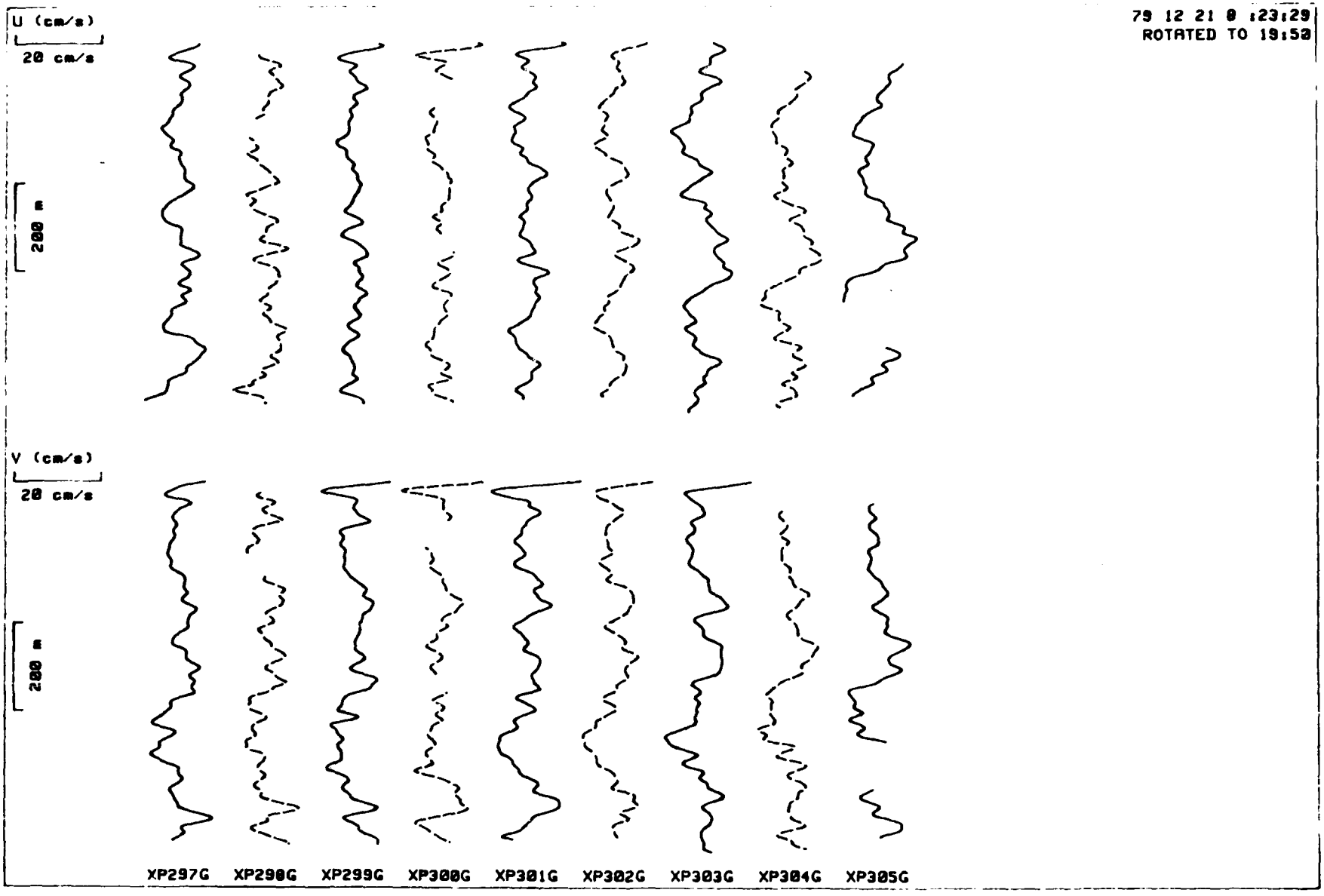

Figure 7.6e. East (U) and North (V) components of residue and rotated profiles for first leg of third L-shaped pattern of first series.

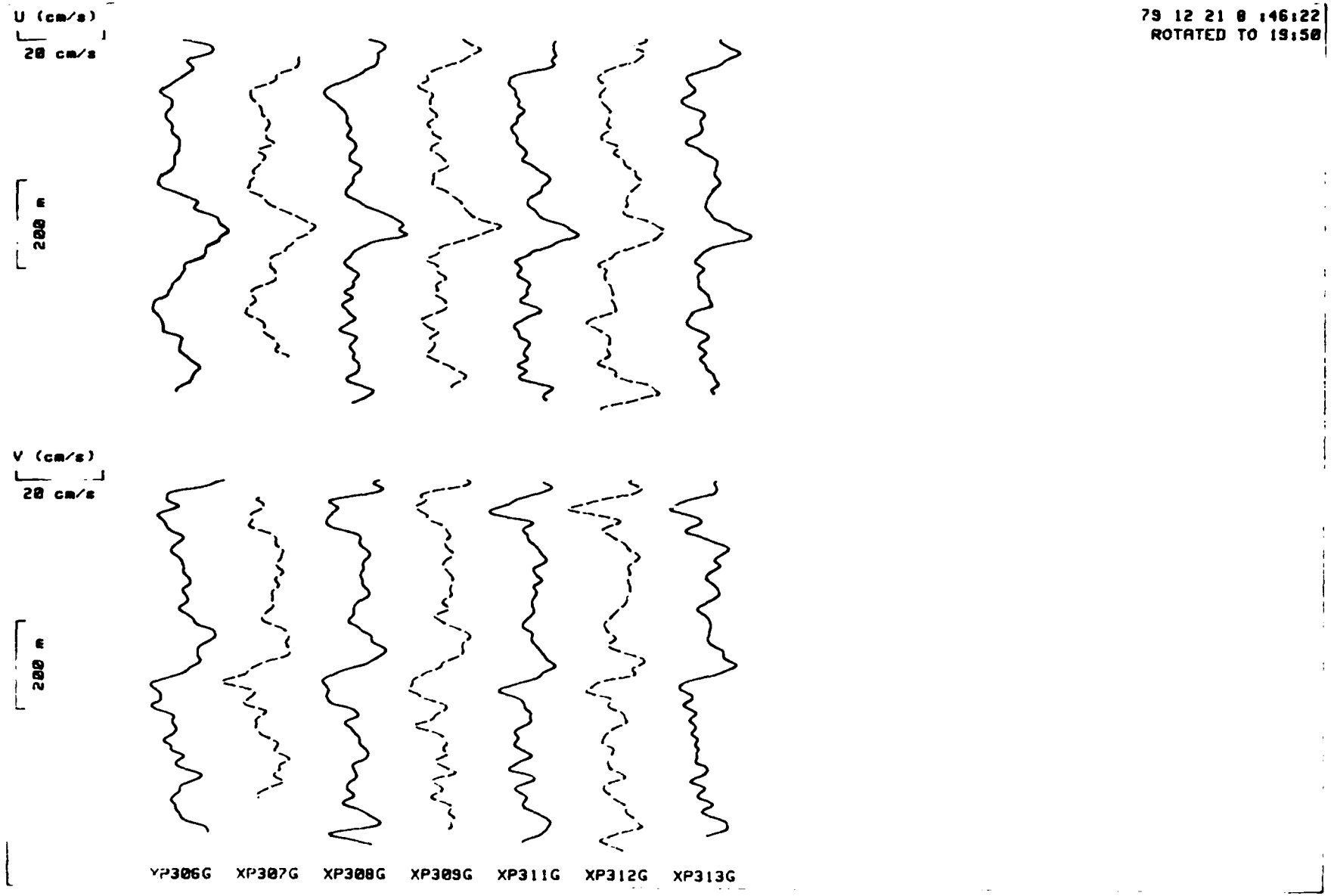

Figure 7.6f. East (U) and North (V) components of residue and rotated profiles for second leg of third L-shaped pattern of first series.

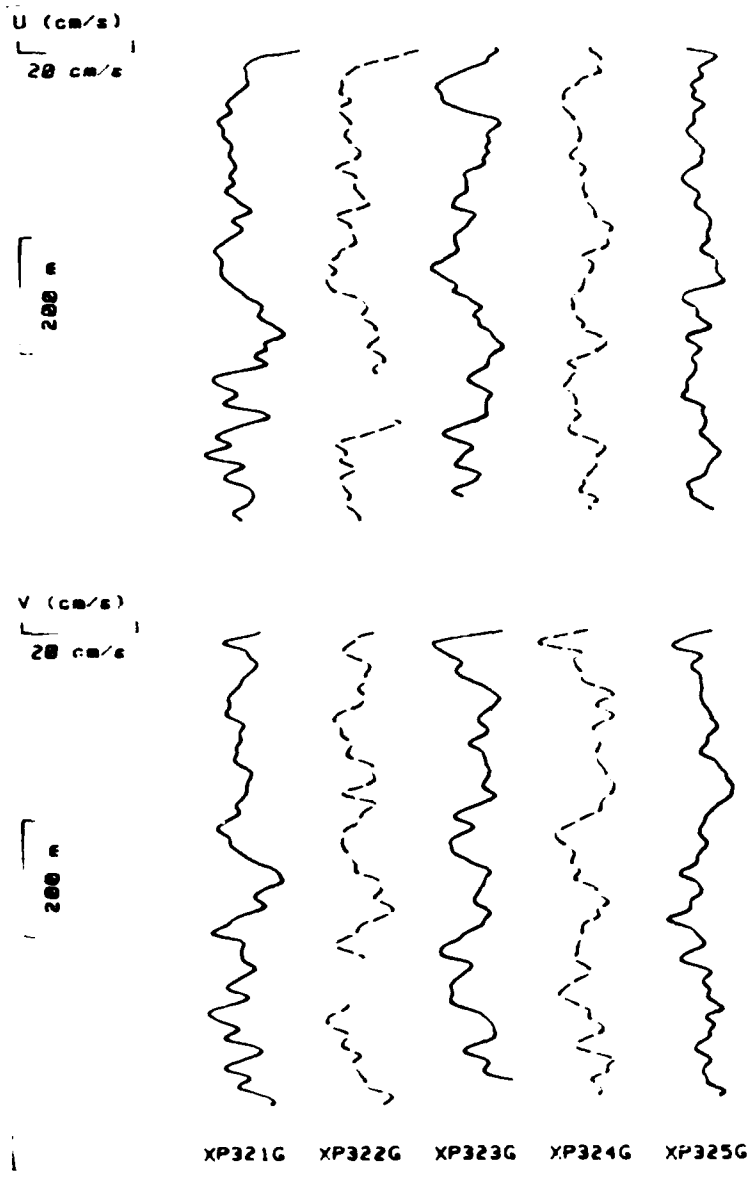

Figure 7.6g. East (U) and North (V) components of residue and rotated profiles for first leg of first L-shaped pattern of second series.

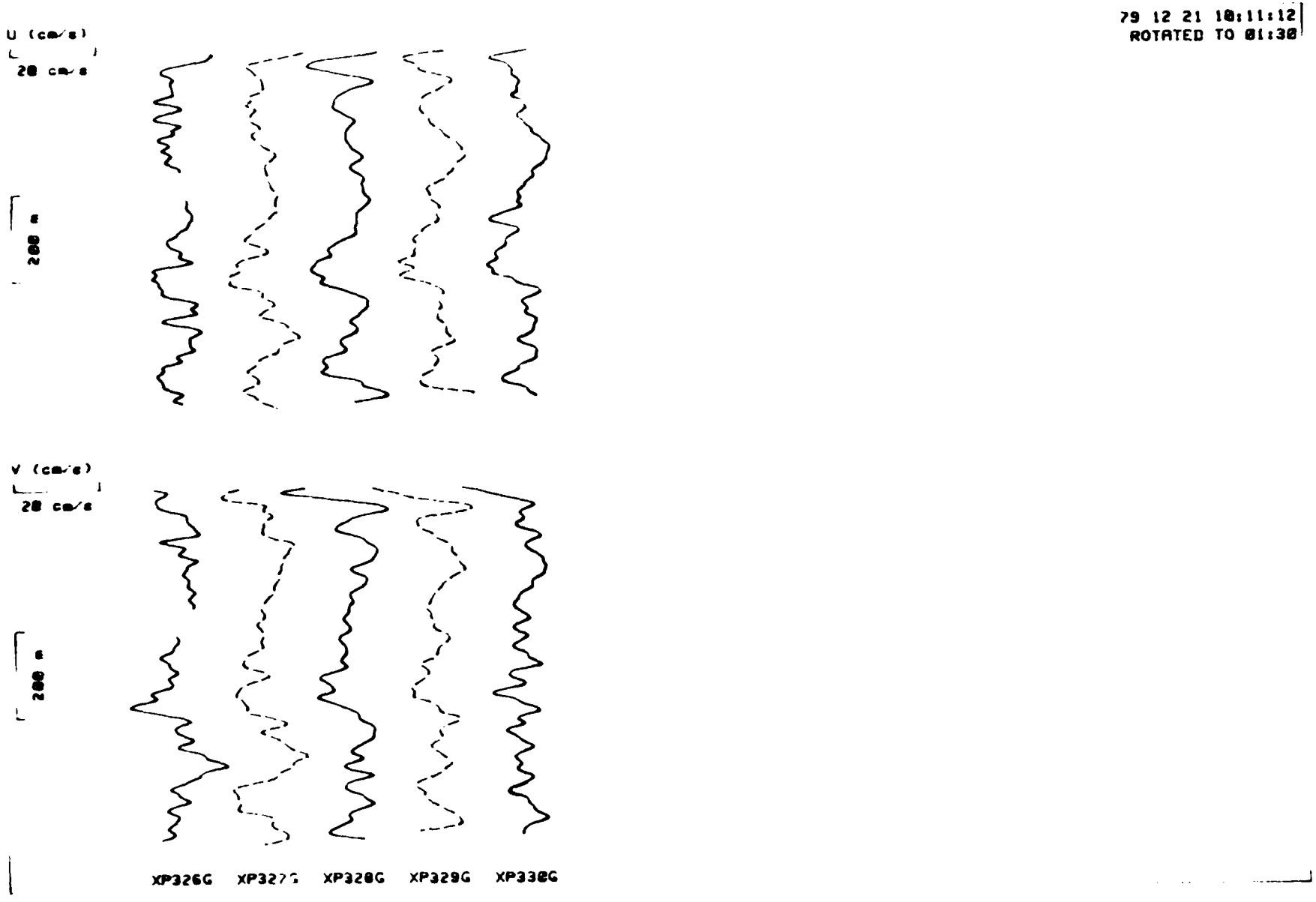

Figure 7.6h. East (U) and North (V) components of residue and rotated profiles for second leg of first L-shaped pattern of second series.

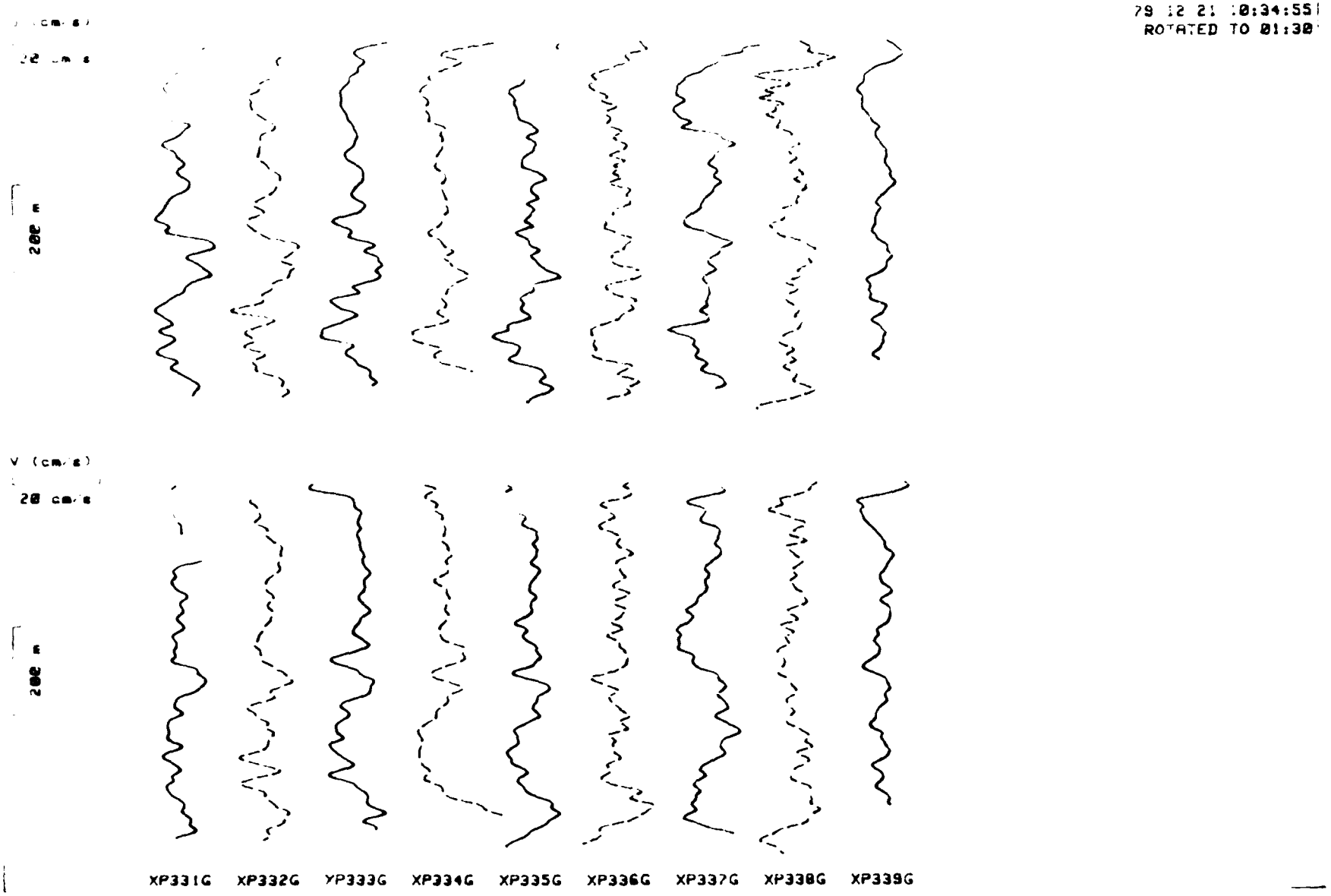

Figure 7.61. East (U) and North (V) components of residue and rotated profiles for first leg of second L-shaped pattern of second series.

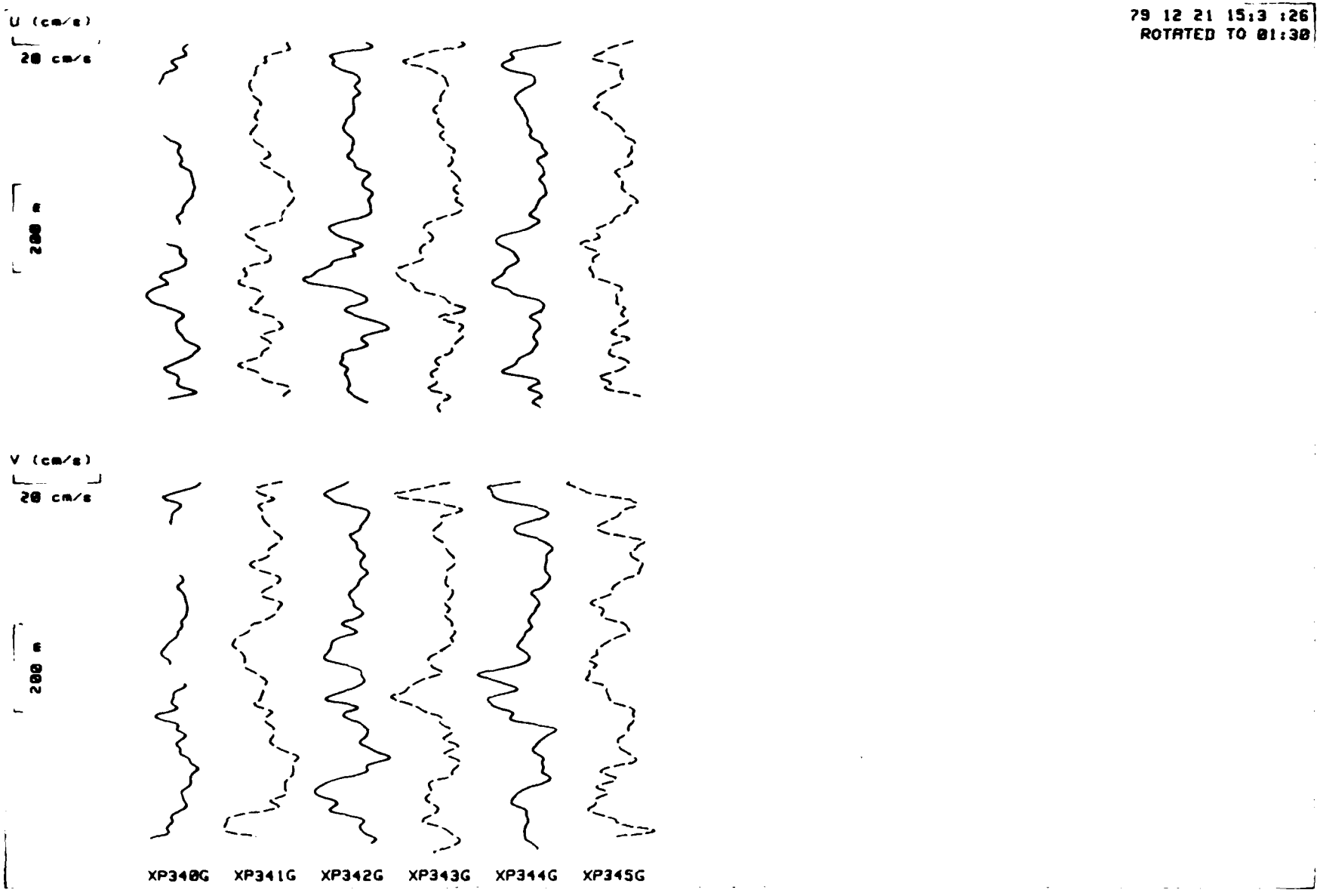

Figure 7.6j. East (U) and North (V) components of residue and rotated profiles for second leg of second L-shaped pattern of second series.

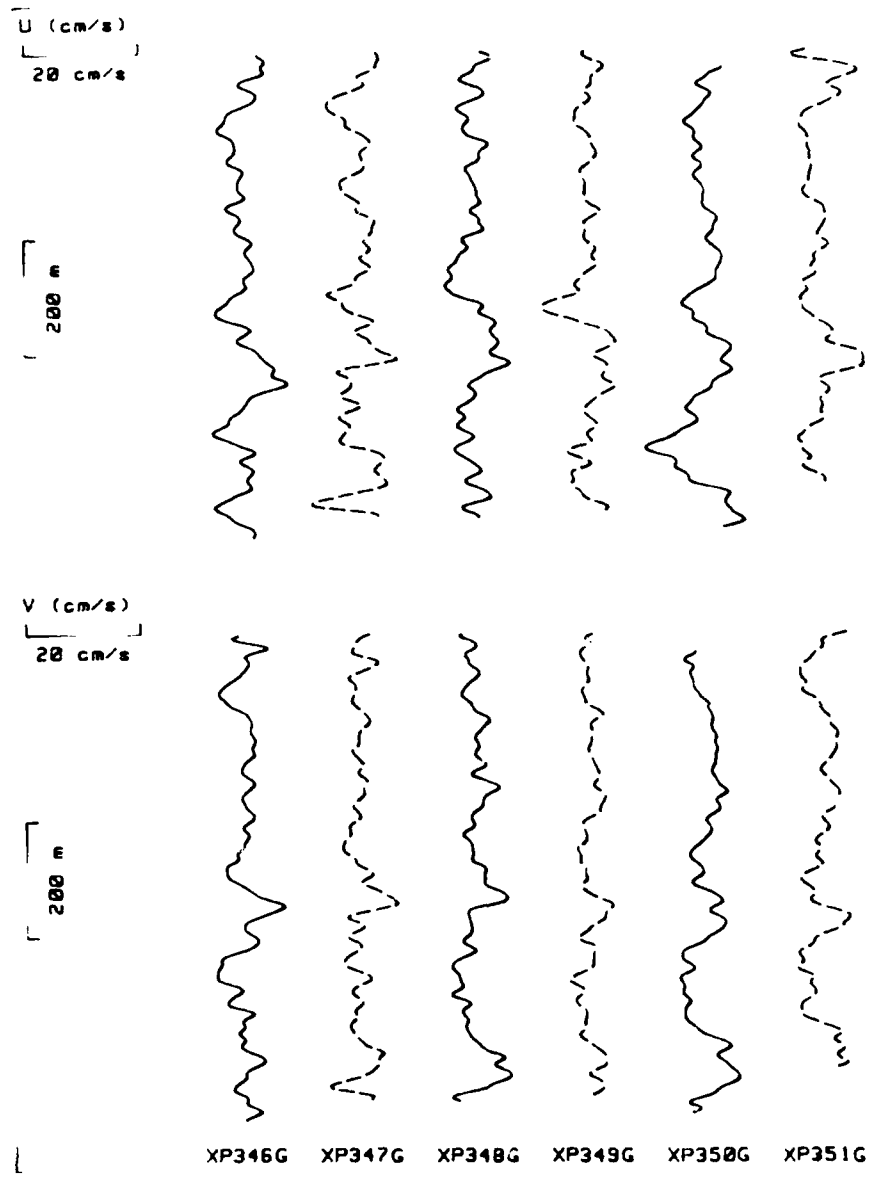

Figure 7.6k. East (U) and North (V) components of residue and rotated profiles for first leg of third L-shaped pattern of second series.

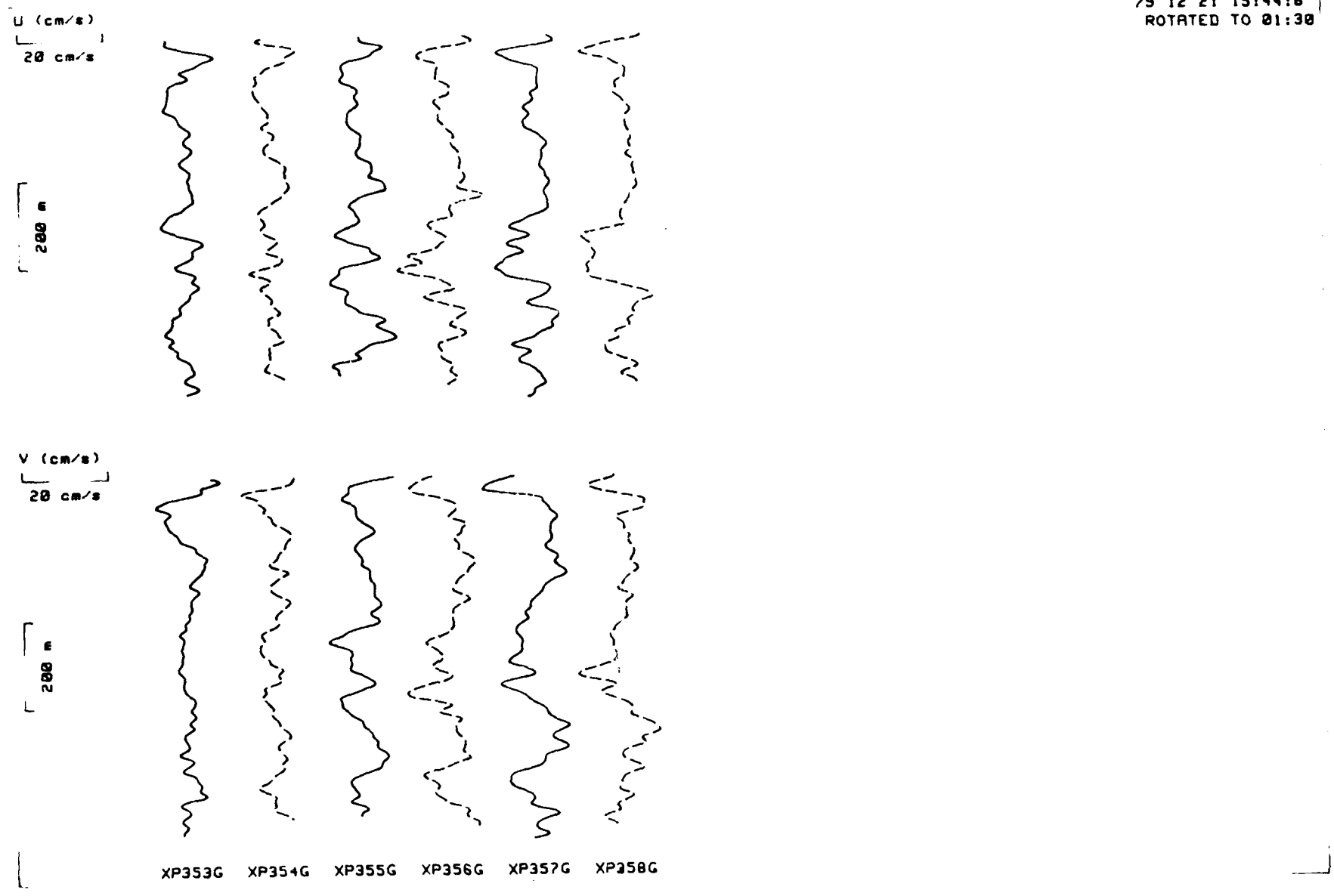

Figure 7.61. East (U) and North (V) components of residue and rotated profiles for second leg of third L-shaped pattern of second series.

Section 8.0

REMOTELY SENSED DATA

by Peter Smith

8.0 REMOTELY SENSED DATA

8.1 INTRODUCTION

The objectives of the Remote Sensing section of this program were threefold. First, data obtained during a pre-cruise survey flight was to provide a basis for planning the USNS KANE's operating area. Second, data collected by aircraft during the KANE's operations were to provide a mesoscale background against which the "L" pattern data collection was to be accomplished. And third, technically advanced remote sensing measurements were to be made of sea surface temperature and roughness, together with surface truth.

To accomplish the first objective, the NAVOCEANO BIRDSEYE aircraft was flown over a three degree square area (71°W-74°W and 29°N-32°N) on 24 August 1979 obtaining AXBT and PRT-5 data. This data was reduced and presented at a precruise planning meeting on 29 August 1979 at NORDA.

The second and third objectives were met during a data collection flight of NAVOCEANO SEASCAN aircraft on 6 September 1979. A planned second flight on 10 or 11 September 1979 was cancelled due to aircraft malfunctions.

The collection of instrumentation employed and the resulting data products are listed in Table 8.1 below.

Table 8.1

INSTRUMENT	LOCATION	TYPE DATA
PRT-5	Shipboard	Thermal IR Irradiance
Waverider	Shipboard	Sea Surface Elevations
PRT-5	Aircraft	Thermal IR Sea Irradiance
PRT-4	Aircraft	Thermal IR Sky Irradiance
RS-310 Scanner	Aircraft	High Resolution IR
KS-87 Camera	Aircraft	Glint Imagery
AXBT	Aircraft	Water Temperature Profile
Video Tape	Aircraft	Visible Imagery & Time Base
TIROS-N VHRR	Satellite	Thermal IR Imagery

A laser sea surface profiler was installed on the aircraft, but failed to function during the exercise.

8.2 AXBT DATA

A pre-cruise AXBT survey was flown on 24 August 79, covering a 3° X 3° square. Two data products of this survey, temperature contours at 100 m and depth contours of the 22°C isotherm, are shown in Figures 8-1 and 8-2, respectively. Both figures delineate a density structure which might be associated with a warm core, anticyclonic eddy centered at about 30°30'N, 72°00'W. The AXBT's have a depth capability of only 350 m and, consequently, were not capable of determining whether this feature extended into the permanent thermocline.

On 6 Sept an AXBT survey of the square, 30°00'N-30°40'N by 71°20'W-72°30'W, was conducted. The flight lines are shown in Figure 8-3 and the AXBT drop pattern in Figure 8-4. Out of 61 BT's dropped, 50 functioned properly. The derived temperature contours at 100 m and depth contours of the 22° isotherm are shown in

Figures 8-5 and 8-6, respectively. The feature identified in the pre-cruise survey appears to have moved to the northwest as evidenced by the increased temperatures in that direction. The "L" pattern location is superimposed to show that the data collection did, in fact, take place in a relatively "quiet" area of the ocean.

8.3 AIRCRAFT IR SCANNER DATA

A Texas Instruments Model RS-310B infrared scanning imager was operated continuously during the flight survey over the 1 degree square study area on 6 September. The scanner was bore-sighted in the nadir direction. The instrument scans 45° to each side at a rate of 192 scans/sec. The angular resolution of the detector was 3 milliradians. After filtering and analog-to-digital conversion, the spatial resolution is 6 m and 9 m at the two operating altitudes of 463 m and 762 m, respectively. The spectral bandpass window extended from 8.5 to 13.5 in the thermal infra-red region.

Two recording modes were used. In the first, a scanning LED light source exposed a continuous film strip to produce an analog image, and in the second, the voltage output of the detector circuitry was recorded on analog tape, filtered, and digitized on computer compatible tape. The tape was subsequently read into an imaging system for enhancement. This process effectively increases the available dynamic range from 18 dB available in the film to about a 25 dB range available in the computer. This latter recording mode was implemented specifically for the Ocean Measurements Program.

The two most obvious features imaged were a temperature front to the west of the operating area and a sea surface "scar" left by the KANE during the execution of the first "L" pattern.

The front was first observed while flying line #1 (See Fig. 8.3) on a northerly course at 30°50'N, 71°55'W. The film image recorded at this location is shown in Figure 8.7. The film image shown is a negative, and so warmer temperatures are shown as darker areas. Since clouds are cooler than the sea surface, they leave a white impression on the film. The frontal line at this location runs along a NE-SW line. The simultaneous records from the downward-pointing PRT-5 and the upward-pointing PRT-4 radiation thermometers are shown below the IR image. From the PRT-5 trace the change in temperature across the front is seen to be 0.4°C 0.1°C. Time increases to the left and hence the cooler water is to the west.

What is assumed to be a continuation of this same front was observed during three other flight lines. The observation points together with the observed frontal oreintations are shown in Figure 8.8. The dashed line represents the postulated overall shape of the front. A computer enhanced, digital image showing the front during a portion of flight line #5 is given in Figure 8.9. The figure shows the data strip broken into 4 sections. Time starts in the upper left corner and increases toward the lower right hand corner. The aircraft was traveling toward the west. This image is positive; hence, clouds appear black, and warmer waters light. A distinct frontal feature is imaged at "A" and a less distinct front is seen at "B". The cooler water, again, lies to the west of the front, consistent with other observations along the front. The temperature gradient at this location was observed to be less than 0.2°C across the front. The direction of the frontal temperature gradient is somewhat inconsistent with the increasing temperature trend toward the northwest at depth indicated by the AXBT survey. It should be noted that the AXBT seeding did not detect a front in this region even

though, according to the IR scanner survey, this was the only front manifested at the surface within the 1^{o} square.

The other feature observed during the flight was manmade-a surface signature left by the KANE during the initial leg of the first "L" pattern, a digitally enhanced image of which is shown in Figure 8.10. Cooler water is dark; warmer water is light. The KANE had occupied a CTD station at "A" and had gotten underway to the northwest until it was overflown at "C". The aircraft was at 463 m altitude, hence, the swath width was about 1 km. The signature appears to vary in width, but the average width appears to be about 20 m. The length of time between the commencement of the "L" pattern by the KANE and the IR scanner image is approximately 50 minutes.

Three possible causes for this signature are proposed: (a) surface contaminants, (b) temperature difference, or (c) surface water turbulence. Since the apparent temperature, Ta, observed by the scanner is equal to the emissivity, ϵ, times the true temperature, T_t, the signature can result from variations in ϵ as well as T_t. Surface contaminants affect ϵ, primarily. The intensity of the signature appears to diminish with time; however, the width remains relatively constant. This would indicate that if a passive contaminant were involved, it would have to diffuse downward. Since the most likely contaminants are lighter than water, the fact that the trail does not broaden argues against their presence.

A mechanism for a thermal signature exists in a shallow thermocline that is generated during the day near the surface. Figure 5.3a shows several such thermal gradients in the area imaged by the scanner. The depth of this effect appears to be about 1 to 5 m, and the temperature difference varies up to about $1^{o}C$. The ship's propeller would have moved some of this water to the surface where it would have contributed to the observed darkening of the image.

Fossil turbulence of the overturned water is a third possibility. The turbulence has the effect of smoothing the surface water, since the surface kinematic boundary condition, necessary for the formation of waves, is not met; i.e., water parcels on the surface do not remain on the surface. The persistence of the turbulence will depend on the underlying and surrounding buoyancy forces. Since dense BT data describing the near-surface stratification exists, this area represents a fertile area for further analysis.

Point "B" of Figure 8.10 exhibits some distortion of the trail. Since no net displacement of the signature appears to occur, the effect is probably not due to frontal boundary.

The high thermal and spatial resolution of the IR scanner enables this instrument to record a thermal front that would have gone undetected using other instruments. (See the PRT-5 trace in Fig. 8.7, for example.) Further digital enhancement of this data has made it possible to resolve thermal features not visible on the image film (for example, the initial section of the surface signature of the KANE shown in Fig. 8.10). It is estimated that enhancement can reveal temperature differences as small as $0.1^{o}C$. Future improvements in the system will allow data logging of time and PRT-5 data on the computer compatible tape and provide for better calibration procedures.

8.4 SHIPBOARD IR DATA

A PRT-5 radiation thermometer was mounted on the 03 level of the KANE and was sighted outboard at the sea surface. Recordings of sea surface temperature were

made during Leg 1 and Leg 2 of the first "L" pattern. At the end of this period the instrument failed, and could not be used during the remainder of the cruise. Figure 8.11 shows two sections of the record. Grey areas on each graph represent rapid oscillations of the recording pen. The source of these oscillations may have been a real sea surface temperature variation or it may have been caused by the spray and turbulence associated with the bow wave of the ship. The variance of this "noise" appeared to increase after sunset, suggesting that convective instabilities in the surface layers caused by diurnal cooling may have produced an even greater variance in the surface temperature during the early evening hours. The KANE was cruising at about 5 kn, hence, a 5 minute oscillation in the record would correspond to a wavelength of about 750 m. The average surface temperature seems to have dropped 0.6°C from 1750 local time to 2240 local time.

8.5 TIROS-N THERMAL IR IMAGERY

At 1936Z on 6 September the TIROS-N AVHRR (Advanced Very High Resolution Radiometer) recorded an IR image of the area of operations. Figure 8-12 displays the image together with a superimposed grid showing the original 3° X 3° square area. The predominance of clouds makes the detection and interpretation of any ocean features difficult. Figure 8-13 shows the 1° square operations area with the "L" pattern and the front detected by the scanner superimposed on the image. There appears to be no correlation between the dark and light variations in the image and the frontal line.

Two factors make detection of sea surface features from above the atmosphere difficult in the summer: (a) suspended atmospheric moisture and (b) the small dynamic range of sea surface temperatures. Temperature frontal gradients in the Gulf of Mexico have been detected in the presence of as much as 4 cm of atmospheric water. The total integrated water vapor content for this experiment can be calculated from the available atmospheric sounding data, but the analysis is beyond the scope of this report.

8.6 GLINT PHOTOGRAPHY

Cox and Munk (1954) have demonstrated that analysis of sun glint images of the sea surface can yield statistical information about the sea surface slopes. They also found a close relationship between the RMS wave slope components in the crosswind and downwind directions and the wind magnitude in these directions. Their theory has been applied to the analysis of the photographs taken during this experiment. A schematic of the geometry and the expected distribution of sea slopes is shown in Figure 8.14.

A software package was developed to analyze glint photos following the Cox and Munk model. Inputs to the model are focal distance of the camera, size of the image, altitude, roll angle, and heading of the aircraft, time, sun declination, latitude, longitude and wind direction. The primary output is a two-dimensional histogram of population density versus slope components in the X and Y directions. From this approximation to the bivariate distribution function of sea slope components, the RMS value of the wave slope components in the crossswind and downwind directions are then estimated. Inverting the expression derived by Cox and Munk, the velocity of the wind, W, in terms of the variances of slope in the crosswind and downwind directions, σ_x^2 and σ_y^2, becomes:

$$W = 5.210 \times 10^2 \sigma_x^2 \pm 2.0 \sigma_x$$

and

$$W = 3.165 \times 10^2 \sigma_y^2 \pm 2.5 \sigma_y$$

where W is in meter/sec.

Data reduction proceeds as follows. The negative transparency is digitized into a 512 X 512 matrix and the image is "warped" for proper registration of the image in the array. Intensities are then adjusted for the D-log E characteristics of the film and the transfer function of the digitizer. Next, the image is scanned pixel, by pixel converting from image coordinates to α, k coordinates at each pixel, where k is the wave slope and α is the azimuthal orientation of the slope. Finally, the component of the slope in the downwind and crosswind directions is calculated and the intensity of the pixel is added to the k_x^i, k_y^j bin of the probability density histogram. It is assumed that the number of glints contained in a given pixel is proportional to the intensity of that particular pixel.

Sources of error are the following:

1. Some slight defocusing occurred due to a failure of the camera to properly register the film on the camera back-plane.

2. The background film noise (fog).

3. Statistical fluctuations in the sea surface.

4. Reflected and scattered light incident on the sea surface.

5. Effect of atmospheric refraction (on sun angle determination).

6. Variations of the length of day relative to mean solar time.

Corrections for errors 4, 5, and 6 can be made during analysis. Error 1 has been eliminated for future experiments. Error 3 is minimized by taking suitable averages. The effect of error 2 has been minimized by contrast stretching; however, this results in the very steepest slopes being lost in the noise.

Eight images, taken in the vicinity of the ship, were analyzed. In order to bring the glint pattern to the center of the image, the plane was rolled by dipping the left (northern) wingtip. One such photo is shown in Figure 8.15. The altitude was 760 m, the field of view was 1.14 km by 1.14 km, and the overlap between frames was 25%. Hence, the fourth frame contained 25% of the field of view of the first frame. The results are shown in Table 8.2.

Table 8.2

Glint-derived Slopes and Wind Speed Near the USNS KANE at Start of Leg A
(30°25.5'N, 71°38.5'W)

Photo	x	W(kn)	y	W(kn)
170441	0.181	17.1	0.194	11.9
170444	0.177	16.3	0.189	11.3
170446	0.178	16.5	0.188	11.2
170449	0.182	17.2	0.190	11.4
170547	0.181	17.1	0.193	11.8
170549	0.182	17.2	0.193	11.8
170705	0.178	16.5	0.190	11.4
170708	0.177	16.3	0.192	11.7

(The photo ID number is the time in hrs-min-seconds.) Surface observations indicate that wind velocities at 26.5 m were near 2 ms^{-1} (4 kn) as shown in

Figure 9.2. Wind velocities derived from the glint data vary between 11 and 17 kn.

The disparity between wind speeds may be due to: (a) the fact that sea state was decaying and, hence, not saturated, or (b) the strong swell moving through the locally generated wave field from the south biased the wind-related slopes toward higher values.

Figure 8.16 shows the wave slope component histograms in the crosswind and downwind directions obtained from photos 170441 and 160635. A slight flattening of the distribution at the peak of the distribution is reflective of the slightly saturated character of the photo images. The variance of the downwind distribution is greater than that of the crosswind distribution as predicted by Cox and Munk (1954).

Three photos, taken on either side of the observed temperature front, were analyzed for wave slope distribution. These images were obtained with zero aircraft roll, so the pattern was slightly truncated. The effect was that the downwind and crosswind distribution functions were truncated and the RMS values were higher than they would have been otherwise. The analysis was undertaken for comparison purposes to determine if a front-related velocity shear may have been present and whether the effect of such currents on the RMS slopes could be observed. The results are shown below in Table 8.3. The photographs were taken near 30°50'N, 71°50'W.

Table 8.3
Glint-derived Wave Slopes near a Surface Front

Photo	x	y	
160635	0.182	0.157	south of front
160639	0.186	0.160	south of front
160627	0.183	0.156	north of front

There appears to be no discernible change in σ across the front, so it is concluded that no appreciable current shear was associated with this thermal front.

8.7 WAVERIDER DATA

The Waverider buoy is a 1 m diameter buoyant sphere containing an accelerometer, integrating circuitry, and a transmitter. The buoy was tethered to the ship whenever the ship stopped for a CTD station during daylight hours and data was logged on board the ship in analog form. The tethering was accomplished through the use of a 10 m length of shock-absorbing bungey cord and an 80 m nylon line. There were seven deployments of the buoy, of which four were digitized. Power spectra for each deployment are displayed in Figures 8.17 and 8.18. Each record was 1 hour long and was digitized with a Nyquist frequency of 1 Hz, yielding spectra with 27 degrees of freedom.

The first deployment on 6 September coincided with the imaging of the set of four glint photos analyzed in section 8.6. The spectrum for this deployment exhibits a pronounced peak at about 0.08 Hz, representing an energetic swell traveling from the south and most likely generated by Hurricane David (see Figure 9.1). The tail of the spectrum exhibits an $\omega^{-2.9}$ dependence, indicating a nonequilibrum condition (Phillips (1966) demonstrates that a ω^{-5} dependence should be expected on the right side of the peak for a fully developed sea.) In order to estimate an RMS wave slope from an elevation record, some assumption about the

directional characters of the spectrum must be made. If a plane wave is assumed, then

$$\zeta = \sum_{n=-N}^{N} C_n e^{i(k_n x - \omega_n t)} \qquad (1)$$

where ζ is the elevation, C_n is the complex amplitude, and $\omega_n = \sqrt{g\, k_n}$.

It can be shown that the resulting expression for the RMS wave slope is:

$$\sigma = \left[\sum_{n=o}^{N} K_n^2 \, (A_n^2 + B_n^2) \right]^{1/2} \qquad (2)$$

where A_n and B_n are the Fourier coefficients of the elevation time series.

For run #1, shown in Figure 8.16, $(A_n^2 + B_n^2)$ decays as $\omega^{-2.9}$ or $k^{-1.9}$. Hence, the series is barely divergent within the accuracy of the statistical estimate. The quantity N in equation (2) above, was taken to be 26, which corresponds to the point at which the spectral energy density disappears into the statistical noise. Then σ, thus obtained, equals 0.069 for run #1 as compared to 0.19 as obtained using glint photography. The former figure is likely low because equation (2) had to be truncated at N = 26, whereas the slow convergence of this series indicates that large contributions to σ may occur at the larger wavenumbers. Use of a pitch-roll buoy may reduce the problem of ambiguity in the directional spectrum. The spectrum on 9 September shows the result of the diminishing winds, and the following two spectra obtained on 10 and 11 September (Fig. 8.18) show the influence of Hurricane Frederick as a low frequency spike appearing in both spectra (see Fig. 9.1).

8.8 SUMMARY

The primary goal during this exercise was to demonstrate the use of photographic and advanced infrared sensing devices over the open sea. Some estimate of the sensitivity of these measurements to actual surface parameters, especially temperature, has been made.

A thermal front occurring in the mixed layer was observed to the west of the ship's operating area. The gradient across this front is opposite to the temperature gradient observed at 100 m depth and appears to cross isotherms at that depth.

The wave slope statistics obtained through analysis of photographs exhibited a 0.4% variance over the observation area, indicating high homogeneity on the wind field. The large disparity between glint-derived winds and actual surface winds is apparently due to the presence of a large swell arriving from the south. The presence of such large modulating waves generated in other areas of the ocean place a limit on the usefulness of the glint method for obtaining surface winds. However, the glint photos do provide valuable slope statistics for the interpretation of microwave scattering and emissivity data.

The data, particularly image data, shown here is only a small fraction of the total data collected during the experiment. There remains a wealth of information that could be analyzed, and one of today's challenges in remote sensing is to develop automated analysis techniques, analogous to those developed for time

series. The glint analysis and the IR image digitization are steps in this direction.

8.9 REFERENCES

Cox, C. S. and Munk, W. H. (1954). Measurements of the Roughness of the Sea Surface from Photographs of Sun Glitter. J. of Am. Optical Society, 44, p.838-850.

Phillips, O. M. (1966). The Dynamics of the Upper Ocean. Cambridge University Press, p. 261.

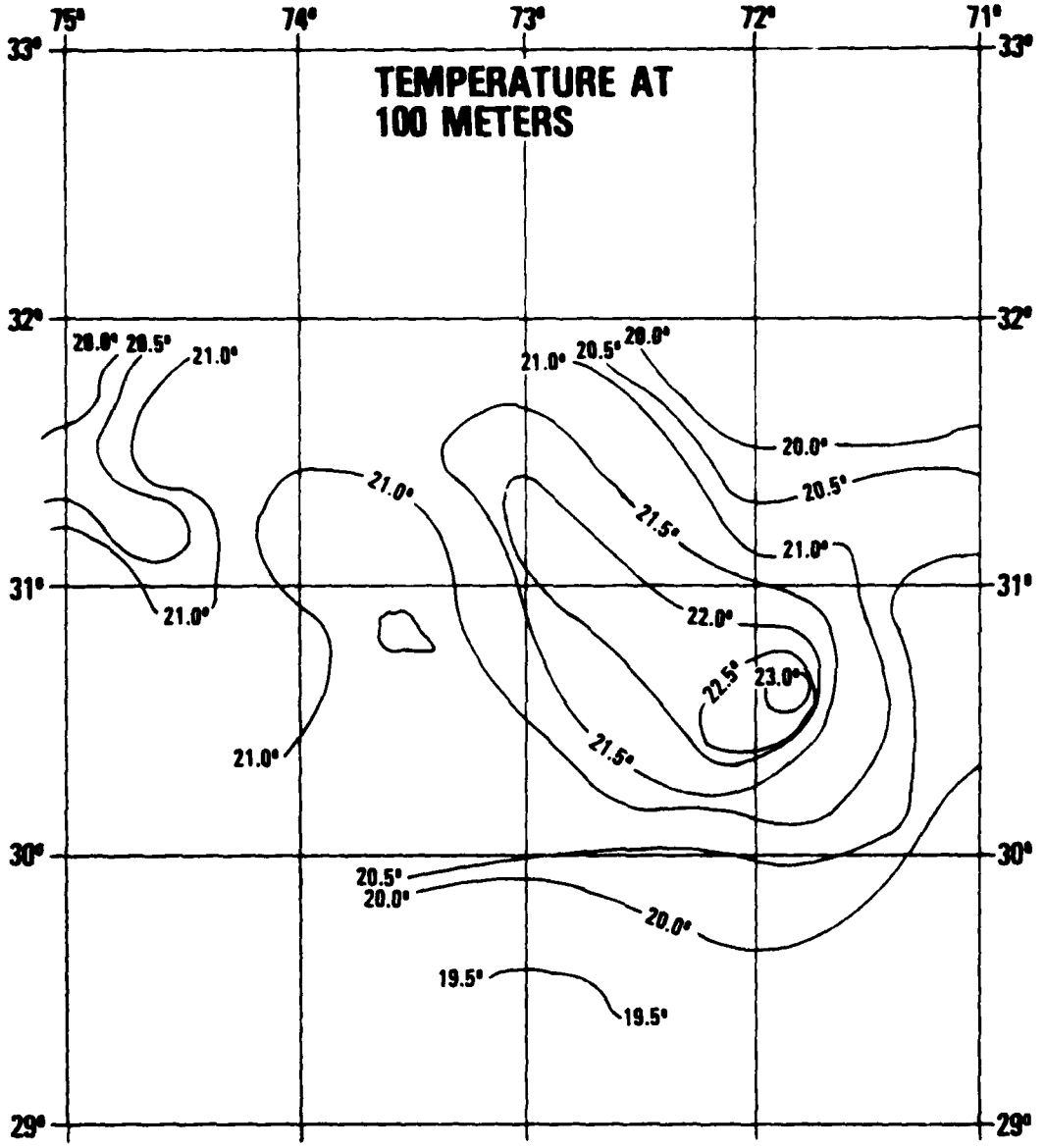

Figure 8.1. Pre-cruise survey 24 Aug 79

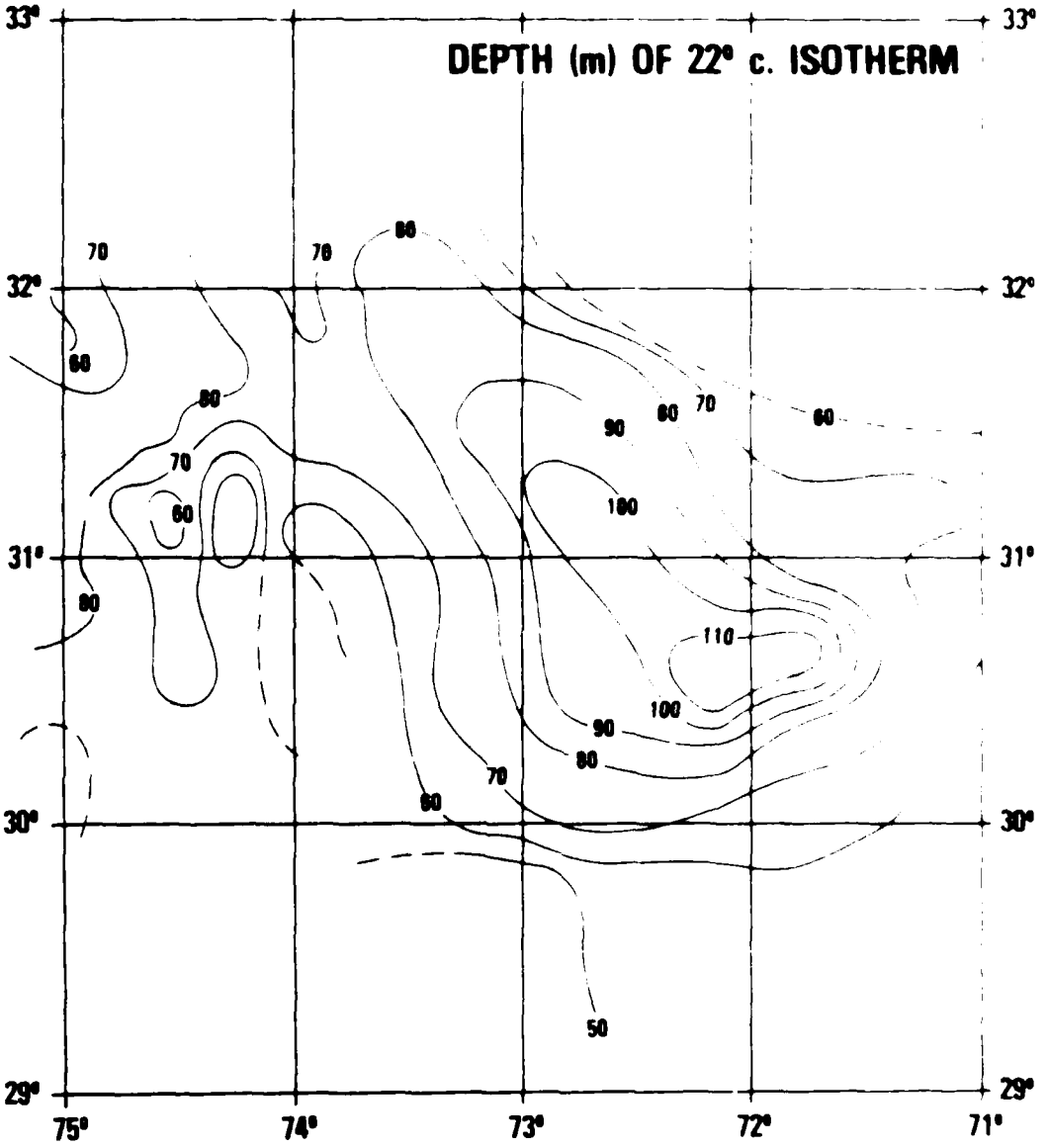

Figure 8.2. Pre-cruise survey 24 Aug 79

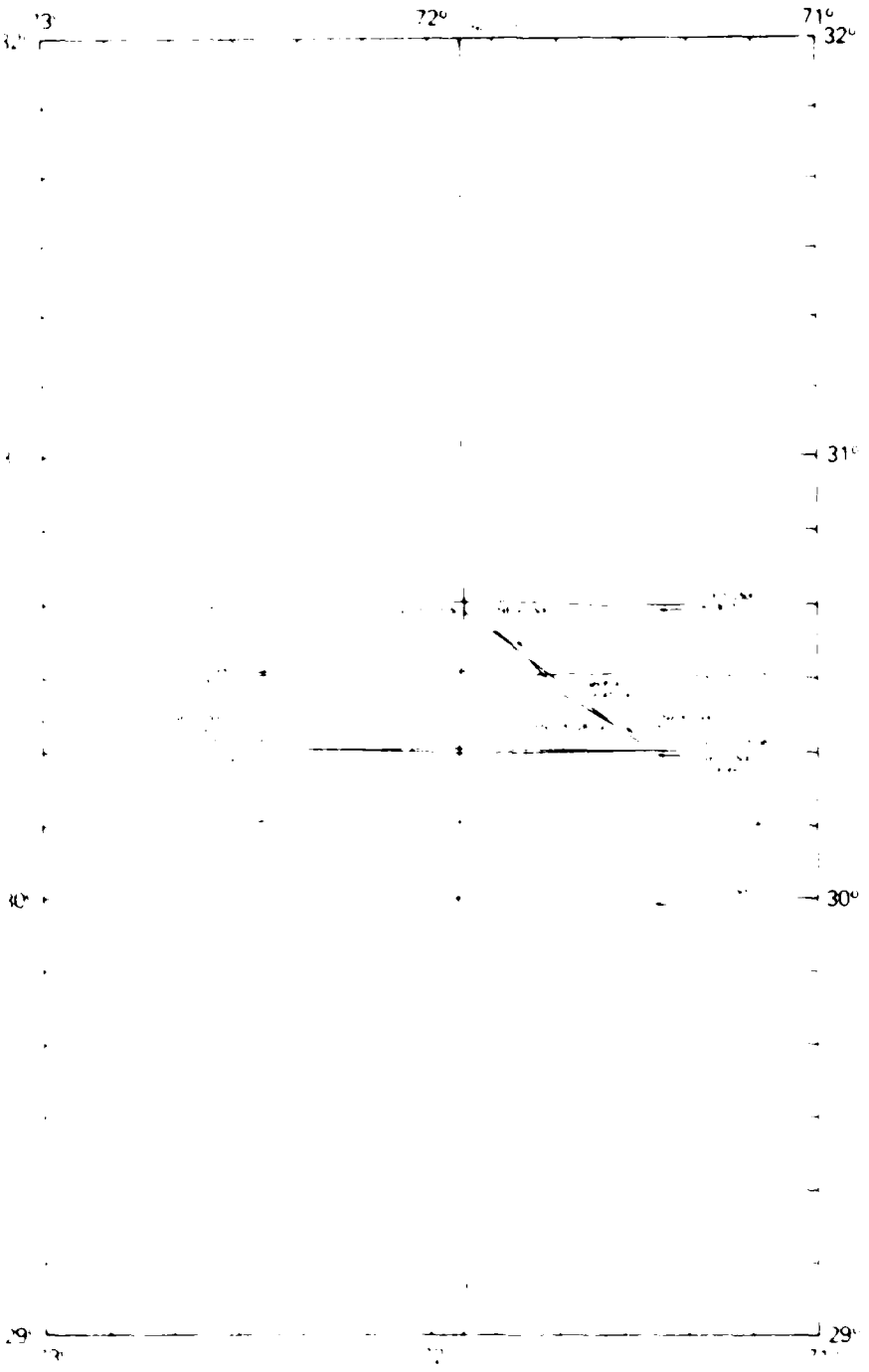
72°
71°
32°
31°
30°
29°

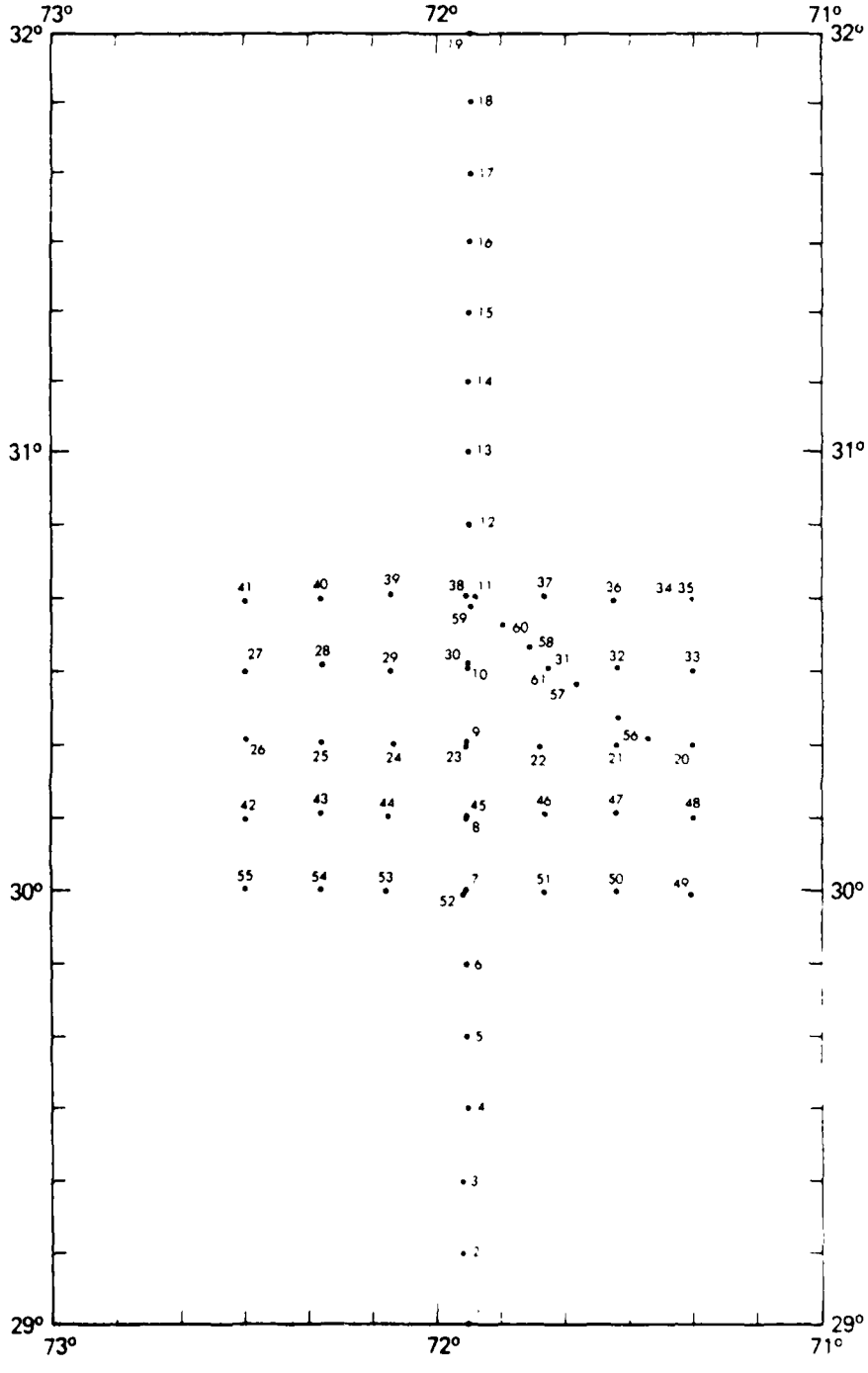

Figure 8.4. AXBT drop pattern 6 Sept 79

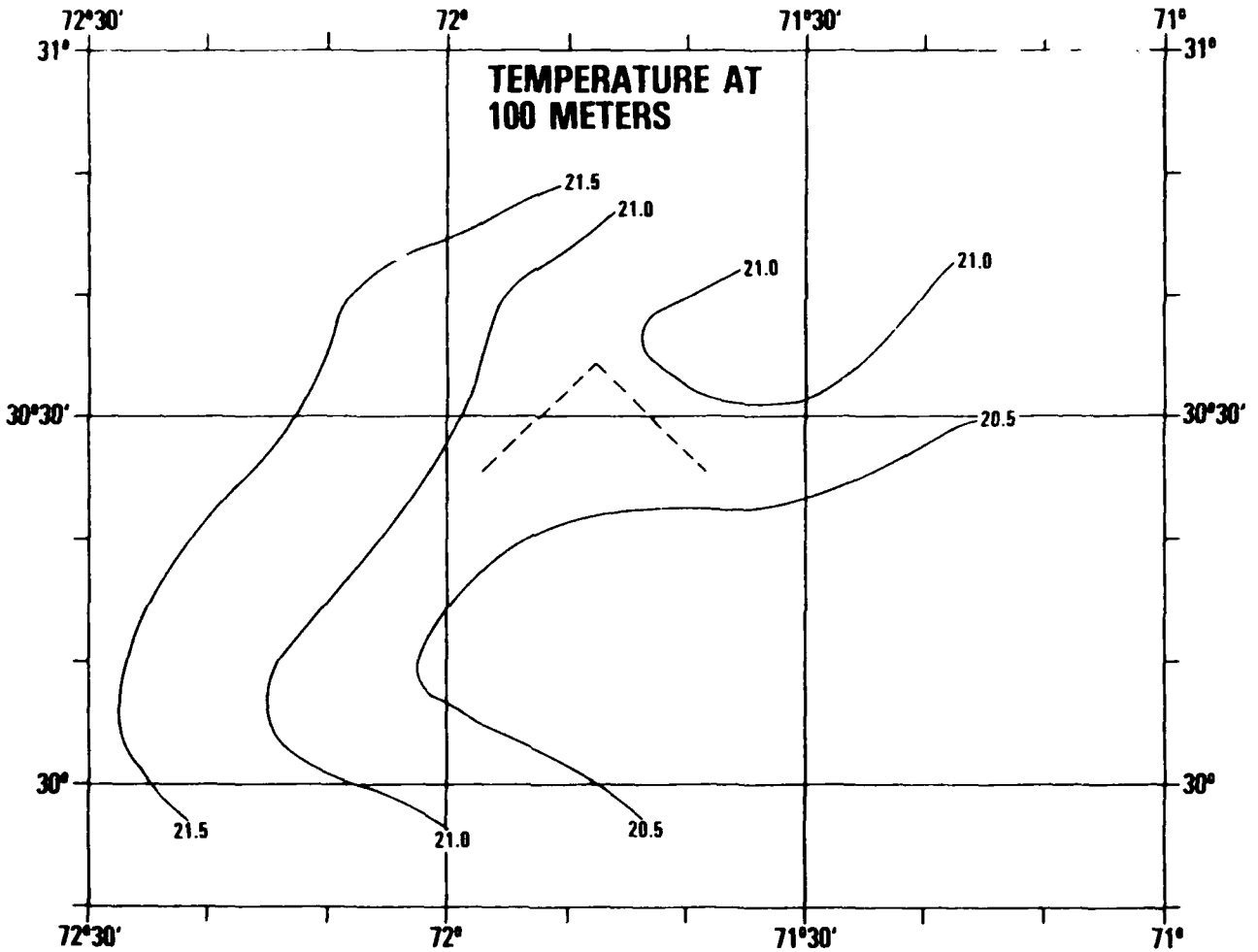

Figure 8.5. Cruise survey 9 Sept 79

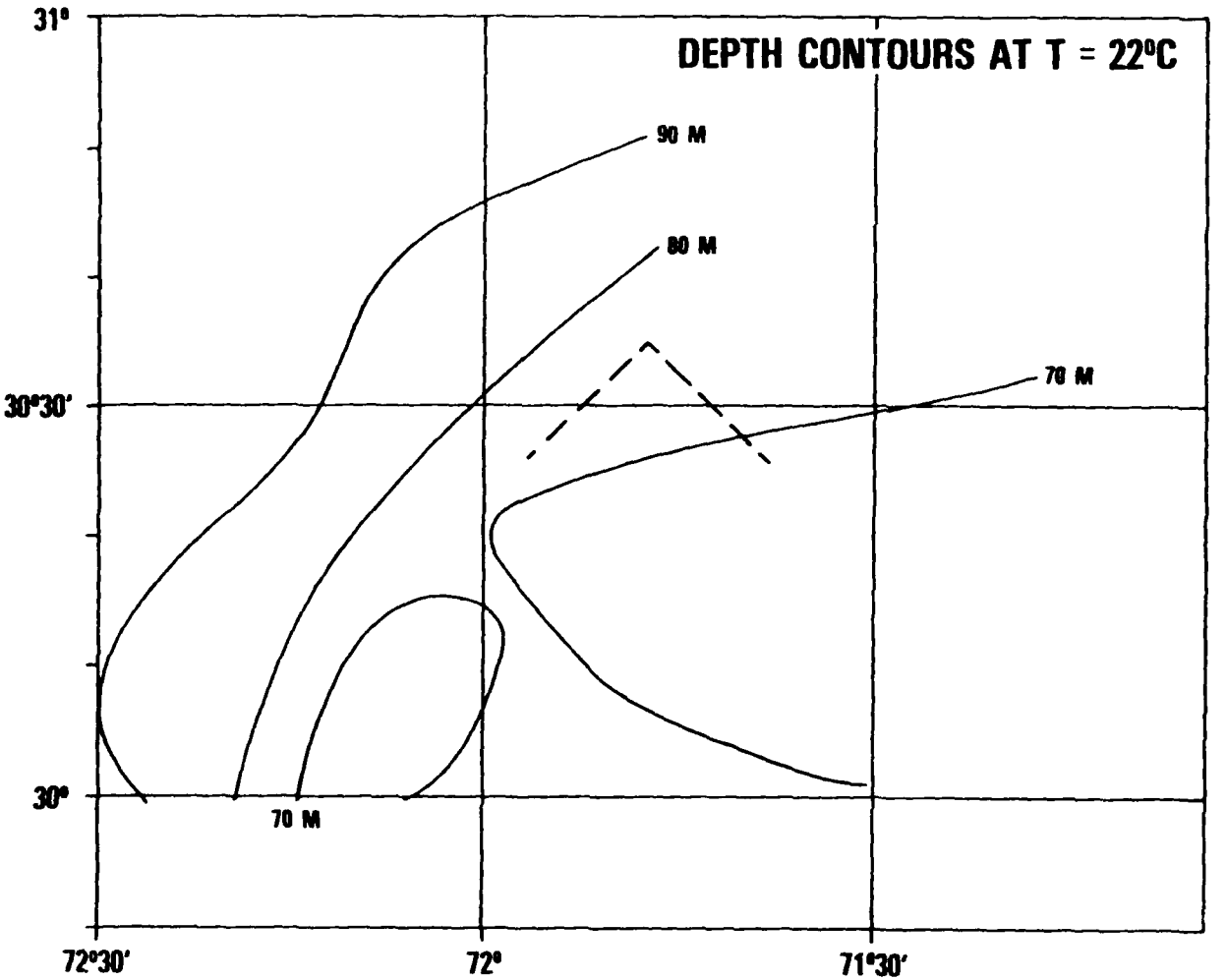

Figure 8.6. Cruise survey 9 Sept 79

THERMAL FRONT LOCATED ON AIRBORNE THERMAL INFRARED
LINE SCANNER AND PRECISION RADIATION THERMOMETER

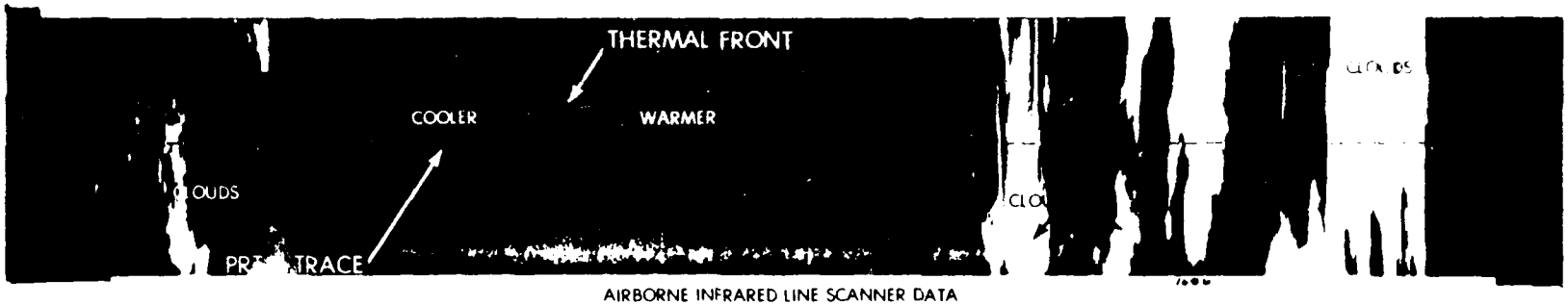

AIRBORNE INFRARED LINE SCANNER DATA

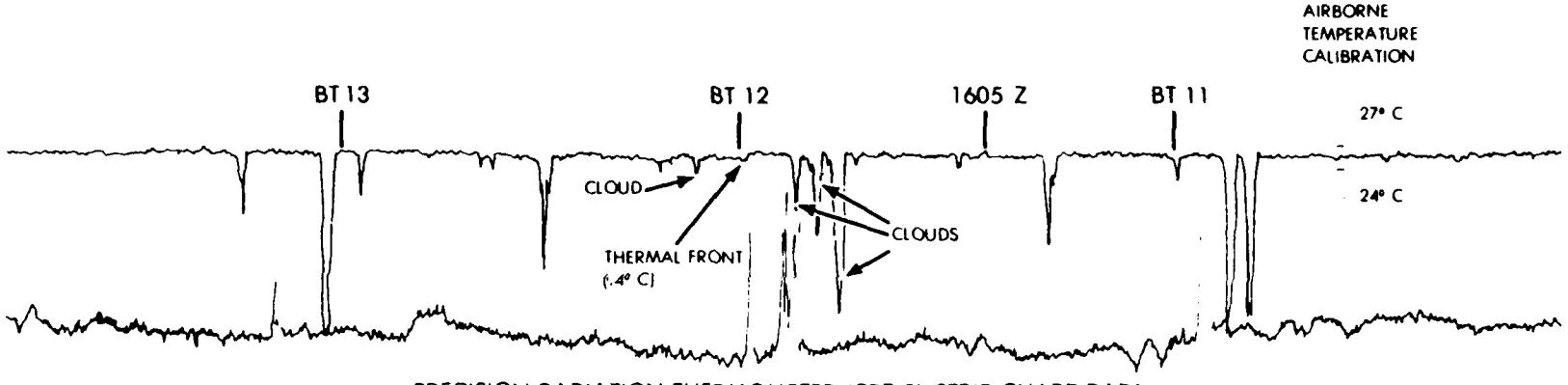

PRECISION RADIATION THERMOMETER (PRT-5) STRIP CHART DATA

ALTITUDE 2500'
LOCATION 30° 50.0' N 71° 55.1' W

Figure 8.7. Thermal front located on airborne thermal infrared line scanner and precision radiation thermometer

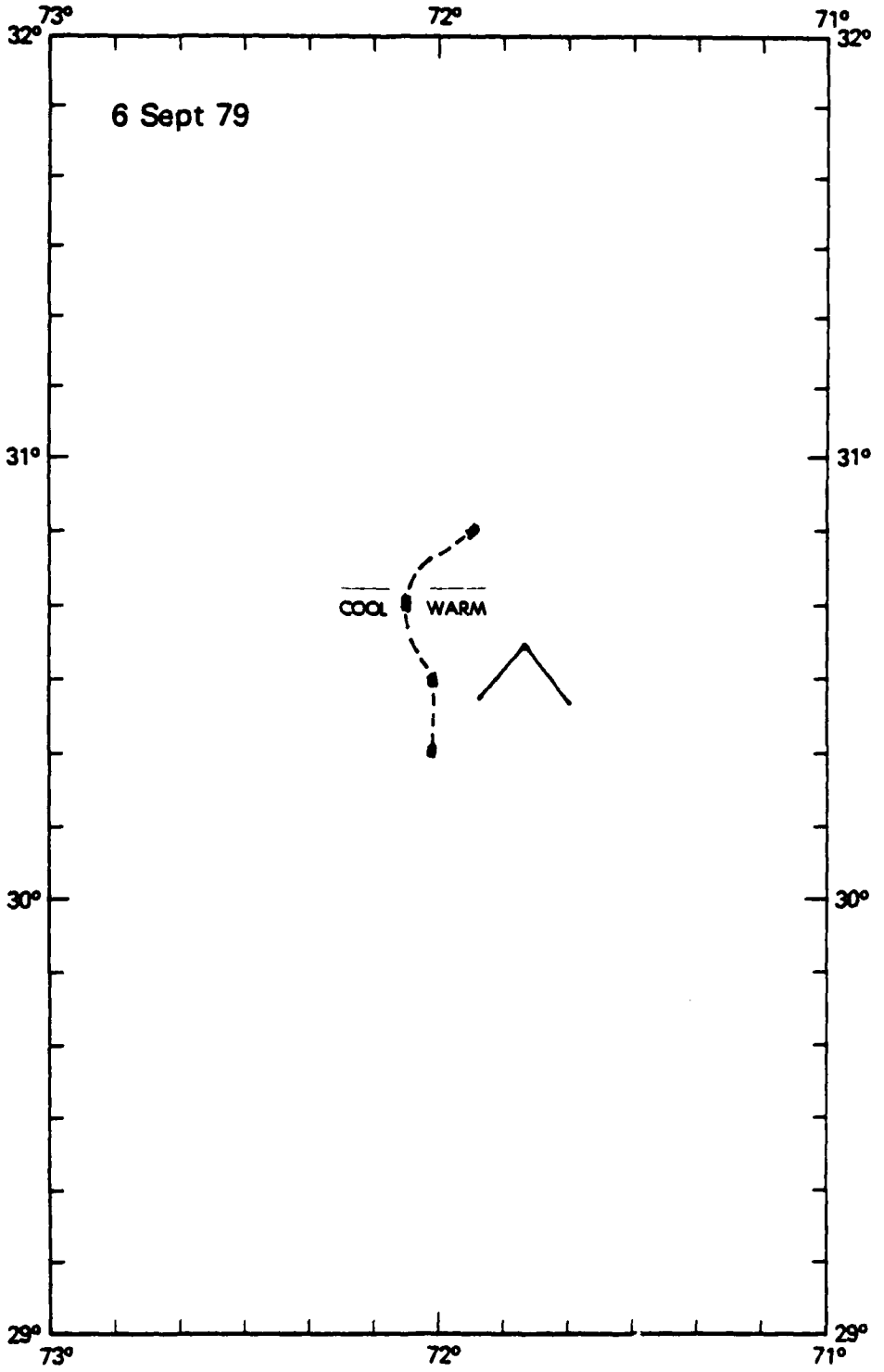

Figure 8.8. Surface thermal front mapped by IR scanner

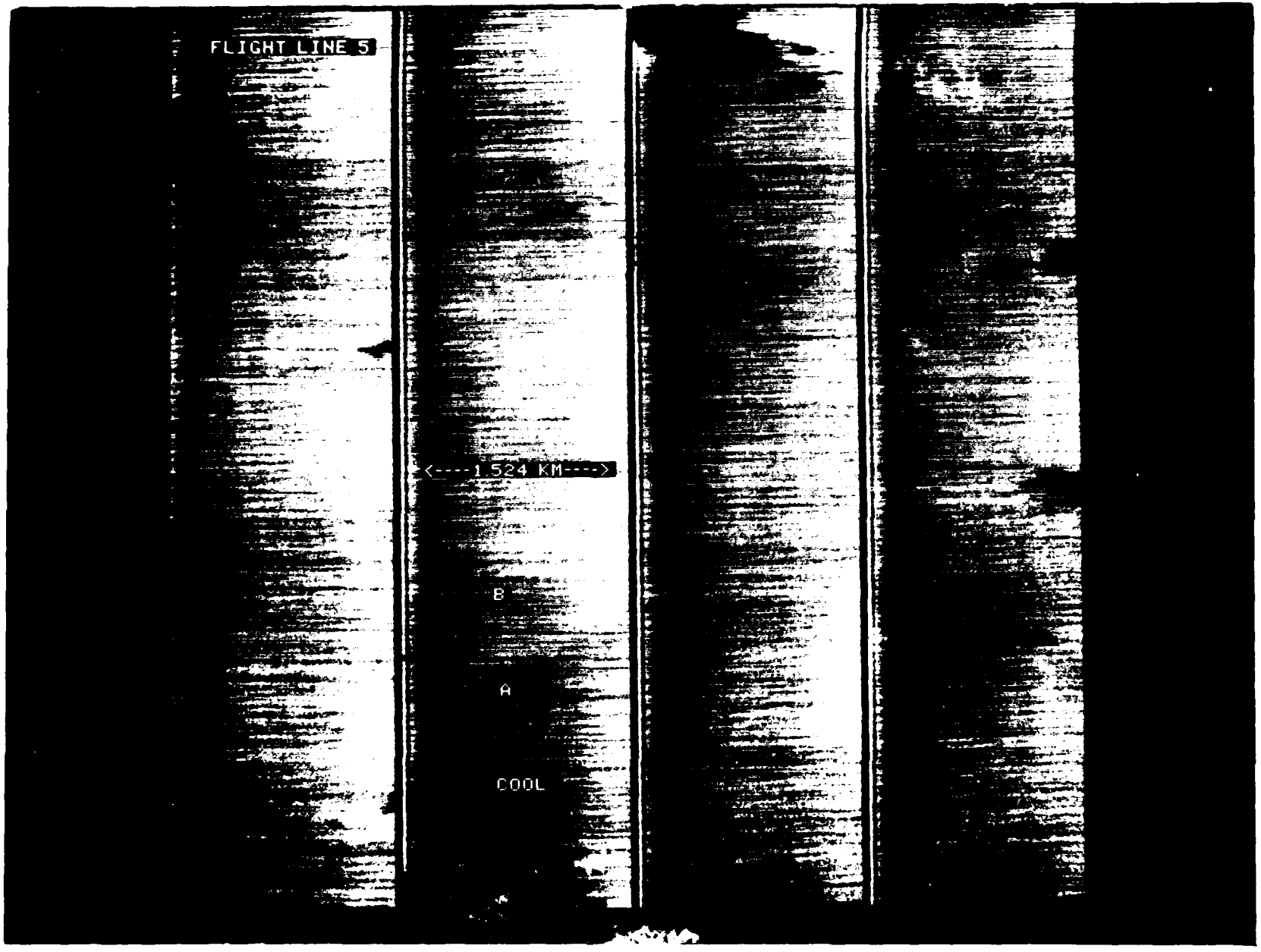

Figure 8.9 Digitized IR scanner image

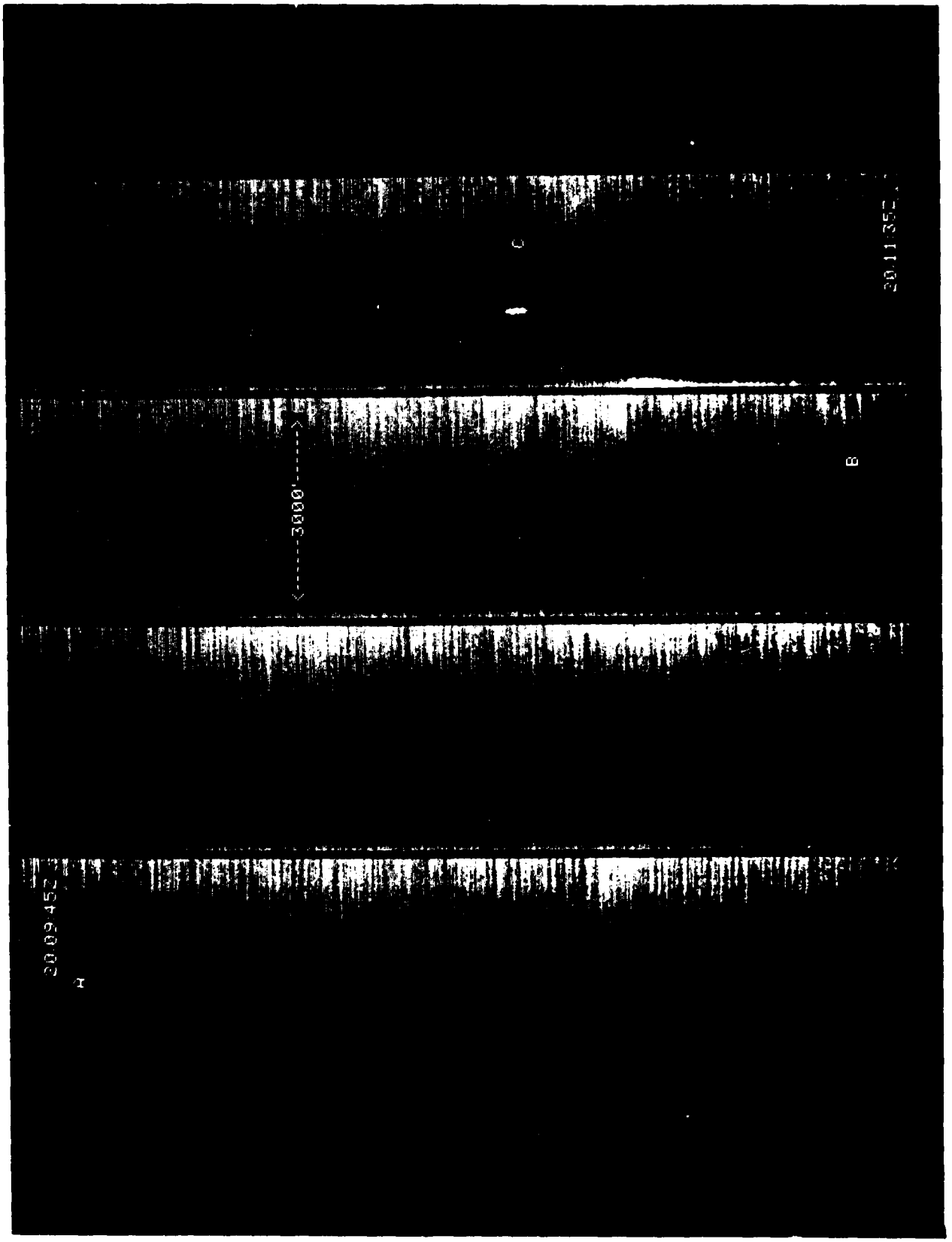

Figure 8.10. Digitized IR scanner image USNS KANE on leg A of "L" pattern

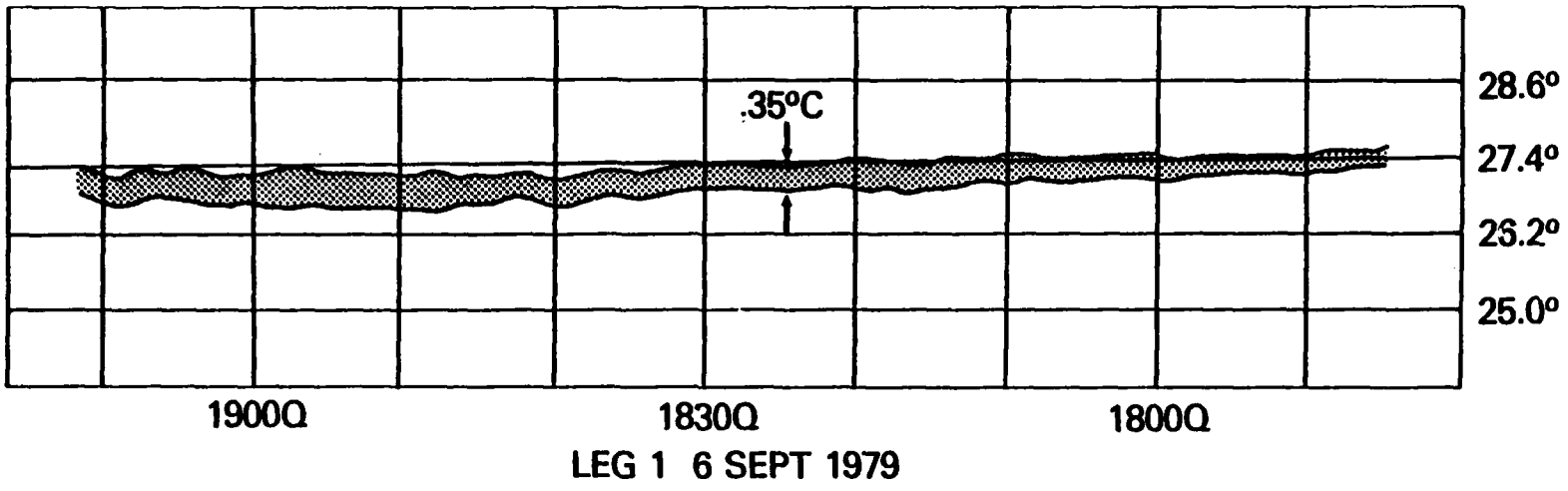

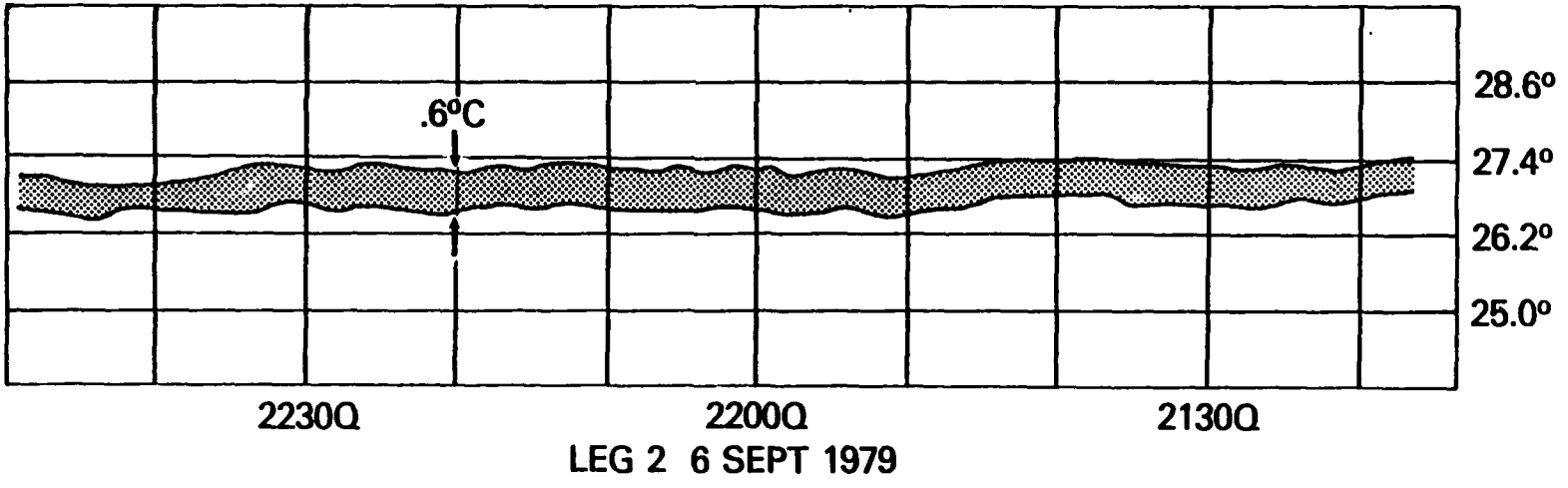

SHIPBOARD PRT-5 RADIATION THERMOMETER RECORD

Figure 8.11. Shipboard PRT-5 radiation thermometer record

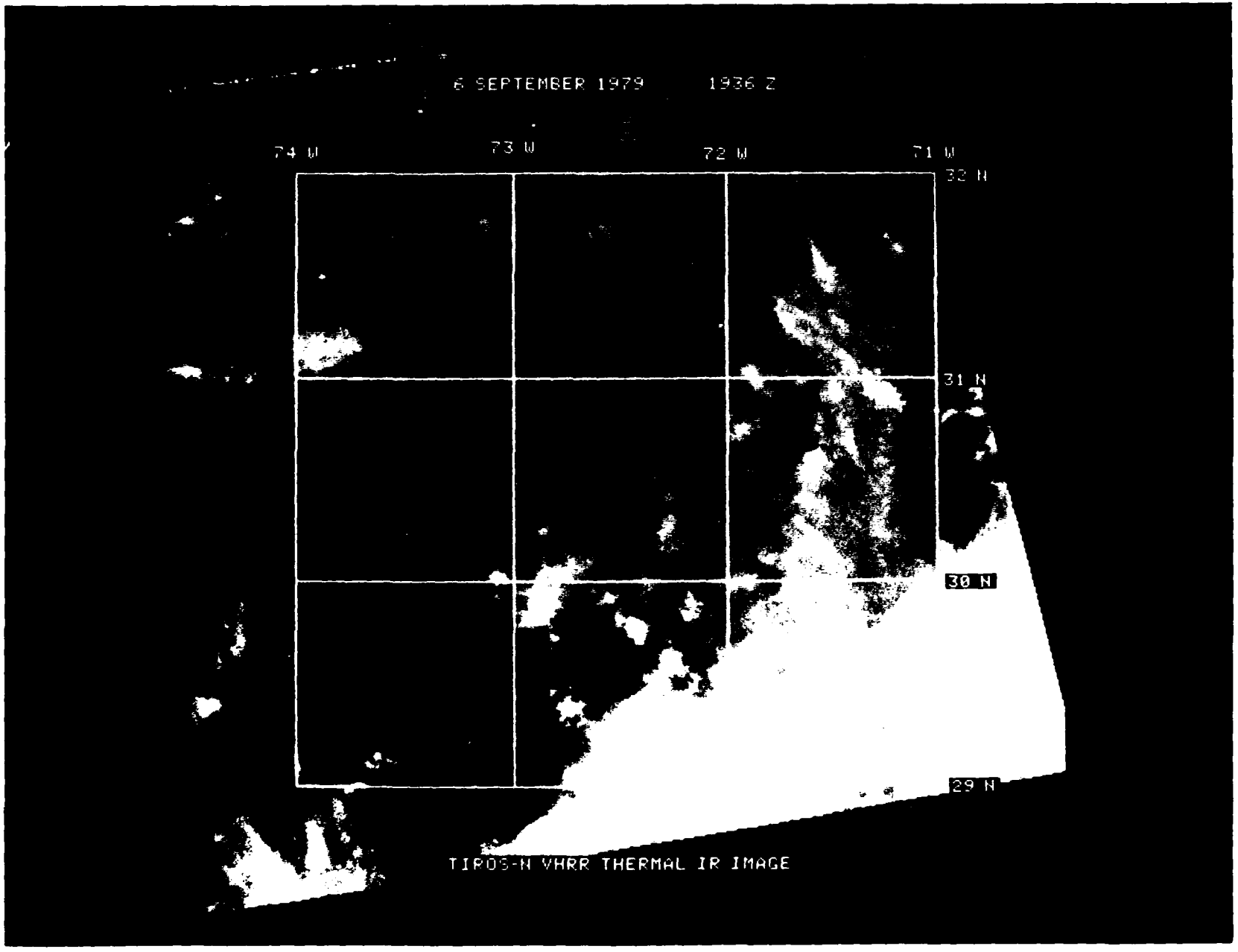
6 SEPTEMBER 1979 1936 Z
74 W
73 W
72 W
71 W
32 N
31 N
30 N
29 N
TIROS-N VHRR THERMAL IR IMAGE

Figure 8.12.

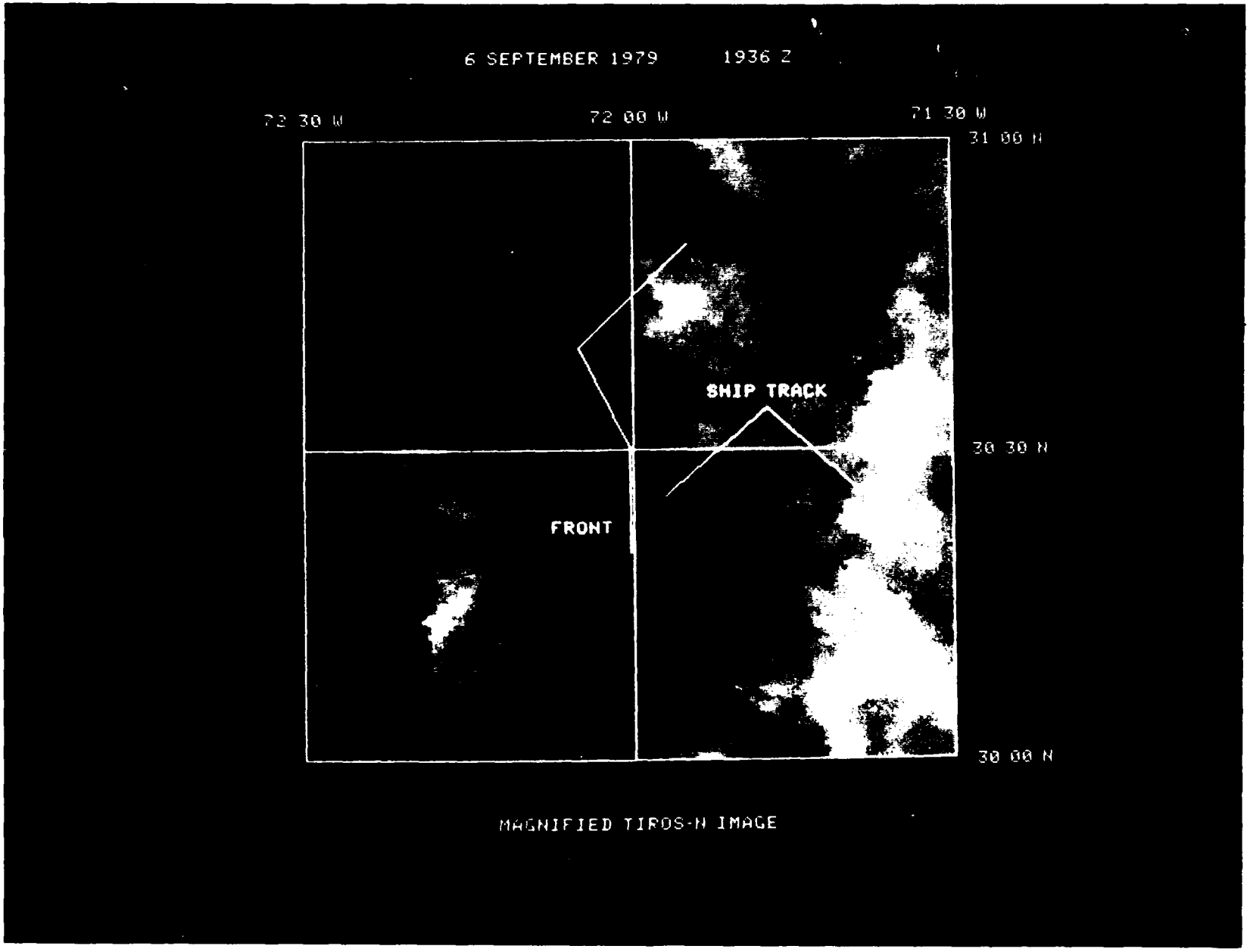
6 SEPTEMBER 1979 1936 Z
72 30 W
72 00 W
71 30 W
31 00 N
30 30 N
30 00 N
SHIP TRACK
FRONT
MAGNIFIED TIROS-N IMAGE

Figure 8.13.

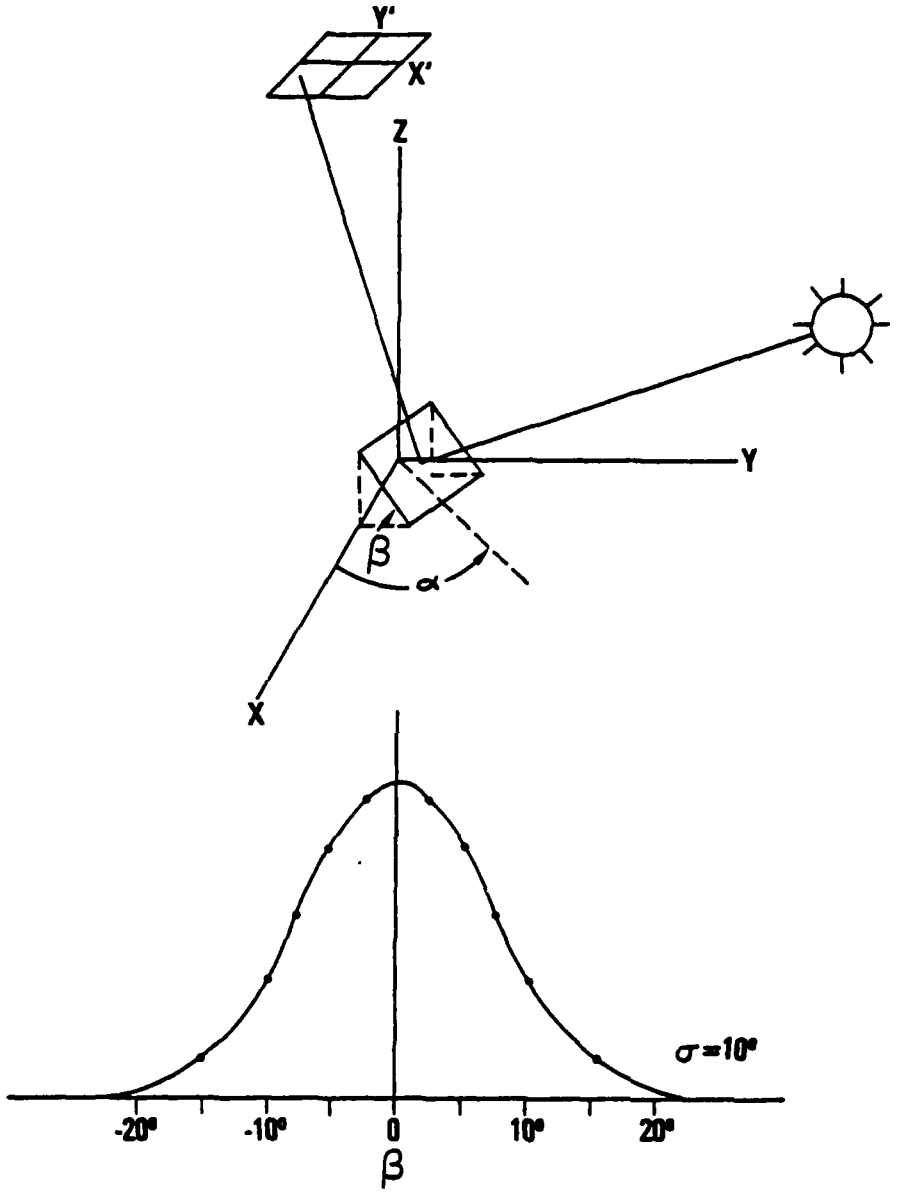

Figure 8.14. Geometry of glint reflection and a hypothetical distribution of wave slope components

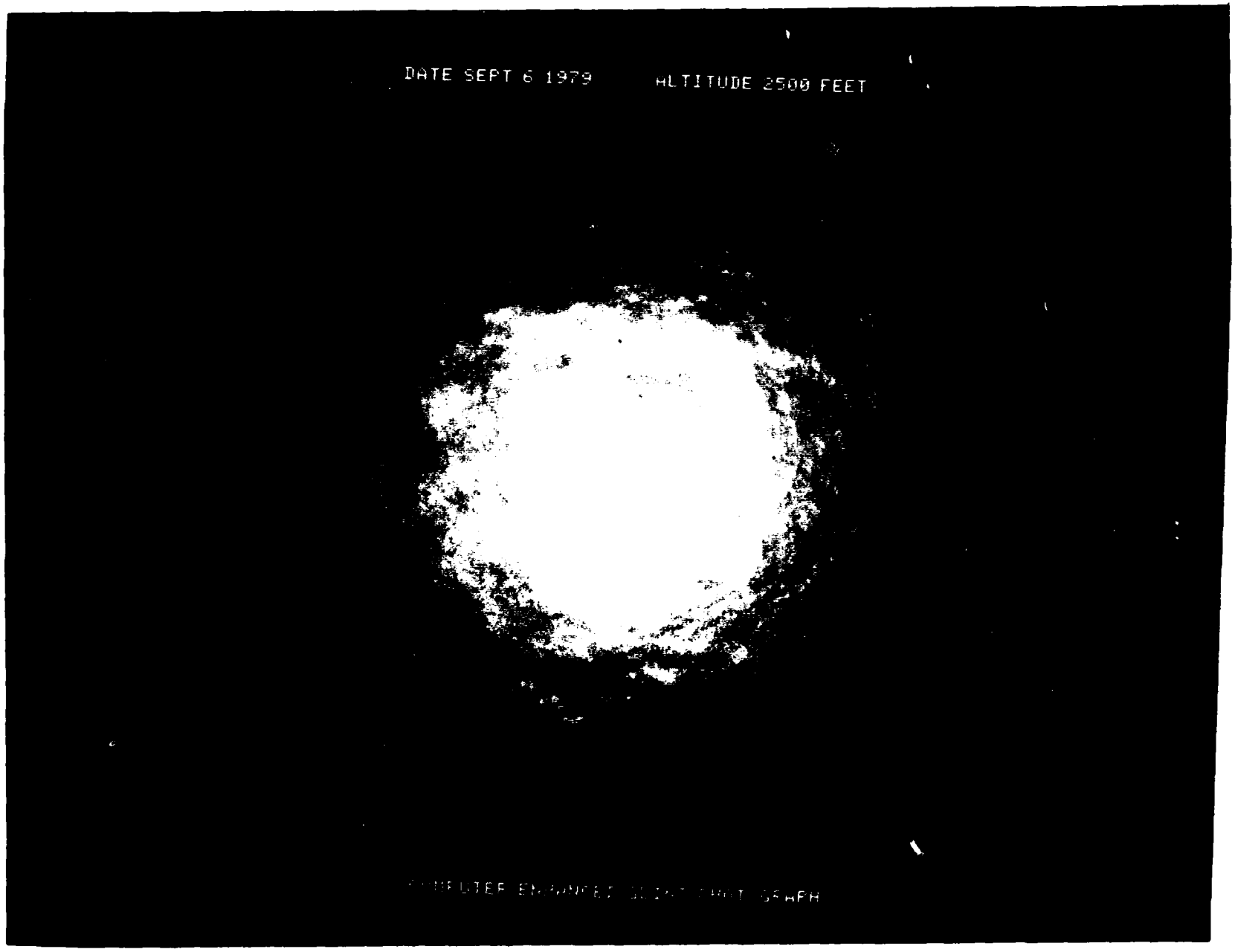

Figure 8.15.

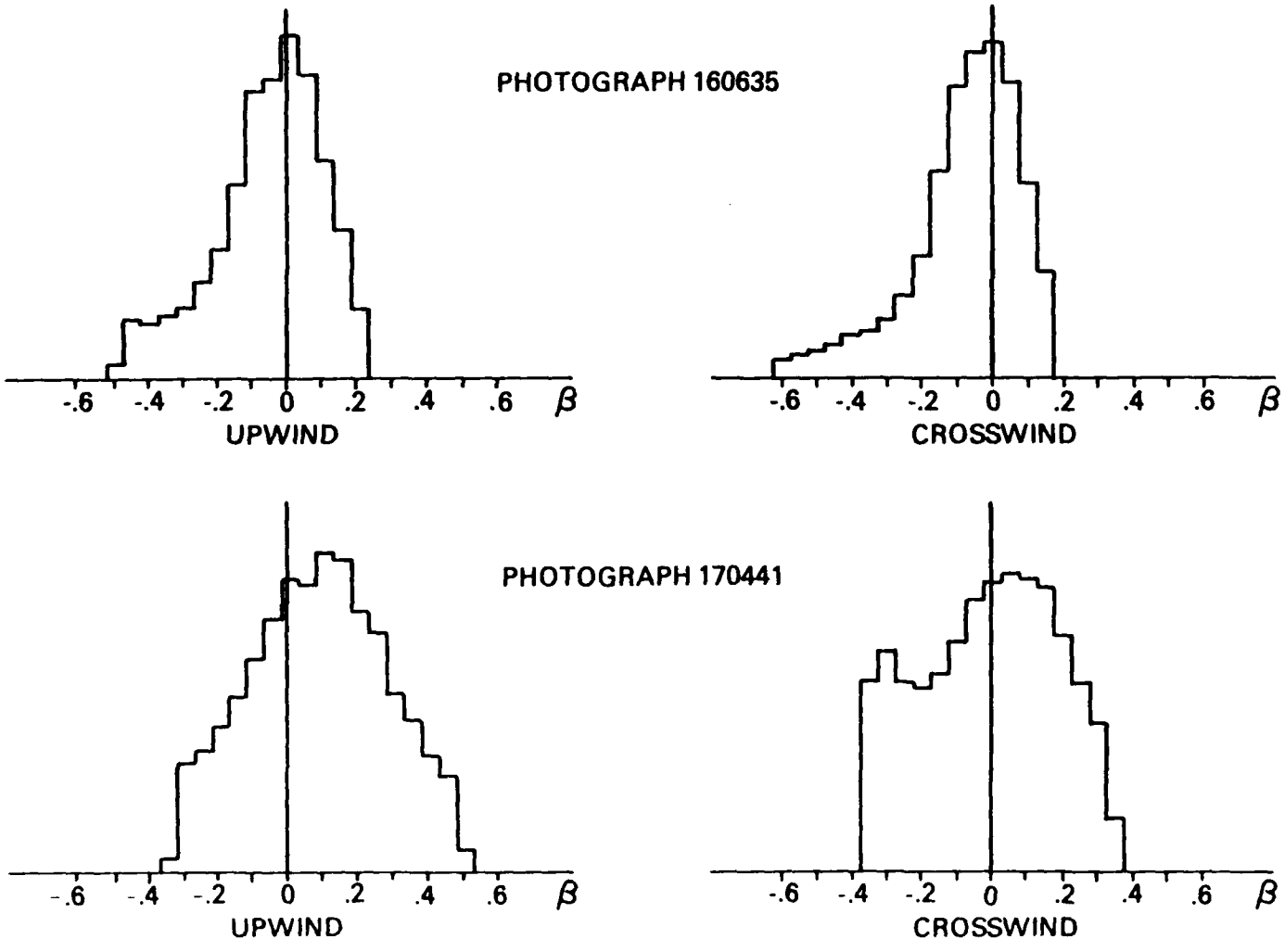

Figure 8.16. Histograms of wave slope component density in the upwind and crosswind directions.

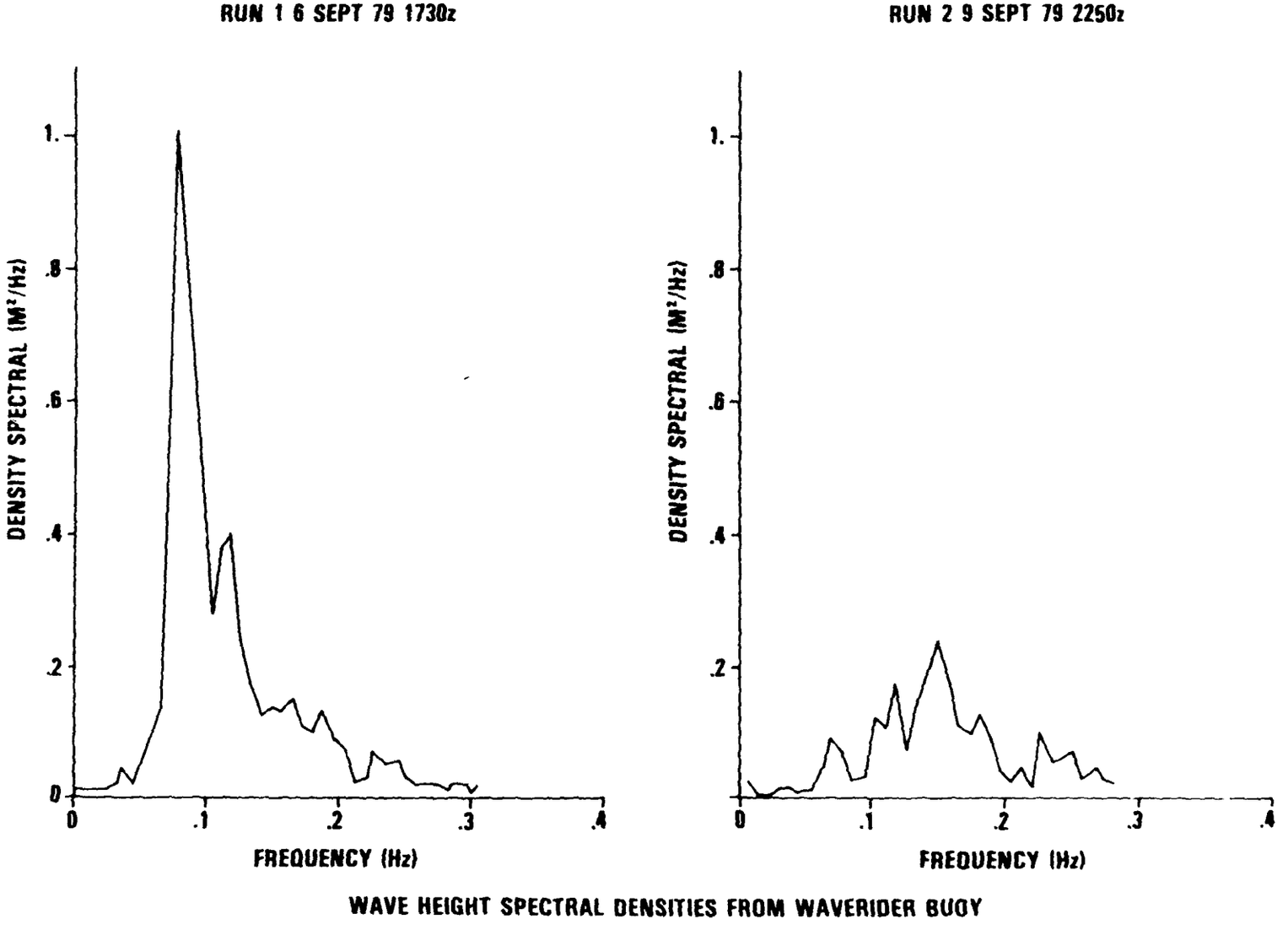

Figure 8.17. Wave height spectral densities from waverider buoy

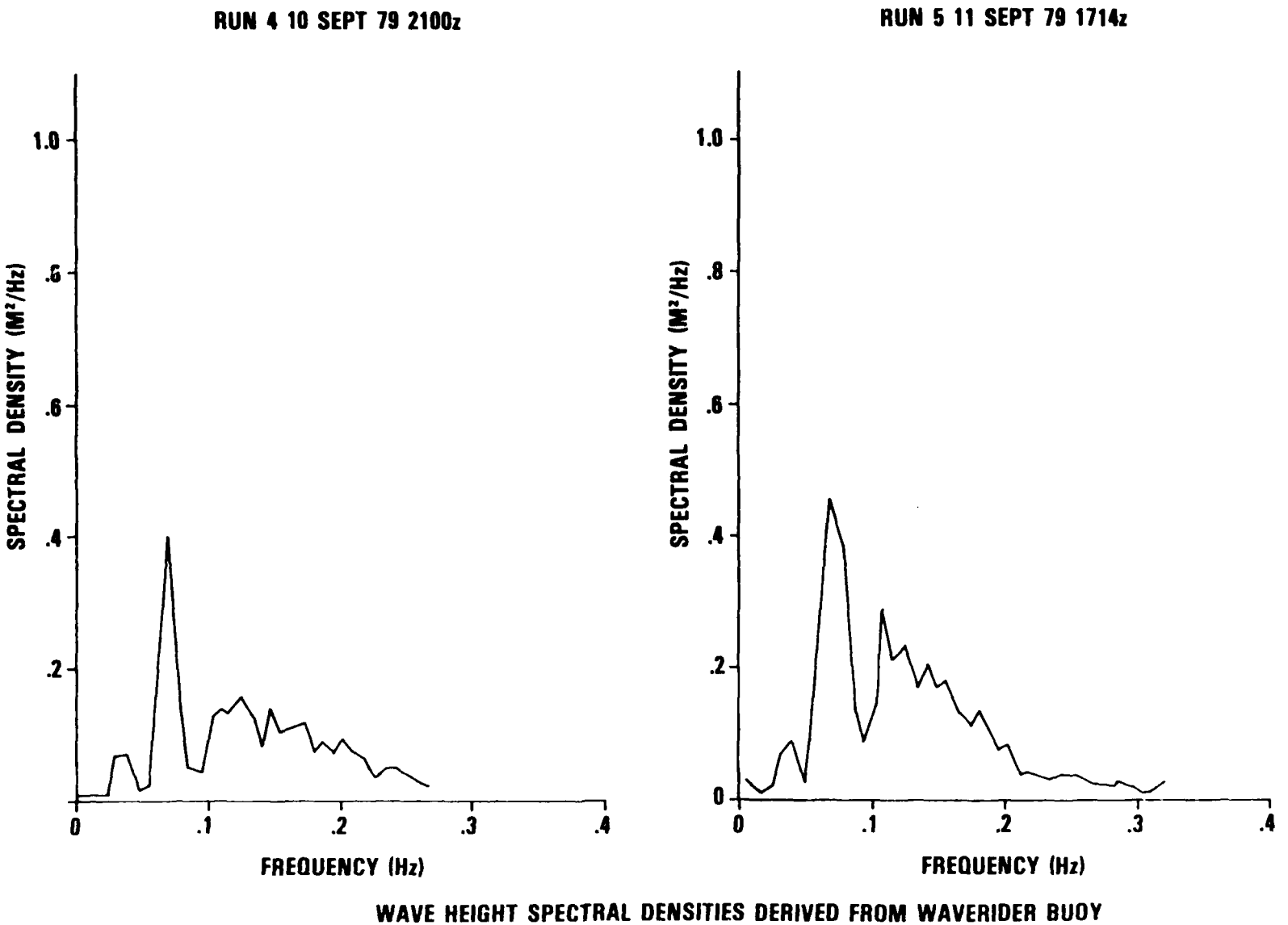

Figure 8.18. Wave height spectral densities derived from waverider buoy

Section 9.0

METEOROLOGICAL DATA

by Walter Grabowski

METEOROLOGICAL DATA

INTRODUCTION

The meteorological observation program consisted of observations taken at three-hour intervals by a U.S. Navy Mobile Environment Team. The following parameters were recorded during each observation:

- Time (GMT)
- Location (latitude and longitude)
- Ship's speed and heading
- Anemometer and corrected wind speed and direction
- Sea-level pressure
- Dry and wet bulb air temperature
- Bucket sea-surface temperature
- Cloud cover (tenths)
- Present and past weather (NOAA Codes)
- Cloud descriptions
- Wave and swell height and direction
- Rainfall

Observations were carried out from 1200 GMT 2 September through 0900 GMT 13 September. The Mobile Environment Team encountered no serious difficulties, and complete observations were recorded at every three-hour interval.

An expanded presentation of this data, including a tabulation of the original observations, is given in a memorandum prepared by Science Applications, Inc., for the Applied Physics Laboratory of Johns Hopkins University, dated February 20, 1980.

INSTRUMENTATION AND ACCURACY

Wind speed and direction were obtained from the ship anemometer, which was located on a spar about 26.5 m above the sea surface. The air temperatures were measured at about 12.5 m above the sea surface with a hand-held psychrometer. The sea-level pressure was measured at the same level. Cloud cover descriptions and wave and swell height and direction were estimated visually. Rainfall was measured with a bucket rain gauge.

The boundary layer of the marine atmosphere is turbulent with velocity variations of the same order as the mean wind speed. The instantaneous wind speeds reported here may be poor approximations to hour-long means, which are strictly required for the estimation of air-sea fluxes from bulk formulas. In addition, significant large scale changes in the wind field can occur over three-hour periods, and these were not adequately resolved with the sampling strategy employed aboard the KANE.

There are three main sources of measurement error in shipboard wind observations. First, the anemometer is probably not more accurate than ± 0.5 ms^{-1}, or perhaps 10% of the actual wind speed. Second, the actual wind speed (that is, with respect to the earth's surface) must be determined from the shipboard observation by a vector subtraction of ship velocity. Since the uncertainty in ship speed is also probably about ± 0.5 ms^{-1}, the combined measurement error in wind speed can easily be 1 ms^{-1}. A third source of error arises from the distortion of the air flow by the ship. There is little information available to estimate this effect. Simple potential fluid flow theory suggests that wind speeds enhanced by as much as 50% could occur at KANE anemometer level with the ship broadside to the wind.

The thermometers in hand-held psychrometers typically have an accuracy of ±0.2°C. A ship is a source of heat and that may give rise to a temperature overestimate. Under strong insolation, the ship structure can become quite warm which, under light wind conditions, may produce an overestimate of air temperature.

Bucket sea-surface temperature (not surface skin temperatures) are probably accurate to ±0.2°C. On a nearly stationary ship it is possible to sample water which has been significantly warmed by the ship. This is not likely to be a problem while a ship is underway.

The sea-level pressure was measured with an aneroid barometer which has an accuracy of ±1 mb or better.

9.3 LARGE SCALE METEOROLOGY

Large scale surface weather charts centered about the experiment site are shown in Figure 9.1. The three hurricanes (David, Frederick, Gloria) are certainly the most dramatic large scale features. Only David passed close enough to the site to affect even slightly the surface weather. A cold front passed across the site on 10 September.

9.4 SHIPBOARD OBSERVATIONS

Shipboard observations began at 1200Z on 2 September. Figure 9.2 displays the observations. The conversion from so-called "Julian" dates to conventional calendar dates is presented below.

Julian Day	Calendar Day
245	2 September
246	3 September
247	4 September
248	5 September
249	6 September
250	7 September
251	8 September
252	9 September
253	10 September
254	11 September
255	12 September
256	13 September

The first two days (245 and 246) of the experiment were characterized by moderate winds of 6-10 ms^{-1} from the southeast, overcast, and a very slowly rising barometric pressure. Wind speeds began to decrease on Day 247 and reached a minimum on day 250, when the winds were coming from the south with a day-averaged speed of only 2 ms^{-1}. Cloud cover from Day 247 to 252 was light. Barometric pressure fell from a high of 1020 mb on Day 248 to an experiment low of 1012 mb on Day 251, after which it gradually increased. The sea and air temperatures on Days 247 through 251 exhibited a rather clear diurnal cycle. Wind speed increased during Day 251 (following the minimum on Day 250) and peak wind speeds of 8 ms^{-1} were recorded. There was a sharp drop in wind speed early on Day 252. Surface air temperature, especially dry bulb, began to decrease, the sky became fully overcast, and rain began. The wind changed from southerly to northerly to easterly over a six-hour period. These events correspond with the passage over the site of a cold front shown on the surface chart of 10 September (Day 253).

Rain was recorded throughout Day 253 and also during Day 254, and winds were about 4 ms^{-1}. Three centimeters of rain fell during a three-hour period late in the day. The wind speed increased on Day 255 to a peak of 10 ms^{-1} and became southerly once again.

9.5 AIR-SEA FLUX ESTIMATES

The large (three-hour) time interval between samples and inaccuracies of the samples make the estimation of air-sea fluxes difficult. The 20-25% error associated with the best of such estimates represents a lower error limit for the estimates presented here. To provide an adequate set of surface flux conditions for mixed layer analysis, the observational data have been linearly interpolated to hourly values. Wind stress, heat flux and mass flux estimates are based on these.

Wind stress and sensible and evaporative heat transfer have been calculated at one-hour intervals using bulk formulas. The formulas are as follows:

$$\tau_s = \rho_a C_D U_a |U_a|$$

$$Q_s = \rho_a C_p C_s |U_a| (T_s - T_a),$$

$$Q_e = \rho_a C_e U_a H (q_s - q_a)$$

where

τ_s = surface stress

Q_s = sensible heat loss

Q_e = evaporative heat loss

ρ_a = air density

C_p = specific heat of air

U_a = air velocity

T_s, T_a = sea surface and air temperature

q_s, q_a = saturated specific humidity at sea surface temperature and actual air specific humidity

H = latent heat of evaporation

C_D, C_s, C_e = transfer coefficients

The transfer coefficients have typical values under neutral atmospheric conditions of about 1.3×10^{-3}. To produce flux estimates, we have performed minor corrections to these values for non-neutral conditions following an approach described in Davidson et al. (1978). The air wind speed, temperature and specific humidity are commonly taken to be measured values at about 10 m. The KANE anemometer is located at about 26.5 m above the sea surface, and a logarithmic wind profile has been used to obtain a 10 m estimate. The specific humidity is computed using the vapor pressure obtained from the psychrometric data (List, 1951). The latent heat of evaporation is taken from Kraus (1972) as

$$H = 576.3 - 0.56\ T_S \ (\text{cal gm}^{-1})$$

The short wavelength solar flux is empirically related to the direct and diffuse (scattered) sky irradiances by (Krauss, 1972)

$$R_S = (R_{DIR} + R_{DIF})\ (1 - 0.71n)\ (1 - r(\alpha))$$

where n is opaque cloud cover in tenths and r (α) is the surface reflectance factor based on the sun's altitude, α. The reflectance has been treated following Deacon and Stevenson (1968) as reported by Kraus (1972). The solar altitude is, in turn, dependent on declination and hour angle of the sun and latitude of the station.

The amount of direct solar radiation is approximated by

$$R_{DIR} = R_o\ a^{\csc(\alpha)} \sin(\alpha),$$

and the amount of diffuse sky radiation is approximated by

$$R_{DIF} = 0.5\ R_o \sin(\alpha)\ (0.9 - a^{\csc(\alpha)}).$$

In these expressions, R_o is the solar radiation reaching the outer atmosphere per unit area per unit time and a is an average clear sky atmospheric transmission coefficient taken to be 0.85 following Price, et al. (1978).

A pyranometer was operating on board the KANE and its records will be compared with the empirical estimates.

The treatment of the long wavelength flux, R_L, is based on the assumption that the sea surface radiates energy to a good approximation as a classic black body. Thus, this term is approximated by the formula of Budyko (1956):

$$R_L = S\sigma\ (T_a+273.16)^4\ (0.39-0.05\sqrt{e_a})\ \ (1-0.6n^2)$$

where S is the emissivity, σ is the Stefan-Boltzman constant, and e_a is the atmospheric water vapor pressure in millibars.

Figures 9.3a-b display estimated wind stress and surface heat flux*. While peak winds were slightly higher during the last two days of the experiment than during the first two days, these estimates suggest that substantially more momentum was transferred to the water during the earlier period. During the low-wind mid-portion of the experiment, evaporative heat loss and infrared radiation loss were nearly equal. During the windier periods at the beginning and end of the experiment, evaporative heat loss dominated the surface heat flux. Figure 9.3c shows the flux of solar radiation into the ocean. The solar flux is here computed hourly using interpolated cloud cover estimates. The effect of the cloud cover during the latter half of the experiment on the solar heat flux is obvious. Figure 9.3d displays the surface heat flux $Q_s + Q_e + R_L$ and the total heat flux $Q_s + Q_e + R_L + R_s$ (computed at three-hour intervals).

*"Surface heat flux" here refers to heat exchange across an infinitesimal surface layer. We consider solar radiation separately, since it is absorbed over a relatively thick O(1m) surface layer. Also since its magnitude is far greater, it is more conveniently displayed on a different scale.

Finally, Figure 9.3c displays mass flux due to evaporation and rain. The rain fluxes are defined as the difference between rain gauge volumes over three-hour periods divided by the three-hour time interval.

Daily heat flux totals have been obtained from the flux estimates presented in the previous section. Heat fluxes from Days 245 and 256 represent only portions of those days.

Day	Heat Gain (cal cm^{-2})
245	50
246	-146
247	232
248	336
249	336
250	340
251	267
252	- 82
253	- 82
254	- 51
255	-205
256	-264

9.6 REFERENCES

Budyko, M. E. (1956). The Heat Balance of the Earth's Surface. Clearinghouse for Federal Scientific and Technical Information, Document P13 131 692.

Davidson, K. L., T. M. Houlihan, C. W. Fairall, and G. E. Schacher (1978). Observations of the Temperature Structure Function Parameter, C_T, Over the Ocean. Naval Postgraduate School Rep. NPS 63-78-005.

Deacon, E. L. and J. Stevenson (1968). Radiation and Associated Observations Made on Indian Ocean Cruises. Tech. Pap. Div. Metrol. CSIRO, Australia.

Kraus, E. B. (1972). Atmosphere-Ocean Interaction. Clarendon Press, Oxford.

List, R. J. (1951). Smithsonian Meteorological Tables, 6th ed. Smithsonian Institution, Washington, D.C.

Price, J. F., C.N.K. Mooers and J. C. Van Leer (1978). Observations and Simulation of Storm-Induced Mixed-Layer Deepening. J. Phys. Oceanogr. 8, p.582-599.

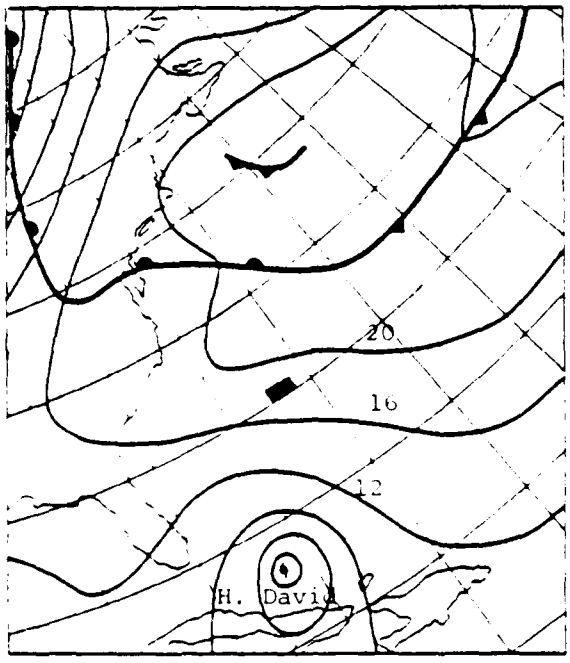

2 Sept.

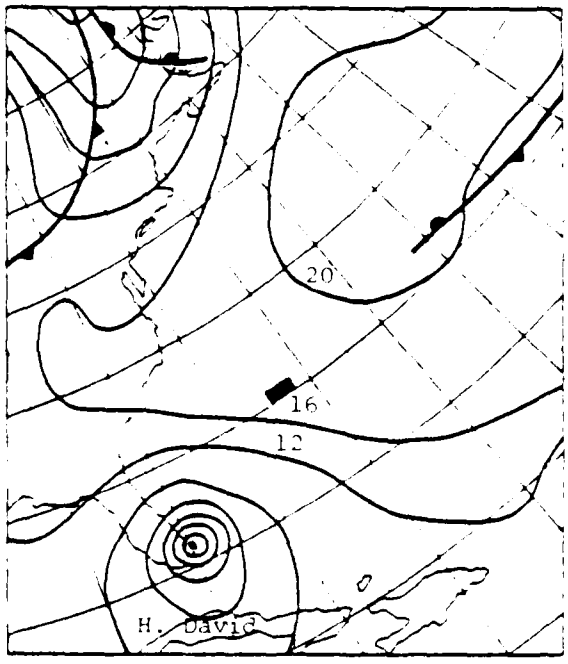

3 Sept.

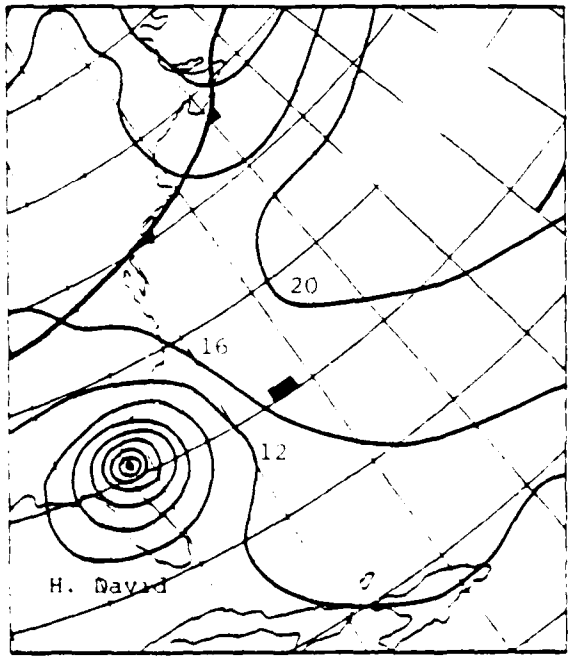

4 Sept.

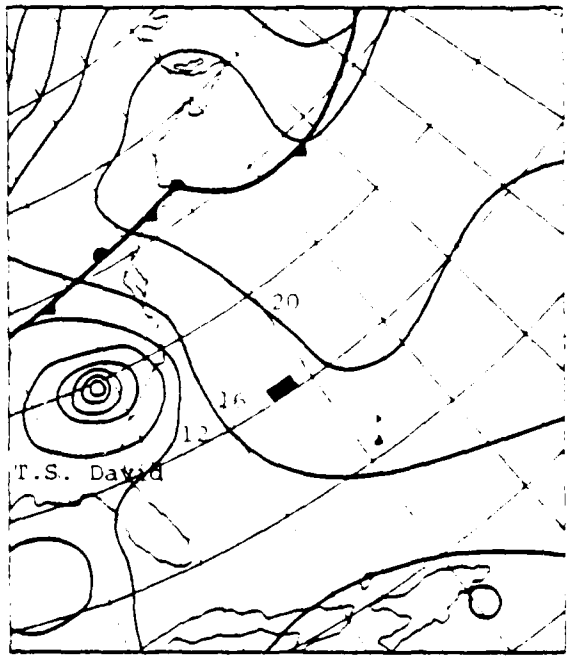

5 Sept.

Figure 9.1. Surface weather charts at 1200Z from 2 to 13 September 1979. The shaded region is the experiment site.

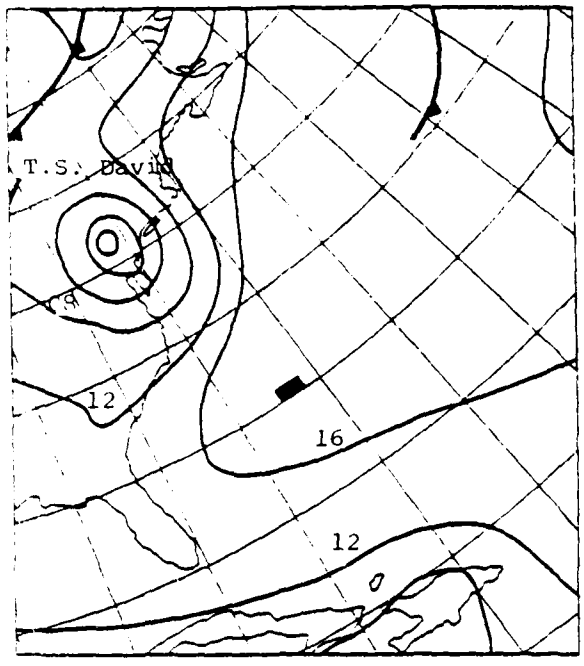

6 Sept.

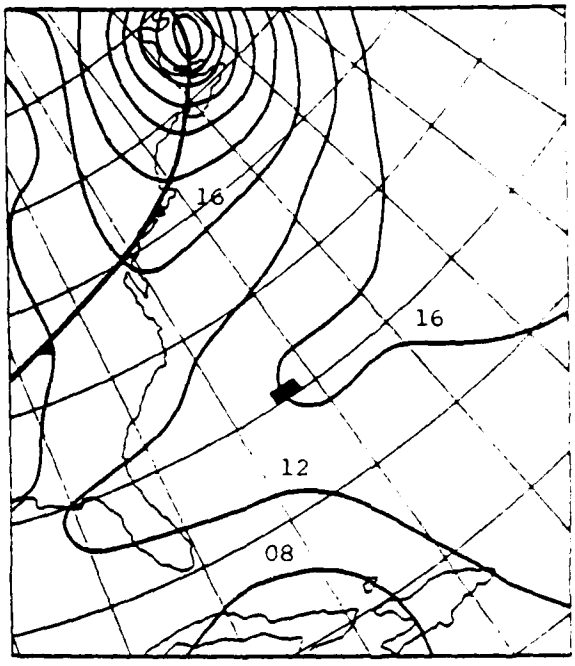

7 Sept.

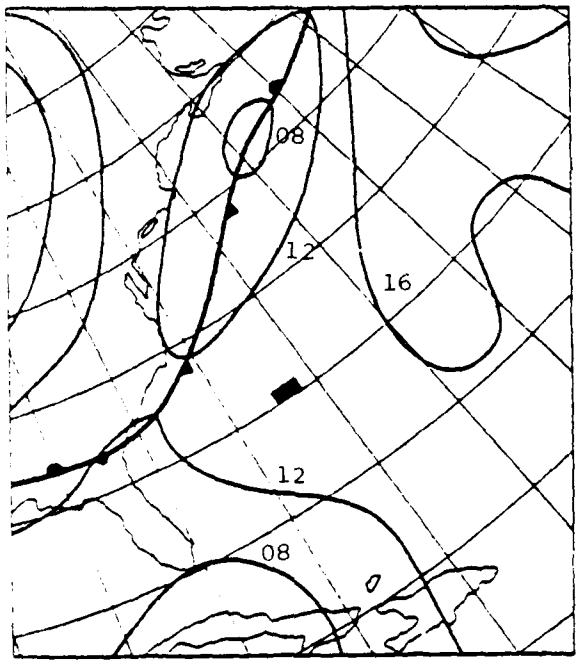

8 Sept.

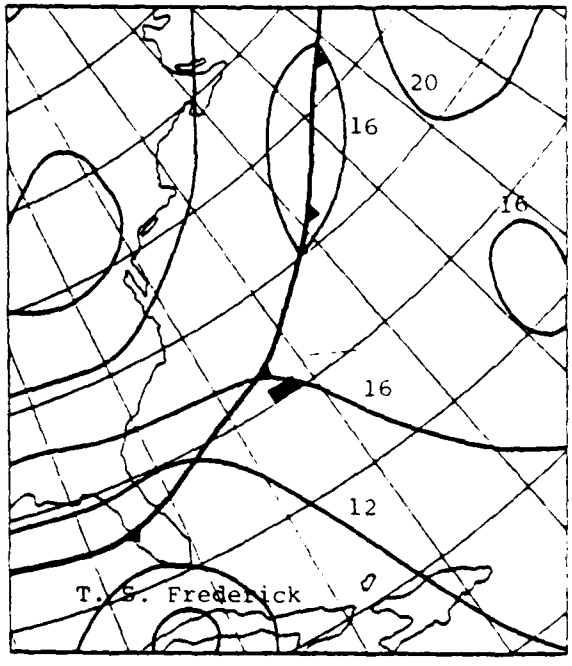

9 Sept.

Figure 9.1. (continued)

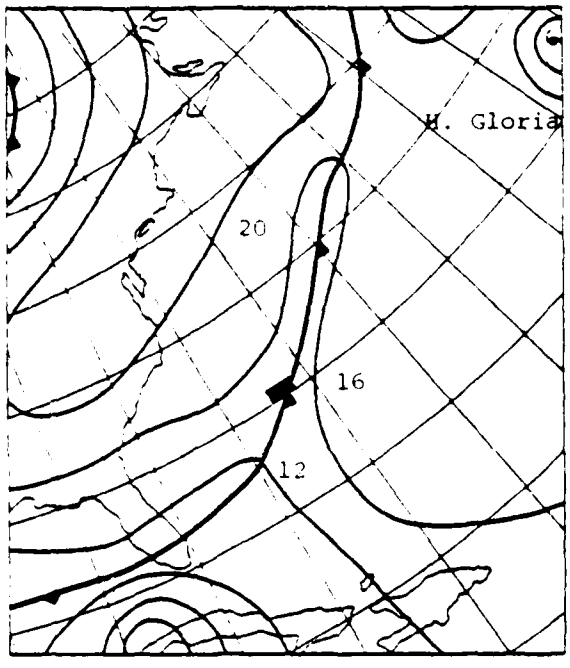

10 Sept.

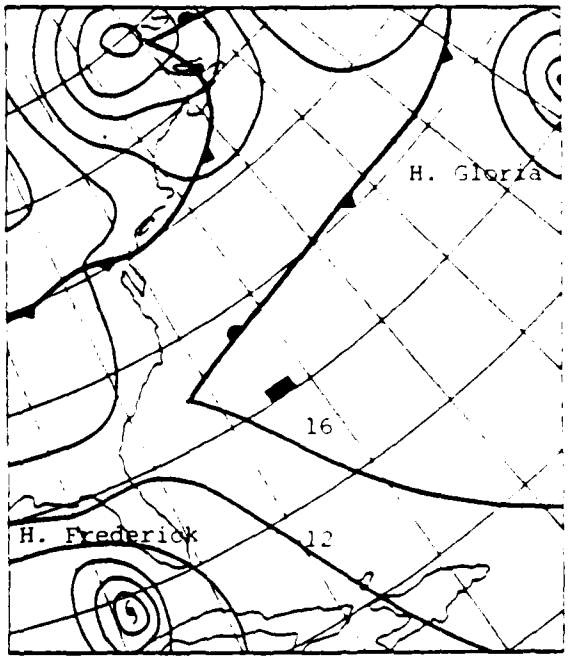

11 Sept.

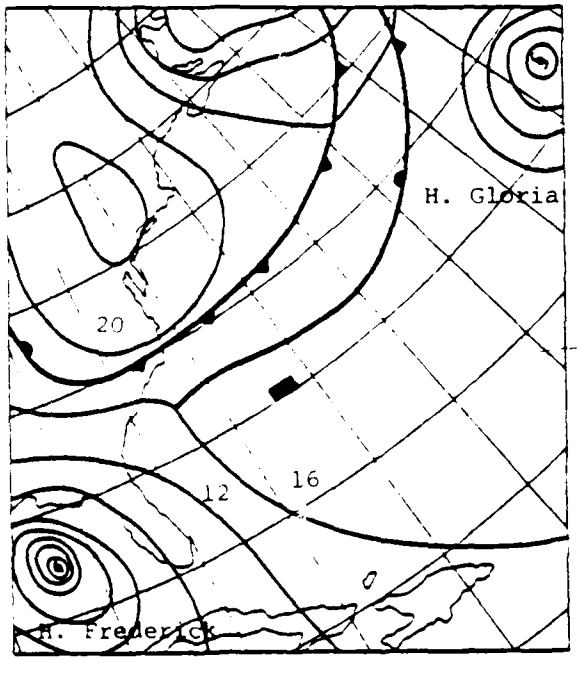

12 Sept.

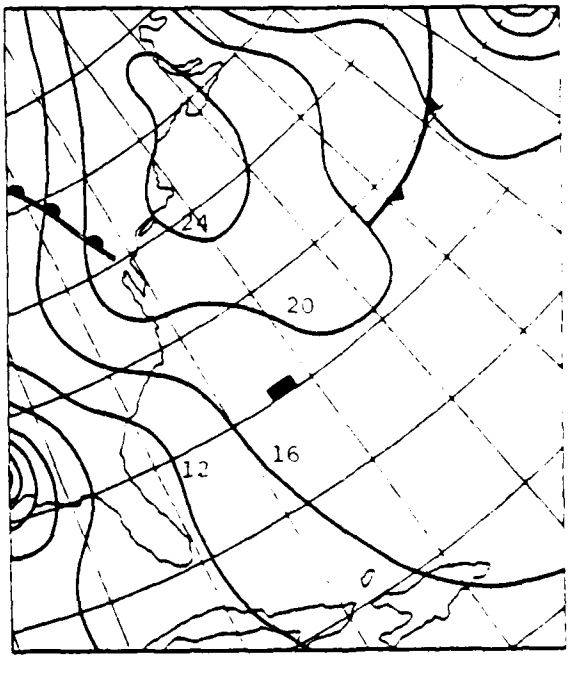

13 Sept.

Figure 9.1. (continued)

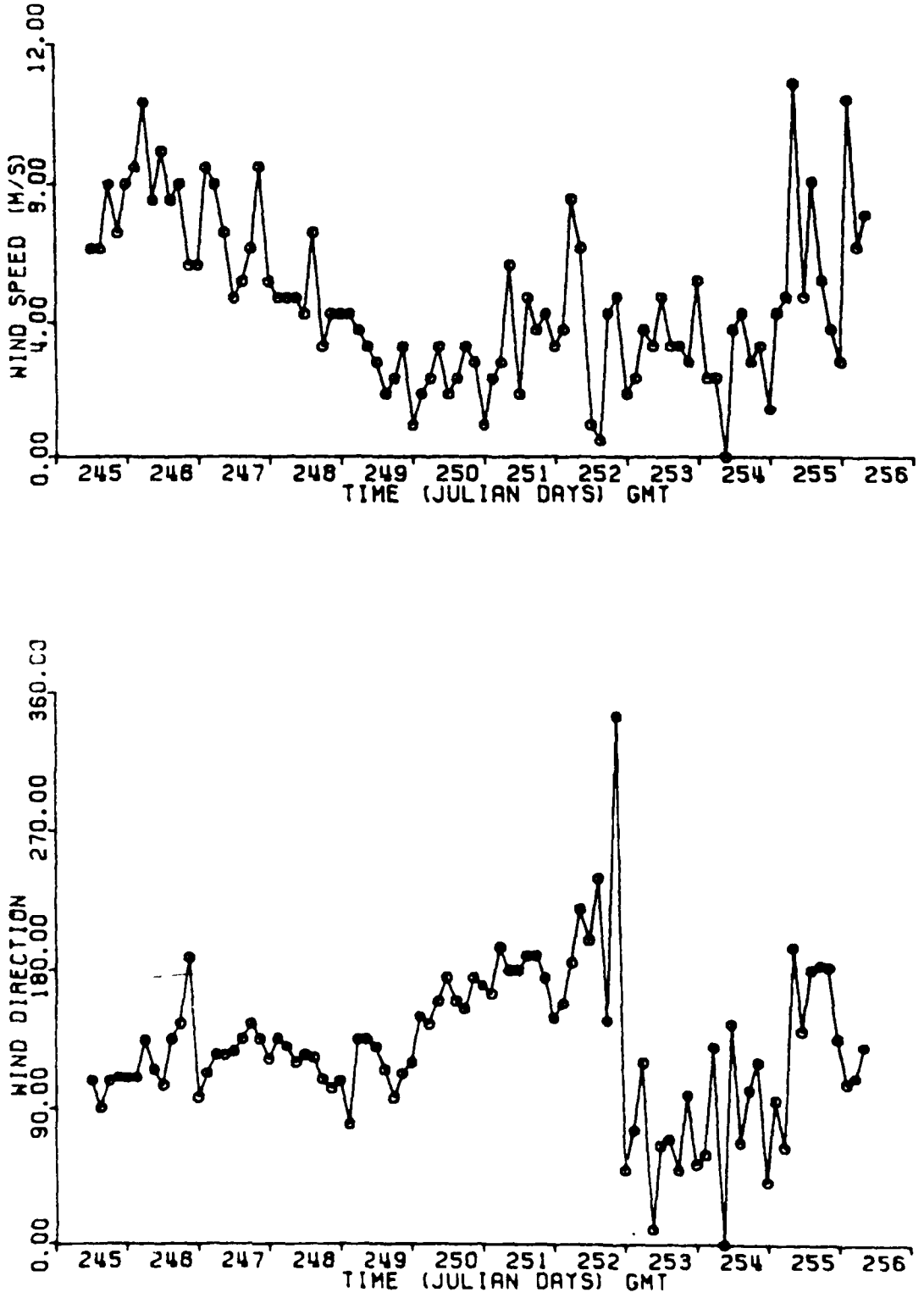

Figure 9.2. Time series of observations from the USNS KANE. Wind speed (a) and direction (b).

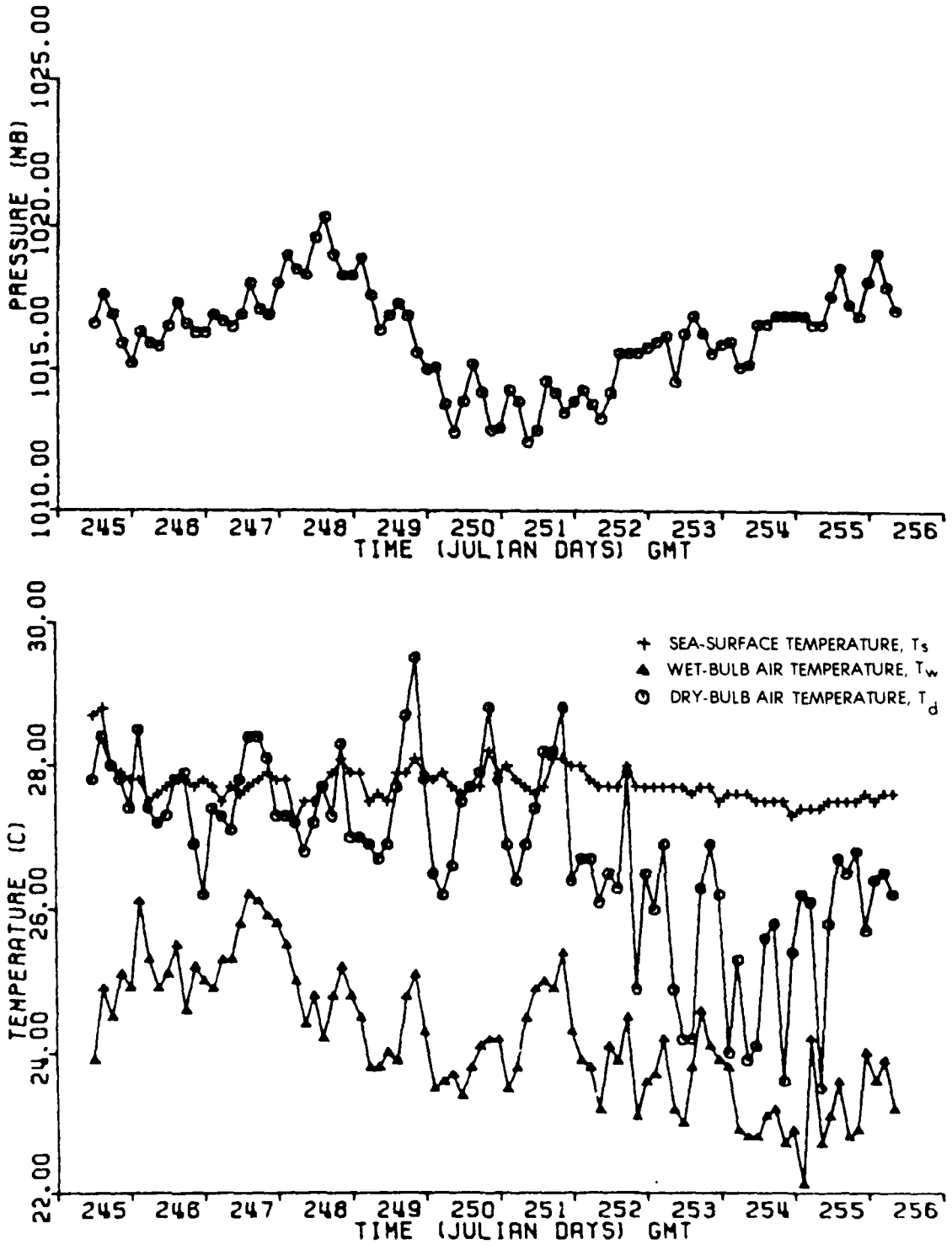

Figure 9.2. (continued) Sea-level pressure (c) and sea-surface, wet-bulb and dry-bulb temperature (d).

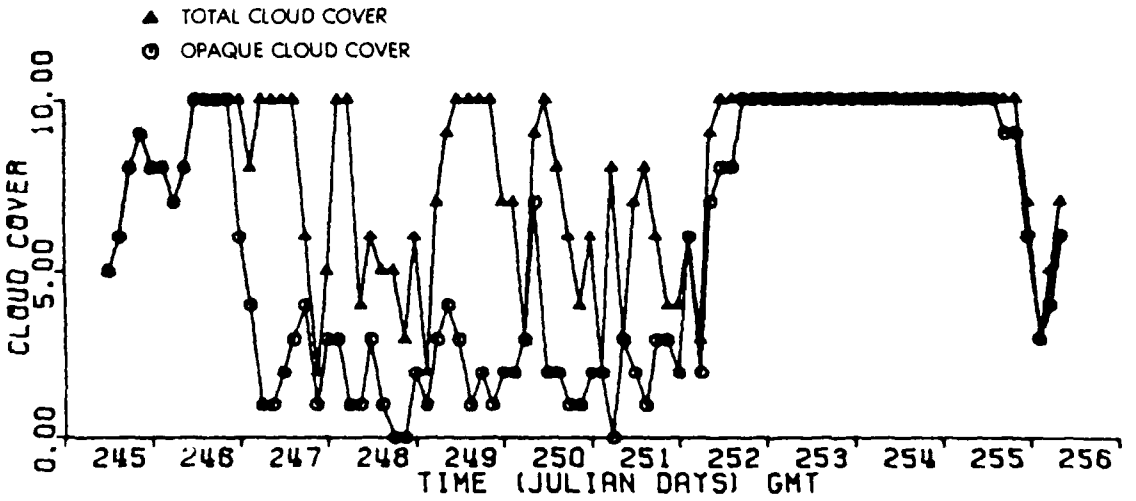

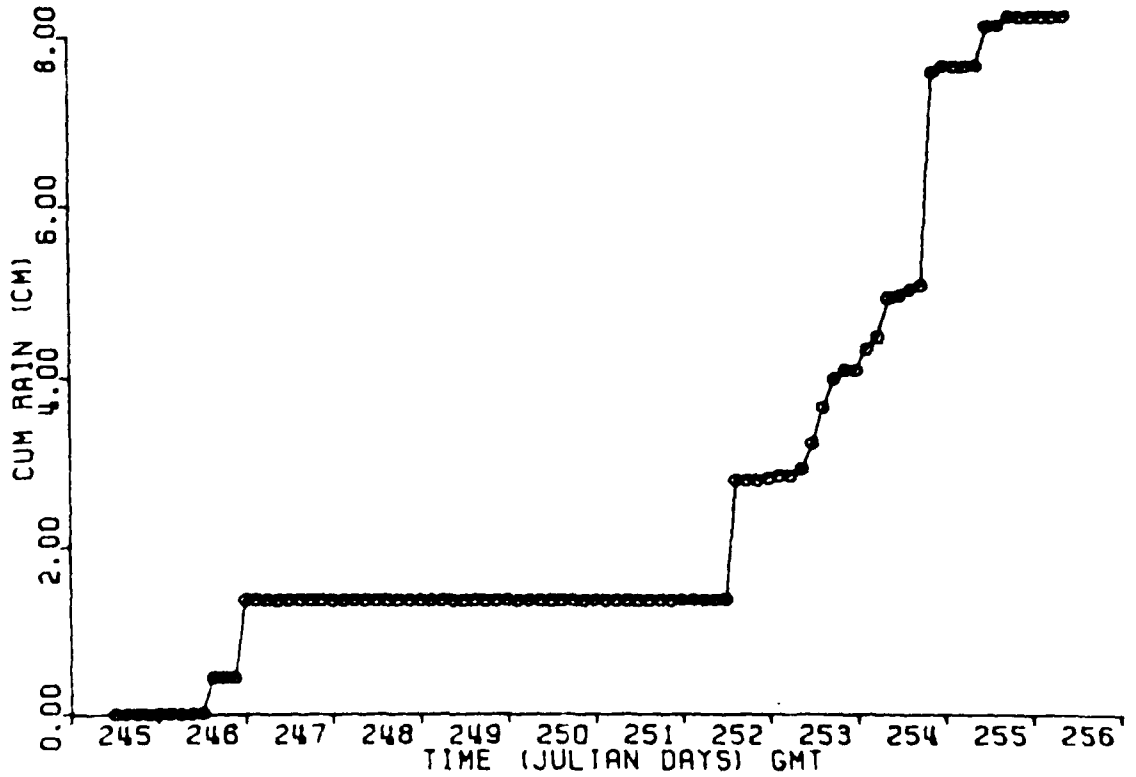

Figure 9.2. (continued) Total and opaque cloud cover (e) and cumulative rainfall (f).

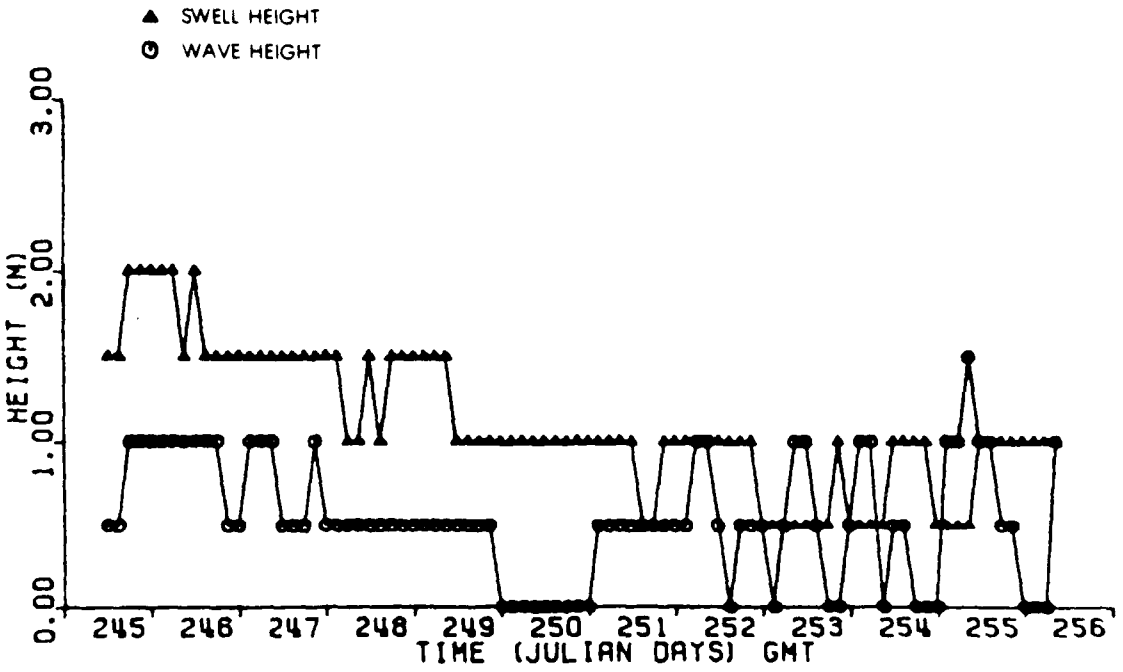

Figure 9.2. (continued) Wave and swell height (g).

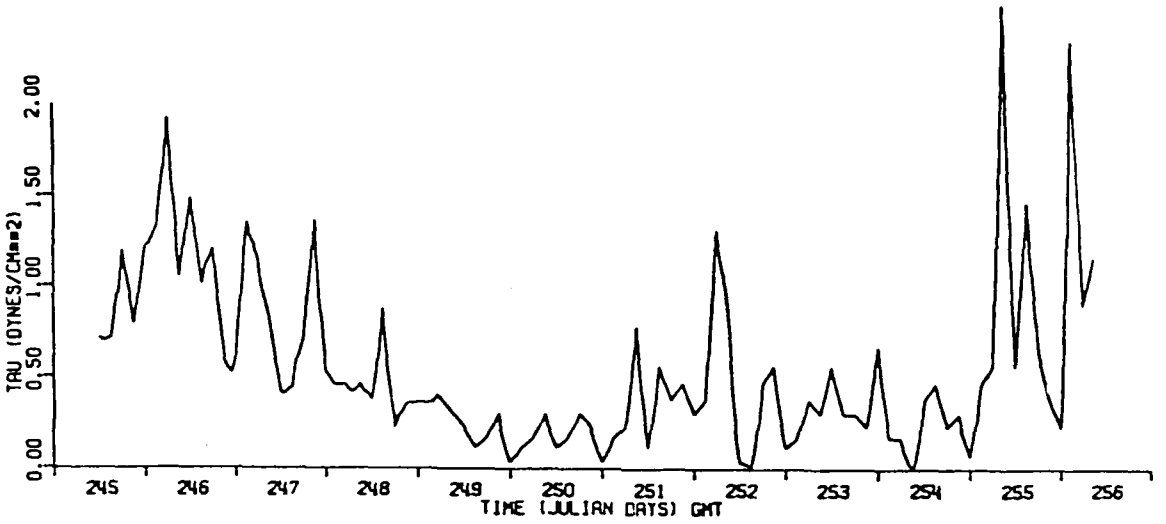

(a)

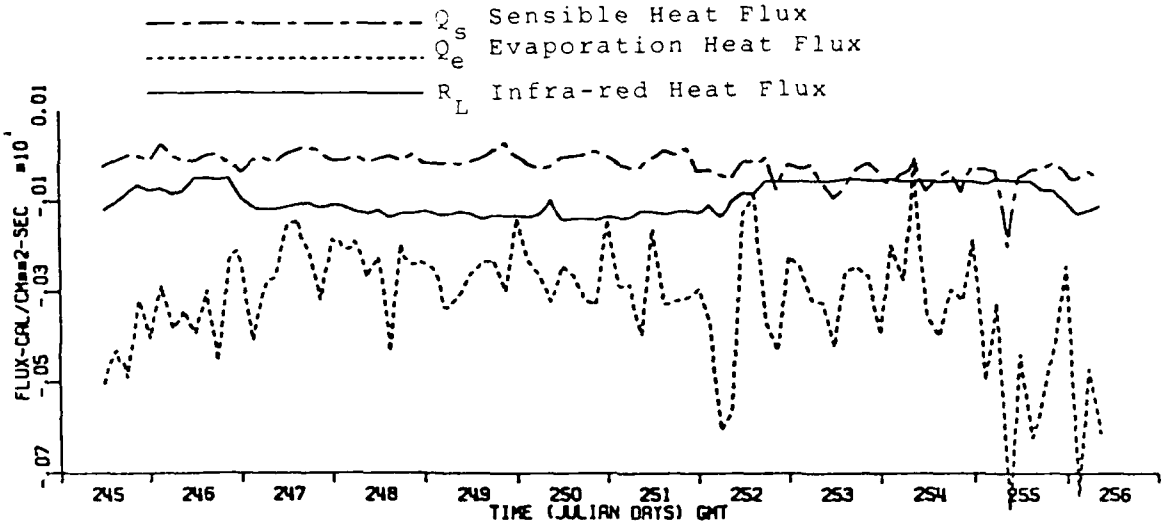

(b)

Figure 9.3. Surface fluxes. Wind stress (a) and sensible, evaporation and infra-red heat fluxes (b).

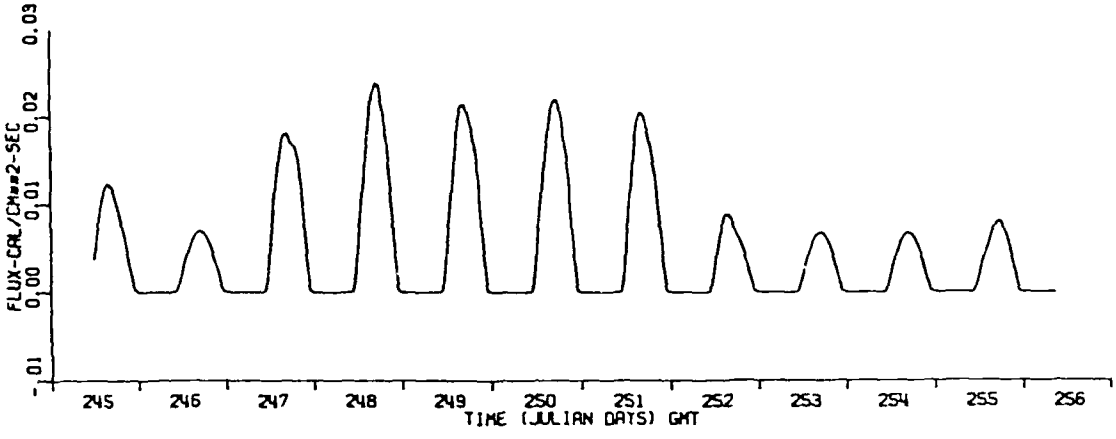

(c)

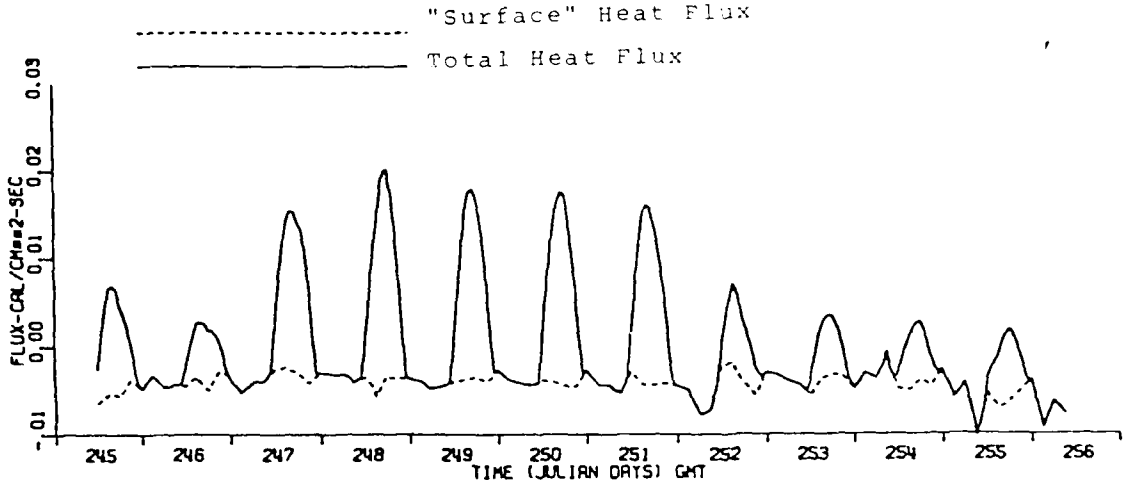

(d)

Figure 9.3. (continued) Solar heat flux (c) and surface and total heat fluxes (d). The surface flux is defined as $Q_S + Q_e + R_L$ and the total flux as the surface plus short wave (F_S) fluxes.

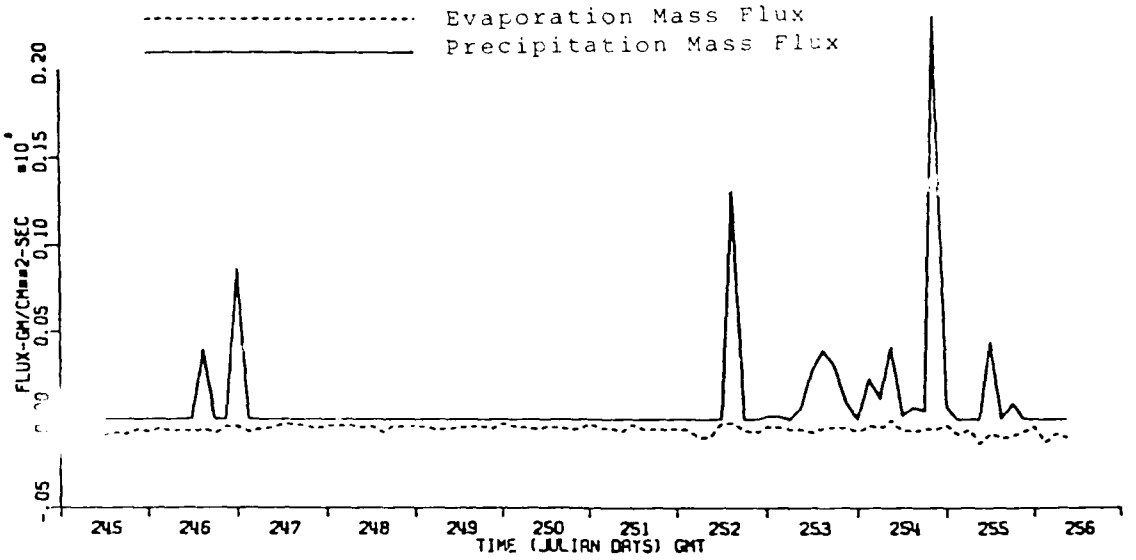

(e)

Figure 9.3. (continued) Evaporation and precipitation mass fluxes (e).

UNCLASSIFIED

SECURITY CLASSIFICATION OF THIS PAGE (When Data Entered)

REPORT DOCUMENTATION PAGE	READ INSTRUCTIONS BEFORE COMPLETING FORM
1 REPORT NUMBER: NORDA Technical Note 58 — 2 GOVT ACCESSION NO: AD-A099014	3 RECIPIENT'S CATALOG NUMBER:
4 TITLE (and Subtitle): Oceanic Environmental Background Observations in the Sargasso Sea During September 1979	5 TYPE OF REPORT & PERIOD COVERED: Final Sep 1979
	6 PERFORMING ORG. REPORT NUMBER:
7 AUTHOR(s): Henry Perkins	8 CONTRACT OR GRANT NUMBER(s):
9 PERFORMING ORGANIZATION NAME AND ADDRESS: NORDA, NSTL Station, MS 39529	10 PROGRAM ELEMENT, PROJECT, TASK AREA & WORK UNIT NUMBERS: 63704N
11 CONTROLLING OFFICE NAME AND ADDRESS: NORDA, Code 500	12 REPORT DATE: March 1980
	13 NUMBER OF PAGES:
14 MONITORING AGENCY NAME & ADDRESS (if different from Controlling Office): Distribution Unlimited	15 SECURITY CLASS. (of this report): Unclassified
	15a DECLASSIFICATION/ DOWNGRADING SCHEDULE:
16 DISTRIBUTION STATEMENT (of this Report):	
17 DISTRIBUTION STATEMENT (of the abstract entered in Block 20, if different from Report):	
18 SUPPLEMENTARY NOTES:	
19 KEY WORDS (Continue on reverse side if necessary and identify by block number): Ocean Measurements, Ocean Currents, Ocean Finestructure, Ocean Mixed Layer, Air-Sea Interaction.	

20 ABSTRACT (Continue on reverse side if necessary and identify by block number)

This document presents the results of an experiment, conducted jointly by the Naval Ocean Research and Development Activity (NORDA) and the Naval Oceanographic Office (NAVOCEANO), to measure the environmental background in the upper layers of the Sargasso Sea during late summer. The experiment focuses on physical oceanography and attendant meteorology on scales ranging from tens of meters to tens of kilometers in the horizontal, and on scales of order one meter or more over the upper several hundred meters of the ocean. The measure-

DD FORM 1 JAN 73 1473 EDITION OF 1 NOV 65 IS OBSOLETE
S/N 0102-LF-014-6601

UNCLASSIFIED

SECURITY CLASSIFICATION OF THIS PAGE (When Data Entered)

20. ABSTRACT (Continued from reverse)

ment platforms were the USNS KANE, a Navy P-3 aircraft (two flights) and the Tiros N and GOES satellites. A summary of the types of data collected is given in Table 1.1.

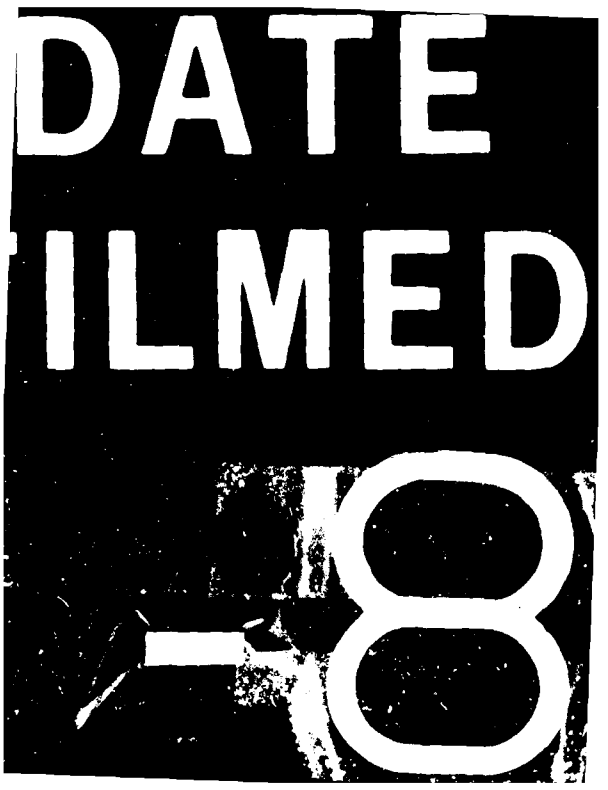
DATE
ILMED
-8